

THE HIGH LUMINOSITY LARGE HADRON COLLIDER

New Machine for Illuminating the Mysteries of the Universe

Second Edition

Editors

Oliver Brüning and Lucio Rossi



**THE HIGH LUMINOSITY
LARGE HADRON COLLIDER**

New Machine for Illuminating the Mysteries of the Universe

Second Edition

ADVANCED SERIES ON DIRECTIONS IN HIGH ENERGY PHYSICS

ISSN: 1793-1339

This is the best review series in high energy physics today. It comprehensively reviews the most important developments in each sector of high energy physics and is of lasting use to all researchers. All volumes are edited by eminent physicists — researchers who have themselves made substantial contributions to their respective fields of research.

Published

- Vol. 31 – *The High Luminosity Large Hadron Collider: New Machine for Illuminating the Mysteries of the Universe Second Edition* (eds. O. Brüning and L. Rossi)
- Vol. 30 – *ATLAS: A 25-Year Insider Story of the LHC Experiment* (by The ATLAS Collaboration)
- Vol. 29 – *Multiple Parton Interactions at the LHC* (eds. Paolo Bartalini and Jonathan Richard Gaunt)
- Vol. 28 – *The State of the Art of Neutrino Physics: A Tutorial for Graduate Students and Young Researchers* (ed. A. Ereditato)
- Vol. 27 – *Technology Meets Research 60 Years of CERN Technology: Selected Highlights* (eds. C. Fabjan, T. Taylor, D. Treille and H. Wenninger)
- Vol. 26 – *The Standard Theory of Particle Physics: Essays to Celebrate CERN's 60th Anniversary* (eds. L. Maiani and L. Rolandi)
- Vol. 25 – *Massive Neutrinos: Flavor Mixing of Leptons and Neutrino Oscillations* (ed. H. Fritzsch)
- Vol. 24 – *The High Luminosity Large Hadron Collider: The New Machine for Illuminating the Mysteries of Universe* (eds. O. Brüning and L. Rossi)
- Vol. 23 – *60 Years of CERN Experiments and Discoveries* (eds. H. Schopper and L. Di Lella)
- Vol. 22 – *Perspectives on String Phenomenology* (eds. B. Acharya, G. L. Kane and P. Kumar)
- Vol. 21 – *Perspectives on Supersymmetry II* (ed. G. L. Kane)
- Vol. 20 – *Lepton Dipole Moments* (eds. B. Lee Roberts and William J. Marciano)
- Vol. 19 – *Linear Collider Physics in the New Millennium* (eds. K. Fujii, D. J. Miller and A. Soni)
- Vol. 18 – *Perspectives on Supersymmetry* (ed. G. L. Kane)
- Vol. 17 – *Perspectives on Higgs Physics II* (ed. G. L. Kane)
- Vol. 16 – *Electroweak Symmetry Breaking and New Physics at the TeV Scale* (eds. T. L. Barklow, S. Dawson, H. E. Haber and J. L. Siegrist)
- Vol. 15 – *Heavy Flavours II* (eds. A. J. Buras and M. Lindner)
- Vol. 14 – *Precision Tests of the Standard Electroweak Model* (ed. P. Langacker)

The complete list of titles in the series can be found at

<http://www.worldscientific.com/series/asdhep>

Advanced Series on
Directions in High Energy Physics — Vol. 31

THE HIGH LUMINOSITY LARGE HADRON COLLIDER

New Machine for Illuminating the Mysteries of the Universe

Second Edition

Editors

Oliver Brüning

CERN, Switzerland

Lucio Rossi

University of Milano, Italy

INFN, Italy

 **World Scientific**

NEW JERSEY • LONDON • SINGAPORE • BEIJING • SHANGHAI • HONG KONG • TAIPEI • CHENNAI • TOKYO

Published by

World Scientific Publishing Co. Pte. Ltd.

5 Toh Tuck Link, Singapore 596224

USA office: 27 Warren Street, Suite 401-402, Hackensack, NJ 07601

UK office: 57 Shelton Street, Covent Garden, London WC2H 9HE

Library of Congress Control Number: 2024930795

British Library Cataloguing-in-Publication Data

A catalogue record for this book is available from the British Library.

**Advanced Series on Directions in High Energy Physics — Vol. 31
THE HIGH LUMINOSITY LARGE HADRON COLLIDER
New Machine for Illuminating the Mysteries of the Universe
Second Edition**

Copyright © 2024 by The Editors.

All rights reserved.

This is an Open Access book published by World Scientific Publishing Company. It is distributed under the terms of the [Creative Commons Attribution 4.0 International \(CC BY 4.0\) License](https://creativecommons.org/licenses/by/4.0/) which permits use, distribution and reproduction in any medium, even commercially, provided that the original work is properly cited.

ISBN 978-981-12-7894-5 (hardcover)

ISBN 978-981-12-7895-2 (ebook for institutions)

ISBN 978-981-12-7896-9 (ebook for individuals)

For any available supplementary material, please visit

<https://www.worldscientific.com/worldscibooks/10.1142/13487#t=suppl>

Desk Editor: Carmen Teo Bin Jie

Printed in Singapore

Foreword

The feasibility study for a proton–proton collider in the Large Electron-Positron Collider (LEP) tunnel started at the end of 1982. The project was approved by the CERN Council in December 1994 and the first beam circulated on 11th September 2008. The discovery of the Higgs boson was announced on 4th July 2012.

The construction and exploitation of the Large Hadron Collider (LHC) over the last decades has been an incredible journey and is a testament to the professionalism, dedication and resilience of all the many teams involved. A 27 km superconducting machine and its experiments, having performed beyond expectations is a triumph for the worldwide collaborative effort it represents. The direct pay-off is the transformative and wide-ranging wealth of physics results.

Underpinning the superb performance of the accelerator systems is a robust, safe and yet remarkably flexible operational model that has allowed full exploitation of the LHC’s potential. This has paved the way for the diverse physics programme pursued by the LHC experiments, which ranges from heavy ion physics to forward physics, and searches for long lived particles (LLP).

With its ambitious but well targeted performance upgrade, the High Luminosity Large Hadron Collider (HL-LHC) project will pave the way to meaningful exploitation of this remarkable machine for another 15 years or so, and allow the physics community to continue to enjoy vigorous life on the Energy Frontier. Besides the headline aim of increasing the delivered integrated luminosity by a factor of 10, the longevity and operational robustness of the machine in the HL-LHC era have been assured to secure an era of continued high-level productivity.

The increased performance of the machine will necessarily be accompanied by wide-ranging upgrades to the experiments, and already their restless eagerness to exploit the future potential is being made clear with further

iterative upgrades proposed by the main experiments together with a burgeoning number of proposals for LLP searches.

The machine side upgrades described herein are challenging. They see pioneering, and challenging, use of niobium-tin superconducting magnets, innovative use of high temperature superconductors, operational deployment of crab cavities with protons, and many other novel developments in accelerator systems ranging through collimation and absorbers, powering, cryogenics, machine protection, vacuum, beam transfer, beam dump systems and beam instrumentation. All this has required, and at time of writing still requires, time constrained R&D, prototyping, a mix of in house, in-kind and industrial production, exquisite levels of quality control, and rigorous testing. In parallel, a profound understanding of energy deposition and beam physics in a novel and a challenging regime has been established. Beside direct application, many of these cutting-edge technological developments are paving the way for future high energy physics projects, and the HL-LHC might be said to be on both the Energy and Technology Frontiers.

In fact, it is impressive that many of these aspects had to be mastered for the original LHC to deliver what we have enjoyed so far. However, across the board, all systems are now taking it to another level to meet the exacting requirements and demands of the HL-LHC. The process is a truly international effort with wide ranging collaboration from both CERN Member States and Non-Member States.

As for the LHC itself, the HL-LHC is fully dependent on its injectors and a key factor in its increased performance is high intensity, high brightness beams from the injector complex. The LHC Injectors Upgrade (LIU) project drew to a close in 2021 having successfully deployed a swath of measures across the complex designed to deliver the required beams and ensure the long life of an aging complex – the Proton Synchrotron (PS) will be 80 in 2039!

The LHC was a major capital investment. We are privileged to have the opportunity to exploit its potential at an even higher level and to continue to serve a vibrant and committed experimental community in what is a profoundly interesting time for particle physics.

Mike Lamont
CERN Director for Accelerators and Technology

Contents

Foreword by <i>Mike Lamont</i>	v
List of Authors	xi
Chapter 1 The High Luminosity Large Hadron Collider – HL-LHC <i>O. Brüning and L. Rossi</i>	1
Chapter 2 The Physics Landscape of the High Luminosity LHC <i>M. Mangano</i>	55
Chapter 3 Upgrade of the Experimental Detectors for High Luminosity LHC <i>F. Hartmann, B. Hippolyte, F. Lanni, T. Nayak, C. Parkes and P. Rumerio</i>	67
Chapter 4 Operational Experience from LHC Run 1 & 2 and Consolidation in View of Run 3 and the HL-LHC <i>M. Lamont</i>	101
Chapter 5 Machine Physics and Performance <i>G. Arduini, R. De Maria, M. Giovannozzi, G. Iadarola, E. Métral, Y. Papaphilippou and R. Tomás</i>	121
Chapter 6 Superconducting Magnet Technology for the IR Upgrade <i>E. Todesco, G. Ambrosio, P. Ferracin, G. L. Sabbi, T. Nakamoto, M. Sugano, R. Van Weelderen, P. Fabricatore, S. Farinon, F. Toral, M. Sorbi, M. Statera, Q. Xu, J. M. Rifflet and H. Felice</i>	165

Chapter 7	RF Systems	199
	<i>R. Calaga, P. Baudrenghien, G. Burt, O. Capatina, E. Jensen, E. Montesinos and A. Ratti</i>	
Chapter 8	Collimation of HL-LHC Beams	225
	<i>S. Redaelli, A. Bertarelli, R. Bruce, F. Carra, A. Lechner, A. Mereghetti and A. Rossi</i>	
Chapter 9	Circuit Layout, Powering and Protection	255
	<i>F. Rodríguez Mateos, T. D. Catalão Da Rosa, F. Menéndez Cámara, S. Yammine and M. Zerlauth</i>	
Chapter 10	Cold Powering of the Superconducting Circuits	267
	<i>A. Ballarino and P. Cruikshank</i>	
Chapter 11	Warm Powering	281
	<i>M. Martino, J.-P. Burnet and S. Yammine</i>	
Chapter 12	Machine Protection in the High Luminosity LHC	297
	<i>A. Apollonio, P. Bélanger, D. Carrillo, R. Denz, F. Rodríguez Mateos, B. Panev, A. Siemko, J. Uythoven, A. Verweij, D. Wollmann and M. Zerlauth</i>	
Chapter 13	Interface with Experimental Detector in the High Luminosity Run	317
	<i>H. Burkhardt and F. Sánchez Galán</i>	
Chapter 14	Cryogenics for the HL-LHC	341
	<i>S. Claudet, G. Ferlin, E. Monneret, A. Perin, M. Sisti, R. Van Weelden, A. Lees, V. Gahier, K. Brodzinski and L. Delprat</i>	
Chapter 15	Energy Deposition and Radiation to Electronics	355
	<i>F. Cerutti, R. Garcia Alia and A. Tsinganis</i>	

Chapter 16	11T Dipole and New Connection Cryostats for Collimators <i>B. Bordini, L. Bottura, A. Devred, L. Fiscarelli, M. Karppinen, G. de Rijk, L. Rossi, F. Savary, D. Schörling and G. Willering</i>	371
Chapter 17	Vacuum System <i>V. Baglin, P. Chiggiato and C. Garion</i>	391
Chapter 18	Beam Instrumentation and Diagnostics <i>E. Bravin, R. Jones, T. Lefevre and R. Veness</i>	407
Chapter 19	Injection and Beam Dump Systems <i>C. Bracco, M. J. Barnes, W. Bartmann, M. Calviani, D. Carbajo Perez, E. Carlier, L. Ducimetiere, M. I. Frankl, B. Goddard, J. Jowett, A. Lechner, N. Magnin, A. Perillo Marcone, T. Polzin, V. Rizzoglio, V. Senaj, L. Vega, V. Vlachodimitropoulos and C. Wiesner</i>	427
Chapter 20	Controls Technologies <i>J. Serrano, G. Daniluk, E. Gousiou and C. Roderick</i>	445
Chapter 21	Beam from Injectors: The LHC Injectors Upgrade (LIU) Project <i>M. Meddahi, G. Rumolo, R. Alemany, H. Bartosik, G. Bellodi, J. Coupard, H. Damerau, G. P. Di Giovanni, A. Funken, R. Garoby, S. Gilardoni, B. Goddard, K. Hanke, A. Huschauer, V. Kain, A. Lombardi, D. Manghunki, B. Mikulec, F. Pedrosa, S. Prodon, R. Scrivens and E. Shaposhnikova</i>	457
Chapter 22	Integration, (De-) Installation and Alignment <i>P. Fessia and H. Mainaud Durand</i>	475

Chapter 23	The HL-LHC Technical Infrastructure <i>L. Tavian</i>	501
Chapter 24	HL-LHC IT String and Hardware Commissioning <i>M. Bajko and M. Pojer</i>	519
Chapter 25	SRF Cryogenic Test Facility for the HL-LHC <i>L. Tavian, G. Vandoni and W. Venturini Delsolaro</i>	537
Chapter 26	The International Network of Test Infrastructures for the HL-LHC Magnets and Cold Powering System <i>M. Bajko</i>	543
Chapter 27	Beam-beam Long Range Compensation: From Concept to Validation <i>Y. Papaphilippou and G. Sterbini</i>	561
Chapter 28	Non-linear Optics Measurements and Corrections <i>E. H. Maclean, F. Carlier, J. W. Dilly, M. Giovannozzi, N. Karastathis, T. H. B. Persson and R. Tomás</i>	579
Chapter 29	The Role of Noise on Beam Stability and Performance in HL-LHC <i>X. Buffat, S.V. Furuseth, E. Métral, T. Pieloni, C. Tambasco and D. Valuch</i>	593
Chapter 30	Crystal Collimation of Heavy-Ion Beams <i>S. Redaelli, R. Bruce, M. D'Andrea, D. Mirarchi and R. Rossi</i>	603
Chapter 31	High Field Accelerator Magnets for Next Generation Colliders – Motivation, Goals, Challenges and R&D Drivers <i>L. Bottura</i>	615

List of Authors

R. Alemany, CERN, BE Department, Genève 23, CH-1211, Switzerland

G. Ambrosio, FNAL, Batavia, IL 60510, USA

A. Apollonio, Former CERN member

G. Arduini, CERN, BE Department, Genève 23, CH-1211, Switzerland

V. Baglin, CERN, TE Department, Genève 23, CH-1211, Switzerland

M. Bajko, CERN, TE Department, Genève 23, CH-1211, Switzerland

A. Ballarino, CERN, TE Department, Genève 23, CH-1211, Switzerland

M. J. Barnes, CERN, SY Department, Genève 23, CH-1211, Switzerland

W. Bartmann, CERN, SY Department, Genève 23, CH-1211, Switzerland

H. Bartosik, CERN, BE Department, Genève 23, CH-1211, Switzerland

P. Baudrenghien, CERN, SY Department, Genève 23, CH-1211, Switzerland

G. Bellodi, CERN, BE Department, Genève 23, CH-1211, Switzerland

A. Bertarelli, CERN, EN Department, Genève 23, CH-1211, Switzerland

P. Bélanger, CERN, BE Department, Genève 23, CH-1211, Switzerland

L. Bottura, CERN, TE Department, Genève 23, CH-1211, Switzerland

C. Bracco, CERN, SY Department, Genève 23, CH-1211, Switzerland

E. Bravin, CERN, SY Department, Genève 23, CH-1211, Switzerland

K. Brodzinski, CERN, TE Department, Genève 23, CH-1211, Switzerland

R. Bruce, CERN, BE Department, Genève 23, CH-1211, Switzerland

O. Brüning, CERN, ATS-DO Unit, Genève 23, CH-1211, Switzerland

X. Buffat, CERN, BE Department, Genève 23, CH-1211, Switzerland

H. Burkhardt, CERN, EP Department, Genève 23, CH-1211, Switzerland

J.-P. Burnet, CERN, ATS-DO Unit, Genève 23, CH-1211, Switzerland
G. Burt, University of Lancaster, Lancaster LA1 4YW, UK
R. Calaga, CERN, SY Department, Genève 23, CH-1211, Switzerland
M. Calviani, CERN, SY Department, Genève 23, CH-1211, Switzerland
O. Capatina, CERN, EN Department, Genève 23, CH-1211, Switzerland
D. Carbajo Pérez, Former CERN member
D. Carrillo, CERN, TE Department, Genève 23, CH-1211, Switzerland
F. Carlier, CERN, BE Department, Genève 23, CH-1211, Switzerland
E. Carlier, CERN, SY Department, Genève 23, CH-1211, Switzerland
F. Carra, CERN, EN Department, Genève 23, CH-1211, Switzerland
T. D. Catalão Da Rosa, Former CERN member
F. Cerutti, CERN, SY Department, Genève 23, CH-1211, Switzerland
P. Chiggiato, CERN, TE Department, Genève 23, CH-1211, Switzerland
S. Claudet, CERN, TE Department, Genève 23, CH-1211, Switzerland
J. Coupard, CERN, EN Department, Genève 23, CH-1211, Switzerland
P. Cruikshank, CERN, TE Department, Genève 23, CH-1211, Switzerland
H. Damerau, CERN, SY Department, Genève 23, CH-1211, Switzerland
G. Daniluk, CERN, BE Department, Genève 23, CH-1211, Switzerland
M. D'Andrea, CERN, BE Department, Genève 23, CH-1211, Switzerland
R. De Maria, CERN, BE Department, Genève 23, CH-1211, Switzerland
L. Delprat, CERN, TE Department, Genève 23, CH-1211, Switzerland
R. Denz, CERN, TE Department, Genève 23, CH-1211, Switzerland
G. P. Di Giovanni, CERN, BE Department, Genève 23, CH-1211,
Switzerland
J. W. Dilly, CERN, BE Department, Genève 23, CH-1211, Switzerland
L. Ducimetiere, SY CERN, Department, Genève 23, CH-1211, Switzerland
P. Fabbriatore, INFN Genoa, Genova, 16146, Italy

- S. Farinon, INFN Genoa, Genova, 16146, Italy
- S. Fartoukh, CERN, BE Department, Genève 23, CH-1211, Switzerland
- H. Felice, CEA Saclay, 91400, France
- G. Ferlin, CERN, TE Department, Genève 23, CH-1211, Switzerland
- P. Ferracin, LBNL, Berkeley, CA 94720, USA
- P. Fessia, CERN, ATS-DO Unit, Genève 23, CH-1211, Switzerland
- M. I. Frankl, Former CERN member
- A. Funken, CERN, SY Department, Genève 23, CH-1211, Switzerland
- S. V. Furusest, EPFL, Lausanne, CH-1015, Switzerland and CERN, BE Department, Genève 23, CH-1211, Switzerland
- V. Gahier, CERN, TE Department, Genève 23, CH-1211, Switzerland
- R. García Alia, CERN, SY Department, Genève 23, CH-1211, Switzerland
- C. Garion, CERN, TE Department, Genève 23, CH-1211, Switzerland
- R. Garoby, Former CERN member
- S. Gilardoni, CERN, SY Department, Genève 23, CH-1211, Switzerland
- M. Giovannozzi, CERN, BE Department, Genève 23, CH-1211, Switzerland
- B. Goddard, CERN, SY Department, Genève 23, CH-1211, Switzerland
- E. Gousiou, CERN, BE Department, Genève 23, CH-1211, Switzerland
- K. Hanke, CERN, ATS-DO Unit, Genève 23, CH-1211, Switzerland
- F. Hartmann, Karlsruhe Institute of Technology, 76131 Karlsruhe, Germany
- B. Hippolyte, USIAS - Université de Strasbourg, 67081, France and CERN, Switzerland
- A. Huschauer, CERN, BE Department, Genève 23, CH-1211, Switzerland
- G. Iadarola, CERN, BE Department, Genève 23, CH-1211, Switzerland
- E. Jensen, CERN, EP Department, CH-1211 Genève 23, CH-1211, Switzerland
- J. Jowett, CERN, EP Department, Genève 23, CH-1211, Switzerland

V. Kain, CERN, BE Department, Genève 23, CH-1211, Switzerland

N. Karastathis, Former CERN member

R. Jones, CERN, BE Department, Genève 23, CH-1211, Switzerland

M. Lamont, CERN, DG Department, Genève 23, CH-1211, Switzerland

F. Lanni, Brookhaven National Laboratory, Upton, NY 11973 USA

A. Lechner, CERN, SY Department, Genève 23, CH-1211, Switzerland

A. Lees, CERN, TE Department, Genève 23, CH-1211, Switzerland

T. Lefevre, CERN, SY Department, Genève 23, CH-1211, Switzerland

A. Lombardi, CERN, BE Department, Genève 23, CH-1211, Switzerland

E. H. Maclean, CERN, BE Department, Genève 23, CH-1211, Switzerland

N. Magnin, CERN, SY Department, Genève 23, CH-1211, Switzerland

H. Mainaud Durand, CERN, BE Department, Genève 23, CH-1211,
Switzerland

M. Mangano, CERN, TH Department, Genève 23, CH-1211, Switzerland

D. Manglunki, CERN, IR Department, Genève 23, CH-1211, Switzerland

M. Martino, CERN, SY Department, Genève 23, CH-1211, Switzerland

M. Meddahi, CERN, ATS-DO Unit, Genève 23, CH-1211, Switzerland

F. Menéndez Cámara, Former CERN member

A. Mereghetti, Centro Nazionale di Adroterapia Oncologica (CNAO),
Pavia, 27100, Italy

E. Métral, CERN, BE Department, Genève 23, CH-1211, Switzerland

B. Mikulec, CERN, BE Department, Genève 23, CH-1211, Switzerland

D. Mirarchi, CERN, BE Department, Genève 23, CH-1211, Switzerland

E. Monneret, CERN, TE Department, Genève 23, CH-1211, Switzerland

E. Montesinos, CERN, SY Department, Genève 23, CH-1211, Switzerland

T. Nakamoto, KEK, 1-1 Oho, Tsukuba, Ibaraki 305-0801, Japan

- T. Nayak, National Institute of Science Education and Research, Bhubaneswar, Odisha 752050, India and CERN, Switzerland
- B. Panev, CERN, TE Department, Genève 23, CH-1211, Switzerland
- Y. Papaphilippou, CERN, BE Department, Genève 23, CH-1211, Switzerland
- C. Parkes, University of Manchester, Manchester M13 9PL, UK
- F. Pedrosa, CERN, EN Department, Genève 23, CH-1211, Switzerland
- A. Perillo Marcone, CERN, SY Department, Genève 23, CH-1211, Switzerland
- A. Perin, CERN, TE Department, Genève 23, CH-1211, Switzerland
- T. H. B. Persson, CERN, BE Department, Genève 23, CH-1211, Switzerland
- T. Pieloni, EPFL, Lausanne, CH-1015, Switzerland
- M. Pojer, CERN, TE Department, Genève 23, CH-1211, Switzerland
- T. Polzin, Former CERN member
- S. Prodon, CERN, FAP Department, Genève 23, CH-1211, Switzerland
- A. Ratti, SLAC, Palo Alto, California, CA 94025, USA
- S. Redaelli, CERN, BE Department, Genève 23, CH-1211, Switzerland
- J. M. Rifflet, CEA Saclay, 91400, France
- V. Rizzoglio, Former CERN member
- C. Roderick, CERN, BE Department, Genève 23, CH-1211, Switzerland
- F. Rodríguez Mateos, CERN, TE Department, Genève 23, CH-1211, Switzerland
- A. Rossi, SY Department, Genève 23, CH-1211, Switzerland
- L. Rossi, University of Milano and INFN-LASA Milano, Italy
- R. Rossi, CERN, BE Department, Genève 23, CH-1211, Switzerland
- P. Rumerio, University of Alabama, AL 35487, USA and Università di Torino, 10124, Italy
- G. Rumolo, CERN, BE Department, Genève 23, CH-1211, Switzerland

- G. L. Sabbi, SLAC, Palo Alto, California, CA 94025, USA
- F. Sánchez Galán, CERN, BE Department, Genève 23, CH-1211, Switzerland
- R. Scrivens, CERN, BE Department, Genève 23, CH-1211, Switzerland
- V. Senaj, CERN, SY Department, Genève 23, CH-1211, Switzerland
- J. Serrano, CERN, BE Department, Genève 23, CH-1211, Switzerland
- E. Shaposhnikova, CERN, SY Department, Genève 23, CH-1211, Switzerland
- A. Siemko, CERN, TE Department, Genève 23, CH-1211, Switzerland
- M. Sisti, CERN, EP Department, Genève 23, CH-1211, Switzerland
- M. Solfaroli, CERN, BE Department, Genève 23, CH-1211, Switzerland
- M. Sorbi, INFN LASA, Milano, 20054, Italy
- M. Statera, INFN LASA, Milano, 20054, Italy
- G. Sterbini, CERN, BE Department, Genève 23, CH-1211, Switzerland
- M. Sugano, KEK, 1-1 Oho, Tsukuba, Ibaraki 305-0801, Japan
- C. Tambasco, EPFL, Lausanne, CH-1015, Switzerland
- L. Tavian, CERN, ATS-DO Unit, Genève 23, CH-1211, Switzerland
- E. Todesco, CERN, TE Department, Genève 23, CH-1211, Switzerland
- R. Tomás, CERN, BE Department, Genève, 23, CH-1211, Switzerland
- F. Toral, CIEMAT, Madrid, 28040, Spain
- A. Tsinganis, CERN, EP Department, Genève 23, CH-1211, Switzerland
- J. Uythoven, CERN, TE Department, Genève 23, CH-1211, Switzerland
- D. Valuch, CERN, SY Department, Genève 23, CH-1211, Switzerland
- R. Van Weelderden, CERN, TE Department, Genève 23, CH-1211, Switzerland
- G. Vandoni, CERN, ATS-DO Unit, Genève 23, CH-1211, Switzerland
- L. Vega, CERN, SY Department, Genève 23, CH-1211, Switzerland

R. Veness, CERN, SY Department, Genève 23, CH-1211, Switzerland

W. Venturini Delsolaro, CERN, SY Department, Genève 23, CH-1211, Switzerland

A. Verweij, CERN, TE Department, Genève 23, CH-1211, Switzerland

V. Vlachodimitropoulos, Former CERN member

C. Wiesner, CERN, TE Department, Genève 23, CH-1211, Switzerland

D. Wollmann, CERN, TE Department, Genève 23, CH-1211, Switzerland

Q. Xu, IHEP, Beijing, 100039, China

S. Yammine, CERN, TE Department, Genève 23, CH-1211, Switzerland

M. Zerlauth, CERN, ATS-DO Unit, Genève 23, CH-1211, Switzerland

This page intentionally left blank

Chapter 1

The High Luminosity Large Hadron Collider – HL-LHC*

O. Brüning^a and L. Rossi^b

^a*CERN, ATS-DO Unit, Genève 23, Switzerland*

^b*University of Milano and INFN-LASA Milano, Italy*

The Large Hadron Collider (LHC) is one of largest scientific instruments ever built. It has been exploring the new energy frontier since 2010, gathering a global user community of 10,000 scientists. To extend its discovery potential, the LHC requires a major upgrade in the 2020s to increase its luminosity (rate of collisions) by a factor of five beyond its design value, and the integrated luminosity by a factor of ten. Being a highly complex and optimized machine, such an upgrade of the LHC must be carefully studied and requires about 10 years to implement. The novel machine configuration, called High Luminosity LHC (HL-LHC), relies on a number of key innovative technologies, each representing exceptional technological challenges, such as: cutting-edge 11-12 tesla superconducting magnets, very compact superconducting cavities for beam rotation with ultra-precise phase control, new technology for beam collimation and 100-metre-long high-power superconducting links with negligible energy dissipation, very precise 2-Q high current power converter, new surface treatment for e-coupled suppression, and many others. All these constitute major breakthroughs in accelerator technology.

* The Project has been initially partially supported by the EC as *FP7 HiLumi LHC Design Study* under grant no. 284404. The HL-LHC Project is mainly supported by CERN with special in-kind contributions and support by: USA-DOE (HL-LHC-AUP, with FNAL, BNL, LBNL and SLAC laboratories), KEK-Tsukuba (Japan), INFN-LASA-Milano and INFN-Genova (Italy), CIEMAT-Madrid (Spain), STFC-Daresbury (UK, with participation of Huddersfield, Lancaster, Liverpool, Manchester, Oxford, Royal Holloway and Southampton Universities), IHEP-Beijing (CN), BINP-Novosibirsk and PNPI-St Petersburg (Russian Federation) until the end of 2021, Uppsala University (SE), TRIUMF-Vancouver B.C. (CA) and PAEC (Pakistan).

This is an open access article published by World Scientific Publishing Company. It is distributed under the terms of the Creative Commons Attribution 4.0 (CC BY) License.

HL-LHC federates efforts, R&D, and construction of a large community in Europe, the USA, Japan, China and Canada, thereby consolidating CERN and LHC as the center of a world-wide collaboration for basic science and technology.

1. Context and Objectives

The Large Hadron Collider (LHC) was successfully commissioned in March 2010 for proton-proton collisions with a 7 TeV center-of-mass energy. It delivered 8 TeV center-of-mass proton collisions from April 2012 until the end of the LHC Run1 in 2012 and pushed the collision energy to 13 TeV center-of-mass during the Run2 period from 2015 until 2018. The LHC is pushing the limits of human knowledge: the discovery of the Higgs boson in 2012 is undoubtedly a major milestone in the history of science.

Thanks to the LHC, Europe has decisively regained world leadership in high-energy physics, a key sector of knowledge and technology development. The LHC can continue to act as catalyst for a global effort: out of the 12400 CERN users, about 8700 are scientists and engineers using the LHC, half of which are from countries outside the EU.

The LHC will remain the most powerful accelerator in the world until 2025, when it is expected that several key components in the LHC machine and Detectors will reach the end of their radiation lifetime at around 400 fb^{-1} integrated luminosity, and the HL-LHC will assure this position for another decade up to 2040. Its full exploitation is the highest priority of the European Strategy for particle physics, adopted by the CERN Council in 2013 and revised in 2020, and is a reference point for the Particle Physics Strategy of the US and for various other States worldwide. To extend its discovery potential, the LHC needs a major upgrade in the 2020s to extend its operability by another decade or more, and to increase its collision rate and thus integrated luminosity. The upgrade design goal is a five-fold increase in the instantaneous collision rate and a ten-fold increase of the integrated luminosity (the total data volume). As a highly complex and already well-optimized machine, such an upgrade must be carefully devised, and actually calls for breakthroughs in a variety of critical collider technologies. The necessary developments require focused research efforts, extending to over 10 years for studies, prototyping, testing, and construction of new equipment.

HL-LHC federates the efforts and R&D of a large international community towards the ambitious HL-LHC objectives and contributes to establishing CERN as a focal point of global research cooperation and leadership in frontier knowledge and technologies. HL-LHC relies on strong participation from various partners beyond CERN, with important in-kind contributions by Non-Member States laboratories in the USA, Japan, China, and Canada, and by Member States leading Institutions/Universities: INFN (Genova and Milano-LASA Italy), CIEMAT (Madrid, Spain), STFC (UK) and other British Universities and Institutions, Uppsala University (FREIA Laboratory, Uppsala, SE), and several other partner institutes. These participations with in-kind contributions, as well as the participation of other Institutes providing skilled personnel and studies, are key ingredients for the execution of the construction phase. The US LHC Accelerator R&D Program (LARP) has been essential for the development of some of the key technologies for the HL-LHC, such as the large-aperture niobium–tin (Nb_3Sn) quadrupoles and the crab cavities.

The LHC baseline program till 2025 is schematically shown in Figure 1, together with the initial HL-LHC exploitation time. After entering in the near-to-nominal energy regime of 13 TeV center-of-mass energy during Run2 in 2015, LHC has reached the design luminosity[†] of $10^{34} \text{ cm}^{-2} \text{ s}^{-1}$ in 2016 and attained the so-called ultimate luminosity $L_{\text{ult}} = 2 \times 10^{34} \text{ cm}^{-2} \text{ s}^{-1}$ in 2018, where the cryogenic limit in the inner quadrupole triplet magnets was reached. In terms of integrated luminosity, about 65 fb^{-1} were collected during the 2018 operation year, bringing the total integrated luminosity of LHC to nearly 190 fb^{-1} . The most sensible projection is to reach about 350 fb^{-1} (and maybe even 400, in case of very smooth operation) by end of Run3 in 2025 which exceeds the LHC design luminosity of 300 fb^{-1} and is assumed to come close to the expected equipment lifetime due to the implied radiation for several key elements in the LHC machine and the main detectors.

In addition to the consideration of radiation damage to the machine and detectors, as indicated in Figure 1, that would require serious long interventions, after 2025 the statistical gain in running the accelerator without an additional considerable luminosity increase beyond its design value will become marginal. The running time necessary to halve the statistical error in the measurements will be more than ten years after 2025. Therefore, to

[†] Luminosity is the number of collisions per square centimetre and per second, $\text{cm}^{-2} \text{ s}^{-1}$.

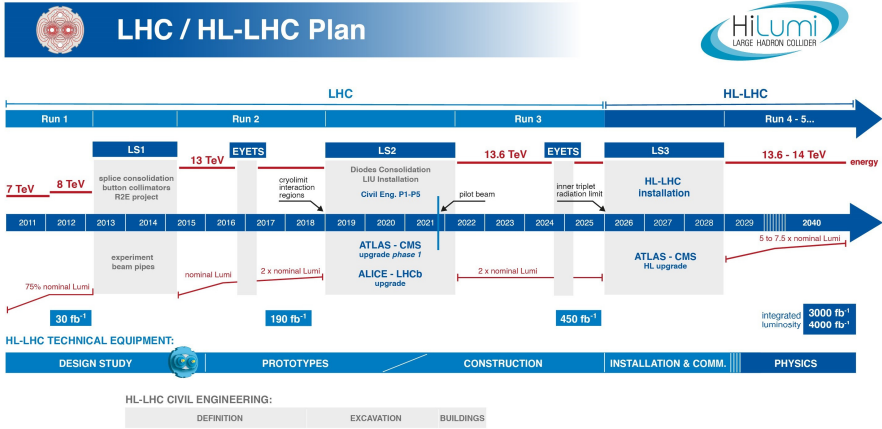


Fig. 1. LHC/HL-LHC baseline plan for the next decade and beyond. In terms of energy of the collisions (upper line) and of luminosity (lower lines). The first long shutdown (LS1) 2013-14 is to allow design parameters of beam energy and luminosity. The second one, LS2 in 2019-2021, is for secure luminosity and reliability as well as to upgrade the LHC Injectors. After LS3, in 2029 the machine will be in the High Luminosity configuration (HL-LHC) and operates till nearly 2040.

maintain scientific progress and to explore its full capacity, the LHC will need to have a decisive increase of its luminosity. Somehow the necessity of an important luminosity upgrade was already inscribed in the LHC design, well before its operation. That is why, when the CERN Council adopted the European Strategy for Particle Physics in 2006 [1], it was agreed the first priority was “to fully exploit the physics potential of the LHC. A subsequent major luminosity upgrade, motivated by physics results and operation experience, will be enabled by focused R&D”. The European Strategy for Particle Physics has been integrated into the ESFRI Roadmap of 2006 and its update of 2008 [2]. The priority to fully exploit the potential of the LHC was confirmed as *first priority* among the “High priority large-scale scientific activities” in the European Strategy for Particle Physics update in 2013 [3] and underlined by the CERN Council in June 2016, when it approved the HL-LHC as an official Upgrade Project at CERN. The European Strategy for Particle Physics update in 2020 reiterated the high priority of the HL-LHC with the following words: “The successful completion of the high-luminosity upgrade of the machine and detectors should remain the focal point of European particle physics, together with continued innovation in experimental techniques.”

The importance of the LHC upgrade in luminosity for the future of High Energy Physics was also affirmed in the 2014 Snowmass process (the USA process of the strategy of particle physics). In the May 2014 resolution of the so-called P5 panel in the USA [4], a critical step was taken in updating the USA strategy for HEP, with the following wording: “*Recommendation 10: ... The LHC upgrades constitute our highest-priority near-term large project.*”

In this context, at the end of 2010 CERN put in place the High Luminosity LHC (HL-LHC) project [5,6]. Started as a Design Study, HL-LHC has become CERN’s major construction project for the next decade after the approval by CERN Council on 30 May 2013 and the insertion of the budget in the CERN Medium Term Plan, approved by the Council in June 2014. Then, in 2015, the Council approved the HL-LHC budget for the period 2016-2021 (MTP2015) and positively acknowledged the remaining HL-LHC budget for the years 2022-2026 in the so-called long term plan information included in the MTP document, for a total of 950 MCHF of material budget. Eventually, the CERN Council approved the entire HL-LHC project, with a total material budget of 950 MCHF for 2015-2026, in the session of June 2016 [7], as one of the first key decisions of Fabiola Gianotti’s directorate. Significantly, the High Luminosity LHC is the first project with explicit approval as a stand-alone project by the Council after the LHC.

The main objective of High Luminosity LHC, as established in the HiLumi LHC submission to EC in the Seventh Framework Programme (FP7-INFRA) of November 2010 [8] is to determine a set of beam parameters and the hardware configuration that will enable the LHC to reach the following targets:

- (1) A peak luminosity of $5 \times 10^{34} \text{ cm}^{-2}\text{s}^{-1}$ with levelling, allowing:
- (2) An integrated luminosity of 250 fb^{-1} per year, enabling the goal of 3000 fb^{-1} in about a dozen years after the upgrade. This luminosity is about ten times the luminosity reach of the first twelve years of the LHC lifetime.

The time horizon foresees the installation of the main hardware for HL-LHC during LS3 (2026-2028) and commissioning the new machine configuration in 2029.

All hadron colliders in the world prior to the LHC have so far produced a total combined integrated luminosity of about 11 fb^{-1} . As reported above, LHC has delivered so far nearly 190 fb^{-1} and should reach and exceed 350 fb^{-1} by 2026. The High Luminosity LHC is a major and extremely challenging upgrade. For its successful realization, several key novel technologies have to

be developed, validated, and integrated. The work initiated with the FP7 Design Study HiLumi LHC which, approved by EC in 2011 with the highest mark [9], was instrumental in initiating a new global collaboration for the LHC that matches the spirit of the worldwide user community of the LHC experiments.

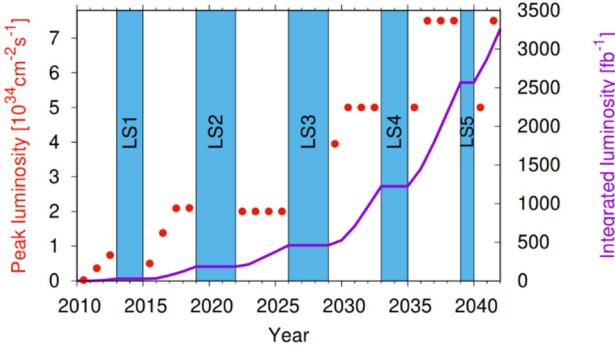


Fig. 2. Luminosity evolution for LHC, extrapolated until end of Run3 and projected for the HL-LHC both in terms of peak and integrated luminosity.

The High Luminosity LHC project is working in close connection with the companion ATLAS and CMS upgrade projects of 2019-2028 and the upgrade of LS2 for both LHCb and ALICE, as discussed in [10]. Furthermore, the performance of the high luminosity machine critically depends on the performance of the injector chain as well, whose main upgrade finished in 2020 under the companion program, the LHC Injector Upgrade (LIU) [11] and the complex has been commissioned in the 2021 and 2022 machine running periods.

2. Approach for the Upgrade

The (instantaneous) luminosity L can be expressed as:

$$L = \gamma \frac{n_b N^2 f_{rev}}{4\pi\beta^* \varepsilon_n} R; \quad R = 1 / \sqrt{1 + \frac{\theta_c \sigma_z}{2\sigma}}$$

γ is the proton beam energy in unit of rest mass

n_b is the number of bunches in the machine: 1380 for 50 ns spacing and 2760 for 25 ns

N is the bunch population. $N_{\text{nominal 25 ns}}: 1.15 \times 10^{11}$ p (\Rightarrow 0.57 A of beam current at 2760 bunches)

f_{rev} is the revolution frequency (11.2 kHz)

β^* is the beam beta function (focal length) at the collision point (nominal LHC design 0.55 m)

ε_n is the transverse normalized emittance (nominal LHC design: $3.75 \mu\text{m}$)

R is a luminosity geometrical reduction factor (0.85 at 0.55 m of β^* , down to 0.5 at 0.25 m)

θ_c is the full crossing angle between colliding beam ($285 \mu\text{rad}$ as nominal LHC design)

σ_x, σ_z are the transverse and longitudinal r.m.s. size, respectively ($16.7 \mu\text{m}$ and 7.6 cm).

2.1. Present luminosity limitations and hardware constraints

There are various limitations to a continuous increase in luminosity, either in beam characteristics (injector chain, beam impedance and beam-beam interactions in the LHC) or in technical systems. Mitigation of potential performance limitations arising from the LHC injector complex are addressed by the LIU project, which has been completed and fully commissioned during the Run3 period. Any potential limitations coming from the LHC injector complex put aside, it was expected that LHC would have reached performance bottlenecked by the beam current and cleaning efficiency at 350 MJ stored beam energy and from the acceptable pile-up level. LHC was supposed to reach the maximum luminosity level of $L = 2 \times 10^{34} \text{ cm}^{-2}\text{s}^{-1}$ only with the ultimate value of bunch population (1.7×10^{11} p/bunch). This maximum luminosity value (sometimes called ultimate luminosity for the LHC) was established in the LHC design as the maximum compatible with the heat deposited in the Inner Triplet (IT) quadrupoles by the collision debris escaping along the beam pipe. Beyond this peak luminosity value, the heat can no longer be removed sufficiently fast from the magnets. This value has actually been reached already in Run2 with a bunch population approximately at nominal value, $1.1\text{--}1.2 \times 10^{11}$ but with smaller than nominal optical beta functions at the IP and smaller than nominal beam emittances. The reason this was possible was because the magnet aperture is

better than anticipated and that the beam emittance delivered by the injectors in LS2 exceeded any expectations: $2.2 \mu\text{m}$ instead of $3.5 \mu\text{m}$ for LHC nominal design intensities thanks to the novel Batch Compression Merging Scheme (BCMS) implemented in the PS [12]. This allowed β^* of 25-30 cm to already be reached in Run2 and made it possible to reach ultimate luminosity much earlier than anticipated. However, the luminosity limit from heat removal appeared exactly as expected, and this means that the peak luminosity cannot increase. This limit was predicted in 2003, based on computations extrapolated from Tevatron experience [13] and based on cryogenic computations. The slight difference of the actual limiting value of $2 \times 10^{34} \text{ cm}^{-2}\text{s}^{-1}$ wrt the initially expected $2.5 \times 10^{34} \text{ cm}^{-2}\text{s}^{-1}$ is due to the fact that an accident on the IT heat exchanger during the hardware commissioning [14] forced a smaller heat exchanger to be retrofitted, which reduced the heat removal capability of the system by 15-20%. Another intrinsic limit, also reported in [15], is that the dose on the triplet would reach the radiation damage limit at around 350-400 fb^{-1} . The radiation damage is not a hard limit. The magnets may still work well above 400 fb^{-1} , especially if the collision configuration is adapted (e.g. changing of the crossing angle [16]). However, running above 400 fb^{-1} implies entering a dangerous zone where a magnet fault can cause an unanticipated long shutdown with bad consequences for the LHC operation and the data taking at the experiments.

Before discussing the new configuration, it is useful to recall the systems that need to be changed, and possibly improved, just because they become more vulnerable to breakdown and accelerated wear out. This goes well beyond the regular on-going consolidation work.

- (1) *Inner Triplet Magnets:* As previously mentioned, at about 350-400 fb^{-1} some components of the low-beta triplet quadrupoles and their corrector magnets will have received a dose of 30 MGy, entering the region of radiation damage. The quadrupoles may withstand 400-700 fb^{-1} , but some corrector magnets of nested type might already wear out at above 350 fb^{-1} . The numbers are difficult to compute exactly because of uncertainties on material properties and on exact heat deposition locations that strongly depend on the detailed collision conditions, such as the crossing angle that varies from fill to fill and during a fill. Regardless, damage must be anticipated because the most likely way of failing is through a sudden electric breakdown, entailing a magnet replacement with a serious

and long intervention in an extremely challenging radiation environment and confined space that requires a careful and time-consuming intervention preparation. Replacing a single triplet may take almost one year: the worst thing for the LHC is a long shutdown that was not planned and where other maintenance and upgrade activities cannot be implemented. That is why replacement of the triplet must be envisaged before actual damage occurs. In addition, if one magnet fails, the other ones are probably close to failing soon as well, i.e. all the triplets in the two high luminosity insertions, P1 and P5, need to be replaced at the same time. Since triplet replacement in one IP (8 quads) requires more magnets than the total spare magnet pool (4 quads) a production of additional magnets would need to be started well in advance. Replacement of the low-beta triplets is a long intervention, requiring at least one year, and must be coupled with a major detector upgrade. Also, the detectors suffer from radiation damage in the Inner Tracker system, whose performance degrades strongly after 350-400 fb⁻¹. The LHC has been designed to have a common lifetime, or to require a synchronized major maintenance, both for accelerator and detectors, in the high luminosity insertions.

- (2) *Cryogenics*: To increase flexibility and balance the power availability for each magnet sector (and thus to maximize the integrated luminosity for a given cryogenic power) we plan to upgrade the cryo-plant in P4. We have abandoned the pursuit of full separation between superconducting RF cavities and magnets cooling. However, the increased capacity of the P4 plant eliminates an initial limitation, especially in view of the higher than expected power consumption in the LHC cold bore tube, driven by e-cloud effects and probably due to bad surface condition. The main cryogenic aspect that may penalize the LHC performance in terms of luminosity in the long term is the coupling of the cooling of the inner triplets (and matching section) magnets with the magnets of the arc. Decoupling the insertion region cooling from one part of the arc would avoid warming up the entire arc in an intervention in the triplet region (an operation of 3 months and not without risk). In addition, the total power available for the insertion region is about 250 W per side of each interaction point, which for P1 and P5 is insufficient to go beyond $2.5\text{--}3 \times 10^{34} \text{ cm}^{-2} \text{ s}^{-1}$.

- (3) *Collimation and absorbers*: The collimation system has been designed for the first phase of LHC life and has performed very well. The new collimators installed during LS1 with beam position monitors integrated in the jaws have drastically reduced the setting-up time. However, in view of the higher intensity beams of HL-LHC, a reduction of the impedance is also needed (the collimator jaws account for ca. half the impedance of the total machine). Therefore, many secondary collimators will be replaced with new lower impedance ones, based on a newly developed MoGr (molybdenum – graphite) composite with a Mo coating. The tertiary collimators protecting the triplets must also be changed. Any small gain in triplet aperture and performance must be accompanied by an adequate consolidation or modification of the collimation system, including a number of collimators and masks intercepting physics debris. A second area that will require a special attention for the collimation system is the Dispersion Suppressor (DS), where a leakage of off-momentum particles into the first and second main superconducting dipoles, has been already identified as a possible LHC performance limitation. The most promising concept is to substitute an LHC main dipole with a dipole of equal bending strength (121 T·m) obtained by a higher field (11 T) and shorter length (11 m) than those of the LHC dipoles (8.3 T and 14.2 m). The gained space is sufficient for placing special collimators. There is actually another concept which has been demonstrated in Run2, which uses crystals to kick the off-momentum particles towards larger amplitudes, such that the secondary collimators can do the job with less complexity and cost. However, this only works for ions. After LS3, when the full HL-LHC beam will be deployed, only the operational experience of Run3 can show if DS collimators, and thus 11T magnets, are required for the proton operation during the HL-LHC exploitation, depending on the observed minimum beam lifetimes. The Injection protection absorbers also need to be replaced with better ones, called TDIS: the higher modularity of the new ones, along with improved robustness, is necessary to deal with the intense new LIU beams. The main fixed absorbers for the collision debris also need to be replaced, following the new magnet aperture. New TAXS and TAXN absorbers are being designed for IR1 and IR5, and even in IR8 a new TAN is needed to accommodate the increased luminosity of LHCb experiment (from $4 \times 10^{34} \text{ cm}^{-2} \text{ s}^{-1}$ to $2 \times 10^{33} \text{ cm}^{-2} \text{ s}^{-1}$).

- (4) *R2E and SC links for remote cold powering*: a considerable effort is under way to study how to replace the radiation sensible electronic boards with rad-hard cards especially, but not only, for the electrical power converter feeding the magnets. A complementary solution is also pursued for the new magnets in IR1 and IR5: removal of the power supplies and associated DFBs (electrical feed-boxes, delicate equipment today in line with the continuous cryostat and containing the current leads) out of the LHC tunnel. Displacement of power converter (and electrical feed-boxes) into lateral new galleries, suitably excavated, is possible without excessive power consumption and increasing the voltage drop at power converter terminals, thanks to a novel technology, Superconducting links (SCLs) whose main body is made out of MgB_2 superconductors.
- (5) *Other Systems*: Other systems will become a bottleneck along with aging of the machine and a higher performance with $> 60 \text{ fb}^{-1}$ per year. Among the most critical are the Halo control, the Beam Dump system and the injection system.

2.2. The high luminosity parameters and upgraded systems

2.2.1. Luminosity levelling and availability

Both consideration of energy deposition; by collision debris in the interaction region magnets and the necessity to limit the peak pile up in the experimental detector, impose “a-priori” a limitation of the peak luminosity. The consequence is that the HL-LHC operation will have to rely on luminosity levelling. As shown in Figure 3 (left), without levelling, the luminosity profile quickly decreases from the initial peak value, due to “proton burning” (protons consumed in collisions). By designing the collider to operate with a constant luminosity that is lower than the maximum obtainable peak luminosity i.e., “levelling” the instantaneous luminosity and avoiding its decay for a good part of the fill, the average luminosity is almost the same - within 20-25% - as the one of a run with higher peak luminosity and without levelling, see Figure 3 (right). However, this has the big advantage of a smaller maximum peak luminosity.

The fact that the maximum levelled luminosity is limited means that in order to maximize the integrated value, one needs to maximize the run length,

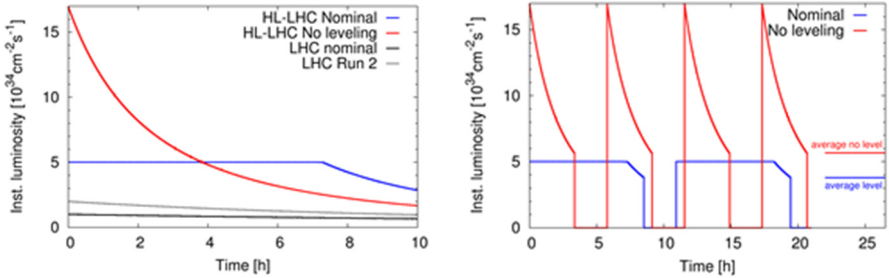


Fig. 3. Left: luminosity profile for a single long run for: LHC nominal peak luminosity (black line), LHC Run2 at ultimate luminosity (grey line), HL-LHC no levelling (red line) and HL-LHC with levelling (blue line). Right: luminosity profile with optimized run time, without (red line) and with levelling (blue line) with indication of the average luminosity for both cases.

which can be obtained by filling the maximum number of protons, i.e. by maximizing the beam current: $I_{beam} = n_b \times N$ and minimizing unintentional aborts in the beam operation due to equipment faults. Other key factors for maximizing the integrated luminosity and obtaining the challenging goal of exceeding $3 \text{ fb}^{-1}/\text{day}$ are: a short average machine turnaround time (the time from end of a fill and start of collision in the successive fill), and a good overall machine “efficiency”, defined as the ratio between actual luminosity produced and the luminosity of a continuous ideal cycle (see Figure 4). Clearly, for maximizing the integrated luminosity, the efficiency matters almost as much as the virtual peak performance. We call the maximum value that one could obtain in principle at the beginning of the fill before proton burning starts to decrease it, the “virtual luminosity”. For example, looking at Figure 3 (left), one can see that HL-LHC virtual luminosity is $17 \times 10^{34} \text{ cm}^{-2}\text{s}^{-1}$, i.e. seventeen times the nominal LHC luminosity. Somehow, the ration between virtual and levelling luminosity gives the idea of the “luminosity reservoir” one can use to continue the levelling.

For the levelled luminosity operation, one injects the beam with the current and emittance values fit for reaching the virtual peak luminosity. However, one or more of the machine parameters controlling the luminosity are “detuned” i.e. not set to the values for maximum luminosity production. This is kept as a “reserve”. Then during the luminosity run, these parameters are slowly “retuned” toward their optimum values to compensate the proton burning (or other source of luminosity loss, like emittance increase). Typical

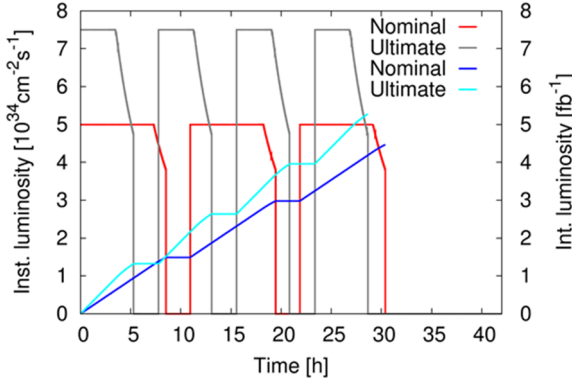


Fig. 4. Luminosity cycle for HL-LHC with levelling and a short decay (optimized for integrated luminosity) assuming 100% efficiency. The set of parameters generating cycle are the 25 ns column of Table 1.

parameters we intend to use as knobs for levelling are the optical beta function at the IP, controlling the beam size at collision (β^*), the crossing angle, and the overlap of the two beams at the IP.

HL-LHC with scheduled 160 days of physics operation needs an efficiency of ca. 50% to reach the HL-LHC goal of 250 fb^{-1} per year. During Run2 the efficiency was pretty stable at values around 50% (with the notable exception of 2015, the start-up year after LS1). However, one has to account for the increased complexity of HL-LHC, with levelling operation, the addition of new hardware (crab cavities, new refrigerator, etc...). Reaching an efficiency as high as achieved in the present LHC but with a (levelled) luminosity five times the nominal one, with much higher bunch population and additional technically complex hardware, will be a strong challenge. The project must therefore be accompanied by a vigorous consolidation for the high intensity and high luminosity regime; the High Luminosity LHC must also be a High Availability LHC.

2.2.2. Upgrade parameters

Table 1 lists the main parameters foreseen for the high luminosity operation for proton collisions. In order to mitigate possible limitations arising from heat deposition from e-cloud effects, HL-LHC maintains a backup scheme based on 25 ns bunch spacing and a filling sequence of 8 bunches followed by

Table 1. High Luminosity LHC parameters for protons (LHC nominal ones for comparison).

Parameter	Nominal LHC (design report)	HL-LHC 25 ns (standard)	HL-LHC 25 ns (BCMS) ⁸	HL-LHC 8b+4e ¹⁰
Beam energy in collision [TeV]	7	7	7	7
N	1,15E+11	2,2E+11	2,2E+11	2,2E+11
n_b ¹²	2808	2760	2744 ¹³	1972
Number of collisions in IP1 and IP5 ¹	2808	2748	2736	1960
N_{tot}	3,2E+14	6,1E+14	6,0E+14	4,3E+14
Beam current [A]	0,58	1,1	1,1	0,78
Half Crossing angle [μ rad]	142,5	250	250	250 ⁹
Norm. long range beam- beam separation at minimum β^*	9,4	10,5	10,5	10,5 ⁹
Minimum β^* [m]	0,55	0,15	0,15	0,15
ϵ_n [μ m]	3,75	2,50	2,50	2,50
ϵ_L [eVs]	2,5	3,03	3,03	3,03
R.M.S. energy spread (q-Gaussian distribution)	-	1,10E-04	1,10E-04	1,10E-04
R.M.S. energy spread (FWHM equiv. Gaussian)	1,13E-04	1,29E-04	1,29E-04	1,29E-04
R.M.S. bunch length [m] (q-Gaussian distribution) ¹¹	-	7,61E-02	7,61E-02	7,61E-02
R.M.S. bunch length [m] (FWHM equiv. Gaussian) ¹¹	7,55E-02	9,00E-02	9,00E-02	9,00E-02
IBS horizontal [h]	105	16,5	16,5	16,5
IBS longitudinal [h]	63	19,2	19,2	19,2
Piwinski parameter	0,65	2,66	2,66	2,66
Total loss factor R0 without crab-cavity	0,836	0,342	0,342	0,342
Total loss factor R1 with crab-cavity	-	0,716	0,716	0,716
beam-beam / IP without crab- cavity	3,1E-03	3,3E-03	3,3E-03	3,3E-03
beam-beam / IP with crab- cavity	3,8E-03	8,6E-03	8,6E-03	8,6E-03

Table 1. (Continued)

Parameter	Nominal LHC (design report)	HL-LHC 25 ns (standard)	HL-LHC 25 ns (BCMS) ⁸	HL-LHC 8b+4e ¹⁰
Peak Luminosity without crab-cavity [$\text{cm}^{-2}\text{s}^{-1}$]	1,00E+34	8,1E+34	8,1E+34	5,8E+34
Virtual Luminosity with crab-cavity: $L_{\text{peak}} \cdot R1/R0$ [$\text{cm}^{-2}\text{s}^{-1}$]	-	1,70E+35	1,69E+35	1,21E+35
Events / crossing without levelling and without crab-cavity	27	212	212	212
Levelled Luminosity [$\text{cm}^{-2}\text{s}^{-1}$]	-	5,0E+34 ⁴	5,0E+34	3,80E+34
Events / crossing (with levelling and crab-cavities for HL-LHC)	27	131	132	140
Peak line density of pile up event [event/mm] (max over stable beams)	0,21	1,28	1,29	1,37
Levelling time [h] (assuming no emittance growth) ⁷	-	7,2	7,2	6,4
Number of collisions in IP2/IP8	2808	2492/2574 ^{6,13}	2246/2370 ¹³	1178/1886 ¹³
N at LHC injection ²	1,20E+11	2,30E+11	2,30E+11	2,30E+11
n_b /injection	288	288	240 ¹³	224
N_{tot} /injection	3,46E+13	6,62E+13	5,52E+13	5,15E+13
ϵ_n at SPS extraction [μm] ³	3,5	2,1	1,7 ⁵	1,7

¹ Assuming one less batch from the PS for machine protection (pilot injection, TL steering with short trains of nominal bunches) and non-colliding bunches for experiments (background studies...).

Note that due to RF beam loading the abort gap length must not exceed the $3\mu\text{s}$ design value.

² An intensity loss of 5% distributed along the cycle is assumed from SPS extraction to collisions in the LHC.

³ A transverse emittance blow-up of 10 to 15% on the average H/V emittance in addition to that expected from intra-beam scattering (IBS) is assumed.

⁴ For the design of the HL-LHC systems (collimators, triplet magnets...), a design margin of 50% on the stated peak luminosity was agreed upon.

⁵ For the BCMS scheme emittances down to $1.7\mu\text{m}$ are expected at LHC injection which might be used to mitigate excessive emittance blowup in the LHC during injection and ramp.

⁶ The lower number of collisions in IR2/8 wrt to the general purpose detectors is a result of the agreed filling scheme, aiming as much as possible at a democratic sharing of collisions between the experiments.

⁷ The total number of events/crossing is calculated with an inelastic cross-section of 81 mb (also for nominal), while 111 mb is still assumed for calculating the proton burn off and the resulting levelling time.

⁸ BCMS parameters are only considered for injection and as a backup parameter set in case one encounters larger than expected emittance growth in the HL-LHC during injection, ramp and squeeze.

⁹ The crossing angle for the 8b+4e alternative could be reduced down to about 400 μrad (9σ) thanks to the lower number of long ranges.

¹⁰ The 8b+4e variant represents a back-up scenario for the baseline 25ns operation in case of e-cloud limitations. The parameters are still evolving but are stated for the sake of performance reach comparison.

¹¹ The RF system is assumed to operate at 16MV with full detuning.

¹² The underlying assumption of reliable operation with a 200/800 ns SPS/LHC injection kicker rise time still remains to be proven during 2018 operation.

¹³ Updated baseline filling schemes and inclusion of LHCb Upgrade II.

4 empty buckets [8b4e] or variations of it. The large extra heat load observed in a few LHC sectors during Run2 and triggered by e-cloud effects by still unidentified mechanisms, remains a possible threat to operation with HL-LHC bunch intensities and filling schemes. For similar reasons, a slightly different parameter set with very small emittance beams (BCMS) is also maintained in case the LHC operation at high beam intensities reveals unexpected sources for emittance blow-up during the beam injection and acceleration.

For ion collisions, there is a similar parameter table as described in Table 2 below, which lists three sets of parameters for the ions: the values from the original LHC design report, the HL-LHC baseline parameters assuming slip stacking in the SPS and an alternative third 75 ns option as backup.

Table 2. High Luminosity LHC parameters for ions.

Parameter	Nominal LHC (design report)	HL-LHC (baseline)	HL-LHC 75 ns option
Beam energy [Z TeV]	7	7	7
Number of bunches per beam	592	1240	733
Bunch spacing [ns]	100	50	75
Bunch intensity [10^7 Pb ions]	7	18	21
Stored beam energy [MJ]	3,8	20,5	14,2

Table 2. (Continued)

Parameter	Nominal LHC (design report)	HL-LHC (baseline)	HL-LHC 75 ns option
Total beam current [mA]	6,12	33	22,7
Normalized transverse emittance e_n [μm]	1,5	1,65	2,3
Longitudinal emittance ε_L [eVs/charge]	2,5	2,42	2,33
R.M.S. energy spread [10^{-4}]	1,1	1,02	1,06
R.M.S. bunch length [cm]	7,94	8,24	8,24
IBS horizontal [h]	13	5,8	10,8
IBS longitudinal [h]	7,7	2,6	2,8
Peak RF voltage [MV]	16	14	14
Number of colliding bunches (IP1/5)	<592	976 - 1240	733
Number of colliding bunches (IP2)	592	976 - 1200	702
Number of colliding bunches (IP8)	0	0 - 716	468
β^* at IP1/5 [m]	0,55	0,5	0,5
β^* at IP2 [m]	0,5	0,5	0,5
β^* at IP8 [m]	10	1,5	1,5
Half crossing, IP1/5 [μrad]	160	170	160
Half crossing, IP2 (external, net) [μrad]	110, 40	170, 100	137, 60
Half crossing, IP8 (external, net) [μrad]	-	-170, -305	160
Peak luminosity, IP1/2/5 [$10^{27}\text{cm}^{-2}\text{s}^{-1}$]	1	-	6,2
Levelled Luminosity, IP1/5 [$10^{27}\text{cm}^{-2}\text{s}^{-1}$]	-	6,4	-
Levelled Luminosity, IP2 [$10^{27}\text{cm}^{-2}\text{s}^{-1}$]	-	6,4	6,4
Levelled Luminosity, IP8 [$10^{27}\text{cm}^{-2}\text{s}^{-1}$]	-	1	1

An upgrade should provide the possibility of performance increase over a wide range of parameters, such that the machine experience and experiments can eventually find the practical best set of parameters in actual operation.

Beam current and brightness: the total beam current may be a hard limit in the LHC since many systems are affected by this parameter. RF power system and RF cavity, Collimation, Cryogenics, Kickers, Vacuum, beam diagnostics, QPS, various controllers, etc. Putting aside radiation effects, in principle, all systems have been designed for principle for $I_{beam} = 0.86$ A, the so called “ultimate” beam current. However, this has yet to be experimentally proven and for the goal of HL-LHC we need to go beyond the ultimate value by 30%

with 25 ns bunch spacing. Especially the power needed for the RF system is a concern. Operating the SRF cavity system in detuning mode and implementing high efficiency klystrons should solve this issue, but remains to be fully demonstrated.

For HL-LHC the beam brightness needs to be increased, which is a property that must be maximized at the beginning of the beam generation and then preserved throughout the entire injector chain and LHC itself. The LIU project has as primary objective to increase the beam brightness at the LHC injection, basically increasing the number of protons per bunch by a factor two above what was achieved in the injector complex during Run2, while keeping the emittance at the same low value.

β^ and cancelling the luminosity reduction factor R* : a classical route to the luminosity upgrade is to reduce β^* , the optical function at the Interaction Points (IPs), by means of larger aperture IT quadrupoles (implying a larger peak field at the coils), alongside an upgrade of the matching sections quadrupoles. A reduction in β^* values implies an increase of beam sizes inside the IT quadrupoles and a wider crossing angle, which, in turn, both require larger aperture IT quadrupole magnets, larger D1 and D2 separation/recombination dipole magnets and a few additional modifications in the matching section. Stronger chromatic aberrations coming from the larger β -functions inside the triplet magnets may exceed the strength of the existing correction circuits, and the peak beta-function inside the IT magnets is also limited by the possibility to match the optics to the regular beta functions of the neighbouring arcs. A previous study has shown that a practical limit in LHC is $\beta^* = 30$ cm, compared to the 55 cm foreseen in nominal operation and the 15 cm foreseen for HL-LHC. A novel scheme called Achromatic Telescopic Squeeze (ATS) uses the adjacent arcs as enhanced matching sections and the increase of the beta-functions in those arcs to boost, at constant strength, the efficiency of the lattice sextupoles for the chromaticity correction. This way, a β^* value of 15 cm can be envisaged and a flat optics with a β^* as low as 5 cm in the plane perpendicular to the crossing plane is enabled. For the β^* reduction the quadrupole magnets need to double the aperture, implying a peak field of 11-12 tesla, 50% above the present LHC, requiring a new, more performant superconducting technology based on Nb₃Sn.

Another drawback of operating with very small β^* values and a small bunch spacing is that it requires a larger crossing angle in order to avoid unwanted

long-range beam-beam encounters. In addition to requiring aperture inside the IT magnets, a large crossing angle entails a reduction of the geometrical luminosity reduction factor ‘R’, see luminosity expression. In Figure 5 the reduction factor R is plotted for a constant normalized beam separation of 10σ vs. β^* values. ‘+’ signs indicated the value for LHC design, actual LHC 2018 Run2) and the value foreseen for HL-LHC (bottom cross along red line).

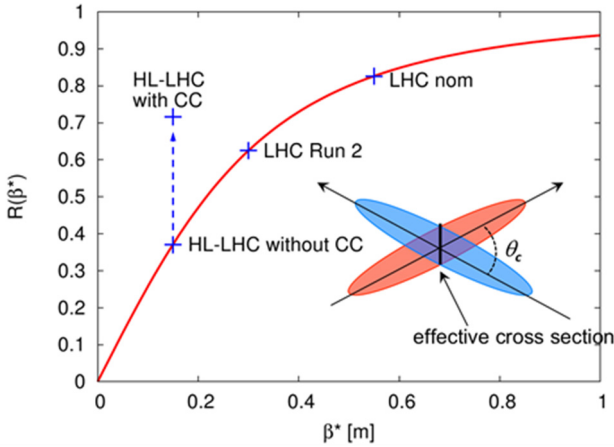


Fig. 5. Behavior of geometrical reduction factor of luminosity vs. β^* for constant normalized beam separation with indicated various operating points. The sketch of bunch crossing shows the reduction mechanism: a reduction of the luminous region [bunch overall] and an increase of the effective bunch cross section at the IP.

An efficient and elegant solution for compensating the geometric reduction factor is the use of special RF crab cavities, capable of generating a transverse electric field, a voltage kick, to rotate each bunch by as close as possible to $\theta_c/2$, such that they collide effectively head on, overlapping almost perfectly at the collision point, see Figure 6 even in presence of a crossing angle. Crab cavities make accessible the full performance reach of the small β^* that the ATS scheme and the large low-beta triplet quadrupoles can generate. Their primary function is therefore boosting the virtual peak luminosity for attaining the full HL-LHC performance. They can also be used as a levelling tool by varying the voltage kick, but unfortunately at constant pileup density. β^* levelling is therefore the baseline operation scenario, but the easy levelling or anti-levelling knob provided by the CC will certainly be an asset for operation.

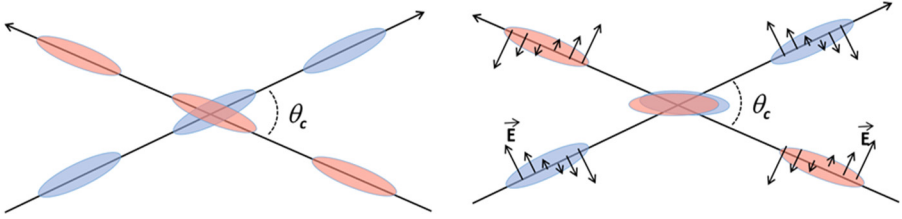


Fig. 6. Effect of the crab cavity on the beam: left, bunch collision geometry without CC; right: with CC small arrows indicate the transverse varying RF Electric field E when crossing the CC (please note that the E kick has same directions before and after collision; however, because of the almost 180 degree betatron phase advance between the two kicks, it correspond to an opposite torque on the bunch [π -bump]).

3. New Equipment and Modifications for HL-LHC

The HL-LHC project tries to address all issues and hardware limitations described in Section 2.1. In this section, we list all new equipment that will be installed within the HL-LHC baseline and all modifications to the present LHC configuration: for a complete description of the equipment and configuration we redirect the reader to each article of this book and to the HL-LHC Technical Design Report [17]. There is some equipment that has been only recently added to the HL-LHC baseline [e.g. at the 2019 Cost & Schedule Review]. These items are listed in a separate dedicated section.

3.1. Magnets and associate equipment

3.1.1. 11T in Nb_3Sn (LS2)

The LHC collimation system has a small but significant loss of particles that may deposit too much energy in the dispersion suppressor (DS) region, (see Chapter 8). This is a cold zone, part of the 3 km continuous cryostat: in particular, the first superconducting dipoles can be quenched in case of both ion beams and proton beams once the upgrade is carried out. As a mitigation measure of this problem, it has been considered to install collimators in the DS region. Since collimators need to be placed in a warm region, the only way to generate space in case the loss peaks occur in a region occupied by a dipole magnet, is to substitute an 8.4 T, 15 m long LHC dipole with two 11 T, 5.5 m long new LHC dipoles. The 4-meter free-space is enough to install a by-pass

system connected to the 1.9 K continuous cryostat hosting at room temperature the 1-meter-long collimator. In P7 of the LHC, we need two systems, one on each side of the insertion, to protect the neighbouring superconducting arcs from the debris escaping from the collimation system in P7.

The 11 T dipole is a very complex new equipment since it requires use of more performant Nb₃Sn superconductors, the key technology also being used for the IT triplet upgrade. The aperture of the magnets is much smaller than the IT triplet, 60 mm vs. 150 mm. However, it is a double bore magnet, like all LHC main dipoles. In addition, the 11 T dipoles have a number of additional constraints because they are part of the regular LHC main dipole electrical and cryogenic circuits. For example, the current is powered in series with the arc magnets while the integrated transfer function must fit perfectly to the one of the LHC main dipoles.

Despite a big effort by the project and the technical teams, and in spite of the initial success of the short magnet development program, featuring the identical size in cross section as the full-size magnets, the initial full length 11 T dipoles (arranged in pairs of 5.5. m long dipoles, with a cold-warm-cold by-pass hosting the collimators in the middle), displayed some unexpected



Fig. 7. Two first 11 T dipoles of the series production under test at the CERN testing infrastructure called SM18.

behavior. Three of the first four dipoles tested at the CERN SM18 facility, see Figure 7, reached the nominal field but showed a peak field degradation after high power quenches and thermal cycles.

In light of these observed degradations, it has been decided to not install the 11T magnets until the origin of the effect has been fully understood and mitigated. In total, considering a full spare unit, six 11 T- 5.5 m long dipoles will be needed for HL-LHC. In parallel, the LHC operation will study in more detail the magnet quench limits in the existing machine and the actual need for the DS collimators during Run3.

Crystal collimators were added to the HL-LHC baseline at the end of 2019, in order to mitigate the risk of performance shortcomings of the 11T magnets. Crystal collimators effectively protect the superconducting arcs for operation with ion beams. However, the need for dispersion suppressor collimators for proton operation cannot be mitigated by the crystal collimators. A final decision on the need for the 11T dipoles for the HL-LHC proton operation will be taken during the LHC Run3 period when more operational data with higher beam intensities following the LIU upgrade in LS2 becomes available.

3.1.2. *IT quadrupoles in Nb₃Sn*

As mentioned in Section 2.2.2, a much larger aperture for the IT aperture is required for reaching very small β^* values. The aperture for HL-LHC IT quadrupoles has been selected to be 150 mm. Using Nb-Ti technology, as in the present LHC magnets, would mean unpractical magnet lengths, almost tripling the length of the present quadrupole triplets and resulting in unacceptably large peak beta function inside the triplets [chromatic aberrations] and generating problems for integration and layout with serious difficulties in other areas (for example requiring a stronger D1-D2 magnet pair). In practical terms, we have decided to go for a gradient and length combination that requires a peak field of about 11.5 T on the coil of the quadrupoles (for 7 TeV beam operation). As already cited, such a field imposes the use of Nb₃Sn superconductor, the only viable choice today for accelerator magnets beyond the 8.5-9 T operational limit of the NbTi technology. It also makes it easier to deal with the heat deposition by the collision debris due to the larger temperature margin of Nb₃Sn as compared to that of NbTi superconductor.

Each Triplet array consists of four cryo-assemblies: Q1, Q2a, Q2b and Q3, like in the LHC. The only difference, from a layout point of view, is the -limited- increase of the total triplet length (from 32 m to 42 m physical length). All Q1/Q2a/Q2b/Q3 magnets will be powered in series, and the cross section is the same for all quadrupoles. We will need four IT triplet assemblies, one per side of the two high luminosity insertions, P1 and P5. Only the magnetic length is different: 7.2 m for the Q2a/b and 8.4 m for Q1 and Q3 magnets. However, for reducing risk and technical difficulties for the Q1 and Q3 magnet production, under requests of our partner of US-HL-LHC-AUP in charge of the design and construction (see next section on collaboration), the Q1 and Q3 quadrupoles will be segmented into two magnets of 4.2 m length each, assembled in the same cold mass and cryostat. In Figure 8, a US quadrupole magnet, i.e. half of Q1 or Q3, is shown before testing. Including spare magnets, practically a fifth IT triplet assembly, the HL-LHC will need to manufacture 30 Nb₃Sn quadrupoles, 10 of 7.2 m length and 20 of 4.2 m length. The triplet assembly will be tested in advance with a special set up in the CERN Magnet Test Hall (SM18) as “HL-LHC IT String” to check installation and operational issues well before commissioning in the machine.

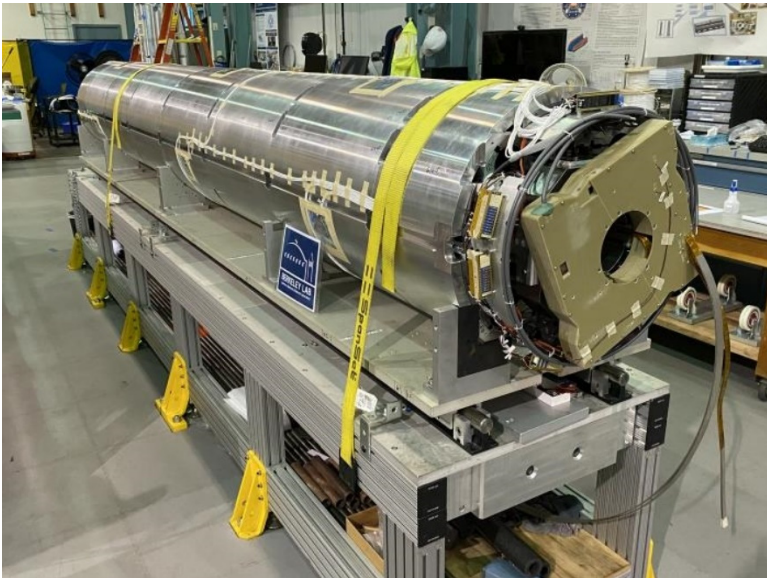


Fig. 8. MQXFA05 at Lawrence Berkeley National Laboratory, USA.

It is worth remembering that not only Nb₃Sn is a new, more complex, technology than the Nb-Ti deployed in the LHC. Because of their high peak field and especially because of their enormous aperture, the HL-LHC triplet magnets have forces and stored energies that are larger than the LHC main dipoles and comparable with dipoles considered for next generation hadron colliders, such as the FCC-hh, or for the main ring of a Muon-collider. This gives the measure of the technical challenge and explains why the HL-LHC is a pivotal project for the technological advancement for energy frontier colliders.

3.1.3. *IR magnets in Nb-Ti*

The increased aperture of the IT triplet requires revision of the aperture of many other magnets too. In the first layout of the HL-LHC, we planned to change almost all magnets of the insertion region, from Q1 down to Q5, with the noticeable exception of Q6. However, further studies and design optimizations allowed us to avoid the change of the Q4 and Q5 magnets. However, in addition to the IT triplet quadrupoles, an upgrade is still required for the separation/recombination dipole pair, called D1 and D2, and the numerous corrector magnets that are associated to the IT triplet quadrupoles and to the D1/D2 pair.

All these magnets are wound with Nb-Ti and operated at 1.9 K. The difficulties for these new magnets come from increased field and size or from the use of new coil/magnets layout as listed below:

- (1) The 6 D1 separation dipoles (4 for installation and 2 spare ones) are single aperture magnets, featuring a peak field of almost 6 T and a length of more than 6 m. The coil aperture of 150 mm implies a stored energy per unit length of 0.35 MJ/m-aperture, sensibly larger than the 0.25 MJ/m-aperture of the LHC dipoles.
- (2) The 6 D2 recombination dipoles (4 for installation and 2 spare ones) are double aperture magnets, with the same field direction in both apertures. Since their field and aperture, 4.5 T and 105 mm, are considerably larger than for the LHC D2 magnets, the field quality and coil design poses much bigger challenges than in LHC (cross talk) and the stored energy of 0.15 MJ/m-aperture is considerable for such magnets.

- (3) The 18 single aperture orbit corrector magnets (dipoles with both horizontal and vertical orientation) for the Inner Triplets have fields similar to the ones in the LHC, but with much larger aperture. Like in the nominal LHC, these dipoles are of nested type, with two concentric dipole coils rotated by 90° with respect to each other. This design makes it very difficult to control tolerance and stress on the coils in presence of large torque: the outer dipole coils have a diameter of almost 200 mm, which poses serious mechanical challenges. The integrated field is 4.5 Tm, a value that makes it misleading to call it a simple “corrector” magnet.
- (4) In total 54 single aperture magnets for the correction of high order (HO) field harmonics, from quadrupoles to dodecapoles errors, are needed for the HL-LHC Inner Triplet regions (the number of magnets includes some 14 spare magnets). These HO magnets will all be *superferric*: the main field is given by an iron pole-yoke circuit that is magnetized by small compact superconducting coils. In this way, one achieves the advantage of compactness, with sharp field decay (a key point because the 150 mm aperture is comparable to the needed magnetic length) and reduces the risk of radiation damage with respect to classical superconducting magnet designs. This configuration is a novelty, too, for colliders see Figure 9.

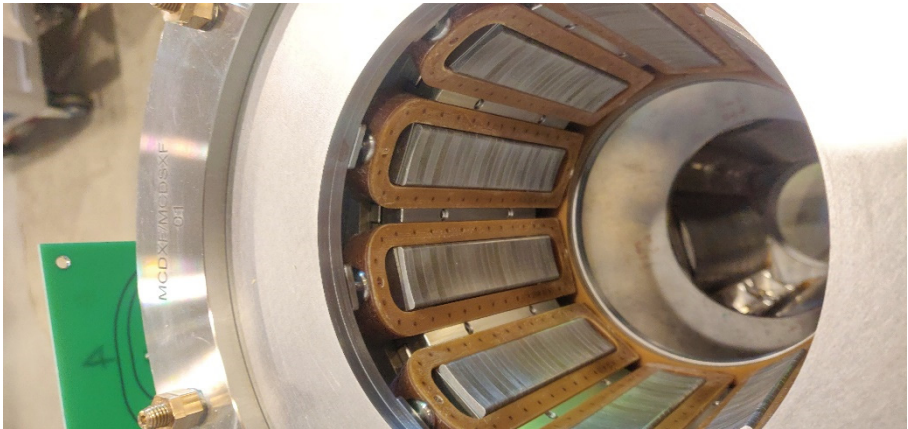


Fig. 9. Inside view of a superferric dodecapole corrector under assembly at INFN-LASA-Milano. Well visible are the rectangular coils surrounding the flat iron poles.

- (5) The 12 double aperture orbit correctors that are assembled in the D2 cold mass will be made with a novel coil layout called Canted-Cosine-Theta (CCT) design, that generates the dipole field via two nested inclined solenoidal coils with opposite winding. The integrated field is 5 Tm, again a very big value for a “corrector” magnet. The length of nearly 2 m calls for a dipole field of 2.6 T, which makes this new magnet design potentially very attractive, which promises to considerably simplify the construction of superconducting magnets working at low-moderate field. This again is a novelty for Colliders, see Figure 10.



Fig. 10. Winding the first CCT prototype at CERN.

3.1.4. *Cold and warm powering*

The new magnet circuits need more electrical power converters (EPCs) that are newer and more powerful. They will be hosted in new, long galleries 8 m above and 30 m aside of the LHC tunnel to provide optimum protection against radiation from the tunnel and to facilitate the access during operation. The connection between EPCs and magnets, about 110-130 m long, will be made via superconducting links. Flexible cryostats host a cable composed of several cables made of MgB_2 superconducting strands. The use of new MgB_2 composite is a novelty for larger systems: it allows cooling via He gas operating between 4 and 20 K with higher temperature margin and much larger energy margin than classical Nb-Ti strands cooled with supercritical helium flow. Consequently, the superconducting links are very stable, almost insensible to quench and the use of gas accommodates for height differences between the EPCs and the magnets in the tunnel and also allows operators to access the galleries of the power converter during operation.



Fig. 11. Handling tests of a superconducting link.

The cold powering system, one of the most innovative technologies in HL-LHC, is then composed by cold distribution feedboxes (DFs for triplet magnets or DFMs for matching section magnets), hosting the connections between Nb-Ti bus bars coming from the magnets and MgB_2 cables. The long MgB_2 cables, starting from DF/DFMs, are located in a flexible cryostat ending into cold boxes placed in the higher-level galleries (called DFHs or DFHMs). Here the cables are spliced to short HTS cables that are connected to the He gas cooled copper current leads, the feedthrough realizing the passage from cold to warm powering. Finally, from current leads to the nearby EPCs the connection is made by heat-sink-cooled copper bars. Another new feature is that between current lead and EPCs, special “disconnecter” boxes are inserted to facilitate the segregation of the circuits, and to improve electrical safety of operators.

The power converters are all of the same class of the LHC ones, except the 18 kA EPC for the new IT magnets that feature the novelty of being Class 0, i.e. better than 1 ppm ripple and ten times more precise than the ones deployed for the LHC main magnets. In addition, the 18 kA EPCs are of 2-Quadrant type. The 2-Q layout allows speeding up IT quadrupole current decrease, a new feature too, beyond present technology requiring new developments.

3.1.5. *Magnet and machine protection*

The protection systems of the HL-LHC feature advanced electronics control and radiation resistance boards in all domains. The main conceptual novelty is probably the use of the new CLIQ (Coupling Losses Induced quench) concept for the quench protection of the IT quadrupoles, together with classical quench heaters. In this case, it should be noted again, that it is the first time ever that the CLIQ concept is used to protect magnets in an accelerator. Its very short reaction time is very much suited to the high current density Nb_3Sn windings to spread the quench over the whole coil in a few milliseconds. Also, this is a key test in real conditions for a critical technology for FCC-hh magnets.

3.2. *Crab cavities*

As mentioned above, crab cavities are used for the first time on a hadron collider. For HL-LHC, they improve the bunch overlap at the interaction point (IP) and thus, compensate for the geometric luminosity reduction factor. Two

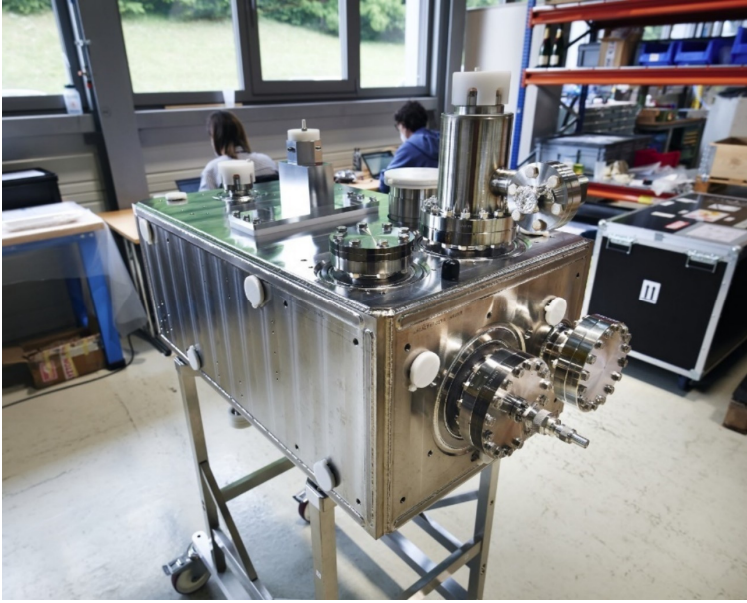


Fig. 12. RFD2 crab cavity within its magnetic shielding manufactured at CERN.

single cell cavities are placed on the incoming beam in the matching section at 160 m from the IP. Each cavity gives a kick of 3.3 MV, resulting in a nominal total kick of 6.6 MV for the incoming beam. A similar voltage kick is given to the outgoing beam (the same beam after collision) at the other side of the IP. Each crab cavity pair is hosted in one cryo-module: the distance between the two counter-circulating beams is so small that, in spite of the extremely compact design of the CC, the beam pipe of the non-kicked beam needs to be hosted in the cryo-module of the CC. Considering the two beams, we have the following layout (please note that vertical-horizontal crossing is opposite as it is in the present LHC):

- (1) P1 (ATLAS, horizontal crossing beams): 4 cavities per IP side, of the RFD type. Two cryo-modules per side, one per beam.
- (2) P5 (CMS, vertical crossing beams): 4 cavities per IP side, of the DQW type. Two cryo-modules per side, one per beam.

In total, considering that each type will require a spare cryo-module, we will have 10 CC cryo-modules, with in total 20 CC cells, half in DQW for vertical deflection at P5 and half in RFD for horizontal deflection in P1.

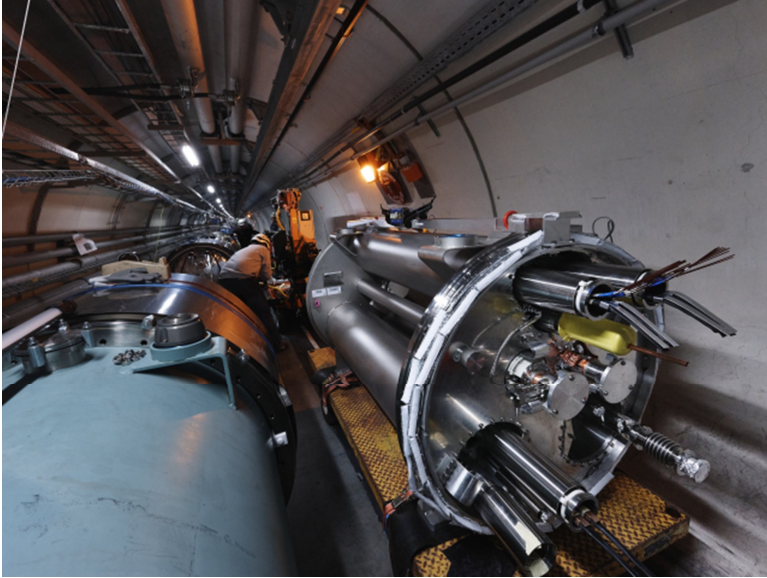


Fig. 13. Installation of a new bypass near the new cryostat installed in 11L2.

3.3. Collimators (*LS2 and LS3*)

The collimation system requires a serious upgrade to face the challenge of the more intense HL-LHC beams. The upgrade can be summarized as follows:

- (1) Upgrade of 18 secondary collimators (8 during LS2) with new jaws, with active absorbing components made of a new molybdenum-graphite composite (MoGr) and then coated with molybdenum. The projected impedance reduction is a big step to assure stable beams with the required HL-LHC intensities.
- (2) Upgrade of the tertiary collimation system (12 units) to cope with larger triplet aperture and increased robustness and the addition or upgrade of 8 collimators and 12 fixed masks to intercept debris from the IP. With the reuse of existing collimators, a total of 28 movable collimators and 12 fixed masks will compose the new tertiary collimation system in operation for Run4.
- (3) Insertion of a new collimation system in the dispersion suppressor (DS) regions around IR2, in a newly designed connection cryostat (installed in LS2). The insertion of the DS collimators in such bypasses placed in

between two 11 T dipoles, around IR7, has been postponed until after LS2 in order to fully assess the need for the collimators in IR7 and the technical maturity of the 11T dipole design. A final decision on the 11T installation for HL-LHC will be taken during Run3.

- (4) Insertion of new crystal primary collimators, 1 crystal per plane on each beam, i.e. four crystals with their goniometer, positioning and control systems, to ensure good collimation cleaning for heavy-ion operation. The installation will start before the end of LS2 and will be completed during Run3. See specific section on new equipment baseline.

3.4. Collider-Experiments interface

The interfaces between collider and experimental detectors need a change because a smaller β^* entails a large beam size at the entrance in the detector region, so the TAS absorber needs to be made larger and upgraded with the new TAXS. The neutral absorber in the matching sections of IR1 and IR5 will be replaced, too, with a new one called TAXN. A new one, called TANB, that is necessary in IR8 to cope with the increased luminosity of the LHCb experiment has already been installed in summer 2019, representing the first HL-LHC equipment installed in the LHC tunnel! The new TANB absorber is shown in Figure 14.

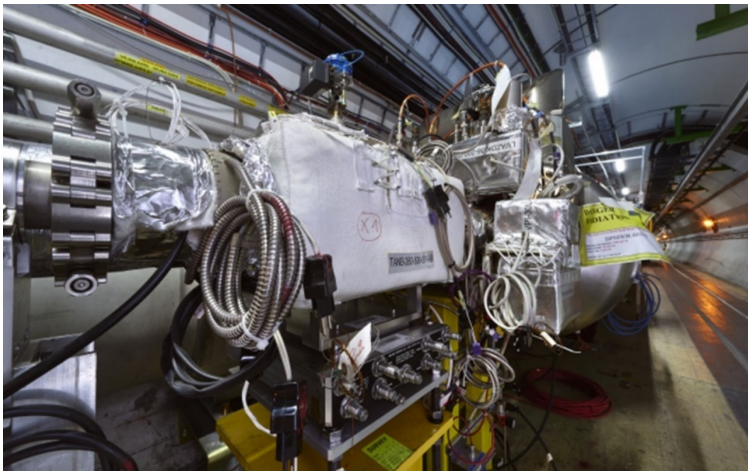


Fig. 14. The TANB absorber.

With the change of the TAXS and of the iron shielding around IP1 and IP5, we profit from the reorganisation of the VAX region, the zone dedicated to the vacuum equipment at the interface between the machine beam pipe and the experimental beam pipe. It is a packed zone with valves, actuators, interlocks and control boards, with very limited accessibility and in high radiation environment. It will be reorganized and rationalized via use of remote-control actuators that allow fully robotic controlled interventions, see Figure 15.

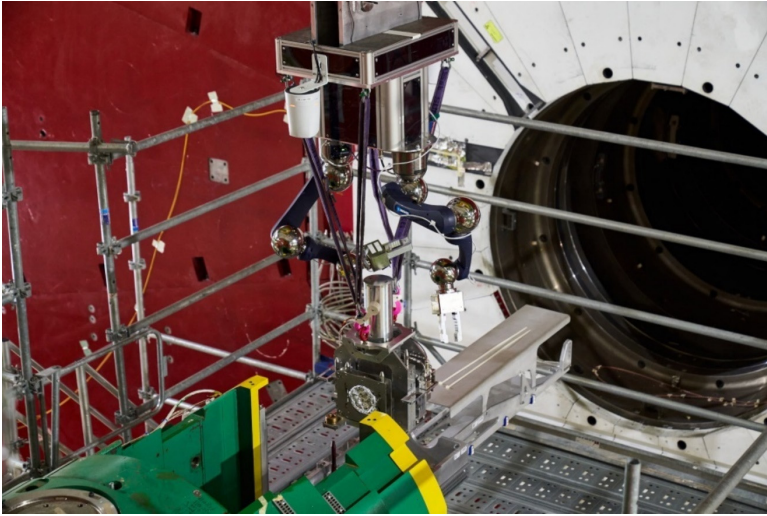


Fig. 15. The CERN CRANEbot handles a VAX module in the CMS cavern.

3.5. Cryogenics

The main cryogenic modifications are, of course, at P1 and P5. In each of these points a new 1.9 K cryo-plant, with the same power as the existing LHC cryo-plants (18 kW@4.2 K with 1.8 kW@1.9K cryo-power), will be installed in LS3, to face the increase of heat deposited at cryogenic temperature in the magnet cold mass by the high luminosity regime. The cryo-lines that supply helium to the magnets will be considerably modified and will be separated from the ones of the arc, which will greatly increase the flexibility for operation (a warm-up in the triplet region will not force warming-up the continuous cryostat of the 3 km long sector). The new cryo-line will start from the Q4-CC interface and will extend until Q1 of the IT assembly.

In addition, an upgrade of the existing cryogenic plant in P4 is under way to increase the cooling capacity of the Sector 3-4. Once the upgrades of the cryogenic systems are completed, the Sector 3-4 will become the weakest cryogenic sector after sector 4-5 will be reinforced by the new cryogenic system in P5. The upgrades are already being implemented since LS2 but will be completed only during LS3.

3.6. *Vacuum*

Apart the obvious changes of the vacuum system entailed by the new magnet layout in IR1 and IR5, it is worth underlining a few modifications of the vacuum system as new technological breakthroughs.

- (1) The beam screen in the IT triplet is of a new design: octagonal in shape, it is suitable for vertical and horizontal beam crossing at the same time. The beam screen supports a heavy shielding in tungsten alloy (INERMET), of thickness varying between 16 mm (for Q1) and 6 mm (for Q2a/b and Q3), to better protect the 1.9 K superconducting coils from the radiation debris. The HL-LHC beam screen works at 60-90 K, a carefully studied temperature range to avoid desorption gas instability



Fig. 16. A beam screen at the cryolab.

while maximizing by a factor five the gain in efficiency for the power removal when compared to the LHC beam screen in the arcs, that works between 10 and 20 K. Figure 16 shows the new beam screen inserted into a cold bore.

- (2) To eliminate the e-cloud effect, all new beam screens will be coated with amorphous carbon (actually carbon nanostructured particulate, deposited via sputtering, that reduce the secondary electron yield $SEY < 1$. Tested already in a few SPS magnets at room temperature, this a-c coating will be used on a cryogenic surface for the first time. The possibility of using an alternative technique called LESS (laser engineered structured surface) is still being studied. In this case the reduction of the SEY is obtained by “scratching” the surface via a green light power laser. While very attractive, since it does not require to be performed in vacuum like the a-c sputtering process, this technique is not yet fully validated for accelerators (possible issues include high wall impedance, possible powder residuum, etc...). A-C coating will also be retrofitted in the IR8 and IR5 triplet regions. In that case, the only choice is sputtering “onsite” during LS3. In LS2 we anticipate, however, some coating of the beam screens, namely Q5L8, in order to validate the procedure and gain experience with the in-situ application technique in advance with minimal risk.

3.7. Beam injection and beam dumping systems

The increased beam intensity in HL-LHC poses great challenges to the beam injection and dumping systems. The need to upgrade these systems even in advance to the full HL-LHC deployment has been evident since Run1. The main upgrades foreseen for the injection and extraction/dumping systems are the following:

- (1) Injection kicker MKI has already suffered beam-induced heating, electrical flashovers, beam losses and electron cloud related vacuum pressure rise during LHC operation. Cr_2O_3 coated alumina chambers, an upgraded beam screen with active cooling of the ferrite rings are the main upgrades of the so called “MKI cool” for HL-LHC.
- (2) A novel design of the main injection absorber, called TDIS, has been designed for HL-LHC and already installed in LS2 to cope with beam above nominal intensities in Run3. TDIS is segmented (the S of the

name), into three shorter absorbers (~ 1.6 m each) accommodated in separate tanks. The two upstream modules will accommodate low-Z graphite absorber blocks, to increase robustness, while the third one hosts higher-Z absorber materials for improved absorption efficiency. Figure 17 shows the TDIS being lowered into the LHC tunnel at Point 1.

- (3) The septa protection absorber (TCDS) will be modified to withstand an asynchronous dump with HL-LHC beam. Solutions with different absorbing material or with extra absorber are possible.

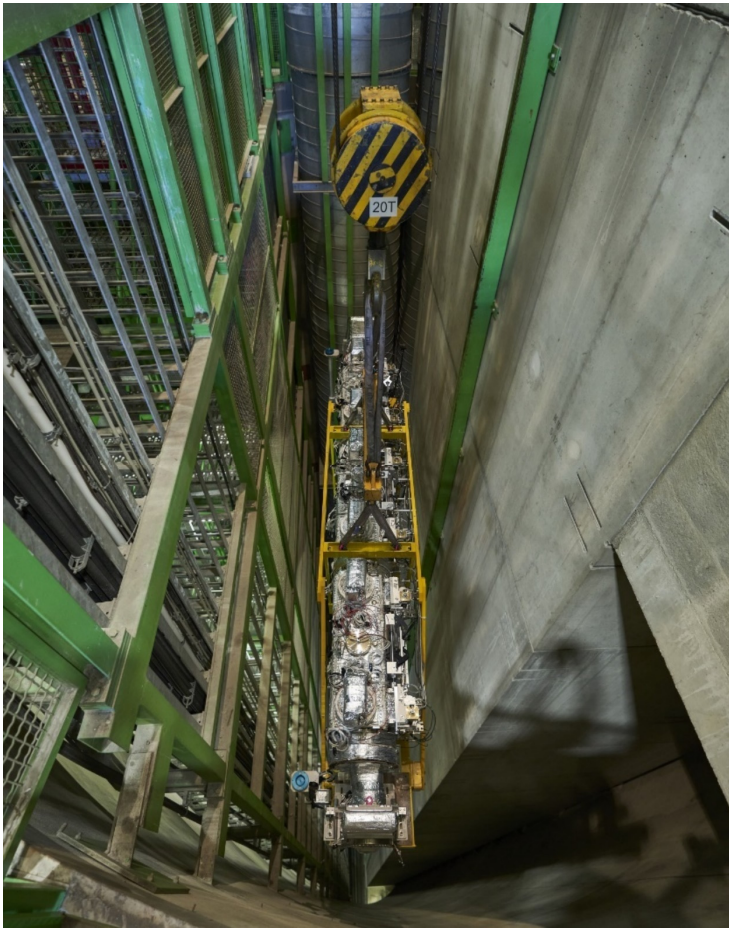


Fig. 17. TDIS lowered into the tunnel at Point 1.

- (4) The HV generators of both MKD and MKB (dumping and dilution kickers, respectively) need to be improved in reliability to reduce failure risk and reaction time.
- (5) An expected failure mode to the dilution kickers MKB, identified during Run2, could have a catastrophic consequence on the beam dump final absorber (TDE) if happening with the full HL-LHC beam. TDE itself has already shown various weaknesses and is unsuitable for safe operation for HL-LHC (and for the ultimate LHC beam, actually). Therefore, the project is preparing complete re-design of the TDE, which still requires further studies and investigations that are currently underway and prepares the option of a partial upgrade of the MKB system by adding an additional horizontal MKB kicker magnet.

3.8. *Beam instrumentation*

The HL-LHC operation modes with luminosity levelling and tighter control on the acceptable beam halo losses also imply improvements in the beam instrumentation for the HL-LHC exploitation era. The HL-LHC project therefore features the following novel diagnostic tools:

- Radiation hard Beam Position Monitor (BPM) designs for the new IT regions, see Figure 18;



Fig. 18. BPM prototype (body and insert) for the new IT regions.

- 3-dimensional bunch imaging from novel vertex;
- Laser Interferometer Beam Position Monitors for accurate beam position controls near the Crab Cavities.

In addition, the project studied and developed in preparation of future upgrade options a beam halo diagnostics based on Coronagraph technology and Gas Curtain beam profile monitors for measuring the beam overlap of the electron beam of a Hollow Electron Lens (HEL) and the circulating proton beam.

3.9. *Beam control*

In order to cope with the expected larger data volumes and harder radiation environments in the LHC tunnel, the HL-LHC includes a dedicated Controls Technologies work package, that looks after the development of modular and more radiation hard controls electronics and data distribution.

3.10. *Full remote alignment*

During the 2016 re-scoping exercise of the HL-LHC project, it was decided to de-scope the very large aperture MQYY quadrupole magnets, Q4 and Q5 in the high luminosity insertion regions, from the project baseline. The implied reduction in mechanical aperture was compensated by the introduction of a Fully Remote Alignment System (FRAS) that minimizes the radiation exposure of the survey team and thus allows more frequent alignment exercises during a given operation year. The system comprises of special support feet with remote controlled interfaces for adjustments and upgrades in the online survey monitors along the long straight sections in IR1 and IR5.

3.11. *Civil engineering and technical infrastructure*

To host all the new technical services and ancillaries for the new HL-LHC equipment (like power converters, new cryo-plant, cc amplifiers, etc...), the project needed to create new underground areas and surface buildings.

HL-LHC creates significant new infrastructures in LHC P1 (ATLAS) and P5 (CMS). They consist in each point of (see Figures 19 and 20):

- A large shaft of 9 m diameter, 65 m deep.



Fig. 19. Aerial view of the HL-LHC work site at Point 1.



Fig. 20. HL-LHC underground cavern at Point 5.

- New underground caverns and main technical galleries, URs, more than 300 m long, located next to the existing long straight sections of the LHC and located approximately 8 m higher than the existing tunnel. The main UR service tunnel has a distance of approximately 30 m from the existing LHC tunnel.
- Four new, smaller galleries (2 per Interaction Point) connecting the new HL-LHC cavern and galleries to the LHC tunnel. In total the new underground volume is 40,000 m³ in P1 and P5, each.
- Five new buildings for a surface of 6000 m² in a new dedicated area, of about 20,000 m².

Most of the new technical equipment will be hosted in the new underground structures which extend in total to about 1 km in length: the two new large (18 kW@4.2K – 2 kW@1.9K) helium refrigerators, electrical power converters with the magnet protection units, the cold powering system, the power amplifier for the SRF CC and all service equipment.

The contracts for the main construction were signed with two consortia (one for each point) in March 2018. The ground-breaking ceremony took place on 15 June 2018 in the presence of CERN Council delegates and local authorities. Construction of the shafts finished almost on time in 2018 and the cavern construction, underground excavation and lining could be finished almost on schedule, well before the LHC resumed operation after LS2 in 2022 (see Figure 1). To assure completion of HL-LHC excavation before beam commissioning for Run3 was the main goal of the “new plan” of HL civil engineering, devised in 2015, when it was clear that vibrations could have hampered LHC luminosity. This is “per se” a great achievement. A second great achievement is the technical success of the works, without serious short-falls and extra-cost (discounting of course the ones related to the unpredictable Covid-19 emergency). The surface construction works are also proceeded very well, with completion of all buildings by 2023 in spite of the Covid-19 related delays.

3.12. Electrical wires for beam-beam compensation: a last option for long-term HL-LHC consolidation

The long-range beam-beam interactions, which the LHC bunches experience in the long straight section at the unwanted parasitic beam encounters, can be

compensated with electrical wires, placed at well-chosen locations and at suitable distances from the circulating beams. While not being part of the HL-LHC baseline, such wires could offer a perspective for future performance improvements in the LHC and the HL-LHC project supports therefore the R&D activity for these devices within its baseline scope. In particular, the HL-LHC project has financed the construction and installation of 4 such devices (electrical wires impeded in the jaws of collimators) next to the experimental insertions at P1 and P5. The installation has been completed during LS1 and the arrangement has been further optimized during LS2 so that further operational experience and understanding can be gained during the upcoming LHC Run3 operation.

4. Performance, Plan and Cost

4.1. Performance

The performance of the HL-LHC, both in terms of peak and integrated luminosity, is reported in the plot of Figure 21. The plot assumes that the days for proton luminosity are increased after LS4 due to end of the ion program and, after LS5, for a decrease in MD (machine development) allocated time and in the numbers of technical stops.

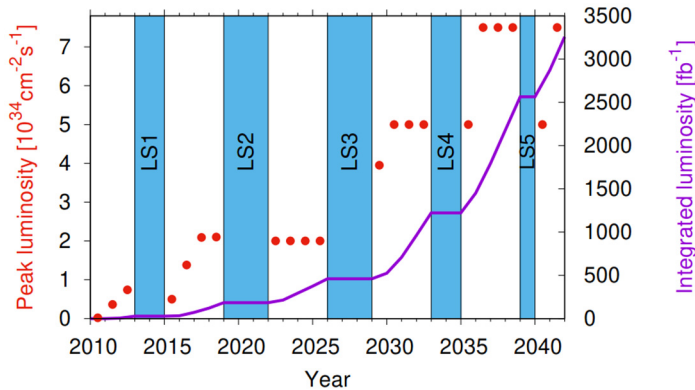


Fig. 21. Peak luminosity (red dots) and integrated luminosity (purple line) vs. time. With the hypothesis of pushing towards ultimate performance (7.5×10^{34}) after LS4, the goal of 3000 fb^{-1} can be reached by 2041, shortly after LS5, while the ultimate target of 4000 fb^{-1} would require a longer Run6 period that extends beyond 2041.

4.2. Time plan: main milestones

The global HL-LHC time plan is illustrated in Figure 1.

The plan is based on the following main technical milestones:

- 2014: Preliminary Design Report (PDR) - achieved
- 2015: End of Design Phase, issue of the first version of Technical Design Report (TDR) - achieved
- 2016: Re-baseline to face C.E. extra-cost. Issue of TDR_v0.1 with re-baseline integrated.
- 2017: Test main hardware: only partially achieved with the few outstanding tests planned for 2023.
- 2018: Test of Crab Cavity prototype in SPS (achieved) and first long Nb₃Sn prototype (achieved)
- 2019-2021: LS2 - DS collimators in P2 (ions). Low-Z collimators. Issue of TDR_v1.0 for construction: achieved
- 2019-2021: Construction and test of Magnet prototypes: achieved
- 2019-2025: Construction of main equipment for LS3
- 2023-2025: Installation and test of Inner Triplet String
- 2026-2028: LS3 – Main installation and commissioning.

From the managerial point of view the main achieved milestones have been:

- 2010: Set up of the project by CERN as Design Study under the Accelerator and Technical Directorate and submission of the FP7-HiLumi LHC Design Study application to EC with 20 partners.
- 2011: Approval and start of FP7-HiLumi LHC DS
- 2013: LHC luminosity upgrade declared as priority project by the European Strategy for Particle Physics (CERN Council in Brussels May 30); HL-LHC kick-off meeting as construction project in Daresbury (UK) on 11th of November. Insertion of most budget for HL-LHC in the CERN Medium Term Plan (MTP).
- 2015: End of FP7-HiLumi LHC DS; 1st Cost & Schedule Review. Insertion of all budgets of HL-LHC in the MTP with indication for beyond (Long term plan)
- 2016: Approval of the HL-LHC with entire budget until 2026 by CERN Council in June session. HL-LHC as EU landmark in the ESFRI roadmap. 2nd C&S Review.

- 2017-19: Securing most of the in-kind contribution outside CERN MS: (USA-CN, JP, CA). USA branch of the project (US HL-LHC-AUP) gets CD1 and CD2.
- 2018: Adjudication of C.E. main contracts and ground-breaking ceremony (15 June 2018)
- 2019: First HL-LHC equipment installed in the LHC tunnel (TANB in P8).
- 2020: First two IT Quadrupole magnets for Q1 (From USA) successfully tested for operation: CD3 (green light to full construction) for the US-HL-LHC-AUP.
- 2022: First IT Quadrupole magnets for Q2 (from CERN) successfully tested, confirming all design choices for the Q2 design.

4.3. Cost

At the time of writing, the Cost-to-Completion of the full HL-LHC project amounts to about 1,040.4 MCHF of material budget, plus ca. 99 MCHF for HL-LHC spare parts under the HL-LHC CONS budget. The total Cost-to-completion includes in-kind contributions from external institutes, for a core value of 93.7 MCHF. The Cost-to-Completion estimate at the time of writing represents ca. 91.4 MCHF more than the initial cost at the end of 2014, as presented at the first Cost & Schedule Review (C&SR) in March 2015. The 91.4 MCHF are split in 66.6 MCHF of real extra-cost, resulting from a rigorous and continuous cost optimization exercise and the inflation hitting all markets in 2022, and 24.8 MCHF of increased scope, i.e., new equipment, partially obtained as in-kind contribution. In addition to the above material budget, about 2200 FTE-y of CERN staff are accounted for the project, corresponding approximately to 470 MCHF of labour cost. The 1,040.4 MCHF include also approximately 82 MCHF of budget for external, associated personnel, which in CERN's budgeting rules is imputed to "material" budget codes.

Table 3 also gives the cost of the HL-LHC consolidation, i.e., the cost of the totality of the items that are not entering directly into construction but are necessary as spares for continued LHC operation beyond Long Shutdown 3, independently of HL-LHC; for example, the replacement of ageing equipment due to radiation damage to electronics. The consolidation cost of 99.0 MCHF is not incorporated in the direct cost of the HL construction project. Together, HL construction and HL consolidation bring the total budget at completion to

1,139.4 MCHF at the time of writing. The budget breakdown is summarized in Table 3, as presented to the 6th Cost and Schedule Review in 2022. For completeness, the evaluation of the overall cost of HL-LHC should include the cost of personnel working for the project in all contributing institutes others than CERN. However, this would require an impractical normalization of the different accounting of personnel cost, overhead policies, and budget structure in each institute – which has not been carried out in detail. Estimating the personnel in-kind budgetary effort as approximately equal to the in-kind material budget contribution yields a personnel contribution of around 440 FTE-y, which at CERN average cost would be approximately equivalent to 95 MCHF.

Table 3. Breakdown of the total Cost-to-Completion of the HL-LHC project, see text for details.

HL-LHC Construction	M CHF
Material (including Money-for-Personnel)	1,040.4
CERN Staff (2271 FTE-year)	472.5
Total HL Construction	1448.0
HL-LHC Consolidation	99.0
HL-LHC Grand Total	1611.9

At the C&SR#5 in November 2021, additional costs for an amount of 14.2 MCHF, related to market conditions, covid related extra cost, performance and schedule risk mitigation, as well as added scopes, were presented to the reviewers and endorsed. The budget required to cover these costs has been requested to the management via the Medium-Term Plan 2022-2027. Market conditions after Covid and the Russian attack on Ukraine impacted the overall project budget, requiring the addition of 51.5 MCHF to cover extra costs of two large cryogenic contracts and other tangible cost changes, partially mitigated by descopings from the insourced Russian contribution.

Figure 22 shows the accumulated Planned budget expenditure versus time, together with the Earned Value and Actual Cost of the material budget, as seen in January 2023. Actual Cost also includes all already committed budget. At the time of writing, about 51% of the budget has been spent, while about 53% of the planned work has been executed - or value earned, in the language of Earned Value Management. The Covid-19 crisis introduced a delay estimated

to 6.5 months. In 2021, the Long Shutdown 3 was rescheduled to 2026, thus allowing to reabsorb the delay and some performance limitations in a new baseline, which results shifted by 14.2-month with respect to the plan approved at the Cost & Schedule review 2019. The baseline PV shown in Figure 22 was presented to C&SR 2022.

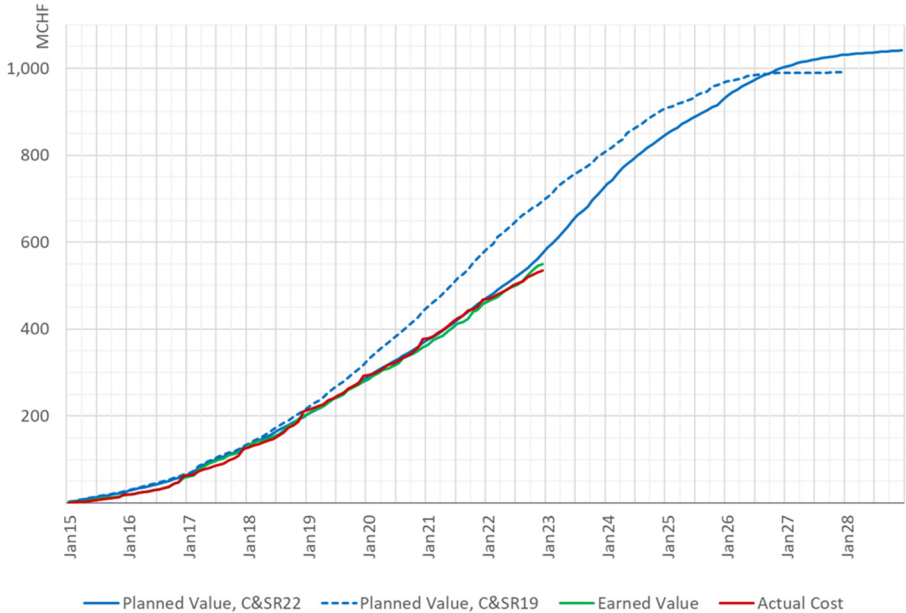


Fig. 22. EVM curves with total cumulative budget, earned value and actual cost, the latter including commitments.

It is worth remembering that according to CERN management rules, the project has been approved without risk contingency, nor managerial reserve, nor price escalation reserve or any other overhead. Therefore, any added cost must be justified and eventually approved by the CERN management, usually after scrutiny and presentation to the Cost & Schedule Review panel. At the C&SR#4 in November 2019, a first comprehensive monetary evaluation of the risk was presented. Based on a detailed risk matrix with vulnerability and impact index assigned to each single item, the extra-cost risk scale was quantified to be in the range of 20-80 MCHF, with the most probable value at 48 MCHF. This led the CERN management to put 50 MCHF of contingency for

HL-LHC in the MTP approved in 2020. At the time of writing, with the additional budget and an increased risk stemming from the volatile market situation, risk is evaluated to 68 MCHF.

5. International Collaboration and Project Governance

5.1. The international collaboration

5.1.1. The initial R&D and design study

The contribution of the international collaboration for the HL-LHC is even more critical than for LHC. The project heavily relied on the US-DOE-Conductor Development Program, launched in 1998, which was instrumental for improving Nb₃Sn to accelerator quality [18]. The other US-DOE program, LARP (LHC Accelerator Research Program), has been fundamental for HL-LHC: the fifteen year-long LARP program was very beneficial for the IT Quadrupole R&D, as well as for other equipment (e.g., Crab cavities) and studies for the upgrade. The two US programs helped to bolster the credibility of the project when it was launched in 2010. At the time, CERN was just starting Nb₃Sn R&D, and the LARP magnet program provided the necessary proof-of-principle of Nb₃Sn magnet technology.

The EC-FP7 Design Study HiLumi LHC was allowed in 2011 to federate several European Laboratories for the initial studies, as well as KEK-Japan and BINP-Russia. It is worth noticing that HiLumi LHC is the nickname to indicate the part of HL-LHC under the FP7 umbrella (six of the 18 work packages: management and technical coordination, optics and beam performance, magnets, crab cavity, collimators, cold powering) even if in practice has become a popular name to indicate the full project.

Figure 23 shows a summary of all R&D International programs that have supported the LHC upgrade, with the various parallel branches converging to the final HL-LHC target.

Before the set-up of the HL-LHC project, the US-LARP and Japan-KEK collaborations were monitored via bilateral “good-will” agreements. A formal FP7-HiLumi Design Study consortium was implemented during the period 2011-2015, with a Collaboration Board and the governing rules of EC funded programs.

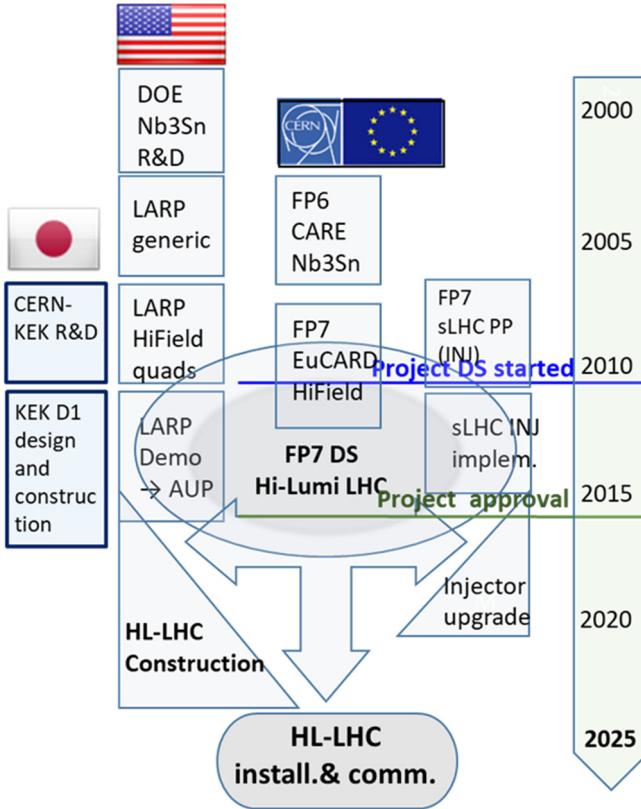


Fig. 23. The International Collaboration set up for the study and various programs toward the High Luminosity LHC.

5.1.2. *Present structure of the international collaborations, HL-LHC MoU and in-kind contributions*

Following the first approval of 2013 and with accelerated pace after the final full approval of 2016, various institutes have joined the project to contribute in-kind. The end of the FP7-HiLumi Consortium, and especially the start of the new construction phase, has required a revision of the governance of the international collaboration.

The HL-LHC Collaboration Board, HLCB, is composed by one member from each Institution that has signed the High Luminosity LHC Memorandum of Understanding (HLMoU). The HLCB membership is possible at two

different levels. Full members of the HLCB are, besides CERN, all institutions providing equipment as in-kind contributions (regardless of their value). Institutes participating in the project with regards to design, studies and other types of support not entailing a cost of hardware, i.e., not covering items in the HL-LHC material budget (CORE value in the language of LHC experiments), are observer members of the HLCB. Only full members have a voting right. However, given the nature of consultant body, supervising all external contributions and advising CERN management on the trend of the project, the

Country	Institutions	Contributions	Logos
	INFN Milano - LASA	High-order orbit corrector magnets	
	INFN Genoa	Separation dipole D2 magnets	
	INFN Ferrara	Crystals	
	CIEMAT	MCBXF nested orbit corrector magnets	
	Uppsala University	Cold testing of superconducting orbit corrector magnets and crab cavities DFHM and DFHX cold boxes	
	Cockcroft Institute - ASTeC & Lancaster University	DQW crab cavities cryostats	
	Royal Holloway University & University of Oxford	Beam Instrumentation EO-BPM	
	University of Liverpool	Beam-gas curtain	
	University of Manchester & University of Dundee	Laser Engineered Surface Structures (LESS)	
	University of Southampton	DFM and DFHX cold boxes	
	PAEC	ATLAS JTT plug 1 shielding	

Fig. 24a. Table of collaborators with in-kind contributions from CERN Member States and Associate Members.













Country	Institutions	Contributions	Logos	
	TRIUMF	RFD crab cavities cryostats		
	IHEP CAS	MCBRD orbit corrector magnets		
	KEK	Separation dipole D1 cold masses		
	BNL	Nb3Sn low-beta triplet quadrupoles Q1/Q3		
	FNAL (leader)			
	LBNL	RFD dressed crab cavities		
	SLAC			

Fig. 24b. Table of Collaborators outside CERN Member States with in-kind contributions.

HLCB statements are approved by consensus without voting. The list of countries and Institutions with full memberships of the HLCB is reported in Figure 24a for countries that are CERN member states, and in Figure 24b for Countries that are non-member states (NMS). The mechanism of accounting for in-kind contributions is different in both cases. When an Institute picks up an equipment for in-kind contribution, its value of the corresponding CERN Material budget value is taken as reference to determine the value of the in-kind contribution to the project (like in the LHC experiments, where it is called CORE value). However, for Institutions of a member state, CERN agrees to pay, either in cash or in material supply, half of the value: the in-kind contribution value is then half of the CERN material budget figure. This is done in order to encourage in-kind contributions from member-states, since these they are already supporting CERN via their annual contribution. This way, a considerable number of additional contributions to HL-LHC, beyond the standard budget contribution of the member states to CERN, has been collected. In EU countries, the in-kind contributions amount to a value of ca. 13 MCHF, i.e., European Institutes are directly responsible for manufacturing equipment worth 26 MCHF in the HL-LHC Cost to Completion budget. The total value of all in-kind contributions amounts to ca. 93.7 MCHF in the HL-LHC Cost to Completion budget. This is big success for a CERN-based accelerator. It is also worth considering that in-kind contributions for HL-LHC are important

not only for their “CORE” value. The staff deployed by the collaborating institute is indeed a critical and necessary addition to the CERN staff for the project, both numerically, as well as in terms of quality and skill terms.

5.2. Project structure and governance

The HL-LHC project is organised in four main offices:

- The Budget and Schedule Office that looks after the overall budget and schedule
- The Collaborations Office that looks after the external collaborations
- The Procurement, Baseline Documentation and Quality Assurance and Risk Office
- The Integration and Installation Office.

In addition to these four main offices, the project features a Communication and Outreach office and a Safety office. Figure 25 illustrates the HL-LHC Project Office structure and illustrates the main links to CERN groups and entities.

The technical work is organised into 19 work packages (WP) that are listed in Figure 26. The first six work packages, WP1 to WP6a, were part of the FP7

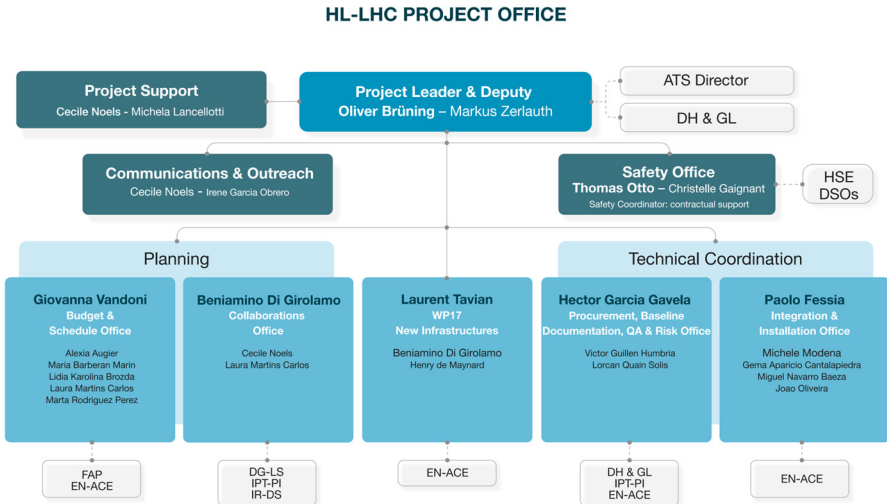


Fig. 25. The HL-LHC Project Office.

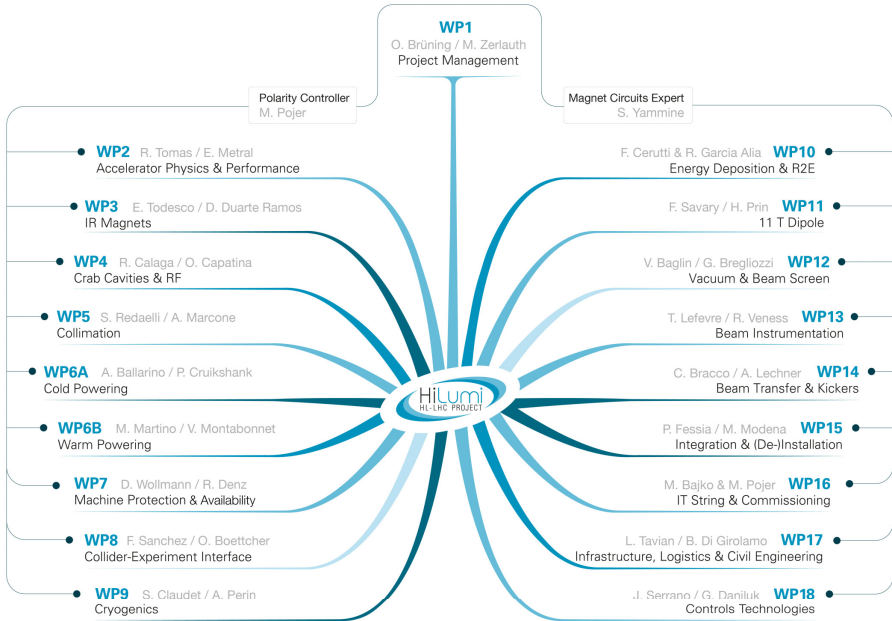


Fig. 26. The HL-LHC work package structure.

Design Study. A ‘Polarity Controller’ and a ‘Magnet Circuits Expert’ ensure the integrity and conformity of the final magnet powering circuits.

Work package 17 has a special role in the project office and is the only HL-LHC work package that is explicitly represented in the HL-LHC Project Office. WP17 looks after the civil engineering work and the construction of the new technical infrastructures for the HL-LHC. It has a direct link with the CERN SCE department that is following the civil engineering contracts for the HL-LHC project.

The Budget & Schedule Office and the Collaborations Office use the Project Steering Meetings (PSM) to interface and monitor the budget and schedule progress of each work package and to establish the link with the associated Departments and Groups at CERN. The regularity of the meetings varies between work packages. But overall, the project features on average ca. two PSM per week. The Procurement, Baseline Documentation and QA & Risk Office and the Integration & Installation Office use the Technical Coordination Committee (TCC) to coordinate their work across all the HL-LHC

work packages and to disseminate the technical information to the CERN Departments and Groups. The project features on average one TCC meeting every two weeks.

In addition to the PSM and TCC meetings, the Project Office interfaces with the upgrade coordinators of the experiments through the Coordination Group and with the SCE Department of CERN through a dedicated SCE Steering committee to follow-up on HL-LHC related civil engineering work.

The HL-LHC project reports to the Director of the Accelerators and Technology Sector and meets regularly with the spokespersons of the experiments and the CERN management, Directors and department heads, through the HL-LHC Executive Committee that is chaired by the ATS Director. The CERN management regularly consults the CERN Machine Advisory Committee (CMAC), at least once per year, and organizes an external Cost & Schedule Review approximately every 12 months in order to evaluate the project progress and to generate the reporting to the CERN Council. Figure 27 illustrates this line of reporting with the CERN management and lists the interfaces of the HL-LHC management with key groups and bodies at CERN [light boxes on the right]. The HL-LHC project governs the international collaborations through dedicated Steering Committees for each collaboration

INTERFACES WITH COMMITTEES & LINKS

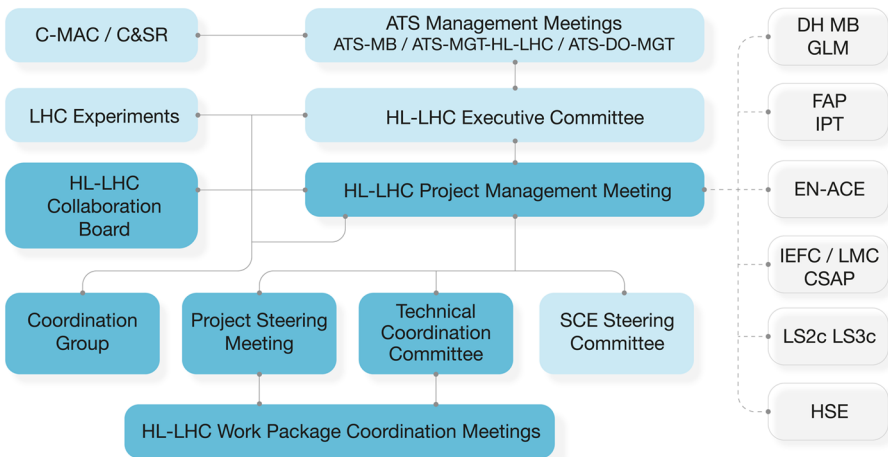


Fig. 27. The HL-LHC interfaces with committees and other CERN units.

and through a Collaboration Board, that involves one representative from each collaboration and meets on an annual basis.

Figure 27 summarizes the main interfaces of the HL-LHC project with Committees and lists links to the key CERN structures.

References

1. European Strategy for Particle Physics, adopted by the CERN Council at a special session at ministerial level in Lisbon in 2006.
<http://cern.ch/council/en/EuropeanStrategy/ESParticlePhysics.html>.
2. European Strategy Forum for Research Infrastructures, ESFRI,
<http://ec.europa.eu/research/esfri>.
3. The European Strategy for Particle Physics Update 2013, CERN-Council-S/106, adopted at a special session in the Brussels on 30 May 2013.
<http://cern.ch/council/en/EuropeanStrategy/ESParticlePhysics.html>.
4. Building for Discovery: Strategic Plan for U.S. Particle Physics in the Global Context, in <http://science.energy.gov/hep/hepap/reports/>.
5. Lucio Rossi, LHC Upgrade Plans: Options and Strategy, *Proceedings of IPAC2011*, San Sebastián, Spain, 01/09/2011, pp. 908-912.
6. Lucio Rossi and Oliver Brüning, High Luminosity Large Hadron Collider - A description for the European Strategy Preparatory Group, CERN-ATS-2012-236.
7. The High-Luminosity LHC (HL-LHC) Project, CERN/SPC/1068, CERN/FC/6014, CERN/3255, 30 May 2016.
8. Commission presents its evaluation of the 7th Framework Programme for Research, 7th Framework Programme for Research, MEMO/16/146, 25 January 2016.
9. EUROPEAN COMMISSION – 7th Framework Programme for Research – EVALUATION SUMMARY REPORT: HiLumi LHC_284404.
10. ECFA High Luminosity LHC Experiments Workshops – 2013 and 2014,
<https://indico.cern.ch/event/252045/> and <https://indico.cern.ch/event/315626/>.
11. H. Damerou et al., Upgrade Plans for the LHC Injector Complex, *Proceedings of IPAC2012*, New Orleans, Louisiana, USA, pp. 1010-1014.
12. H. Damerou et al., RF Manipulations for Higher Brightness LHC-Type Beams, CERN, Geneva, Switzerland, Rep. CERN-ACC-2013-0210, 2013,
<https://cds.cern.ch/record/1595719>.
13. J. Strait et al., Towards a New LHC Interaction Region Design for a Luminosity Upgrade, *Proceedings of the 2003 Particle Accelerator Conference (PAC2003)*, Portland, OR, USA, 12-16 May 2003, Vol. 1, pp. 42-44; also available as: CERN-LHC-Project Report 643.
14. R. van Weldon, CERN, private communication.
15. R. M. Scanlan, *IEEE Trans. Appl. Supercond.* 11, 2150 (2001).

16. S. Farthoukh et al., LHC Configuration and Operational Scenario for Run 3, CERN-ACC-2021-0007, 12 November 2021.
17. High Luminosity Large Hadron Collider (HL-LHC): Technical design report, I. Béjar Alonso I. Béjar Alonso, O. Brüning, P. Fessia, M. Lamont, L. Rossi, L. Taviani, M. Zerlauth, *CERN Yellow Reports: Monographs*, CERN-2020-010, CERN, Geneva, 2020, 10.23731/CYRM-2020-0010.
18. N. Mokhov, I. Rakhno, J. Kerby and J. Strait, Protecting LHC IP1/IP5 Components Against Radiation Resulting from Colliding Beam Interactions, CERN-LHC-Project-Report-633; FERMILAB-FN-0732, April 2003.

This page intentionally left blank

Chapter 2

The Physics Landscape of the High Luminosity LHC

M. Mangano

CERN, TH Department, Genève 23, CH-1211, Switzerland

This contribution reviews the physics potential of the HL-LHC experimental programme. The first 10 years of the LHC has demonstrated the vast open range of opportunities for measurements and discoveries of new phenomena. Starting from the results of the first two runs of the LHC, extensive experimental and theoretical studies have now defined a broad set of goals for the future high-luminosity phase of the project, reviewed here. The precision measurement of the Higgs boson properties, which has greatly expanded our knowledge today, represents the primary guaranteed deliverable. This target is complemented by a vast array of additional measurements, ranging from the continued search for phenomena beyond the Standard Model, to the study of the Standard Model dynamics and parameters, flavour phenomena, and the study of matter at high density and temperature.

1. Introduction

The first 10 years of data collection and analysis by the LHC experiments delivered three key takeaways: (i) the discovery^{1,2} of the Higgs boson,³⁻⁵ (ii) the lack of evidence for particles and interactions beyond those described by the Standard Model (SM)⁶⁻⁸ and (iii) the excellent corroboration between the data and the theoretical modeling of proton-proton (pp) collisions at center of mass energies ranging between $\sqrt{S} = 2.76$ and 13 TeV. Each of these points contributes to sharpening the definition of the landscape for the future of the LHC programme.

This is an open access article published by World Scientific Publishing Company. It is distributed under the terms of the Creative Commons Attribution 4.0 (CC BY) License.

The prospects for LHC physics with a dataset of 3000 fb^{-1} had been outlined in the early 2000's, in a series of studies collected in Ref. [9]. The abundance of physics results obtained during the first two LHC runs, the experience gained by the experiments with the operation and the performance of their detectors, and the immense work done to characterize the features of their future high-luminosity upgrades, contributed to a recent thorough assessment of the HL-LHC physics potential.¹⁰ The five Working Group reports contained in that document cover all areas of LHC research, from the SM¹¹ and the Higgs,¹² to searches for new physics beyond the SM¹³ (BSM), flavour,¹⁴ and studies of QCD matter at high densities and temperature.¹⁵ These documents provide the most comprehensive and up-to-date overview of the key role to be played by the HL-LHC in shaping the future progress of high-energy physics, which we will briefly summarize here.

The observation of the Higgs boson provides a compelling and concrete case to define and quantify the goals and targets of the long-term LHC exploration. Within the SM, the value of the Higgs mass allows to predict uniquely its production and decay properties. A large number of decay final states is accessible for exploration at the LHC, each of them sensitive, in different ways, to the possible effects of BSM physics. One of the primary goals of the future LHC programme is therefore to greatly extend the range and precision of Higgs studies, improving the accuracy of the measurements, searching for yet unobserved decay modes, and probing in more detail the mechanism of electroweak symmetry breaking (EWSB). Precision targets in the range of few percent provide a concrete reference to benchmark the performance of the future detector and accelerator improvements against.

The expectation that the LHC should find evidence for BSM phenomena is justified by decades of theoretical work on the foundations of the SM and its conceptual shortcomings, as well as on possible interpretations of experimental facts that cannot be explained within the SM, such as dark matter (DM), the baryon asymmetry of the universe and neutrino masses. The lack of BSM signals from the first runs of the LHC does not dampen that expectation. It just constrains the set of suitable BSM models, possibly reducing the appeal of some frameworks, as they would now require a finer tuning of their parameters to remain viable. The search for BSM signals therefore remains a top priority for the LHC. Two directions emerge: searching for particles of higher mass, and searching for final states that are harder to

distinguish from the SM backgrounds. The increase in energy from 13 to 14 TeV will mildly extend the LHC search potential at high mass, but the higher statistics will push it towards the kinematic limit, and, perhaps more importantly, will allow to pursue the more *stealthy* manifestations of new physics. High luminosity will also allow to exploit the potential for very precise measurements, building on the great progress that has taken place over the last 10 years.

In addition to the Higgs discovery, and to the tighter constraints on the existence of BSM phenomena, the first years of LHC physics have proven two facts, which corroborate the reliability of the projections for the physics potential of the HL-LHC phase. On one side, the performance of the detectors matches, and often surpasses, the expectations. This is particularly true of the ability to operate in a regime of very high pile-up, a critical test for effective data taking in the environment expected with the HL-LHC. On the other, the theoretical modelling of the properties of pp collisions at these energies has proven very accurate. Dedicated precise measurements of SM processes and cross sections have shown that data and theory agree over a broad dynamical range of phenomena, including the very complex final states with mixtures of gauge bosons, heavy quarks, and multijets, which characterize BSM processes. Where the theoretical predictions are limited in precision by the lack of higher-order calculations or by uncertainties in the knowledge of the quark and gluon content of the proton (the so-called parton distribution functions, PDFs), great progress is taking place to match the precision needs, by improving the calculations, and by using the LHC data themselves, to validate the theoretical progress and to refine the knowledge of PDFs. This progress will continue with more data and more powerful theoretical tools. For the specific case of PDFs, further insight could also arise from a programme of ep collisions, as proposed by the LHeC project.¹⁶ Its results would surely fulfill, and even exceed, the precision requirements of the HL-LHC.

1.1. Status and prospects of Higgs studies

Since the discovery of the Higgs in July 2012, it has since been studied in greater detail, using the additional statistics of Run 2, and continuously refining the experimental analyses. There is no reasonable doubt by now that this particle is a scalar,^{17,18} consistent with being an excitation of the

Higgs field, responsible for the breaking of the $SU(2) \times U(1)$ electroweak (EW) symmetry, and for the masses of the W and Z bosons, as well as of the known quarks and leptons. While the simplest theoretical model describing the Higgs boson is what is built into the SM itself, it is well known that there are several alternative ‘‘Higgs mechanisms’’. A Higgs mechanism is defined by the spectrum of the Higgs states, and by the dynamics that leads the Higgs field to acquire a non-zero vacuum expectation value, resulting in the EWSB. In the SM version of the Higgs mechanism,⁷ there is a single complex $SU(2)$ doublet, corresponding to four real degrees of freedom. The symmetry breaking is driven by the minimization of the mexican-hat-shaped potential, described by two parameters associated to the mass of the Higgs boson and its expectation value. Three of the four degrees of freedom become the longitudinal modes of the W^+ , W^- and Z^0 massive vector bosons, and the fourth is left as *the* SM Higgs boson.

Alternatives to the SM Higgs mechanism include theories with a more extended spectrum and/or with a different EWSB dynamics. For example, several theories, most notably supersymmetric models, have two doublets, instead of one, leading to a total of three neutral and one charged scalar particles. Other extensions include the possibility of further doublets, or of different $SU(2)$ representations, including singlets, or vectors, in which case doubly-charged Higgs fields could also appear. In other scenarios, EWSB may arise from an underlying strong dynamics, the Higgs field emerging as a composite particle, a bound state of elementary fermions confined together (for a review see e.g. Ref. [19]). In some theories with extra space dimensions, the Higgs scalar could be a component of vector fields living in higher dimensions.

In the SM, the production and decay properties of the Higgs boson are completely determined by its mass and by the masses of the SM particles. In BSM theories such as those described above, those properties can change, whether because of a richer Higgs spectrum, or of a different EWSB dynamics, or because the other new BSM particles can influence the Higgs couplings: additional decay channels can be open, or new intermediate virtual states can modify the loop-mediated Higgs effective couplings, such as those to gluons and photons.

The dominant production and decay channels of the Higgs have all been observed with a significance exceeding 5 standard deviations.^{20,21} These measurements lead to a quantitative agreement with the SM predictions at level of

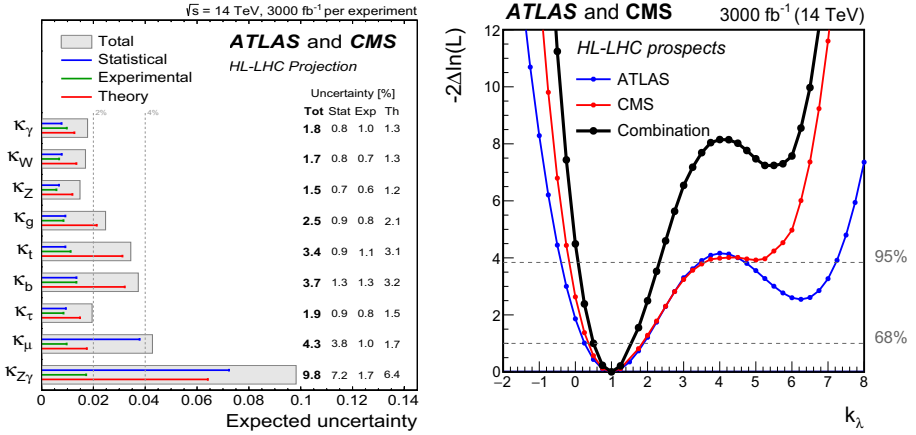


Fig. 1. HL-LHC projections for the precision of the Higgs couplings measurements (left) and for the significance of the Higgs self-coupling extraction (right) (for details see Ref. [12]).

$\sim 10\%$, which can still be greatly improved with additional statistics, leaving plenty of room for possible surprises. The latest HL-LHC projections for the main Higgs couplings, documented in the recent report,¹² are summarized in the left plot of Figure 1. The κ_X quantities represent the ratios of the measured and the SM values of the Higgs coupling to the particle X . For example, κ_Z refers to the coupling of the Higgs to the Z boson, which determines the decay $H \rightarrow ZZ \rightarrow 4$ leptons; κ_t refers to the coupling with the top quark, which can be measured in the process $pp \rightarrow t\bar{t}H$, where the Higgs boson is emitted from the top or antitop quarks. Deviations from the SM behaviour would be signalled by $\kappa_X \neq 1$, and the horizontal bars in the plot show the precision with which the various κ will be measured, including the three sources of systematics: purely experimental, statistical, and the systematics arising from the uncertainties in the theoretical prediction of the various production rates, due to higher-order corrections or PDF uncertainties. The expected precision, e.g. better than 2% for the couplings to the EW gauge bosons, exceeds all earlier estimates, reflecting the fantastic performance of the experiments and the experience gained in operations with a high pile-up environment. For most cases, theoretical uncertainties dominate the systematics, a limitation that will likely be overcome with the hard work of the theoretical community. The projected experimental systematics shown in Figure 1 are never a dominating factor, indicating that each additional ab^{-1} of statistics is well justified

and highly desirable. As shown in the figure, this is particularly true of the rare Higgs final states that have not been seen so far, such as $\mu^+\mu^-$ and $Z\gamma$, which will likely be discovered only during the HL-LHC phase. The HL-LHC statistics, furthermore, will bring us closer to a measurement of the extremely challenging $H \rightarrow c\bar{c}$ decay, and will push the sensitivity to possible flavour-changing couplings of the Higgs (e.g. $H \rightarrow e\mu$, $H \rightarrow \tau\mu$, $t \rightarrow Hc$), whose detection would signal new physics. A large number of even more exotic Higgs decays, which are signatures of BSM phenomena, has been proposed for exploration.²²

One of the key properties of the Higgs boson, which still needs experimental validation, is its self-coupling. Its strength, uniquely specified within the SM, probes the global shape of the Higgs potential, and could expose the existence of BSM Higgs interactions. In turn, these could shed light on the nature of the cosmological phase transition, which took place as the universe's temperature cooled down below the EW scale, settling the Higgs field in the ground state that we have today. The existence of a strong first order phase transition (SFOPT), instead of the mild cross-over predicted by the SM, could leave imprints in a stochastic gravitational wave background, within the reach of a next generation of space-based interferometers.

The prospects for the Higgs self-coupling measurement at the HL-LHC are discussed in Ref. [12], and summarized in the right plot of Figure 1. As before, κ_λ is the ratio of the measured value of the self-coupling, relative to its SM expectation. The y-axis shows the number of standard deviations with which a given value of κ_λ can be excluded (expressed in terms of confidence levels at the 68% and 95% points on the right side of the plot). The minimum at $\kappa_\lambda \sim 5$ reflects a negative interference among different contributions to the Higgs-pair production cross section, which reduce the rate and the statistical power of the measurement. The black line represents the combination of the individual ATLAS and CMS projections. The significant improvement arising from the combination confirms the crucial role played for this fundamental measurement by the integrated luminosity. The precision around the SM value $\kappa_\lambda = 1$, at the 68% of confidence level (CL), is about $\pm 50\%$, a significant improvement over earlier estimates. This will give sensitivity to a large fraction of the parameter space characteristic of BSM models with a SFOPT, complementing possible evidence emerging from the direct creation of the new scalar particles present in those theories.¹²

1.2. Prospects for BSM searches

Physicists have long anticipated the existence of new phenomena at the TeV scale, in order to address issues like the existence of DM and the hierarchy problem, namely the extremely unnatural fine tuning of the Higgs bare mass, necessary to justify the smallness of the Higgs mass with respect to the Planck scale. The LHC experiments have found no evidence so far for such new phenomena, setting limits that often well exceed the TeV scale. But the search for hints of new phenomena remains one of the top priorities of the future HL-LHC programme, and an extensive study of prospects is documented in Ref. [13]. Following are some indicative examples.

The HL-LHC statistics will benefit BSM searches in at least three different ways. Firstly, as already discussed above, more precise measurements of the Higgs boson and SM processes will increase the sensitivity to possible small deviations. Secondly, the increase in energy from 13 to 14 TeV will complement the increase in luminosity, pushing to the upper edge the mass reach for new very heavy particles. Finally, greater statistics will allow to probe the existence of new phenomena that, while being easily accessible in terms of available energy, tend to be very elusive, either because of very small couplings (low production rates or small decay branching ratios), or because of features that make them hard to single out from the large backgrounds.

These features are shown by the examples of Figure 2. The left plot shows the HL-LHC sensitivity to a new W' gauge boson decaying to electrons or

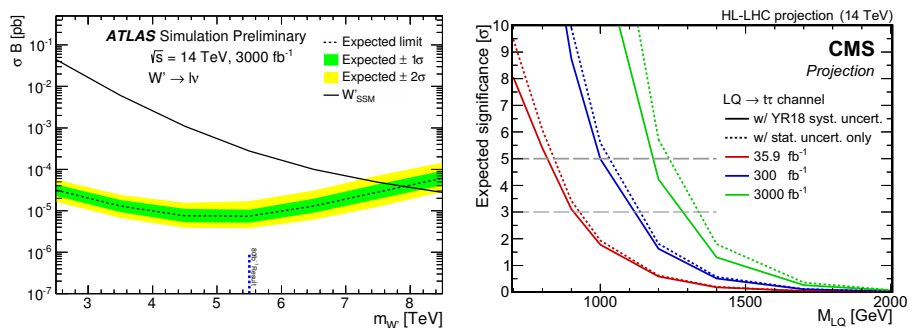


Fig. 2. Left: 95% CL upper limit on the production times decay rate of new W' gauge bosons decaying to $\ell\nu$ ($\ell = e, \mu$). The blue marker shows the current mass limit from 80 fb⁻¹ of Run 2 data. Right: signal significance for the observation of a possible leptoquark (LQ), decaying to top quarks and tau leptons. From Ref. [13].

muons. The dotted line gives the 95% CL limit that can be set on the total production rate (cross sections (σ) times branching ratio (B) for the decay to leptons), as a function of the new W' mass. The green and yellow bands represent the uncertainty in this projection, based on statistical and systematic effects, at a CL of 1 and 2 sigma (68 and 95%), respectively. The interpretation of these limits in terms of models of new physics depends on the specific prediction for $\sigma \times B$ arising in a specific BSM theory. As an example, the black line gives the $\sigma \times B$ rate of a W' coupled with the same strength as the SM W boson. The mass exclusion increases from today's ~ 5.5 TeV (the blue marker) to almost 8 TeV, a 50% increase. A similar relative increase is foreseen in the search for leptoquarks (LQs) decaying with branching ratio $B = 1$ to a τ lepton and a top quark, as shown by the right plot in Figure 2. Here the production proceeds via the strong interaction, and different models are only characterized by the different LQ mass. The three sets of lines correspond to the number of standard deviations that could arise, for a given M_{LQ} , with different amounts of integrated luminosities. Solid (dotted) lines refer to the consideration of the full set (statistical only) of uncertainties.

If we focus instead on the increase in sensitivity at a fixed mass value, e.g. for a possible W' at 5.5 TeV, the left plot shows that the HL-LHC could probe a W' with a production rate about 50 times smaller than today's reach. As far as theory is concerned, the search for very weakly coupled particles is as significant as that of very heavy ones, and, for this, the increase in luminosity is typically more effective than the increase in beam energy!

Examples of elusive signatures that could be exposed by the HL-LHC are given in Figure 3. On the left, we show the prospects for the search of the supersymmetric partners of the Higgs and weak gauge bosons (generically labeled as gauginos, $\tilde{\chi}$), in regions of parameter space where the small mass differences lead to difficult signatures. The study considers associated production of pairs of the lightest ($\tilde{\chi}_1^0$) and next-to-lightest ($\tilde{\chi}_2^0$) neutral gauginos, and of the lightest charged gauginos ($\tilde{\chi}_1^\pm$). For mass differences $\Delta m(\tilde{\chi}_1^\pm, \tilde{\chi}_1^0)$ and $\Delta m(\tilde{\chi}_2^0, \tilde{\chi}_1^0)$ above few hundred MeV, the decays considered include, for example, $\tilde{\chi}_1^\pm \rightarrow \tilde{\chi}_1^0 \ell^\pm \nu$ and $\tilde{\chi}_2^0 \rightarrow \tilde{\chi}_1^0 \ell^+ \ell^-$. These lead to leptons with small momentum ("soft leptons"). For smaller mass splittings, down to the pion mass, the searches use $\tilde{\chi}_1^\pm \rightarrow \tilde{\chi}_1^0 \pi^\pm$ decays, where the charged tracks left by the long-lived $\tilde{\chi}_1^\pm$ cross only the first tracking layers, before its decay to the undetectable $\tilde{\chi}_1^0$ and soft pion ("disappearing tracks"). The corresponding

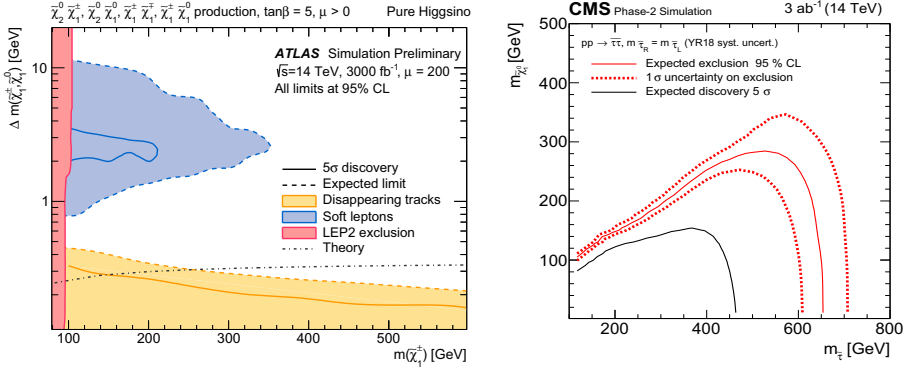


Fig. 3. Exclusion and discovery reach for elusive, weakly interacting supersymmetric particles. Left: the fermionic partners of gauge and Higgs bosons, in the region of parameters with $O(\text{GeV})$ mass differences. Right: the partner of the tau lepton ($\tilde{\tau}$). From Ref. [13].

discovery ranges (exclusion limits) are shown by the blue and yellow regions delimited by the solid (dashed) lines. The line labeled as “theory” reflects the mass difference expected in a class of models with small mass splittings. On the right, we show the sensitivity to the discovery (black solid line) or to the exclusion (red solid line, with $\pm 1\sigma$ uncertainty shown by the dashed lines) of the supersymmetric partners of the tau leptons ($\tilde{\tau}$). The results are presented in the plane of the $\tilde{\tau}$ mass vs the mass of the lightest gaugino, assuming the decay $\tilde{\tau} \rightarrow \tilde{\chi}_1^0 \tau$. No limit is available today from the LHC. All these exotic searches will be possible thanks to the large statistics, and to the improved performance of the upgraded detectors.

A further class of hard-to-detect signatures of new physics has recently gained great attention,²³ namely long-lived particles (LLPs). Particles with macroscopic lifetimes, in the range of several cm up to hundreds of meters, could be present in several BSM theories. Their detection challenges the standard triggers and reconstruction techniques, but new strategies, together with new features of the HL-LHC upgraded detectors (e.g. timing resolutions of $O(\text{few tens})$ picoseconds), open new and exciting prospects. Dedicated detectors for HL-LHC are also being proposed for such searches. The HL-LHC datasets will allow to explore otherwise untestable scenarios.

1.3. *Final remarks*

With the discovery of the Higgs boson, a long era of more or less guaranteed discoveries is over. The W and Z bosons, the top quark, and the Higgs, were already seen, prior to their discovery, as the necessary components of an extremely compelling theoretical framework, the SM, whose predictions have steadily grown in reliability over the years. The high-energy accelerators of the last 40 years were built to discover and study, in detail, these particles, whose existence and whose properties were anticipated with great confidence. While there is similar confidence in the existence of new physics beyond the SM, today there is no certainty as to precisely what this new physics should be, and where or how it will appear in accelerators. There is no guarantee that it will be discovered during the Run 3 of the LHC, or even in the subsequent phases of its upgrade. The programme of precision Higgs physics and continued exploration of EWSB is therefore the most concrete and robust deliverable that the LHC upgrade can promise, and whose future returns can be anticipated today.

The potential achievements of the HL-LHC programme presented in Ref. [10] will greatly enrich our knowledge of particle physics, even in absence of BSM discoveries, and by themselves motivate the upgrade effort. Alongside the few goals summarized here, a large set of ancillary measurements will take place, in order to improve the precision of the theoretical predictions, to reduce the experimental systematics, and to improve the knowledge of the complete set of observables and parameters of the SM. Among these, we mention the measurement of the top quark and W boson masses, and of the weak mixing angle $\sin^2 \theta_W$.

The study of flavour physics, and of the properties of QCD matter at high-density, have also proven to be an essential complement to the Higgs and BSM physics studies, taking full benefit of the versatility of the beam configurations provided by the LHC. Flavour studies, and heavy ion collisions, do not rely directly on the highest possible pp luminosity. But recent studies have shown very clearly that these components of the LHC physics programme have a lot to gain from continued operations during the HL-LHC era. New targets for integrated luminosity have been set for the programme of flavour physics of the LHCb experiment,^{14,24} and a strong physics case has been presented¹⁵ to justify the extension of heavy ion collisions, including runs with lighter beam

types. These demands pose new challenges to the HL-LHC project, but they underscore the great expectations built by the physics community as a result of the extreme success of LHC's operations to date.

The longevity of a hadron collider is a great asset, as the Tevatron, for example, has well illustrated. Following the discovery of the top quark, several of the Tevatron's most impressive legacy results, like the oscillations of B_s mesons, the observation of single top production, the precision measurement of the W and of the top quark masses, among others, were all achieved within 20 years after the first collisions. The delivery of a slightly larger integrated luminosity, could have also enabled the Tevatron to discover the Higgs boson by the end of its Run 2. These examples underscore the potential of a hadron collider to deliver surprises over a very long life span, provided a sufficiently rapid luminosity doubling time is attainable. The HL-LHC project²⁵ will guarantee this longevity to the LHC programme.

References

1. G. Aad *et al.* [ATLAS Collaboration], Phys. Lett. B **716** (2012) 1 [arXiv:1207.7214 [hep-ex]].
2. S. Chatrchyan *et al.* [CMS Collaboration], Phys. Lett. B **716** (2012) 30 [arXiv:1207.7235 [hep-ex]].
3. F. Englert and R. Brout, Phys. Rev. Lett. **13** (1964) 321.
4. P. W. Higgs, Phys. Rev. Lett. **13** (1964) 508.
5. G. S. Guralnik, C. R. Hagen and T. W. B. Kibble, Phys. Rev. Lett. **13** (1964) 585.
6. S. L. Glashow, Nucl. Phys. **22** (1961) 579.
7. S. Weinberg, Phys. Rev. Lett. **19** (1967) 1264.
8. A. Salam, Weak and electromagnetic interactions - in Elementary particle physics: relativistic groups and analyticity, N. Svartholm, ed p. 367. Almqvist & Wiskell, 1968. Proceedings of the eighth Nobel symposium. Conf. Proc. C **680519** (1968) 367.
9. F. Gianotti, M. L. Mangano, T. Virdee, S. Abdullin, G. Azuelos, A. Ball, D. Barberis and A. Belyaev *et al.*, Eur. Phys. J. C **39** (2005) 293 [hep-ph/0204087].
10. A. Dainese, M. Mangano, A. B. Meyer, A. Nisati, G. Salam and M. A. Vesterinen, "Report on the Physics at the HL-LHC, and Perspectives for the HE-LHC," CERN Yellow Rep. Monogr. **7** (2019), doi:10.23731/CYRM-2019-007.
11. P. Azzi *et al.*, CERN Yellow Rep. Monogr. **7** (2019) 1 doi:10.23731/CYRM-2019-007.1 [arXiv:1902.04070 [hep-ph]].
12. M. Cepeda *et al.*, CERN Yellow Rep. Monogr. **7** (2019) 221 doi:10.23731/CYRM-2019-007.221 [arXiv:1902.00134 [hep-ph]].
13. X. Cid Vidal *et al.*, CERN Yellow Rep. Monogr. **7** (2019) 585 doi:10.23731/CYRM-2019-

- 007.585 [arXiv:1812.07831 [hep-ph]].
14. A. Cerri *et al.*, CERN Yellow Rep. Monogr. **7** (2019) 867 doi:10.23731/CYRM-2019-007.867 [arXiv:1812.07638 [hep-ph]].
 15. Z. Citron *et al.*, CERN Yellow Rep. Monogr. **7** (2019) 1159 doi:10.23731/CYRM-2019-007.1159 [arXiv:1812.06772 [hep-ph]].
 16. J. L. Abelleira Fernandez *et al.* [LHeC Study Group], J. Phys. G **39** (2012) 075001 doi:10.1088/0954-3889/39/7/075001 [arXiv:1206.2913 [physics.acc-ph]].
 17. S. Chatrchyan *et al.* [CMS Collaboration], Phys. Rev. Lett. **110** (2013) 081803 [arXiv:1212.6639 [hep-ex]].
 18. G. Aad *et al.* [ATLAS Collaboration], Phys. Lett. B **726** (2013) 120 [arXiv:1307.1432 [hep-ex]].
 19. B. Bellazzini, C. Csáki and J. Serra, arXiv:1401.2457 [hep-ph].
 20. G. Aad *et al.* [ATLAS Collaboration], Phys. Rev. D **101** (2020) no.1, 012002 doi: 10.1103/PhysRevD.101.012002 [arXiv:1909.02845 [hep-ex]].
 21. A. M. Sirunyan *et al.* [CMS Collaboration], Eur. Phys. J. C **79** (2019) no.5, 421 doi: 10.1140/epjc/s10052-019-6909-y [arXiv:1809.10733 [hep-ex]].
 22. D. Curtin, R. Essig, S. Gori, P. Jaiswal, A. Katz, T. Liu, Z. Liu and D. McKeen *et al.*, arXiv:1312.4992 [hep-ph].
 23. J. Alimena *et al.*, arXiv:1903.04497 [hep-ex].
 24. LHCb Collaboration, R. Aaij *et al.*, Physics case for an LHCb Upgrade II - Opportunities in flavour physics, and beyond, in the HL-LHC era, arXiv:1808.08865.
 25. Rossi, Lucio (ed.) (CERN); Brüning, Oliver (ed.) (CERN), “The High Luminosity Large Hadron Collider: the new machine for illuminating the mysteries of Universe”, World Scientific (2015) doi:10.1142/9581.

Chapter 3

Upgrade of the Experimental Detectors for High Luminosity LHC

F. Hartmann^a, B. Hippolyte^b, F. Lanni^c, T. Nayak^d, C. Parkes^e and P. Rumerio^f

^a*Karlsruhe Institute of Technology, 76131 Karlsruhe, Germany*

^b*USIAS - Université de Strasbourg, 67081, France and CERN, Switzerland*

^c*Brookhaven National Laboratory, Upton, NY 11973, USA*

^d*National Institute of Science Education and Research, Bhubaneswar, Odisha 752050, India and CERN, Switzerland*

^e*University of Manchester, Manchester M13 9PL, UK*

^f*University of Alabama, AL 35487, USA and Università di Torino, 10124, Italy*

The HL-LHC upgrade plans of ALICE, ATLAS, CMS and LHCb are briefly outlined in this chapter.

1. Introduction

The high-luminosity upgrade of the LHC (HL-LHC)^{1–3} will enable the four experiments to enter a new era, allowing searches of new phenomena and precision measurements.

ATLAS and CMS will upgrade their detector systems to cope with a pileup of 200 collisions per bunch crossing, corresponding to an ultimate, leveled instantaneous luminosity of $\mathcal{L} = 7.5 \times 10^{34} \text{ cm}^{-2}\text{s}^{-1}$, and to an integrated luminosity of 4 ab^{-1} . These conditions will pose unprecedented challenges in terms of particle rates and radiation levels: L1 trigger rates will reach up to approximately 1 MHz, while the inner tracking detectors will be designed to withstand fluence up to $2.3 \times 10^{16} \text{ n}_{\text{eq}}/\text{cm}^2$ and total ionizing doses in excess of 1 Grad. Plans will be described in Sections 2 and 3 respectively.

Section 4 describes the proposed LHCb Upgrade II detector, which would operate at an instantaneous luminosity of $1.5 \times 10^{34} \text{ cm}^{-2} \text{ sec}^{-1}$, almost an order of magnitude above Upgrade I, for a minimum of 300 fb^{-1} integrated luminosity.

Finally, ALICE is completing major upgrades for long shutdown 2 (LS2) that will result in a more precise, reliable, and faster experimental setup in the HL-LHC era, as summarized in Section 5. High statistics Pb–Pb data, amounting to at least 13 nb^{-1} , will be accumulated, together with O–O, pp, p–O and p–Pb collisions. The future plan after Run-4 calls for a compact, next-generation multipurpose detector as a follow-up to the ALICE experiment, conceived to handle luminosities a factor of 20 to 50 times higher than RUN-3.

2. The HL-LHC Upgrade of the ATLAS Detector

The ATLAS Phase-II upgrades, illustrated concisely in Figure 1, are designed to cope with the conditions expected for the ultimate HL-LHC configuration with up to $\mu = 200$ inelastic collisions per bunch crossing.

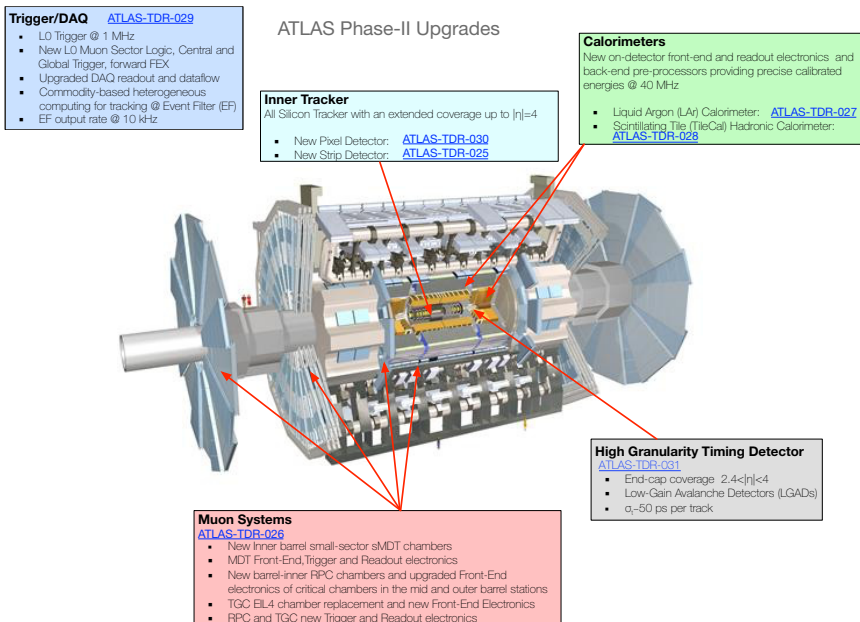


Fig. 1. ATLAS detector and the HL-LHC upgrade programme of its sub-systems.

2.1. Inner Tracker

The Inner Tracker (ITk) layout is shown in Figure 2. Five layers of pixel detector modules are installed at the inner radii around the beam pipe in the barrel region. Several pixel rings in the forward region extend the pseudo-rapidity coverage of the tracker system to $|\eta| < 4$. The outer tracker is made of four barrel layers and six end-cap disks of strip detectors modules on both sides of the layers, covering a pseudo-rapidity range of $|\eta| < 2.7$. The Pixel and Strip Detector volumes are separated by a Pixel Support Tube (PST). The ITk layout has been optimised to reach, at the HL-LHC conditions, similar or better performance as the present tracker: to cope with the higher pileup, the granularity of the sensors is increased, resulting in an average occupancy of 0.16% in the Pixel and 1.2% in the Strip detectors. The ITk design targets to have about half as much material compared to the current ID, minimising the effects of losses due to hadronic interactions and bremsstrahlung.

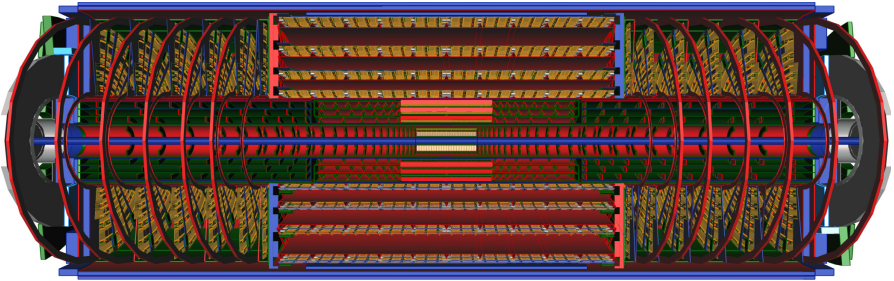


Fig. 2. Layout of the HL-LHC Inner Tracker (ITk) of ATLAS.

2.1.1. ITk Pixel Detector

The design of the ITk-Pixel system⁴ features a short central barrel region, inclined modules that cover the intermediate η -region, and rings perpendicular to the beam direction in the very forward region.

The innermost two Pixel layers are designed to be replaceable, as the maximum expected neutron fluence exceeds $2 \times 10^{16} \text{ 1MeV n}_{\text{eq}}\text{cm}^{-2}$. Different sensor technologies are used in the different regions of the detector: 3D sensors and thin ($100 \mu\text{m}$) n-in-p planar sensors in the inner layers, $150 \mu\text{m}$ thick n-in-p planar sensors in the outer three layers and in the end-cap rings. The pixel size

is $25 \times 100 \mu\text{m}^2$ in the central barrel region of the first layer and $50 \times 50 \mu\text{m}^2$ elsewhere.

Pixel modules are made by bump-bonding the silicon sensors on the front-end read-out ASICs, fabricated in 65 nm CMOS technology. The modules are glued to a flex circuit interfacing to the readout data transmission, and power distribution systems.

2.1.2. *ITk Strip Detector*

The ITk outer system is made of approximately 18000 modules of silicon Strip sensors.⁵ A module is built by gluing kapton flexible hybrids to the sensors. The hybrids also host the readout ASICs in 130 nm CMOS technology. The modules are assembled onto CO₂ cooled carbon fibre structures (“staves” and “petals”, respectively, in the barrel and end-cap regions).

392 staves are installed in the four barrel layers. Each barrel stave is populated with 28 Strip modules on both the top and bottom side. The Strip sensors are 24.1 mm long (short-strips) in the two innermost layers, and 48.2 mm (long-strips) in the outer two.

In the end-caps 32 identical petals, each housing 9 modules on each side, are assembled on every disk. Six different sensor geometries allow to cover the wedge-shaped petal surface, i.e. pointing to the beam axis.

2.2. *Calorimeters*

The on-detector and off-detector readout electronics of both the Liquid Argon (LAr) and Tile (TileCal) calorimeters^{6,7} are entirely replaced during the Phase-II upgrades (Figure 3). In the new readout scheme, after a first stage of (pre)-amplification, the signals are split into two overlapping linear gain scales, filtered by shaping amplifiers and digitized at 40 MHz. The digitized samples are multiplexed and transmitted off-detector optically to pre-processor modules, where energy and time of the deposits in the calorimeter elements are reconstructed at each bunch crossing.

In the LAr system 1524 new Front-End Boards (FEB2s) are installed on detector, each processing the signals from 128 calorimeter cells. 372 LAr Signal Processor (LASP) modules receive off-detector the front-end data through approximately 31900 fibers, for a throughput in excess of 280 Tb/s. In addition,

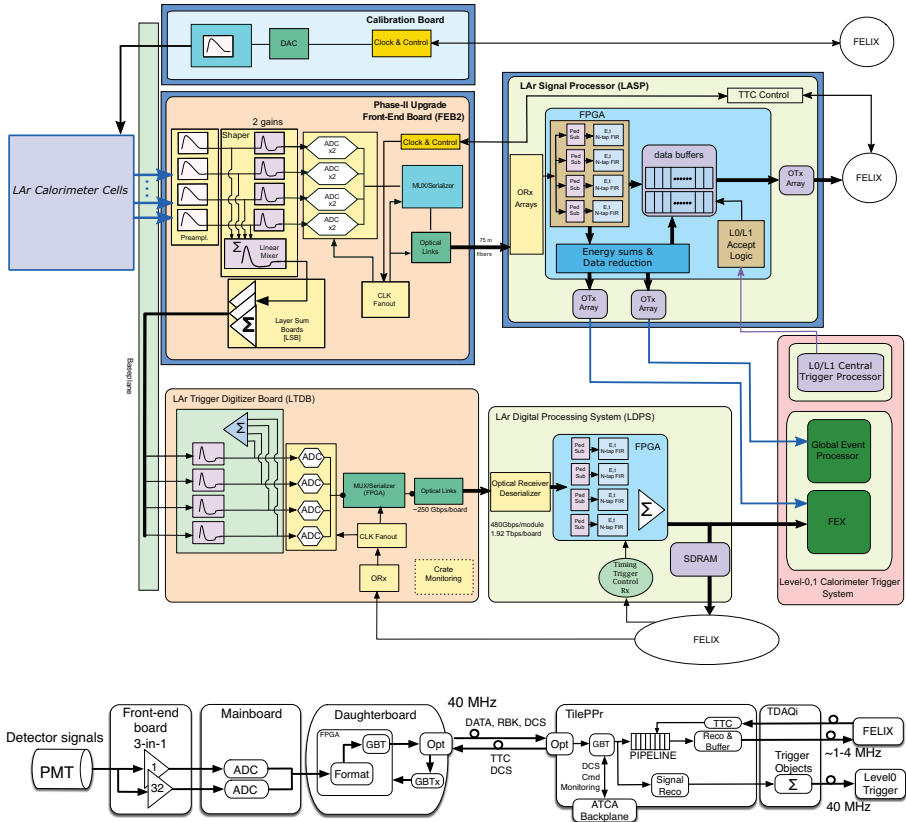


Fig. 3. High-level diagrams of the LAr (top) and TileCal (bottom) calorimeter readout.

an upgraded calibration system allows to inject calibration signals directly into the LAr cells with a precision better than 0.1% over the full 16-bit dynamic range.

In TileCal the PMTs, the front-end electronics, the power, and the cooling services are supported by new mechanical structures, segmented in four independent “Mini-drawers”, each servicing a TileCal module, i.e. one of the 256 wedges constituting the barrel and end-cap detectors. A total of 4096 fibres, each running at 9.6 Gb/s bandwidth – i.e. for a total of 1.3 Tb/s throughput, interface the on-detector front-end to 32 PPr modules. The off-detector PPr modules interface to the DAQ system and to the Level-0 Trigger processors through the TDAQi modules.

2.3. Muon Detectors

The main challenge for the ATLAS Muon Spectrometer⁸ is to maintain excellent selection and tracking capability at the HL-LHC conditions in terms of background rates, pile-up and integrated radiation doses. Figure 4 shows the spectrometer upgraded detectors in the two orthogonal planes.

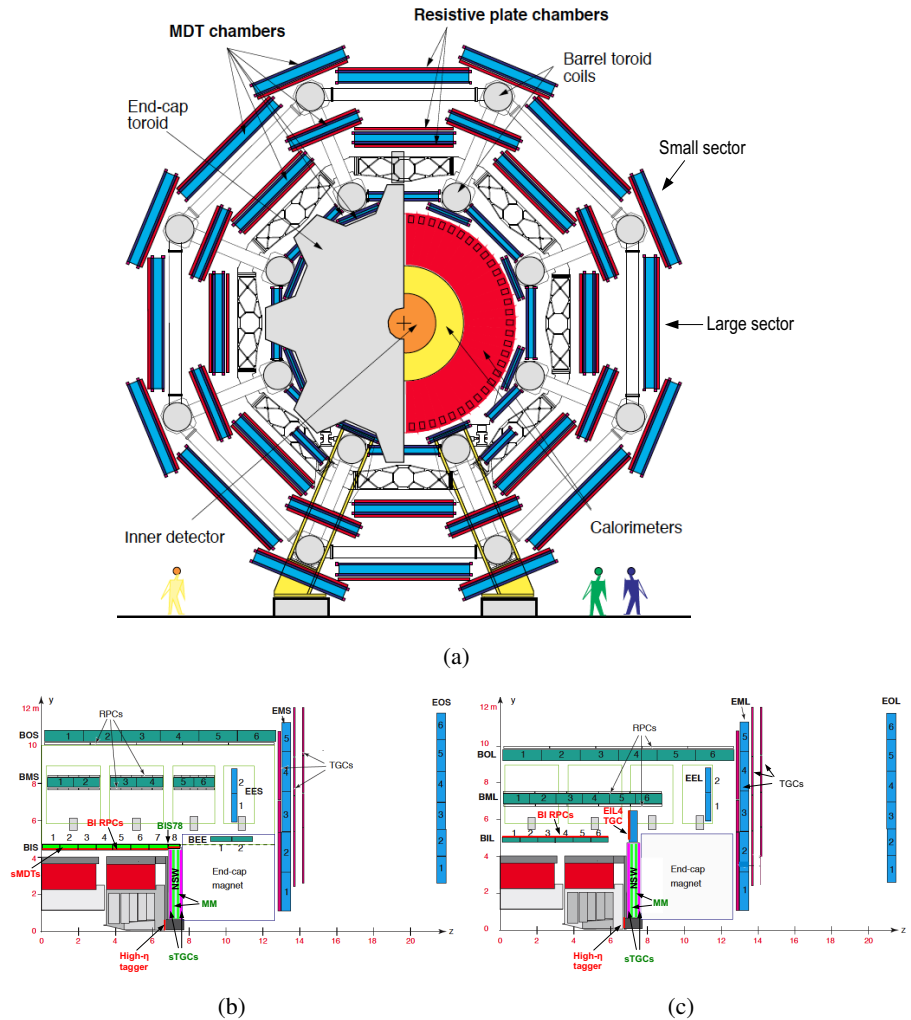


Fig. 4. Muon spectrometer layout in the r - ϕ plane (a), and in the r - z plane for the small (b) and large (c) sectors respectively.

2.3.1. *RPC and MDT upgrades in the barrel spectrometer*

New Resistive Plate Chambers (RPC) with increased rate capability are installed in the inner barrel layer (BI) to improve the acceptance and robustness of the trigger selection. The installation of the BI chambers is challenging in terms of available space, in particular in the small sectors of the muon spectrometer, where it is possible only if the existing Monitored Drift Tubes (MDT) chambers are replaced with new small diameter MDT (sMDT) detectors. Also, selected RPC chambers in the middle (BM) and outer barrel (BO) layers in the areas of highest rate, i.e. at $|\eta| > 0.8$, are refurbished during the winter shutdowns after LS3, with new electronics and readout planes, to operate the chambers at reduced high voltage without efficiency loss.

2.3.2. *TGC upgrade in the barrel-endcap transition*

In the barrel-endcap transition region new Thin Gap Chambers (TGC) triplets replace the current TGC doublets (EIL4 in Figure 4c). The triplets, with finer readout granularity, allow to implement a more robust majority logic, i.e. requiring hits in two out of three planes, and to use a smaller coincidence window, suppressing the rate of random coincidences generated by low- p_T charged particles (typically slow protons) produced inside the endcap toroid cryostats.

2.3.3. *Electronics upgrades*

A large fraction of the on- and off-detector readout and trigger electronics is upgraded for compatibility with the Level-0 trigger requirements. The RPC and TGC trigger and readout chains are redesigned with data streamed off-detector and made available to the Level-0 trigger processors. The front-end electronics of the MDT detectors is also upgraded: raw data are sent to dedicated processors where precise measurements of the hit coordinates allow the Level-0 trigger processor to sharpen trigger efficiency turn-on curves at high p_T , and reduce the background rate significantly.

2.4. *High Granularity Timing Detector*

The High Granularity Timing Detector (HGTD) is a precision timing system based on Low Gain Avalanche Detectors (LGAD), installed in the region $2.4 <$

$|\eta| < 4.0$.⁹ It improves the rejection of pileup jets with $30 < p_T < 50\text{GeV}$ in the forward region up to a factor of 40% at the start of the detector lifetime to 25% at the end of lifetime, and reduces the inefficiencies of forward lepton isolated tracks by a factor two. HGTD comprises two layers of pixelated sensors ($1.3 \times 1.3 \text{ mm}^2$) installed on the end-cap cryostats for an active area of 6.3 m^2 (see Figure 5a). Full-sized (15×15) LGAD arrays, shown in Figure 5c, have achieved in testbeams a time resolution of 30 ps.

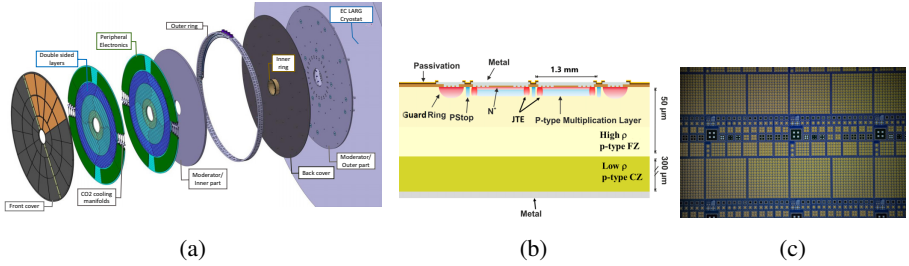


Fig. 5. (a) HGTD detector layout and mechanical structure. (b) Cross-section of an LGAD sensor including a JTE around each sub-pad. (c) Microscope picture of an HGTD LGAD prototype with full size sensors (15×15 array) tested on beam.

2.5. Trigger and DAQ

The baseline configuration¹⁰ features a Level-0 (L0) hardware trigger with a readout rate of 1 MHz and a latency of $10 \mu\text{s}$, followed by the Event Filter (EF) system performing the final event selection, and outputting data at 10 kHz - see Figure 6.

2.5.1. Level-0 Trigger System

The existing Muon Trigger processors are entirely replaced with upgraded modules that process the information from the RPC, TGC and sTGC and MicroMegas detectors in the forward region (New Small Wheel). They are complemented by additional processors that improve the precision of the muon p_T measurement using the information of the MDT detectors.

The Phase-I Calorimeter Feature Extractors (FEXes) modules are maintained during the HL-LHC operations, and their firmware optimized for the

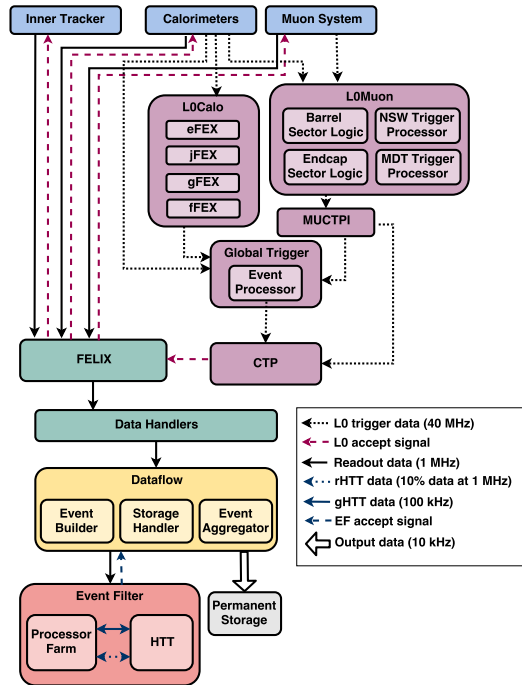


Fig. 6. High-level diagram of the Trigger/DAQ architecture.

expected pile-up conditions and the extra-latency available in Run-4. Additional FEXes units are installed to process data from the forward calorimeter.

The Global Trigger system performs offline-like algorithms, and executes topological algorithms extending the functionality of the Run-2 Topological Processor.

2.5.2. Data Acquisition System

Detector data are transmitted to the Front-End Link eXchange (FELIX) nodes, a common interface between the detector-specific links and the commodity network downstream. Along the network, data are received by the Data Handlers, where detector-specific processing is implemented, and transferred to the Dataflow sub-system, which transports, aggregates, buffers and compresses event data for utilization in the EF. The system is designed to sustain a throughput of 5.2 TB/s.

2.5.3. Event Filter System

The Event Filter (EF) system, a large commodity CPU-based processing farm, is upgraded to maintain the rejection by employing offline-type particle reconstruction, and achieve an output rate of 10 kHz. The total data throughput to storage is 60 GB/s.

The design of the EF tracking sub-system described in the TDAQ Technical Design Report (TDR) was based on a custom-electronics Hardware Tracking for the Trigger (HTT) based on Associative Memory ASICs deployed on ATCA processing modules.¹⁰ Recently, the baseline design has changed in favor of a commodity solution that may benefit of accelerators as co-processors. The opportunity to drop tight latency constraints, originally required by the optional use of tracking in earliest stage of the trigger chain, has been the driving reason behind the decision of this baseline change. A TDR amendment is in preparation and its release is planned at the beginning of 2022.

3. The HL-LHC Upgrade of the CMS Detector

To exploit the high-luminosity upgrade of the LHC, the CMS experiment has to combat higher overall particle rates, higher pileup of superimposed proton-proton collision events per LHC bunch crossing, and higher instantaneous and integrated radiation doses to the detector elements. All CMS systems for the HL-LHC (CMS Phase-2 upgrade) are designed to withstand an integrated luminosity of 4 ab^{-1} , equivalent to a fluence of $2.3 \times 10^{16} \text{ n}_{\text{eq}}/\text{cm}^2$ at the innermost radius of the Pixel detector, to cope with a pileup of 200 collisions per bunch crossing, and to sustain a Level-1 (L1) trigger rate of 750 kHz with a latency of $12.5 \mu\text{s}$. The whole system including the trigger concept implements the Particle Flow (PF) paradigm.¹¹ The tracking system and endcap calorimeters will be completely replaced with much finer granularity systems and — for the first time for an all-silicon tracker detector — L1-trigger capability. The Tracker coverage will be extended to $|\eta| = 4.0$. Figure 7 gives a concise overview. A new MIP (Minimum Ionizing Particle) timing detector (MTD) will add a fourth dimension to reconstructed tracks. The barrel Electromagnetic Calorimeter will be refurbished with new electronics, which will stream data at full 40 MHz. The full Muon front-end and back-end system will be renewed to cope with the higher particle rates while the forward region will be significantly extended to $|\eta| = 2.8$.

CMS HL-LHC Upgrade

Technical proposal CERN-LHCC-2015-010 <https://cds.cern.ch/record/2020886>

Scope Document CERN-LHCC-2015-019 <https://cds.cern.ch/record/2055167>

L1-Trigger/HLT/DAQ

<https://cds.cern.ch/record/2714892>

<https://cds.cern.ch/record/2283193>

- Tracks in L1-Trigger at 40 MHz
- PFlow selection 750 kHz L1 output
- HLT output 7.5 kHz
- 40 MHz data scouting

Calorimeter Endcap

<https://cds.cern.ch/record/2293646>

- 3D showers and precise timing
- Si, Scint+SiPM in Pb/W-SS

Tracker <https://cds.cern.ch/record/2272264>

- Si-Strip and Pixels increased granularity
- Design for tracking in L1-Trigger
- Extended coverage to $\eta \approx 3.8$

Barrel Calorimeters

<https://cds.cern.ch/record/2283187>

- ECAL crystal granularity readout at 40 MHz with precise timing for e/ γ at 30 GeV
- ECAL and HCAL new Back-End boards

Muon systems

<https://cds.cern.ch/record/2283189>

- DT & CSC new FE/BE readout
- RPC back-end electronics
- New GEM/RPC $1.6 < \eta < 2.4$
- Extended coverage to $\eta \approx 3$

Beam Radiation Instr. and Luminosity

<http://cds.cern.ch/record/002706512>

- Bunch-by-bunch luminosity measurement: 1% offline, 2% online

MIP Timing Detector

<https://cds.cern.ch/record/2667167>

Precision timing with:

- Barrel layer: Crystals + SiPMs
- Endcap layer: Low Gain Avalanche Diodes

Fig. 7. The HL-LHC upgrade of the CMS detector.

3.1. CMS Phase-2 Tracker

The Phase-2 Tracker will consist of an Inner Pixel Tracker (IT) based on silicon pixel modules and an Outer Tracker (OT) composed of silicon modules with strip and macro-pixel sensors. The main challenge is to increase radiation tolerance, reduce mass, and increase granularity to cope with high pileup and ensure efficient tracking, two-track separation in high energetic jets, and good 3D pattern recognition. A multi-year campaign to study radiation tolerance led to the choice of *n-in-p* sensors in all OT and IT layers with the potential exception of 3D sensors for the innermost pixel layer. Many novel design choices achieve a significant reduction in material budget and, consequently, multiple scattering. This significantly improves transverse momentum (p_T) resolution, and lowers the photon conversion rate and electron bremsstrahlung. The main strategies to reduce mass are: implementing fewer layers, using DC-DC converters in the OT and serial power in the IT (with significant reduction of power cable mass), adopting ultra-light structural materials and CO₂ cooling (smaller pipes, lighter liquid), and reducing the number of connectors, extra boards, cables, etc. Figure 8 shows one quadrant with 4 inner pixel barrel layers plus twelve forward disks, spanning the full detector length, extending

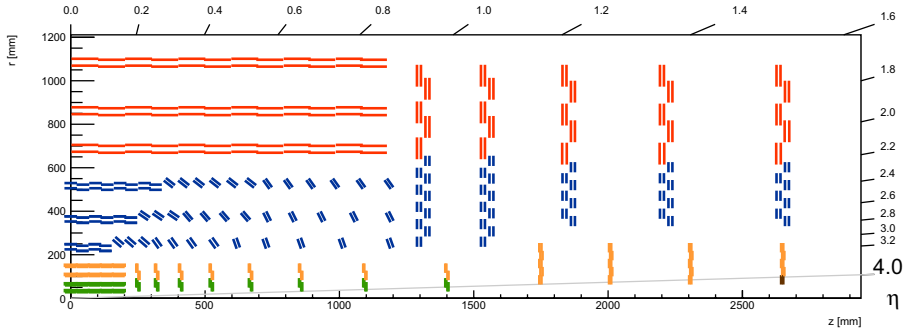


Fig. 8. The HL-LHC upgrade of the CMS Tracker. The red/blue outer layers are composed of 2S and PS p_T -modules, respectively (see Figure 9). The orange pixel layers/disks consist of 1×2 chips modules while the green ones consist of 2×2 chip modules. The Tracker, all in all, has seven pixel layers, of which 4 are based on micro- and 3 are macro-pixels. The innermost ring of endcap 12 (brown) is located beyond $|\eta| = 4.0$ and serves as an independent luminometer.¹²

the coverage to $|\eta| = 4.0$. A partially inclined geometry is implemented in the OT, saving about 5 m^2 of active elements. With respect to the existing detector, the pitch in the outer strips section will stay roughly the same while the strip length will be reduced from 20 to 5 cm and from 10 to 2.5 cm and even to long macro-pixels of 1.5 mm length. The inner pixel cell size will be reduced by a factor six from $15000 \mu\text{m}^2$ to $2500 \mu\text{m}^2$ (50×50 or $25 \times 100 \mu\text{m}^2$). The six OT barrel layers and five endcap disks are composed of novel p_T -modules with intrinsic capability to distinguish high and low p_T -track segments. The OT has about 42M strips plus 127M macro-pixels, which are complemented by roughly 2B micro-pixels in the IT.

CMS will introduce a Level-1 track trigger that fully reconstructs all $p_T > 3 \text{ GeV}$ tracks to $\eta < 2.5$ at the 40 MHz bunch crossing rate. Front-end-chips in p_T -modules read channels from two closely spaced sensors in a single frame (strips parallel) and correlate the signals. With the strong bending power of the CMS magnet, only segments of high- p_T tracks (stubs) will be contained in a small ‘pass-window’ in the second sensor, cf. Figure 9.

With 1.5-mm-long macro-pixels in three layers, primary vertex identification (PV) is possible with a precision of about 1 mm at the L1 trigger. About 80% of the transmitted data are trigger data, for which modern Field Programmable Gate Arrays (FPGAs) fully reconstruct tracks faster than $4 \mu\text{s}$.^{12,13}

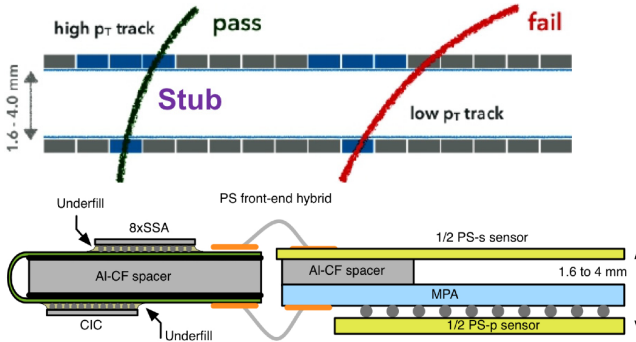


Fig. 9. ‘Stubs’, depicted in the upper part of the figure, are transmitted to the L1 trigger for every bunch crossing. The lower figure shows a PS-module (Pixel-Strip-sensors: $2.5 \text{ cm} \times 100 \mu\text{m}$ and $1.5 \text{ mm} \times 100 \mu\text{m}$). Signals are routed via flex cables to the other hybrid side, which correlates hits in-situ in the ASICs and identifies p_T ‘stubs’.

3.2. CMS Phase-2 MIP Timing Detector MTD

With increased pileup, the identification of primary vertices (PV) becomes significantly more difficult, especially in the very forward direction. With pileup of 200, one expects about two primary vertices per millimetre resulting in $\sim 15\%$ reconstructed PVs to be merged. Collisions within one bunch crossing have a time spread of $\sim 180 \text{ ps}$, thus precise timing information (time resolution $\sigma_t = 30 - 50 \text{ ps}$) allows to unfold the tracks versus time thereby reducing the pileup to an *effective* value similar to today’s pileup. A 4D vertex reconstruction (space + time) are superior to 3D reconstruction especially for low- p_T tracks. CMS estimates a 20% gain in signal yield for di-Higgs events due to improvement in object isolation and b -tagging. The time information also allows particle identification for low- p_T tracks, which is important for dedicated heavy ion runs. The MTD also largely increases the sensitivity to discover long-lived stable particles.

CMS will instrument¹⁴ the barrel region with LYSO crystal bars ($3 \times 3 \times 50 \text{ mm}^3$) read out by $3 \times 3 \text{ mm}^2$ SiPMs of $15 \mu\text{m}$ cell pitch on both crystal ends. The endcap regions will be equipped down to $\eta \approx 3$ with two layers of Low Gain Amplifier Diodes (LGADs) with cell sizes of $1.3 \times 1.3 \text{ mm}^2$ on sensor sizes of $21 \times 42 \text{ mm}^2$ with $20 \times 20 \text{ mm}^2$ bump bonded readout chips. Both detectors will be operated at a temperature of -30°C or lower realized via CO_2 cooling to limit SiPM dark count rate and LGAD leakage current.

Figure 10 illustrates the global geometry and location of the thin MTD layers. In addition, the time resolution of the barrel electromagnetic calorimeter¹⁵ will be $\sigma_t = 30$ ps for energy deposits greater than 30 GeV, while for the endcap high-granularity calorimeter¹⁶ it is expected to be $\sigma_t = 25$ ps for deposits equivalent to 50 fC (= 12 MIPs for the 300 μm sensors).

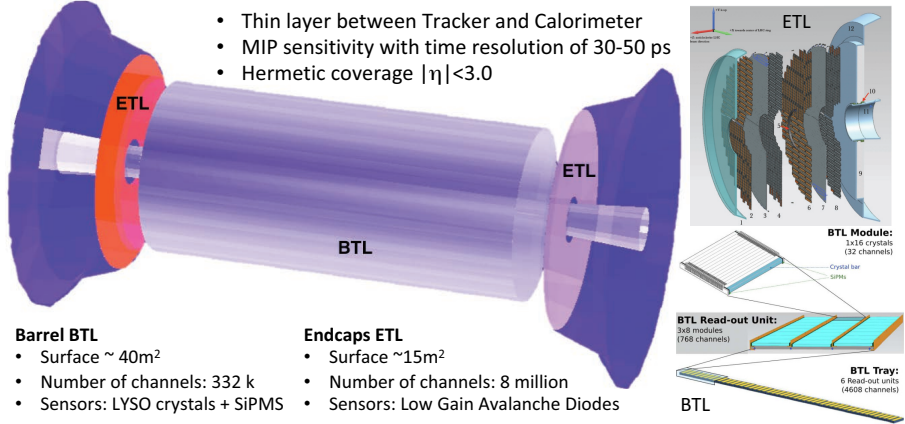


Fig. 10. The HL-LHC MIP Timing Detector MTD. The BTL will be integrated within the Tracker Support Tube, while the ETL will have its own thermal screen between Tracker and HGCAL.¹⁴

3.3. CMS Phase-2 Barrel Calorimeter

Both the homogeneous electromagnetic section (EB), made of lead-tungstate crystals, and the sampling hadronic section (HB), made of brass absorber and scintillator tiles coupled to wavelength-shifting and clear fibers, will withstand the radiation exposure in this barrel region for the entire HL-LHC run with sustainable degradation. The EB Avalanche Photodiodes (APD) and the HB Silicon Photomultipliers (SiPM), installed with new front-end electronics in LS2 as the last item of the CMS Phase-1 upgrade, will also be retained as they will experience a significant but manageable increase in dark current, which will be ameliorated by lowering the operational temperature. The EB front-end electronics and both the EB and HB back-end electronics will be upgraded¹⁵ in LS3 in order to sustain the challenging HL-LHC operating conditions, including the increased L1-trigger rate and latency.

The upgraded EB front end is designed to provide 30 ps timing resolution for photons from di-photon Higgs decays. This will enable precise primary vertex determination, mitigate the effects of the increasing APD dark current noise, suppress anomalous APD signals in the L1 trigger, and provide single crystal information to the L1 trigger (compared to a 5×5 crystal matrix in the legacy system), which will improve electromagnetic shower isolation and permit to retain calorimeter trigger thresholds at the level needed for Higgs precision studies. To carry out this upgrade, the 36 EB *supermodules* shown in Figure 11(a) will be extracted, refurbished, and reinstalled during LS3. Figure 11(b) shows the architecture of the new front-end electronics of EB, which will feature analogue ASICs implemented in 130 nm technology, and digital ASICs and ADCs implemented in 65 nm technology.

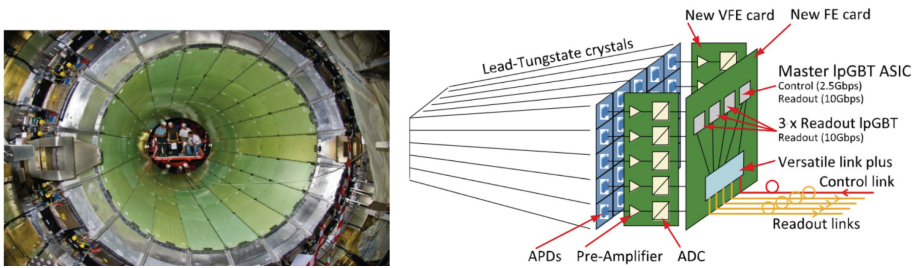


Fig. 11. (a) The 36 wedges (*supermodules*) of the electromagnetic section (EB) of the CMS barrel calorimeter inserted inside the hadronic section (HB). (b) Schematic of the upgrade of the EB front-end electronics architecture for one of the 2448 5×5 crystal matrices.

3.4. CMS Phase-2 High Granularity Calorimeter

A long-standing concept for the International Linear Collider, a high granularity calorimeter, based on silicon pad detectors plus scintillator/SiPM cells, will be realised for the CMS Phase-2 Endcap Calorimeter.^{16,17} It effectively ‘tracks’ particles inside the calorimeter, embodying the particle flow concept. The global layout and a photo of a silicon prototype sensor are displayed in Figure 12. Close to 600 m^2 active surface (~ 25000 silicon modules) will be instrumented with $\sim 6\text{M}$ channels of 0.5 and 1 cm^2 hexagonal pad cells at smaller and larger radius, respectively. The detector is very dense to preserve lateral compactness of showers, and it has a fine lateral granularity to enable two-shower separation and narrow jet identification as well to reduce the

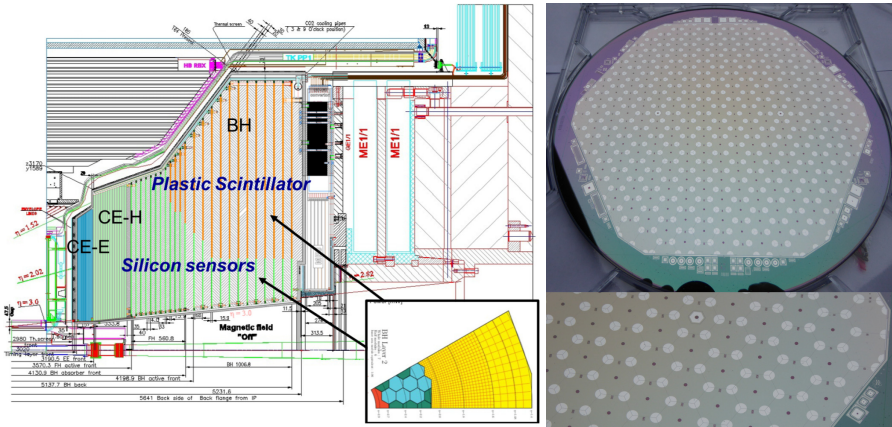


Fig. 12. The CMS Endcap Calorimeter layout is shown on the left; a prototype sensor from an 8 inch silicon wafer is on the right.

inclusion of energy from particles originating in pileup interactions. Fine longitudinal segmentation enables fine sampling of the development of showers, retaining good electromagnetic energy resolution (e.g. for $H \rightarrow \gamma\gamma$), pattern recognition, and discrimination against pileup. For cell signals of 12 fC (about 3 MIPs) a timing precision of 100 ps can be achieved. Streaming reduced data at 40 MHz to the L1 Trigger is achieved by summing up the energy of several cells from every other layer. The electromagnetic part (CE-E) will have 28 sampling layers embedded in Cu/CuW/Pb absorbers, equivalent to around $26 X_0 + 1.7 \lambda$. The hadronic section (CE-H) has 22 layers with stainless steel absorbers, corresponding to about 9λ . Deeper hadronic layers (BH) at larger radius, with lower radiation exposure, will be equipped with $\sim 400k$ small plastic scintillator tiles (from 4 to 32 cm^2), each optically coupled to a SiPM. The volume will be kept at a temperature of -30°C via CO_2 cooling. Silicon sensor thicknesses will be 100, 200 and $300 \mu\text{m}$, with thinner sensors, being more radiation tolerant, placed at smaller radius. To span the necessary dynamic range of 1 to 5000 MIPs, the readout features a charge amplifier/shaper (low range) plus a time-over-threshold circuit (high range).

3.5. CMS Phase-2 Muon Detector System

CMS will significantly overhaul its extensive muon detector and electronics systems to address longevity limitations in the existing systems, increase re-

dundancy, and cope with the increased particle rates due to the higher HL-LHC instantaneous luminosity.¹⁸ The forward region will be extended with high granularity detectors up to $|\eta| = 2.8$ (2.4 today). Figure 13 illustrates the Muon system for the HL-LHC era. Extensive longevity studies show that the DT, CSC and RPC chambers will remain operational during the full HL-LHC period with reduced voltages, while their front-end electronics might not withstand the total expected radiation. New electronics will increase rate capability and trigger latency as required, improve time resolution for RPCs (1.5 ns), and make the DT time resolution (2 ns) available at L1 trigger. Trigger primitives of DTs and RPC will be generated in off-detector FPGA systems to enable more complex topologies, e.g. improving the sensitivity for discovering long-lived stable particles. The high spatial resolution and MHz/cm² capability of the GEM technology is crucial for instrumenting the high- η region. Three GEM stations (GE1/1, G2/1 and ME0) plus two improved RPC stations (RE3/1 and RE4/1) at high η will significantly improve trigger efficiency and, due to better spatial resolution, p_T resolution. The CSC upgrade, installation of GE1/1 and of GEM and RPC endcap services is taking place during LS2.

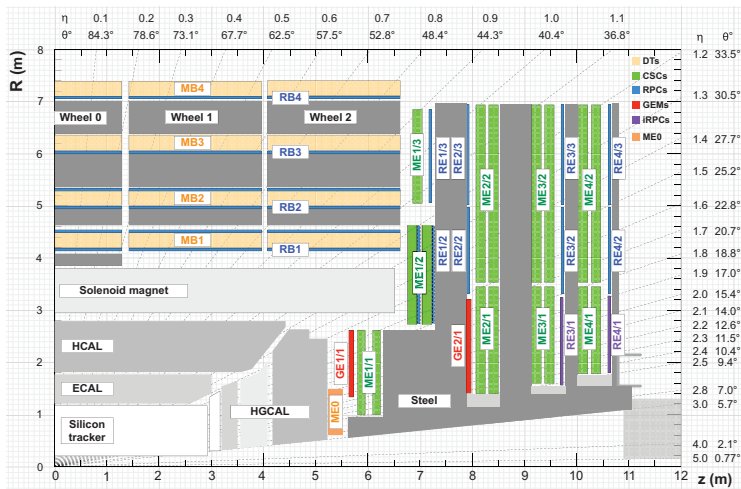


Fig. 13. The HL-LHC Muon Detector System. An R-z cross section of a quadrant of the CMS detector, including the new Phase-2 upgrades (RE3/1, RE4/1, GE1/1, GE2/1, ME0). The locations of the various muon stations are shown in color (MB = DT = Drift Tubes, ME = CSC = Cathode Strip Chambers, RB and RE = RPC = Resistive Plate Chambers, GE and ME0 = GEM = Gas Electron Multiplier).

3.6. CMS Phase-2 Trigger and Data Acquisition

A new Trigger and Data Acquisition (TDAQ) system^{19,20} will process data at an unprecedented rate of 50 Tb/s, corresponding to the Level-1 trigger event rate of 750 kHz, to select and record events at 7.5 kHz. The Phase-2 TDAQ system will continue to be based on a two-level trigger strategy. The custom hardware Level-1 (L1) trigger will take full advantage of advances in FPGA and optical link technologies. The inputs to the L1 trigger, namely the Trigger Primitives (TPs), are generated at 40 MHz in the subdetector back-end electronics, based on the Advanced Telecommunications Computing Architecture (ATCA) standard. For the first time, tracking information from the Outer Tracker will be sent to the L1 trigger and will be crucial for keeping trigger thresholds and efficiencies consistent with LHC Run 1 values. High-resolution clusters will be produced from the Endcap and Barrel Calorimeter TPs. Muon TPs will incorporate data from the additional chambers covering pseudorapidity up to $|\eta| = 2.8$. A new Correlator Trigger system will match tracks with the calorimeter and muon information, apply object identification algorithms, and provide a list of sorted trigger objects to a Global Trigger. This will apply sophisticated algorithms, particle flow and machine learning to produce an L1-accept signal with a fixed latency of $12.5 \mu\text{s}$ to be distributed to the subdetector backend electronics, initiating readout through a standardized ATCA data concentrator board included in every subdetector back-end crate. Then, the High-Level Trigger (HLT)²⁰ will process full detector event data through software algorithms running asynchronously on standard processors. Accepted events will be recorded for efficient long-term storage and subsequent offline reconstruction.

3.7. CMS Precision Proton Spectrometer PPS for HL-LHC

After successful operation of the Precision Proton Spectrometer (PPS) since 2016, the CMS Collaboration is planning to pursue the study of central exclusive production (CEP) events, $pp \rightarrow pXp$, at the HL-LHC with detection of the state X in the central detectors and of the leading protons in the PPS stations with a large, not continuous, acceptance on masses of X from ~ 50 GeV to ~ 3 TeV.²¹ More specifically, we target a kinematic acceptance for the centrally produced X state of 44–160 GeV with a cryogenic (“cold”) station at 420 m, and 264–370 GeV, 520–960 GeV, and 1–2.72 TeV with three non-cryogenic

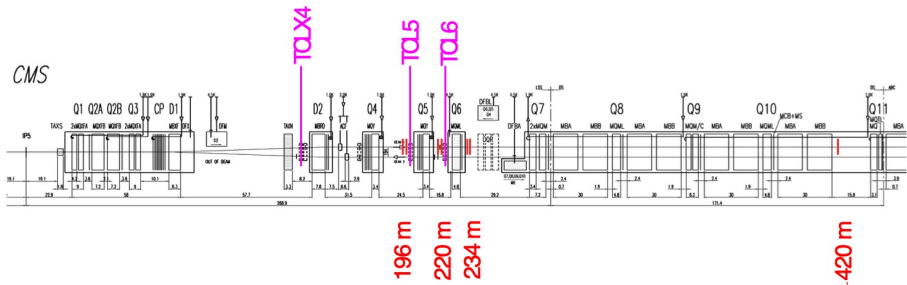


Fig. 14. Phase-2 layout of Long Straight Section LSS5, where the PPS detectors are planned to be located.

(“warm”) stations at 234, 220 and 196 m, respectively. The foreseen locations of the detectors, which will be on both sides of IP5, are indicated in Figure 14. Tracking and timing detectors are planned. The Higgs mass is only accessible with the 420 m station in the cold section.

The three warm stations can be instrumented with upgraded Roman Pot technology while the cold station needs a cryogenic bypass as the signal protons arrive in between the beam pipes, and new development is necessary. The required sensitive area is only a few cm^2 but with $\text{PU} = 200$, pad sizes should be in the order of $100\text{--}200\ \mu\text{m}$ and sensor radiation tolerant up to $1.5 \times 10^{16}\ \text{n}_{\text{eq}}/\text{cm}^2$. The preferred technologies are diamond for timing and 3D for tracking. To achieve a good vertex determination via time of flight, the goal is to reach a σ_T of 15–20 ps/arm with ~ 15 planes (50–60 ps/plane). The MTD in the central detector is instrumental to make the track association.

4. The HL-LHC Upgrades of the LHCb Detector

The LHCb Upgrade II programme²² aims to make full use of the capabilities of a forward acceptance detector during the HL-LHC operational period, foremost in its core areas of CP violation and rare decays in flavour physics. Its capabilities range far beyond these into forward and high- p_T physics, spectroscopy, heavy ion and fixed target physics, dark-sector searches and beyond. The LHCb Upgrade I is currently under construction and will start data taking in 2022 after LHC Long Shutdown 2 (LS2). The future LHCb for the HL-LHC era will be installed in a consolidation phase during LS3, with primary operations of LHCb Upgrade II starting in Run 5 after LS4 operating

at an instantaneous luminosity of $1.5 \times 10^{34} \text{ cm}^{-2} \text{ sec}^{-1}$, nearly an order of magnitude above Upgrade I. LHCb Upgrade II will accumulate a data sample corresponding to a minimum of 300 fb^{-1} . The general concepts were presented in an Expression of Interest in 2017,²² and a Physics Case in 2018.²³ The data sample collected by the end of the HL-LHC period will be more than a factor thirteen higher than that collected in the pre-HL-LHC period. The energy scale probed through precision measurements scales as the fourth root of the sample size, so the step from the pre-HL-LHC to the post-HL-LHC, and post Belle II, period corresponds to a factor of 1.9 or more in reach or corresponding to an LHC energy increase from 14 TeV to 27 TeV.

4.1. Tracking with timing detectors

At a luminosity of $2 \times 10^{34} \text{ cm}^{-2} \text{ s}^{-1}$, the maximum considered, the mean number of visible proton-proton interactions per crossing will be 56, producing around 2500 charged particles within the LHCb acceptance. Efficient real-time reconstruction of charged particles and interaction vertices represents a significant challenge. It is foreseen to modify the existing spectrometer components to increase the granularity, reduce the amount of material and to exploit the use of precision timing.²²

4.1.1. The vertex detector

The LHCb upgrade physics programme is reliant on an efficient and precise vertex detector (VELO) that enables real time reconstruction of tracks in the software trigger system. To cope with the large increase in pile-up, new techniques to assign correctly each b hadron to the primary vertex (PV) will be realized by the development of a new 4D hybrid pixel detector with enhanced rate and timing capabilities in the ASIC and sensor. Improvements in the mechanical design of the Upgrade II VELO will allow for periodic module replacement. The principle behind the use of timing information for PV association is illustrated, for a single event, in Figure 15a. Studies show that without timing, the Upgrade II PV mis-association levels may reach $\sim 20\%$, and this can be reduced to $\sim 5\%$ with a timing precision of 50–100 ps. Studies have also shown that the track reconstruction efficiency and fake rate can be addressed by decreasing the pixel pitch from the current $55 \mu\text{m}$, particularly for the innermost region of the VELO. Timing will speed up track reconstruction,

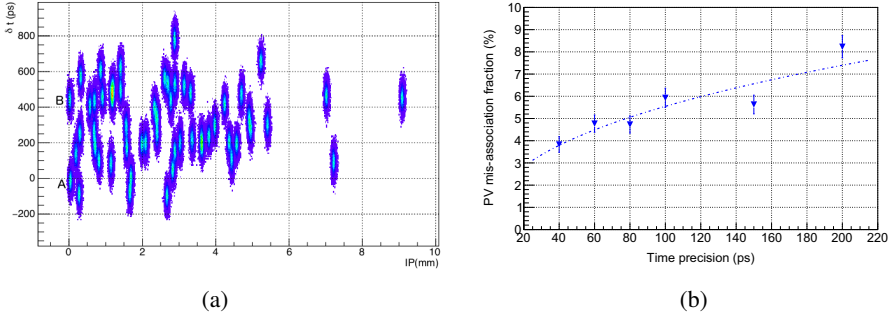


Fig. 15. (a) Example event containing a $B^0 \rightarrow \pi^+\pi^-$ candidate, illustrating the PV association challenge. Each PV is drawn as a 2D Gaussian distribution with the appropriate values and uncertainties for both spatial (x -axis) and temporal (y -axis) metrics used to associate the B meson to a single origin PV. Adding the temporal information allows the correct PV [‘A’, closest to $(0, 0)$] to be identified where the spatial information alone would lead to the wrong choice (‘B’).

(b) Fraction of $B^0 \rightarrow \pi^+\pi^-$ candidates which are associated with an incorrect primary vertex in Upgrade II conditions ($\mathcal{L} = 1.5 \times 10^{34} \text{ cm}^{-2}\text{s}^{-1}$), for the outer radial region ($20 < r < 35 \text{ mm}$) of the VELO, to be compared with the 20% PV mis-association fraction corresponding to a detector with no time information.

reducing drastically combinatorics at an early stage, saving CPU resources. Also a ‘mixed’ solution is considered where the inner region has a smaller pitch (emphasising resolution) and the outer region has a larger pitch emphasising more precise timing. Studies of the performance are shown in Figure 15b.

4.1.2. Downstream tracking

Changes to the downstream tracking system are also foreseen. In Upgrade I this comprises a silicon strip detector located upstream (UT) and three tracking stations located downstream of the magnet (T-stations) realised by a twelve-layer scintillating fibre tracker (SciFi). This covers the full acceptance, corresponding to 30 m^2 per layer. In conjunction with the VELO, these stations provide a high precision momentum measurement and provide the track directions as input to the particle identification systems. For Upgrade II the higher occupancies necessitate increased detector granularity. Second, the rate of incorrect matching of upstream and downstream track segments needs to be minimised. The inner part of the T-stations will be replaced with a high granularity

silicon detector, with the large area covered by scintillating fibres. Based upon occupancy studies it is proposed to cover the inner region with six planes of silicon.²² The design of this new silicon detector is expected to be based on HV-CMOS technology, the first of its kind at the LHC. Pixels Sizes of around $300 \times 100 \mu\text{m}$ are under study.

4.1.3. Magnet stations

For Upgrade Ib in LS3, it is proposed to extend the spectrometer coverage for low momentum tracks (for example the slow pion from the decay $D^{*+} \rightarrow D^0\pi^+$) by instrumenting the internal surfaces of the magnet with scintillating fibres. A spatial resolution of the order of a mm is sufficient in the bending-plane to obtain the required momentum resolution. The use of a stereo arrangement of layers will be implemented to achieve the required y segmentation.

4.2. Particle identification

High quality particle identification (PID) is essential for almost all precision flavour measurements. These developments will improve granularity and, for certain subdetectors, add fast timing of the order of a few tens of picoseconds, in order to associate signals with one, or a small number, of pp interactions in the bunch crossing.

4.2.1. Hadron identification: the RICH system and the TORCH

The RICH system of Upgrade II will be a natural evolution of the current detectors and those being constructed for Upgrade I. There will be two counters, an upstream RICH 1 optimised for lower momentum tracks, and a downstream RICH 2, both occupying essentially the same footprint as now. Higher granularity and fast timing photodetectors will resolve the increased track multiplicity. Several candidate technologies are under consideration, with SiPMs being a leading contender. Other possibilities include vacuum devices such as MCPs, HPDs and MaPMTs.

As well as reducing the occupancy it will be necessary to improve the Cherenkov angle resolution by around a factor of three in both counters with

respect to the specifications of Upgrade I. This goal can be achieved by redesigning the optics ensuring that the response of the photodetectors is weighted towards longer wavelengths, and taking advantage of the smaller pixel size.

There is an exciting possibility, under consideration, to enhance the low-momentum hadron-identification capabilities of the experiment by installing a TORCH detector, measuring time-of-flight through detecting internally reflected Cherenkov light produced in a thin (~ 1 cm) quartz plane with MCP photodetectors. A time resolution of 70 ps per photon and an expected yield of ~ 30 photons per track will allow for kaons and low-momentum proton identification in the region below 10 GeV/ c . These improvements would benefit flavour tagging, reconstruction of multi-body final states, physics with baryons and spectroscopy studies. A suitable location for the TORCH within LHCb would be upstream of RICH 2.

4.2.2. *Electromagnetic calorimeter*

The electron, photon and π^0 identification provided by the current electromagnetic calorimeter (ECAL) has proved of great importance. The principal challenges for the ECAL at Upgrade II will be threefold. Firstly, the radiation environment will be extremely severe, with a total dose of around 200 Mrad foreseen for the innermost modules. Indeed, severe degradation in performance is already expected for these innermost modules by the time of LS3, requiring replacement. Secondly, the very high luminosity of 10^{34} cm $^{-2}$ s $^{-1}$ operation will lead to overlapping showers and a corresponding degradation in energy resolution and shower finding efficiency. This problem can be tackled by reducing the Molière radius of the converter and moving to a smaller cell size, for example 2×2 cm 2 in the inner region. Finally, the high number of candidates in every event, for example of π^0 mesons, will lead to an unacceptably large combinatoric background. Hence fast timing information will be essential to associate the candidates to individual pp interactions in the bunch crossing.

One option being pursued is a homogeneous crystal calorimeter with longitudinal segmentation. Materials are being investigated, which offer good radiation hardness, excellent energy resolution and very fast response. Another possibility is a sampling calorimeter, either Shashlik or SpaCal, with a

tungsten-alloy converter, with a crystal component for providing a fast-timing signal. An alternative source of fast timing would be a preshower layer involving silicon pads.

4.2.3. *The muon system*

Operating the current muon system in Upgrade I conditions would lead to a degraded performance due to dead-time induced inefficiencies and an increased rate of ghost hits, all coming from the higher background flux. Future improvements comprise of a modification to the electronics to increase the granularity, the replacement of certain detectors with new pad chambers, and additional shielding around the beam pipe. For Upgrade II luminosities, extra shielding will be required to suppress the flux of punchthrough. This can be achieved by replacing the HCAL with up to 1.7 m of iron, which would provide an additional four interaction lengths compared to the current situation. New detectors will be installed in the innermost region of all stations, with a design possessing both high granularity and high rate capabilities. A promising solution is the micro-resistive WELL detector (μ -RWELL²⁴), a novel MPGD with good prospects for satisfying these criteria. In the lower flux region μ -RWELL or new MWPC detectors could be installed.

4.3. *Trigger and data processing*

At an instantaneous luminosity of up to $2 \times 10^{34} \text{ cm}^{-2} \text{ s}^{-1}$, the LHCb detector is expected to produce up to 400 – 500 Tb of data per second, which will have to be processed in real time and reduced by at least 4 – 5 orders of magnitude before recording the remainder to permanent storage. The ongoing evolution of radiation-hard optical links and commercial networking technology, is expected to allow transferring this volume of the data off the detector and into a processor farm. The Upgrade II data processing will be based around pile-up suppression, in which detector hits not associated with the individual pp interaction of interest are discarded as early as possible in the processing chain.

Timing information from the detectors allows for a particularly fast separation of reconstructed objects according to the pp interaction that produced them LHCb has already demonstrated the ability to perform a full offline-

quality detector alignment, calibration, and reconstruction in near-real-time in Run 2, as well as the ability to perform precision physics measurements using this real-time data processing. Given the ongoing trend towards more and more heterogeneous computing architectures, with CPU server farms increasingly supplemented with GPU or FPGA accelerators, it will be critical to study such hybrid architectures.

5. The HL-LHC Upgrade of the ALICE Detector

During LS2, the ALICE Collaboration is enhancing its physics capabilities with a major upgrade of the detectors, electronics and data-processing systems which will improve the precision of the extracted characteristics of the high density, high temperature phase of strongly interacting matter, the quark-gluon plasma (QGP), together with the exploration of new phenomena in Quantum Chromodynamics (QCD). The major focus for Runs 3 and 4 will be on rare probes such as heavy-flavour particles, quarkonium states, real and virtual photons and low-mass dileptons as well as on the study of jet quenching and exotic nuclear states.^{25,26} The ALICE upgrade strategy is formulated under the assumption that, in Run 3, the LHC will progressively increase the luminosity of Pb beams to reach an interaction rate of 50 kHz (instantaneous luminosity of $6 \times 10^{27} \text{ cm}^{-2}\text{s}^{-1}$). ALICE will then be able to accumulate ten times more integrated luminosity (more than 13 nb^{-1}) than what has been collected so far.

5.1. General layout of upgraded ALICE

Figure 16 shows a sketch of the upgraded ALICE experimental setup which includes a newly built Inner Tracking System (ITS) with a new high-resolution, low-material-budget silicon tracker, which extends to forward rapidities with the new Muon Forward Tracker (MFT), an upgraded Time Projection Chamber (TPC) with Gas Electron Multiplier (GEM) detectors along with a new readout chip for faster readout, new Fast Interaction Trigger (FIT) detector, new readout electronics for the muon spectrometer, Time-of-flight (TOF) detector, Transition Radiation Detector (TRD), Electromagnetic Calorimeter (EMCAL), Photon Spectrometer (PHOS), Zero Degree Calorimeter (ZDC), and an integrated online-offline (O^2) computing system to process and store the large data volume. The beryllium beam pipe near the interaction point (IP)

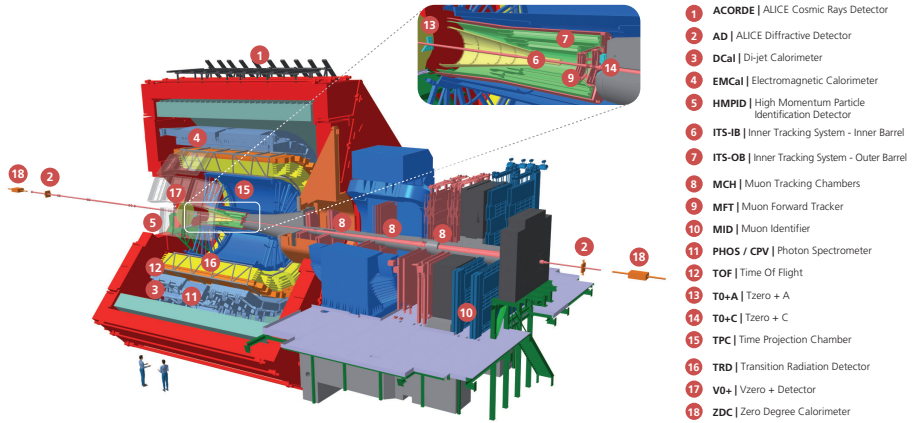


Fig. 16. ALICE upgraded experimental set-up for the HL-LHC.

is also newly installed with a smaller outer radius of 19 mm compared to the former one of 29.8 mm.

5.2. Inner tracking with the ITS and the MFT

The new ITS and the MFT are two all-pixel detectors (see Figure 17) based on CMOS monolithic active pixel sensor (MAPS) technology. In the MAPS technology, both the sensor for charge collection and the readout circuit for digitization are hosted in the same piece of silicon instead of being bump-bonded together. The chip developed by ALICE, and called ALPIDE, uses a 180 nm CMOS process. With this chip, the silicon material budget per layer is reduced by a factor of seven compared to the present ITS. The ALPIDE chip is $15 \times 30 \text{ mm}^2$ in size and contains more than half a million pixels organized in 1024 columns and 512 rows. Its low power consumption ($<40 \text{ mW/cm}^2$) and excellent spatial resolution ($5 \mu\text{m}$) optimally matches the requirements for measuring rare probes such as heavy flavour hadrons in an environment with a large track density.

The ITS (covering the region, $\eta < 1.5$) consists of seven cylindrical layers of ALPIDE chips with 12.5 billion pixels, covering a total area of 10 m^2 . The pixel chips are installed on staves with radial distances ranging from 22 mm to 400 mm to the IP. The new beam pipe allows for the first detection layer to be placed closer to the IP at a radius of 22.4 mm compared to 39 mm during Runs

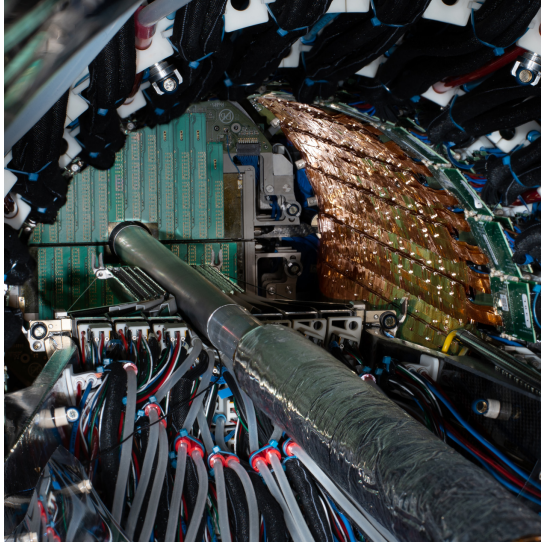


Fig. 17. The figure shows the installed inner (left, middle) and outer (gold colour) barrels of the ITS, along with the MFT (green panel) in the ALICE cavern.

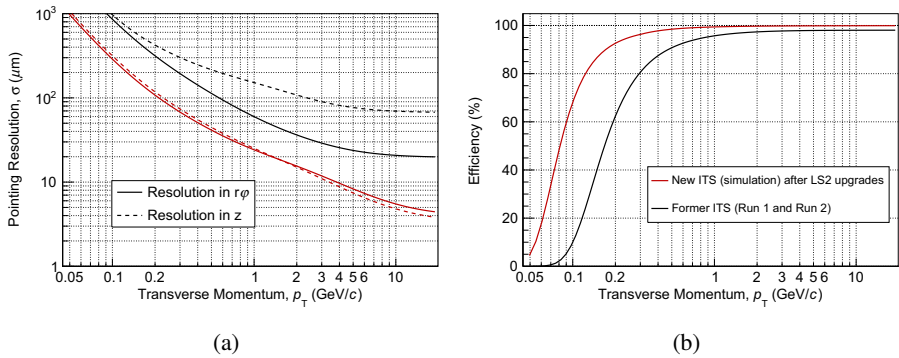


Fig. 18. Expected pointing resolution (a) and efficiency (b) of the upgraded ALICE ITS as a function of the track p_T .

1 and 2. The new ITS detector will improve the impact parameter resolution (Figure 18a) by a factor of three in the transverse plane and by a factor of five along the beam axis. It will also extend the tracking capabilities to much lower p_T , allowing ALICE to perform measurements of heavy-flavour hadrons down to zero p_T (see Figure 18b).

The new MFT detector, located at forward rapidity ($2.45 < \eta < 3.6$), is designed to add vertexing capabilities to the muon spectrometer and will enable several new measurements. As an example, it will allow to distinguish J/ψ mesons that are produced directly in the collision from those that come from decays of mesons which contain a beauty quark. The MFT consists of five disks, each with two MAPS detection planes, placed perpendicular to the beam axis between the IP and the hadron absorber of the muon spectrometer.

5.3. Novel configuration with GEM detectors for the TPC and improved readout

The TPC is the key device for tracking and charged particle identification in ALICE. It consists of a 90 m^3 cylinder filled with gas and divided in two drift regions by the central electrode located at its axial centre. The field cage secures the uniform electric field along the z-axis. The new TPC readout chambers employ a novel configuration of stacks of four GEM detectors (see Figure 19) instead of multi-wire proportional chambers (MWPC). That will allow for continuous readout at 50 kHz with Pb–Pb collisions at no cost to detector performance. The replacement of the chambers in the TPC from MWPC to the GEM detectors had been one of the major activities of the LS2 period. At the end of the year 2020, a major milestone was achieved with the completion of the TPC upgrade, after many years of intense R&D, construction and assembly.

The readout of the TPC as well as the one of the muon chambers is performed by SAMPA, a newly developed, 32-channel front-end analog-to-

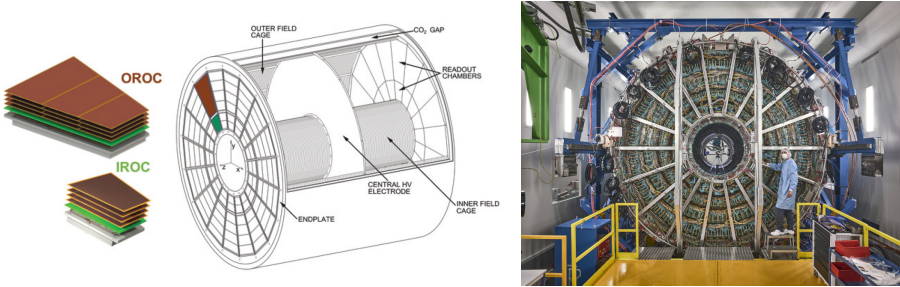


Fig. 19. Configuration of the GEM detectors employed for the ALICE TPC (left) and a photograph showing the installed readout chambers (right).

digital converter (ADC) ASIC with integrated digital signal processor. The newly designed ALICE readout system presents a change in general approach as all Pb–Pb collisions that are produced in the accelerator, at a rate of 50 kHz rate will be read out in a continuous stream. Triggered readout will be used by only a fraction of the detectors and for commissioning and calibration runs and for proton-proton collisions. The central trigger processor (CTP) is being upgraded to accommodate the higher interaction rate.

5.4. Fast interaction trigger (FIT)

The Fast Interaction Trigger (FIT) serves as an interaction trigger, online luminometer, initial indicator of the vertex position, and the forward multiplicity counter. In the offline mode, it provides the precise collision time for the TOF-based particle identification, yields the centrality and interaction plane, and measures cross sections of diffractive processes. The FIT relies on three state-of-the-art detector technologies underpinning components grouped into five arrays surrounding the LHC beamline, at -1, +3, +17, and -19 metres from the interaction point as shown in the left panel of Figure 20. Among the three components that make up the FIT detector, the FT0 is the fastest: comprising 208 optically separated quartz radiators, its expected time resolution for high-multiplicity heavy-ion collisions is about 7 picoseconds. The second component, is a segmented scintillator called FV0. Finally, the Forward Diffractive Detector (FDD), consisting of two nearly identical scintillator arrays, can tag photon-induced or diffractive processes by recognising the absence of activity in the forward direction. A photograph of the installed FV0 and FT0-A is shown in the right panel of Figure 20.

5.5. An integrated online-offline computing system (O^2)

The improved ALICE detector is capable of collecting events at 100 times faster rate during LHC Run-3 compared to previous Runs (1 and 2). The total data volume produced by the front-end cards of the detectors will increase significantly, reaching a sustained data throughput of up to 3 TB/s. This necessitated the development and implementation of a completely new readout and computing system. The ALICE computing model is redesigned in order to minimise the data volume from the detectors as early as possible during the

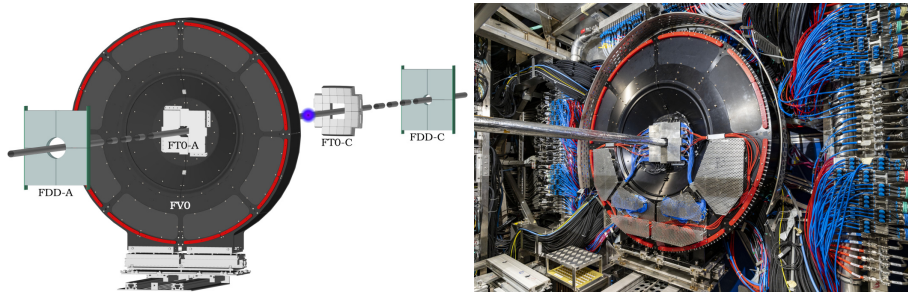


Fig. 20. Layout of the new Fast Interaction Trigger (FIT) of ALICE and a photograph showing the installed detector in the cavern.

data processing. This is achieved by online processing of the data including detector calibration and reconstruction of events in several steps synchronously with data taking. At its peak, the estimated data throughput to the mass storage is 90 GB/s. To reach this goal, a new computing facility is being installed on the surface, near the experiment. It will feature a data storage system with a capacity large enough to accommodate an important fraction of a full year data taking. It will also provide the interface to the permanent data storage at the Tier-0 computing centre at CERN as well as other data processing centres.

5.6. ALICE upgrade during Long Shutdown 3

During LS3 period, ALICE will further upgrade²⁷ ITS to a newly designed vertex detector consisting of curved wafer-scale ultra-thin silicon sensors arranged in perfectly cylindrical layers, featuring an unprecedented low material budget of 0.05% radiation length per layer, with the innermost layer positioned at only 18 mm radial distance from the interaction point. Such a novel detector (ITS3), replacing the three innermost layers of the ITS would significantly improve the measurement of low momentum charmed hadrons and low-mass dielectrons in heavy-ion collisions.

In addition, a new forward electromagnetic and hadronic calorimeter (FoCal)²⁸ covering $3.2 < \eta < 5.8$ will be installed during LS3, which will provide ALICE with unique capabilities to measure small- x gluon distributions via prompt photon production and will significantly enhance the scope of ALICE for inclusive and correlation measurements with mesons, photons, and jets to explore the dynamics of hadronic matter at small x down to $\sim 10^{-6}$.

5.7. ALICE during the HL-LHC era

The running scenario in HL-LHC era foresees a high statistics Pb-Pb collision sample of at least 13 nb^{-1} accompanied with O-O as well as pp, p-O, and p-Pb collisions.²⁶ The future plan after Run 4 calls for a compact, next-generation multipurpose detector as a follow-up to the ALICE experiment.²⁹ The aim is to build a nearly massless barrel detector consisting of truly cylindrical layers based on curved wafer-scale ultra-thin silicon sensors with MAPS technology. This detector is conceived to handle luminosities a factor of 20 to 50 times higher than what will be possible for the upgraded ALICE detector, enabling a new, rich physics program.

The major upgrades during the LS2 and LS3 will allow ALICE to enter the HL-LHC era with a more precise, reliable and faster experimental set-up. The experiment will provide high-precision measurements and pave the way for the next generation of nearly mass-less barrel detectors.

References

1. G. Apollinari, I. Béjar Alonso, O. Brüning, M. Lamont, and L. Rossi, *High-Luminosity Large Hadron Collider (HL-LHC): Preliminary Design Report*. CERN Yellow Reports: Monographs, CERN, Geneva (2015). doi: 10.5170/CERN-2015-005. URL <http://cds.cern.ch/record/2116337>.
2. O. Brüning and L. Rossi, eds., *The High Luminosity Large Hadron Collider: the new machine for illuminating the mysteries of Universe*. vol. 24 (2015). ISBN 978-981-4675-46-8, 978-981-4678-14-8. doi: 10.1142/9581.
3. I. Béjar Alonso, O. Brüning, P. Fessia, M. Lamont, L. Rossi, L. Taviani, and M. Zerlauth, eds., *High-Luminosity Large Hadron Collider (HL-LHC): Technical Design Report*. vol. 10/2020 (2020). doi: 10.23731/CYRM-2020-0010.
4. The ATLAS Collaboration. Technical Design Report for the ATLAS Inner Tracker Pixel Detector. Technical Report CERN-LHCC-2017-021. ATLAS-TDR-030, CERN, Geneva (June, 2018). URL <https://cds.cern.ch/record/2285585>.
5. The ATLAS Collaboration. Technical Design Report for the ATLAS Inner Tracker Strip Detector. Technical Report CERN-LHCC-2017-005. ATLAS-TDR-025, CERN, Geneva (April, 2017). URL <https://cds.cern.ch/record/2257755>.
6. The ATLAS Collaboration. ATLAS Liquid Argon Calorimeter Phase-II Upgrade Technical Design Report. Technical Report CERN-LHCC-2017-018. ATLAS-TDR-027, CERN, Geneva (June, 2018). URL <https://cds.cern.ch/record/2285582>.

7. The ATLAS Collaboration. Technical Design Report for the Phase-II Upgrade of the ATLAS Tile Calorimeter. Technical Report CERN-LHCC-2017-019. ATLAS-TDR-028, CERN, Geneva (June, 2018). URL <https://cds.cern.ch/record/2285583>.
8. The ATLAS Collaboration. Technical Design Report for the Phase-II Upgrade of the ATLAS Muon Spectrometer. Technical Report CERN-LHCC-2017-017. ATLAS-TDR-026, CERN, Geneva (December, 2017). URL <https://cds.cern.ch/record/2285580>.
9. The ATLAS Collaboration. Technical Design Report: A High-Granularity Timing Detector for the ATLAS Phase-II Upgrade. Technical Report CERN-LHCC-2020-007. ATLAS-TDR-031, CERN, Geneva (June, 2020). URL <https://cds.cern.ch/record/2719855>.
10. The ATLAS Collaboration. Technical Design Report for the Phase-II Upgrade of the ATLAS Trigger and Data Acquisition System. Technical Report CERN-LHCC-2017-020. ATLAS-TDR-029, CERN, Geneva (June, 2018). URL <https://cds.cern.ch/record/2285584>.
11. The CMS Collaboration, Particle-flow reconstruction and global event description with the CMS detector, *JINST.* **12**(10), P10003 (2017). doi: 10.1088/1748-0221/12/10/P10003.
12. The CMS Collaboration. The Phase-2 Upgrade of the CMS Tracker. Technical Report CERN-LHCC-2017-009. CMS-TDR-014, CERN, Geneva (Jun, 2017). URL <https://cds.cern.ch/record/2272264>.
13. I. Tomalin et al., An FPGA based track finder for the L1 trigger of the CMS experiment at the High Luminosity LHC, *JINST.* **12**, P12019 (2017). doi: 10.1088/1748-0221/12/12/P12019.
14. The CMS Collaboration. A MIP Timing Detector for the CMS Phase-2 Upgrade. Technical Report CERN-LHCC-2019-003. CMS-TDR-020, CERN, Geneva (Mar, 2019). URL <http://cds.cern.ch/record/2667167>.
15. The CMS Collaboration. The Phase-2 Upgrade of the CMS Barrel Calorimeters. Technical Report CERN-LHCC-2017-011. CMS-TDR-015, CERN, Geneva (Sep, 2017). URL <https://cds.cern.ch/record/2283187>.
16. The CMS Collaboration. The Phase-2 Upgrade of the CMS Endcap Calorimeter. Technical Report CERN-LHCC-2017-023. CMS-TDR-019, CERN, Geneva (Nov, 2017). URL <https://cds.cern.ch/record/2293646>.
17. The CMS Collaboration. Technical Proposal for the Phase-II Upgrade of the CMS Detector. Technical Report CERN-LHCC-2015-010. LHCC-P-008. CMS-TDR-15-02, Geneva (Jun, 2015). URL <https://cds.cern.ch/record/2020886>.
18. The CMS Collaboration. The Phase-2 Upgrade of the CMS Muon Detectors. Technical Report CERN-LHCC-2017-012. CMS-TDR-016, CERN, Geneva (Sep, 2017). URL <https://cds.cern.ch/record/2283189>.
19. The CMS Collaboration. The Phase-2 Upgrade of the CMS Level-1 Trigger. Technical Report CERN-LHCC-2020-004. CMS-TDR-021, CERN, Geneva (June, 2020). URL <http://cds.cern.ch/record/2714892>.
20. CMS Collaboration. The Phase-2 Upgrade of the CMS Data Acquisition and High Level Trigger. Technical report, CERN, Geneva (Mar, 2021). URL <https://cds.cern.ch/record/2759072>.

21. The CMS Precision Proton Spectrometer at the HL-LHC – Expression of Interest. Technical report (Mar, 2021). URL <https://cds.cern.ch/record/2750358>.
22. R. Aaij et al., Expression of Interest for a Phase-II LHCb Upgrade: Opportunities in flavour physics, and beyond, in the HL-LHC era. (CERN-LHCC-2017-003) (2017).
23. R. Aaij et al., Physics case for an LHCb Upgrade II - Opportunities in flavour physics, and beyond, in the HL-LHC era (2018).
24. G. Bencivenni, R. De Oliveira, G. Morello, and M. Poli Lener, The micro-Resistive WELL detector: a compact spark-protected single amplification-stage MPGD, *JINST.* **10**, P02008 (2015). doi: 10.1088/1748-0221/10/02/P02008.
25. B. Abelev et al., Upgrade of the ALICE Experiment: Letter Of Intent, *J. Phys. G.* **41**, 087001 (2014). doi: 10.1088/0954-3899/41/8/087001.
26. Z. Citron et al., *Report from Working Group 5: Future physics opportunities for high-density QCD at the LHC with heavy-ion and proton beams*, In eds. A. Dainese, M. Mangano, A. B. Meyer, A. Nisati, G. Salam, and M. A. Vesterinen, *Report on the Physics at the HL-LHC, and Perspectives for the HE-LHC*, vol. 7, pp. 1159–1410 (Dec, 2019). doi: 10.23731/CYRM-2019-007.1159.
27. The ALICE Collaboration. Letter of Intent for an ALICE ITS Upgrade in LS3. Technical Report CERN-LHCC-2019-018; LHCC-I-034, CERN, Geneva (December, 2019). URL <https://cds.cern.ch/record/2703140>.
28. The ALICE Collaboration. Letter of Intent: A Forward Calorimeter (FoCal) in the ALICE experiment. Technical Report CERN-LHCC-2020-009; LHCC-I-036, CERN, Geneva (June, 2020). URL <https://cds.cern.ch/record/2719928>.
29. D. Adamova et al., A next-generation LHC heavy-ion experiment (Jan, 2019).

This page intentionally left blank

Chapter 4

Operational Experience from LHC Run 1 & 2 and Consolidation in View of Run 3 and the HL-LHC

M. Lamont

CERN, DG Department, Genève 23, CH-1211, Switzerland

By the end of Run 2 in December 2018, the LHC had seen seven full years of operation and a wealth of knowledge and experience has been built up. The key operational procedures and tools are well established. The understanding of beam dynamics is profound and utilized online by well-honed measurement and correction techniques. Key beam-related systems have been thoroughly optimised and functionality sufficiently enhanced to deal with most of the challenges encountered. Availability has been optimised significantly across all systems. This collected experience will form the initial operational basis for Run 3 and subsequent HL-LHC operation.

A brief review of Run 1 and Run 2 is given below, firstly to outline the progress made, and secondly to highlight the issues encountered and surmounted along the way. A synthesis of operational features of the machine and the lessons learnt is then presented. The chapter concludes with brief look at consolidation activities in view of the need to sustain high availability and safe operation given the considerable challenges of the HL-LHC operational regime and the time-frame over which it will operate.

1. Overview of Run 1

Following the recovery from the September 2008 incident, Run 1 saw initial commissioning at reduced energy and the inevitable problems of bootstrapping the operations of a 27 km superconducting collider. Nonetheless, having bedded in the core operational and machine protection systems, healthy levels of performance were achieved. A brief overview of 2010–2013 operations follows, which aims to highlight the main issues addressed.

This is an open access article published by World Scientific Publishing Company. It is distributed under the terms of the Creative Commons Attribution 4.0 (CC BY) License.

1.1. 2010

Essentially, 2010 was devoted to commissioning and establishing confidence in operational procedures and the machine protection system. At this stage the operational basics were sorted out while climbing a steep learning curve.

Ramp commissioning to 3.5 TeV was smooth and led to very public first collisions at 3.5 TeV unsqueezed on the 30th March 2010 (see Figure 1). Squeeze commissioning subsequently reduced the β^* to 2.0 m in all the four main experiments. After the squeeze was commissioned, there was a period of Stable Beams interleaved with continued system commissioning.

The decision was then taken to operate with bunches of nominal intensity. Consequently, there was a halting push through the introduction of nominal bunch intensity and further operational debugging up to a total stored beam energy of around 1 to 3 MJ. This led, eventually, to a period of steady running that was used to fully verify machine protection and operational procedures.

To increase the number of bunches, the move to 150 ns bunch trains was made and the crossing angles across the interaction regions were deployed. A phased increase in total intensity was then performed. Each step-up in intensity was followed by operational and machine protection validation and



Fig. 1. Tense times in the control room on 30th March 2010 on the occasion of first high energy colliding beams in the LHC.

a few day running period to check system performance. The 2010 proton run finished with beams of 368 bunches of around 1.2×10^{11} protons per bunch, and a peak luminosity of $2.1 \times 10^{32} \text{ cm}^{-2}\text{s}^{-1}$. The operational year ended with a successful four week lead-lead ion run.

1.2. 2011

The beam energy remained at 3.5 TeV in 2011 and the year saw combined exploitation and the exploration of performance limits. Following a ramp-up to around 200 bunches (75 ns bunch spacing) taking about 2 weeks, there was a scrubbing run of 10 days which included 50 ns injection commissioning. After an encouraging performance, the decision was made, to operate with 50 ns bunch spacing, and a staged ramp-up in the number of bunches then took place up to a maximum of 1380 bunches.

Having raised the number of bunches to 1380, performance was further increased by reducing the emittances of the beams delivered by the injectors and by gently increasing the bunch intensity. The result was a peak luminosity of $2.4 \times 10^{33} \text{ cm}^{-2}\text{s}^{-1}$ and some healthy delivery rates, topping at 90 pb^{-1} in 24 hours.

A reduction in β^* in ATLAS and CMS from 1.5 m to 1 m delivered the next step up in peak luminosity. This step was made possible by careful measurements of the available aperture in the interaction regions concerned. These measurements revealed excellent aperture consistent with a very good alignment and close to design mechanical tolerances. The reduction in β^* and further gentle increases in bunch intensity produced a peak luminosity of $3.8 \times 10^{33} \text{ cm}^{-2}\text{s}^{-1}$, well beyond expectations at the start of the year.

1.3. 2012 and 2013

2012 was a production year at an increased beam energy of 4 TeV. The choice was made to continue to exploit 50 ns bunch spacing and run with a total number of bunches of around 1380. Based on the experience of 2011, the decision was taken to operate with tight collimator settings, which allowed a more aggressive squeeze to a β^* of 0.6 m. Peak luminosity got up close to its peak pretty quickly. This was followed by determined and long running attempts to improve peak performance. This was successful to a certain extent, revealing some interesting issues at high bunch and total beam intensity,

but had little effect on integrated rates. Beam instabilities, although never debilitating, were a recurring problem and there were phases when they cut into operational efficiency.

It was a very long operational years and included the extension of the proton-proton run until December resulting in the shift of a four week proton-lead run to 2013. Integrated rates were healthy at around the 1 fb^{-1} per week level and this allowed a total for the year of about 23 fb^{-1} to be delivered to both ATLAS and CMS, who had, on the back of the data delivered in 2011 and the first half of 2012, announced the discovery of the Higgs boson on the 4th July 2012.



Fig. 2. Lyn Evans accepting the plaudits in CERN's main auditorium on 4th July 2012 following the announcement of the Higgs boson discovery by ATLAS and CMS.

1.4. Long Shutdown 1 (LS1)

The primary aim of LS1 (2013 to 2014) was the consolidation of the superconducting splices in the magnet interconnects following the incident of 2008. The successful completion of this work allowed, in principle, the current in the main dipole and quadrupole circuits to be increased to the nominal value for 7 TeV operation. The subsequent main dipole magnet training campaign confirmed systematic de-training and the need for a very long training programme to get to 7 TeV, and the decision was taken to operate the machine at a beam

energy of 6.5 TeV during Run 2. Besides splice consolidation, a significant amount of maintenance and other consolidation work was performed on all accelerator systems.

2. Overview of Run 2

Important milestones were reached by the LHC during Run 2 and these included the demonstration of reliable operation with 6.5 TeV beams and exploitation with 25 ns bunch spacing and over 2500 bunches. The design luminosity of $1 \times 10^{34} \text{ cm}^{-2}\text{s}^{-1}$ was passed and a peak of $2.1 \times 10^{33} \text{ cm}^{-2}\text{s}^{-1}$ reached. Around 160 fb^{-1} was delivered to ATLAS and CMS, along with 6.7 fb^{-1} to LHCb and 33 pb^{-1} to ALICE.

2.1. 2015

The principle aims were to re-commission the machine without beam following the major consolidation and upgrades that took place during LS1, and, from a beam perspective, to safely establish operations at 6.5 TeV with 25 ns bunch spacing. The beam configuration targeted was close to nominal i.e. 25 ns bunch spacing with around 2800 bunches of near nominal bunch intensity (1.15×10^{11} protons per bunch). A relatively relaxed β^* of 80 cm in ATLAS and CMS was chosen to provide some aperture margin in the Inner Triplets and thereby less rigorous demands on the collimator settings were required to protect said aperture.

Recommissioning at 6.5 TeV with a bunch spacing of 25 ns was anticipated to be more of a challenge than previous operations at 4 TeV with 50 ns beams. The increased energy implies lower quench margins and thus lower tolerance to beam loss. The hardware (beam dumps, power converters, magnets) is pushed closer to maximum with potential knock-on effects to availability. 25 ns beam was anticipated to have significantly higher electron-cloud than that experienced with 50 ns. It also implies higher total beam current and also higher intensity per injection.

UFOs (“Unidentified Falling Objects”) are micrometer sized dust particles that lead to fast, localized beam losses when they interact with the beam. The phenomenon had already appeared during Run 1 and they were expected to become more of an issue at higher energy. All of these factors came into play in 2015, making for a challenging year.

Two scrubbing runs delivered good beam conditions for around 1500 bunches per beam after a concerted campaign to re-condition the beam vacuum. However, electron cloud, as anticipated, was still significant at the end of the scrubbing campaign.

The initial 50 ns and 25 ns intensity ramp-up phase was tough, having to contend with a number of issues, including magnet circuit earth faults, UFOs, an unidentified aperture restriction in a main dipole, and radiation affecting specific electronic components in the tunnel. Combined, these problems made operations difficult during this phase but nonetheless the LHC was still able to operate with up to 460 bunches and to deliver some luminosity to the experiments albeit with poor efficiency.

The second phase of the ramp-up following a technical stop at the start of September was dominated by the electron cloud generated heat load and the subsequent challenge for cryogenics, which had to wrestle with transients and operation close to their cooling power limits. The ramp-up in number of bunches was consequently slow but steady, culminating in the final figure for the year of 2244 bunches per beam.

The overall machine availability was respectable with around 32% of the scheduled time spent in Stable Beams during the final period of proton-proton physics from September to November. By the end of the 2015 proton run, 2244 bunches per beam were giving peak luminosities of $5.5 \times 10^{33} \text{ cm}^{-2}\text{s}^{-1}$ in the high luminosity experiments with a total delivered integrated luminosity of around 4 fb^{-1} delivered to both ATLAS and CMS. Levelled luminosity of $3 \times 10^{32} \text{ cm}^{-2}\text{s}^{-1}$ in LHCb and $5 \times 10^{30} \text{ cm}^{-2}\text{s}^{-1}$ in ALICE was provided throughout the run.

2.2. 2016 – 2018

2016 started with four weeks of relatively smooth commissioning with beam with the machine fully validated for $\beta^* = 40 \text{ cm}$. The first part of the operating period was hit by a number of serious problems in both the LHC and the injectors – in particular a leak from a cooling circuit to the beam vacuum in the SPS beam dump which limited the beam intensity to the LHC. However, after recovery from the main LHC problems, things progressed well. The number of bunches was increased to 2040 per beam – the maximum with the SPS limit of 72 bunches per injection. A bunch population of 1.1×10^{11}

gave a peak luminosity of $\approx 8 \times 10^{33} \text{ cm}^{-2}\text{s}^{-1}$. Design luminosity was reached on the 26th June thanks to the reduced β^* and lower transverse beam sizes from the injectors, following significant effort to optimise beam brightness via: continuous optimisation; the change of the PS Booster's working point; and the deployment of the batch compression, merging and splitting (BCMS) scheme in the PS.² An increase in the peak luminosity of around +20% and a new record of $1.2 \times 10^{34} \text{ cm}^{-2}\text{s}^{-1}$ was obtained as a result.

The smaller emittances allowed the reduction of the crossing angle from $370 \mu\text{rad}$ to $280 \mu\text{rad}$ and a concomitant increase in the geometrical reduction factor from around 0.59 to 0.70. Performance was also helped by the use of a reduced bunch length in Stable Beams. Thus, despite the limit in the number of bunches and a limit in bunch intensity from injection kicker vacuum issues, the peak performance of 40–50% over nominal was obtained.

2016 was also blessed by unprecedented machine availability: the machine was available for operation 72% of the time scheduled for physics. Overall Stable Beam efficiency was of order 49% (to be compared to 36% in 2012, and 30% for the short production period in 2015).

2017 saw a further reduction in beam size at the interaction point ($\beta^* = 30 \text{ cm}$), which, together with small beams from the injectors, gave a peak luminosity of $2.1 \times 10^{34} \text{ cm}^{-2}\text{s}^{-1}$. Despite the effects of an accidental ingress of air into the beam vacuum during the winter technical stop, referred to as “16L2” after the location of the contamination, around 50 fb^{-1} was delivered to ATLAS and CMS.

2018 essentially followed the set-up of 2017 with a squeeze with ATS optics³ to 30 cm in ATLAS and CMS. Soon after the intensity ramp up the debilitating effects of 16L2 returned, limiting the maximum bunch intensity to approximately 1.2×10^{11} protons per bunch.

Despite the limitation from 16L2, the peak luminosity was systematically close to the $2 \times 10^{34} \text{ cm}^{-2}\text{s}^{-1}$ and somewhat more integrated luminosity was possible thanks to the levelling strategy pursued:

- continuous crossing angle reduction (“anti-levelling”) in Stable Beams, from an initial $160 \mu\text{rad}$ smoothly to $130 \mu\text{rad}$ as a function of the beam current;
- β^* levelling: for the first time the LHC was operated with a dynamically changed optics in Stable Beams, with the β^* in ATLAS and CMS being reduced from 30 cm to 27 cm to 25 cm while colliding.

3. Performance

3.1. Run 1

One of the main features of operations in Run 1 was the use of the high bunch intensity with 50 ns bunch spacing offered by the injectors. The injector complex has succeeded in delivering beam with significantly higher bunch intensities with lower emittances than nominal. This is particularly significant for the 50 ns beam. Happily the LHC was capable of absorbing these brighter beams, notably from a beam-beam perspective. The clear cost was increased pile-up for the high luminosity experiments, which they successfully dealt with.

The corresponding values for the main luminosity related parameters at the peak performance of the LHC through the years are shown in Table 1. The design report values are shown for comparison. Remembering that the beam size is naturally larger at lower energy, it can be seen that the LHC has achieved 77% of design luminosity at 4 sevenths of the design energy with a β^* of 0.6 m (cf. design value of 0.55 m) with half nominal number of bunches.

Table 1. Run 1: Proton performance related parameter overview.

Parameter	2010	2011	2012	Design value
Energy [TeV]	3.5	3.5	4	7
Bunch spacing [ns]	150	75/50	50	25
Number of bunches	368	1380	1380	2808
Bunch population (10^{11})	1.2×10^{11}	1.45×10^{11}	1.7×10^{11}	1.15×10^{11}
β^* in IP 1 and 5 [m]	3.5	1.0	0.6	0.55
Normalised emittance (μm)	≈ 2.0	≈ 2.4	≈ 2.5	3.75
Peak luminosity [$\text{cm}^{-2}\text{s}^{-1}$]	2.1×10^{32}	3.7×10^{33}	7.7×10^{33}	1×10^{34}
Pileup	4	17	37	19
Stored beam energy [MJ]	≈ 28	≈ 110	≈ 140	362

3.2. Run 2

Following a conservative and indeed difficult 2015, peak luminosity in ATLAS and CMS was resolutely pushed throughout the run, principally by:

- a staged reduction of the β^* down to 30 cm at the start of Stable Beams;

- operational use of luminosity levelling via separation, crossing angle reduction and change of β^* – all during Stable Beams;
- provision of high-brightness beams from the injectors (BCMS).

This resulted in a peak luminosity of over twice design and was in fact limited there by the cryogenic cooling capacity of the inner triplets.

Table 2. Run 2: Proton performance related parameter overview.

Parameter	2015	2016	2017	2018
Energy (TeV)	6.5	6.5	6.5	6.5
No. of bunches	2244	2220	2556 – 1868	2556
No. of bunches per train	144	96	144 – 128	144
Bunch population (10^{11})	1.2	1.25	1.25	1.1
β^* [cm] in IP 1 and 5 [cm]	80		40	40 → 30 → 27 → 25
Normalised emittance [μm]	2.6 – 3.5	1.8 – 2	1.8 – 2.2	1.8 – 2.2
Peak Luminosity [$\text{cm}^{-2}\text{s}^{-1}$]	0.6×10^{34}	1.5×10^{34}	2.0×10^{34}	2.1×10^{34}
Half Crossing Angle (μrad)	185	185 → 140	150 → 120	160 → 130

This peak performance was accompanied by impressive availability and a low level of premature dumps following a concerted program of measures outlined in more detail below (5).

The resultant integrated luminosity delivered to ATLAS and CMS is shown in Figure 3.

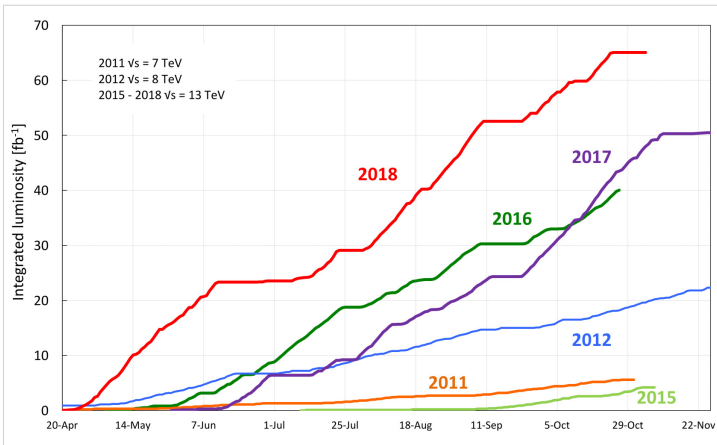


Fig. 3. Average integrated luminosity delivered to ATLAS and CMS during Run 1 and 2.

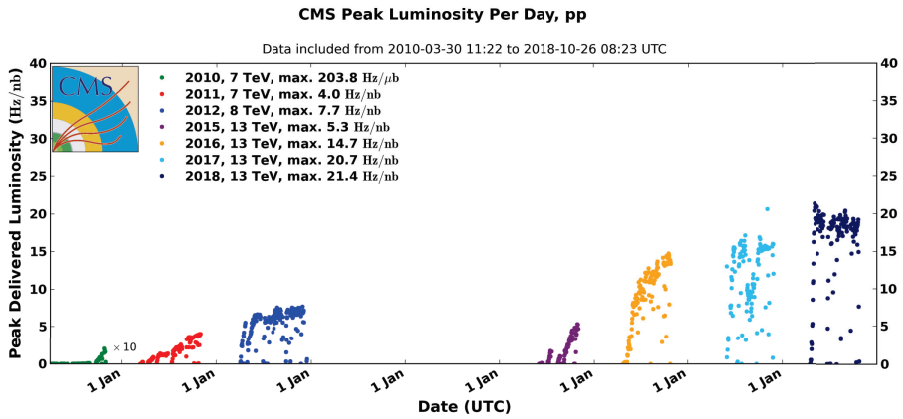


Fig. 4. CMS peak luminosity by day 2010–2018.

CMS’s peak luminosity by day is shown in Figure 4. This illustrates nicely the results of all the measures outlined above.

An interesting snapshot of the LHC’s overall performance during Run 1 and Run 2 is given by ATLAS’s collection of performance records as of the end of 2018 – see Figure 5.

Record	Value	Date
Peak Stable Luminosity Delivered	$2.10 \times 10^{34} \text{ cm}^{-2} \text{ s}^{-1}$	06.05.18 04:19
Maximum Average Events per Bunch Crossing*	88.6	26.10.18 08:11
Maximum Stable Luminosity Delivered in one fill	766.8 pb^{-1}	06.11.17 03:35
Maximum Stable Luminosity Delivered in one day	912.4 pb^{-1}	22.07.18
Maximum Stable Luminosity Delivered for 7 days	5.182 fb^{-1}	2 to 8 September, 2018
Longest Time in Stable Beams for one fill	1 day, 6 hrs, 4 min	09.07.18 22:59
Longest Time in Stable Beams for one day	1 day, 0 min	10.07.18
Longest Time in Stable Beams for 7 days	4 days, 22 hrs, 27 min	17 to 23 October, 2018
Fastest Turnaround to Stable Beams	1 hr, 46 min	14.10.18
Maximum Colliding Bunches	2544	05.05.18
Maximum Charge per Bunch Colliding*	1.83×10^{11}	26.10.18 08:11
Maximum Charge per Beam Colliding	3.08×10^{14}	09.08.17 23:45
Maximum Total Charge per Beam	3.09×10^{14}	09.08.17 23:45
Average Specific Luminosity	$6.94 \times 10^{30} \text{ cm}^{-2} \text{ s}^{-1} (10^{11} \text{ p})^{-2}$	08.08.18 03:47

Fig. 5. LHC performance records at the end of 2018 as noted by ATLAS. * indicates a record achieved during machine development.

3.3. Other users

Throughout Run 1 and Run 2, the operational flexibility of the LHC has allowed the pursuit of a rich variety of physics programmes ranging through lead-lead, lead-proton, xenon-xenon, and an interesting, and sometimes demanding, forward physics programme.

The time limited ion programme inevitably represents a challenge for LHC operations.⁴ The team has to commission new configurations and provide stable physics operation within time frame of one month and meet demanding requirements from the experiments which include multiple changes of beam conditions (intensity ramp-up, solenoid reversal, beam reversal, low/high/levelled luminosity, special beam energies, Van der Meer scans). Nonetheless, heavy-ion operation of LHC has surpassed initial expectations, both quantitatively (3.5 times design luminosity after about 10 weeks of Pb-Pb operation since 2010) and qualitatively (asymmetric p-Pb collisions, unforeseen in the design, have yielded almost 6 times their nominal luminosity and a rich harvest of unexpected physics results). The fact that it has been possible to rapidly recommission the LHC in multiple new configurations efficiently is testament

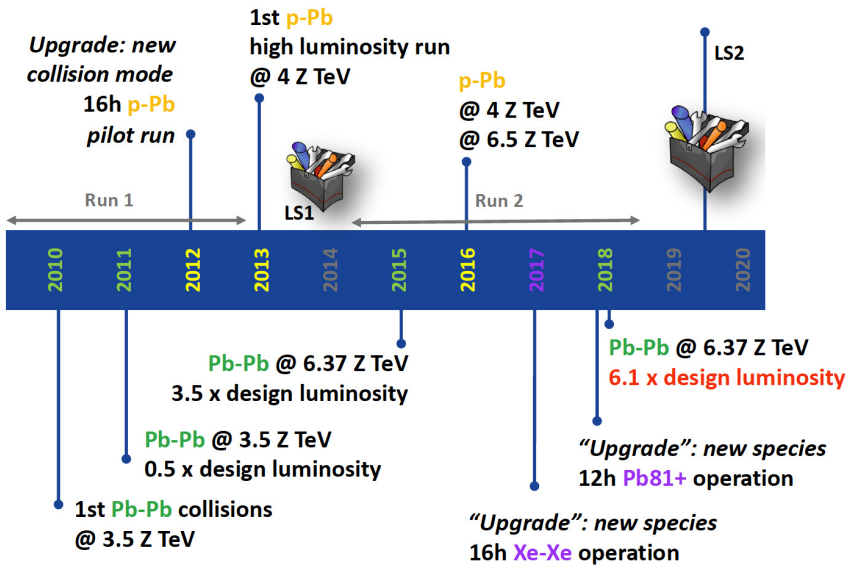


Fig. 6. Timeline of the heavy-ion runs during Run 1 and Run 2. Figure courtesy John Jowett and Michaela Schaumann.⁵

to the understanding and level of control that has been established; the salient points are summarized below.

4. Overview of LHC Operational Characteristics

The performance described above is built on the back of some excellent system performance and some fundamental operational characteristics of the LHC. Very good understanding of the beam physics and a good level of operational control was established and the following features related to beam-based operation may be elucidated.

- The linear optics is well measured and is remarkably close to the machine model. The bare beta-beating is acceptable and has been corrected to excellent. The availability of multi-turn orbit measurements and impressive analysis tools should be noted.
- There is excellent single beam lifetime and on the whole the LHC enjoys very good vacuum conditions.
- Head-on beam-beam is not a limitation although long-range beam-beam has to be taken seriously with enough separation at the long-range encounters guaranteed by sufficiently large crossing angles. The tolerance to high head-on beam-beam tune shifts can be partially attributed to: well-corrected lattice errors, via both an excellent magnet model and a superb optics measurement and correction programme; low external noise, and other perturbations. A full analysis may be found at Ref. [1].
- Better than nominal beam intensity and beam emittance is delivered by the injectors and it has proved possible to collide nominal bunch currents with smaller than nominal emittances with no serious problems.
- Collective effects have been seen with high bunch intensities and with nominal bunch intensities in the presence of electron cloud. Single and coupled bunch instabilities have been suppressed using a range of tools (high chromaticity, Landau damping octupoles and transverse feedback).
- There is better than expected aperture due to good alignment and respect of mechanical tolerances.

- There is excellent field quality, coupled with good correction of non-linearities. The magnetic machine is well understood and the modelling of all magnet types has delivered an excellent field description at all energies. This model includes persistent current effects which have been fully corrected throughout the cycle.
- A strict pre-cycling regime means the magnetic machine is remarkably reproducible. This is reflected in the optics, orbit, collimator set-up, tune and chromaticity. Importantly orbit stability (or the ability to consistently correct back to a reference) means that collimator set-up remains good for a year's run.
- There is low tune modulation, low power converter ripple, and low RF noise. Power converters are delivering remarkably stable and accurate currents ranging from single digits to several thousand amps. Tracking between power converters in the ramp and squeeze is exceptional and the whole system is complemented by a very good front-end control system.
- Efficient, stable, operating procedures and supporting software are in place.

5. Operational Cycle and Availability

The nominal operation cycle provides the framework driving luminosity production. Given the high stored beam energy, the nominal cycle must be fully mastered for effective, safe operation. As of Run 2, the operational cycle was well established for 50 and 25 ns and bunch population exceeding nominal.

The turnaround time is defined as the time taken to go from the dump of a physics fill at top energy back into colliding beams following a refill. Following converted effort over the years and numerous operational improvements, by 2018 the minimum turnaround time had been reduced to around 110 minutes.

Availability is defined as the overall percentage of the scheduled machine time left to execute the planned physics program after removing the total time dedicated to fault resolution. Faults cover an enormous range from a simple front-end computer reboot to the loss of a cold compressor of the cryogenics system with a corresponding loss of time to operations from 10 minutes to potentially days. Availability has, in general, been excellent considering the size, complexity, and operating principles of the LHC. The percentage of sched-

uled proton-proton physics time spent delivering collisions to the experiments (“Stable Beams”) was around 36% in 2012. Following a prolonged campaign of consolidation and targeted system improvements, the corresponding number in 2017 and 2018 was around 50%. As of the end of Run 2, there is good overall system performance and availability based on solid foundations and vigorous follow-up of problems. This is the result of a sustained, targeted effort across the board by all teams, backed by effective fault tracking. Beam related issues such as radiation to electronics, UFOs, beam induced heating have all been relentlessly addressed.

Operations also depends heavily on the superb performance of machine protection and associated systems. These include the beam interlock system, the beam dump system, the beam loss monitors, and the collimation system. There is rigorous machine protection follow-up, qualification, and monitoring; all non-conformities are carefully examined. The importance of this to the success of the LHC so far cannot be over stressed and due credit must be given to the teams involved for ensuring the safety of the machine during beam based operation over the two runs.

Remarkable operational flexibility has been demonstrated, and allowed the team to handle, for example, the slower than expected electron cloud conditioning, and the effects of the accidental air ingress in Sector 12 – the now infamous 16L2.

6. Issues

There have inevitably been a number of challenges during the exploitation of the LHC. Initially, single event effects (SEEs) caused by beam induced radiation to tunnel electronics was a serious cause of inefficiency. However, this problem had been foreseen and its impact was considerably reduced following sustained program of mitigation measures. There were several shielding campaigns prior to the 2011 run including relocation “on the fly” and equipment upgrades. The 2011/12 Christmas stop saw some “early” relocation and additional shielding and further equipment upgrades. Further improvement followed an extensive campaign of relocation, shielding, and hardware upgrades during LS1.

6.1. UFOs

UFOs (Unidentified Falling Objects) are microscopic particles of the order of 10 microns across. These fall from the top of the vacuum chamber or beam screen, become ionised by collisions with circulating protons and then are repelled by the positively charged beam. While interacting with the circulating protons they generate localised beam loss which may be sufficient to dump the beam or, in the limit, cause a quench. They have now been very well studied and simulated. There were occasional dumps in 2012 following adjustment of BLM thresholds at the appropriate time-scales (the beam loss spike caused by a UFO is typically of order 1 ms). With the increase in energy to 6.5 TeV and the move to 25 ns the UFOs become harder (energy) and more frequent (25 ns). Indeed, during the first half of 2015 they were a serious issue but happily there was conditioning and the UFO rate fell to acceptable levels as the year progressed. It should also be noted that it was fortunate that UFO rates have conditioned down, accompanied, as elsewhere, by excellent diagnostics, well thought through mitigation actions and understanding through simulation.

6.2. Beam induced heating

Beam induced heating has been an issue and essentially all cases have been local and, in some way, due to non-conformities either in design or installation. The guilty parties have been clearly identified. Design problems have affected the injection protection devices and the mirror assemblies of the synchrotron radiation telescopes. Installation problem have occurred in a low number of vacuum assemblies. These singularities have all been addressed and the issue is not expected to be problem in the long term.

6.3. Beam instabilities

Beam instabilities were an interesting problem that dogged operations through 2012. It should be noted that this problem paralleled a gentle push in bunch intensity with the peak going into stable beams reaching around 1.7×10^{11} protons per bunch i.e. ultimate bunch intensity. In 2015 operations with 25 ns bunch spacing and lower bunch population meant that intrinsically instabilities should have been less of an issue. However, high electron cloud proved to be a

driver and defence mechanisms were deployed in the form of high chromaticity, high octupole field strength and the transverse damper system.

6.4. *Electron Cloud*

Electron cloud is the result of an avalanche-like process in which electrons from gas ionisation or photo-emission are accelerated in the electromagnetic field of the beam and hit the beam chamber walls with energies of few hundreds of eV, producing more electrons. The electron impact on the chamber wall causes gas desorption as well as heat load for the cryogenic system in the cold regions. High electron densities in the beam chamber can lead to beam oscillations and blow-up of the particle bunches due to the electromagnetic interaction between electrons and protons. Electron bombardment of a surface has been proven to reduce drastically the secondary electron yield (SEY) of a material. In a process known as scrubbing, deliberate invocation of high electron cloud with beam thus provides a means to reduce or suppress subsequent electron cloud build-up.

Although electron cloud was not an issue with 50 ns beam, 25 ns operation proved to be a challenge in 2015, and extensive scrubbing – both dedicated at low energy and while delivering collisions to the experiments – was required. Conditioning thereafter has been slow and the heat load from electron cloud to the cryogenics system remained a limitation in 2018.

7. Conclusions

After seven full years of operation, in the beam parameter regime concerned, the extended LHC team has managed to develop an impressive mastery of the LHC and the delivery of the requisite beam from the injectors. A concise summary of the salient observations is attempted below.

- Good peak luminosity via exploitation of all available parameters (β^* , bunch population, bunch length, crossing angle, transverse emittance).
- Stunning availability following sustained effort from hardware groups accompanied by effective fault tracking.
- Few premature dumps allowing long fills: the UFO rate conditioned down and radiation to electronics effects have been largely mitigated, again after a sustained and successful campaigns.

- Excellent and improved system performance across the board, for example, the new developments of the transverse damper system; collimator alignment software; improved injection kicker performance via hardware modifications.
- The magnets, circuits and associated systems are behaving well at 6.5 TeV.
- Good beam lifetime through injection, ramp, and squeeze with tight control of tune and closed orbit, reflecting that operationally things are very well under control.
- Excellent luminosity lifetime in general with only moderate emittance blow-up in Stable Beams and minimal non-luminosity beam loss after the first hour or so.
- Well established and tuned magnet model, good compensation of persistent current decay and snapback, which couple with a strict magnet cycling give excellent magnetic reproducibility.
- The optics of the machine has been measured and corrected to a impressive level, both linear and higher orders, and a superb level of understanding has been established.
- Aperture is fine and compatible with the collimation hierarchy.
- The collimation system has consistently demonstrated excellent performance and impressive robustness.
- A reliable and well designed machine protection system coupled with a disciplined regime has assured safe exploitation.

2016 was really the first year when it all came together: injectors; operational efficiency; system performance; understanding and control; and availability. In 2017, and 2018, the LHC was able to build on this to move into a true exploitation regime, accompanied, as always, by continued efforts to improve integrated luminosity delivery.

The LHC has moved haltingly from commissioning to exploitation, and is now enjoying the benefits of the decades long international design, construction, and installation effort – it's clear that the foundations and fundamentals are good. It's present performance is worthy reflection of this effort and the huge amount of experience and understanding gained and fed-forward over the last years. Remarkably, not only can a 27 km superconducting collider work, it can work well!

8. Consolidation in view of HL-LHC

The Accelerators & Technology sector strives for a maximum reliability and availability of the whole accelerator complex and the associated experimental areas. Given the age, complexity, and operational lifetime of the complex, the provision of spares and consolidation of the existing equipment and associated technical infrastructure are key issues in ensuring that the needs of the Organisation's diverse physics program are assured. This, of course, includes the flagship LHC programme, which is and will be intimately dependant on the performance of the injectors.

The ongoing consolidation programme consists in the replacement (or renovation) of equipment and related technical infrastructure at the end of the normal lifetime, i.e. when:

- An equipment can no longer be used with sufficient reliability;
- The equipment has been exposed to levels of radiation that compromise its functionality;
- Commercially available spare parts are lacking;
- Technical support is no longer available for components or software;
- The systems no longer meets safety regulations and standards.

The performance and availability of all technical systems is actively monitored with the Accelerator Fault Tracking system. This can give some indication of potential issues and the need for targeted consolidation. However, consolidation of most major systems has to be anticipated before impacting the performance of the machine. For example, the end of life of electronic components, where there are long lead times for product design, prototyping, tendering, and production. Other factors such as maintenance cost, availability of expertise, availability of spares, standardisation, modern functionality/reliability have also to be taken into consideration.

Typical, during an operational year, active consolidation continues as far as possible during technical stops, along with provision of spares, and development and production of components for a major programme of deployment in the long shutdowns. The LHC consolidation program has over 100 consolidation activities ongoing at any one time, and besides long-term activities, the consolidation program also had to respond to a number of punctual demands resulting from issues arising from regular operations.

On the magnet front, spares for the many types of magnets, both superconducting and room temperature must be assured. Of note, as of 2021, is the ongoing production of five spare main quadrupole magnets. A number of corrector magnets have been lost over the years, and remain in the machine, and are either electrically by-passed or simply removed from operations. In the interest of nominal performance, and to avoid the potential loss of a debilitating number of magnets, plans to recover these circuits in the future long shutdowns should be made.

The machine protection group continues targeted revision and renovation of the key elements of the quench protection and energy extraction systems, in particular the tunnel electronics. Vacuum, heavily implicated around the whole machine, continues a rolling program of upgrades which includes mobile pumping stations, bake-out systems, and other elements. In close collaboration with HL-LHC project, the collimation team has developed and partially deployed the next generation of robust, low impedance collimators.

Beam instrumentation is targeting upgrades of its big distributed systems (beam position monitors and beam loss monitors). This will take several years and in 2017 they started on the BLM system, part of the effort being dedicated to the development of radiation hard front-end electronics for the HL-LHC era. In addition, they perform consolidation and upgrades of a number of stand-alone systems (wire-scanners, bunch current transformers, interlocked BPMs); here the goal is performance enhancing consolidation, taking the opportunity of not only replacing equipment, but also leveraging experience and technology to improve system performance to match the needs of the HL-LHC era.

The use of industrial controls is widespread and a number of teams (e.g cryogenics, cooling and ventilation) are renovating and upgrading their systems. The control group continues maintenance of its fundamental infrastructure (field bus installations, repeaters, timing system, control room hardware).

Technical Infrastructure (cooling, ventilation, electrical distribution, lifts, cranes etc.) has a long-term rolling consolidation program with staged replacement and renovation of the enormous amount of site wide systems. Cooling and ventilation continues renovation of HVAC units in surface buildings and industrial control renovation. Heavy engineering will continue to execute its rolling replacement of lifts, overhead cranes and hoists.

In Long Shutdown 2, the LHC beam dump system (LBDS) saw urgent consolidation of the beam dump blocks following issues in Run 2. This experience will be fed forward into the design of new dump blocks which will be produced for the HL-LHC intensities. The LBDS pulse forming networks (PFNs), switches and electronics are the subject of diligent scrutiny and appropriate consolidation as befits their criticality.

References

1. Sondre Vik Furuseth and Xavier Buffat. Modeling of nonlinear effects due to head-on beam-beam interactions. *Physical Review Accelerators and Beams*, 21(8):081002, August 2018.
2. Heiko Damerau, Steven Hancock, Alexandre Lasheen, and Damien Perrelet. RF Manipulations for Special LHC-Type Beams in the CERN PS. In *9th International Particle Accelerator Conference*, 6 2018.
3. S. Fartoukh *et al.*, *Achromatic telescopic squeezing scheme and by-products: From concept to validation*, Phys. Rev. Accel. Beams **24**, 021002.
4. J. Jowett, Colliding Heavy Ions in the LHC, 9th International Particle Accelerator Conference doi:10.18429/JACoW-IPAC2018-TUXGBD2
5. Jowett, John M. and Schaumann, Michaela, Overview of Heavy Ions in LHC Run 2 Proceedings of the 9th LHC Operations Evian Workshop CERN-ACC-2019-059, 15-25 2019.

Chapter 5

Machine Physics and Performance

G. Arduini, R. De Maria, M. Giovannozzi, G. Iadarola, E. Métral,
Y. Papaphilippou and R. Tomás

CERN, BE Department, Genève 23, CH-1211, Switzerland

The main beam and machine parameter choices and the underlying beam dynamics considerations are reviewed together with the main challenges and expected performance.

1. Overview of the Performance Goals and Main Choices

The maximum instantaneous luminosity L_{inst} of the HL–LHC will be limited by the maximum event pile-up per bunch crossing that the high luminosity experiments ATLAS and CMS, located at the Interaction Points (IP) 1 and 5 respectively, will be able to handle. After the upgrade they are expected to cope with values of at least 140 and up to 200 events per bunch crossing. These values correspond to instantaneous luminosities of approximately $5 \times 10^{34} \text{ cm}^{-2}\text{s}^{-1}$ and $7.5 \times 10^{34} \text{ cm}^{-2}\text{s}^{-1}$ for the maximum number of bunches that can be injected in the LHC (approximately 2750).¹ The HL–LHC project^{2,3} aims to achieve a ‘virtual’ peak luminosity that is considerably higher than the maximum imposed by the acceptable event pile-up rate, and to control the instantaneous luminosity to a lower value L_{lev} during the physics fill (‘luminosity levelling’) so that the luminosity production can be sustained over longer periods to maximize the integrated luminosity. The luminosity evolution can be estimated taking into account the beam population N_{beam} reduction due to the collisions (the so called ‘burn-off’) in n_{IP} collision

This is an open access article published by World Scientific Publishing Company. It is distributed under the terms of the Creative Commons Attribution 4.0 (CC BY) License.

points⁴ as

$$\frac{dN_{beam}}{dt} = -n_{IP}\sigma_{tot}L_{inst} , \quad (1)$$

where the burn-off cross-section has been conservatively taken to be the total cross-section σ_{tot} (111 mb at 7 TeV^{1,5}). No other sources of intensity reduction or emittance blow-up are considered in this simplified model. In operation with luminosity levelling an effective beam lifetime τ_{eff} can be defined from Eq. (1) as,^{4,6}

$$\tau_{eff} = \frac{N_{beam}}{n_{IP}\sigma_{tot}L_{lev}} , \quad (2)$$

illustrating that τ_{eff} is proportional to beam intensity. Figure 1 shows the expected yearly-integrated luminosity as a function of the ‘virtual’ peak luminosity L_{virt} for $L_{lev} = 5 \times 10^{34} \text{ cm}^{-2}\text{s}^{-1}$ and $7.5 \times 10^{34} \text{ cm}^{-2}\text{s}^{-1}$. The corresponding optimum fill length (i.e. the length of time for each fill that will maximize the average luminosity production rate) is also shown. The annual integrated luminosity is determined for a minimum turnaround time of 145 minutes,⁷ a scheduled physics time for luminosity production of 160 days per year with an efficiency for physics (defined in Ref. [8,9]) of 50%. In order to reach the goal of integrating $250 \text{ fb}^{-1}/\text{year}$ the peak virtual luminosity L_{virt} must exceed $1.5 \times 10^{35} \text{ cm}^{-2}\text{s}^{-1}$ if $L_{lev} = 5 \times 10^{34} \text{ cm}^{-2}\text{s}^{-1}$. Larger values are of particular interest if $L_{lev} = 7.5 \times 10^{34} \text{ cm}^{-2}\text{s}^{-1}$ or higher.

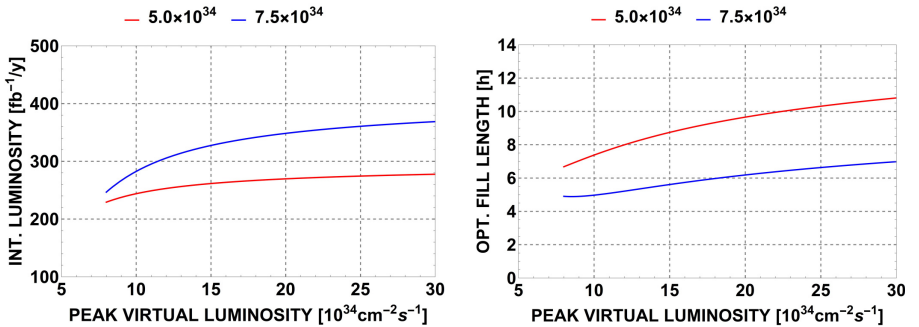


Fig. 1. Left: Expected annual integrated luminosity. Right: optimum fill length as a function of the ‘virtual’ peak luminosity L_{virt} for $L_{lev} = 5 \times 10^{34} \text{ cm}^{-2}\text{s}^{-1}$ and $7.5 \times 10^{34} \text{ cm}^{-2}\text{s}^{-1}$. A circulating current of 1.1 A (corresponding to $N_{beam} = 6.1 \times 10^{14}$ p) and two ($n_{IP}=2$) high-luminosity IPs have been assumed.

The instantaneous luminosity L_{inst} is given by:¹⁰

$$L_{inst} = \frac{n_b N^2 f_{rev} \gamma}{4\pi \beta^* \epsilon_n} R(\beta^*, \sigma_z, d_{bb}) \quad (3)$$

where n_b is the number of colliding bunches per beam, N is the bunch population, f_{rev} is the beam revolution frequency, γ is the relativistic gamma factor and assuming equal R.M.S. normalized emittances ϵ_n in collision for both beams and transverse planes. The Twiss beta function β^* at the IP determines, together with ϵ_n , the R.M.S. beam size $\sigma^* = \sqrt{\epsilon_n \beta^* / \gamma}$ at the IP (assuming that the contribution to the beam size due to the dispersion and the momentum spread of the beam can be neglected). Here and below it is assumed that the beam is ultra-relativistic.

A crossing angle θ_c is needed to separate bunches immediately upstream and downstream of the IP to avoid unwanted parasitic collisions. This leads to a reduced geometric overlap between the colliding beams, and hence to a reduction in luminosity. The crossing angle needs to be increased when reducing the β^* in order to maintain a sufficiently large normalized long-range beam-beam separation d_{bb} , defined as $d_{bb} = \theta_c \beta^* / \sigma^*$. The luminosity is also reduced by the ‘‘hourglass effect’’ that arises from the increase of the β function upstream and downstream of the IP along the bunch longitudinal distribution. The hourglass effect is enhanced by a reduction in β^* and by an increase in bunch length σ_z . The luminosity reduction factor R in Eq. (3) takes both the crossing angle and the hourglass effect into account. Equation (3) shows the parameters that can be varied to maximize the instantaneous luminosity. The following considerations have been used as guidelines to define the HL-LHC machine and beam parameters at the project conception:¹¹

- The maximum number of bunches n_b is limited by:
 - the minimum time interval between bunch crossings at the IP that can be handled by the detectors: this is limited to 25 ns;
 - the maximum number of bunches n_{SPS} that can be transferred safely from the SPS to the LHC;
 - the rise-time of the injection kickers in the SPS and LHC, extraction kickers in the PS and SPS, and abort gap kicker in the LHC;
 - the need to inject one train consisting of a few bunches (typically 12 nominal bunches for 25 ns spacing), for machine protection

considerations, before injecting one nominal batch;¹²

- the need for non-colliding bunches for background evaluation by the experiments and a sufficient number of collisions for the lower luminosity experiments.¹³
- The maximum bunch population N should be well below the single bunch Transverse Mode Coupling Instability (TMCI) threshold in the LHC, expected to be 3.5×10^{11} p/bunch.¹⁴
- The maximum cryogenic power available to cool the beam screen limiting the beam current circulating in the LHC, $I_{beam} = eN_{tot}f_{rev}$ (where e is the proton charge and N_{tot} the total beam population) to approximately 1.1 A.¹⁵
- The total available power for the main 200 MHz SPS RF system after the LHC Injector Upgrade limiting the maximum bunch population to $N_{SPS} = 2.4 \times 10^{11}$ protons at SPS extraction for 288 bunches. An intensity loss of about 5% distributed along the cycle is assumed from SPS extraction to collisions in the LHC.
- The beam brightness $B = N/\epsilon_n$ is limited by:
 - The maximum brightness achievable in the injectors $B_{SPS} \approx 1.5 \times 10^{11}$ p/ μm after the full injector upgrade¹⁶
 - The total head-on beam-beam tune shift $\Delta Q_{bbHO} \approx 0.03$.¹¹
 - Intra-beam scattering (IBS) inducing transverse and longitudinal emittance blow-up, particularly at injection but also in the acceleration, squeeze, and collision phases.
- The minimum β^* is constrained by:¹⁷
 - The triplet aperture as the beam size at the triplet and $\theta_c = d_{bb}\sqrt{\epsilon_n/\gamma\beta^*}$ required to maintain a sufficiently large normalized beam-beam long-range (BBLR) separation d_{bb} and minimize the corresponding tune spread ΔQ_{bbLR} increase with $1/\sqrt{\beta^*}$;
 - The maximum β function at the triplet that can be matched to the regular optics of the arcs within the distance available in the matching section between the triplets and the arcs;
 - The strengths of the arc sextupoles available to correct the chromaticity generated by the triplets (proportional to the maximum value of the β function β_{max}).

Table 1 shows the beam parameters in collision, selected on the basis of the above considerations.

Table 1. HL–LHC nominal parameters for 25 ns operation^{18,19} for two production modes of the LHC beam in the injectors.⁸

Parameter	Nominal LHC (design report)	HL–LHC (standard)	HL–LHC (BCMS) [#]
Beam energy in collision [TeV]	7	7	7
Particles per bunch, N [10^{11}]	1.15	2.2	2.2
Number of bunches per beam	2808	2760	2744
Number of colliding bunches in IP1 and IP5*	2808	2748	2736
Total beam population N_{tot} [10^{14}]	3.2	6.1	6.0
Beam current [A]	0.58	1.10	1.10
Half-crossing angle in IP1 and IP5 [μrad]	142.5	250	250
Minimum norm. beam–beam long–range separation [σ]	9.4	10.5	10.5
Minimum β^* [m]	0.55	0.15	0.15
ϵ_n [μm]	3.75	2.50	2.50
Longitudinal emittance ϵ_L [eVs]	2.50	3.03	3.03
R.M.S. energy spread [10^{-4}] (q-Gaussian distribution)	-	1.1	1.1
R.M.S. energy spread [10^{-4}] (FWHM equiv. Gaussian)	1.13	1.29	1.29
R.M.S. bunch length [cm] (q-Gaussian distribution)	-	7.61	7.61
R.M.S. bunch length [cm] (FWHM equivalent Gaussian)	7.55	9.0	9.0
IBS horizontal [h]	105	16.5	16.5
IBS longitudinal [h]	63	19.2	19.2
Radiation damping [h]	26	26	26
Piwinski parameter	0.65	2.66	2.66
Total reduction factor R_0 without crab cavities at min. β^*	0.836	0.342	0.342
Total reduction factor R_1 with crab cavities at min. β^*	-	0.716	0.716
Beam–beam tune shift/IP [10^{-3}]	3.1	8.6	8.6

Table 1. (Continued)

Parameter	Nominal LHC (design report)	HL-LHC (standard)	HL-LHC (BCMS) [#]
Peak luminosity without crab cavities $L_{peak} [10^{34} \text{ cm}^{-2}\text{s}^{-1}]$	1.00	8.11	8.07
Peak luminosity w. crab cavities $L_{virt} = L_{peak} R_1/R_0 [10^{34} \text{ cm}^{-2}\text{s}^{-1}]$	-	17.0	16.9
Events/crossing w/o levelling and without crab cavities	27	212	212
Levelled luminosity [$10^{34} \text{ cm}^{-2}\text{s}^{-1}$]	-	5.0	5.0
Events/crossing μ (with levelling and crab cavities)	27	131	132
Max. line density of pile-up events during fill [evts/mm]	0.21	1.3	1.3
Levelling time [h] (assuming no emittance growth) [‡]	-	7.4	7.3
Number of collisions in IP2/IP8	2808	2492/2574**	2246/2370**
N at injection [10^{11}] ^{††}	1.20	2.30	2.30
Maximum number of bunches per injection N_{SPS}	288	288	240
Total beam population per injection [10^{13}]	3.46	6.62	6.62
ϵ_n at SPS extraction [μm] ^{‡‡}	3.50	2.10	1.70

[#] BCMS parameters are only considered for injection and as a backup parameter set in case one encounters larger-than-expected emittance growth in HL-LHC during injection, ramp, and squeeze.

* Assuming one less batch from the PS for machine protection (pilot injection, transfer line steering with 12 nominal bunches) and non-colliding bunches for experiments (background studies, etc.). Note that due to RF beam loading the abort gap length must not exceed the 3μ design value.

[‡] The total number of events/crossing is calculated with an inelastic cross-section of 81 mb, while 111 mb is assumed as a pessimistic value for calculating the proton burn off and the resulting levelling time.^{1,5}

** The lower number of collisions in IR2/8 compared to the general-purpose detectors is a result of the agreed filling scheme, aiming as much as possible at an equal sharing of collisions between the experiments.

^{††} An intensity loss of 5% distributed along the cycle is assumed from SPS extraction to collisions in the LHC.

^{‡‡} A transverse emittance blow-up of 10-15% on the average H/V emittance in addition to that expected from IBS is assumed (to reach $2.5 \mu\text{m}$ of emittance in collision for 25 ns operation).

In addition the following main choices have been made to enhance L_{virt} :²⁰

- installation of large aperture triplet quadrupoles close to the IP to allow sufficient aperture for large crossing angles and small β^* ;
- installation of crab cavities, i.e. RF deflecting cavities providing opposite transverse kicks to the head and tail of the bunches upstream and downstream of the IP to suppress the crossing angle at the IP and provide head-on collisions.

2. Optics and Layout Choices

As mentioned above, the smaller values of β -function at the interaction points impose the use of large-aperture magnets. In addition, the higher luminosity implies also a larger amount of collision debris that should be absorbed outside the coils of the superconducting magnets to avoid depositing energy there, thus inducing the risk of quenching or reducing the magnets' lifetime. This means that the larger coil aperture shall be used not only for increasing the available space for the beams, but also for installing appropriate shielding materials. Furthermore, external absorber devices have to be added to the layout to provide additional shielding power. These devices are either fixed masks, installed in front of the superconducting magnets, or collimators with movable jaws. It is worth stressing that the larger coil aperture of the triplet quadrupoles imposes the use of a new technology for the superconducting cable, Nb₃Sn based cables instead of Nb-Ti as in the LHC. The length and strength of the triplets has been optimized to reduce the peak- β function in the triplets,²¹ compatibly with the hardware constraints, in order to reduce the smallest reachable β^* and the optical aberrations.

Two more aspects have been considered in the design of the new layout, namely the optimisation of the crab cavities and the system of orbit correctors used to generate the separation and crossing angle bumps. Crab cavities require well-defined optical conditions (large β functions) to be fulfilled in order to achieve optimal performance. The system of orbit correctors has been also highly optimised²² to reduce the strength needs without compromising its performance or that of the crab cavities.²³ A final improvement has been provided by the implementation of a full remote alignment system²⁴ that allows a substantial reduction of the required strength. The latest layout of the new

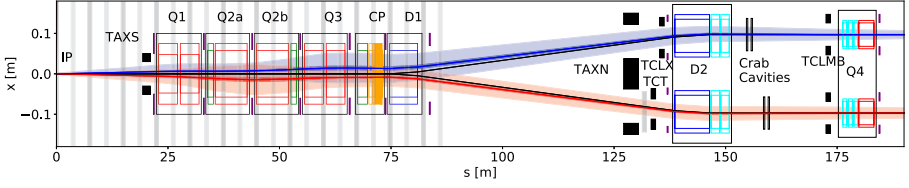


Fig. 2. Overall layout of the insertion region between the IP and Q4. The dark blue and dark red areas represent the 2σ beam envelope for the $\beta^* = 15$ cm round optics. The lighter regions correspond to the 11.9σ value of the beam envelope for a normalized emittance of $2.5 \mu\text{m}$ and including tolerances in β -beating and orbit distortions. This represents the required minimum beam-stay clear in the IR magnets shown to be protected by the collimation system in collision. The shaded grey areas in the triplet region represent the locations of the parasitic beam-beam encounters in which the BPM (marked in purple) should not be installed.

insertions, i.e. version 1.4, is shown in Figure 2 for the region between the interaction point and the Q4 quadrupole, including TAXS, TAXN (collision debris absorbers), D1, D2 (combination separation dipoles), and TCLX-TCTX (tertiary collimators).

Note that the HL–LHC layout has been incrementally updated since version 1.0^{25–27} following the development of the new hardware, cost optimisation exercises, new requests from the experiments, and also the experience gathered during the LHC Run 2^{28–30} (the comprehensive and up-to-date list of the changes with respect to the LHC layout is available in Ref. [20]).

As far as the optics is concerned, different settings of the experimental insertions³¹ elements provide the conditions for the proton⁷ and ion programmes,³² as well as special runs for luminosity calibration (the so-called Van der Meer scans). The baseline scenario of the proton programme relies on the Achromatic Telescopic Squeeze (ATS) optics scheme³³ with equal $\beta^* = 15$ cm in the transverse planes (so-called round optics). Alternative configurations, based on optical solutions featuring unequal β^* values in the transverse planes are also available (so-called flat optics). The advantage of flat optics is that a smaller-than-nominal β^* value can be used in the plane orthogonal to the crossing plane (as low as 7.5 cm), while a larger one is used in the crossing plane (see Section 8). Note that for the proton physics runs, the ALICE experiment is supposed to take data with $\beta^* = 10$ m, while LHCb with β^* as low as 1.5 m to provide the necessary luminosity for the possible LHCb Phase-II upgrade.³⁴ For the ion programme, low β^* optics have been

designed for all experiments (50 cm for ATLAS, ALICE, CMS, and 1.5 m for LHCb).

Luminosity levelling is assumed in all experiments, which is achieved by varying β^* and the crossing angle (for ATLAS and CMS), or the parallel separation (for ALICE and LHCb). This implies that a dynamic change of the optics is part of the collision process. Nevertheless, one should consider that the injection and collision optics are different. An optics transition is performed during the energy ramp³⁵ so that at the end of the energy ramp, the optics is ready for bringing the beams into collisions.

As a last point, the overall HL–LHC ring optics has been reviewed and improved also in the non-experimental insertions. Worth mentioning is the optics in IR4, hosting the RF cavities and most of the instrumentation devices, which fulfills the specific constraints for RF cavities, pick-ups, kickers, and beam profile measurement devices, as well as suitable optical conditions for the possible use of electron lenses.³⁶ Furthermore, the optics in IR6, hosting the beam dump, has been developed so to fulfill special phase advance constraints needed for machine protection considerations.^{37,38}

3. Linear Optics Correction and Specification for Power Converter Performance

Optics control in the HL–LHC is challenging due to the very low β^* of 15 cm at the two high luminosity IPs and the increased β functions in the arcs during the telescopic squeeze. The peak β -beating achieved in LHC in the range between 7% and 11%^{39–41} cannot be guaranteed for HL–LHC. Simulations⁴² and experiments⁴³ suggest that a peak β -beating of 20% is a more realistic target, which was then used to define the aperture margins of the machine.⁴⁴ The tightest tolerance on optics comes from the experiments requiring a luminosity imbalance not larger than 5%, which requires a β^* control to better than 2.5% at the IPs. To measure β^* the gradient of the quadrupoles closest to the IP are modulated while measuring the tune. This technique is called K-modulation.^{45,46} In the following all HL–LHC hardware aspects relating to optics control and new possible measurement techniques are discussed.

The tight tolerances in the optics control impose tight requirements on the magnetic measurement and powering precision as well as on alignment. For illustration, a Gaussian error distribution in the integrated gradient of

the HL–LHC triplet quadrupoles with a R.M.S. of 10^{-4} produces a R.M.S. β -beating of 7.2‰ at $\beta^*=15$ cm.

The integrated gradient of HL–LHC triplet quadrupoles will be within 0.1‰ standard deviation of the design value, which is the accuracy of the measurement. The precision of the measurement is $\pm 2 \times 10^{-4}$ which allows pairing quadrupoles of similar strength within the Q2 module.⁴⁸

The longitudinal location of the nodal points of the triplet quadrupoles are expected to follow a uniform distribution with a maximum deviation of ± 2 mm. For a definition of nodal points see.⁴⁹ Similarly, the magnetic length has an accuracy of ± 5 mm.⁴⁹ The tilt angle around the beam axis of each quadrupole in the triplet is specified to be within ± 2 mrad, while the measurement accuracy of the average tilt of the two quadrupoles in a cold mass is ± 0.5 mrad. The local magnetic field angle in each section of the quadrupole should be within ± 2 mrad⁴⁹ from the average field angle of the whole magnet.

The accuracy of β^* from K-modulation is determined by the knowledge of the integrated gradient and alignment of the closest quadrupoles to the IP (Q1A left and right to the IP) and of the machine tune drifts over the time scale of the measurement. The resolution of the tune measurement contributes to the β^* uncertainty and therefore needs to be optimized by correcting chromaticity and amplitude detuning and further reduced thanks to repeated measurements.

Table 2. Power converter stability specifications for HL–LHC circuits. All uncertainties are 2σ in units of $10^{-6}I_{rated}$, where σ is the rms.⁵⁰

Circuit name	I_{rated} [A]	PC class	Stability	
			20 min	12 h
RB ^a , RQ(D/F) ^a	13000	1	0.4	2
RQX	18000	0	0.2	1
RTQX(1/3), RCBX	2000	2	1.2	15.5
RTQXA1 ^b	60	4	5	40
RQSX ^d , RCBRD, RTB9 ^c	600	3	2	34
RC(S/O/D/T)X, RCB(C/Y) ^a	120	4	5	40
RD(1/2)	14000	0	0.2	1
RQ4 ^a	4000	2	1.2	15.5
RQ(5/6) ^a	5000	2	1.2	15.5

^a Existing circuit assumed not to be upgraded.

^b Compatible with the use of the trim as $I_{max} = 35$ A in operation.

^c Standard 600 A PC is assumed even though $I_{max} = 250$ A in operation.

^d Standard 600 A PC is assumed even though $I_{max} = 200$ A in operation.

From power converter (PC) stability specifications, Table 2,⁵⁰ tune drifts can be estimated and used in realistic simulations of K-modulation incorporating all mentioned uncertainties.⁵¹

As a benchmark the tune jitter was measured in LHC for various optics and compared to expected values from power converter specifications.⁵² Model predictions were close or below measurements by up to a factor 2. This might indicate that there are other sources of tune drifts not yet identified, making current simulations optimistic. Figure 3 (left) shows the expected β^* accuracy from K-modulation versus β^* and assuming that the tune jitter, δQ , scales as $1/\beta^*$, which is confirmed in simulations. The tune modulation amplitude is also scaled with $1/\beta^*$ as the Q1A maximum current is 35 A. The maximum tune modulation is limited to 0.01 to avoid beam loss. The green curve corresponds to the current HL-LHC baseline having a β^* accuracy of 7.5% at $\beta^*=15$ cm and reducing to the target of 2.5% at $\beta^*=25$ cm. The yellow curve corresponds to an upgrade of the ATS arcs' dipole power converters to class 0 (see Chapter 11 for the definition of the classes of power converters). The β^* accuracy is improved to 4% at $\beta^*=15$ cm. The point at $\beta^*=7.5$ cm corresponds to the case of a flat optics with $\beta^* = 30/7.5$ cm and the β^* uncertainty is as large as 33% without any upgrade of the main dipole PC stability. The upgrade here also improves accuracy by a factor 2 but still remaining far from the target. Figure 3 (right) shows the contributions to the β^* uncertainty when

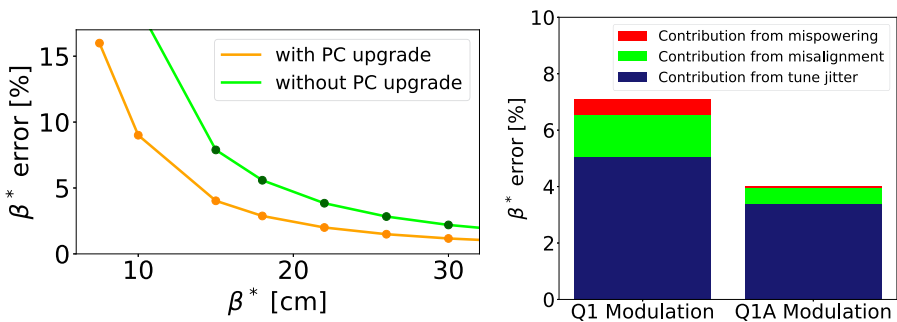


Fig. 3. Left: Expected β^* accuracy from K-modulation versus β^* for the current HL-LHC baseline (green) and an upgrade of the ATS arcs' dipole power converters to class 0 (yellow). The case with $\beta^*=7.5$ cm corresponds to the flat optics with $\beta^* = 30/7.5$ cm. Right: contributions to the β^* accuracy when modulating Q1A and the two modules of Q1 at $\beta^*=15$ cm and $\delta Q = 2.9 \times 10^{-5}$ (upgraded of four dipole power converters to class 0).

modulating only the Q1A current and when the current of both Q1 magnets is modulated at $\beta^*=15$ cm and $\delta Q = 2.9 \times 10^{-5}$, being the tune jitter the largest contribution in both cases. Modulating only Q1A improves β^* accuracy by almost a factor 2 at $\beta^*=15$ cm. For that reason an independent trim circuit has been added to allow modulating the strength of the Q1A magnet.^{53,54} Since the Q1A tune modulation amplitude decreases with β^* the full Q1 should be used for K-modulation measurements above $\beta^*=25$ cm.

As mentioned above, these estimates are optimistic as unknown sources of tune jitter may appear, yet the HL-LHC baseline does not reach the target β^* measurement accuracy. Alternative or complementary β^* control techniques will be required in HL-LHC. Luminosity waist scans have been experimentally tested in Run 2, demonstrating a performance better than K-modulation in the measurement of the waist location, as shown in Figure 4.⁵⁵ Yet, these scans cannot measure the individual β^* in the different planes and beams. Therefore Beam Position Monitors (BPM) with better resolution, such as those equipped with the DOROS electronics,⁵⁶ will also be needed in HL-LHC to measure the β at the waist location from the phase advance across the interaction region drift.⁵⁵ Optics-measurement-based BPM calibration techniques⁵⁷ will be needed to further improve measurement results. Machine learning techniques are also being explored.^{58,59}

The triplet quadrupole tilt errors are corrected by minimizing the coupling resonance driving terms from beam measurements. Assuming the above tilt

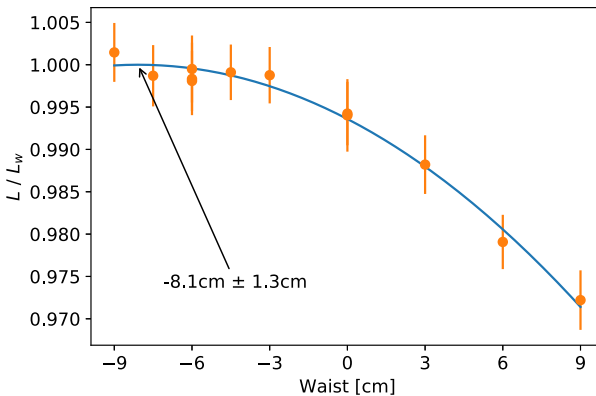


Fig. 4. Luminosity waist scan as proof-of-principle for accurate waist position measurement.⁵⁵

tolerances there is about a factor 2 margin in the strength of the triplet skew quadrupole corrector, MQSX.⁵⁵ Imperfect local coupling correction at the IP can lead to luminosity loss even with perfect global coupling. HL–LHC luminosity is about a factor 4 more sensitive to left-right unbalanced MQSX coupling correction than LHC.^{60,61} A technique to improve the locality of the coupling correction was tested in 2018 by applying a rigid shift of all IP betatron waists.⁶²

The completion of the linear optics commissioning requires that non-linear corrections are in place to avoid beam losses while exciting forced betatron oscillations, to ensure high quality tune measurements and to minimize feed-down effects. Chapter 28 describes the various challenges involved in the non-linear commissioning.

The HL–LHC triplet Nb₃Sn superconductor features an unstable behaviour when subject to a change in voltage. This is referred to as “flux jumps”. Measurements have revealed that these are expected to happen in the first half of the energy ramp, inducing a relative change in the gradient by about 0.2×10^{-4} with a rise time of about 50 ms. Simulations of flux jumps on orbit,⁶³ tune and emittance growth⁶⁴ show that these do not pose a threat for the HL–LHC performance.

4. Dynamic Aperture and Field Quality

Dynamic aperture (DA) is defined as the average amplitude in transverse phase space where the oscillation amplitudes remain within the defined mechanical aperture over a specified time interval. It is one of the key quantities for the design of modern colliders, based on superconducting magnets, such as Tevatron,^{65–67} HERA,^{68–71} RHIC,⁷² and the CERN Large Hadron Collider (LHC) (see e.g., Ref. [47] for a detailed overview). Note that the DA reduces typically with increasing time intervals and that for design purposes it is customary to assume a conservative definition based on the minimum amplitude.

In a mathematical sense, stable motion implies bounded motion for arbitrary time, whereas in a physical context, particle stability can be linked to a maximum number of turns, N_{\max} , which depends on the specific application, for which bounded motion occurs. If an ensemble of initial conditions defined on a polar grid ($x = r \cos \theta$, $y = r \sin \theta$ $0 \leq \theta \leq \pi/2$, where x, y are expressed in units of σ_x, σ_y of the beam dimension) is tracked for up to N_{\max}

turns to assess their stability, then the DA can be defined as:⁷³

$$DA(N) = \frac{2}{\pi} \int_0^{\pi/2} r_s(\theta; N) d\theta \equiv \langle r_s(\theta; N) \rangle_\theta. \quad (4)$$

where $r_s(\theta; N)$ stands for the last stable amplitude (disregarding any stable domain disconnected from the origin) for up to N turns in the direction θ , for $N < N_{\max}$. Given the choice of the co-ordinates, $DA(N)$ is expressed in units of beam sigma. The DA can be considered a function of time and whenever its border is inside the phase-space region occupied by the beam, particles will be pushed towards high amplitudes and eventually lost. This is the essence of the proposed relationship between DA and particles losses,⁷⁴ namely

$$\frac{I(N)}{I(1)} = 1 - \int_{DA(N)}^{+\infty} e^{-\frac{r^2}{2}} r dr = 1 - e^{-\frac{DA^2(N)}{2}}, \quad (5)$$

where $I(N)$ represents the beam intensity at turn N . The relation (5) establishes a direct link between DA and losses and can be used to model the beam lifetime. In this way, the possibility to set a tolerances on the DA based on the target beam losses or lifetime is available. This provides a very solid approach, based on physical observables such as losses, in the design phase of a particle accelerator. Parenthetically, Eq. (5) is the basis of an innovative method to experimentally determine the DA,⁷⁵ which complements the standard method,⁷⁶ as well as of novel models to describe luminosity evolution in the presence of burn off and losses due to DA.^{77,78} DA computation consists of simulating the evolution of a large number of initial conditions, distributed to provide good coverage of the phase space under study. Given the CPU-intense nature of these simulations, studies explored techniques for finding easy-to-compute dynamical quantities, such as the so-called early indicators,⁷⁹ or to achieve parallelisation over the initial conditions.⁸⁰ In addition, models to fit, and eventually extrapolate, the dependence of the DA on the number of turns^{81–83} have been looked for. The idea behind is that long-term behaviour of the DA, a computationally heavy task, can be extrapolated from numerical simulations performed over a smaller number of turns. Recently, refined models have been proposed⁸³ that improve the numerical stability of the model parameters: this paves the way to determine and study the dependence of the model parameters on the HL–LHC configuration in view of optimising the overall performance, also extrapolating to realistic time scales. In this respect, the approach studied seems mature, allowing the standard paradigm

of analysing the DA at a fixed number of turns to be abandoned, and instead considering the properties of its extrapolation and of the model parameters. It is worth stressing that these advanced techniques rely on a modern tracking code and postprocessing tools. The SixTrack code⁸⁴ is in fact kept up-to-date thanks to a vigorous plan aimed at improving and developing it.⁸⁵

For the sake of completeness, it is important to mention that in parallel to the activities aimed at achieving a better understanding of the DA, research work is carried out to develop new diffusive models^{86,87} to describe the beam dynamics in the HL-LHC, using the LHC as an experimental test bed. The novelty of this research is the functional form of the diffusion coefficient that is derived from the stability-time estimate of the Nekhoroshev theorem,^{86,87} which has been proven to be compatible with experimental results. Following these encouraging outcomes, the next steps will be to establish a relationship between the approach based on the DA and that based on the diffusion equation, the use of symplectic tracking to compute the diffusion coefficient, and then to predict the beam distribution evolution, including also noise effects.

Part of these concepts have been applied to the analysis of the DA of the HL-LHC, whose main results have been collected in Ref. [88]. Detailed studies of the DA as a function of the main ring parameters, such as linear tunes, chromaticities, strength of the Landau octupoles, and phase advance between the two high-luminosity insertion regions, have been carried out. The dependence on the field quality of the main HL-LHC magnet families has been a major activity. In this respect, given that magnetic measurement results are becoming available, their impact on the DA has been assessed in detail, also in view of providing guidance to the magnets' acceptance process prior to installation in the tunnel (parenthetically, these intense tracking campaigns profited from the support of the volunteer-computing platform LHC@Home⁸⁹). Of course, each configuration has been probed for both magnetic channels corresponding to the two beams. The ring configuration did not include the beam-beam effects and the target minimum DA has been set to 12σ at injection and 10σ at flat-top energy for the nominal HL-LHC emittance of $2.5 \mu\text{m}$ and a relative momentum deviation of 2.7×10^{-4} .²⁰ These values ensure that the impact of the magnets' field quality is in the shadow of that of the beam-beam effects (the target DA with beam-beam being around 6σ , see next section). While at injection energy the field quality is fully compatible with the target DA, this is not completely the case at flat top

and special care has been taken to study and improve the way the non-linear corrector magnets should be operated. This topic is particularly challenging and is discussed in more detail in Chapter 28.

5. Incoherent Collective Effects

5.1. Beam-Beam

The incoherent beam-beam interaction has been a limiting factor for the beam and luminosity lifetime of past and present colliders. In combination with machine imperfections, magnetic non-linearities and noise effects, it can limit the DA at collision and thereby impact performance by imposing limits on beam brightness (in particular due to the head-on effect) or on the minimum normalized BBLR separation. Although in the HL-LHC, the crossing angle impact to the virtual luminosity is mitigated by the crab crossing, a reduced crossing angle is always beneficial for reducing the requirements on insertion magnets' aperture, the irradiation of the triplet magnets by luminosity debris⁹⁰ and to maximize β^* reach.

The fact that the incoherent BBLR effects dominate the reduction of the DA at collision was evidenced since the design phase of the LHC.^{47,91,92} Driven by beam dynamics considerations in LHC simulations,⁹³ the target value for the 10⁶-turn minimum DA was chosen to be 6 σ for the nominal HL-LHC emittance of 2.5 μm and a relative momentum deviation of 2.7×10^{-4} .⁹⁴ An experimental analysis of the observed beam lifetime has been initiated since LHC Run 1.⁹⁵ A clear demonstration of the correlation between beam lifetime and DA at collision was provided during Run 2.⁹⁶⁻¹⁰⁰ In Figure 5, the simulated minimum DA (over a set of initial transverse amplitude ratios) and the measured burn-off corrected lifetime (in logarithmic scale) during crossing angle reduction experiments is being presented for two type of beams (BCMS in orange and "8b+4e" in blue).^{96,101} The beam lifetime after subtraction of the luminosity burn-off must be significantly larger than the burn-off lifetime to minimize the impact of the DA reduction due to non-linearities at collision. For example, a burn-off corrected lifetime 10 times longer than the burn-off lifetime will reduce the total beam lifetime by 10%. Therefore DA limits should be set to guarantee a burn-off corrected lifetime of a few hundred hours taking into account that the burn-off beam lifetime ranges between 10

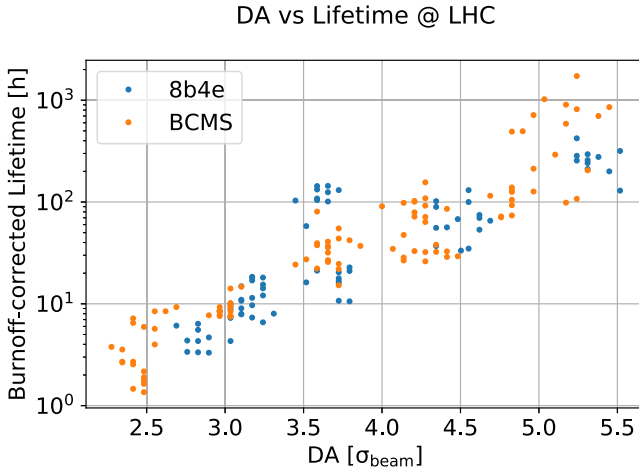


Fig. 5. Measured burn-off-corrected lifetime plotted against the corresponding simulated DA along two MD fills for crossing angle reach studies, for BCMS (orange) and “8b+4e” (blue) beam types.^{96,101}

and 20 h during the fill for the HL-LHC nominal scenario with two high luminosity IPs. A minimum DA of 6σ (or 5σ in the presence of magnetic field errors) is therefore mandatory also to account for additional effects that cannot be simulated yet (e.g. as the impact of electron cloud (e-cloud) on lifetime observed at the end of Run 2^{98,99}).

Multi-parametric DA studies have validated the operational scenario⁷ both for nominal and ultimate luminosity with a constant half crossing angle of $250\ \mu\text{rad}$ in IP1 and IP5, including the margins for reducing it during the collision process, through working point (WP) optimisation.^{97,102,103} In Figure 6, DA tune scans at the start (top) and at the end (bottom) of the levelling process are presented, with the black lines representing to iso-DA contours. The Landau octupoles are powered at $-300\ \text{A}$ (i.e. at approximately half of their maximum current) and partially compensate the BBLR tune-spread,^{104,105} whereas the chromaticity is set to 15 units. Adjusting the WP to (62.315, 60.320) at the end of levelling is crucial for guaranteeing DA of 6σ (bottom), leaving very little margin for further optimisation. Although at the start of levelling (top) there is more margin with respect to DA, because of the large head-on tune-spread the optimal WP is found at (62.320, 62.325). This means that the WP should be varied along the diagonal during the levelling process,

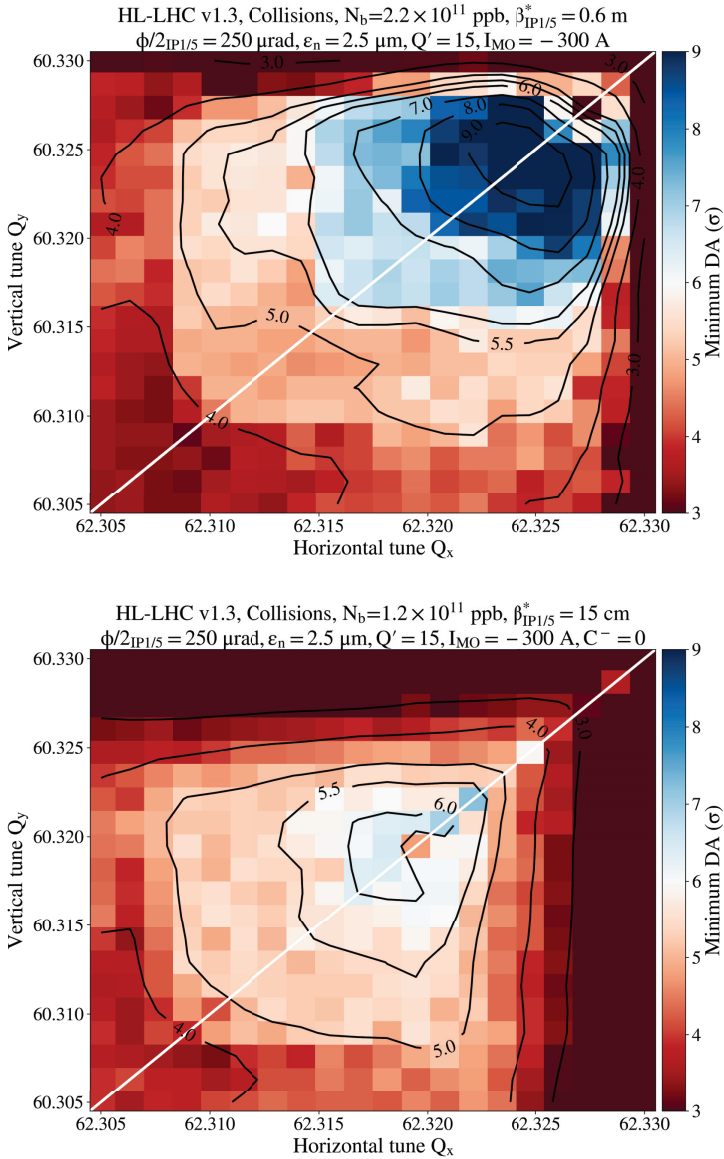


Fig. 6. DA tune scans at the start (2.2×10^{11} ppb, top) and the end of levelling (1.2×10^{11} ppb, bottom), at a half crossing angle of $250 \mu\text{rad}$ with octupoles at -300 A and chromaticity of 15 units. No field errors have been considered here.^{97,102,103}

even if the crossing angle is kept constant during the fill, a complication that could be solved with additional non-baseline measures such as the BBLR compensation with DC wires (see Chapter 27).

The correlation of the (half) crossing angle with the bunch population in terms of DA at $\beta^* = 15$ cm and the optimised working point is shown in the top part of Figure 7. On top of the iso-DA lines, the iso-luminosity contours are overlaid in units of $10^{34} \text{ cm}^{-2}\text{s}^{-1}$. The 6σ DA with a constant half crossing angle of $250 \mu\text{rad}$ and target luminosity of $5 \times 10^{34} \text{ cm}^{-2}\text{s}^{-1}$ can be maintained until the intensity drops to around 1.2×10^{11} ppb, through the above-mentioned WP optimisation. At the ultimate luminosity of $7.5 \times 10^{34} \text{ cm}^{-2}\text{s}^{-1}$, and for the same crossing angle, the DA is slightly below 6σ . Operation at high luminosity of LHCb ($1.5 \times 10^{34} \text{ cm}^{-2} \text{ s}^{-1}$) appears to be also compatible with the above DA target, although it might limit the possibility of further optimizing the crossing angle throughout the levelling phase by reducing it further, for $\beta^* > 15$ cm, up to a target DA (adaptive crossing angle scenario).^{9,97,102,103} The impact of magnetic field imperfections is presented in the bottom part of Figure 7, where DA simulations are performed assuming 60 different realizations of the machine. A statistical analysis is performed for the nominal (blue) and ultimate (red) luminosity operation. The average DA spread is found to be at the level of 0.3σ . Therefore, the beam–beam interaction is the main DA degradation mechanism, while the magnetic imperfections have a minor additional effect. It should be stressed that even for the worst seed, a 5σ DA can be guaranteed.

The interplay between the non–linearity of the beam–beam interaction with machine non-linearities and various sources of noise can further enhance diffusion, thereby leading to emittance blow-up and beam losses. The main sources of noise studied for the HL-LHC is the ripple in the phase and amplitude of crab cavities voltage and in the current of magnet power converters. The white random phase noise in the crab cavities can be efficiently suppressed by the transverse feedback (ADT) with a damping time of 10 turns.^{106,108–110} The crab cavity relative voltage amplitude noise is estimated as 5×10^{-5} ,¹⁰⁶ causing a luminosity loss of about 2%¹⁰⁷ for both nominal and ultimate scenarios. From measurements during the crab cavity prototype tests in the SPS it was initially expected that the HL-LHC emittance growth estimates would be too pessimistic.¹¹¹ However recent studies show that the emittance growth suppression in the SPS is due to collective effects only appearing in

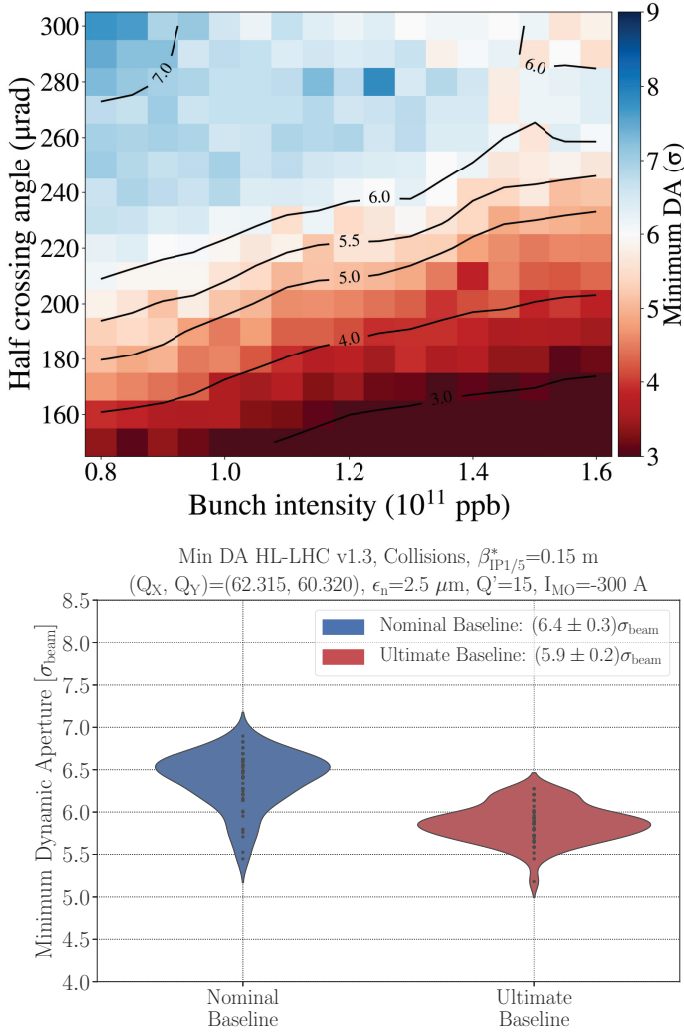


Fig. 7. DA correlation of half crossing angle and bunch population towards the end of levelling (top) and statistical result of the impact of magnetic field imperfections in DA for the nominal (blue) and ultimate (red) scenario at the end of levelling (bottom).^{97,102,103}

the SPS¹¹² and therefore not relevant for HL-LHC. The only hope to mitigate the emittance growth from crab cavity amplitude noise in the HL-LHC is via a dedicated feedback, not foreseen in the project baseline.

The requirements for magnet power supply current noise have been studied for low^{50,54} and high-frequencies.¹¹³ The observations in the present LHC of noise spectral lines at around 8 kHz is of concern. A simulation and measurement campaign to clearly identify its origin and impact on DA and thereby lifetime is presently undertaken.^{113,114}

5.2. Emittance degradation mechanisms

The emittance evolution in the present LHC is dominated by IBS, electron cloud, noise, synchrotron radiation (at flat top) and some additional mechanisms yet to be fully identified.^{98,115,116} A model for the emittance evolution based on semi-analytical IBS models including coupling and a numerical parametrisation of growth rates for all possible dependent parameters has been built and was used as a tool to identify instrumentation issues and follow-up luminosity performance during Run 2,^{117,118} coupled with a fully automated numerical framework for data monitoring and off-line analysis. This model, in combination with the measured data in particular during the last year of Run 2, was then used to estimate HL-LHC performance.¹¹⁵ For the nominal and the ultimate scenarios, the extra transverse emittance growth at collisions results in a 2% degradation of the integrated luminosity per day (additional to the CC noise contribution).

6. Beam Induced Heat Loads on Cryogenic Beam Screens

The LHC and HL-LHC cryogenic magnets are equipped with actively cooled beam-screens, which intercept beam induced heating mainly due to synchrotron radiation, impedance and e-cloud effects.⁴⁷ The nominal operating temperature is 20 K for most of the beam screens, with the exception of the new inner triplet assemblies and the D1 dipoles in IR1 and IR5, which will be operated at higher temperature (60 - 80 K).

Large heat loads on the beams screens have been observed during the LHC Run 2, when the LHC was routinely operated with the 25 ns bunch spacing, as assumed in the LHC design and in the the HL-LHC baseline.^{119,120} Figure 8 (left) shows the heat loads measured in the LHC arcs during two consecutive fills in 2017. The first is a regular physics fill using the 25 ns bunch spacing and a bunch population of 1.1×10^{11} p/bunch, while the second is a

test fill performed with the same bunch population but with a bunch spacing of 50 ns. It can be noticed that, with the 25 ns spacing, the heat loads are much larger than expected from impedance and synchrotron radiation and, in some of the arcs, are very close to the design cooling capacity of 160 W/half-cell (corresponding to 8 kW/arc). With the 50 ns, instead, the heat loads are much smaller and compatible with the expectation from impedance and synchrotron radiation. Moreover, with the 25 ns, beams large differences are observed among the eight LHC arcs. These differences are unexpected as the arcs are by design identical, and their origin is presently being investigated.^{120,121}

Such a large difference between fills performed with different bunch spacings, together with other experimental observations with different beam conditions, allow excluding that the observed differences among sectors are originated by an artefact in the cryogenic measurement and point to e-cloud effects as the only plausible cause.¹²²

Figure 8 (right) shows the estimated heat loads on the arc beam screens as a function of the bunch population for one of the sectors having the largest heat load.¹²³ The contributions from different sources are indicated with different colours. The e-cloud contributions are calculated inferring the Secondary

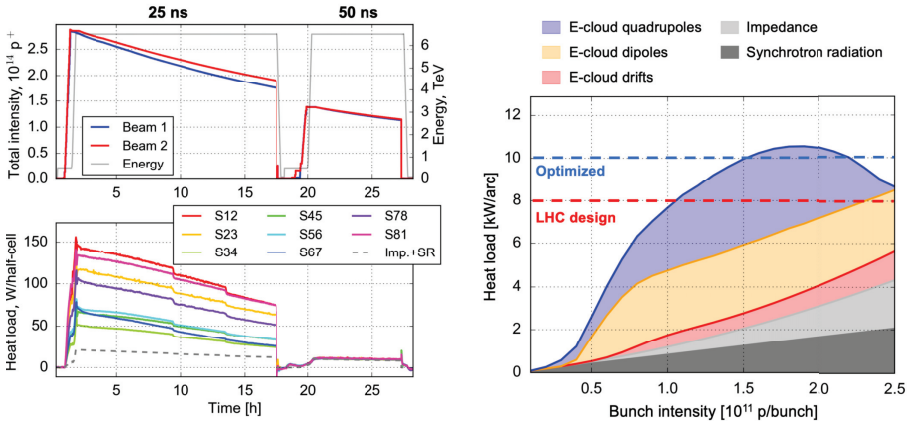


Fig. 8. Left: Heat loads measured during a regular luminosity fill with 25 ns bunch spacing and during a subsequent test fill with 50 ns bunch spacing, both with 1.1×10^{11} p/bunch. Right: Heat load expected for the sector showing the highest load (S81) as a function of the bunch population. The different contributions are indicated in different colors. The cooling capacity for the LHC design and the optimized cryogenics configuration is shown by the dashed lines.

Electron Yield (SEY) of the beam screen surface from the heat loads measured during LHC operation and assuming that this will remain unchanged (after conditioning) in the HL–LHC era.

The increase in bunch population, from 1.1×10^{11} p/bunch presently used at the LHC to 2.3×10^{11} p/bunch foreseen for HL–LHC, implies a significant increase in the contributions from impedance and synchrotron radiation. Nevertheless, only a relatively mild increase of the total heat loads is expected for bunch intensities above 1.2×10^{11} p/bunch, due to the fact that the contributions from e-cloud are not expected to increase significantly for larger bunch population.

The red line in Figure 8 (right) represents the available cooling capacity for the arc beam screens in the design configuration of the LHC cryogenics.⁴⁷ This would not be sufficient to cope with the expected heat loads. During Run 2, the LHC cryogenics has been operated in an optimized configuration (using one cold-compressor unit to serve two consecutive sectors) profiting from the lower-than-expected heat loads at 1.9 K. The compatibility of this optimized configuration with the HL–LHC operational scenarios is being verified. With this optimized configuration, a higher cooling capacity becomes available for the arc beam screens,¹²⁴ as indicated by the blue line in Figure 8 (right), which is very close to the maximum load expected during the HL–LHC luminosity fill.

The dependence of the e-cloud heat load on the bunch population is a critical input for the estimates made above, which were based on numerical simulations of the e-cloud buildup. Direct experimental checks of these simulation results were not possible in Run 2 using long bunch trains for intensities above 1.2×10^{11} p/bunch, due to intensity limitations in the injectors. Nevertheless, towards the end of 2018, trains of 12 bunches with high bunch population (up to 1.9×10^{11} p/bunch) became available from the injectors and could be used for tests in the LHC. The results of those experiments are shown in Figure 9 (left). The data clearly show that the heat loads from e-cloud tend to saturate above 1.5×10^{11} p/bunch. When comparing the measurement results against simulations, very good agreement is found especially for the high-load sectors, as shown in Figure 9 (right).¹²³

The beam screen in the new magnetic elements developed for HL–LHC will receive a surface treatment (coating with amorphous carbon) to reduce the surface SEY and suppress the e-cloud.^{125,126} The treatment will be applied

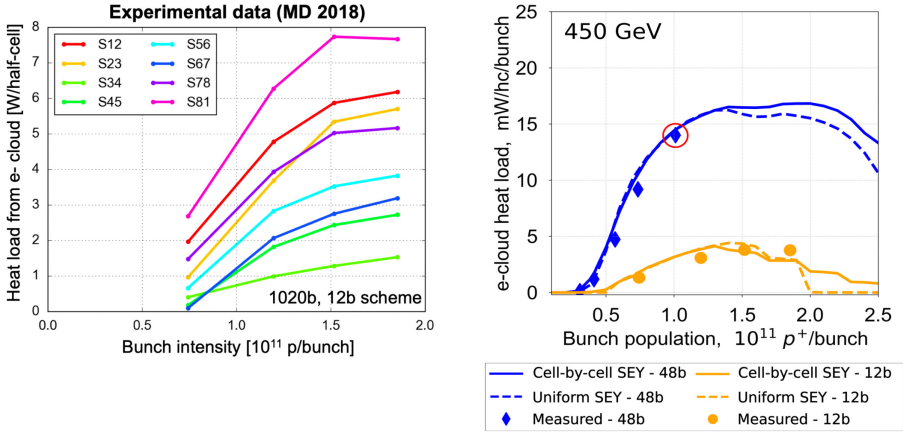


Fig. 9. Left: Heat loads measured for different bunch intensities at 450 GeV in the eight LHC arcs using trains of 12 bunches. The load expected from impedance and synchrotron radiation is subtracted. Right: Comparison of simulation results against measured heat-load data for one of the sectors showing the highest heat load. The continuous line is calculated assuming different SEY in the different half-cells. The dashed line is based on a simplified model assuming uniform SEY over the entire arc. The data point used to infer the SEY values is circled in red.

also on critical elements already present in the LHC, in particular all the inner triplets and some of the matching quadrupoles in IR1, IR2, IR5 and IR8.

In case the intensity limitations from the heat loads on the beam screens are found to be stronger than expected, the heat loads can be mitigated exploiting the flexibility in the filling pattern design. A reduction of the heat loads by about 8% can be achieved using trains of 48 bunches instead of trains of 72 bunches, with practically no impact on the number of circulating bunches.¹²⁷ A stronger reduction of the heat loads can be achieved exploiting the “8b+4e” filling pattern made of short trains of 8 bunches separated by gaps of 4 empty slots. With this scheme the number of circulating bunches is reduced to 1972 bunches per beam. Hybrid schemes mixing standard and “8b+4e” bunch trains can also be envisaged, which allow maximizing the number of bunches, compatibly with the available cooling capacity.¹²⁸ The effectiveness of the “8b+4e” scheme for electron cloud suppression as well as that of the hybrid schemes have been proven experimentally in the LHC.^{123,129}

7. Coherent Collective Effects

7.1. The HL-LHC impedance

The current HL-LHC impedance model has been constructed by adding the contributions of the main accelerator components interacting with the beam, mainly from analytical models and simulations.¹³⁰ The relative contributions of the different equipment to the transverse (dipolar) and longitudinal impedance models are plotted for 1 kHz to 10 GHz at top energy (for the pre-squeeze at $\beta^* = 50$ cm) in Figure 10 (the impedance model at injection energy can also be found in¹³⁰). The LHC effective impedance is significant at high energy, when the primary (TCP) and secondary (TCSG) collimators in the betatronic collimation section in LSS7, become its dominant contributors, over a wide range of frequencies, because of their small gaps. As the impedance is composed of several complex functions of frequency, it is not possible to represent the impedance by a single number to have an idea of the importance of the collimators. Instead, what can be done is to look at the Landau octupole current required to stabilise the HL-LHC beam at 7 TeV for the assumed chromaticity and transverse damper gain (the Landau octupole current, the chromaticity and transverse damper are the three knobs available in the LHC and HL-LHC to stabilise the transverse coherent instabilities, as discussed in more detail below). It can be seen in particular that 98% of the required Landau octupole current is coming from the collimators and that the IR7 collimators alone (both primaries and secondaries) contribute to 79%.¹³⁰ During Run 2, systematic measurements have been performed to characterize the present LHC impedance model for both beams in both planes. These are in agreement with expectations, with an uncertainty that is estimated to be less than 50%.^{131,132}

The expected strength of the Landau octupoles corresponding to the onset of transverse instabilities is in good agreement with observations¹³³ but only when stability is considered on short time scales (shorter than few minutes). For longer time scales, typical of transition times between different phases of the cycle, noise sources acting on the beam and inducing dipolar oscillations at the level of $10^{-4} \sigma$ (with σ being the rms beam size) are observed to affect beam stability at approximately twice the threshold Landau octupole strength. The origin of this noise and the mechanisms leading to transverse instabilities

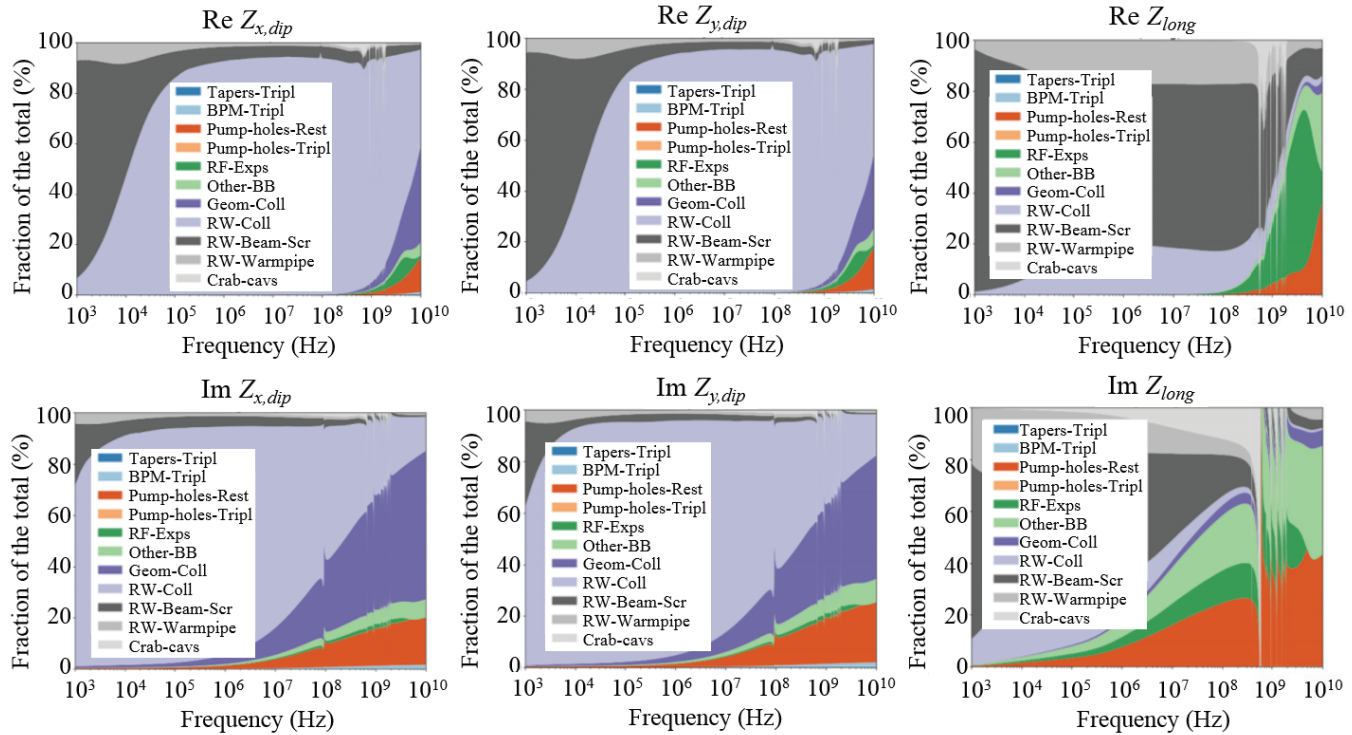


Fig. 10. Relative impedance contributions of the different considered elements to the total HL-LHC impedance at top energy (for the pre-squeeze at $\beta^* = 50$ cm) as a function of frequency (left: horizontal, middle: vertical, right longitudinal - top: real, bottom: imaginary).

are being investigated in detail (see Chapter 29) as a possible explanation of the above discrepancy.

New low-impedance collimators will be installed to replace and enhance, with the addition of embedded beam position monitors, the functionality of the existing ones:^{20,134} 2 Molybdenum-Graphite (MoGr) primary collimators per beam (TCPPM) and up to 9 Molybdenum coated ($5\ \mu\text{m}$ coating thickness) MoGr secondary collimators per beam will be installed. A significant effort has also been put in maintaining a low geometric impedance of the collimators by optimizing their design.

The impedance reduction with Mo-coated MoGr collimators has been tested and validated through extensive laboratory and beam-based measurements.^{131,135} In addition, attention must be paid to the impedance of new pieces of equipment, in particular for those being installed in regions with high β functions (e.g. crab cavities), which are enhancing the effects of transverse impedance. For the crab cavities, a limit of $1\ \text{M}\Omega/\text{m}$ on the transverse shunt impedance of each High-Order Mode (HOM) has been chosen as a guideline to avoid that this equipment visibly affects the corresponding stability thresholds expressed by the additional Landau octupole strength required to stabilize the corresponding transverse instabilities.¹³⁶ The HOMs, whose frequencies are potentially dangerous for beam induced heating and have to be closely monitored during production, have been identified taking into account recent tests at SPS.^{137–139} An overall description of the studies carried out, of the design guidelines provided and actions taken is available in Ref. [130].

The major beam induced RF heating issues that occurred in the first years of high intensity LHC operation were efficiently tackled with the help of the respective equipment groups (see Table 20 of Ref. [130]). The main showstoppers to reach the HL-LHC intensity were identified as the extra beam screen heat load due to e-cloud (see Section 6) and the injection kicker (MKI) operating temperature limit (for which a new design is being studied to reduce the temperature increase of the ferrite core).^{130,140} The design of the new Injection Absorber (TDIS) includes an adequate cooling system to cope with the expected deposited power.^{130,141} With the increase of bunch intensity, other devices may heat up beyond their acceptable limit and this is why all available temperature probes are carefully followed up during the run for signs of issues. Additional monitoring is recommended wherever possible.

7.2. *Beam stability*

Three main mitigation methods exist for both LHC and HL-LHC to stabilize the beam transversally: (i) Landau octupoles, with a possible boost from the ATS optics; (ii) chromaticity and (iii) transverse damper. The first mitigation method, Landau damping, is a general physical process that arises when a collection of particles, which have a spectrum of resonant frequencies, is considered and interact in some way. In particle accelerators we are usually concerned with an interaction that makes the beam unstable (due to the impedance for instance) and we want to find out whether or not the spread of resonant frequencies will stabilise it. Indeed, if the particles have a spread in their natural frequencies, the motion of the particles can lose its coherency and the beam can be stabilised. The Landau octupoles are used to generate this spread through amplitude detuning. For HL-LHC, the frequency spread can be increased thanks to the ATS optics, which increases the effect of the Landau octupoles by increasing the beta function at their location. The second mitigation method, chromaticity (which is modified through sextupoles), shifts the beam spectrum with respect to the impedance and therefore modifies the interaction between the beam and the impedance and the associated instabilities. Finally, the third mitigation method, transverse damper, is an electronic device which first detects the motion of the beam at some location (with a beam position monitor) and then kicks the beam to put it back on the design orbit (with a kicker magnet): it can be seen as a kind of negative impedance.

However, these three methods can have detrimental effects on the dynamic aperture and beam lifetime and a trade-off needs to be found: the value and sign of both the current in the Landau octupoles and chromaticity need to be optimised as well as the gain, the bandwidth and the noise of the transverse damper. From the LHC design report,⁴⁷ it was clear that due to the huge impedance produced by the collimators, transverse beam stability at high energy would require the use of chromaticity, or transverse damper, or both, as the octupole current alone would not be enough to stabilize the beam.^{47,131}

The scenarios for operation at nominal and ultimate luminosity are described in Ref. [7] and they take into account the experience gained during Run 1 and Run 2.^{142–146} The following effects have been or are gradually being taken into account: beam coupling impedance, electron cloud, head-on and long-range beam-beam forces, realistic transverse feedback and machine opti-

cal parameters like tunes, linear coupling,¹⁴⁷ linear and non-linear chromaticity, Landau octupole strength and other non-linearities and, more recently, the effect of noise^{144,148} (see Chapter 29). However, about a factor 2 stronger Landau octupoles are still required as compared to expectations. Several investigations are ongoing to further reduce all the uncertainties of the model: (i) interplay of noise, transverse damper and impedance, (ii) better impedance model and (iii) understanding discrepancies at low chromaticity.¹⁴⁹ Potential additional mitigation paths are being analysed: modifying IR7 optics to reduce the effective collimator impedance and using asymmetric collimation schemes.¹³¹ The baseline scenario provides stability with margin dictated by the present experience compatibly with sufficient dynamic aperture¹³¹ (see Figure 11, where the required relative increase of the peak beta functions induced in the arcs with the ATS optics, called telescopic index or tele-index, are specified for both Landau octupoles polarity).

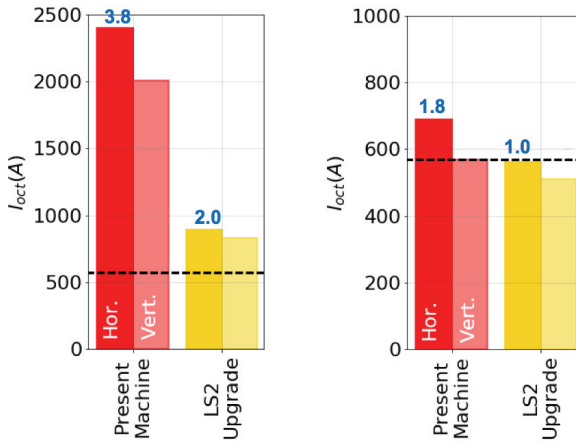


Fig. 11. Required Landau octupole current to stabilise the beam in the presence of both impedance (for the horizontal and vertical planes, with the present and HL-LHC LS2 upgrade cases) and beam-beam effects and for the most stringent scenario going in collision to produce the ultimate luminosity: (left) for the negative sign of the Landau octupole current and (right) for the positive sign of the Landau octupole current. The numbers in blue indicate the required boost from the ATS optics, i.e. the required tele-index, which describes the relative increase of the peak beta functions induced in the arcs, to achieve stability while keeping the octupole current at its maximum (570A, black line). These values have been obtained by considering a factor two in the required Landau octupole current, based on the LHC experience in 2018.¹³¹

The operation with 25 ns beams relies heavily on beam-induced scrubbing and the pace of the intensity ramp-up after the Long Shut-Down 2013-2014 (LS1) (when practically all LHC beam screens and vacuum chambers were vented to air for interventions) has been determined by electron cloud effects both from the heat load and beam stability points of view,^{150,151} as expected. Although a significant reduction of the SEY has been obtained during Run 2 through scrubbing, significant differences in the final value of the SEY, inferred from measurements of the heat load, have been observed in different sectors, in different cryogenic cells and in different magnets within the same sector and cryogenics cell, respectively^{119,122} (see Section 6). Coherent beam instabilities are expected and observed^{144,152} in the LHC at injection as a result of the residual electron cloud, in particular in the quadrupoles. Machine settings with high chromaticity and Landau octupoles⁷ are considered to be sufficient to stabilize the HL-LHC beam taking into account the non-monotonic dependence of the electron cloud density as a function of the bunch population.^{120,153,154} However, these settings will have a stronger impact on the DA compared to the LHC.¹⁵⁵ Simulation studies are ongoing in order to identify the optimal configuration, which will be experimentally tested during Run 3. Transverse coupled-bunch instabilities driven by e-cloud effects could be simulated recently for the first time at CERN on a High Performance Computing cluster after parallelization of the simulation codes.¹⁵⁶ Detailed analyses and scans at injection are ongoing.

Amorphous carbon (a-C) coating of the beam screens of the superconducting magnets together with the non-monotonic dependence of the electron cloud density in the arcs on the bunch population should prevent electron cloud instabilities at high energy after scrubbing and in particular at the higher bunch populations.¹²⁶ Instabilities driven by e-cloud^{153,154} could be observed in LHC at the end of long physics fills (so-called “pop-corn instabilities”) due to the increase of electron density in the centre of the dipole magnets. If this occurs, the beams can be stabilized by increasing the chromaticity up to 15-20 units. Note that the a-C coating is expected to have a negligible effect on the overall machine impedance and related effects.¹⁵⁷

The longitudinal beam parameters of the HL-LHC beams in collision described in Ref. [7] for the various phases of the HL-LHC cycle, have been updated with respect to those listed in Ref. [9] to guarantee the longitudinal beam stability.

7.3. Beam-beam coherent effects

The higher bunch population and lower β^* required in HL-LHC as compared to LHC imply stronger beam-beam interactions. The bunch-to-bunch differences introduced by missing beam-beam interactions, so-called PACMAN effects, were studied for the LHC and determined to not affect its performance.^{158,159} They generate bunch-to-bunch orbit, tune and chromaticity offsets that were re-assessed for HL-LHC, with emphasis on the impact on physical aperture, beam loading on crab cavities, single particle and coherent stability of the beam. The new concept of PACMAN linear coupling driven by skew long-range beam-beam interactions was also introduced and implemented in the self-consistent code TRAIN,¹⁶⁰ adapted to the HL-LHC layout and optics.

Orbit, tune and chromaticity effects due to head-on and long-range beam-beam interactions are tolerable without dedicated mitigation measures in the nominal and ultimate scenarios.^{161,162} Although small PACMAN orbit effects are not negligible (0.1σ) and should be included in the definition of the aperture requirements, the luminosity loss due to the PACMAN orbit effects was shown to be negligible (of the order of 0.1%) in the high luminosity experiments and tolerable (i.e. smaller than the luminosity variation from intensity and emittance bunch to bunch fluctuations of the order of 10%) in the low luminosity ones. Nevertheless, the PACMAN orbit effect has an indirect impact on the long term stability of single particle trajectories since it imposes that the PACMAN bunches collide with a small offset, which modifies the non-linear forces that they experience at the IP. Linear coupling (driven by skew long-range beam-beam interactions) imposes tight tolerance on the alignment of the crossing angles bumps in the different IPs and its control will rely on measurement and correction of the orbit in the interaction region. Indeed, the PACMAN coupling generated by the combination of the crossing angle, the parallel separation bump and the orbit effects resulting from beam-beam long-range interaction at the opposing interaction region is already at the edge in terms of its detrimental effect on Landau damping (a maximum global coupling, described by the closest tune approach, of the order of 0.001 is recommended for the operational scenarios).

When operating with low β^* , or large crossing angles, or both, head-tail oscillations affect significantly the coherent forces between the beams. This mechanism allows for high-order mode-coupling instability of collid-

ing beams. The transverse damper, whose bandwidth limits its action to a constant kick over the bunch, is mostly efficient against the mode-coupling instability of low-order modes.¹⁶³ Numerical simulations accounting for the three-dimensional interaction of the two beams at the IPs for thousands of turns revealed that Landau damping by synchrotron side-bands is sufficient to maintain the beam stability in the configurations anticipated for HL-LHC.¹⁶⁴ Such a heavy simulation campaign relied on the implementation of a new high-performance computing cluster allowing fast parallel computations.

8. Alternative and Potential Operational Scenarios

Various alternatives to the present baseline configuration with the aim of either improving the potential performance or providing options for addressing possible limitations or changes in parameters¹⁶⁵ are briefly described in the following sections and summarized in Figure 12.

8.1. “8b+4e” and hybrid filling schemes

This scheme highly suppresses the formation of the electron cloud as discussed in Section 6. The lower number of bunches of the “8b+4e” scheme implies a lower peak luminosity at the same number of pile-up events per crossing. The single bunch parameters evolve as for the baseline during the physics fill. Therefore integrated luminosity simply scales linearly with the number of bunches. To maximize luminosity it is possible to mix “8b+4e” and BCMS trains to adapt the heat-load to the available cryogenic power.

8.2. Other filling schemes

The number of bunches in the PS trains could be increased from 72 to 80 in order to increase the integrated luminosity without affecting longitudinal peak pile-up density, as defined in.¹⁶⁵ Various fillings schemes have been considered offering integrated luminosity increases between 1.9% and 6.8% for all IPs.¹⁶⁶ The implications for machine protection in the SPS and in the LHC injection transfer lines due to the larger number of bunches per injection (from 288 to 320) are being analyzed.

8.3. Flat optics with crab cavities

A flat optics might be used with β^* of 7.5 cm and 18 cm in the separation and crossing planes, respectively, to improve the performance. Possible limitations on β^* may appear if IP5 has a vertical crossing angle. A crossing angle of 11.4σ could be reached at the end of the fill for bunch populations of 1.1×10^{11} p/bunch applying approximate scaling from DA studies.^{103,167–169} It must be noted that this configuration has not been fully validated yet and the operation at ultimate luminosity might not be possible unless β^* is increased or beam-beam long-range compensation schemes are implemented (see Chapter 27). The performance for this configuration is shown in Figure 12 and it exceeds the HL–LHC nominal performance in terms of integrated luminosity.

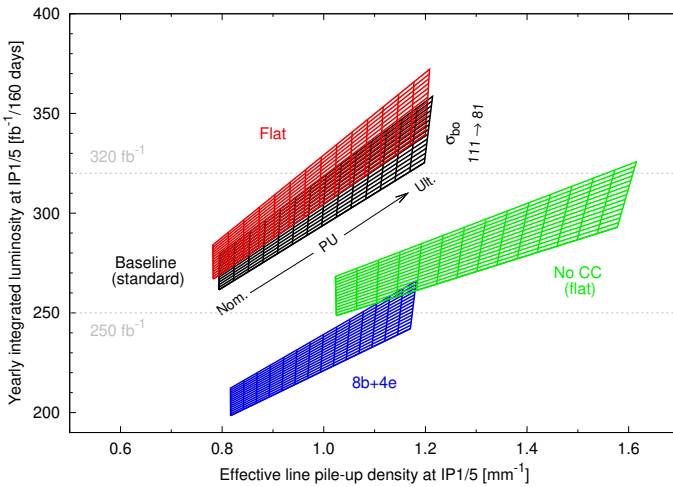


Fig. 12. Summary chart showing integrated luminosity per year versus effective pile-up density for the various scenarios considered. The impact of assuming less conservatively the effective cross section, from 111 mb to 81 mb for the estimate of the burn-off lifetime is also shown, indicating the importance of minimizing losses due to reduced DA and the potential gain in integrated luminosity.

8.4. Flat optics without crab cavities

Although crab-cavities have been successfully operated with beam in the SPS at reduced voltage, a back-up scenario has been developed in case of a major

crab cavity failure in HL–LHC. In this scenario, it is possible to partially recover the performance loss by resorting to flat optics with larger beam size in the crossing plane at the IP. The IP β functions that maximize luminosity are 7.5 cm and 31.5 cm. These β functions might not be possible if the IP5 crossing angle is in the vertical plane and an increase might be needed in this case. Also in this case beam-beam long range compensation schemes (see Chapter 27) might be required. Assuming flat optics in the absence of crab cavities reduces the performance by 5% in the nominal and 12% in the ultimate scenarios. The beam-beam long-range compensation could allow reducing the normalized long-range beam-beam separation from 12.6σ to 11.0σ improving the integrated luminosity from 249 fb^{-1} to 252 fb^{-1} .

References

1. ATLAS and CMS Collaborations, *Expected pile-up values at HL–LHC*, ATL-UPGRADE-PUB-2013-014, CERN (30 September 2013).
2. O.S. Brüning, *The High Luminosity LHC project*, in 6th Int. Particle Accelerator Conf. (IPAC 2015), Richmond, VA, USA, pp. 4096–4101.
3. L. Rossi and O.S. Brüning, *Progress with the High Luminosity LHC project at CERN*, in 10th Int. Particle Accelerator Conf. (IPAC 2019), Melbourne, Australia, pp. 17–22.
4. F. Zimmermann and O.S. Brüning, *Parameter Space for the LHC Luminosity Upgrade*, in Proc. 3rd Int. Particle Accelerator Conf. (IPAC’12), New Orleans, LA, USA, May 2012, paper MOPPC005, pp. 127–129.
5. D. Contardo, *private communication*, 3 December 2014.
6. F. Zimmermann, *HL–LHC: Parameter space, constraints & possible options*, LHC performance workshop, Chamonix 2011.
7. E. Métral et al., *Update of the HL–LHC operational Scenarios for Proton Operation*, CERN-ACC-NOTE-2018-0002.
8. G. Arduini, O. Brüning, R. De Maria, R. Garoby, S. Gilardoni, B. Goddard, B. Gorini, M. Meddahi, G. Rumolo and R. Tomás Garcia, *Beam parameters at LHC injection*, CERN-ACC-2014-0006 (2014).
9. G. Apollinari et al. (ed.), *High-Luminosity Large Hadron Collider (HL–LHC): Technical Design Report V.0.1*, Geneva, Switzerland, Rep. CERN-2017-007-M, 2017.
10. W. Herr, B. Muratori, *Concept of luminosity*, CAS - CERN Accelerator School: Intermediate Course on Accelerator Physics, Zeuthen, Germany, 15–26 Sep 2003, CERN-2006-002, pp. 361–378.
11. O.S. Brüning, *HL–LHC parameter space and scenarios*, Proc. Chamonix 2012 Workshop on LHC Performance, Chamonix, France, 6–10 Feb 2012, Ed. C. Carli, CERN-2012-006 (2012), pp. 315–324.
12. V. Kain et al., *Injection protection — Are we taking it seriously? How can we make*

- it safer?*, Proc. 2nd Evian Workshop on LHC Beam Operation, Evian, France, 7–9 December 2010, Ed. B. Goddard, CERN-ATS-2011-017, pp. 143–149.
13. R. Jacobsson, *Future wishes and constraints from the experiments at the LHC for the proton–proton programme*, ICFA Mini-Workshop on Beam–Beam Effects in Hadron Colliders (BB2013), CERN, Geneva, Switzerland, 18–22 Mar 2013, Eds. W. Herr and G. Papotti, CERN-2014-004 (2014), pp. 167–176.
 14. E. Métral, *Pushing the limits: Beam*, Proc. Chamonix 2011 Workshop on LHC Performance, Chamonix, France, 24–28 January 2011, Ed. C. Carli, CERN-ATS-2011-005, pp. 252–260.
 15. R.W. Assmann, *Implications of higher intensities in the LHC*, Proc. Chamonix 2011 Workshop on LHC Performance, Chamonix, France, 25–29 January 2010, Ed. C. Carli, CERN-ATS-2010-026, pp. 328–333.
 16. H. Bartosik, G. Iadarola, Y. Papaphilippou, G. Rumolo and E. Shaposhnikova, *Can we ever reach the HL–LHC requirements with the injectors?*, Proc. Review of LHC and Injector Upgrade Plans Workshop, Archamps, 29–31 October 2013, Eds. B. Goddard, F. Zimmermann, CERN-2014-006, pp. 95–104.
 17. S. Fartoukh and F. Zimmermann, *The accelerator physics challenges*, CERN-ACC-2014-0209 (2014) Advanced Series on Directions in High Energy Physics: Volume 24 (2015), World Scientific Chapter 4, pp. 45–96.
 18. G. Arduini, R. Tomás García, *HL–LHC Engineering Change Request — BEAM/MACHINE PARAMETERS IN COLLISION — UPDATE — LHC-_-EC-0039 v.1.0*, EDMS 1908458.
 19. HL–LHC Technical Coordination Committee Parameter Table v. 7.0.0 (18/03/2018). https://espace.cern.ch/HiLumi/TCC/_layouts/15/WopiFrame.aspx?sourcedoc=/HiLumi/TCC/SiteAssets/HL_LHC_Parameter_Table.xlsx&action=default
 20. G. Apollinari *et al.* Eds., *High–Luminosity Large Hadron collider (HL–LHC) — Technical Design Report V 1.0*, to be published.
 21. R. De Maria, *General method for final focus system design for circular colliders*, Phys. Rev. ST Accel. Beams **11**, p. 031001, 2008.
 22. D. Gamba and R. De Maria, *IP Orbit Correction Update for HL–LHC*, in Proc. 9th Int. Particle Accelerator Conf. (IPAC’18), Vancouver, Canada, Apr.–May 2018, pp. 3048–3051. doi:10.18429/JACoW-IPAC2018-THPAF039.
 23. P. Baudrenghien and R. Calaga, *Update on CCRF noise and operational aspect*, presented at the 96th HiLumi WP2 Task Leader Meeting – Tuesday, 13 Jun. 2017, <https://indico.cern.ch/event/645814/>.
 24. A. Herty *et al.*, *HL–LHC Full Remote Alignment Study*, presented at the 10th Int. Particle Accelerator Conf. (IPAC’19), Melbourne, Australia, May 2019, paper THPGW057.
 25. R. De Maria, S. D. Fartoukh, A. V. Bogomyagkov, and M. Korostelev, *HLLHCv1.0: HL–LHC Layout and Optics Models for 150 mm Nb3Sn Triplets and Local Crab-cavities*, in Proc. 4th Int. Particle Accelerator Conf. (IPAC’13), Shanghai, China, May 2013, paper TUPFI014, pp. 1358–1360.
 26. R. De Maria, S. D. Fartoukh, and M. Fitterer, *HL–LHCv1.1 Optics Version for the HL–*

- LHC Upgrade*, in *Proc. 6th Int. Particle Accelerator Conf. (IPAC'15)*, Richmond, VA, USA, May 2015, pp. 2090–2093. doi:10.18429/JACoW-IPAC2015-TUPTY037.
27. R. De Maria, R. Bruce, M. Giovannozzi, F. Plassard, and D. Gamba, *HL-LHC Optics and Layout VI.4*, presented at the 10th Int. Particle Accelerator Conf. (IPAC'19), Melbourne, Australia, May 2019, paper MOPMP019.
 28. R. Bruce et al., *Review of LHC Run 2 Machine Configurations*, in Proc. 9th LHC Operations Evian Workshop, Evian, Switzerland, January 2019.
 29. R. Tomás et al., *LHC Run 2 Optics Commissioning Experience in View of HL-LHC*, presented at the 10th Int. Particle Accelerator Conf. (IPAC'19), Melbourne, Australia, May 2019, paper MOPMP033.
 30. X. Buffat et al., *Transverse Instabilities*, in Proc. 9th LHC Operations Evian Workshop, Evian, Switzerland, January 2019.
 31. R. De Maria et al., *HLLHC VI.4 Optics repository*, <http://lhc-optics.web.cern.ch/lhc-optics/HLLHCVI.4/>.
 32. J. Jowett, M. Schaumann and R. Versteegen, *Heavy-ion operation of HL-LHC*, in Adv. Ser. Dir. High Energy Phys. 24 (2015) pp. 359–371.
 33. S. Fartoukh et al., *Achromatic telescopic squeezing scheme and by-products: From concept to validation*, Phys. Rev. Accel. Beams **24**, 021002.
 34. I. Efthymiopoulos et al., *LHCb Upgrades and operation at $10^{34} \text{ cm}^{-2} \text{ s}^{-1}$ luminosity – A first study*, CERN-ACC-NOTE-2018-0038.
 35. R. De Maria and M. Solfaroli, *Smooth and Beta-Beating-Free Optics Transitions for HL-LHC*, presented at the 10th Int. Particle Accelerator Conf. (IPAC'19), Melbourne, Australia, May 2019, paper MOPMP020.
 36. S. Redaelli, et al., *Plans for Deployment of Hollow Electron Lenses at the LHC for Enhanced Beam Collimation*, in Proc. 6th Int. Particle Accelerator Conf. (IPAC'15), Richmond, VA, USA, May 2015, pp. 2462–2465. doi:10.18429/JACoW-IPAC2015-WEBB1.
 37. R. Bruce, et al., *Reaching record-low β^* at the CERN Large Hadron Collider using a novel scheme of collimator settings and optics*, Nucl. Instrum. Methods Phys. Res. A, vol. **848**, pp. 19–30, 2017.
 38. C. Bracco et al., *Update on optics constraints for injection and dump protection elements*, presented at the 30th HL-LHC TCC meeting on 8 June 2017, <https://indico.cern.ch/event/638356/>.
 39. R. Tomás, et al., *Record low beta beating in the LHC*, Phys. Rev. ST Accel. Beams **15**, p. 091001 (2012).
 40. E.H. Maclean, et al., *New approach to LHC optics commissioning for the nonlinear era*, Phys. Rev. Accel. Beams **22**, 061004, 2019.
 41. E.H. Maclean, et al., *Detailed review of the LHC optics commissioning for the nonlinear era*, CERN-ACC-2019-0029.
 42. F. Carlier, et al., *Optics Measurement and Correction Challenges for the HL-LHC*, CERN-ACC-2017-0088.
 43. J. Coello et al., *MD2148: Flat optics*, CERN-ACC-NOTE-2018-0051.

44. R. Bruce, *et al.*, *Updated parameters for HL-LHC aperture calculations for proton beams*, CERN-ACC-2017-0051.
45. R. Tomás, *et al.*, *Review of linear optics measurement and correction for charged particle accelerators*, Phys. Rev. Accel. Beams, vol. **20**, p. 054801 (2017).
46. F. Carlier and R. Tomás, *Accuracy and Feasibility of the β^* Measurement for LHC and High Luminosity LHC using K-Modulation*, Phys. Rev. Accel. Beams **20**, 011005, Jan. 2017.
47. O. Brüning (ed.) *et al.*, *LHC Design Report*, Geneva, Switzerland, Rep. CERN-2004-003-V-1, Jun. 2004.
48. R. Carcagno, *Functional Specifications MQXFA Magnets*, CERN EDMS No. 1535430.
49. R. Carcagno, S. Feher, *Functional Specifications LMQXFA Cold Mass*, CERN EDMS No. 1686197, <https://edms.cern.ch/document/1686197>.
50. D. Gamba *et al.*, *Update of beam dynamics requirements for HL-LHC electrical circuits*, CERN-ACC-2019-0030.
51. M. Hofer, *et al.*, *K-modulation for future High energy colliders*, presented at the IPAC'19, Melbourne, Australia, May 2019, paper MOPMP022.
52. D.W. Wolf, "Analysis of tune modulations in the LHC", Bachelor thesis, CERN-THESIS-2018-251.
53. R. Tomás Garcia, *Trim in QI for the beta* measurements*, 27th Technical Coordination Committee, 30th March 2017, INDICO 590417.
54. D. Gamba *et al.*, *Beam dynamics requirements for HL-LHC electrical circuits*, CERN-ACC-2017-0101.
55. J. Coello *et al.*, *New local optics measurements and correction techniques for the LHC and its luminosity upgrade*, Phys. Rev. Accel. Beams **23**, 041001, April 2020.
56. M. Gasior, G. Baud, J. Olexa, and G. Valentino, *First Operational Experience with the LHC Diode ORbit and OScillation (DOROS) System*, in Proc. 5th Int. Beam Instrumentation Conf. (IBIC'16), Barcelona, Spain, Sep. 2016, pp. 43–46. doi:10.18429/JACoW-IBIC2016-MOPG07
57. A. Garcia-Tabares *et al.*, *Optics-measurement-based beam position monitor calibrations in the LHC insertion regions*, Phys. Rev. Accel. Beams **23**, 042801, April 2020.
58. E. Fol, R. Tomás and G. Franchetti, *Supervised learning-based reconstruction of magnet errors in circular accelerators*, The European Physical Journal Plus vol. **136**, Article number: 365 (2021).
59. E. Fol, R. Tomás, J. Coello de Portugal, and G. Franchetti, *Detection of faulty beam position monitors using unsupervised learning*, Phys. Rev. Accel. Beams **23**, 102805, 2020.
60. R. Tomás *et al.*, *LHC Run 2 Optics Commissioning Experience in View of HL-LHC*, presented at IPAC'19, Melbourne, Australia, May 2019.
61. M. Hofer and R. Tomás, *Effect of local linear coupling on linear and nonlinear observables in circular accelerators*, Phys. Rev. Accel. Beams **23**, 094001, 2020.
62. T. Persson, *et al.*, *LHC Optics Corrections in Run 2*, Proc. of 9th LHC Operations Evian Workshop, 2019, pp. 59–66.

63. D. Gamba, *Impact of flux jumps on orbit stability*, 150th HiLumi WP2 Meeting. <https://indico.cern.ch/event/823530/>
64. J. Coello et al., *Impact of Flux Jumps in Future Colliders*, Phys. Rev. Accel. Beams **23**, 011001, January 2020.
65. N. M. Gelfand, *Calculations of the Dynamic Aperture at the Tevatron*, in Proceedings of SSC Workshop on Accelerator Physics Issues for a Superconducting Super Collider, edited by M. Tigner, UM-HE-84-1, 124, 1984.
66. V. Visnjic, *Dynamic aperture of low beta lattices at Tevatron collider*, in Proceedings of 1991 Particle Accelerator Conference, edited by J. Chew and L. Lizama (IEEE Computer Society Press, Piscataway - NY), 1701, 1991.
67. V. Visnjic, *Dynamic aperture of the future Tevatron Collider*, in Proceedings of Workshop On Nonlinear Problems In Future Particle Accelerators, edited by W. Scandale and G. Turchetti (World Scientific, Teaneck, NJ), 1991.
68. R. Brinkmann, F. Willeke, *Persistent Current Field Errors and Dynamic Aperture of the Hera Proton Ring*, DESY-HERA-88-08, 1988.
69. F. Zimmermann, F. Willeke, *Long term stability and dynamic aperture of the HERA proton ring*, DESY-HERA-91-08, 1991.
70. F. Zimmermann, *Dynamic aperture and transverse proton diffusion in HERA*, SLAC-PUB-6458, 1994.
71. O.S. Brüning et al., *Comparison of measured and computed dynamic aperture for the SPS and the HERA proton ring*, Part. Accel. **54**, 223 (1996).
72. Y. Luo et al., *Dynamic aperture evaluation at the current working point for RHIC polarized proton operation*, in Proceedings of 2007 Particle Accelerator Conference, edited by C. Petit-Jean-Genaz (IEEE Computer Society Press, Piscataway - NY, 2007), 4363, 2007.
73. E. Todesco and M. Giovannozzi, Phys. Rev. E **53**, 4067 (1996).
74. M. Giovannozzi, Phys. Rev. ST Accel. Beams **15**, 024001 (2012).
75. E.H. Maclean, M. Giovannozzi, and R.B. Appleby, *Innovative method to measure the extent of the stable phase-space region of proton synchrotrons*, Phys. Rev. Accel. Beams **22**, 034002 (2019).
76. E.H. Maclean, R. Tomás, F. Schmidt, and T.H. B. Persson, *Measurement of nonlinear observables in the Large Hadron Collider using kicked beams*, Phys. Rev. ST Accel. Beams **17**, 081002 (2014).
77. M. Giovannozzi, F. Van der Veken, *Description of the luminosity evolution for the CERN LHC including dynamic aperture effects, Part I: The model*, Nucl. Instrum. & Methods A **905**, 171.
78. M. Giovannozzi, F. Van der Veken, *Description of the luminosity evolution for the CERN LHC including dynamic aperture effects. Part II: application to Run 1 data*, Nucl. Instrum. & Methods A **908**, 1.
79. E. Todesco, M. Giovannozzi and W. Scandale, *Fast indicators of long-term stability*, Part. Accel. **55**, 273 (1995).
80. M. Giovannozzi and E. McIntosh, *Development of parallel codes for the study of nonlinear*

- beam dynamics*, Int. Jou. Mod. Phys. C **8**, 155 (1997).
81. M. Giovannozzi, W. Scandale, E. Todesco, *Prediction of long-term stability in large hadron colliders*, Part. Accel. **56**, 195 (1996).
 82. M. Giovannozzi, W. Scandale, E. Todesco, *Dynamic aperture extrapolation in presence of tune modulation*, Phys. Rev. E **57**, 3432 (1998).
 83. A. Bazzani, M. Giovannozzi, E.H. Maclean, C.E. Montanari, F.F. Van der Veken, W. Van Goethem, *Advances on the modelling of the time evolution of dynamic aperture of hadron circular accelerators*, submitted for publication (2019).
 84. SixTrack web site: <http://cern.ch/sixtrack>
 85. R. De Maria *et al.*, *SixTrack Version 5: Status and New Developments*, presented at the 10th Int. Particle Accelerator Conf. (IPAC'19), Melbourne, Australia, May 2019, paper WEPTS043.
 86. A. Bazzani, O. Mazzarisi, M. Giovannozzi, E.H. Maclean, *Diffusion in stochastically perturbed Hamiltonian systems with application to the recent LHC dynamic aperture experiment*, in Nonlinear Dynamics and Collective Effects in Particle Beam, World Scientific, ed. by S. Chattopadhyay, M. Cornacchia, S. Di Mitri, p. 70.
 87. A. Bazzani, M. Giovannozzi, E.H. Maclean, *Analysis of the CERN Large Hadron Collider non-linear beam dynamics at top energy by means of a new diffusion mode*, submitted for publication (2019).
 88. Y. Cai, R. De Maria, M. Giovannozzi, Y. Nosochkov, F.F. Van der Veken, *Dynamic aperture studies for HL-LHC V1.0*, CERN-ACC-2018-0054 (2018).
 89. J. Barranco, *et al.*, *LHC@Home: a BOINC-based volunteer computing infrastructure for physics studies at CERN*, Open Eng. **7**, 378 (2017).
 90. F. Cerutti *et al.*, *Heat deposition and radiation dose vs operation mode and mitigation schemes*, Presentation in the LHC Performance Workshop 2018, 29 January – 1 February 2018, Chamonix, France. <https://indico.cern.ch/event/676124/contributions/2767903/>.
 91. Y. Papaphilippou and F. Zimmermann, *Weak-strong beam-beam simulations for the Large Hadron Collider*, Phys. Rev. ST Accel. Beams, **2**, 104001, (1999). <https://link.aps.org/doi/10.1103/PhysRevSTAB.2.104001>.
 92. Y. Papaphilippou and F. Zimmermann, *Estimates of diffusion due to long-range beam-beam collisions*, Phys. Rev. ST Accel. Beams, **5**, 074001, (2002). <https://link.aps.org/doi/10.1103/PhysRevSTAB.5.074001>.
 93. Y. Luo and F. Schmidt, *Dynamic aperture studies for LHC optics Version 6.2 at Collision*, CERN LHC-Project-Note-310, (2003). <https://cds.cern.ch/record/692074>.
 94. T. Pieloni, D. Banfi, and J. Barranco Garcia, *Dynamic Aperture Studies for HL-LHC with beam-beam effects*, May 2017. <https://cds.cern.ch/record/2263345>.
 95. W. Herr, *et al.*, *Long range beam-beam effects*, in the LHC, Proc. ICFA Mini-Workshop on Beam-Beam Effects in Hadron Colliders, CERN, Geneva, Switzerland, 18–22 March 2013, Eds. W. Herr and G. Papotti, CERN-2014-004, pp. 87–92 (2014).
 96. D. Pellegrini, *et al.*, *Incoherent beam-beam effects and lifetime optimization*, 8th Evian Workshop on LHC Beam Operation, Evian, France, 12–14 December 2017.

- https://indico.cern.ch/event/663598/contributions/2782389/attachments/1574018/2521763/Pellegrini_Evian_Paper.zip.
97. Y. Papaphilippou, et al., *Long range beam-beam effects for HL-LHC*, Presentation in the LHC Performance Workshop 2018, 29 January – 1 February 2018, Chamonix, France. <https://indico.cern.ch/event/676124/contributions/2768610/>.
 98. S. Papadopoulou, et al., *Transverse emittance blow-up*, 9th Evian Workshop on LHC Beam Operation, Evian, France, 30 January – 1 February 2019, INDICO: 751857.
 99. S. Kostoglou, et al., *Luminosity, lifetime and modelling*, 9th Evian Workshop on LHC Beam Operation, Evian, France, 30 January – 1 February 2019, INDICO: 751857.
 100. K. Paraschou and G. Iadarola, *Status of the studies on Electron cloud incoherent effects*, 165th HiLumi WP2 Meeting.
 101. H. Damerau, H. Bartosik, R. Garoby, S. Gilardoni, S. Hancock, B. Mikulec, Y. Papaphilippou, G. Rumolo, E. Shaposhnikova, R. Tomás, *LIU: Exploring Alternative Ideas*, Proc. Review of LHC and Injector Upgrade Plans Workshop, Archamps, 29–31 October 2013, Eds. B. Goddard, F. Zimmermann, CERN-2014-006, pp. 127–137.
 102. N. Karastathis, et al., *Refining the HL-LHC Operational Settings With Inputs From Dynamic Aperture Simulations: A Progress Report*, J. Phys.: Conf. Ser., **1067**, 022005, (2018). <https://doi.org/10.1088/1742-6596/1067/2/022005>.
 103. N. Karastathis, et al., *Beam-beam simulation in the HL-LHC*, Presentation in the 8th HL-LHC Collaboration Meeting, 15–18 October 2018, CERN, Geneva, Switzerland. https://indico.cern.ch/event/742082/contributions/3085158/attachments/1736226/2808306/nkarast_HLCollab_18102018.pptx.
 104. J. Shi, L. Jin and O. Kheawpum, *Multipole compensation of long-range beam-beam interactions with minimization of nonlinearities in Poincaré maps of a storage-ring collider*, Phys. Rev. E, **69**, 036502, (2004). <https://link.aps.org/doi/10.1103/PhysRevE.69.036502>.
 105. J. Barranco Garcia and T. Pieloni, *Global compensation of long-range beam-beam effects with octupole magnets: dynamic aperture simulations for the HL-LHC case and possible usage in LHC and FCC*, May 2017. <https://cds.cern.ch/record/2263347>.
 106. P. Baudrenghien, *Expected performances of the CC in terms of voltage and (phase) noise*, Presentation in the 96th WP2 Meeting, 13 June 2017, CERN, Geneva, Switzerland. https://indico.cern.ch/event/645814/contributions/2622537/attachments/1475139/2291022/Meeting_13_06_2017.pptx.
 107. L. Medina et al., *Effective pile-up density as a measure of the experimental data quality for High-Luminosity LHC operational scenarios*, CERN-ACC-2018-0003.
 108. X. Buffat, *Emittance growth due to crab cavity noise and expected orbit spread at the crab cavity*, Presentation in the 96th WP2 Meeting, 13 June 2017, https://indico.cern.ch/event/645814/contributions/2622559/attachments/1475256/2284820/2017-06-13_CCnoise-offset.pdf.
 109. J. Qiang, et al., *Simulation of beam-beam interaction with crab cavities for LHC upgrade*, Nucl. Instrum. Methods Phys. Res., A, **900**, 53-59, (2018).
 110. A. Alekou, et al., *Deliverable 2.10: Summary of the observations in the SPS and update*

- of the estimates for HL-LHC concerning phase and amplitude noise levels and RF multipoles, CERN-ACC-2020-0002.
111. P. Baudrenghien, *LLRF lessons learned from SPS tests, observed emittance growth*, Presentation in the 8th HL-LHC Collaboration Meeting, 15–18 October 2018, CERN, Geneva, Switzerland. <https://indico.cern.ch/event/742082/contributions/3084929/attachments/1734377/2804529/HL--LHC18v5.pptx>.
 112. N. Triantafyllou et al., “New results of the SPS Crab Cavity noise emittance blow-up analysis”, 187th HiLumi WP2 Meeting, February 2021.
 113. S. Kostoglou, et al., *Summary of observations on noise for LHC and projections for HL-LHC*, Presentation in the 63rd Technical Coordination Committee, 13th December 2018, CERN, Geneva, Switzerland. https://indico.cern.ch/event/779650/contributions/3244747/attachments/1770859/2877606/TCC_noise_131218.pptx.
 114. S. Kostoglou, et al., *An update on the LHC noise observations and studies*, Presentation in the Beam-Beam and Luminosity Studies meeting, 7 June 2019, CERN, Geneva, Switzerland. https://indico.cern.ch/event/817173/contributions/3445813/attachments/1858887/3054263/MD4147_BBLM_v1.0.pptx.
 115. S. Papadopoulou, et al., *Emittance growth in the LHC and impact on HL-LHC performance*, Presentation in the 8th HL-LHC Collaboration Meeting, 15–18 October 2018, CERN, Geneva, Switzerland. https://indico.cern.ch/event/742082/contributions/3085157/attachments/1736429/2808930/HILUMImeet_18102018_stef.pdf.
 116. R. Tomás, J. Keintzel and S. Papadopoulou *Emittance growth from luminosity burn-off in future hadron colliders*, Phys. Rev. Accel. Beams **23**, 031002, March 2020.
 117. F. Antoniou, G. Arduini, Y. Papaphilippou, and G. Papotti, *Building a Luminosity Model for the LHC and HL-LHC*, in Proc. 6th Int. Particle Accelerator Conf. (IPAC’15), Richmond, VA, USA, May 2015, pp. 2042–2045. doi:10.18429/JACoW-IPAC2015-TUPTY020.
 118. F. Antoniou, et al., *Can we predict luminosity*, in proc. of 7th Evian Workshop on LHC beam operation, Evian Les Bains, France, 2016. https://indico.cern.ch/event/578001/contributions/2366376/attachments/1388316/2222614/Evian2016_Lumi_F.Antoniou.pdf.
 119. G. Iadarola, G. Rumolo, P. Dijkstal, L. Mether, *Analysis of the beam induced heat loads on the LHC arc beam screens during Run 2*, CERN-ACC-NOTE-2017-0066 (2018).
 120. G. Iadarola, et al., *Electron cloud and heat loads in Run 2*, in Proc. 9th LHC Operations Evian Workshop, Evian, Switzerland, January 2019.
 121. L. Tavian, *Report from the task force on beam induced heat load*, presented at the LHC Performance Workshop 2018, CERN, 31 Jan 2018, <https://indico.cern.ch/event/676124>.
 122. G. Iadarola, *e-cloud and heat load in the LHC arcs*, presented at the Accelerator and Beam Physics Forum, CERN, Geneva, Switzerland, Jul. 2018, <https://indico.cern.ch/event/740046/>.

123. G. Skripka, *Scaling of e-cloud effects with bunch population*, presented at the 143th HiLumi WP2 Meeting, CERN, Geneva, Switzerland, Mar. 2019, <https://agenda.infn.it/event/13351>.
124. K. Brodzinski, *Measurement of available beam screen cooling capacity on cryoplants*, presented at the LHC Machine Committee, CERN, 10 Apr 2019, <https://indico.cern.ch/event/812689/>
125. G. Skripka, G. Iadarola, *Beam-induced heat loads on the beam screens of the inner triplets for the HL-LHC*, CERN-ACC-NOTE-2018-0009 (2018).
126. G. Iadarola, E. Métral, G. Rumolo, *Beam induced heat loads on the beam screens of the twin-bore magnets in the IRs of the HL-LHC*, CERN-ACC-2016-0112 (2016).
127. G. Iadarola, *Heat-Load budget in the arcs at 7 TeV*, presented at the LHC Run-III Configuration Meeting, CERN, 22 Jun 2018, <https://indico.cern.ch/event/732916>.
128. G. Iadarola, *Digesting the LIU high brightness beam: is this an issue for HL-LHC?*, presented at the LHC Performance Workshop 2018, CERN, 31 Jan 2018, <https://indico.cern.ch/event/676124>.
129. G. Iadarola, et al., *MD421: Electron cloud studies on 25 ns beam variants (BCMS, 8b+4e)*, CERN-ACC-NOTE-2017-0028 (2017).
130. D. Amorim et al., *HL-LHC impedance and related effects*, CERN-ACC-NOTE-2018-0087.
131. E. Métral et al., *Impedance models, operational experience and expected limitations*, International Review of the HL-LHC Collimation System, CERN, 11-12/02/2019.
132. D. Amorim et al., *Comparison of LHC impedance model predictions to beam-based measurements*, 169th HSC section meeting, CERN, 18/02/2019.
133. L. Carver et al., *Current status of instability threshold measurements in the LHC at 6.5 TeV*, in Proc. 7th Int. Particle Accelerator Conf. (IPAC'16), Busan, South Korea, May 2016, pp. 1434–1437. CERN-ACC-2016-234.
134. S. Antipov et al., *Staged implementation of low-impedance collimation in IR7: plans for LS2*, CERN-ACC-2019-0001.
135. S. Antipov et al., *Single-collimator tune shift measurement of the three-stripe collimator at the LHC*, in Proc. 9th Int. Particle Accelerator Conf. (IPAC'18), Vancouver, BC, Canada, May 2018, pp. 3036–3039. doi: DOI: 10.18429/JACoW-IPAC2018-THPAF035.
136. S. Antipov et al., *Effect of crab cavity high order modes on the coupled-bunch stability of High-Luminosity Large Hadron Collider*, Phys. Rev. Accel. Beams **22**, 054401 (2019).
137. F. Giordano and B. Salvant, *Update on crab cavity beam induced heating*, 127th HSC section meeting, CERN, 20/11/2017.
138. S. Antipov et al., *Update on beam stability due to HOMs and beam induced heating reflecting the recent changes in RFD crab cavity*, 129th HSC section meeting, CERN, 04/12/2017.
139. S. Antipov et al., *Update on DQW crab cavity HOMs*, 140th HiLumi WP2 meeting, CERN, 29/01/2019.
140. V. Vlachodimitropoulos et al., *Study of an Improved Beam Screen Design for the LHC Injection Kicker Magnet for HL-LHC*, in Proc. 8th Int. Particle Accelerator Conf. (IPAC'17),

- Copenhagen, Denmark, May 2017, paper WEPVA094, pp. 3471–3474.
141. C. Bracco, *The new injection protection dump TDIS, Engineering Change Request*, LHC-TDIS-EC-0001, EDMS document 1936580, Jul. 2018. <https://edms.cern.ch/document/1936580/>.
 142. E. Métral *et al.*, *Summary of the 2-day internal review of LHC performance limitations (linked to transverse collective effects) during run I (CERN, 25-26/09/2013)*. CERN-ACC-NOTE-2014-0006.
 143. E. Métral *et al.*, *Summary of the half-day internal review of the LHC performance limitations (linked to transverse collective effects) during run II (CERN, 29/11/2016)*, CERN-ACC-NOTE-2017-0005.
 144. X. Buffat *et al.*, *Transverse instabilities*, 9th Evian Workshop on LHC Beam Operation, Evian, France, 30 January – 1 February 2019.
 145. E. Métral *et al.*, *Beam stability from impedance (including effect of coating) and overall summary for the nominal scenario including all effects*, 7th HL–LHC Collaboration meeting, Madrid, Spain, 13-16/11/2017.
 146. G. Iadarola, *Digesting the LIU high brightness beam: is this an issue for HL–LHC?*, LHC Performance Workshop 2018, Chamonix, France, 29 January – 2 February 2018.
 147. L.R. Carver *et al.*, *Transverse beam instabilities in the presence of linear coupling in the Large Hadron Collider*, Phys. Rev. Accel. Beams **21**, 044401 (2018).
 148. X. Buffat, *Transverse beams stability studies at the Large Hadron Collider*, Ph.D. thesis, EPFL, Lausanne, Switzerland, 2015, doi:10.5075/epfl-thesis-6321.
 149. E. Métral *et al.*, *Destabilising effect of the LHC transverse damper*, in Proc. 9th Int. Particle Accelerator Conf. (IPAC'18), Vancouver, BC, Canada, Apr.–May 2018, pp. 3076–3079. doi:10.18429/JACoW-IPAC2018-THPAF048.
 150. K. Li *et al.*, *Electron cloud observations during LHC operation with 25 ns beams*, in Proc. 7th Int. Particle Accelerator Conf. (IPAC'16), Busan, South Korea, 8–13 May 2016, pp. 1458–1461. CERN-ACC-2016-255.
 151. G. Rumolo *et al.*, *Electron cloud in the CERN accelerator complex*, in Proc. 57th ICFA Advanced Beam Dynamics Workshop on High-Intensity and High-Brightness Hadron Beams, Malmö, Sweden, 3–8 July 2016, Eds. D. Gous, M. Marx, R. Mueller (GSI, Germany), J. Olander, V.R.W. Schaa, G. Trahern, pp. 266–271. CERN-ACC-2016-0099.
 152. K. Li *et al.*, *Update on Landau octupoles settings at injection*, 65th LHC Beam Operation Committee meeting, CERN, 23/08/2016.
 153. A. Romano, *Electron cloud formation in CERN particle accelerators and its impact on the beam dynamics*, CERN-THESIS-2018-299.
 154. A. Romano *et al.*, *Electron cloud buildup driving spontaneous vertical instabilities of stored beams in the Large Hadron Collider*, Phys. Rev. Accel. Beams **21** (2018) 061002.
 155. N. Karastathis, *Dynamic Aperture at HL-LHC Injection*, presented at the 149th HiLumi WP2 Meeting, CERN, Geneva, Switzerland, May 2019, <https://agenda.infn.it/event/823612>.
 156. G. Iadarola, *HPC for e-cloud computing*, 367th LHC Machine Committee, CERN, 07/11/2018.

157. S. Antipov et al., *Impact of carbon coating on impedance and beam stability*, 124th HiLumi WP2 meeting, CERN, 03/07/2018.
158. W. Herr, *Features and implications of different LHC crossing schemes*, CERN, Geneva, Switzerland, LHC Project Report 628, 2003.
159. H. Grote, *Self-consistent orbits with beam-beam interactions in the LHC*, in Proc. EPAC 2000.
160. Train TWiki, <https://twiki.cern.ch/twiki/bin/view/ABPComputing/TrainWikiPage>.
161. A. Ribes Metidieri, *Studies of PACMAN effects in the HL-LHC*, 123th HiLumi WP2 meeting, CERN, 12/06/2018.
162. A. Ribes Metidieri and X. Buffat, *Studies of PACMAN effects in the HL-LHC*, in preparation.
163. S. White et al., *Transverse mode coupling instability of colliding beams*, Phys. Rev. Accel. Beams **17**, 041002 (2014).
164. L. Barraud and X. Buffat, *Mode coupling instability of colliding beams in the HL-LHC*, in preparation.
165. L. Medina et al., *Assessment of the performance of High Luminosity LHC operational scenarios: integrated luminosity and effective pile-up density*, Canadian Journal of Physics, <https://doi.org/10.1139/cjp-2018-0291>.
166. G. Iadarola, *HL-LHC filling schemes: possible optimization*, 140th HiLumi WP2 meeting, <https://indico.cern.ch/event/788818/>.
167. A. Valishev, S. Fartoukh and D. Shatilov, *BBLR compensation for HL-LHC*, 3rd Joint HiLumi LHC – 22nd LARP Collaboration Meeting, 7–8 May 2014, BNL, USA, https://indico.bnl.gov/event/730/contributions/17058/attachments/15282/18810/BBLR_Valishev-2014.05.08.pptx.
168. D. Banfi, J. Barranco, T. Pieloni, A. Valishev, *Update on crossing angle scaling with bunch intensity*, 20th HiLumi WP2 Task Leader Meeting, 25 October 2013, CERN.
169. D. Banfi, J. Barranco, T. Pieloni, A. Valishev, *Beam-beam effects for round and flat optics: DA simulations*, 4th Joint HiLumi LHC - LARP Annual Meeting, 17–21 November 2014, KEK, Japan, <https://indico.cern.ch/event/326148/contributions/1711470/attachments/633056/871236/DaniIoKEK.pptx>.

Chapter 6

Superconducting Magnet Technology for the IR Upgrade

E. Todesco^a, G. Ambrosio^b, P. Ferracin^c, G. L. Sabbi^d, T. Nakamoto^e, M. Sugano^e,
R. Van Weelderena, P. Fabbri^f, S. Farinon^f, F. Toral^g, M. Sorbi^h, M. Statera^h,
Q. Xuⁱ, J. M. Rifflet^j and H. Felice^j

^a*CERN, TE Department, Genève 23, CH-1211, Switzerland*

^b*FNAL, Batavia, IL, USA*

^c*LBNL, Berkeley, CA, USA*

^d*SLAC, Menlo Park, CA, USA*

^e*KEK, Tsukuba, Japan*

^f*INFN Genoa, Italy*

^g*CIEMAT, Madrid, Spain*

^h*INFN LASA, Milano, Italy*

ⁱ*IHEP, Beijing, China*

^j*CEA Saclay, France*

In this section we present the magnet technology for the High Luminosity LHC. After a short review of the project targets and constraints, we discuss the main guidelines used to determine the technology, the field/gradients, the operational margins, and the choice of the current density for each type of magnet. Then we discuss the peculiar aspects of the design of each class of magnet, with special emphasis on the triplet.

1. Targets

The HL-LHC aims at gathering 3000 fb^{-1} over ten years. As discussed in the previous section, this ambitious target can be obtained by operating with a peak luminosity levelled at $5 \times 10^{34} \text{ cm}^{-2} \text{ s}^{-1}$. The plan is to obtain it through

This is an open access article published by World Scientific Publishing Company. It is distributed under the terms of the Creative Commons Attribution 4.0 (CC BY) License.

higher intensity/lower emittance and a larger focusing on the Interaction Point (IP). This second part is given by the magnetic lattice; the target is to be able to reduce the beam size in the IP by a factor two, and therefore, at zero order approximation, one has double the size of the quadrupoles aperture in front of the IP (triplet).

Some of the previous proposals, done during the LHC luminosity upgrade studies [1,2,3], aimed at a reduction of the beam size of 30%, increasing the triplet aperture 30% (see Figure 1 for an historical view of the aperture proposed for the triplet). The HL-LHC target of reducing the beam size in the IP by a factor of two was based on theoretical studies (see for instance [4]), and was enabled by advances in magnet technology, i.e., test results from model quadrupoles of progressively larger aperture (Figure 1).

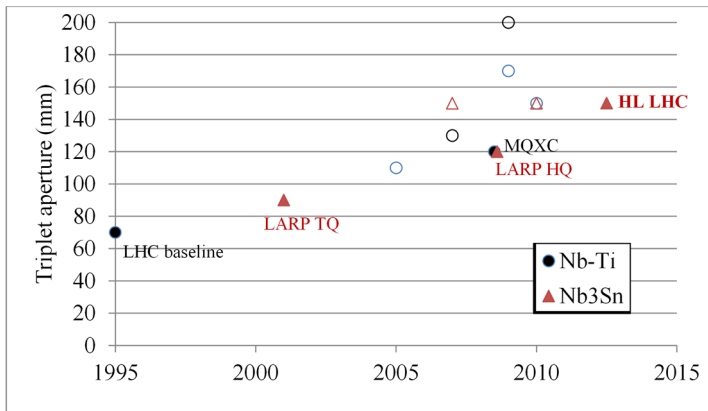


Fig. 1. Proposed aperture for the inner triplet versus time: triangle (Nb_3Sn), circles (Nb-Ti), built hardware in full markers, and proposal in empty markers.

A critical design parameter for a superconducting quadrupole is the peak field in the coil, which is a function of the aperture times the gradient. For Nb-Ti dipole coils the peak field limit in operational conditions is $\sim 8\text{-}9$ T [5], whereas for Nb_3Sn this limit is ~ 15 T. One can prove that for quadrupoles Nb_3Sn can give 50% more gradient w.r.t. Nb-Ti for the same aperture [6] (see Figure 2): this allows for shorter magnets compared to Nb-Ti. As explained in the previous chapter, a compact triplet means not only more space for other components, in a critical region of the tunnel, but also additional performance: a shorter triplet means that the beam size has less longitudinal

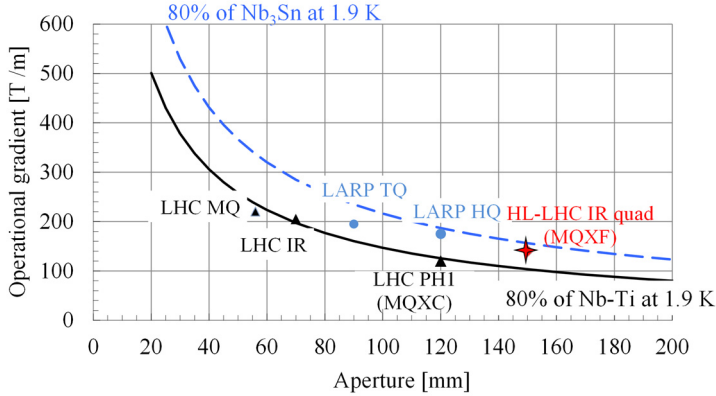


Fig. 2. Operational gradient versus aperture in Nb-Ti and Nb₃Sn quadrupoles.

space to grow, and therefore for the same aperture one can squeeze more the beam in the IP. Moreover, a shorter triplet allows reducing the number of long range beam-beam interactions and to reduce chromatic aberrations. So, Nb₃Sn is the enabling technology to reach the ambitious target of the HL-LHC project. Finally, another fundamental aspect is to use the additional aperture to house a massive shielding to reduce the heat load and the radiation damage, as discussed in the next section.

2. Constraints

2.1. Radiation damage and heat load

The design of the final focus system of the upgraded LHC needs to account for the special conditions related to its proximity to the interaction points. The first important constraint for the magnetic system is the radiation damage, which is proportional to the integrated luminosity. Some essential components employed for magnet fabrication (epoxy resins) undergo severe degradation at 50-100 MGy. Therefore, one needs to set a safe dose limit of 10-20 MGy or switch to the complexity related to radiation resistant materials, as used for nuclear fusion, which can operate in the range of 100 MGy and more. For the HL-LHC we set a target for radiation damage at ~30 MGy.

The second relevant constraint for the magnetic system is the heat deposition on the coil, which is proportional to the peak luminosity. In the

stationary regime of continuous heat deposition, it induces a temperature gradient between the helium bath ($T_{\text{bath}}=1.9$ K) and the temperature of the coil $T_{\text{coil}}=(1.9+\Delta T)$. In the LHC triplet, the limit to the heat load is given by the requirement of having superfluid helium in the coil, at a temperature of 1.9 K giving a $\Delta T < 0.27$ K margin to the lambda point [7]. The actual design limit is set to one third of the theoretical ΔT in order to account for uncertainties in the thermal analysis or variations in the heat load and cooling conditions. For the present inner triplet quadrupoles built with Nb-Ti conductor, this corresponds to a power deposition limit of 4 mW/cm^3 , with a safety factor 3. For Nb₃Sn, with the same safety factor, one can withstand 12 mW/cm^3 [8].

Simulations of energy deposition in the HL-LHC show that without any shielding one has about 200 MGy peak dose and a peak heat load of 20 mW/cm^3 . This regime is not acceptable for both aspects. The peak is localized in the horizontal and vertical planes. Shielding is very effective: with a 6-mm-thick tungsten shielding, one can bring these values down by a factor five, i.e. to 40 MGy and 4 mW/cm^3 [9].

Using an additional shielding in the quadrupole Q1 close to the IP (see Figure 3), where the aperture requirement is smaller due to a smaller size of the beam, one can further reduce these values by a factor two. Therefore,



Fig. 3. Prototype of beam screen and tungsten shielding in Q1.

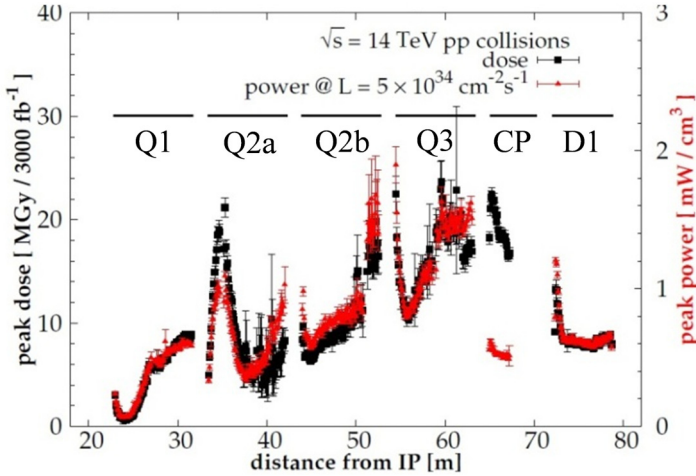


Fig. 4. Heat deposition in the coil (left scale), and radiation damage (right scale) for the 150 mm aperture triplet.

one ends up with a radiation dose similar to what is expected for the LHC, having a factor ten less integrated luminosity, (20-25 MGy) and an even lower heat load (2 mW/cm³), see Figure 4.

The absorbers installed in the magnet bore address two of the most significant challenges of the LHC luminosity upgrade, namely the radiation damage and the heat load. To maintain the required space for the beam the final aperture of the quadrupoles has been fixed to 150 mm, i.e. slightly more than twice the present triplet.

Two additional requirements point in the direction of a thick shielding as the only viable choice for the project. The total heat load on the triplet and separation dipole is 1.5 kW over 55 m, i.e. 30 W/m. The massive shielding allows to intercept about 800 W in the beam screen+shielding and remove it at intermediate temperature with higher efficiency. The remaining 700 W load needs to be removed from the cold mass at 1.9 K. This requires two heat exchangers of 70 mm diameter, barely fitting into the magnet cross-section. A larger heat load would require larger heat exchangers, and larger magnet diameter, which is already at the limit of the constraints imposed by the tunnel diameter.

The second aspect is the degradation of copper Residual Resistivity Ratio (RRR) due to the radiation dose. This parameter is defined as the ratio between

the resistivity at room temperature and at 1.9 K, related to the purity of copper, RRR must be >150 to guarantee the conductor stability and a proper protection in case of quench. Recent studies pointed out that with 200 MGy the RRR is reduced by one order of magnitude [10]. Therefore, a dose of 200 MGy would also endanger the magnet operation and its protection. This degradation is partially wiped out by a warm-up to room temperature, so one could have problems in case of very long runs without warm-up. However, with the 6-mm-thick shielding, the copper RRR degradation becomes negligible.

2.2. *Field quality*

The beta functions in the triplet become very large during the operation with collisions for physics, reaching peak values of ~ 20 km, i.e. five times larger than the nominal LHC values. In these conditions, the beams become very sensitive to magnetic field errors: for this reason, the field quality constraints are very tight. On the other hand, at injection the interaction region gives a small contribution to the total budget of field imperfection of the accelerator and therefore the field quality targets can be significantly relaxed. The field quality optimization should therefore concentrate on high field conditions. A large set of corrector magnets (up to order 6) is foreseen in the layout to be able to correct field errors and/or add nonlinearities to counter beam instabilities; in fact, since the beam size is very large in the correctors, they are very effective to correct any nonlinear unwanted component of the whole LHC.

2.3. *Fringe field and magnet size*

We roughly double the magnet apertures w.r.t. the LHC baseline, but the size of the cold mass is limited by the maximum cryostat size. In the LHC we have a cryostat with a 980 mm diameter that is not far from the limit imposed by the tunnel transverse size. In HL-LHC, the cold mass size is increased from 570 to 630 mm to partly compensate for the aperture, with a weight increase of less than 20%. Larger cold mass diameters would have been difficult since some clearance is needed between the cryostat and the magnet.

In these conditions it is unavoidable to have a large magnetic field outside the cryostat: the transverse fringe field reaches ~ 50 mT on the cryostat surface.

There is no specification of the allowed field in the LHC tunnel; this value depends on the specific instrumentation in situ (vacuum valves, beam position monitors, beam loss monitors, quench protection equipment ...) and in some cases one can envisage a displacement or shielding of the instrument (which is less invasive than shielding the magnet. A target of 50 mT maximum field on the cryostat is considered to be compatible with HL-LHC operation). An alternative solution is an active magnetic shielding, but at the price of an increased complexity of interconnections and number of components.

3. Main Design Choices

3.1. Foreword: loadline, critical surface, and margin

A superconducting magnet has most of the field produced by transport current, plus a second order contribution given by the iron magnetization: therefore, in a first approximation the field is proportional to the current density in the coil: the relation peak field in the coil B_p versus current density j is called the loadline.

A superconducting coil can tolerate up to a given combination of field, current density and operational temperature: this is a property of the superconductor called the critical surface. Materials that can tolerate larger values of field and current density have a better performance, allowing to reach larger fields or to make more compact coils. When the loadline crosses the critical surface, one has the maximum theoretical reachable field. It is called short sample limit since the critical surface is usually measured for a short sample of conductor.

A critical choice for magnet design is the width of its winding. The peak field is proportional to the current density and to the width of the coil, so with large coil widths, the loadline in the B - j graph has a lower slope and one can reach higher fields using lower current densities (see Figure 5). However, a magnet with larger coil is less effective, less compact, and therefore requires more superconductors. With larger and larger coils an asymptotic field is reached, the gain in the short sample limit becoming more and more marginal: one needs to find the optimal coil width. The history of the accelerator magnets shows a progressive increase of coil widths to achieve higher fields [11].

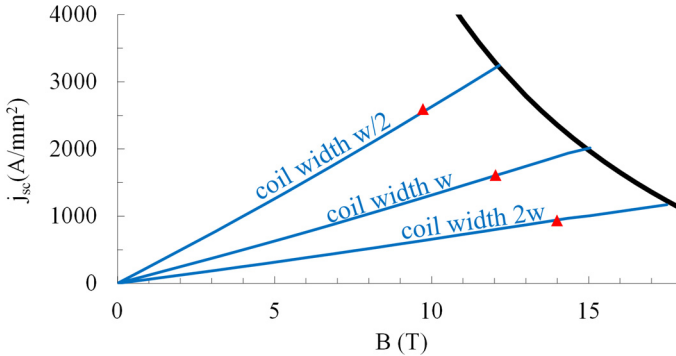


Fig. 5. Critical current versus field for Nb₃Sn at 1.9 K, and loadlines for a coil with width w , $w/2$ and $2w$; red dots indicate operational points with 20% margin.

There are two more aspects that add to what may seem a pure cost and size problem (see also [12,13]): firstly, larger current densities imply larger mechanical stress induced by the electromagnetic. This aspect is particularly critical for HL-LHC since accumulation of azimuthal stress is also proportional to the magnet aperture, and therefore large values are reached even for intermediate fields of the order of 6 T. The second aspect is protection: in case of a transition from the superconductive to the resistive state, the energy of the magnetic field has to be dissipated in the coil. A too large energy density brings the coil to an unsafe temperature (usually considered to be above 350 K) or temperature gradient that damages it. Both stress and protection aspects point to avoid current densities in the coil (including insulation, but not wedges) well above 600 A/mm².

Finally, the design needs to account for production and operation margins. Main magnets in particle accelerators usually operate at 50%-80% of the short sample limit, and correctors around 50%, according to the magnet type and technology. Since the operational targets are usually established before magnet prototyping and production, their selection needs to take into account cost, risk and performance considerations. In the following, we will carry out the main choices for the HL-LHC magnets: technology, coil width and operational margin. A first baseline was developed in 2013 [12] and went through few minor iterations; the final layout is given in [13]. A list of the parameters is given in Table 1.

Table 1. Parameters of HL-LHC main magnets and dipole correctors

		MQXFA/B	MCBXFA/B	D1	D2	MCBRD
Magnet Aperture	(mm)	150	150	150	105	105
Integrated Field	T (m)	-	2.5/4.5	35	35	5
Integrated Gradient	(T)	556.9/948.1	-	-	-	-
Field	(T)	132.6	2.10/2.15	5.60	4.50	2.60
Mag. Length	(m)	4.20/7.15	2.10/1.20	6.26	7.78	1.92
N. Apertures		1	1	1	2	3
Material		Nb ₃ Sn	Nb-Ti	Nb-Ti	Nb-Ti	Nb-Ti
Strand Diameter	(mm)	0.850	0.480	0.825	0.825	0.825
Peak Field	(T)	11.4	4.13	6.58	5.26	2.94
Op. Temp.	(K)	1.9	1.9	1.9	1.9	1.9
Current	(A)	16230	1580-1400	12047	12328	392
J Overall	(A/mm ²)	462	306-270	449	478	368
Loadline Fraction		0.77	0.50	0.77	0.68	0.47
Stored Energy	(MJ)	4.91/8.37	0.77 – 0.239	2.13	2.26	0.143

3.2. Technology, peak field, margin

In a final focus system, performance is given by large aperture and short length in the region from the interaction point up to the separation dipole. This leads to use in the triplet the Nb₃Sn technology at 1.9 K, which allows doubling the aperture of the present Nb-Ti triplet with a moderate increase of the magnet length (see Figure 6). A point of equilibrium between maximization of performance and risking conditions associated with a low margin, was found at 78% on the loadline (see Figure 7).

For the separation/recombination dipole D1 (single aperture), which is presently a resistive magnet (see Figure 6), we opt for a superconducting magnet with 5.6 T operational field, based on Nb-Ti technology, with a 77% operational point on the loadline [14]. Here the initial value of 75% was changed to be able to fit the magnet in the vertical test station; the possibility of vertical testing represents a considerable risk reduction. This field value still fits to the field quality constraints imposing a limited variation of multipoles with nominal current to avoid reaching an uncontrolled situation.

With respect to the LHC, the reduction in the length of D1 in the upgraded IR more than compensates for the additional space needed by the triplet; in

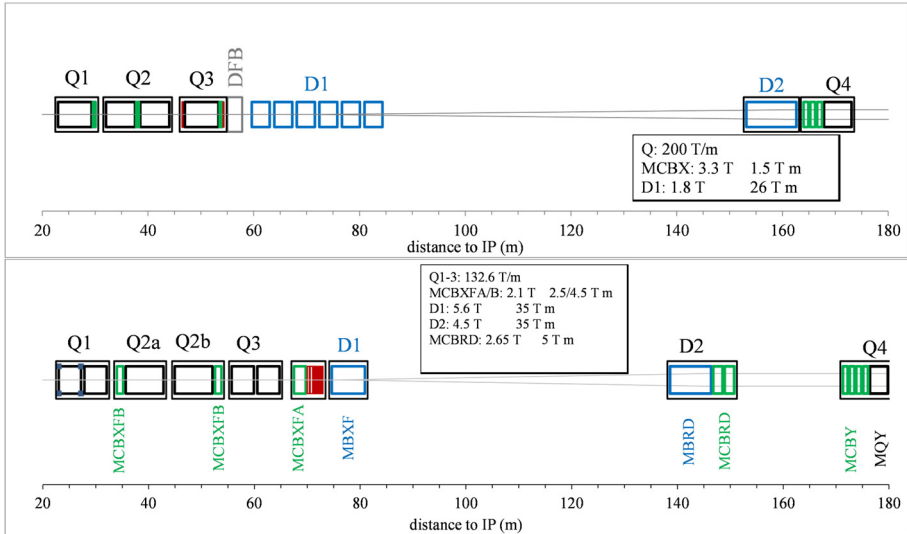


Fig. 6. Layout of the LHC (upper part) and of HL LHC (lower part) interaction region from first quadrupole (Q1) to separation dipole (D1).

fact, the end of D1 in the HL-LHC layout is 4 meters closer to the interaction point as compared to the LHC. The option of a Nb₃Sn magnet, considered in the past [15], has been discarded as the gain of a few meters (3 m, with an 11 T dipole) is not considered critical in this location and has no effect on performance.

The maximum field in the separation/recombination dipole D2 (double aperture) is also mainly determined by field quality constraints, i.e. avoiding a too large saturation in the iron. The issue is not the value itself, that can be corrected via the geometric contribution, but avoiding having a large derivative of b_3 with respect to the operational field, that in the LHC should keep a flexibility in the range 6.5 to 7.5 TeV. For this reason we chose an operational field of 4.5 T based on the Nb-Ti technology, giving a more comfortable operational point at 68% on the loadline. The initial layout also considered a larger aperture Q4 [16], but this option was discarded in 2017, since the additional aperture was not considered to bring a significant performance improvement. However, one short model and two prototypes were built.

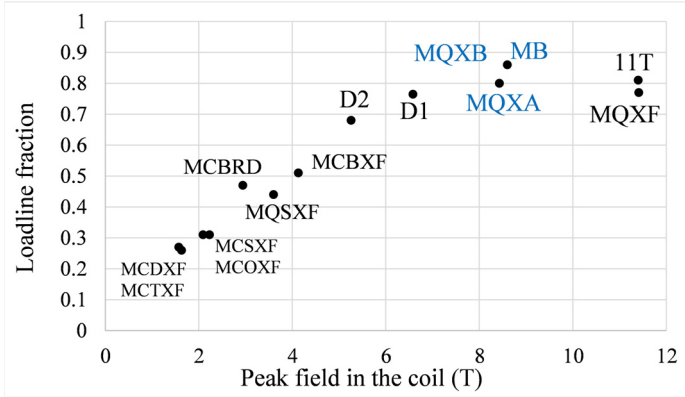


Fig. 7. Peak field in the coil versus loadline fraction of HL-LHC IR main magnets and correctors, 11 T. Blue points: LHC main dipole (MB) and LHC IR quadrupoles (MQXA and MQXB).

The correctors were selected to operate with lower loadline fraction (30% to 50%), as in most accelerators, as there is no need to increase the performance and the cost of additional margin is low compared to the case of the main magnets. The plot summarizing the peak field versus the loadline fraction is given in Figure 7, where the LHC magnets are also shown.

3.3. Cable, coil width and stress

The accumulation of stress in the midplane is proportional to the magnet aperture, to the field and to the current density. Therefore HL-LHC magnets naturally have much larger stress than the LHC magnets, just because of the larger aperture. Values approaching 200 MPa can damage insulation for Nb-Ti magnets or degrade conductor performances for the Nb₃Sn magnets. Therefore, one has to carefully check during the initial design phase that the field, aperture and current density values correspond to reasonable values of stress.

A way to reduce the stress enhancement is to use a larger coil width and reduce the current density, i.e. having a less effective magnet. In HL-LHC, we increased the coil width of the quadrupoles to a double layer of 18 mm width cable; moreover, both D1 and D2 were designed with coils reusing the Nb-Ti cable of the LHC, i.e. increasing the coil width by 50% with respect to the LHC superconducting D2 recombination dipoles, based on BNL RHIC dipole design [17] and 10-mm-width cable.

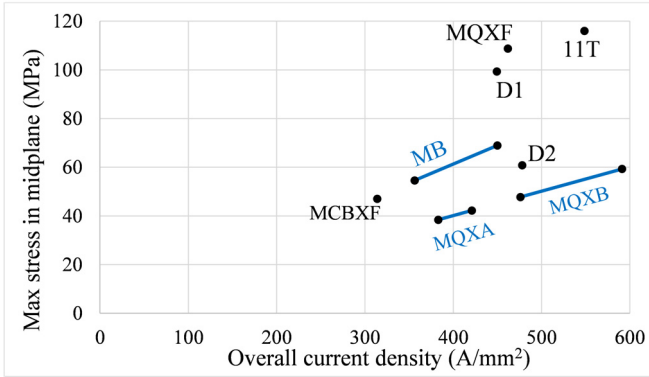


Fig. 8. Overall current density versus maximum midplane stress (in absence of structure and coil deformations) for HL-LHC IR main magnets, 11 T. Blue: LHC main dipole (MB) and LHC triplet (MQXA and MQXB), where two points are given (joint by a line to ease the readability) since the inner and outer layer have different current densities.

The plot summarizing the overall current density versus the accumulated stress in the midplane is given in Figure 8: due to the large aperture, both the HL-LHC triplet MQXF and the separation dipole D1 have challenging values above 100 MPa, 50% to 100% larger than what present in the LHC dipoles.

3.4. Cryostat and interconnections

The maximum length of a cryostat that can be lowered in the tunnel is 15 m, corresponding to the main dipole case. Having quadrupoles with lengths ranging from 7 to 8 m, plus a series of orbit correctors, we are forced to have one cryostat per quadrupole (in LHC Q2a and Q2b share the same cryostat, see Figure 7). The US AUP project, in charge of Q1 and Q3, has opted for a solution based on having two 4.2-m-long quadrupoles closely connected to form one cryostat for the Q1 and Q3 units. This reduces the risk associated to the magnet length, even though it increases costs due to double number of coils and magnet assemblies, and requires doubling the manufacturing lines. The Q2 units are designed with one 7.15-m-long quadrupole magnet (magnetic length), making a further step in the length of Nb₃Sn coils towards the 15 m target needed for main dipoles of a future accelerator fully based on Nb₃Sn. The interconnections have been designed to minimize the distance between the magnets given the requirements for installation and interconnection.

3.5. Cooling

The cooling of the triplet is provided through heat exchangers. Since the total load on the cold mass is about 15 W/m, one has to use two heat exchangers of 70 mm diameter. The alternative options of one heat exchanger of 110 mm diameter would simplify the interconnections but is not viable since it is not compatible with the magnet mechanical structure. The ideal position for a hole in the yoke of a quadrupole is at 45°, i.e. in the low field region and where less material is needed for structural reasons. A 70 mm heat exchanger is large but still fits the cold mass iron yoke. The short orbit correctors have to share the heat exchanger, i.e. the hole must be in the same positions.

4. The Triplet Quadrupoles Q1-Q3

4.1. Historical development

The development of Nb₃Sn quadrupoles for the LHC luminosity upgrade was first initiated with the US conductor development program [18] and, in 2004, by the US LHC Accelerator Research Program (LARP), a collaboration of US National Laboratories and CERN [19]. At that time the target was to reach a β^* of 25 cm and a 30% increase of the aperture, from 70 to 90 mm was considered an adequate choice both in terms of machine requirements and technological challenges. After some preliminary tests using racetrack coils, the 1-m-long Technological Quadrupole (TQ) series were developed to address key manufacturing and design issues for cos2 θ coils [19]. Two mechanical structures were tested, one based on stainless steel collars [19] and the other on Al shell pre-loaded using water-pressurized bladders and interference keys [19,20]. After testing several models, the bladder and key structure demonstrated a better capability of controlling stress and a better reproducibility of performance and was selected for the length scale-up from 1 m to 3.4 m (Long Quadrupole - LQ series, see Figure 9), with successful tests starting from 2009 [21].

Meanwhile, several studies were pointing at the possibility of using apertures larger than 90 mm to increase the upgrade performance [5]. In order to study the feasibility of larger apertures, and demonstrate the capability to incorporate field quality and alignment requirements, LARP started the

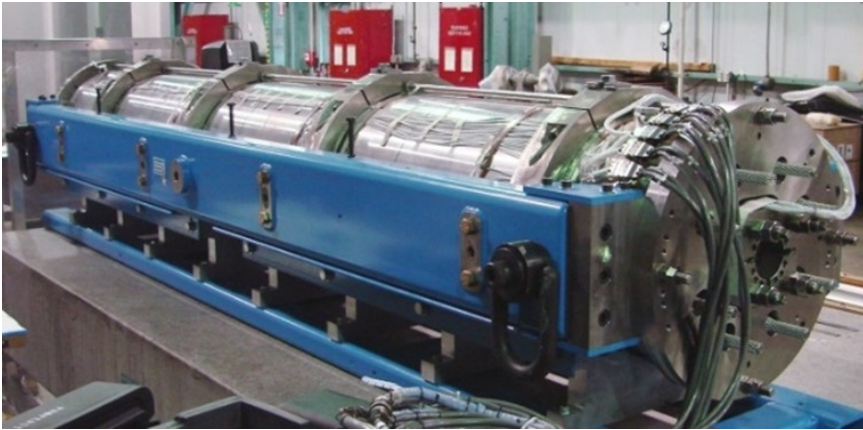


Fig. 9. LQ, the first 3.4-m-long Nb₃Sn magnet built by LARP collaboration.

development of the 120-mm-aperture High-field Quadrupole HQ in 2008 [22]. A successful HQ test at CERN in early 2012 supported the decision to further increase to 150 mm aperture for the triplet quadrupoles (MQXF) [12,23]. The most advanced solutions used in TQ, LQ and HQ are now being applied to the larger aperture quadrupole. So MQXF is essentially a scaling of the design of HQ. The guideline is to keep all features that have been shown to work in the LARP magnets.

4.2. Strand and cable

As the aperture in QXF is 25% larger than in HQ, a corresponding increase of the coil width is desirable. In order to minimize deviations from established LARP designs, a two-layer coil layout is maintained and the increase in coil width is obtained with an increase in cable width, requiring a larger strand and/or more strands per cable. The option of having one additional layer was excluded to avoid complexity in the coil fabrication. The number of strands is limited by cable mechanical instabilities which affect the winding process, and/or damage to the superconducting strands during the cabling operation. For MQXF, it has been decided to limit the number of strands to 40, which is also the upper limit of the CERN winding machine. TQ cable had 27 strands and 10 mm width, and HQ had 35 strands with 15 mm width. The number of strands and the cable width fixes the strand diameter to 0.85 mm. This is a

marginal increase compared to the HQ case, which had 0.8 mm. In all cases we tried to minimize the changes w.r.t. HQ magnets to rely on established design solutions and avoid significant delays to overcome new issues.

With respect to LARP workhorse, the RRP 0.7 mm strand with 54/61 layout, it was decided to use the latest developments used in HQ, i.e. finer filaments with 108/127 layout; the critical current density was reduced by about 10-20% with respect to the highest values reached for the RRP technology, and the specification was at 1280 A/mm² at 4.22 K and 15 T.

The cable made use of a stainless steel core (25 μm thick) to increase the inter-strand resistance. Previous LARP quadrupoles, built without cored cables, showed a clear indication of a very low inter-strand resistance (of the order of 0.1-0.5 $\mu\Omega$) [24], producing (i) a severe degradation of quench performance with increasing ramp rate, affecting the capability to perform a fast discharge without quench and (ii) a degradation of field quality, visible as non-allowed components with large dependence on ramp rate, and decay of several units even at high field, with times of the order of a few seconds (see Figure 10). The second short model HQ02, built with cored cable, proved to cure these issues with an increase of the effective inter-strand resistance by more than one order of magnitude (see Figure 11). Insulation is based on a braided fiberglass tape.

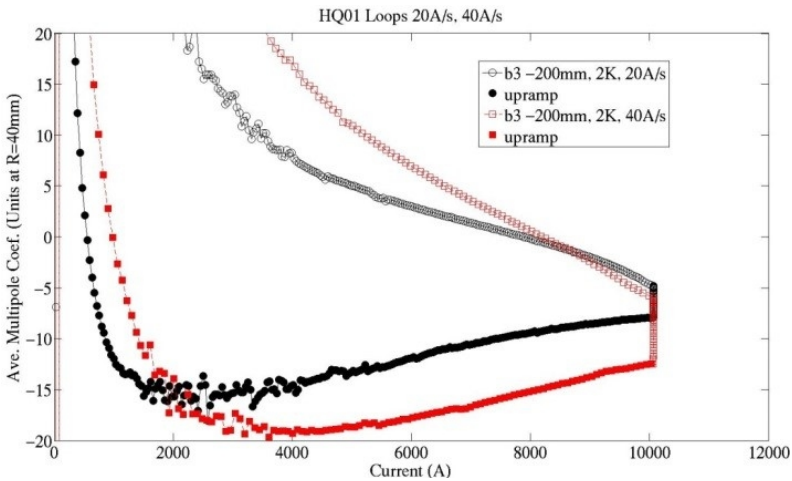


Fig. 10. Dependence of b_3 along the ramp for different ramp rates: case of cable without core (HQ01e).

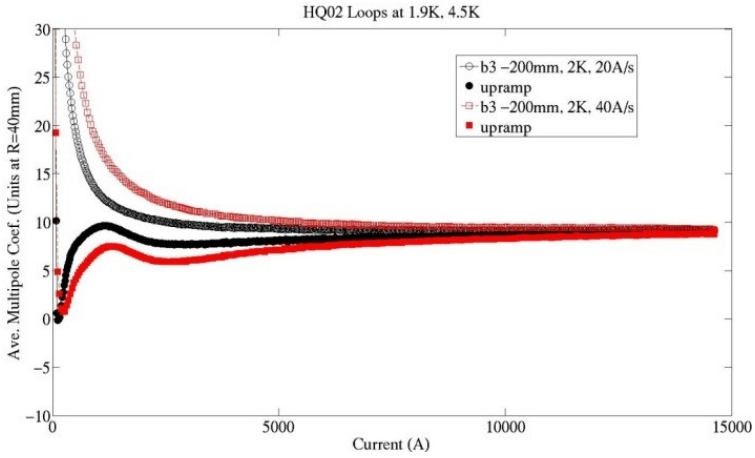


Fig. 11. Dependence of b_3 along the ramp for different ramp rates: case of cable with core (HQ02a).

4.3. Coil

The coil is a double layer, four block coil [23]. Two wedges provide the required flexibility to tune the field quality to optimal values. The basic layout of the conductor blocks (Figure 12) is similar to what has been used in HQ. In particular, similar pole angles are chosen for both layers. This approach has

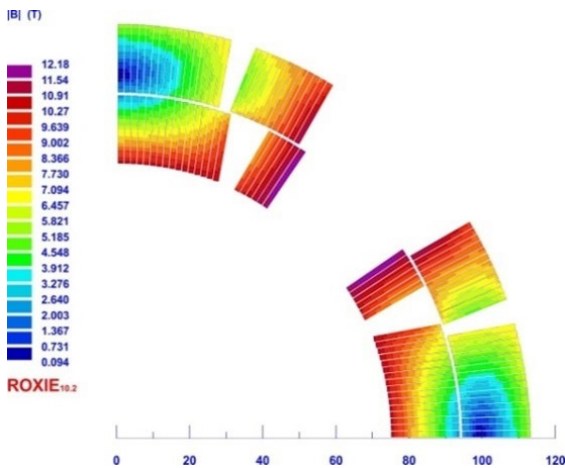


Fig. 12. MQXF coil cross-section (one quarter shown), and field in operational conditions.

been shown to minimize the peak coil stresses. In operational conditions the peak field in the coil is 11.4 T, corresponding to a ratio between peak field and gradient times aperture of about 1.15. The coil is reacted after winding, with a reaction cycle to form the Nb_3Sn superconductor followed by impregnation with CTD-101K. The 7.15-m-long coils of Q2 are shown in Figure 13.



Fig. 13. MQXF coils manufactured at CERN.

4.4. *Mechanical structure*

The magnetic forces are contained by an aluminium shell (see the MQXF cross-section in Figure 14 [23]). During the assembly at room temperature, a prestress of the order of 100 MPa is applied to the coil through the insertion of keys in the slots opened by bladders. During the cool down, the Al cylinder stress increases by an order of 30 additional MPa. This procedure has been used in several models, proving to be an efficient and accurate way to control the stress in the magnet, and allow to select a preload to fully or partially balance the electromagnetic forces. As the magnet is energized, the pre-load provided by the mechanical structure is replaced by the internal loads

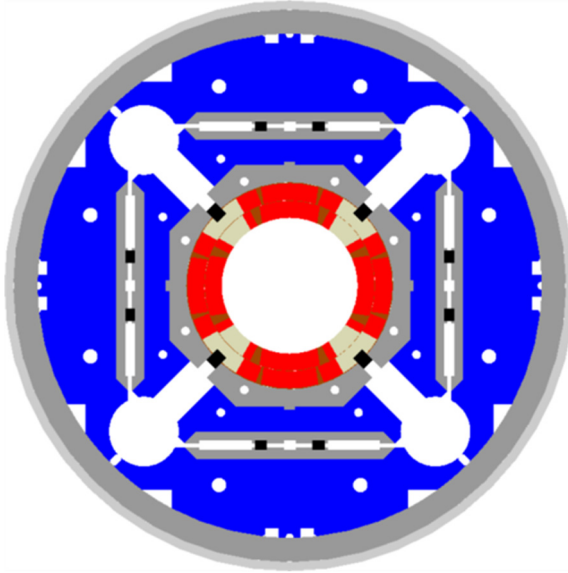


Fig. 14. MQXF cross-section.

generated inside the coils by the electro-magnetic forces. Full alignment is maintained at all steps of coil fabrication, magnet assembly and powering. An additional stainless-steel vessel is needed for He containment. The axial structure is based on stainless steel tie rods providing a preload on the magnet ends equivalent to the magnetic forces; this solution has been validated on the LARP magnets.

4.5. Protection

The inductance of the QXF magnets is 8-10 mH/m, the lowest value being at nominal current and the highest in the linear regime of non-saturated iron, i.e., at injection. The current is 17.5 kA, so a dump resistor is limited to $50 \mu\Omega$ to avoid having voltages that exceed 900 V at the beginning of the current dump. In these conditions, a dump extracts a negligible fraction of the energy stored in the magnetic field, and as in the LHC dipoles, the only solution is to use the thermal inertia of the magnet coil to dissipate the energy of the magnetic field. A design constraint to remain below ~ 350 K in all points of the coils during a quench was adopted.

Both Nb-Ti and Nb₃Sn windings have a similar enthalpy from 2 K to 300 K of the order of 0.6 J/mm³. So, the first physical quantity to check is the energy density, i.e., the stored energy divided by the volume of the coil. Note that due to the time scale involved in these phenomena (a fraction of second), the structure components as collars and yoke are too far from the coils to participate to share the burden of the heat dissipation – that’s why we consider the energy density only over the coil volume. For typical Nb-Ti magnets this value is around 0.05 J/mm³. In our case, as in many other Nb₃Sn magnets, we are at twice this value, so still well within the enthalpy limit but with half the margin.

The key point is to prevent excessive energy dissipation at the initial quench location, which can lead to coil damage due to high local temperature and stress, by ensuring rapid transition of the entire winding to the normal conducting state in the fastest possible time. This is done as in most accelerator magnets through quench heaters, i.e., strips of stainless steel which are powered as soon as the quench is detected, and whose heat is transferred via conduction to the coil, pushing it above the critical temperature.

A simple way to compare the protection challenge is to compute the time budget (time margin) for the protection system available to quench all magnet, setting 300 K as the maximum temperature reached by the coil [25]. An advantage of this quantity is that it depends only on the magnet design, and not on the quench features (high field or low field, propagation, etc.) and on the protection system. On the other hand, to make the estimate of the warmest point reached in the magnet (so-called hotspot temperature) one needs other hypothesis on the quench location, efficiency of heaters, propagation, etc.

The time margin is of the order of 100 ms for Nb-Ti magnets. In general, one needs a few ms to build enough resistance to have a measurable voltage (voltage thresholds are usually set at 100 mV). Then a validation window of 10 ms is used to avoid having false signals. Then the switch of the circuit disconnecting the power converter and dumping the current on the external resistor or on a diode is opened (2 ms). At the same time the heaters are fired. Typical times between the heater firing and the quench of the coil induced by the heaters is 10-20 ms (among the numerous literature, see [26] for an extensive overview). Therefore, 40 ms is a minimal value necessary to have a safe protection system: this is what is achieved in MQXF design. Note that for TQ and HQ magnet this margin is only 18 and 25 ms respectively.

The MQXF protection system relies on outer layer heaters. With respect to the LARP choices, the thickness of the insulation between the heater strip and the coil has been increased from 25 μm to 50 μm to reduce the risks related to insulation failures between the coil and the heaters. On the top of the outer layer quench heaters, two additional options were studied to add the redundancy and the robustness to failure scenarios that are required for operation. Note that the magnet has to be protected in case of two simultaneous failures.

The first redundant system that was explored is the use of inner layer quench heaters, having the interesting feature of directly quenching the inner layer, and not relying on the heat propagation from outer to inner layer. Inner layer quench heaters were intensively studied in LARP and in the initial part of MQXF program, showing a good efficiency in quenching the inner layer of the coil, but they were finally abandoned due to partial detachment of the heaters after successive quenches.

The second option was the use of a novel method [27] based on the injection of a fast pulse of currents in the opposite coils to provoke a quench thanks to the heat dissipation induced by the dI/dt (see Figure 15). This method, named CLIQ, proved to be extremely effective in quenching both layers and

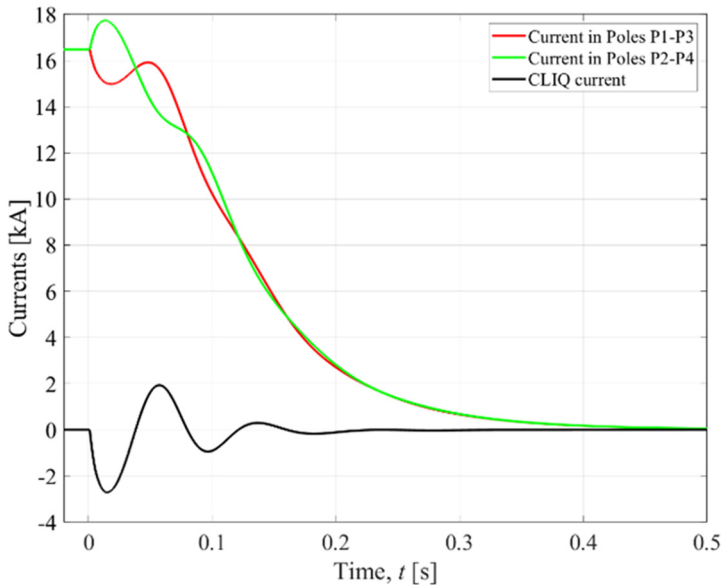


Fig. 15. Current decay during a quench induced via the CLIQ system.

is now part of the MQXF baseline, together with outer quench heaters [28]. In case of no failures, the use of CLIQ and outer layers quench heaters guarantees a hotspot temperature during quench below 300 K.

4.6. Field quality and shimming

When the beams are squeezed in the interaction point, the optical functions in the triplet are very large and the beam dynamics becomes very sensitive to any field imperfection in the triplet. Field quality of the triplet must satisfy tight constraints. The main challenges are (i) a reproducibility of the transfer function of less than one unit and (ii) control of the low order harmonics within few units. On the other hand, the nonlinearities coming from the large iron saturation (about 10%, as in HQ, see Figure 16) can be compensated through an adequate powering of the magnets, provided that the effect is reproducible. Results from the LARP program show that this level of reproducibility is obtained, and that there is a good understanding of the quadrupole main component behaviour as a function of the current and of the ramp direction.

The low order harmonics are related to the asymmetries of the components and of the assembly. Here, in the initial part of the production cases several units of non-allowed low-order harmonics (a_3, b_3, a_4, b_4) have been found. For

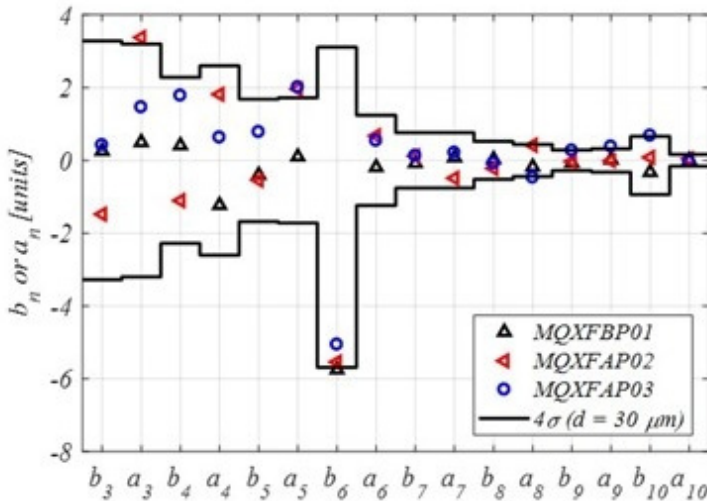


Fig. 16. Average field harmonics measured in three prototypes, and tolerance range.

this reason, a magnetic shimming [29] has been foreseen to compensate for a few large harmonics (typically two at the same time). The technique is based on inserting magnetic rods in holes in the collars and magnetic bars in the spaces used by the bladders. By placing magnetic shims in an asymmetric way, one can compensate up to several units of low order harmonics [30]. The more mature part of the production has shown a reduction of the non-allowed low order harmonics (see Figure 16), towards levels achieved in Nb-Ti collared magnets.

Usually, a lot of emphasis is put on the first allowed harmonics b_6 . In fact, this harmonic is not the most critical for the beam, as it is a high order. Moreover, from the point of view of the magnet builder, it is pretty easy to control b_6 through the cross-section geometry. At injection one has about 20 units given by the magnetizations, which are within the beam dynamics targets.

4.7. Present status

The program includes six short models as a joint effort of CERN and AUP; for MQXFA, two prototypes, 5 pre-series and 16 series magnets are foreseen. For MQXFB, two prototypes and 10 series magnets. An overview on the performance of the short model and prototype magnet build so far goes behind the scope of this chapter, and we refer to [13] as the most recent reference available at the moment of writing.

5. Correctors

5.1. Single-aperture nested orbit correctors

The orbit correctors are needed to compensate for alignment errors of the triplet, to steer the closed orbit of the accelerator, and to open the crossing angle in the interaction point. For HL-LHC, two correctors providing 2.5 T m in each plane are needed close to each Q2, and one providing 4.5 T m between Q3 and D1 (see Figure 6). The aperture has to match the triplet and D1 aperture, i.e., 150 mm diameter. For comparison, in the LHC we have nested magnets providing 3 T in each plane, with 70 mm aperture. A nested configuration is needed to reduce the gap between the quadrupoles, which produces an increase of the beta functions and therefore of the beam size in the

triplet, requiring a larger aperture. The main challenge of the nested magnet is the management of the large torque (10 000 N·m per meter length of the magnet) due to the electromagnetic forces.

For the HL-LHC we consider a nested magnet with an operational field of 2.1 T, giving a magnetic length of 1.2 m and 2.1 m for each magnet type. This is achieved with Nb-Ti two-layer coils based on a Rutherford cable composed of 18 strands of 0.45 mm diameter. This cable [31] has been developed for the corresponding corrector magnet in S-LHC preparatory phase program, set up in the frame of the previous project LHC upgrade Phase I, now superseded by HL-LHC. In HL-LHC we opted for a double layer to increase the margin, and to lower the operation current below 2 kA, thus avoiding significant cost associated to the numerous (total of 24) power converters [32].

The peak field is 3.5 T, close to twice the nominal field. This is due to the presence of two perpendicular fields (giving a factor $\sqrt{2}$) plus the ratio coil peak field/bore field, which is ~ 1.3 . Large ratios of peak field/bore field are unavoidable in dipoles where the coil width is thin with respect to the aperture. The nested option is challenging from the point of view of the mechanical structure, and to ensure reliability we require that the torque has to be controlled through a mechanical locking, see Figure 17 as proposed in [31].

The design, and construction of three prototypes (two providing 2.5 T m and one providing 4.5 T m) and 18 series magnets is an in-kind contribution of CIEMAT laboratory. The magnets are individually tested in the FREIA test station, shipped to CERN, where they are integrated in a cold mass which is then integrated in the cryostat and tested in horizontal position.

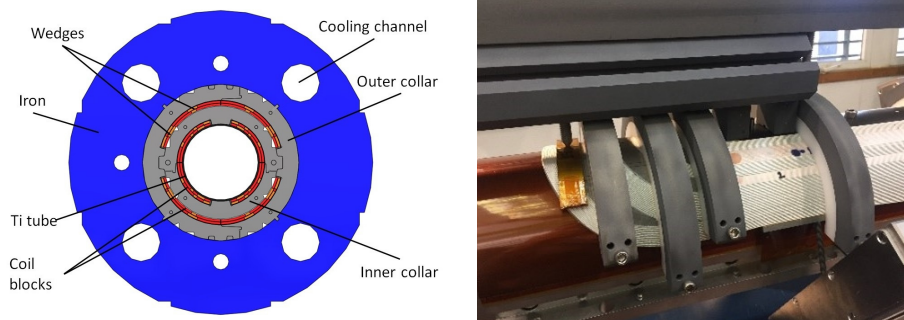


Fig. 17. Cross-section of the orbit correctors (left) and winding of the coil (right).

5.2. Superferric correctors

The correction of the triplet imperfections and misalignment requires a skew quadrupole, and a large set of high order correctors. The first requirement is a skew quadrupole, with $0.7 \text{ T}\cdot\text{m}$ integrated force, to correct the construction and alignment errors in the triplet field direction. Then we have normal and skew sextupole, octupole, decapole and dodecapole corrector magnets. Among them the sextupole is particularly relevant for the chromatic correction. Requirements for the normal and skew terms are the same, with the exception of the normal b_6 which is four times larger than a_6 since this is an allowed multipole of the quadrupole and therefore has a larger systematic and random component (see Table 2).

Table 2. Parameters of the HL-LHC correctors

Multipole	Coil	Intehrated	Peak Field	Loadline
	Length (m)	Gradient (T·m)	in Coil (T)	Fraction
a2	0.457	0.700	3.6	0.44
b3/a3	0.192	0.095	2.23	0.31
b4/a4	0.172	0.069	2.09	0.31
b5/a5	0.172	0.037	1.63	0.26
b6	0.498	0.086	1.57	0.27
a6	0.123	0.017	1.50	0.27

In the LHC we have nested correctors, with up to five magnets nested. This solution saves space but makes operation more complex. For a non-nested solution, a key point is to have very short heads, otherwise all the space is lost in heads and interconnections. In the framework of the S-LHC studies, a superferric technology [31,33] was used to build some prototypes with 140 mm aperture. This solution was adopted for HL-LHC [34]: the magnets have the same cross-section as a resistive magnet (see Figures 18 and 19), with Nb-Ti coils serving to magnetize the iron poles and yoke. In this case, (i) the field quality is given by the shape of the iron poles and not by the precise location of the coils, and (ii) the field is limited at $\sim 1.5\text{-}2 \text{ T}$ due to iron saturation. The magnet operates at a loadline fraction between 0.25 and 0.35 (see Figure 7).

One advantage is that coils are not directly exposed to the aperture, so the magnet is resistant to radiation and additional shielding can be put to

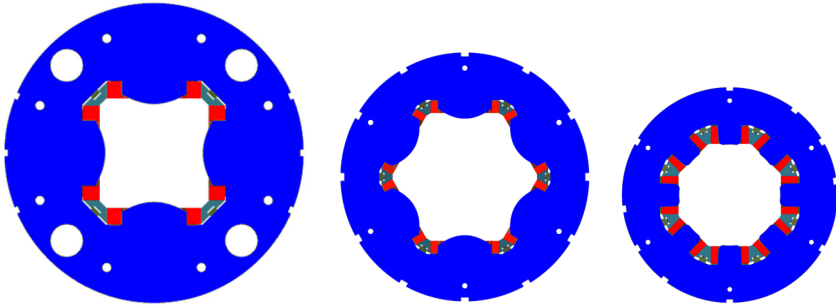


Fig. 18. Cross-section of the skew quadrupole of the sextupole and of the octupole correctors.

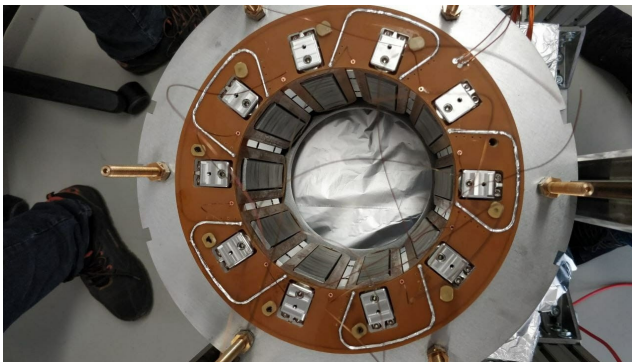


Fig. 19. Superferrous decapole corrector.

protect the coils. The second advantage is that the heads can be made extremely short, with small diameter cable and sharp bends, so what is lost in the non-nested option is partially recovered by the shorter heads. It has been also checked that the longitudinal interference between different correctors is negligible even with short interconnection of 80 mm. The last advantage is that operational current is ~ 100 A, since the conductor is a small single wire. This also simplifies the numerous current leads needed to power this large set of correctors.

The design, and construction and test of five prototypes and 54 series magnets is an in-kind contribution of INFN-Milano-LASA. The magnets are manufactured in SAES-RIAL, tested in LASA and then shipped to CERN, where they are integrated in the cold mass with the orbit correctors or with the Q2 magnet, and then integrated in the cryostat and tested in horizontal position.

5.3. Orbit correctors in recombination dipole

Close to the recombination dipole two additional orbit corrector, with 5 T m integrated field in each plane, is present in the HL-LHC lattice. This corrector is absent in the LHC layout. As for the recombination dipole, the field is limited by nonlinearities in field quality induced by the cross-talk between the two apertures. Since each aperture has to work in any powering condition, the only way out is to have iron shielding between the two apertures, place the horizontal field in one aperture and the vertical in the other one to minimize the cross talk as in the LHC, and limit the operational field to 2.6 T, for a magnetic length of 2.2 m.

These requirements make this magnet ideal for the application for the titled solenoid design (also called canted cos theta or double helix in the literature). This idea first proposed in [35] and later developed in [36,37], is based on winding the conductor on grooves machined in an helix shape on an Al former. The two tilted solenoids (see Figure 20) provide a perfect dipolar field, and the opposite solenoid components cancel out. The lower efficiency of the design (some conductor is used to generate the solenoidal fields in the two concentric windings that compensate each other) is compensated by the required much simpler tooling. Moreover, for this range of field, the conductor cost is not a major component of the magnet cost.

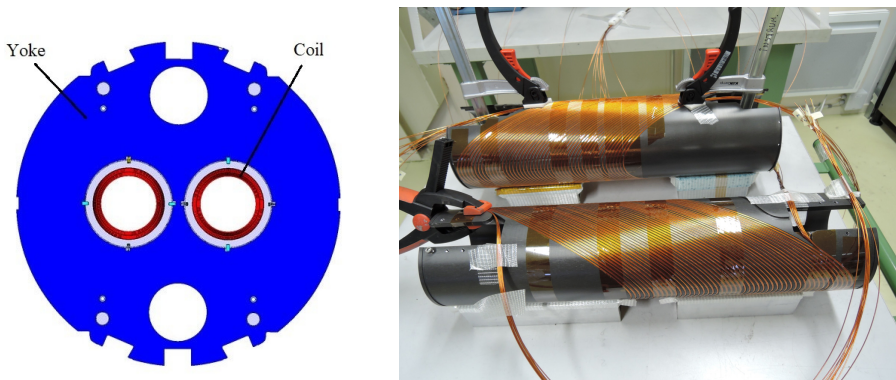


Fig. 20. Cross section of the orbit correctors in the recombination dipole (left) and its active part in a short model version: the tilted solenoid coils.

The conductor is a 0.825 mm diameter Nb-Ti strand, and 10 wires are wound in each groove. The magnet is working a 0.50 loadline fraction. The design and one prototype have been developed at CERN [38], and a technology transfer with IHEP (Beijing) has been carried out in view of an in-kind contribution by China.

A total of 14 magnets (2 prototypes, 8 series and 4 spares) are planned. Prototypes were developed in WST (Xi'an), series is ongoing in BAMA (Suzhou), with magnet test in IMP (Lanzhou). After shipping to CERN, they are integrated in the D2 cold mass, and then integrated in the cryostat and tested in horizontal position.

6. Separation Dipole

The LHC separation dipoles at IR1 and IR5 are 20-m-long resistive magnets, made of 6 modules of 3.4 m length, providing 26 T·m (see Figure 6). The new specification of integrated field in IR1 and IR5 is 35 T·m. The replacement of the resistive units with a single Nb-Ti magnet allows recovering the additional space which is needed by the longer triplet and by the insertion of crab cavities in the interaction region layout. Selecting the same aperture and the same shielding as for the triplet quadrupoles, one can verify that the collision debris induces a heat load and a radiation dose within the project targets; therefore, one can replace the resistive magnet with a superconductive one.

The main challenges in the magnet design are the large aperture giving rise to large accumulation of electromagnetic forces in the magnet midplane, fringe fields, and field quality. The large aperture gives 100 MPa pressure in the midplane due to electromagnetic forces, so a proper mechanical structure must be developed. With such a large aperture, the fringe field also becomes an issue: with a 5 T operational field in 150 mm aperture, one needs ~200 mm of iron to avoid fringe fields. In case of 15 mm coil width and 15 mm spacers, the magnet size reaches $150 + (15 + 15 + 200) * 2 = 610$ in mm diameter, i.e. about the same size of the triplet quadrupole cold mass. This suggest to (i) do not push field to very large values, restricting the study to one-layer coil (ii) have a mechanical structure where forces are taken by the yoke and collars are simple spacers: in this way, more iron is available for shielding.

The baseline [14] is to set the working point at 77% of the loadline, with a Nb-Ti 15-mm-width cable as in the LHC main dipole, providing 5.6 T

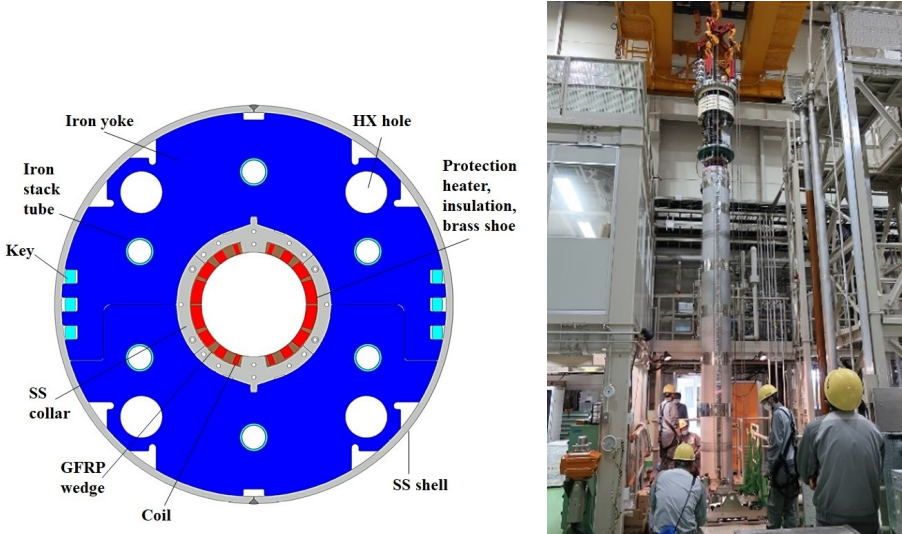


Fig. 21. Cross-section of the separation dipole (left) and prototype magnet in the test station (right).

operational field (see Figure 21). In this way a 6.3-m-long magnet provides the required 35 T·m. The iron is largely saturated at nominal field, with a 12% decrease of ratio field/current w.r.t the linear case. Such a large saturation has a relevant impact on field quality, which becomes the main challenge. A careful iron shaping can reduce this effect, following the example of what has been done for the RHIC dipoles [17]. The impact on b_3 can be reduced from the initial values of several tens of units (for a circular iron without holes) to a few units along the operational range. Optimization is done at high field, with a target for the energy reach in the window 6.5 TeV to 7 TeV.

The mechanical structure is similar to the MQXA [39], with support given by the iron yoke locked by keys. This structure has the advantage of reducing the collar size, leaving more space to iron and reducing the fringe field. It allows a very efficient collaring, providing the compression of the coil needed to avoid pole unloading during powering.

The design, construction and test of three short models, one prototype, four series and two spare magnets is an in-kind contribution of Japan via KEK laboratories. The magnet cold masses are shipped to CERN after vertical test, where they are integrated in the cryostat.

7. Recombination Dipole

The recombination dipole needs the same integrated force of $35 \text{ T}\cdot\text{m}$ to bring the beams back to parallel trajectories, with the nominal spacing of 192 mm. In the LHC this is done by a two-in-one 10-m-long superconducting magnet with $\sim 3 \text{ T}$ operational field, and 80 mm aperture. Due to the larger beam size one needs to increase this aperture to 105 mm at IR1 and IR5. In these conditions, since the beam spacing is unchanged, even with a 15-mm thin coil and 15 mm spacing for collars, only a few cm are left between the two apertures, which have the field pointing the same direction. In these conditions, the main design challenge is to decouple the magnetic field in the two apertures and ensure good field quality. For these reasons, we consider an operational field of 4.5 T (1 T lower than D1), giving a magnet length of 8 m. Even with this conservative design choice, using iron yoke as a shield between two apertures would have a limited efficiency and would lead to large saturation effects, which is difficult to compensate. Therefore, a different approach was proposed [40], following an idea proposed in [41]: the iron yoke is removed from the central part, and the resulting large but current-independent cross-talk between the apertures is corrected with a slightly (order of 1 mm) asymmetric arrangement of the conductor blocks. With this approach, it is possible to reach 4.5 T at 1.9 K with a 35% margin, and satisfying the field quality requirements.

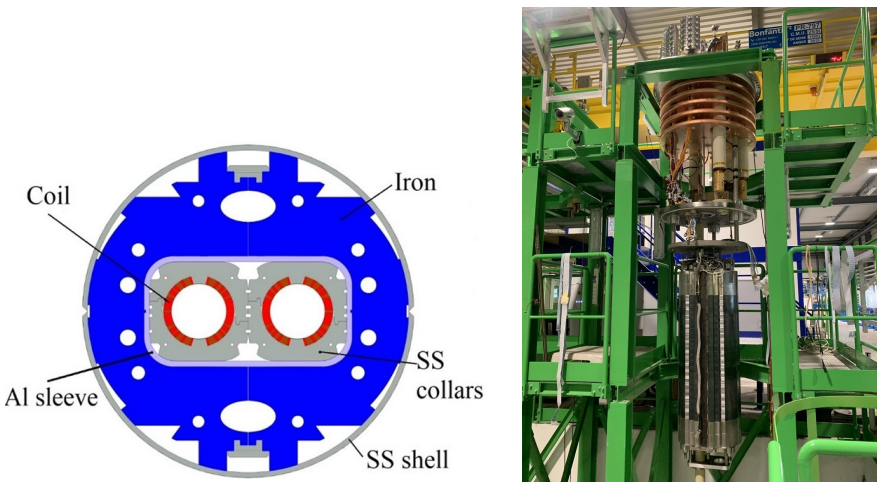


Fig. 22. Cross-section of the recombination dipole (right) and short model in the test station.

The mechanical structure (see Figure 22) relies on separate collars to increase the flexibility in manufacturing for such a small series of magnets (total of 6). The collars completely support the electromagnetic forces, and allow giving a full preload during assembly. The two apertures are assembled in a novel concept, i.e. a Al sleeve providing alignment and mechanical support to the electromagnetic forces between the two apertures (tending to separate the aperture, as the fields are in the same direction).

One short model, one prototype, four series and two spare magnets are provided an in-kind contribution by INFN-Genova, who took care of the design, with manufacture by ASG in Genova. The magnets are shipped to CERN, where they are integrated in a cold mass with the orbit correctors, and then integrated in the cryostat and tested in horizontal position.

8. The Large Aperture Two-in-one Quadrupole

In the initial layout, a larger aperture quadrupole was considered for Q4, namely increasing from the LHC values of 70 mm to 90 mm aperture. The magnet relies on a double layer Nb-Ti coil, with 120 T/m gradient, a 0.77 loadline fraction, a peak field of 6.4 T and an operating current of 4.55 kA [16]. The magnet has been removed from the baseline in 2016 after a review of the beam dynamics requirements.

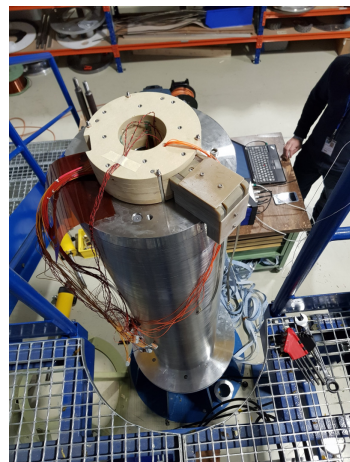
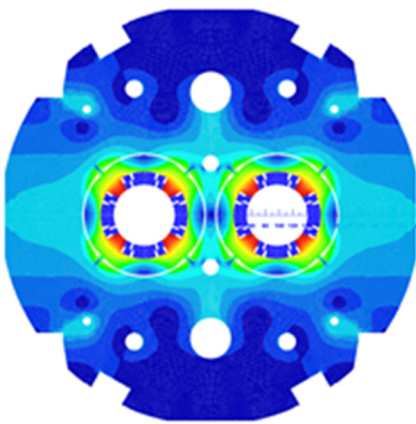


Fig. 23. Cross-section of the large aperture two-in-one quadrupole (left) and short model ready for test in CEA (right).

References

1. O. Bruning, et al., LHC luminosity upgrade: a feasibility study, *LHC Project Report* **626** (2002).
2. J. P. Koutchouk, et al., A solution for phase-one upgrade of the LHC low-beta quadrupoles based on Nb-Ti, *LHC Project Report* **1000** (2007).
3. R. Ostojic, et al., Conceptual design of the LHC interaction region upgrade: phase I, *LHC Project Report* **1163** (2008).
4. J. P. Koutchouk, Investigations of the parameter space for the LHC luminosity upgrade, *European Particle Accelerator Conference* (2006) 556-558.
5. L. Rossi, State of the art superconducting accelerator magnets, *IEEE Trans. Appl. Supercond.* **12** (2002) 219-227.
6. L. Rossi, E. Todesco, Electromagnetic design of superconducting quadrupoles, *Phys. Rev. STAB* **9** (2006) 102401.
7. N. Mokhov, et al., Protecting LHC IP1/IP5 component against radiation resulting from colliding beam interactions, *LHC project report* **633** (2003).
8. V. V. Kashikhin, et al., Quench margin measurement in Nb₃Sn quadrupole magnet, *IEEE Trans. Appl. Supercond.* **19** (2009) 2454-2457.
9. L. Esposito, et al., Fluka energy deposition studies for the HL-LHC, *International Particle Accelerator Conference*, (2013) 1379-1381.
10. R. Flukiger, T. Spina, The behaviour of copper in view of radiation damage in the LHC luminosity upgrade, *CERN Yellow Report* **2013-006** (2013) 76-82.
11. A. Tollestrup, E. Todesco, The development of superconducting magnets for use in particle accelerators: from Tevatron to the LHC, *Rev. Sci. Accel. Tech.* **1** (2008) 185-210.
12. E. Todesco, et al., A first baseline for the magnets in the high luminosity LHC insertion regions, *IEEE Trans. Appl. Supercond.* **24** (2014) 4003305.
13. E. Todesco et al. Review of the HL-LHC interaction region magnets towards series production *Supercond. Sci. Technol.* **34** (2021) 054501.
14. T. Nakamoto, et al. Model magnet development of D1 beam separation dipole for the HL-LHC upgrade *IEEE Trans. Appl. Supercond.* **25** (2015) 4000505.
15. A. Den Ouden, et al., Progress in the development of an 88-mm bore 10 T Nb₃Sn dipole magnet, *IEEE Trans. Appl. Supercond.* **11** (2011) 2268-2271.
16. H. Felice, et al., Development of MQYY: a 90-mm Nb-Ti double aperture quadrupole magnet for HL-LHC *IEEE Trans. Appl. Supercond.* **28** (2018) 4500105.
17. M. Anerella, et al., The RHIC magnet system, *Nucl. Instrum. Meths.* **A 499** (2003) 280-315.
18. R. M. Scanlan and D. R. Diedrich, Progress and plans for the U.S. HEP conductor development program *IEEE Trans. Appl. Supercond.* **13** (2003) 1536-1541.
19. S. Gourlay, et al., Magnet R&D for the US-LHC accelerator program (LARP) *IEEE Trans. Appl. Supercond.* **16** (2006) 324-327.

20. S. E. Bartlett et al., An R&D approach to the development of long Nb₃Sn accelerator magnets using the bladder and key approach *IEEE Trans. Appl. Supercond.* **15** (2005) 1136-1139.
21. G. Ambrosio, et al., Test results and analysis of LQS03 third long Nb₃Sn quadrupole by LARP, *IEEE Trans. Appl. Supercond.* **23** (2013) 4002204.
22. H. Felice, et al. Design of HQ – a high field large bore Nb₃Sn quadrupole magnet for LARP *IEEE Trans. Appl. Supercond.* **19** (2009) 1235-1239.
23. P. Ferracin, et al., Development of MQXF: the Nb₃Sn low beta quadrupole for the Hilumi LHC, *IEEE Trans. Appl. Supercond.* **26** (2016) 4000207.
24. X. Wang, et al., Multipoles induced by interstrand coupling currents in LARP Nb₃Sn quadrupoles, *IEEE Trans. Appl. Supercond.* **24** (2014) 4002607.
25. E. Todesco, Quench limits in the next generation of magnets, CERN Yellow Report 2013-006 (2013) 10-16.
26. T. Salmi, et al., Modeling heat transfer from quench protection heaters to superconducting cables in Nb₃Sn magnets, CERN Yellow Report **2013-006** (2013) 30-37.
27. E. Ravaioli, et al., New coupling loss induced quench protection system for superconducting accelerator magnets *IEEE Trans. Appl. Supercond.* **24** (2014) 0500905.
28. E. Ravaioli, et al., Quench protection of the first 4-m-long prototype of the HL-LHC Nb₃Sn quadrupole magnets *IEEE Trans. Appl. Supercond.* **29** (2019) 4701405.
29. R. Gupta, Tuning shims for high field quality in superconducting magnets, *IEEE Trans. Magn.* **32** (1996) 2069-2073.
30. S. Izquierdo Bermudez, et al., Magnetic analysis of the MQXF quadrupole for the High-Luminosity LHC *IEEE Trans. Appl. Supercond.* **29** (2019) 4901705.
31. R. Ostojic, et al., Conceptual design of the LHC interaction region upgrade: phase I, LHC Project Report **1163** (2008).
32. J. Garcia Matos, et al., Magnetic and mechanical design of the nested orbit corrector for HL-LHC *IEEE Trans. Appl. Supercond.* **26** (2016) 4102005.
33. F. Toral, et al., Development of radiation resistant superconducting corrector magnets for the LHC upgrade, *IEEE Trans. Appl. Supercond.* **23** (2013) 4101204.
34. G. Volpini, et al. Nb-Ti superferric corrector magnets for the LHC luminosity upgrade *IEEE Trans. Appl. Supercond.* **25** (2015) 4002605.
35. D. I. Meyer and R. Flasck A new configuration for a dipole magnet for use in high energy physics applications *Nucl. Instrum. Methods* **80** (1970) 339-41.
36. C. L. Goodzeit, et al., The double-helix dipole – a novel approach to accelerator magnet design *IEEE Trans. Appl. Supercond.* **13** (2003) 1365-1368.
37. S. Caspi et al., Canted cos theta magnet (CCT) a concept for high field accelerator magnets *IEEE Trans. Appl. Supercond.* **24** (2014) 4001804.
38. G. Kirby et al., Hi-Lumi LHC twin aperture orbit correctors magnet system optimisation *IEEE Trans. Appl. Supercond.* **27** (2017) 4002805.
39. Y. Ajima, et al., “The MQXA quadrupoles for the LHC low-beta insertions, *Nucl. Instrum. Meths.* **A 550** (2005) 499-513.

40. P. Fabricatore et al, Development of a short model of the superconducting separation dipoles D2 for the High Luminosity Upgrade of the LHC *IEEE Trans. Appl. Supercond.* **28** (2018) 4000105.
41. V. Kashikin and A. Zlobin, Design study of 2-in-1 large aperture IR dipole (D2) for the LHC luminosity upgrade Particle Accelerator Conference (2007) 464-466.

This page intentionally left blank

Chapter 7

RF Systems

R. Calaga^a, P. Baudrenghien^a, G. Burt^b, O. Capatina^c, E. Jensen^d,
E. Montesinos^a and A. Ratti^e

^a*CERN, SY Department, Genève 23, CH-1211, Switzerland*

^b*University of Lancaster, Lancaster LA1 4YW, UK*

^c*CERN, EN Department, Genève 23, CH-1211, Switzerland*

^d*CERN, EP Department, Genève 23, CH-1211, Switzerland*

^e*SLAC, Palo Alto, California, CA 94025, USA*

The HL-LHC beams are injected, accelerated to and stored at their nominal energy of 7 TeV by the existing 400 MHz superconducting RF system of the LHC. A new superconducting RF system consisting of eight cavities per beam for transverse deflection (aka crab cavities) of the bunches will be used to compensate the geometric loss in luminosity due to the non-zero crossing angle and the extreme focusing of the bunches in the HL-LHC.

1. HL-LHC RF Systems

1.1. *Accelerating RF*

In the LHC, a “half-detuning” scheme was originally proposed and implemented to provide a constant voltage (amplitude and phase) while keeping the klystron power constant over one turn. The klystron drive phase is flipped between and beam and no-beam segments with the loaded Q optimized for minimum power.⁴ Due to doubling of the beam currents in the HL-LHC, an optimal detuning scheme (aka “full-detuning”) is required to cope with the transient beam loading effects during the energy ramp and collisions.^{1,2} A modulation of the klystron and cavity phase make the phase of bunches with

This is an open access article published by World Scientific Publishing Company. It is distributed under the terms of the Creative Commons Attribution 4.0 (CC BY) License.

respect to the RF clock to progressively slip along the bunch train, but then recover during the long abort gap. With this scheme the klystron power is independent of the beam current and maintained constant over one full turn at the expense of bunch-to-bunch phase modulation. This scheme was experimentally tested in 2016 and has been operational since then in the LHC during the acceleration ramp and flat-top.³ During injection of the HL-LHC beams from the SPS in to the LHC however, the original half-detuning scheme to strictly preserve the bunch-to-bunch spacing is a pre-requisite.

1.2. Crab Crossing

For higher luminosity operation, proton beams are squeezed to very small β^* at IP1 and IP5 (well below the nominal 55 cm). Controlling the effect of the large number of parasitic collisions requires a non-zero crossing angle. A non-zero crossing angle in combination with small β^* however implies a geometric reduction of the luminosity $R_\phi = (1 + \phi^2)^{-1/2}$ due to non-perfect overlap of the colliding bunches. This effect is illustrated in Figure 1 and compared to crab crossing scheme where the head and the tail of the bunches transported along different orbits to maximize the overlap at the interaction point.



Fig. 1. Bunches colliding with a crossing angle without crab crossing (left); with the crab crossing (right).

The HL-LHC upgrade will use deflecting (or crab) cavities to compensate for geometric luminosity loss. Two schemes were considered for crab crossing in the HL-LHC, the global scheme and the local scheme. The global scheme would require a single crab cavity system per beam, installed e.g. near point 4, where presently all LHC RF systems are installed with an appropriate phase advance between the crab cavities and the IPs. The transverse kick introduced by this cavity, different for the head and the tail of each bunch, is equivalent to a closed orbit distortion, i.e. head and tail would follow their individual closed

orbit around the ring, their tilt wobbling around the unperturbed closed orbit of the bunch centre. It is clear that this scheme introduces severe constraints on the betatron phase advance between the location of the crab cavities and the IPs. It is also inconsistent with the different crossing angles implemented in IP1 (horizontal crossing) and IP5 (vertical crossing). Furthermore, the collimator settings would have to allow for the wobbling bunches.

The local scheme on the other hand introduces a localized perturbation upstream of the IP where crabbing is required and compensates for it downstream, such that through the rest of the ring the bunches remain unperturbed. This scheme requires up to 4 pairs of cavities per beam and per IP for a full compensation of the HL-LHC crossing angle. So up to 32 cavities are required if only the high luminosity regions (IP1, IP5) are considered. This scheme does not have the optics constraints of the global scheme between the two IPs and allows for the different crossing planes in IP1 and IP5. On the other hand it requires more cavities and in particular cavities that are compact enough for the nominal beam pipe distance of 194 mm. As a result of an intense R&D effort within the HL-LHC collaboration, three novel compact cavity geometries were successfully developed and tested for the HL-LHC.

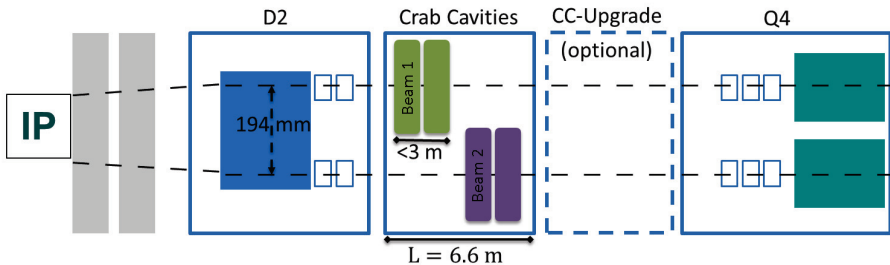


Fig. 2. Schematic layout of the crab cavities in the LHC Point 1 and 5 w.r.t the interaction point.

A local scheme with crab cavity pairs across the IPs is therefore established as the baseline using compact crab cavities at 400 MHz (see Figure 2). Design of the cavities, the cryomodules and the RF system is described in the following sections. A validation of the crab crossing with protons in the Super Proton Synchrotron (SPS) as the first phase towards the implementation in HL-LHC is also described.

1.3. *Transverse Damper*

The LHC requires a transverse feedback to damp injection oscillations and provide stability for impedance-driven transverse instabilities, thus guaranteeing preservation of beam intensity and emittance. The existing coupled bunch feedback system (ADT), installed in Point 4 of the LHC, was fully commissioned in 2010.⁹ It dampens transverse instabilities within a bandwidth of 20 MHz, correcting the oscillations of the centre of gravity of the individual bunches about their orbit. Beyond 20 MHz, the kicker and ADT power amplifier system cannot be used. For the HL-LHC, studies on a larger bandwidth transverse damper were performed in view of the high bunch intensity, but the present ADT system was deemed sufficient for HL-LHC operation.

2. Crab Crossing and Technology Choice

The HL-LHC parameters for a 7 TeV proton beam calls for superconducting crab cavities at a frequency of 400.79 MHz. The frequency choice is primarily driven by the long proton bunches, but it is also convenient to use the same frequency as the accelerating RF system. A total crab cavity voltage of approximately 12 MV is required at 400.79 MHz per IP side per beam to perform the complete bunch rotation. Assuming a maximum voltage of 3.4 MV per cavity, four cavities per side per beam per collision point, i.e. a total of 32 cavities are needed for full compensation. However, only half the system, 16 cavities, are to be installed after the re-baselining in 2016, allowing a partial compensation.⁸ Two cavities are assembled into a cryomodule as a fundamental unit to provide an integrated kick voltage of 6.8 MV.

2.1. *Physical Constraints*

Seen from the IP, the cavities are placed outside the recombination dipole D2, where the beams are completely separated and in their individual beam pipes spaced by 194 mm, and the β -functions in the crossing plane are sufficiently large to minimize the required voltage. Due to remaining optical constraints, the ideal betatron phase advance of $\pi/2$ between IP and crab cavities may not be realized exactly; the orbit bump from the crossing angle is closed prior to the entry into the crab cavities to minimize beam loading effects with trajectory

offsets. The tightest constraint results from narrow beam pipe spacing in the transverse plane. Measuring from the electric centre of the cavity (where the integral $\int_{-\infty}^{\infty} E_z e^{j\frac{\omega}{c}z} dz$ of the operating mode vanishes), the beam pipe at both ends of the cavity must leave a disk of radius 42 mm clear; this will allow the transverse alignment of the cavity without reducing the aperture for the beam. To allow passage of the 2nd beam pipe (distance centre to centre 194 mm) it is required that the cavity transverse size does not extend beyond 145 mm from the same electric centre. Since both vertical and horizontal crossing are used, these tight constraints have to be respected in the crossing plane and the plane orthogonal to it. In the longitudinal plane, the constraints are primarily dictated by the proximity to the neighbouring elements, namely the D2 recombination dipole and the Q4 matching section quadrupole. A total of 13.3 m is reserved for two pairs of four cavities per IP.⁵

2.2. RF Cavities

In order to sustain the surface fields at a kick voltage of 3.4 MV per cavity for the HL-LHC in continuous wave (CW), superconducting technology using high purity bulk Niobium is essential; space restrictions, voltage requirements, and impedance considerations strongly rule out a normal conducting option. Transverse space restrictions led to the concept of ‘compact’ cavities.

2.2.1. Cavity Geometry

As a result of an intense R&D within the FP7 HiLumi LHC, EuCARD and LARP programs and with other external collaborators, three compact designs at 400 MHz emerged as potential candidates.^{6,7} The three proposed designs are at least four times smaller in the plane of crossing compared to a conventional elliptical cavity with a ratio of the kick gradient to the peak surface fields lower by a factor of 2 or better. After validation of the superconducting prototypes within the collaborations, two designs were retained towards their implementation in HL-LHC for vertical and horizontal kick, the Double Quarter Wave (DQW) and the RF Dipole (RFD). The final mechanical design of the cavities including all external interfaces is shown in Figure 3.

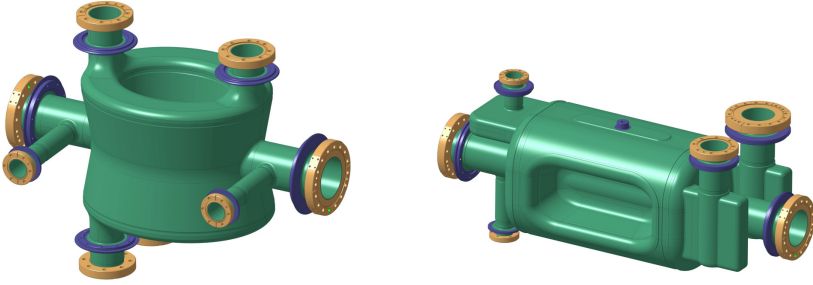


Fig. 3. Schematic view of the cavity with interfaces (left) DQW; (right) RFD.

Table 1. RF parameters for the DQW and RFD cavities.

Quantity	Unit	Value
Frequency	MHz	400.79
Bunch length	ns	1.0-1.2 (4σ)
Maximum cavity radius	mm	≤ 145
Nominal kick voltage	MV	3.4
R/Q (linac convention)	Ω	430
Q_0		$\geq 10^{10}$
Q_{cxt} (fixed coupling)		5×10^5
RF power	kW-CW	40 (80 peak, 1 ms)
LLRF loop delay	μ s	≈ 1
Cavity detuning (if parked, optional)	kHz	≈ 1.0

2.2.2. RF Multipoles

The main deflecting field of the chosen crab cavity geometries contain higher order components of the main deflecting field dependence due to the lack of azimuthal symmetry. Due to the placement of the cavities at high beta-function locations, the higher order components of the main deflecting mode can affect long-term particle stability. RF multipole components b_n of the RF deflecting field can be approximated and hence expressed in a similar fashion to magnets:¹⁰

$$b_n = \int_0^L \frac{1}{qc} F_{\perp}^n dz = \frac{jn}{\omega} \int_0^L E_{acc}^n dz \quad [\text{T m}^{2-n}] \quad (1)$$

Due to symmetries inherent to each design, only odd multipoles have a non-zero component. However, due to fabrication errors and ancillary components,

the first and most important even multipole, b_2 , is non-zero. Specifications from beam dynamics indicate that this value be smaller than 10 units leading to a tune shift of the order of $\Delta Q \approx 10^{-4}$. The first systematic multipole is the sextupolar component, b_3 . Long-term simulations with the optical functions of the HL-LHC indicate that the b_3 component should be limited to approximately $1500 \pm 10\%$ units, which results in an acceptable degradation of the dynamic aperture below 1σ for orbit offsets of 1.5 mm.¹¹ Both the DQW and the RFD designs are below the specified tolerance for b_3 . It is expected that they can be controlled to smaller values than the neighbouring D2 dipole magnet. For $n \geq 4$, assuming a very approximate scaling of the additional kick from an orbit offset via b_n , the b_n must be kept below $\propto O(10^n)$. More precise specifications for higher order terms require long-term tracking simulations.

2.3. Dressed Cavities

The ensemble of the helium tank, cold magnetic shield, fundamental power coupler, HOM couplers and the frequency tuning system is referred to as dressed cavity and described below.

2.3.1. Helium Tank

The helium tank will contain saturated superfluid helium at 2 K, cooling the cavity and allowing the extraction of the heat dissipated in the cavity and adjacent cold components. The titanium grade 2 was chosen as the optimum material for the helium tank, allowing for rigid connection of cavity ports to it. The helium tank has a structural role, and its rigid connection to the cavity ports ensures optimum boundary conditions for the cavity during mechanical loading, in particular during maximum pressure loading and tuning. Therefore, a novel concept using a bolted design with additional leak proof welds to minimize the stress on the cavity during the assembly of the Helium vessel Figure 4. Due to the large apertures in the external magnetic shield for couplers and beam pipes, a single layer is not sufficient to completely shield the earth's magnetic field to the required level ($\leq 1 \mu\text{T}$) with sufficient safety margin. A second cold shield (in purple) is integrated inside the helium vessel (light blue), as presented in Figure 4. The internal shield is 1 mm thick and will be made from Aperam Cryophy[®] to operated at 2 K.

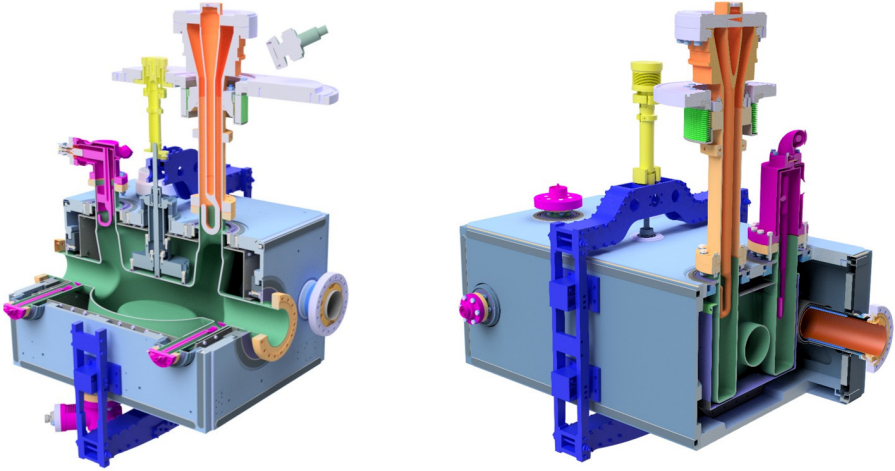


Fig. 4. Left: Sectional view of the DQW cavity inside its helium tank with the power coupler (top right, orange), HOM coupler (left, top and bottom, violet), and tuner (centre, top, and bottom). Right: Schematic sectional view of the RFD cavity inside its helium tank with the power coupler (orange) and HOM couplers (violet).

2.3.2. RF Power Coupler

In deflecting cavities operated in the crabbing mode, kick voltage and beam current are in quadrature ($\phi_s = 0$, synchrotron convention). The longitudinal impedance of the operating crabbing mode vanishes on axis, i.e. there is no beam loading for a centred beam; the RF generator does not exchange energy with the beam. The RF power required to maintain the required cavity voltage thus only depends on the cavity wall losses and remains small for a superconducting cavity with large Q_0 and Q_L . The input coupling and thus Q_L should be chosen to just allow sufficient bandwidth for unavoidable frequency transients due to external perturbations.

The situation is different for a beam circulating at an offset Δx . The beam-induced voltage due to an orbit offset is given by

$$\Delta V = I_b \cdot \frac{R}{Q_0} \cdot Q_L \cdot \Delta x \quad (2)$$

where I_b is the average beam current, $R_T = R/Q_0 \cdot Q_L$ is the transverse shunt impedance in Ω/m . With the Q_L resulting from the bandwidth requirement

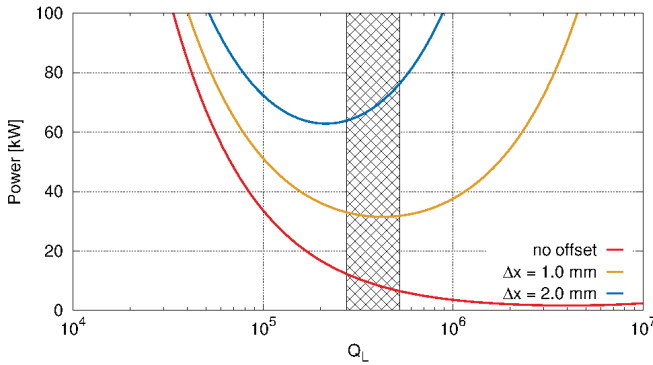


Fig. 5. Forward power vs. cavity Q_L for centred (red), 1 mm offset (green), and 2 mm offset (blue) beams. Assumed $R_T Q = 430 \Omega$, 3.4 MV RF, 1.1 A DC beam current.

discussed above, sufficient RF power is required to compensate for the resulting beam loading caused by unavoidable orbit offsets. Figure 5 shows the required forward power as a function of Q_L for a beam that is centred (red), off-centred by 1 mm (green) and 2 mm (blue). The RF power is limited to 40 kW-CW with a capability of provide 80 kW peak for approximately 1 ms to cope with transients. Therefore, the orbit must be kept within ± 0.5 mm at top energy of the LHC; further 0.5 mm is assumed for intra-cavity alignment and mechanical tolerances. At injection and ramp, the operating voltage is kept at 10-15% of the nominal voltage. Therefore, beam offset tolerance are much relaxed with the available 40 kW-CW RF power.

The crab cavity power coupler will use a single coaxial disk-type window to separate the cavity vacuum and the atmospheric pressure. The antenna shape uses a “hook” design to principally couple magnetically to the deflecting mode. The exact hook shape is specific to each cavity type as the coupling mechanisms on the cavity are not identical between DQW and RFD cavities. The ambient pressure side of the coupler will be air-cooled while the antenna itself will be water-cooled. The waveguide design includes the possibility of DC polarization in order to suppress multipacting.

2.3.3. Higher Order Mode Couplers

On resonance, the large impedance of the fundamental deflecting (dipole) mode is cancelled between the positive and negative sideband frequencies,

which are symmetric around ω_{RF} . The active feedback will reduce the growth rates by a large factor.

For higher order modes (HOMs), both narrow-band and broadband impedance should be minimized during the entire machine cycle as the LHC will accelerate and store beams of currents exceeding 1.1 A (DC). The tolerable longitudinal impedance has approximately a quadratic behaviour vs. f in the region of interest with its minimum between 300 and 600 MHz. The total maximum allowed impedance from each HOM, summing over all cavities in one beam, assuming that the HOM fall exactly on a beam harmonic, is specified to be $\leq 200 \text{ k}\Omega$. The same limit was imposed for higher frequencies. Modes with frequencies above 2 GHz are expected to be Landau-damped due to natural frequency spread and synchrotron oscillations.

In the transverse plane, the impedance threshold is set by the bunch-by-bunch feedback system with a damping time of $\tau_D = 5 \text{ ms}$. Four effective cavities per beam are assumed due to the two different cavity types with different HOM spectra. The single bunch studies show that integrated R_T/Q

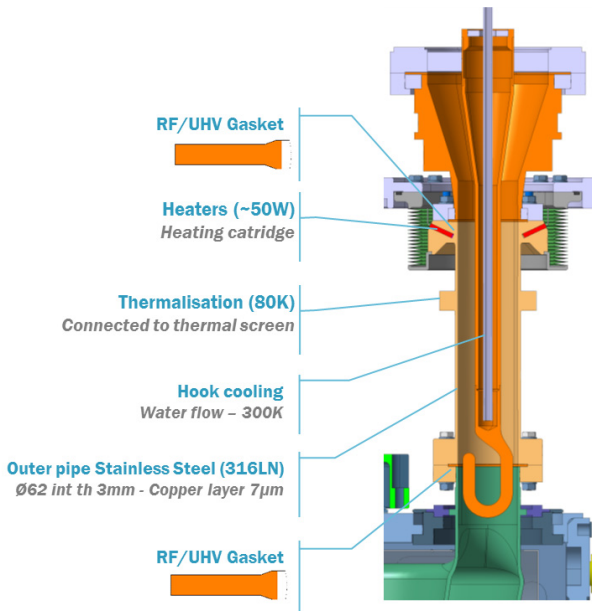


Fig. 6. Fundamental power coupler for the DQW cavity. Similar concept is adopted for the RFD with its own coupling hook.

over the frequency for all the HOMs per cavity should be suppressed to below $4 \text{ k}\Omega/\text{m}$ (without accounting for β -function) from stability considerations.⁵ From multi-bunch considerations and assuming the pessimistic case that the HOM frequency coincides with the beam harmonic, the maximum total transverse impedance in each plane is set to be $1 \text{ M}\Omega/\text{m}$.⁵ Analogous to the longitudinal modes, frequencies above 2 GHz are expected to be Landau-damped due to natural frequency spread, chromaticity, and Landau octupoles. Due to the very tight impedance thresholds, the distribution of HOM frequencies as mentioned above due to manufacturing errors can help relax the tolerances.

Several HOM coupler designs were developed and optimized to provide a high transmission over a large bandwidth of 0.5 - 2 GHz while suppressing the coupling to the fundamental mode. Figure 7 shows the final HOM geometries for the DQW and the RFD respectively. The DQW uses three on-cell HOM couplers with hook-type magnetic coupling to reach the impedance specifications. An additional mushroom-type antenna placed on the cavity beam pipe is required to damp certain high frequency modes confined near the beam pipe region. The RFD uses two hook-type HOM couplers, one for each transverse plane. Both couplers are mounted on dedicated waveguide stubs which act to limit the fundamental mode field near the HOM coupler antenna. The horizontal HOM coupler requires a notch filter at 400 MHz to suppress the coupling to the deflecting mode while the vertical HOM coupler relies on the orientation of the waveguide stub parallel to the deflecting field which acts as a natural filter. Simulations show that the HOM coupler must have a superconductive surface due to the high fields of the fundamental mode and

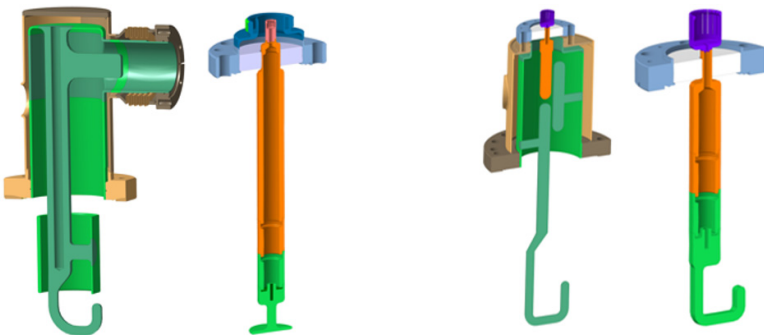


Fig. 7. HOM couplers for the DQW (left) and the RFD (right).

limit the heat load to the 2 K Helium bath for both cavities. Active cooling for the in-cell HOM couplers in the DQW cavity to minimize thermal gradients of the superconductive surface is used (see Figure 7).

The beam power deposited in the longitudinal HOMs can become significant when the frequencies coincide with bunch harmonics. The HOM couplers were dimensioned to cope with maximum of 1 kW average power to be able to cope with HL-LHC type beams.

2.3.4. Frequency Tuning

The final resonance frequency of the cavity will depend on a number of fabrication and handling steps and cool-down. A ‘slow’ mechanical tuning system is required to compensate for the uncertainties of the above steps by altering the cavity shape – this will dominate the tuner requirement. At 2 K it must be possible to tune the cavity to $f_{res} = f_{operation} \pm \Delta f_{LFD}$, where Δf_{LFD} denotes Lorentz force detuning occurring during cavity filling. The operational tuning range required in the LHC is approximately a few kHz. A large tuning range ($\approx \pm 200$ kHz) is specified to cope with frequency variations from cool-down and other mechanical deformations. However, the resolution of the tuner should allow at least ten steps inside the cavity bandwidth (≈ 800 Hz); backlash and hysteresis must be small.

The tuning system is similar for both cavities (DQW and RFD). It consists of an actuation system that is placed outside the cryomodule, and operated at room temperature and at atmospheric pressure, which makes it accessible and thus maintainable.¹⁸ The actuation system consists of a high resolution stepper motor (1.8 deg/step), a harmonic gearbox (100:1 ratio), a roller screw, and linear guide bearings. The estimated mechanical resolution of the tuning system at the connection to the cavity is estimated to be in the order of 10 nm or less, which is equivalent to a few tens of Hz for both cavities, allowing for at least 10 micro-steps inside the cavity RF frequency bandwidth. The details of the prototype actuation system are shown in Figure 8. Since the cavity will be operated in CW mode and frequency variations are expected to be small, fast active tuning is not needed in the final design. The cryostat vacuum exerts a non-negligible force on the tuner mechanism, as it remains floating with respect to the vacuum vessel. A pressure compensation feature is added to minimize this force.

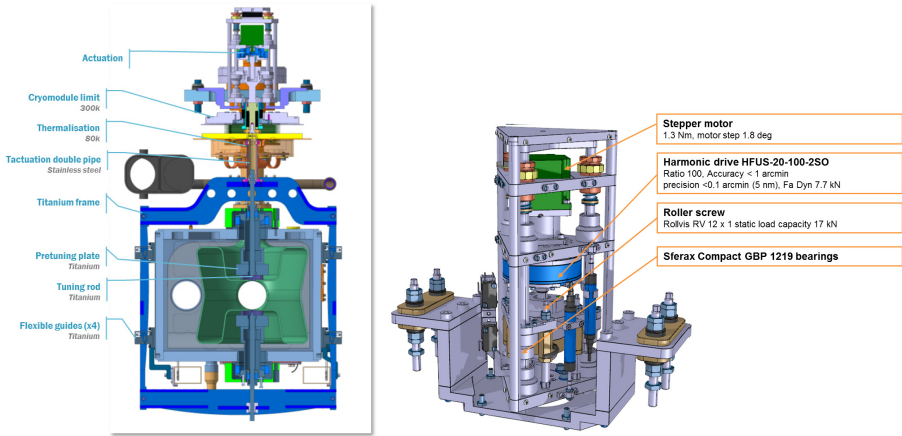


Fig. 8. Left: Cross-sectional view of the tuning system for the DQW cavity. Right: Actuation system of the prototype tuning system for DQW and RFD cavities.

2.4. Cryomodule

Machine architecture and integration studies for the LHC led to the choice of housing two individual cavities in one stand-alone cryomodule, individually connected to a cryogenic distribution line cryostat running in parallel with the main line. A total of six cold-to-warm transitions for the beam tube and four connections to the cryogenic distribution line are required for each cryomodule (Figure 9). This includes the adjacent beam pipe and related transitions which pass through the Helium jacket of the cavities. The combined static

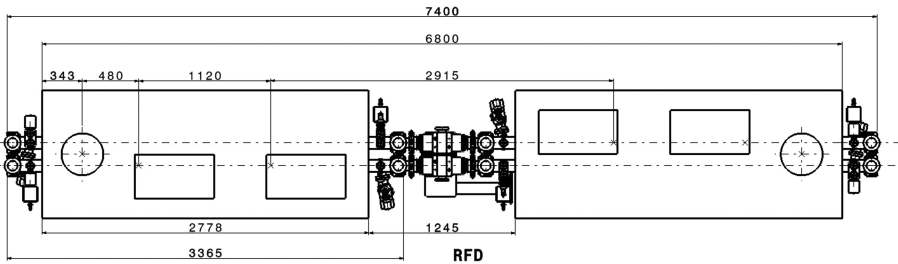


Fig. 9. Cryomodule layout for one side of the interaction region in the LHC for the RFD cryomodule. The layout of the adjacent beam pipe with its own cold-to-warm transitions are not shown.^{19,20}

and dynamic cryogenic heat load at 2 K for the two cavities at operating nominal field is expected to be ≤ 50 W.²⁶ The exact length of the cryomodule depends on the cavity type and, for the longest cavity, results in a total of 7.4 m for two cryomodules (6.9 m for two cryomodules DQW) per side of the LHC interaction region for both beams including gate valves from the interconnection plane (see Figure 9). For each two-cavity module, two gate valves outside the cryomodule vacuum and corresponding vacuum equipment for pumping and monitoring outside at ambient temperature are foreseen.

The vacuum vessel is designed in two main parts – a lower vacuum tank and a top plate. It uses a top-down assembly procedure for the cavity string inside the vessel. This allows the possibility of cavity alignment with optical devices (laser trackers, for example) while making fine adjustments through the adjustable supports before closing the cryomodule. The cavity supporting concept uses the external conductor of the RF coupler as the main mechanical support of the dressed cavities. Two additional supporting points using flexural blades are used to keep cavity alignment stability within requirements. In the RFD cavity, the power coupler is transversely offset from the cavity axis, which requires additional vertical support. The complete cavity string is loaded into the vacuum vessel from the top, with plug valves fitted and closing end-plates integrated in the cavity string. This allows the closure of the beam vacuum in the clean-room environment to minimize contamination of the superconductive surfaces. All external connections except the beam pipes are on the top of the cryomodule. This allows easy access to the cavities and ancillaries. The designs for both cavity variants are kept as similar as possible.

2.5. Cavity Alignment

Successful operation of the RF cavities depends on their correct position. The transverse and longitudinal alignment tolerances are described in the LHC performance requirements:⁴

- Cavity rotation in the X-Y plane (“roll”, R_z , Figure 10): it is required that this rotation has to be $< 0.3^\circ = 5.2$ mrad (3σ) per cavity;
- Cavity “yaw” (R_Y) and “pitch” (R_X) with respect to the cryostat axis should be $< 0.057^\circ = 1$ mrad (3σ), Figure 10;
- Transverse displacement of cavities w.r.t each other inside a cryomodule: intra-cavity alignment in the transverse plane with respect to

the cryostat axis should not exceed the 0.5 mm (3σ) tolerance set by beam loading and multipolar specifications.

The orientation and position of the cavity inside the cryomodule is adjusted by means of a plate rigidly connected to the dressed cavity in 3 supporting points. The rigid connection between the cavity and the alignment plate is obtained by means of the fundamental power coupler (FPC) and a set of additional blade type flexural supports.

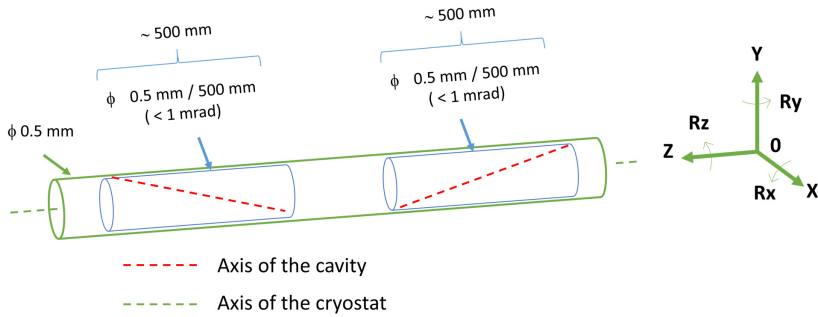


Fig. 10. Crab cavity alignment tolerances inside a two-cavity cryomodule.

The position of each cavity inside the cryomodule is measured by the frequency scanning interferometry (FSI) system.¹⁶ The FSI system offers absolute interferometric distance measurement capability at sub-micron level at cold operating conditions and during the cavity cool down process. Only passive components (mirror, collimator, fibres) are needed at the cavity flange measurement points, which makes the application suitable for a high radiation level of operation. The FSI unit consists of a reference interferometer and a measurement interferometer that use tuneable lasers (from 1410 to 1510 nm). An additional second laser tuned in the direction opposite to the reference laser is required to correct the errors arising from drifts and to account for internal frequency and phase changes from the laser itself. The gas cell ensures stability of the reference interferometer. Each cavity features several FSI heads and several lengths between the FSI system heads and the reflective targets are measured in order to determine the position of the dressed cavities. An improvement from the experience gained from the SPS beam tests using multiple targets for added reliability and robust targets is under study for the eventual use in HL-LHC.

3. RF System and Controls

An independent powering system using SPS-type IOTs, modified to operate at 400 MHz, delivering 40 kW in CW and 80 kW peak is the current baseline for RF power. However, recent advances in solid-state technology allowed pursuing the study of an Solid State Power Amplifier [SSPA] based system in parallel to potentially replace the IOTs and to provide a flexible platform.

3.1. RF Power

The IOTs provide adequate power overhead in a compact footprint. This scheme would also allow for fast and independent control of the cavity set point voltage and phase to ensure accurate control of the closed orbit and the crossing angle in the multi-cavity scheme. Most importantly, fast control of the cavity fields will minimize the risk to the LHC during an abrupt failure of one of the cavities, ensuring machine protection before the beams can be safely extracted. For such fast and active feedback, a short overall loop delay between the RF system and the cavity is required. The overall architecture and approximate volume of the RF infrastructure is shown schematically in Figure 11, the circulators (brown) are placed in an RF gallery placed directly above the the



Fig. 11. Schematic of the RF system layout (four per IP side) in the underground cavern above the LHC tunnel lateral view (top); and top view (bottom). The amplifiers and transmission lines are shown in green routed towards the tunnel located towards the right.

LHC tunnel with 1 m diameter vertical cores connecting the RF power lines. The circulator-to-cavity transmission lines will be WR2300 waveguide (blue) whilst amplifier-to-circulator transmission lines will be coaxial (green). The RF gallery is then connected to the main service gallery via a perpendicular tunnel, which is used to host power amplifiers and LLRF and also used for passage. Both the high power and the low level control systems are placed in the nearby underground gallery (UA) with access during beam operation.

3.2. RF Feedback and Controls

Limitations from the round-turn loop delay for the RF signal for cavity control should be taken into account for the fast feedback to cope with effects from fast RF failures. The amplifier driven by a feedback system feeds a compensating current to cancel the beam current. The cavity impedance is then effectively reduced by the feedback gain. Therefore, the limiting factor in the RF chain is the round-turn-loop delay. Therefore, a short distance between the cavity and the power amplifiers is preferred.¹⁵ Above a certain feedback gain, the loop delay will drive the feedback into electrical oscillations. The minimum effective impedance is

$$R_{min} \approx \frac{R}{Q_0} \omega_0 T, \quad (3)$$

where ω_0 is the RF frequency, R/Q the classic cavity parameter and T the group delay of the feedback loop. Therefore, a radiation free cavern close to the crab cavity location in the LHC tunnel is required to keep the RF feedback delay to less than about 1.5 μ s. This allows a significant reduction of the cavity impedance seen by the beam.

A rapid and unforeseen change of the field in one cavity (see Section 5.4) should trigger the LHC Beam Dump System (LBDS) to extract the beam in a minimum time of three turns (270 μ s). The RF controls should minimize the effect on the beam within the 3 turns to avoid abrupt displacements which can potentially damage the machine elements. Therefore, independent power systems of each cavity with a short delay cavity controller are used.¹⁵ A central controller between the two systems across the IP makes the required corrections to adjust the cavity set points as necessary. Figure 12 shows the proposed LLRF architecture.

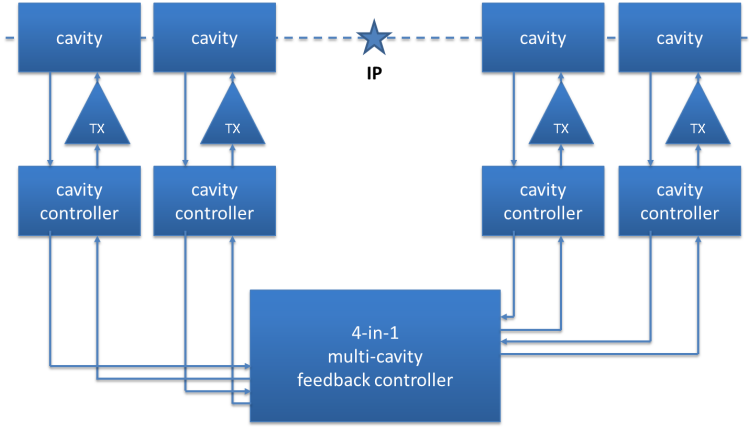


Fig. 12. Proposed LLRF architecture for one ring at one IP for operation with an installation of four cavities per IP per beam.

3.3. RF Noise and Stability

Cavity voltage amplitude jitter introduces a residual crossing angle at the IP proportional to the error as shown in Figure 13 (left). It is sufficient that this residual crossing angle is much smaller ($< 1\%$) than the geometric crossing angle leading to required voltage control from electronics:²¹

$$\frac{\Delta V}{V} \ll \frac{1}{\Phi}, \quad (4)$$

where Φ is the Piwinski parameter. A phase error in the RF wave causes an offset of the bunch rotation axis translating into a transverse offset at the IP (cf. Figure 13, right). The offset at the IP is given by

$$\Delta x = \frac{c \cdot \theta_c}{\omega_{RF}} \delta\phi_{RF} \quad (5)$$

where θ_c is the full crossing angle (cf. Figure 13) and ϕ_{RF} is the crab cavity phase w.r.t to the synchronous particle. For the HL-LHC parameters, the voltage error ratio should be kept to below 0.1%. The challenging aspect is to control the phase jitter across the IP to below $5 \cdot 10^{-3}$ degrees to minimize transverse emittance growth. This corresponds to a transverse displacement of 5% of the beam size at the IP.²²

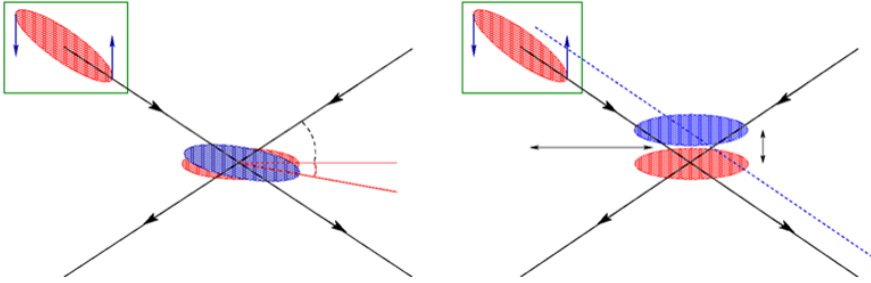


Fig. 13. Schematic of cavity voltage amplitude error leading to a residual crossing angle (left) and a phase error leading to an offset at the IP (right).

The amplitude and phase control must be achieved also during filling and ramping with small (or zero) field in the cavities. Smooth transition between no-crabbing and crabbing must be realized. A single reference generated in a surface building above the accelerating cavities is sent over phase-compensated links to respective crab cavities at IP1 (ATLAS) and IP5 (CMS). An alternative would be to re-generate the bunch phase from local pick-ups.¹⁵

4. Integration in SPS and LHC

The first proof of principle system with two DQW cavities in a cryomodule was tested in the special SPS test bench in 2018. The primary aim of these tests was to validate the technology with proton beams, demonstrate the ability to make the system transparent and establish a robust operational control of a multi-cavity system for the different modes of operation.

4.1. SPS Beam Tests

The SPS ring of a special test region was equipped with a special bypass on a movable table and featuring Y-chambers with mechanical bellows that can be displaced horizontally (see Figure 14). This allowed for the crab module to be placed out of the circulating beam during regular operation of the SPS and to be moved in only during dedicated machine development and not during regular operation. This setup was essential both due to aperture limitations of the crab cavities and the risk associated with leaving the cavities in the beam line with different modes of operation in the SPS.¹³

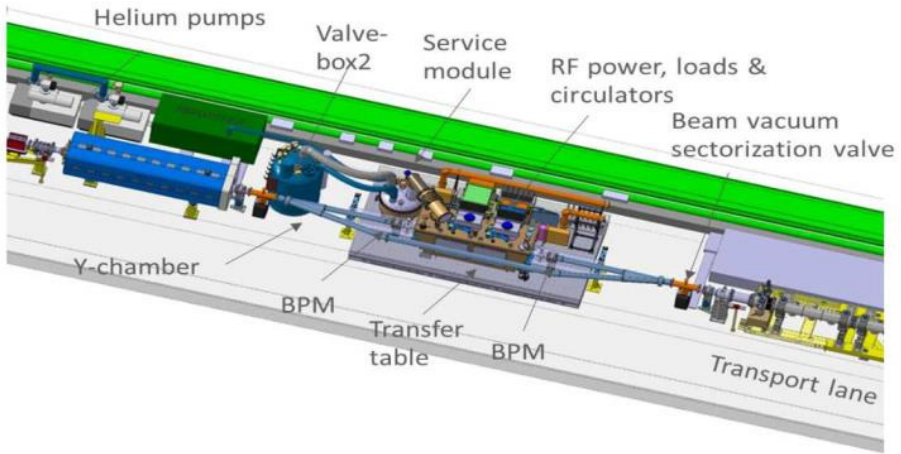


Fig. 14. SPS-LSS6 bypass for the installation of a 2-cavity crab cavity module for the first beam tests with protons.¹³

A complete cryogenic system on the surface (SPS-BA6) and in the tunnel (SPS-LSS6) was installed to deliver 2 K helium for the test operation of the crab cavities. The measured static load of 18 W is almost exactly as the estimated load from design simulations. Two coaxial transmission lines were used to feed RF power of up to 40 kW from the amplifiers (IOTs) installed on the surface. Placement of the passive RF elements (circulators and RF loads) was required to allow for the horizontal movement of the bypass remotely. All beam-pipes in this vacuum sector are coated with a thin film of amorphous carbon, to reduce secondary electron yield and consequently mitigate electron cloud.¹⁴

A detailed campaign of dedicated experiments were carried out in the SPS with proton beams in 2018. Crabbing of the proton bunches were demonstrated (see Figure 15) for the first time and several aspects related to the RF synchronization, cavity transparency, beam quality preservation and intensity related effects.²⁵

4.2. HL-LHC Integration

The RF system demands an independent control of each of the 4 cavities per IP side with the shortest delay loops between the RF amplifier and the

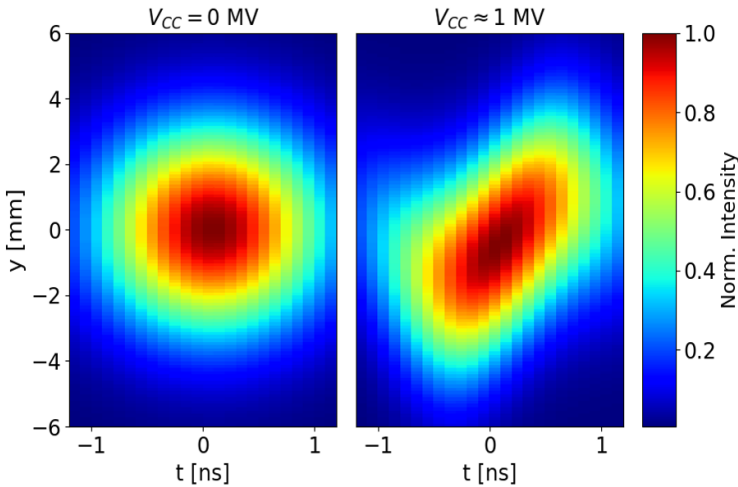


Fig. 15. A comparison of the intra-bunch motion measured with the Head-Tail monitor. The left shows the case where the crab cavities are switched off while the right shows the case where synchronous crabbing is seen with one cavity powered to 1 MV.

cavity (see Figure 12 and Eq. (3)). IOTs provide adequate power overhead in a compact footprint which is presently chosen as the baseline to provide the 40 kW-cw power to each cavity. An IOT based system was successfully operated in during the SPS tests. This scheme would also allow for fast and independent control of the cavity set point voltage and phase to ensure accurate control of the closed orbit and the crossing angle in the multi-cavity scheme. Most importantly, fast control of the cavity fields will minimize the risk to the LHC during an abrupt failure of one of the cavities, ensuring machine protection before the beams can be safely extracted. For such fast and active feedback, a short overall loop delay between the RF system and the cavity is required. A service gallery a few meters above the tunnel (UA galleries) allows for sufficient shielding to sensitive RF electronics and access to the RF equipment during beam operation (see Figure 16). Special cores are placed above the cavities to bring the RF power from the output of the circulators to the cavity to minimize the RF equipment inside the tunnel (see Figure 11). Recent advances in solid-state technology allowed pursuing the study of an SSPA based system in parallel to potentially replace the IOTs and to provide a flexible platform.

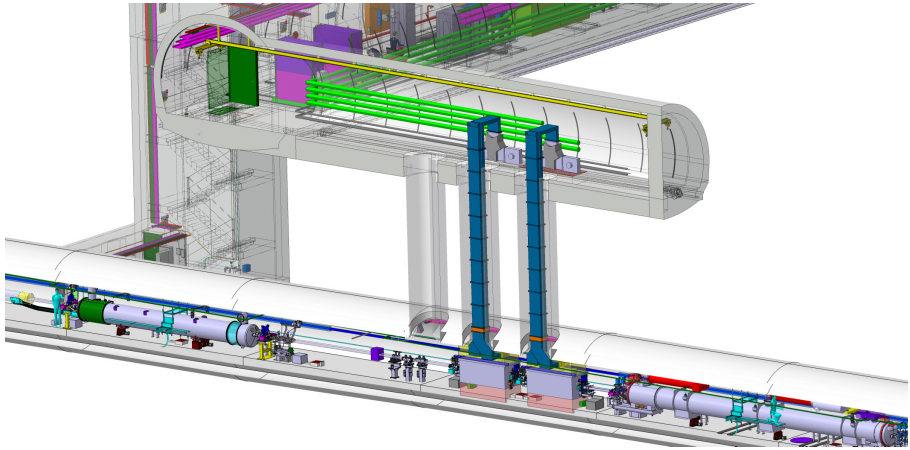


Fig. 16. Preliminary sketch of a high-power RF, controls and LLRF layout in the underground RF cavern.⁵

5. Operational Scenarios

The crab cavities must cope with the various modes of the collider cycle: filling, ramping, and physics.

5.1. *Cavity Transparency*

During filling of the nominally 2748 bunches into the LHC, energy ramping, or operation without crab cavities, the system will be inhibited by making the cavities transparent to the beam (crabbing off). Since more than one cavity is used, counter-phasing to make the effective kick voltage zero while always keeping accurate control of the cavity field is used as the baseline scenario. The counter-phasing ensures both zero effective voltage and beam stability on tune – in fact, it was found that this is the preferred scenario.¹⁵ At flattop, we drive counter-phasing to zero and synchronously change the voltage in all crab cavities as desired. The counter-phasing of two crab cavities was successfully demonstrated in the SPS beam tests in 2018.

Another possibility is to operate with ‘crabbing off’ while simultaneously detuning the cavity; but a small field and RF feedback should be kept for the required active tuning system. This is referred to as ‘parking’. Parking the

cavity half the distance between two revolution frequency side-bands would be ideal for stability. If detuning is used, with a positive non-integer tune ($Q_h = 64.3$, ω_b/ω_{rev} above an integer), the cavity should be tuned above the RF frequency to make the mode $l = -64$ stabilizing (see Figure 17, left).

During a LHC physics run, with crabbing on, the active RF feedback will reduce the peak cavity impedance and transform the high Q resonator to an effective wide-band impedance that covers several revolution frequency lines. The actual cavity tune then has no big importance for stability anymore. Growth rates and damping rates are much reduced, and we have no more dominant mode as shown in Figure 17, right.

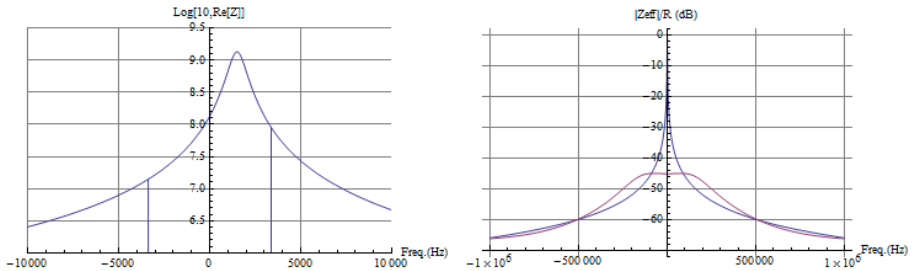


Fig. 17. Left: Real part of the deflecting mode impedance with a detuning of 1.5 kHz from 400 MHz. The vertical lines represent the difference in $Re\{Z\}$ evaluated at $\pm 0.3 f_{rev}$ for the computation of damping rate (mode $l = -64$). Right: Modulus of the cavity impedance seen by the beam with the RF feedback on (red) and off (blue) normalized to the cavity impedance at the fundamental mode.

5.2. Injection power Transients

Injection mismatch at the LHC ring causes beam oscillation along the ring, resulting in beam orbit offsets at the LHC crab cavity. Due to transverse oscillations that can reach up to 2 mm, the power requirement exceeds that available from the 40 kW-CW specification and full compensation of transient beam loading is not possible. A fast transverse damper is used to damp the injections oscillations within 50 turns. Simulations shown that the required crab cavity RF power rapidly converges to the steady state value within 15 turns and should be compatible with the peak power available in the crab cavity RF system.²³

5.3. Effects of Full-Detuning

As explained in subsection 1.1 at the beginning of this chapter, phase modulation of the accelerating cavities is required to minimize the transient beam loading effects (full-detuning). The RF phase of the crab cavities cannot be modulated to follow this phase modulation due to their high loaded quality factors. If the crab cavities are operated from the fixed RF frequency references, it will result in a 60 ps maximum displacement of a bunch centre from the zero phase in the crabbing field. However, the crab cavities are synchronized and for identical bunch phase shifts on the two counter-rotating beams, the bunch centres have the same transverse displacement at the IP. For the longitudinal displacement of the luminous region this may be acceptable given the 1 ns bunch length; the resulting transverse offset of the bunch centroid in the IP however (see above under “RF Noise and Stability”) will require that the LLRF synchronizes bunch by bunch correctly taking the actual phase modulation into account. The cumulative effect of this phase shift and the RF curvature was shown in simulations to be negligible.²⁴

5.4. Fast Failures and Machine Protection

Crab cavity failures can lead to a fast voltage and/or phase change with a short time constant. This can lead to large, global head–tail oscillations, or coherent betatron oscillations with a change in transverse beam trajectories of 1.7σ for a single cavity failure; the effect is cumulative with the number of failing cavities. These failures can be broadly classified into two categories:

- Fast failures, single or few turns. For example, a sudden cavity quench or breakdown.
- Slow failures, several tens of turns or greater (caused by vacuum degradation, voltage and phase drifts, or similar).

Due to the relatively high quality factor in the superconducting cavity, the stored energy inside the cavity can typically only be extracted with a time constant determined by Q_L , which results from the coupling to the cavity via the power coupler. The stored energy will decay with a time constant $\tau = 2 \cdot Q_L / \omega$. For $Q_L = 5 \times 10^5$, the time constant is approximately 400 μs . The three turn delay time (270 μs) for a beam dump trigger is an important consideration during a RF source failure, where the cavity field decays to

roughly half its value before the beam can be safely aborted. In the case of a quench, the time constant of field decay may be dominated by the quench dynamics rather than Q_L . The situation is similar to strong and sudden electron loading due to multipacting or other phenomena.

Two kinds of interlocks are foreseen: slow (on BPMs) and fast (on RF). To minimize the perturbation on the beam during a cavity failure, the MFB will adjust the field in the other cavities on both sides of the IP, such that the orbit distortion due to cavity failure remains local. The rapid change in field will also result in a detuning of the cavity; however, the mechanical tuning system is unable to adjust the tune within 400 μs . Since a rapid breakdown of a failed cavity may become unpredictable, it is probably safest to ramp down the cavities synchronously. However, small and slow changes in one of the cavities can be adjusted for without aborting the beam.

The BPM interlock post-mortem, i.e. the last recorded trajectories could be used to study the effect on beam during a cavity failure. Operationally, it is preferred to have a low Q_{ext} ($\sim 10^5$), as the cavity frequency is less sensitive to perturbations. However, it is assumed that machine protection may benefit from a high Q_{ext} ($\geq 5 \times 10^5$) to help avoid fast reaction on the frequency and phase changes of cavity. Consequently, the cavity will be more sensitive to external perturbations.

References

1. D. Boussard, RF power requirements for a high intensity proton collider, Proceedings of Particle Accelerator Conference (PAC'91) (1991), pp. 2447-2449.
2. P. Baudrenghien, T. Mastoridis, Proposal for an RF roadmap towards ultimate intensity in the LHC, Proceedings of International Particle Accelerator Conference (IPAC'12) (2012), pp. 154-156.
3. T. Mastoridis, P. Baudrenghien, J. Molendijk, Cavity voltage phase modulation to reduce the high-luminosity Large Hadron Collider RF power requirements, Phys. Rev. Accel. Beams, 20 (2017), p. 101003.
4. LHC Design Report, CERN-2004-003-V-3, CERN, 2004.
5. HL-LHC Design Report, CERN-2017-007-M, CERN, 2017.
6. S. Verdu-Andres et al., Design and vertical tests of double-quarter wave cavity prototypes for the high-luminosity LHC crab cavity system, Phys. Rev. Accel. Beams 21, 082002; B. Xiao et al., Design, prototyping, and testing of a compact superconducting double-quarter wave crab cavity, Physical Review Special Topics - Accelerators and Beams 18, 041004. (2015).

7. S. U. De Silva and J. R. Delayen, “Design evolution and properties of superconducting parallel-bar rf-dipole deflecting and crabbing cavities”, *Phys. Rev. ST Accel. Beams* 16, 012004 (2013); S. U. De Silva and J. R. Delayen, “Cryogenic test of a proof-of-principle superconducting rf-dipole deflecting and crabbing cavity”, *Phys. Rev. ST Accel. Beams* 16, 002001 (2013).
8. R. Calaga, “Comments on crab cavity voltage (unpublished)”, 2012.
9. W. Hofle, D. Valuch, Transverse Feedback: high intensity operation, AGC, IGC, lessons for 2012, LHC Beam Operation Workshop, Evian, December 2011, CERN-ATS-2012-083, CERN, Geneva (2012), p. 97-100.
10. M. Navarro-Tapia, R. Calaga, A. Grudiev, RF multipoles from crab cavities, in the proceedings of IPAC13, Shanghai, 2013.
11. J. Barranco et al., *Phys. Rev. Accel. Beams* 19, 101003 (2016).
12. L. Arnaudon et al., Conceptual specification of the crab cavity RF system, EDMS 1363181, 2014, <https://edms.cern.ch/document/1363181>.
13. R. Calaga et al., SPS tests of HL-LHC crab cavities, in Proc. IPAC18, Vancouver, 2018.
14. C. Yin Vallgren et al., “Amorphous carbon coatings for mitigation of electron cloud in the CERN SPS”, in Proc. IPAC10, Kyoto, Japan, May 2010, pp. 2033–2035.
15. P. Baudreghien, LLRF for Crab Cavities, presented at the 2nd HiLumi-LHC Meeting, Frascati, 2012.
16. M. Sosin et al., Alignment reference.
17. Dressed cavity citation.
18. K. Artoos et al., Development of SRF cavity tuners for CERN, in the proceedings of the SRF 2015, Whistler, 2015; K. Artoos et al., Status of the HL-LHC crab cavity tuner, in the proceedings of the SRF 2019, Dresden, 2019.
19. T. Capelli et al., in the proceedings SRF 2019, Dresden, 2019.
20. M. Garlasche et al., in the proceedings of the IPAC 2018, Vancouver, 2018.
21. K. Oide, K. Yokoya, *Physical Review A*, 40, 315 (1989).
22. R. Calaga et al., in the proceeding of the LHC performance workshop 2010, Chamonix, 2010.
23. E. Yamakawa et al., Beam loading study for HL-LHC and measurements in SPS crab cavities, STFC-Report-2018, to be published.
24. E. Yamakawa et al., Luminosity reduction caused by phase modulations at the HL-LHC crab cavities, *Nuclear Inst. and Methods in Physics Research, A* 908 (2018) 338–346.
25. R. Calaga et al., “First demonstration of the use of crab cavities on hadron beams”, *Physical review, accelerators and beams* 24, 062001 (2021).
26. F. Carra, “DWQCC cryomodule thermal budget and heat loads,” EDMS n. 1729079 (2017); J.S Swieszek et al., RFD CC cryomodule thermal budget and heat loads, EDMS n. 2310389, <https://edms.cern.ch/document/2310389>, (2020).

Chapter 8

Collimation of HL-LHC Beams

S. Redaelli^a, A. Bertarelli^b, R. Bruce^a, F. Carra^b, A. Lechner^c,
A. Mereghetti^d and A. Rossi^c

^a*CERN, BE Department, Genève 23, CH-1211, Switzerland*

^b*CERN, EN Department, Genève 23, CH-1211, Switzerland*

^c*CERN, SY Department, Genève 23, CH-1211, Switzerland*

^d*Centro Nazionale di Adroterapia Oncologica (CNAO), Pavia, Italy*

High-performance collimation systems are essential for operating modern hadron accelerators with large beam intensities efficiently and safely. In particular, at the LHC the collimation system ensures a clean disposal of beam halos in the superconducting environment. The challenges of the HL-LHC study pose more demanding requests for beam collimation. In this chapter, the upgraded collimation system for HL-LHC is presented. Various collimation solutions were elaborated to address the HL-LHC requirements and challenges. These are reviewed in the following, identifying the main upgrade baseline and pointing out advanced collimation concepts under consideration for further enhancement of the collimation performance.

1. Introduction

Because of the high stored energy of about 700 MJ for each of the full HL-LHC beams and the small transverse beam sizes [1], the HL-LHC beams have the potential for creating significant damage from uncontrolled beam losses. Even a local beam loss of a tiny fraction of the full beam in a superconducting magnet could cause a quench, and larger beam losses could easily cause damage to accelerator components. A variety of processes can cause unavoidable beam losses during normal and abnormal beam operation. Therefore, all beam losses must be tightly controlled. For this purpose, a multistage

This is an open access article published by World Scientific Publishing Company. It is distributed under the terms of the Creative Commons Attribution 4.0 (CC BY) License.

collimation system has been installed in the LHC [2,3] to safely dispose of beam losses. Unlike other high-energy colliders, where the main purpose of collimation is typically to reduce experimental backgrounds, the LHC and the HL-LHC require efficient beam collimation during all stages of operation from injection to top energy. The requirement to operate efficiently and safely with high-intensity hadron beams at small colliding beam sizes entails significant challenges, which drive the key design aspects of the collimation system at the HL-LHC [4].

In addition to cleaning the unavoidable beam halo to prevent quenches of superconducting magnets, the collimation system must fulfil other important roles [5]. The collimators are the closest elements to the circulating beam and they must provide passive protection to any aperture bottleneck, in particular the triplet magnets around the experiments, with sufficient margins [6,7]. They help concentrate the radiation dose and activation to confined areas and provide local protection of equipment to improve its lifetime. In addition, collimators also clean collision debris products, with dedicated active collimators on the outgoing beams of each high-luminosity experiment [8,9]. Furthermore, collimation plays a role in keeping under control machine- and halo-induced experimental background [10,11]. Collimation also provides a crucial role for passive machine protection in case of any failure, e.g. injection and dump kicker failures [12] (see also Chapter 19).

For these requirements, the LHC collimation system features an unprecedented complexity compared to previous particle accelerators. The LHC collimation system used in Run 1 (2010–2013) [13] and Run 2 (2015–2018) [14] consisted of up to 108 movable collimators and 10 fixed-aperture absorbers, and provided an excellent cleaning efficiency above 99.99% [3], i.e. less than 10^{-4} of the primary beam losses reached the superconducting magnets. The highest cold losses occur in the dispersion suppressors (DSs) around IR7. Nevertheless, the system must be upgraded to cope with the new HL-LHC challenges. The LHC collimation system was designed to safely withstand beam lifetime drops down to 0.2 h during 10 s at maximum beam current at 7 TeV, corresponding to peak losses of up to 500 kW [3]. This increases to 945 kW for HL-LHC if a simple scaling by the total stored beam energy is applied. The Pb ion beam upgrade, targeting more than 20 MJ stored beam energy at luminosities around $7 \times 10^{27} \text{ cm}^{-2} \text{ s}^{-1}$ [15] is also very challenging for beam collimation. In addition, given the low electrical conductivity

of the present primary and secondary collimator materials and their vicinity to the beam, these collimators contribute significantly to the machine impedance, which will become much more critical for beam stability with the higher HL-LHC brightness. Finally, the higher peak luminosity goal of the HL-LHC, about 5 times larger than the initial LHC design, demands an upgrade of the collimation around the high-luminosity collision points, both in terms of magnet protection and physics debris disposal.

2. The HL-LHC Multi-Stage Collimation System

The backbone of the HL-LHC collimation system will remain as it is for the current LHC, the betatron (IR7) and momentum (IR3) multi-stage cleaning systems installed in two separated warm insertions [2]. A very efficient halo cleaning is achieved by precisely placing blocks of materials close to the circulating beams, while respecting a pre-defined multi-stage collimator hierarchy (illustrated schematically in Fig. 1). Primary (TCP) and secondary (TCS) collimators are placed closest to the beam. Active shower absorbers (TCLA) catch the showers produced by upstream stages. Tertiary collimators

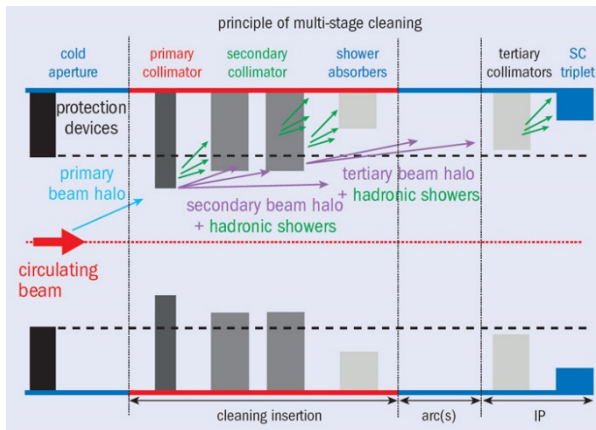


Fig. 1. Schematic illustration of the LHC multi-stage collimation cleaning system. Primary and secondary collimators (darkest grey) are closest to beam and are made of robust carbon-fibre-carbon composites. Shower absorbers and tertiary collimators (lighter grey) sit at larger apertures and are made of a tungsten alloy to improve absorption, in the shadow of protection devices (black). Collimators of different families are ordered in a pre-defined collimation hierarchy that must be respected to ensure the required system functionalities.

(TCTs) are located in front of the aperture bottlenecks in the final focusing system close to the experiments.

About 50% of the present LHC system will remain operational in HL-LHC, and the rest of the system will be replaced. Three main pillars of the HL-LHC collimation upgrade can be identified:

- Improved protection of the DS regions around IR7 and IR2 to mitigate local beam losses through new collimators (TCLD and TCPC). In IR2, one TCLD per side will be installed in the empty connection cryostat, to be used only for Pb ion operation; In IR7, one TCLD per side could be installed together with 11 T dipoles needed to make space for the collimator. However, the installation of the TCLDs in IR7 cannot take place before Long Shutdown 3 (LS3) and new primary crystal collimators TCPCs will be used in IR7 during ion operation in order to increase the cleaning efficiency and to lower the losses in the DS regions around IR7 (see Chapter 30).
- Reduction of the collimator-induced impedance to allow the operation of the larger-brightness beams of the HL-LHC: 9 out of 11 LHC secondary TCSG collimators will be replaced by a new low-impedance design (TCSPM).
- Improvement of the collimation of incoming and outgoing beams in the experimental insertions IR1 and IR5. Four tertiary collimators per beam and per high luminosity IR are needed to protect matching section and inner triplet from beam losses; three physics debris collimators and three fixed masks per beam and per high luminosity IR are needed to protect matching section and DS from collision debris.

In order to minimize the time spent outside physics operation, an improvement of the collimator setup time and the minimization of faults also requires a consolidation of the present system. The list of LHC (as of Run 2) and HL-LHC ring collimators are given in Table 1. Collimator types (with their collimation plane) and family names are introduced together with the number of units and their active material. The 2018 settings for $\beta^*=25$ cm and the HL-LHC baseline settings for $\beta^*=15$ cm are also listed. New collimators that are part of the HL-LHC upgrade will be installed in the DSs around IR2 and in IR7 (“DS cleaning” upgrade), in IR1/5 (IR upgrade) and IR7 (low-impedance upgrade). Approved consolidation activities include the replacement of four primary collimators with low-impedance ones made of molybdenum carbide-

Table 1. Collimators used in LHC and HL-LHC, including their abbreviated names, plane (H=horizontal, V=vertical, S=skew), the number of installed units, the material (CFC=carbon-fibre composite, W=heavy tungsten alloy (Inermet180), MoGr=molybdenum-graphite, CuCD=copper-diamond) and the operational openings in collision in units of beam σ . The LHC settings are given for p-p operating at $\beta^*=25$ cm, as used in 2018, and the HL-LHC settings for $\beta^*=15$ cm. In both cases, a reference proton emittance of $2.5 \mu\text{m}$ has been used. The IR2 TCLD's and the crystal primary collimators are used only in ion operation.

Functional type	Name	Plane	Number		Material		Physics settings [σ]	
			LHC	HL	LHC	HL	LHC	HL
Primary IR3	TCP	H	2	2	CFC	CFC	17.7	17.7
Secondary IR3	TCS	H	8	8	CFC	CFC	21.3	21.3
Absorber IR3	TCLA	H, V	8	8	W	W	23.7	23.7
Passive absorber IR3	TCAP	--	4	4	W	W	--	--
Primary IR7	TCP	H, V, S	6	2	CFC	CFC	5.9	6.7
Primary crystal IR7	TCPC	H, V	--	4	Si	Si	--	6.5
Low-impedance primary IR7	TCP	H, V	--	4	--	MoGr	--	6.7
Secondary IR7	TCS	H, V, S	22	4	CFC	CFC	7.7	9.1
Low-impedance secondary IR7	TCS	H, V, S	--	18	--	MoGr	--	9.1
Absorber IR7	TCLA	H, V, S	10	10	W	W	11.8	12.7
Passive absorber IR7	TCAP	--	8	8	W	W	--	--
Passive absorber mask IR7	TCAPM	--	--	2	--	Steel	--	--
Dispersion suppressor IR7	TCLD	H	--	2	--	W	--	16.6
Dispersion suppressor IR2	TCLD	H	--	2	--	W	--	30
Tertiary IR2/IR8	TCT	H, V	8	8	W	W	17.7/ 43.8	17.7/ 43.8
Tertiary IR1/IR5	TCT	H	4	8	W	CuCD or W	9.2	10.4
Tertiary IR1/IR5	TCT	V	4	8	W	W	9.2	10.4
Physics debris IR1/IR5	TCL	H	12	12	Cu/W	W	18-41	14
Physics debris IR1/IR5 mask	TCLM	--	--	12	--	Cu and W	--	--
Dump protection IR6	TCDQ	H	2	2	CFC	CFC	8.6	10.1
	TCSP	H	2	2	CFC	CFC	8.6	10.1

graphite (MoGr) and of new passive absorber masks, planned for LS2. The other devices that are part of the present system will remain unchanged and operational for the HL-LHC era. Crystal primary collimators (TCPCs) for ion beam collimation, discussed in detail in Chapter 30, are also listed. Most collimators consist of two movable blocks, called ‘jaws’, placed symmetrically around the beam. The collimators are built as high-precision devices, with the key features of (i) a jaw flatness of about $40\ \mu\text{m}$; (ii) a surface roughness below $2\ \mu\text{m}$; (iii) a $5\ \mu\text{m}$ positioning resolution (mechanical, controls); (iv) an overall setting reproducibility below $20\ \mu\text{m}$ [16]; (v) a minimum gap below $0.5\ \text{mm}$; (vi) the capability to withstand heat loads of up to $6\ \text{kW}$ in a steady-state regime (1 h beam lifetime) and of up to $30\ \text{kW}$ in transient conditions (0.2 h beam lifetime) [17].

The initial LHC collimator design [18] has been improved by adding two beam position monitors (BPM pickups) on both extremities of each jaw [17,19-21]. This allows for fast collimator alignment as well as a continuous monitoring of the beam orbit with the possibility to interlock the beam position. After prototype tests in the SPS [22], several collimators with this design were installed and operated in LHC Run 2 [21]. All new HL-LHC collimators incorporate this feature that improves significantly the operational flexibility and β^* reach, contributing in particular to reaching $\beta^*=25\ \text{cm}$ in 2018 [7]. The improved flexibility in the IRs is particularly relevant for HL-LHC that will rely on complex levelling schemes, with frequent changes of orbit and optics. It is noted that the BPM feature cannot be integrated in the design of the crystal collimators that will thus be aligned with the standard BLM-based method.

3. Collimation Upgrade in the High-Luminosity Interaction Regions

The LHC Run 1 and Run 2 operation showed that protection of the IR superconducting magnets and experiments is a key asset for machine performance and efficient operation; the available aperture, to be protected in all operational phases, determines the transverse collimation hierarchy. With the pushed β^* and the increased beam intensity and luminosity of HL-LHC, protecting the machine aperture becomes even more challenging. In order to provide adequate protection, the HL-LHC collimation layout in IR1 and IR5 includes two pairs of TCTs (horizontal and vertical) on each *incoming beam*, as well as three physics debris absorbers (TCLs) and three fixed masks on each *outgoing*

beam. The layouts of Beam 1 and Beam 2 are symmetric, requiring a total of 20 movable collimators and 12 fixed masks. Fig. 2 shows the HL-LHC layout in IR1 together with the nominal LHC layout deployed in Run 1. The layout in IR5 is similar and contains the same upgrades.

The LHC tertiary collimators are located at positions that protect the triplet; in order to provide the necessary absorbance, they make use of a heavy tungsten alloy (Inermet 180). They effectively protect the downstream elements but are not robust against high beam losses, in particular during very fast beam failures that might occur if the beam dumping system does not trigger synchronously with the abort gap (an “asynchronous beam dump”). With the increase in bunch intensity of HL-LHC, this accident scenario becomes even more critical. Margins on collimator settings are added to the collimator hierarchy to minimize this risk [7]. In Run 2 a new optics with a specially matched phase advance between the extraction kickers and the TCTs was deployed, which was used to significantly push further the β^* performance of the LHC. A TCT design with improved robustness would provide an alternative way to reduce the hierarchy margins without introducing constraints on the optics. This gives more flexibility in the optics design, which is useful in particular for the HL optics baseline that features many other constraints.

The extensive experimental experience of beam impacts on collimator material samples at the CERN facility HiRadMat [23-26], where several new materials were studied, indicates that MoGr can improve the TCTP robustness by a factor of several hundreds, while copper-diamond (CuCD), featuring higher density (and hence better cleaning efficiency) and larger electrical conductivity, would still give about a factor 15 improvement in robustness [24]. Therefore, CuCD is the preferred material choice for the horizontal TCTs, although Inermet180, as used in the LHC TCTs, would not prevent reaching the HL-LHC baseline performance with the present optics baseline. The final decision will be taken in 2022 based on experience with a prototype collimator, which is being built with jaws in CuCD, and on the assessment of the final production costs for CuCD. The vertical tertiary collimators are still made of Inermet 180, since the critical losses from an asynchronous beam dump occur only in the horizontal plane.

In addition to improvements from increased robustness, the HL-LHC layout has additional aperture constraints [1] because the normalized aperture of the magnets up to Q5 is now smaller than in the present layout. Thus,

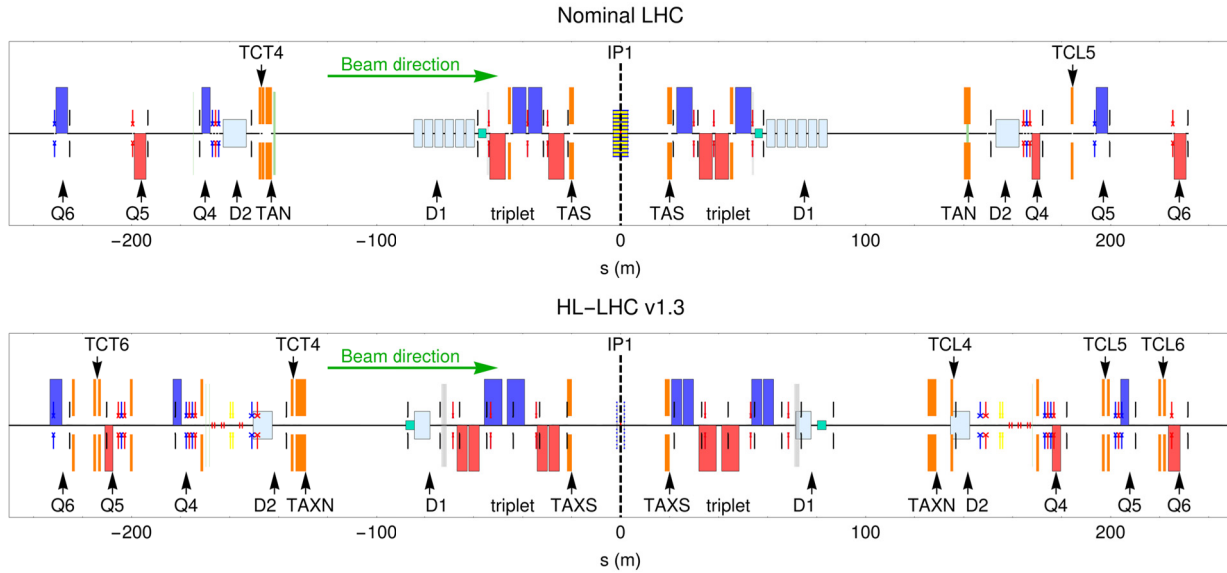


Fig. 2. The schematic layout in the experimental insertion IR1 for the nominal LHC as used in Run 1 (top) and HL-LHC v1.3 (bottom). Collimators are indicated in orange, quadrupoles in blue and red for the two polarities, and dipoles in light blue.

additional tertiary collimators are required in IR1/IR5 to protect the Q4 and Q5 quadrupole magnets. The present baseline includes a pair of new TCTP collimators in front of Q5, including one horizontal and one vertical, and another pair of TCTPs just upstream of the TAXN to protect the triplet, as for the nominal LHC.

The expected beam losses in the experimental insertions have been verified in simulations. Tracking simulations of the collimation mechanism using SixTrack [27,28] show that the proposed layout provides adequate protection of all magnets against cleaning losses [8]. Simulations of asynchronous beam dumps show that no direct losses are to be expected on the magnets, and losses of up to about 2×10^{10} protons could occur on the TCTs [12]. These losses consist of spread-out secondary protons, scattered out of upstream collimators, about a factor 5 below the onset of plastic deformation even for Inermet 180. This result relies on a matched fractional phase advance below 30° between the extraction kickers and the TCTs, as implemented in HL-LHC v1.3.

Further simulations of energy deposition during an asynchronous beam dump hitting a TCT show that there is no risk of damaging neither the experimental detectors nor the downstream magnets. Experimental background coming from the TCTs during normal operation is not expected to be problematic based on other recent studies [11].

The collimators on the outgoing beams, downstream of the high-luminosity experiments, must intercept both scattered primary beam particles and secondary particles generated by the collisions. The protection of the triplet from luminosity debris is discussed in Chapter 10, and here the focus is instead on the protection of the matching section. In Run 1, protection of the matching section was achieved by a single horizontal collimator in Cell 5, called TCL5. For Run 2, new TCLs were added in Cells 4 and 6, to cope with the higher luminosities and requirements from forward-physics experiments.

In HL-LHC, the ultimate levelled luminosity of $7.5 \times 10^{34} \text{ cm}^{-2}\text{s}^{-1}$ will be about a factor three higher than the peak achieved at the beginning of the collision process during Run 2 in the LHC, which is a significant challenge for the collimation of physics debris. In addition, the absorber TAXN (the upgrade of the TAN, see Chapter 13) is less effective – because of the geometry of the reference trajectory and crossing angle, a significantly larger fraction of the scattered particles can pass through its opening than in the LHC (see also Chapter 15).

Therefore, several improvements are foreseen for the HL-LHC. The TCL4 needs to be upgraded to have thicker jaws [4] in order to intercept a larger fraction of the particles that have passed through the TAXN opening. This new collimator is called TCLX. In addition, fixed masks have to be installed on the IP side of Q4, Q5, and Q6. The TCL5 and TCL6 are also needed, and the material of all TCLs will be changed to a tungsten heavy alloy for better protection. Using this new layout, the highest power load in any magnet coil in the matching section stays below 1.5 mW/cm^3 at peak ultimate luminosity of $7.5 \times 10^{34} \text{ cm}^{-2}\text{s}^{-1}$, which is far below the estimated quench limits. It should be noted also that the TCTs also play a role in protecting the outcoming-beam bore from the collision debris.

The design of the new IR collimators is challenging. Due to the larger β -functions in the HL-LHC high-luminosity insertions, the TCTs and TCLs in Cell 4 have to be opened to rather large gaps in mm to achieve the smaller normalized design openings in σ . To keep a maximum operational flexibility, a half gap of up to 40 mm could be needed, while it is limited to 30 mm in the present collimator design, so modifications are necessary. In addition, the transverse physical space available at this location in the HL-LHC tunnel is limited.

In order to provide the needed stroke and still fit in the horizontal space, a new two-in-one collimator design for the horizontal TCT and the TCL4 has been developed. A single vacuum tank houses the movable jaws acting on one beam and the vacuum chamber of the opposing, non-collimated, beam. A 3D model of this design is shown in Fig. 3. For the vertical TCT in Cell 4, a two-in-one design is not needed, however, a special design still has to be developed to implement the larger stroke of up to 40 mm.

4. Dispersion Suppressor Collimation Upgrades

The cleaning upgrades in the dispersion suppressor (DS) regions for HL-LHC is primarily driven by the increased risk of quenches from off-momentum losses. The DSs around IR7 are the main bottleneck in the LHC in terms of collimation leakage. A small fraction of protons interacting with the collimators in IR7 escape from the IR with a reduced magnetic rigidity. These protons, which are mainly single diffractive protons emerging from the TCPs, represent a source of local heat deposition in the cold DS magnets downstream

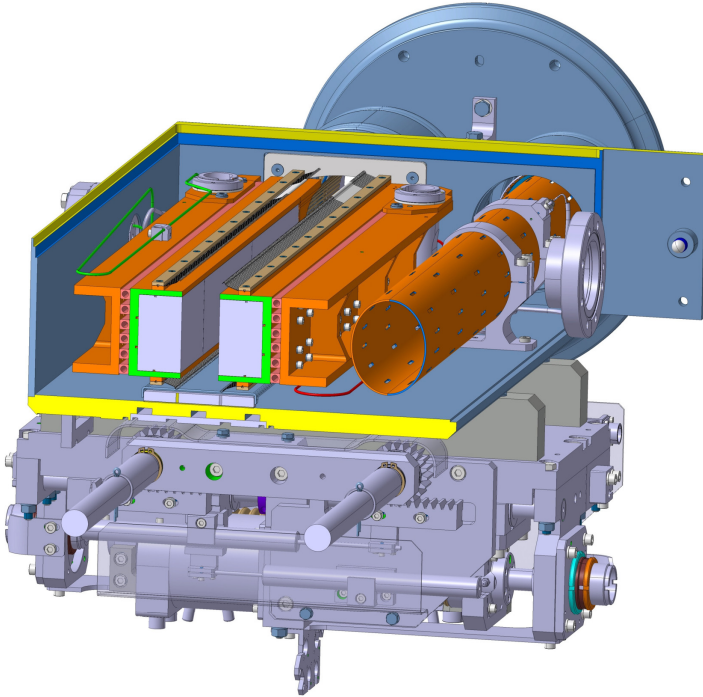


Fig. 3. Design of two-in-one collimators with a common vacuum tank housing both the movable jaws (left part) and the vacuum chamber of the opposing beam.

of IR7, where the dispersion starts to increase (see [29] and references therein). These losses are among the highest losses in cold magnets around the ring. In case of large drops in the beam lifetime, the impacted magnets risk quenching and the beams should be dumped by the BLMs before. This would result in costly downtime and reduced HL-LHC availability. The same mechanism inducing DS losses applies to secondary ion fragments produced in IR7 collimators during heavy ion operation. Although the intensities of heavy-ion beams are lower, they undergo numerous nuclear and electromagnetic interactions with the material of the primary collimators, creating an abundance of secondary ions with different mass and charge. Collimation of heavy-ion beams is therefore much less efficient than that of proton beams.

The design goal for the LHC, used also for HL-LHC, is that quenches and beam dumps should be avoided for a beam lifetime of 0.2 h for up to 10 s, or 1h beam lifetime for extended time periods [3]. This implies that the cleaning

system must sustain a higher power loss due to the higher beam intensity. Although such pessimistic lifetimes were rarely encountered in the LHC, this criterion is maintained in the HL-LHC design phase, where neither the quench limits at 7 TeV nor the operational performance are yet well known.

The acceptable losses in the DSs around IR7 were investigated with experimental quench tests with protons and Pb ions [30,31], and a quench was achieved in the heavy-ion test with a 6.37 Z TeV Pb beam [31,32]. A campaign of tracking studies using the SixTrack-FLUKA coupling [27] and energy deposition studies with FLUKA [33] managed to reproduce the experimental results within about a factor 3 [34,35]. This is considered a good agreement, given that the losses span many orders of magnitude and that there are large uncertainties and unknowns, in particular in terms of imperfections. Since the simulations underestimate the quench level inferred from beam experiments, all simulations for HL-LHC are scaled up by this factor.

Similar simulations have then been performed for HL-LHC for protons and Pb ions. If no upgrade is done, the peak power load in the superconducting coils in the DS, averaged over the cable width, is estimated at around 21 mW/cm³ for protons and 57 mW/cm³ for Pb ions during a beam lifetime drop to 0.2 h [4]. This should be compared with a quench limit of around 20 mW/cm³, inferred from the quench tests and corresponding simulations. The proton losses are just above the limit and the Pb ion losses exceed it by almost a factor of 3. It is therefore clear that there is a need for a cleaning upgrade, at least for Pb ion beam operation.

To mitigate the risk of quenches, it is therefore foreseen to add local collimators, referred to as TCLDs, in the DSs, where the dispersion has already started rising. In IR7 this is only feasible with a major change of the cold layout. In order to make space for the new collimators, it is envisaged to replace, for each TCLD in IR7, an existing main dipole with two shorter 11 T dipoles. The 60 cm long TCLD, made of the tungsten alloy Inermet 180, will be located in the middle between the two 11 T magnets, as shown in Fig. 4. A photograph of the TCLD collimator is given in Fig. 5: as received at CERN and as installed in the IR2 DS (Feb. 2020). The TCLD will be integrated in a specially designed assembly, containing a beam pipe for the other beam, as well as a cryo-bypass. The system design is particularly complex due to the very limited space imposed by the surrounding cryogenic equipment. Therefore, the active length of the material had to be reduced to only 60 cm.

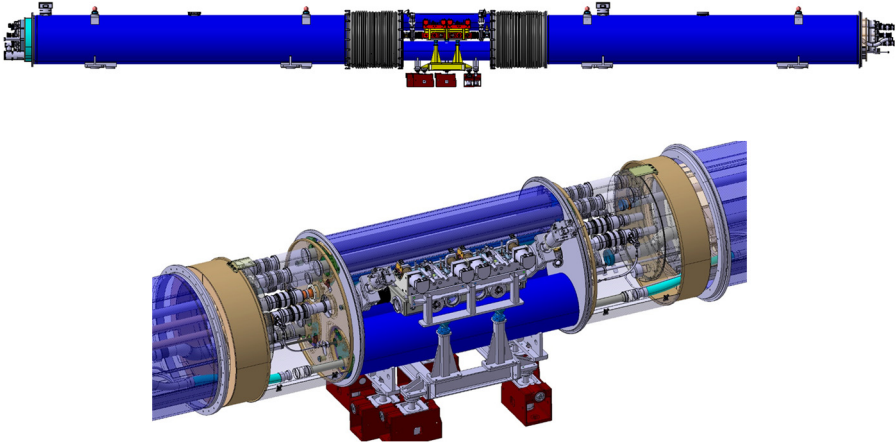


Fig. 4. Top: Schematic view of the assembly of two shorter 11 T dipoles with a collimator in between, which can replace one standard main dipole. Bottom: 3D model of a TCLD assembly showing the collimator (in grey, at the centre), the two short dipole cryostats and the connection cryostat. (Courtesy of L. Gentini).

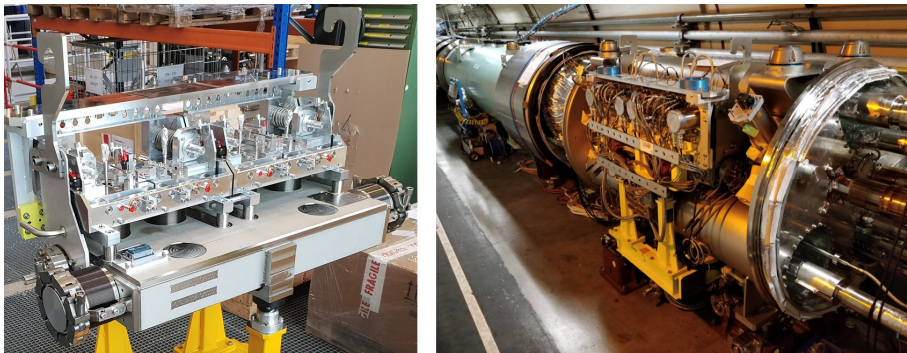


Fig. 5. TCLD collimator for the installation in DSs around IR2 and IR7 (left) and device installed in the connection cryostat in the DS on the left side of IP2 (right). The flange-to-flange distance is 1080 m.

The best performance would be obtained with two TCLD units per beam, however, a single unit gives already a significant performance improvement. It is therefore planned to install one TCLD in IR7 per beam in the HL-LHC baseline, replacing the present main dipole MB.A9 in Cell 9. The old and new IR7 layouts are shown in the left part of Fig. 6.

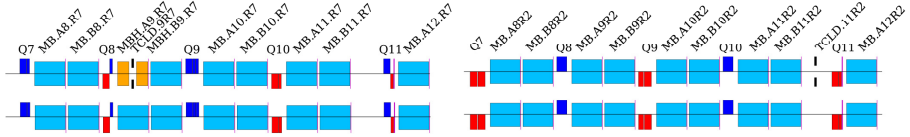


Fig. 6. HL-LHC (top) and LHC (bottom) layouts of the IR7 DS (left) and IR2 DS (right) of B1, with the new TCLD collimators, with and without 11 T dipoles. B2 layouts are symmetric. The beam goes from left to right.

Simulations of this new layout indicate that the power load on the superconducting cables in the main magnets decreases to about 8 mW/cm^3 for protons and 4 mW/cm^3 for Pb ions, thus leaving a comfortable margin to the quench limit. It should be noted that the superconducting cable of the 11 T dipoles instead receives a higher power load of 48 mW/cm^3 with protons (33 mW/cm^3 with Pb ions). However, the quench limit of the new 11 T magnet is estimated to be about 70 mW/cm^3 [36], which is significantly higher than for the present magnets, hence making the losses acceptable, although not with a very large margin. Various mitigation measures to increase this margin are under study, e.g. optimized alignment of the 11 T dipole and a local orbit bump to displace the losses in the 11T magnet to the TCLD. It is thus concluded that the proposed layout with new TCLDs in IR7 mitigates the risk of unacceptably high losses in the DS. These conclusions should be reassessed based on the operational experience in Run 3.

A DS collimation upgrade is needed also for heavy ion collisions in IP2. When two Pb ion beams collide, secondary ion beams with different magnetic rigidity are created, which are lost in the adjacent DS [9,29,37]. These ions represent a source of local heat deposition in the impacted magnet that could lead to a quench. The dominating processes are bound-free pair production (BFPP), where electron-positron pairs are created and one (BFPP1) or two (BFPP2) electrons are caught in a bound state of one of the colliding nuclei, thus changing its charge, and electromagnetic dissociation (EMD), where one nucleus emits one (EMD1) or two (EMD2) neutrons, thus changing mass. Further photon-induced processes also take place, but the four mechanisms mentioned here have the highest cross-sections. An example of ion beams produced in collisions of $^{208}\text{Pb}^{82+}$ nuclei in IR2 is given in Fig. 7.

The production of losses above quench limits from these secondary beams was demonstrated experimentally in 2015 at a Pb beam energy of 6.37 Z TeV,

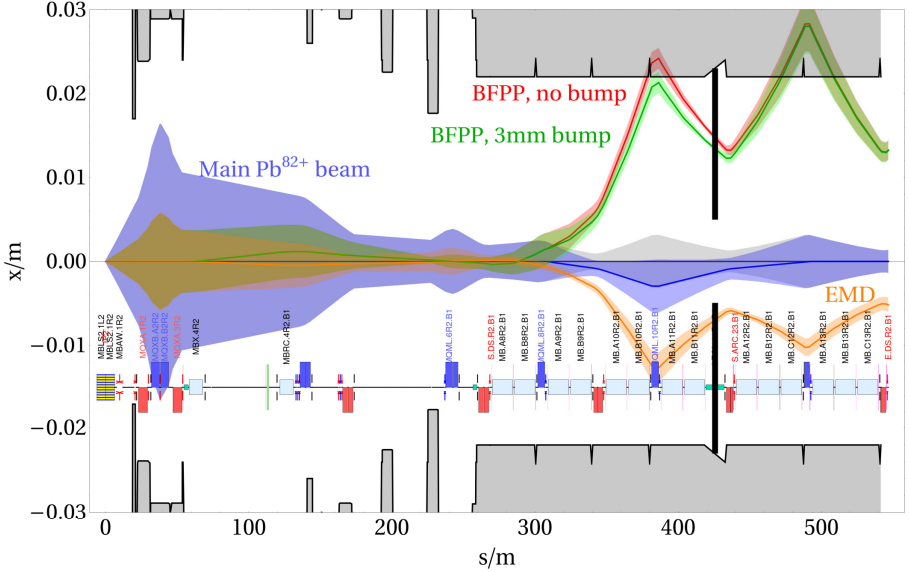


Fig. 7. 1σ envelope of the main Pb^{82+} beam (violet) together with the dispersive trajectories of ions undergoing BFPP1 (red) and EMD1 (brown), coming out of the ALICE experiment (IP2). The DS collimator jaws appear as black lines. The green line indicates the shifted BFPP1 orbit using a closed orbit bump, which is necessary to intercept the beam with the collimator. The EMD1 beam can be intercepted with the other jaw.

when a dipole quenched at a luminosity of $2.3 \times 10^{27} \text{ cm}^{-2} \text{ s}^{-1}$ [37]. In HL-LHC, with 7 Z TeV energy and a luminosity of about $7 \times 10^{27} \text{ cm}^{-2} \text{ s}^{-1}$ (about seven times the nominal one) [38], the BFPP beam carries 180 W of power. The simulated steady-state load in physics operation on the coils of the MB.B10 dipole is about 50 mW/cm^3 on both sides of the ALICE experiment [38]. Similar ion losses also occur in the DS regions around ATLAS and CMS, however at different locations than in IR2. It is therefore clear that mitigation measures are needed.

In IR1 and IR5, the BFPP1 beam is lost towards the end of the last dipole in Cell 11. This location is close to the connection cryostat. Therefore, the risk of quenches can be mitigated by redirecting the losses on the cryostat beam screen using local orbit bumps. Such bumps have been routinely used in the 2015 [40] and 2018 [41] Pb-Pb runs at 6.37 Z TeV. In the latter run, a peak luminosity of $6.2 \times 10^{27} \text{ cm}^{-2} \text{ s}^{-1}$ was reached in IP1 and IP5, which is almost the HL-LHC target luminosity. Simulation studies also confirm

that orbit bumps are a robust solution, indicating that, at a luminosity of $7 \times 10^{27} \text{ cm}^{-2} \text{ s}^{-1}$ and at a beam energy of 7 Z TeV, the power deposition in the coils of downstream magnets and in bus bars would remain safely below the quench level [38].

This solution does not work in IR2, where the BFPP1 beam is instead lost further upstream in Cell 10. It is therefore foreseen to install one TCLD per side in IR2, as shown schematically in Fig. 6. This TCLD intercepts the BFPP1 and EMD1 beams in a location where these ions are well separated from the main beam. The IR2 TCLDs will be installed in the connection cryostat in Cell 11 without need for 11 T dipoles, with the old and new layout shown in the right part of Fig. 6 (right graph). A closed orbit bump is required to make the BFPP1 beam miss the aperture at the first maximum of its trajectory and instead hit the TCLD. The EMD1 beam, which carries $\sim 65 \text{ W}$ at a luminosity of $7 \times 10^{27} \text{ cm}^{-2} \text{ s}^{-1}$, could be intercepted with the other jaw. Similar orbit bumps were successfully deployed operationally in IR1 and IR5 [41].

In order to minimize design and production efforts, the collimator length and material are chosen to be the same as for the TCLDs around IR7. Particle shower simulations with this layout suggest that the power deposition density in the coils of downstream magnets is below 1 mW/cm^3 if the BFPP1 and EMD1 beams impact at least 2 mm from the collimator edges, eliminating the risk of quenching both the magnets and the bus bars in the new connection cryostat [38]. Losses in the DS also occur during proton operation, but simulations have shown that the induced power load is safely below the quench level. Therefore, relying on the orbit bumps to alleviate BFPP losses, no collimation upgrade is needed in the DSs of IR1 and IR5.

5. Upgrades for Impedance Improvement

The LHC impedance budget is largely dominated by the contribution of the LHC collimators [1], which should be reduced to guarantee beam stability (see also Chapter 5). Since this was known already at the LHC design stage, the collimation system has been designed so that every TCS slot in IR3 and IR7 features a companion slot for the future installation of a low-impedance secondary collimator [3], for a total of 22 cabled slots in IR7 and 8 in IR3. Simulations predict that beam stability can be re-established for all HL-LHC scenarios if the carbon-fibre composite (CFC) of present TCSs is replaced, at

least in the betatron cleaning insertion, with a material having an electrical conductivity a factor of 50 to 100 higher than CFC [42]. However, the TCSs should also maintain a high cleaning efficiency, and they could be exposed to large beam losses and must therefore be robust against beam failure.

The latter requirement rules out the possibility to deploy high-Z metals because of their relatively low melting point and comparatively large thermal expansion that impairs their resistance to thermal shocks [43]. The present baseline for the upgraded secondary collimators relies thus on novel carbon-based materials, in particular molybdenum carbide-graphite (MoGr). This is a ceramic composite, jointly developed by CERN and Brevetti Bizz (IT), in which the presence of carbides and carbon fibres strongly catalyses the graphitic ordering of carbon during high temperature processing. This enhances its thermal and electrical properties [42]. To further improve their surface electrical conductivity, these materials will be coated with 5 μm pure molybdenum.

The foreseen HL-LHC upgrade consists therefore of the installation of Mo-coated MoGr collimators in 9 out of 11 TCS slots per beam. The installation is foreseen in two stages: a first installation in the Long Shutdown 2 (LS2, in the period 2019–2021), involving 4 collimators per beam, followed by a second installation in LS3 (2025–2026), when the remaining ones will be installed. This schedule gives already an impedance reduction and operational experience with the new collimators in Run 3, while allowing possible further iterations on the collimator design for the last units. The choice of the slots for installation during LS2 [44] was mainly driven by maximising the impedance reduction for the first upgrade phase, while avoiding installation slots with the highest expected thermo-mechanical loads, as an extra safety measure for validating the design.

The HL-LHC impedance upgrade includes a contribution to low-impedance material also for the TCPs that are otherwise renewed as a part of the consolidation project. In LS2, the 4 IR7 TCPs in the horizontal and vertical planes in both beams will be replaced with the new design using uncoated MoGr and introducing the BPM functionality [19]. Since TCPs are continuously exposed to primary beam losses, coating the active jaw part is not considered viable. The MoGr provides an improvement of about a factor 5 in resistivity compared to CFC, while ensuring a similar robustness against beam failure.

The impedance of the present and future machine configurations was studied through detailed calculations. Fig. 8 shows the expected octupole current required to stabilise the HL-LHC beam for the ultimate scenario [44] (see also [45] and Chapter 5 of this book), i.e. the most demanding one from the point of view of beam stability, together with the maximum allowed octupole current of 570 A. Estimations are done taking into account all sources of machine impedance, including crab-cavities, and a factor 2 as it was observed at the end of Run 2, also after optimization of coupling that was confirmed to be a major detrimental mechanism for beam stability [46]. As seen, beam stability requires an impedance upgrade. Moreover, the estimation for the present upgrade almost matches the maximum octupole current, with an almost negligible deterioration due to the two TCS slots not upgraded. Expectations for the LS2 upgrade show a significant improvement already achieved with only four collimators per beam (where also the TCP is upgraded through the consolidation program to uncoated MoGr). This discrepancy is

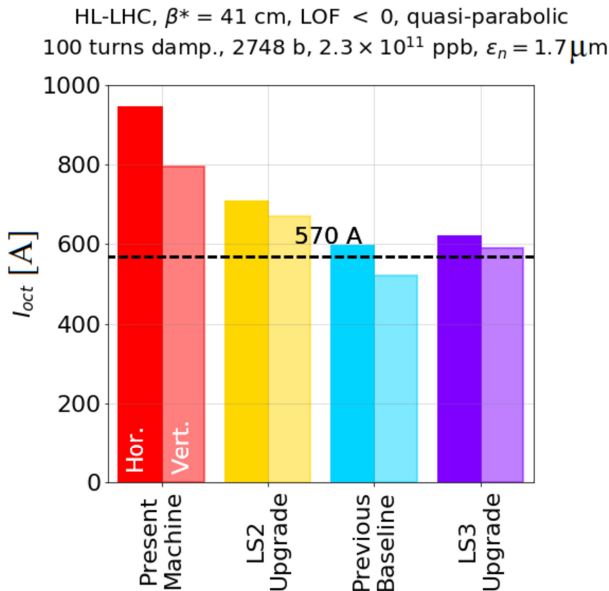


Fig. 8. Expected octupole current required to stabilise the HL-LHC beam for the ultimate scenario [44], with the relevant simulation parameters. Expectation values include the factor 2 discrepancy between predictions and operational values observed in Run 2 (after optimisation of the parameters such as linear coupling).

being investigated in detail and seems to be related to noise injected in the beam by power supplies or by the transverse damper [47].

The thermo–mechanical response of the new collimator has been simulated to ensure that it will survive regular and accidental beam losses [24]. Simulations are done in three steps, including particle tracking, energy deposition, and thermo-mechanical analysis. The studies demonstrate that the most loaded low-impedance collimator, which intercepts about 100 kW during a 0.2 h beam lifetime, survives without permanent damage but is subject to a jaw deformation of 500 μm , exceeding the tolerance of 100 μm . However, the deformation is directed away from the beam, meaning that the expected impact on the cleaning efficiency is very small. Nevertheless, this particular TCS will be upgraded only in LS3, giving time to further improve the design if needed based on the operational experience of Run 3.

The new collimator design must be validated for operation in the LHC. For this purpose, a rich programme of validation tests has been carried out. Irradiation tests of MoGr at GSI and BNL are well advanced, and the latest results indicate that MoGr, even when coated with Mo, can survive the expected dose in HL-LHC, although the analysis is not yet finalized at the time of writing (see for example [48] for the un-coated case). Experimental beam-impact tests at HiRadMat were carried out very successfully to demonstrate that a full-scale MoGr jaw prototype could be hit by a full train during an injection failure without apparent damage [24]. The coating was assessed in another HiRadMat test [49], where an 8 μm -thick Mo coating layer exhibited a surface scratch less than 2 mm wide following a direct impact equivalent to the HL-LHC injection failure. Such a damage is non-catastrophic from the impedance point of view; moreover, thanks to the limited transverse extension of the damage, an undamaged portion of jaw surface can be exposed to the beam by moving the collimator in the non-collimation plane thanks to the so-called 5th axis functionality.

Tests of a prototype collimator with circulating beams in the LHC have been carried out in 2017. Each jaw of the prototype was built with MoGr bulk and has three different surface “stripes” for impedance tests: uncoated MoGr, Mo coating and TiN coating. The collimator was installed right next to the CFC TCS with the smallest beam size in the collimation plane, hence maximizing the effect on impedance. Both collimators are vertical, allowing for a direct comparison. Fig. 9 shows the tune-shift measurements with the

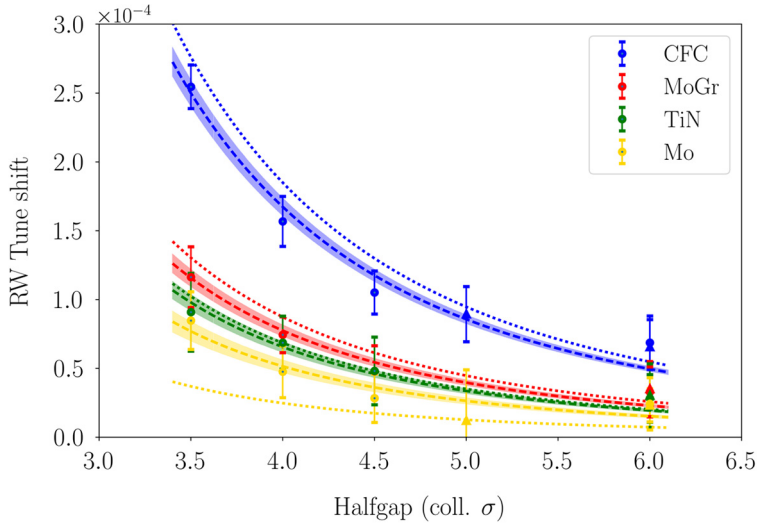


Fig. 9. Tune shift measurements carried out in 2017 (dots), fit to experimental data (dashed line) and predictions (dotted lines) for the three stripes of the TCSPM prototype and the CFC of regular TCSGs as a function of the minimum collimator opening [44]. The collimator opening is expressed as half gap, in units of local beam σ (for a normalised emittance of $3.5 \mu\text{m}$).

MoGr prototype and the adjacent CFC TCS, taken while varying the collimator opening [45]. The measurements are compared to numerical simulation results. In general, a good agreement is seen between simulations and measurements, with the exception of the Mo coating, which shows a factor 2 discrepancy. Further measurements in laboratory showed that the quality of the microstructure of the coating and of the jaw roughness could explain this difference [50]. The MoGr prototype was kept in the LHC throughout 2018 and used throughout the run at the same settings as the adjacent TCS, without any fault or odd behavior in key operational parameters and observables.

6. Reference Cleaning Performance for the Baseline Upgrade System

Putting together all upgrades described in the previous sections, the global performance of the upgraded HL-LHC collimation system should be assessed. This has been done using the SixTrack-FLUKA coupling [27], which tracks an initial distribution of beam halo particles through the magnetic lattice of

the ring. When a particle enters a collimator, its coordinates are sent to FLUKA, which simulates the particle-matter interaction and then sends any surviving particles above a minimum threshold back to SixTrack for further tracking. A particle is considered lost either when it hits the aperture (the particle coordinates are checked against a detailed aperture model with 10 cm longitudinal precision) or if it interacts inelastically inside a collimator. The exception to this is single diffractive events, where the incident proton could survive and exit the collimator. These protons, which often have significant energy offsets, are tracked further. The simulation output contains coordinates of all loss locations.

The simulation output, presented as a loss distribution around the ring, is shown in Fig. 10 for the reference case of horizontal betatron losses at 7 TeV for Beam 1. The baseline collision optics with $\beta^*=15$ cm, version 1.3, was used together with the collimator settings in Table 1. As can be seen, the main losses occur at the betatron collimators in IR7 and losses at other positions in the ring are orders of magnitude lower. The most important losses outside of IR7 occur at the momentum collimators in IR3 and at the dump protection collimators in IR6, while significant losses occur also at the TCTs at the experiments. It should be noted that almost no cold losses occur outside of IR7, which is an excellent result, possible only thanks to the very efficient cleaning of the TCLD. The highest cold losses in the ring occur at the first 11 T magnet, just upstream of the TCLD as discussed in Section 4. The resulting energy deposition here is below the estimated quench limit even for the pessimistic case of a 0.2 h beam lifetime, meaning that the collimation system successfully protects the cold elements. These results are qualitatively representative also for vertical losses (similar loss pattern) and for losses in B2 (similar loss pattern, but with the beam going in the opposite direction). Off-momentum losses in IR3 are not expected to limit the performance of HL-LHC [51].

Similar cleaning simulations have been performed also for Pb ion beams. As observed in the LHC machine [51,53], the nuclear fragmentation makes the collimation system less efficient with ion beams than with protons, however, this is to a large part compensated by the lower stored beam energy. The TCLD cleans almost completely the particles that would otherwise be lost around the ring, and the only significant cold losses are in the IR7 DS, on the 11 T magnet upstream of the TCLD. The energy deposition studies in Section 4 show that these losses are well below the quench level.

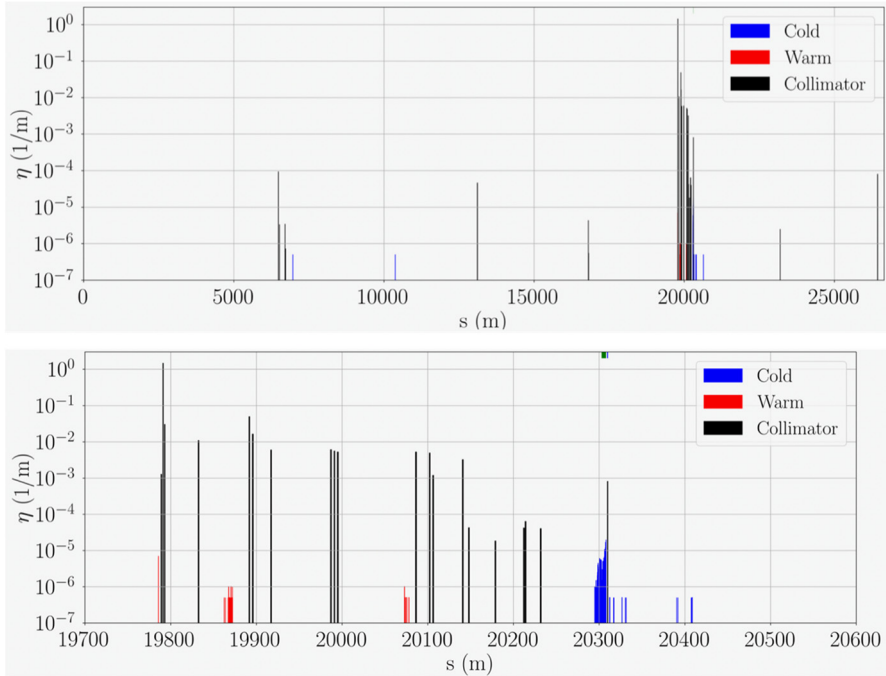


Fig. 10. The simulated losses around the HL-LHC ring (top) with a zoom in the betatron cleaning in IR7 (bottom). The losses, simulated for horizontal betatron losses in lattice version HL-LHC v1.3 at $\beta^*=15$ cm, are expressed in terms of local cleaning efficiency as in [3]. Courtesy of E. Belli.

7. Enhanced Beam Collimation with Hollow Electron Beams

In this section we discuss a new, more advanced, collimation concept that has been very recently (2019) integrated into the upgrade baseline following the Cost & Schedule Review in 2019 through a substantial in-kind contribution (under signature at the time of writing). The concept of hollow electron lenses (HELs) collimation is presented. These two items, which are schematically illustrated in Fig. 11, are part of the approved studies within WP5. Focus was put in recent years to review the needs for these upgrades for HL-LHC and to demonstrate the required technology in tests without and with beam. Both crystal collimation and HELs address, in different ways, further improvements of the betatron collimation system (crystal collimation will be discussed in Chapter 30).

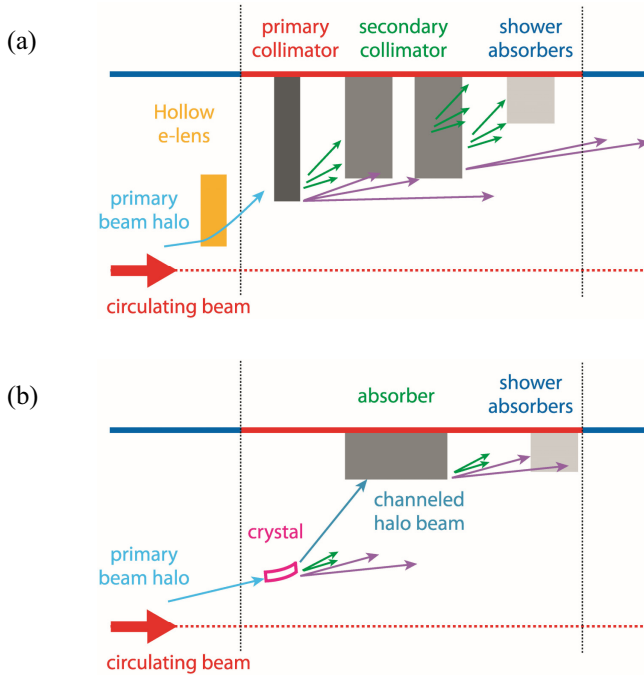


Fig. 11. Illustrative view of the beta betatron collimation system (a) with integrated hollow e-lens or equivalent halo diffusion mechanism; (b) with an ideal crystal-based collimation system. Halo control techniques are used to change the diffusion speed of halo particles, and rely on the full collimation system remaining in place for their disposal. The crystal-based scheme entails a change of concept for betatron collimation, where the whole beam losses are concentrated, ideally, in one single beam absorber per plane.

Operational experience in 2012 indicated that the LHC collimation would profit from halo control mechanisms. The operation of Run 2 at 6.5 TeV showed a less severe impact from halo losses [54]; however, scaling them to HL-LHC beam parameters is still a source of concerns. In particular, the presence of over-populated tails in the LHC beams was consistently observed in dedicated measurements at the LHC [55,56]. Simple extrapolations to the HL-LHC beam intensities lead to the estimate that more than 30 MJ can be stored at transverse amplitudes between $3.5\text{-}4.0\sigma$ and the aperture of primary collimators. This scenario, in particular considering that crab-cavities might produce new fast-loss failure scenarios at HL-LHC, requires an active control of tails. The HELs are the most promising solution to achieve this goal.

Halo control mechanisms were used in other machines like HERA and the Tevatron [57], and more recently in the RHIC [58]. The idea is that, by controlling the diffusion speed of halo particles, one can (1) act on the time profile of the losses, for example by reducing rates of losses that would otherwise take place in a short time, and (2) control the population of halo particles in a certain range of transverse apertures.

In a HEL, a hollow electron beam runs parallel and concentrically to the proton or ion beam. The hollow beam produces an electromagnetic field only affecting halo particles above a given transverse amplitude determined by its inner radius, changing their transverse diffusion speed. Such a device is integrated into the existing collimation system – which remains responsible for the safe and efficient disposal of halo particles – as follows: the electron beam’s inner radius is smaller than the TCP aperture, producing a region of depleted halo between the beam core and the primary collimator aperture. A solid experimental basis achieved at the Tevatron indicates that this solution is promising and can be applied to the LHC as well [57 and references therein].

The potential advantages of electron lens collimation are multiple.

- Control loss rates on primary collimators, with potential mitigation of peak loss rates in cold magnets.
- Mitigate risk of damage from beam losses in case of fast failures with tens of MJ in the tails.
- Reduce tail populations and peak loss rates in the case of orbit drifts.
- Tighten the collimator hierarchy for a smaller β^* reach, thanks to reduced tails (compatibly with other constraints like impedance budget).
- Scraping the beam at very low amplitudes ($>3\sigma$) without the risk of damage, as expected for bulk scrapers.
- Tune the impact parameters on the primary collimators with a possible improvement in cleaning efficiency.

The HEL for the HL-LHC [59] is targeted at enabling active control of beam tails above 3 to 4 real beam sigmas, with tail depletion efficiencies of the order of 90% over times of tens of seconds. This should be possible, ideally, in all phases of the operational cycle but specifically at top energy when beam losses are a concern (usage at injection is considered as an asset for the initial commissioning phase). The present design parameters of the HL-LHC lenses, optimized for 7 TeV, are given in Table 2 and a 3D drawing is given in

Fig. 12. Note that the HEL design should ensure: (i) the possibility of pulsing the current turn-by-turn (as required to drive resonances in the halo particle's dynamics); (ii) a train-by-train selective excitation (leaving 'witness' trains with populated halos for diagnostics and machine protection purposes).

The main HEL components are (1) the electron beam generation and disposal systems: electron gun and collector; (2) the superconducting magnet system composed by main 5 T solenoids, solenoids at the e-beam generation and correctors to stabilize and steer the electron beam; (3) beam instrumentation for the optimization of the electron beam: beam position and transverse profile monitors (see Chapter 18). The LHC Point 4 that houses the superconducting RF system is considered for installation of the HEL, and suitable

Table 2. Hollow electron beam equipment parameters.

Parameter	Value or range
Geometry	
Length of the interaction region, L [m]	3
Desired transverse scraping range at 7 TeV [$\sigma, \epsilon = 2.5\mu\text{m}$]	3.6-7.5
Range of inner electron beam radii at 7 TeV [mm]	1.1-2.3
Inner vacuum chamber diameter [mm]	60
Magnetic fields at 7 TeV and magnet parameters	
Main solenoid field, B_m [T]	5.0
Range of gun solenoid field, B_g [T]	0.2-4.0
Nominal gun solenoid field, B_g [T]	0.375
Range of compression factors, $\sqrt{B_m/B_g}$	1.1-5.0
Target compression factor, $\sqrt{B_m/B_g}$	3.7
Electron gun and high-voltage modulator	
Inner/outer cathode diameters [mm]	8.05-16.1
Peak yield at 10 kV, I [A]	5
Cathode-anode voltage [kV]	10
Accelerating voltage [kV]	15
Rise time (10% -90%) [ns]	200
Electron pulse duration for pulsed operation [μs]	1.2-86.0
Repetition rate [kHz]	11.4-34.2

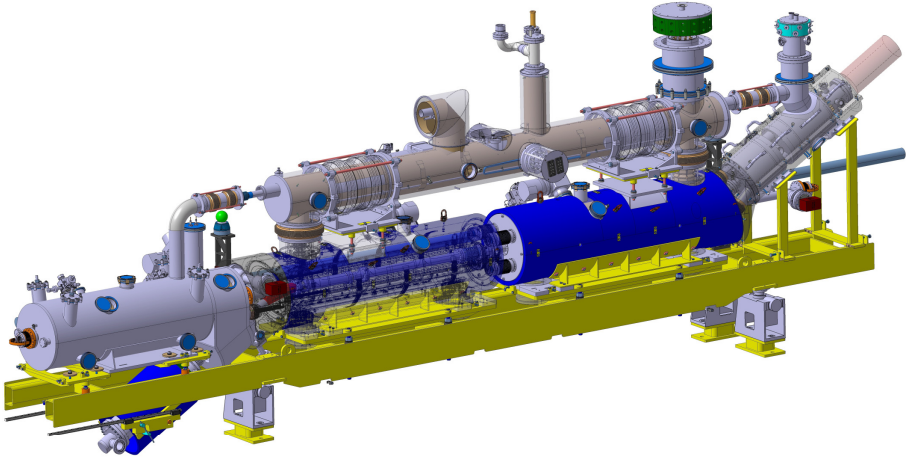


Fig. 12. Present design of the HL-LHC hollow e-lens (version Nov. 2020). An ‘S’ shape is proposed in order to self-compensate potential kicks from the e-beams asymmetries seen by the proton beam at entry and exit. Courtesy of D. Perini.

locations have been identified for the integration of two HELs, one per beam. The HEL does not generate significant local beam losses as the particles slowly expelled from the tails are disposed of in IR7 through the standard multi-turn cleaning mechanism.

References

1. I. Béjar Alonso et al., High-Luminosity Larger Hadron Collider (HL-LHC): Technical Design Report, CERN Yellow Reports: Monographs, 10/2020.
2. O. Brüning (Ed.) et al., LHC Design Report Vol. 1, CERN-2004-003-V-1 (2004).
3. R. Assmann et al., The final collimation system for the LHC, Proc. EPAC2006, Edinburgh, 2006. Conf. Proc. C060626 (2006) 986-988. Also as CERN-LHC-PROJECT-REPORT-919 (2006).
4. S. Redaelli et al., Chapter 5: Collimation system, CERN Yellow Rep. Monogr. 10 (2020) 87-114.
5. S. Redaelli, Beam Cleaning and Collimation Systems, CERN Yellow Report CERN-2016-002, pp.403-437. Contribution to: 2014 Joint International Accelerator School.
6. R. Bruce, R.W. Assmann and S. Redaelli, Calculations of safe collimator settings and β^* at the Large Hadron Collider, Phys. Rev. ST Accel. Beams 18, 061001 (2015).
7. R. Bruce et al., Reaching record-low β^* at the CERN Large Hadron Collider using a novel scheme of collimator settings and optics, Nucl. Instrum. Methods Phys. Res. A 848 (2017).

8. D. Mirarchi et al., Cleaning Performance of the Collimation System of the High Luminosity Large Hadron Collider, Proceedings, 7th International Particle Accelerator Conference (IPAC 2016): Busan, Korea, May 8-13, 2016, doi 10.18429/JACoW-IPAC2016-WEPMW007.
9. R. Bruce et al., Observations of Beam Losses Due to Bound-Free Pair Production in a Heavy-Ion Collider, Phys. Rev. Letters 99.14 (2007).
10. R. Bruce et al., Sources of machine-induced background in the ATLAS and CMS detectors at the CERN Large Hadron Collider, Nucl. Instrum. Methods Phys. Res. A 729 (2013) 825–840.
11. R. Bruce et al., Collimation-induced experimental background studies at the CERN Large Hadron Collider, Phys. Rev. Accel. Beams 22, 021004 (2019).
12. E. Quaranta et al., Modeling of beam-induced damage of the LHC tertiary collimators, Phys. Rev. Accel. Beams 20 (2017) no.9, 091002.
13. B. Salvachua Ferrando et al., Cleaning performance of the LHC Collimation System up to 4 TeV, Proc. IPAC13, Shanghai, China, 2013. <http://accelconf.web.cern.ch/accelconf/ipac2013/papers/mopwo048.pdf>.
14. N. Fuster Martinez et al., Run 2 Collimation Overview, Proceedings of the 2019 Evian Workshop on LHC Beam Operations, pp. 149-164, <https://cds.cern.ch/record/2750291?ln=fr>.
15. Z. Citron et al., Future physics opportunities for high-density QCD at the LHC with heavy-ion and proton beams, CERN-LPCC-2018-07 (2018).
16. S. Redaelli et al., Final implementation and performance of the LHC collimator control system, Proc. PAC09, Vancouver (CA). Conference: C09-05-04, FR5REP007.
17. F. Carra et al., Mechanical engineering and design of novel collimators for HL-LHC, Proc. IPAC2014, Dresden, Germany, 2014. <http://accelconf.web.cern.ch/IPAC2014/papers/mopro116.pdf>.
18. A. Bertarelli et al., The mechanical design for the LHC Collimators, Proc. EPAC2004, Lucerne, Switzerland, 2004. <https://accelconf.web.cern.ch/e04/PAPERS/MOPLT008.PDF>.
19. A. Dallochio et al., LHC collimators with embedded beam position monitors: A new advanced mechanical design, Proc. IPAC2011, San Sebastian, Spain, IPAC-2011-TUPS035 (2011).
20. G. Valentino et al., Successive approximation algorithm for BPM-based LHC collimator alignment, Phys. Rev. ST Accel. Beams 17, 021005 (2014).
21. G. Valentino et al., Final implementation, commissioning, and performance of embedded collimator beam position monitors in the Large Hadron Collider, Phys. Rev. Accel. Beams 20, 081002 (2017).
22. D. Wollmann et al., Beam feasibility study of a collimator with in-jaw beam position monitors, Nucl. Instrum. Methods Phys. Res., Sect. A 768, 62 (2014).
23. A. Bertarelli et al., An experiment to test advanced materials impacted by intense proton pulses at CERN HiRadMat facility, Nucl. Instr. Meth. B 308 (2013) 88.

24. G. Gobbi et al., Novel LHC collimator materials: High-energy Hadron beam impact tests and nondestructive post irradiation examination, *Mechanics of Advanced Materials and Structures* 1-13, DOI: 10.1080/15376494.2018.1518501 (2019).
25. F. Carra et al., Mechanical robustness of HL-LHC collimator designs, *J. Phys.: Conf. Ser.* 1350 012083 (2019).
26. A. Bertarelli et al., Dynamic testing and characterization of advanced materials in a new experiment at CERN HiRadMat facility, *J. Phys.: Conf. Ser.* 1067 082021 (2018).
27. S. Redaelli (Ed.), *Proceedings of ICFA Mini-Workshop on Tracking for Collimation in Particle Accelerators*. CERN-2018-011-CP (2018).
28. R. Bruce et al., Simulations and measurements of beam loss patterns at the CERN Large Hadron Collider, *Phys. Rev. ST Accel. Beams* 17 (2014), p.081004. doi: 10.1103/PhysRevSTAB.17.081004.
29. R. Bruce et al., Beam losses from ultraperipheral nuclear collisions between 208Pb82+ ions in the Large Hadron Collider and their alleviation, *Phys. Rev. ST Accel. Beams* 12 (2009) 071002.
30. B. Auchmann et al., Testing Beam-Induced Quench Levels of LHC Superconducting Magnets, *Phys. Rev. ST Accel. Beams* 18 (2015) 061002.
31. P. D. Hermes et al., LHC Heavy-Ion Collimation Quench Test at 6.37Z TeV, CERN-ACC-Note-2016-0031 (2016).
32. P. D. Hermes, Heavy-ion collimation at the Large Hadron Collider - Simulations and measurements, Ph.D. thesis, University of Munster, DE (2016). CERN-THESIS-2016-230.
33. A. Ferrari, P.R. Sala, A. Fassò, and J. Ranft, FLUKA: a multi-particle transport code, CERN 2005-10 (2005), INFN/TC_05/11, SLAC-R-773.
34. A. Lechner et al., Validation of energy deposition simulations for proton and heavy ion losses in the CERN Large Hadron Collider, *Phys. Rev. Accel. Beams* 22 (2019) 7, 071003.
35. E. Skordis et al., Study of the 2015 Top Energy LHC Collimation Quench Tests Through an Advanced Simulation Chain, doi:10.18429/JACoW-IPAC2017-MOPAB012.
36. L. Bottura et al., Quench performance and assumptions: magnets and cryogenics, presentation at the International Review of the HL-LHC Collimation System (2019). INDICO: 780182.
37. M. Schaumann et al., Bound-free pair production from nuclear collisions and the steady-state quench limit of the main dipole magnets of the CERN Large Hadron Collider, *Phys. Rev. Accel. Beams* 23 (2020) 121003.
38. R. Bruce et al., Performance and luminosity models for heavy-ion operation at the CERN Large Hadron Collider, *Eur. Phys. J. Plus* 136, 745 (2021). <https://doi.org/10.1140/epjp/s13360-021-01685-5>.
39. C. Bahamonde Castro et al., Power deposition in LHC magnets due to bound-free pair production in the experimental insertions, *Proceedings of IPAC2016, Busan, Korea, TUPMW006*, pp. 1418-1421.
40. J.M. Jowett et al., The 2015 heavy-ion run of the LHC, *Proceedings of IPAC16, Busan, Korea, TUPMW027*, pp. 1493-1496. DOI: 10.18429/JACoW-IPAC2016-TUPMW027.

41. J.M. Jowett et al., Overview of ion runs during run 2, Proc. 9th LHC Operations Evian Workshop, Evian, France (2019).
42. J. Guardia-Valenzuela et al., Development and properties of high thermal conductivity molybdenum carbide - graphite composites, *Carbon* 135 (2018) 72-84.
43. A. Bertarelli, Beam Induced Damage Mechanisms and Their Calculation, CERN Yellow Report CERN-2016-002, pp. 159-227. Contribution to: 2014 Joint International Accelerator School.
44. S. Antipov et al., Staged implementation of low-impedance collimation in IR7: plans for LS2, CERN-ACC-2019-0001, CERN, Geneva, Switzerland (2019). <https://cds.cern.ch/record/2654779/files/CERN-ACC-NOTE-2019-0001.pdf>.
45. S. Antipov et al., Transverse beam stability with low-impedance collimators in the High-Luminosity Large Hadron Collider: Status and challenges, *Phys. Rev. Accel. Beams* 23 (2020) 3, 034403, <https://inspirehep.net/literature/1760250>.
46. L.R. Carver et al., Transverse beam instabilities in the presence of linear coupling in the Large Hadron Collider, *Phys. Rev. Accel. Beams* 21 (2018) 4, 044401.
47. S.V. Furusest et al., Loss of transverse Landau damping by noise and wakefield driven diffusion, *Phys. Rev. Accel. Beams* 23 (2020) 11, 114401.
48. N. Simos et al., Proton irradiation effects in Molybdenum-Carbide-Graphite composites, *J. Nucl. Mater.* 553 (2021) 153049.
49. M. Pasquali et al., Dynamic Response of Advanced Materials Impacted by Particle Beams: The MultiMat Experiment, *Journal of Dynamic Behavior of Materials* 5 (2019) 3, 266-295.
50. N. Biancacci et al., Resistivity Characterization of Molybdenum-Coated Graphite-Based Substrates for High-Luminosity LHC Collimators, *Coatings* 2020, 10(4), 361; <https://doi.org/10.3390/coatings10040361>.
51. H. Garcia Morales et al., Off-momentum cleaning simulations and measurements at the Large Hadron Collider, *Nuclear Instruments and Methods in Physics Research Section A: Accelerators, Spectrometers, Detectors and Associated Equipment* 1010 (2021), p. 165494. doi: <https://doi.org/10.1016/j.nima.2021.165494>.
52. P.D. Hermes et al., Measured and simulated heavy-ion beam loss patterns at the CERN Large Hadron Collider, *Nucl. Instrum. Meth. A* 819 (2016) 73-83.
53. N. Fuster-Martínez et al., Simulations of heavy-ion halo collimation at the CERN Large Hadron Collider: Benchmark with measurements and cleaning performance evaluation, *Phys. Rev. Accel. Beams* 23 (2020) 11, 111002.
54. Review of the needs for a hollow e-lens for the HL-LHC, 6th – 7th October 2016, CERN, Geneva, Switzerland. <https://indico.cern.ch/event/567839>.
55. G. Valentino et al., Beam diffusion measurements using collimator scans at the LHC, *Phys. Rev. Spec. Top. Accel. Beams* 16 (2013) 021003.
56. A. Gorzawski et al., Probing LHC halo dynamics using collimator loss rates at 6.5 TeV, *Phys. Rev. Accel. Beams* 23 (2020) 4, 044802.
57. G. Stancari, A. Valishev, G. Annala, G. Kuznetsov, V. Shiltsev, D.A. Still et al., Collimation with hollow electron beams, *Phys. Rev. Lett.* 107 (2011) 084802 [arXiv:1105.3256].

58. X. Gu et al., Halo removal experiments with hollow electron lens in the BNL Relativistic Heavy Ion Collider, *Phys. Rev. Accel. Beams* 23 (2020) 3, 031001.
59. S. Redaelli et al., Hollow electron lenses for beam collimation at the High-Luminosity Large Hadron Collider (HL-LHC), *JINST* 16 (2021) 03, P03042.

Chapter 9

Circuit Layout, Powering and Protection

F. Rodríguez Mateos^a, T. D. Catalão Da Rosa^b, F. Menéndez Cámara^b,
S. Yammine^a and M. Zerlauth^c

On behalf of the HL-LHC Magnet Circuit Forum

^a*CERN, TE Department, Genève 23, CH-1211, Switzerland*

^b*Former CERN members*

^c*CERN, ATS-DO Unit, Genève 23, CH-1211, Switzerland*

The HL-LHC upgrade will impose changes to the magnet circuits in Points 1, 5 and 7 with respect to the present LHC configuration. This chapter describes those changes and describes the powering characteristics and protection strategies applicable to the new magnet circuits. The electrical design criteria for magnets and other elements of the circuit are also presented.

1. HL-LHC Circuits Upgrade

During LS2 and LS3, the HL-LHC upgrade will impose with the installation of new magnets in the high luminosity insertion regions (IR) of ATLAS and CMS many changes to the magnet circuits of the LHC. Figure 1 shows the magnet types and the circuit corresponding circuit layout for the HL-LHC insertion regions. These magnets will be installed in the machine during LS3. In addition to these changes, two main dipole magnets (MB) are planned to be replaced by 11T dipole cryo-assemblies in order to add two additional collimators around Point 7. The two concerned magnets are to be installed in Cell 9 on the left and right side of LHC Point 7. Figures 2 and 3 illustrate the circuit upgrade for one 11T cryo-assembly installed in sectors 67 and 78 of

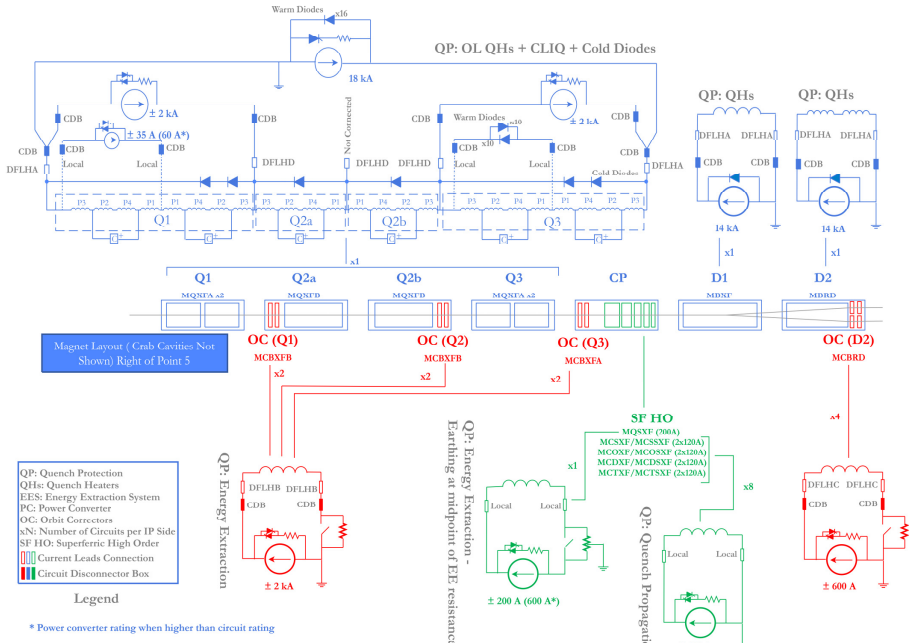


Fig. 1. HL-LHC insertion region magnet and circuit layout the right of Points 1 and 5.

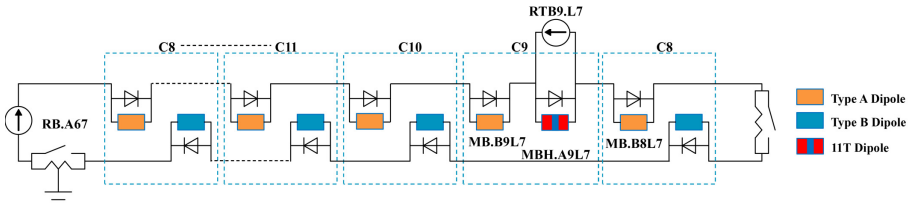


Fig. 2. 11T dipole cryo-assembly replacement of an MB magnet for circuit RB.A67.

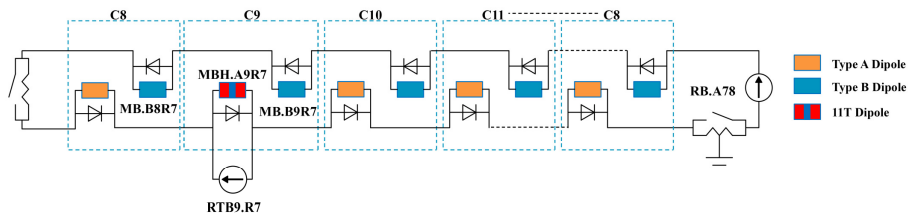


Fig. 3. 11T dipole cryo-assembly replacement of an MB magnet for circuit RB.A78.

the LHC respectively. The next paragraphs will detail each of the concerned circuits.

1.1. *Inner Triplet Main Circuit*

For the HL-LHC, the new inner triplet quadrupoles MQXFA and MQXFB will replace the current MQXA and MQXB magnets in optical positions Q1-Q2a/b-Q3 of the low- β triplet in the LHC IR1 and IR5 (around ATLAS and CMS experiments, respectively). In addition, the circuit configuration relies on having one main circuit with trim power converters acting on half of Q1 (i.e. Q1a), Q1 and Q3 as shown in Figure 1. The circuit powering and protection scheme is composed of the following components:

- **Power Converters:** The main power converter of the Inner Triplet circuit will have a rating of 18 kA. R&D work is well advanced [1] to develop a new type of 2-quadrant power converter in order to apply positive and negative voltage to the magnets which is mandatory to ramp-down the current in the shadow of the main LHC dipole magnets. Two trim power converters will inject or extract currents up to 2 kA in Q1 and Q3. In addition, one 35 A power converter will be connected to the first half of the Q1 magnet (i.e. Q1a) for k-modulation purposes as described in Chapter 5. A decoupling technique with inter power converter communication is applied to the controllers in order to achieve stability [2].
- **Cold Powering:** A superconducting (sc) link, dedicated for the inner triplet circuits (from Q1 to D1) will bring the current to the superconducting magnets through the new UL galleries as shown in Chapter 23. The interface between the sc link and the warm powering is defined at the level of the current leads connected to the distribution feedbox (DFHX) in the new UR galleries (refer to Chapter 23) whereas, the interface between the sc link and the magnets is located at the level of the distribution feedbox (DFX) placed inside the LHC tunnel as described in Chapter 23.
- **Circuit Disconnecter Boxes (CDBs):** The CDBs will provide the galvanic separation of the warm powering, i.e. the cables from the HL-LHC current leads respecting the electrical safety standards. The disconnectors will also feature safer and easier execution of the Electrical Quality Assurance tests.

- **DC Connections:** For the 18 kA and the 2 kA trim circuits, water-cooled cables will be installed between the power converters and the CDBs. Air-cooled cables will be installed for the 2 kA trim circuits between the CDBs and the current leads of the DFHX, whereas, copper bus-bars with electrically insulated cooling plates will connect the 18 kA CDBs to the corresponding current leads. All these items are placed inside the UR galleries. For the k-modulation circuit, air-cooled cables connect the power converter to the CDB and then to the local feedthroughs on the Q1 magnet cryostat.
- **Quench Protection:** The triplet magnets will be protected by means of outer layer quench heaters and CLIQ (Coupling Loss Induced Quench) [2] units as described in Chapter 12. Useful to further reduce the hot spot temperature and necessary to mitigate risks in a multiple fault event, the innovative CLIQ system has been adopted in the protection baseline after a series of validation tests on single magnets. The CLIQ units are electrically connected to the circuit as shown on Figure 1. Furthermore, cold diodes are introduced to the Inner Triplet circuit in order to balance voltages during magnet quenches and to mitigate the possible delays in firing the quench protection systems between different magnets. Cold diodes also limit the transient currents through the superconducting link and warm parts of the circuit during asymmetric quenches (that could arise due to different quench resistances in the magnets). The protection strategy of the inner triplet main circuits is based on the simultaneous firing of all the quench protection systems (quench heaters and CLIQ) when a quench is detected in any superconducting element of the circuit (i.e. magnet, bus-bars, sc link and current leads).

1.2. Triplet Orbit Correctors

For the inner triplet circuit, there will be a total of 6 orbit correctors (1 vertical and 1 horizontal in Q2a, Q2b and the Corrector Package (CP) cold masses respectively). These dipole corrector circuits have a rating of ± 2 kA. The circuit layout of these correctors, as shown in Figure 1, contains the following components:

- **Power Converters:** One power converter per circuit rated at ± 2 kA.

- **Cold Powering:** The MCBXF correctors will be powered via the sc link, the DFHX and the DFX boxes.
- **CDBs:** A CDB will be introduced in each circuit to ensure a safe disconnection of the water-cooled cables from the current leads.
- **DC Cabling:** Water-cooled cables will be installed between the power converters and the CDBs and air-cooled cables will be installed between the CDBs and current leads of the DFHX.
- **Quench Protection:** The baseline for quench protection is energy extraction for the long and the short versions of magnets (MCBXFA/B).

1.3. Inner Triplet High Order Correctors

Nine higher order correctors (skew quadrupole, normal and skew sextupole, octupole, decapole and dodecapole) are required to compensate magnetic errors in the inner triplet magnets as shown in Chapter 6. The quadrupole corrector circuit has a rating of ± 200 A whereas all the eight other correctors have a rating of ± 120 A. The circuit layout of these correctors, as shown in Figure 1, contains the following components:

- **Power Converters:** One power converter per circuit (total of 9 circuits) of ratings ± 200 A or ± 120 A will be used. The power converters will be located in the already existing technical galleries of LHC.
- **Cold Powering:** The cold powering interface of the higher order correctors will be located at the level of the corrector package cryostat (i.e. the magnets will be powered through local current leads penetrating the cryostat walls).
- **DC Cabling:** Air-cooled copper cables will be installed between the power converters and the corresponding current lead feedthroughs, located on the corrector package cryostat.
- **Quench Protection:** All magnets except the skew quadrupole are self-protected. The crowbar resistance of the power converter contributes to dissipate the coil's energy in case of a quench or the detection of other powering failures requiring the extraction of the circuit energy. For the skew quadrupole, an additional energy extraction system is required to protect the magnets, whereas the earthing system is connected to the midpoint of the extraction resistor to limit the magnet voltage to ground during a quench.

1.4. *Separation Dipole D1*

For the HL-LHC, D1 in Points 1 and 5 will become a superconducting magnet in contrast with the LHC configuration where D1 is a series of 6 warm magnets, powered in series between both sides of the IP. The circuit layout contains the following components as shown in Figure 1:

- **Power Converters:** One power converter per circuit rated at 14 kA. This converter will be a 1-quadrant type since the mere presence of the DC cabling resistance leads to a discharge in the shadow of the LHC main dipole circuit.
- **Cold Powering:** The D1 circuit will be powered via the sc link, the DFHX and the DFX boxes.
- **CDBs:** A CDB will be introduced to ensure a safe disconnection of the water-cooled cables from the current leads.
- **DC Cabling:** Water-cooled cables will be placed between the power converters and CDB and copper bus-bars with electrically insulated cooling plates between the CDB and the current leads of the DFHX.
- **Quench Protection:** The baseline for quench protection is quench heaters.

1.5. *Recombination Dipole D2*

The new recombination dipole magnet D2 will be a superconducting magnet with two beam apertures. The two aperture coils are powered in series. The circuit layout contains the following components as shown in Figure 1:

- **Power Converters:** One power converter rated at 14 kA. This converter will be a 1-quadrant type since the mere presence of the DC cabling resistance leads to a discharge in the shadow of the LHC main dipole circuit.
- **Cold Powering:** The D2 circuit will be powered via a second superconducting link, dedicated to the powering of the D2 and its corrector magnets. This includes the DFHM installed in the UR, as well as a DFM module for the connection of the sc link to the D2 magnet in the LHC tunnel.
- **CDBs:** A CDB will be introduced to ensure a safe disconnection of the water-cooled cables from the current leads.

- **DC Cabling:** Water-cooled cables will be placed between the power converters and CDB and copper bus-bars with electrically insulated cooling plates between the CDB and the current leads of the DFHM (matching section electrical feed-box) as described in Chapter 10.
- **Quench Protection:** The baseline for quench protection of the D2 magnet is quench heaters.

1.6. *D2 Orbit Correctors*

Four orbit correctors are needed for the D2 recombination magnets (one vertical and one horizontal for each aperture). These corrector magnets will have a rating of ± 600 A. The circuit layout of these correctors contains the following components as shown in Figure 1:

- **Power Converters:** One power converter per circuit rated ± 600 A.
- **Cold Powering:** The D2 orbit corrector circuits will be powered via the DFHM, sc link and DFM (dedicated matching section link as for D2).
- **CDBs:** A CDB per circuit will be introduced to ensure a safe disconnection of the DC cables from the current leads.
- **DC Cabling:** Air-cooled copper cables will be placed between the power converters and the CDBs and between the CDBs and the current leads of the DFHM.
- **Quench Protection:** The magnet will be protected by means of an energy extraction system.

1.7. *The Modified RB Circuit with the 11T Dipole and Trim Circuit*

Two main dipole magnets (MB) will be replaced by 11T cryo-assemblies (MBH) in order to allow the introduction of two additional collimators in the dispersion suppressor regions of sectors 67 and 78. Besides this replacement, a trim circuit over the 11T dipole cryo-assemblies will be added to compensate for the differences in transfer function between the MB and the MBH magnets. The MBH magnet will be powered in series with the main dipole circuit of the respective sector, the 11T dipole trim circuit consists of the following components:

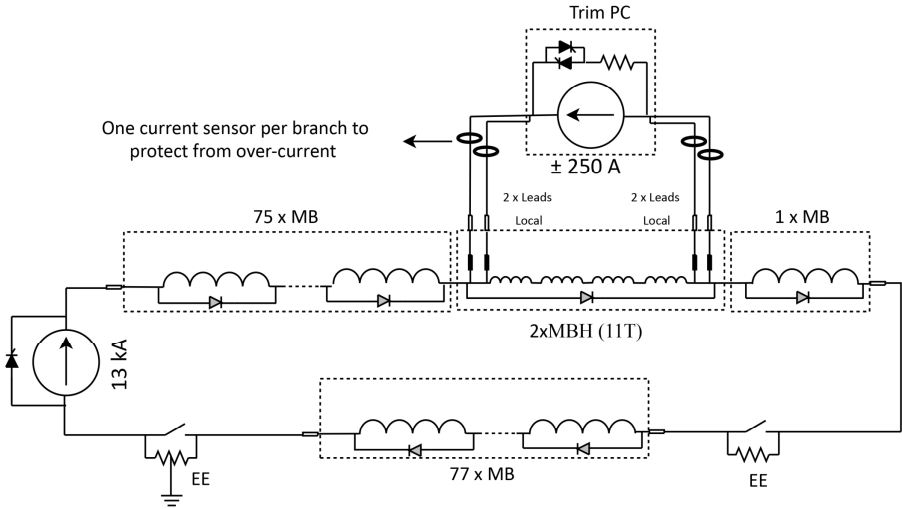


Fig. 4. Circuit layout of the modified RB circuit including the 11T magnet and its trim power converter.

- **Power converters:** One power converter per circuit rated at ± 250 A, see Figure 4.
- **Cold Powering:** The cold powering interface will be at the level of the 11T dipole cryostat (i.e. local powering) with two current leads per polarity.
- **DC Cabling:** Copper cables will be placed between the power converters placed in LHC technical galleries (RR73 and RR77) and the local current leads of the 11T dipole with two cables per polarity due to the number of current leads required.
- **Quench Protection:** The protection scheme used for the 11T dipole magnet is quench heaters. The existing energy extraction system will extract the energy of the RB circuit (the 11T dipole magnet is connected in series with the remaining 153 main dipole magnets). The trim superconducting bus-bars and the current leads are included in the quench protection system of the 11T magnet. When an overvoltage is detected on these elements, the quench heaters of the 11T magnet are fired and consequently the energy extraction systems will be activated.

2. Electrical Test Levels for Magnets and Cold Powering Equipment

Electrical tests are performed in all components belonging to the superconducting magnet chains in order to verify that the integrity of insulation and electrical parameters across the systems are within the expected nominal limits. Electrical tests are also required, among others, in the process to certify acceptance before cryostating, at reception at the test station and before installation of components in the tunnel.

Table 1. Voltage test level requirement for the HL-LHC project

Maximum expected coil voltage at quench (V)	To ground	$V_{sim(ground)}$
	To quench heater	$V_{sim(heater)}$
Test voltage at NOC at 'Manufacturing Facilities and Test Stations' stage (V)	To ground	$V_{test1(ground)} = 2 * V_{sim(ground)} + 500$
	To quench heater	$V_{test1(heater)} = 2 * V_{sim(heater)} + 500$
Test voltage at warm* before first helium bath (V)	To ground	$V_{test2(ground)} = 2 * V_{test1(ground)}$
	To quench heater	$V_{test2(heater)} = 2 * V_{test1(heater)}$
Test voltage at warm* after helium bath (V)	To ground	$V_{test3(ground)} = V_{test1(ground)} / 5$
	To quench heater	$V_{test3(heater)} = V_{test1(heater)} / 5$
Test voltage at NOC at 'Tunnel' stage (V)	To ground	$V_{test4(ground)} = 1.2 * V_{sim(ground)}$
	To quench heater	$V_{test4(heater)} = 1.2 * V_{sim(heater)}$

* T = 20±3 °C and humidity lower than 60%.

Table 1 summarizes the test level requirements defined for the HL-LHC project in order to account for different cryogenic conditions and component stages in its lifetime in addition to including safety factors similarly to what was defined for the LHC [2]. The test strategy is equally applicable for coil-to-ground and coil-to-heater voltages. Moreover, the electrical qualification shall be performed in several steps, the entirety of which is denominated as Electrical Quality Assurance (EIQA). In some cases (i.e. MQXF and 11T Dipole magnet), test voltages at intermediate cryogenic levels are proposed. A

description of the main inputs for the test voltage requirements defined in Table 1 is presented below:

- **Maximum expected coil voltage at quench (V_{sim}):** This value is obtained by performing simulations on the worst-case scenarios for each magnet or circuit.
- **Test voltage at warm before first exposure to helium (V_{test2}):** the test value that must be applied at warm, after manufacturing and at reception, if the magnet has not been previously immersed in helium. This test value shall not be applied if any magnet component has been previously introduced in helium.
- **Test voltage at Nominal Operating Conditions (NOC) at ‘Manufacturing Facilities and Test Stations’ stage (V_{test1}):** the voltage level that the magnet should withstand whenever it is tested at NOC during this stage, in order to make sure that the dielectric material properties are not modified/damaged during the cool down process and after cold test programme.
- **Test voltage at warm after exposure to helium (V_{test3}):** This will be the value to consider whenever the magnet needs to be tested at warm, once the components have been immersed in helium (hence risk of helium pockets).
- **Test voltage at NOC at ‘Tunnel’ stage (V_{test4}):** Once the magnet has been tested and qualified at the first stage, this value shall be applied whenever the components need to be tested at NOC in the ‘Tunnel’ stage.

Figure 5 presents a global flowchart of the test sequences and possible scenarios, starting from the final manufacturing step to machine powering and operation. The flowchart intends to clarify the test levels to apply whenever an EIQA test – represented as hexagons in the flowchart – is required and lists the correct test value. The *final* output of the upper flowchart diagram represents the closure of a short model or prototype magnet test programme, which will not proceed to ‘Tunnel’ stage, contrarily to a series magnet.

The flowchart also includes the approach for magnets required to return back to manufacturing for refurbishment or replacement of some parts. To notice that, despite the several flowchart cycles in the ‘Manufacturing Facilities and Test Stations’ stage which a magnet could experience, the test level at warm V_{test2} should not be performed except for the first time the magnet

is assembled. If testing at warm after helium bath is required, even after returning to manufacturing, it is recommended that the magnet should be tested at the less stringent test level V_{test3} .

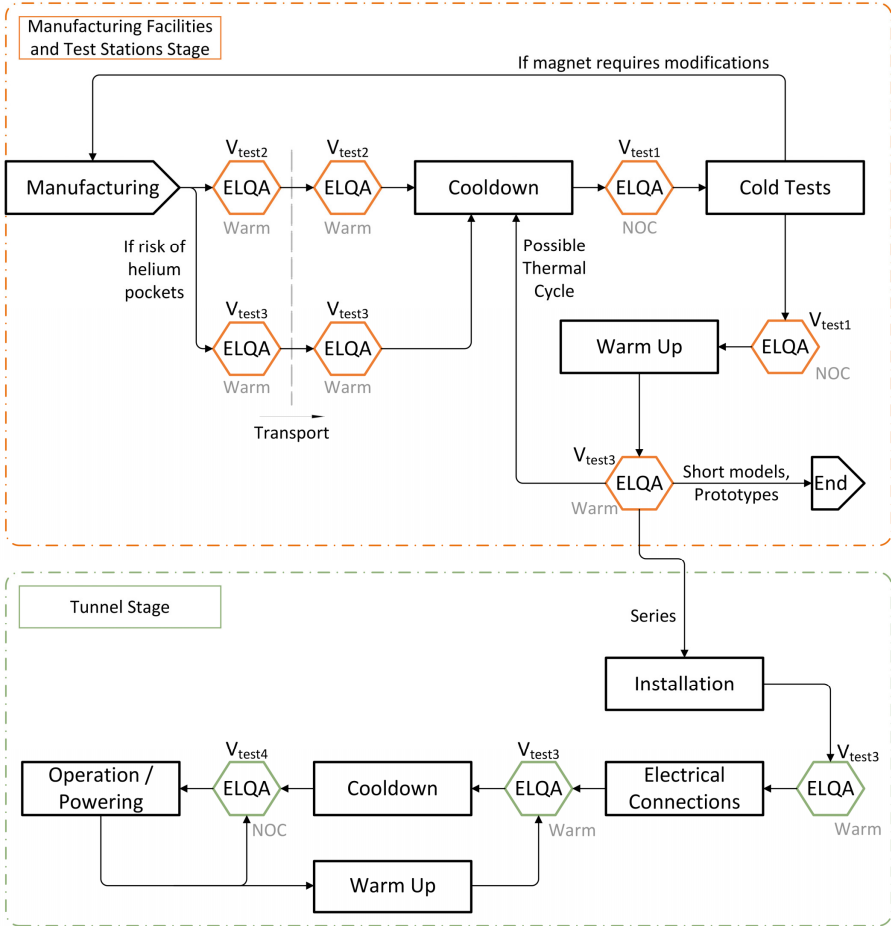


Fig. 5. Flowchart of the defined stages and test levels to apply at each ELQA step.

References

1. E. Coulinge, S. Pittet and D. Dujic, "Design Optimization of Two-Quadrant High-Current Low-Voltage Power Supply," *IEEE Transactions on Power Electronics*, vol. 35, no. 11, Nov. 2020.

2. S. Yammine and H. Thiesen, "Modelling and Control of the HL-LHC Nested Magnet Circuits at CERN," in *20th Workshop on Control and Modeling for Power Electronics (COMPEL)*, Jun. 2019.
3. E. Ravaioli et al., "Quench Protection Studies for the High Luminosity LHC Nb3Sn Quadrupole Magnets," *IEEE Transactions on Applied Superconductivity*, vol. 31, no. 5, pp. 1-5, Aug. 2021.
4. F. Rodríguez-Mateos, "Voltage Withstand Levels for Electrical Insulation Tests on Components and Bus Bar Cross Sections for the Different LHC Machine Circuits," EDMS 90327, <https://edms.cern.ch/document/90327>, 2004-10-27.

Chapter 10

Cold Powering of the Superconducting Circuits

A. Ballarino and P. Cruikshank

CERN, TE Department, Genève 23, CH-1211, Switzerland

This chapter describes the cold powering, i.e. the transfer of current from room temperature to the liquid helium environment, of the High-Luminosity LHC (HL-LHC) [1] magnets. Target R&D was done to develop novel systems relying on long superconducting transfer lines, with up to $|120|$ kA current capability, called Superconducting Links, based on MgB_2 superconductor. The Superconducting Links are part of the so-called Cold Powering Systems that include complex terminations at the two extremities for interfacing with the magnets and the power converters. High Temperature Superconducting REBCO based current leads, housed in a cryostat of novel concept, make the electrical transition between room temperature and 17 K. Two types of system were conceived and designed for the powering of the HL-LHC magnets in the Triplets and the D2 separation dipole in the Matching Sections. Following the successful completion of a staged and focused R&D, which included qualification of prototype systems, series production has been launched. Aspects associated with the integration and operation of the systems in the final LHC configuration were also studied in-depth and optimized.

1. Introduction

The powering of the High-Luminosity magnets requires the transfer of large quasi-DC currents from the power converters, located in the new UR technical galleries, to the LHC machine tunnel [2]. Two different types of Cold Powering System will provide this functionality: the system for the HL-LHC Triplets, which will feed the low-beta quadrupoles, the D1 beam separation

This is an open access article published by World Scientific Publishing Company. It is distributed under the terms of the Creative Commons Attribution 4.0 (CC BY) License.

dipoles and the corrector magnets, and that for the HL-LHC Matching Sections, which will feed the D2 beam recombination dipoles and the corrector magnets. In total, eight systems are needed for integration in the LHC at Point 1 (P1) and Point 5 (P5): two systems, one of each type, right and left of each Interaction Point. They will ensure the electrical transfer from room temperature to the liquid helium environment, and they will span in the LHC underground areas over a physical distance of up to about 120 m.

Two main features distinguishes how the High-Luminosity magnets are powered compared to that in the present LHC configuration:

(1) A significantly higher current has to be transported (up to a total of around 120kA for the Triplets, compared to the currently required 40 kA), because of the high operating current of the low-beta quadrupoles and separation dipoles (in the case of D1, the present resistive low field dipoles will be replaced by superconducting magnets).

(2) The use of hundreds of meters long superconducting MgB_2 lines (hereafter called “SC links”) needed for providing the electrical connection between the current leads, in the UR galleries, and the magnets in the LHC machine tunnel. The need for high-current superconducting power transmission was due to the location of the power converters in the radiation-free UR galleries.

The above requirements called for the development of complex and novel superconducting systems.

2. Cryogenic and Electrical Functionalities

The Cold Powering Systems for HL-LHC provide the electrical connection between the current leads, near the power converters, and the magnets, in the LHC main tunnel. They span the temperature range from 4.5 K to room temperature and rely on cooling via forced flow of helium gas generated, in the coldest part of the system (DF in Figure 1), by liquid helium boil off. Helium gas at low pressure – about 1.3 bara – enters the SC Links in the LHC tunnel and exits, at room temperature (RT), in the UR galleries after having cooled the SC Links and the current leads. The system is designed such that it minimizes the helium mass flow rate and the global cryogenic cost of the refrigeration.

Each Cold Powering System comprises of (see Figure 1):

- a SC Link, i.e. a flexible cryostat with MgB_2 cable assemblies inside;
- at the cold termination of the SC Link (4.5 K), a DF cryostat, which contains the splices between the MgB_2 cables of the SC Link and the Nb-Ti cables passing through the λ -plate and reaching the magnets' cold mass;
- at the warm termination of the SC Link (17 K), a DFH cryostat, which contains the splices between the MgB_2 cables and the REBCO termination of the High Temperature Superconducting (HTS) current leads;
- current leads, incorporating a section made from REBCO HTS material;
- the electrical and cryogenic instrumentation required for operation and protection.

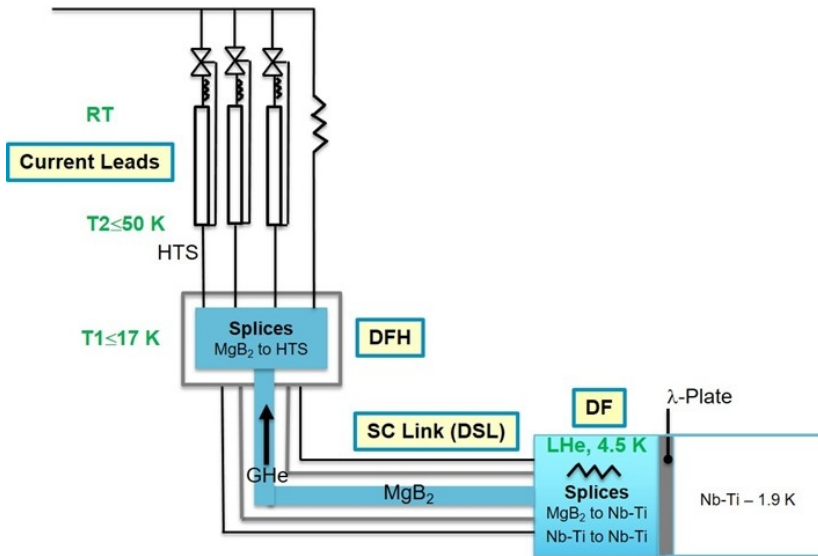


Fig. 1. Schematic of a Cold Powering System and operating temperature range. Helium gas is generated from liquid helium boil off inside the DF cryostat, in the LHC tunnel. It is recuperated at room temperature (RT) at the exit of the current leads.

2.1. SC Links

A SC Link consists of a flexible cryostat housing the MgB_2 cables required for feeding the SC magnet circuits. The cables are made from MgB_2 reacted wire [2-5], developed at an early stage of the project in a collaboration between

CERN and industry. The cables were also initially developed and qualified at CERN, and then industrialized for the final prototypes and series production.

In contrast with superconducting transmission lines developed for electric power distribution, where one (single phase) or a maximum of three (three-phase) cables are contained in the same cryogenic envelope, the SC Links for HL-LHC contain tens of cables rated at different DC currents ranging from a minimum of 0.6 kA up to a maximum of 18 kA. For the powering of the High-Luminosity Triplets, each of the four SC Links to be integrated at LHC P1 and P5 contains four cables rated at 18 kA, three cables rated at 7 kA, and twelve cables rated at 3 kA (see Figure 2) [6]. These cables are twisted together to form a final assembly that has an external diameter of about 90 mm. The 3 kA cables are concentric, i.e. the two polarities of a circuit are part of the same cable and are separated by polyimide insulation. The peak magnetic field experienced by the cables is about 0.8 T. The total current transferred by the assembly of these nineteen cables is about $|120|$ kA DC - 60 kA per polarity. For the powering of the magnets in the Matching Sections, each of the four SC Links to be integrated at LHC P1 and P5 contains three cables rated at 18 kA and eight cables rated at 0.6 kA. The external diameter of the cable assembly is about 60 mm.

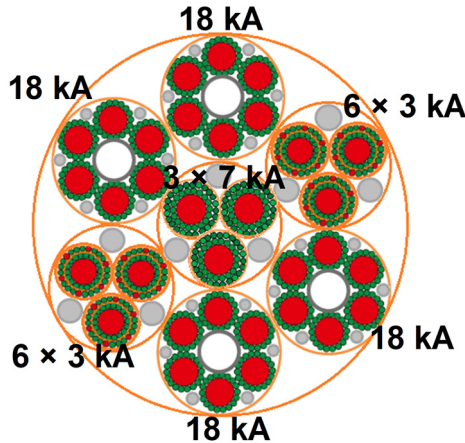


Fig. 2. Schematic of the MgB_2 cable assembly conceived for the powering of the HL-LHC Triplets. Green are MgB_2 wires, red is copper stabilizer, gray are fillers, and orange is electrical insulation. The external diameter of the cable assembly is about 90 mm. To minimize the peak field in the cable assembly, the two 18 kA cables nearby have opposite polarity.

The MgB_2 cables are designed to transfer the maximum design current at a temperature of at least 25 K. The maximum temperature experienced in nominal operating conditions is 17 K.

The cryostat of the SC Links consists of two concentric corrugated pipes. Despite operation at temperatures well below that of liquid nitrogen, it does not include an active thermal shield. The optimization of the Cold Powering System is such that the static heat load of the cryostat, which is about 1.5 W/m, is absorbed by the helium mass flow required for the cooling of the current leads: the cooling of the SC Link itself is therefore fully transparent to the system, in that it uses the enthalpy of the gas, needed for the operation of the current leads, to warm up from 4.5 K to 17 K. A specific development was done with industry to verify the possibility of achieving the desired low static heat load. The advantages of the passive cryostat, which does not have an actively cooled thermal shield and uses two, instead of four, corrugated pipes are: more flexible, and simplifies the global system, e.g. no need of controlling the helium mass flow cooling the shield, and lower cost.

The MgB_2 cable assemblies are pulled inside the cryostats at the surface. They are assembled in one single unit length with no splices inside the SC Link. At one termination, the MgB_2 cables are connected at the surface to Nb-Ti cables: this termination of the SC Link is housed inside the DF cryostats. The Nb-Ti cables operate in a bath of saturated liquid helium. They will be spliced, in the tunnel, to the Nb-Ti busbar passing through the λ -plate (see Figure 1) and connecting to HL-LHC magnets.

2.2. DF Cryostats

The DF cryostats are connected to the colder termination of the SC Links [7,8]. They contain the splices between MgB_2 and Nb-Ti cables (see Figure 1). Their main functionalities are:

- ensuring that the Nb-Ti cables and splices are submerged in liquid helium;
- to generate the gaseous helium required to cool the full length of the SC Link and HTS current leads at the DFH extremities.

These two functions are achieved by maintaining a helium bath, in a fountain configuration, equipped with heaters to create the boil-off. Level gauges are used to monitor and control the helium in-flow from the cryogenic

distribution line (QXL). The design is such that, in case of interruption of the cryogenic supply with the system at full current, all conductors and splices are sufficiently cooled during the current ramp down and do not undergo a resistive transition; the helium vessel and fountain configuration are designed with buffer volumes to ensure adequate autonomy.

Two types of DF cryostats are required: the DFX as part of the Cold Powering System powering the Triplets and the DFM for the Cold Powering System powering the Matching Sections. Eight DF units are needed in total for installation in the LHC underground.

2.3. Current Leads

The current leads are the same type as was used in the LHC machine [9]. They consist of a HTS part, operated between 17 K and 50 K, and a resistive part making the electrical connection in the temperature range between 50 K and room temperature. However, they differ from the HTS current leads in the LHC machine in that:

- The HTS material in the HL-LHC current leads is REBCO tape. In the LHC, BSCCO 2223 tapes, with a silver-gold matrix, were used in the form of vacuum soldered stacks [9].
- The HL-LHC current leads are cooled by the helium gas entering the HTS part of the current leads at about 17 K. The gas is generated at 4.5 K in the DF cryostat and warmed-up, while absorbing the static and dynamic heat loads of the system, to about 17 K, at the inlet of HTS part of the current lead, and to room temperature at the exit of the resistive part of the current leads. In the LHC current leads, the cold termination of the HTS dips into a saturated liquid helium bath and the HTS section is self-cooled, while the resistive part is cooled by forced flow of helium gas made available at about 20 K by the LHC cryogenic system.

Each Cold Powering System requires either nineteen current leads, for the Triplets, or twelve current leads, for the Matching Sections. In total, one hundred and twenty-four HTS current leads are needed to power the HL-LHC magnets.

2.4. DFH Cryostats

The DFH cryostats house the HTS gas cooled current leads. The SC Link cable assembly enters the DFH by means of a shuffling module where the individual cables are separated and guided to the so-called splice box, where the MgB_2 cables are connected to the HTS part of the current leads (see Figure 1). Helium gas at about 17 K, flowing from the SC Link, is channeled over each splice and then through the associated current lead from where it is recovered at room temperature. Regulation of gas flow at each current lead is achieved by control valves. In stand-by conditions, with no powering of the circuits, excess helium flow from the SC Link is diverted through a by-pass channel within the DFH (see Figure 1).

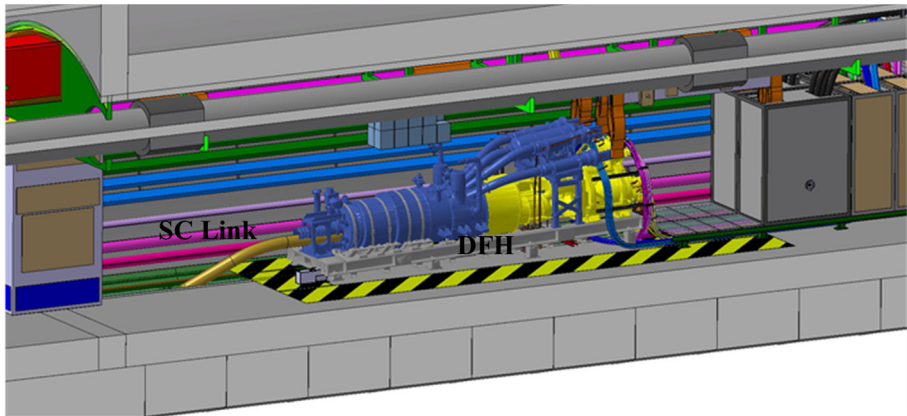


Fig. 3. DFH Cryostat with current leads in the LHC underground. The DFH incorporate nineteen HTS current leads and the corresponding REBCO to MgB_2 splices. It has a total length of about 4.5 meters.

The innovative design of the DFH allows its full assembly with the associated SC Link prior to installation in the underground areas. There are multiple benefits of this concept, such as: allowing the combined cryogenic testing in nominal operating conditions of superconducting cables, splices, current leads, and instrumentation. This will be achieved via a dedicated system test in the CERN SM18 test facility, with no decoupling of the SC Link required for underground installation. During transportation, the SC Link is spooled so that the combined assembly can be handled in a common support frame.

Two types of DFH cryostats are required: the DFHX as part of the Cold Powering System for the Triplets, and the DFHM, a rescaled smaller version for the powering of the Matching Sections. Eight DFH units are needed in total are needed to power the four high luminosity insertions for ATLAS and CMS.

2.5. Instrumentation

Each Cold Powering System incorporates the instrumentation required for its operation. This includes voltage taps, needed for protection – in case of resistive transition of the superconducting parts of circuits or over-heating of the resistive part of the current leads – and monitoring of the splices, and temperature sensors used for helium gas flow control. A large number of voltage tap signals are part of the MgB_2 cable assembly, cabled in bundles.

2.6. Prototype Cold Powering Systems

During the R&D phase, demonstration systems were developed and tested at CERN. The most complete ones were the so-called Demo 2 and Demo 3 systems. Demo 2 was a demonstrator system for the Triplets. It consisted of:

- a 62.5 m long SC Link, i.e. a double wall cryostat, produced in industry, with inside a full cross section MgB_2 cable assembly, cabled in industry with industrial cabling machines;
- a demonstrator DF;
- a demonstrator DFH including two prototype 18 kA REBCO Current Leads designed and constructed at CERN.

Demo 3 was a demonstrator system for the Matching Sections. It used the same components as Demo 2, but the SC Link contained inside the cryostat a full cross section MgB_2 cable assembly for the Matching Sections.

To enable simultaneous powering of several circuits, the SC Links of Demo 2 and Demo 3 could be fed with current from both terminations. In addition to the prototype REBCO current leads in the DFH, a pair of conventional current leads were connected also at the DF side. The extensive campaign of tests performed enabled successful qualification of Demo 2 and Demo 3 systems [10-12]. This included validation of cryogenic, electrical and mechanical performance both in nominal and transient conditions, as well as realization of complex handling and installation that confirmed feasibility of



Fig. 4. View of a demonstration Cold Powering System – Demo 2 – tested at CERN for cryogenic and electrical qualification. The SC Link is 62.5 m long and it contains a full cross section MgB_2 cable assembly of the type needed for the powering of the HL-LHC Triplets.

procedures proposed for final integration of the systems in the LHC underground areas. Attaining world record currents for MgB_2 , Demo 2 and Demo 3 are the first ever power transmission lines made with MgB_2 superconductor and were operated at temperatures of up to 31 K.

3. Integration

The use of the SC Links in the HL-LHC Cold Powering Systems enables the removal of radiation sensitive power converters from high exposure areas of the LHC tunnel and facilitates integration challenges in the densely populated LHC tunnel upstream of the high-luminosity interaction points. The power converters are displaced to the so-called UR underground technical galleries, which are radiation free, and are located near the current leads housed on the DFH cryostats. The SC Links connect the DFH, in the UR technical gallery, to the DF in the LHC tunnel via a sixty-meter-long horizontal UL gallery followed by an eight-meter vertical shaft of about one meter diameter (see Figure 5). In all there are four UL galleries, each with two SC Links routed side by side, one SC Link feeding the Triplets and the other the Matching Sections. To facilitate logistics in the UR galleries and the first meters of the adjoining UL gallery and for safety aspects, the SC Links are placed in covered trenches.

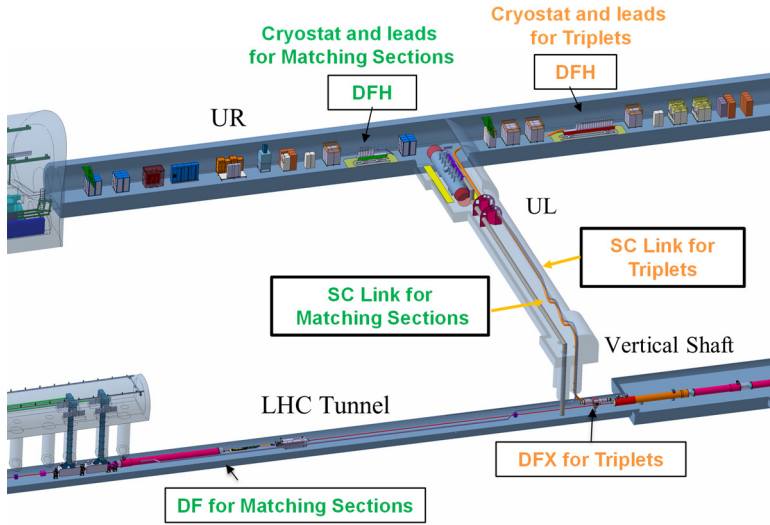


Fig. 5. Schematic view of a Cold Powering System installed in the LHC underground areas.

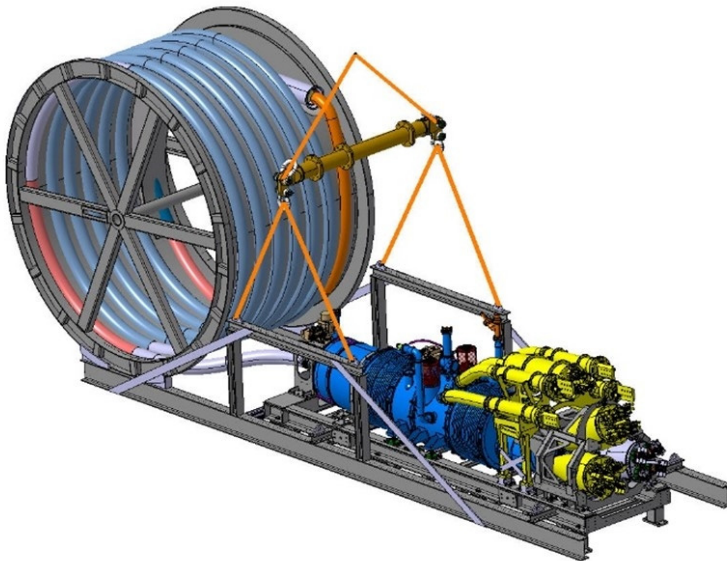


Fig. 6. Configuration of the SC Link after connection to the DFH and ready for being transported in the LHC underground areas. The diameter of the drum onto which the SC Link is spooled is about four meters. The total weight of the system is about 5 tons.

Each SC Link will be lowered into the HL-LHC underground areas spooled onto a drum with a diameter of about four meters and already connected to its DFH. The system as it will be transported is represented in Figure 6. It will be tested at the surface in nominal operating conditions prior to installation.

To cope with thermal contraction of the SC Link cable assembly, each SC Link will be installed with a snaking path having a nominal wavelength of 4 meters and minimum 0.25 m peak-to-peak amplitude of the cryostat axis. Furthermore, to mitigate execution tolerances of the civil engineering infrastructure and link manufacturing, the lateral space allocation is enhanced to allow larger peak-to-peak amplitudes as required.

For the Triplets, the DFX in the LHC tunnel receives the SC Link through its upper flange directly below the eight meters vertical core. The DFM is located above the D2 beam recombination dipole magnet, approximately forty meters from the vertical core; after emerging from the core, its superconducting link is routed about forty meters horizontally in the LHC above the helium transfer line (QXL), again with a snaking path.

4. Safety Aspects

Unlike the existing underground areas of the LHC, the UR underground technical galleries remain accessible during accelerator operation. HL-LHC Cold Powering failure modes leading to cryogenic or electrical hazards in the UR have been identified and analysed [13]. Mitigation by design, safety devices and procedures have been presented and documented [14]. Failure modes leading to helium release and/or electrical arcs are considered up to the Worst Case Incident (WCI) – the extremely rare scenario of a short circuit with electrical arc not detected by the protection system. The analysis demonstrates that access to the UR underground areas remains acceptable in conjunction with technical mitigation, e.g. Oxygen Deficiency Hazard detectors, and organizational measures, e.g. identification of no-stay areas when circuits are powered at nominal current. Mitigation of hazards includes staging of safety valve opening pressures such that helium is preferentially released to the LHC tunnel rather than the UR. Helium and vacuum envelopes, and sensitive instrumentation feedthroughs are protected from accidental damage. Perhaps of most significance, each SC Link with its splices and current leads

will be fully tested under operational conditions before its installation in the underground areas.

5. IT String

The so-called Inner Triplets (IT) String will be built and operated prior to the installation of HL-LHC series components in the underground areas during the Long Shutdown 3, which is presently foreseen to start by beginning 2025. Its configuration is that of an insertion region with the Nb₃Sn quadrupole triplets, the corrector magnets and the D1 separation dipole, with all technical systems required for powering to nominal conditions. The IT String will be equipped with a Cold Powering System comprising the pre-series units of DFH, DF and a 73 meters long SC Link. While the main goal will be to learn about collective behavior of technical systems, significant learning will also come from the installation and commissioning phases as the Cold Powering interfaces to many other HL-LHC systems. Following its exploitation in the IT String, the Cold Powering System will be demounted and stored as spare for the HL-LHC accelerator.

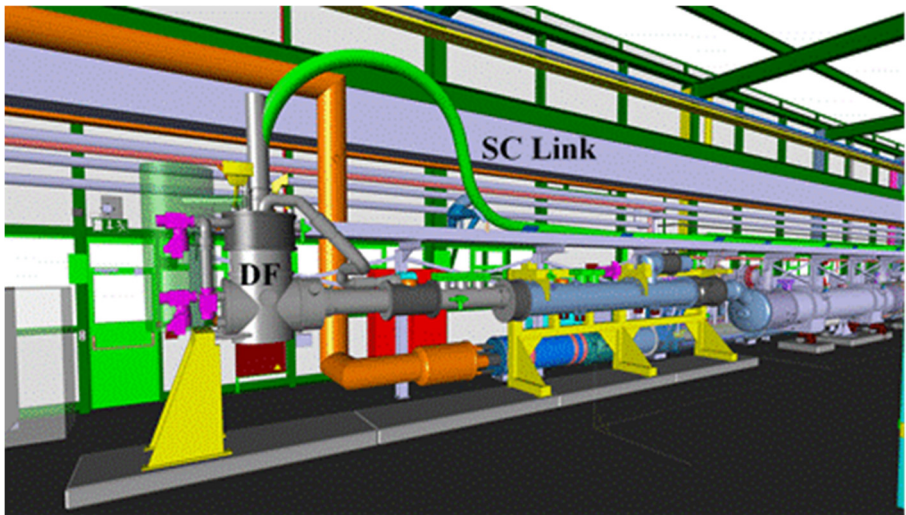


Fig. 7. Configuration of the SC Link after installation in the CERN SM18 cryogenic test facility for the powering of the IT String. After a long horizontal path, the SC Link enters vertically inside the DF, which interfaces with the magnets' cold mass.

6. Conclusions

The Cold Powering Systems for the HL-LHC magnets are based on innovative technologies that include helium gas-cooled MgB_2 electrical transfer lines transporting currents of up to $|120|$ kA over a distance of more than a hundred meters in the LHC underground areas and HTS REBCO based current leads incorporated in compact cryostats of novel concept. The extensive development campaign carried out at CERN was completed in 2020 with the successful qualification of demonstrator systems. Construction of series components has now been launched. The challenging aspects associated with the handling and installation at the surface and in the LHC underground areas have been studied and give confidence in the possibility of integrating the flexible transfer lines in the accelerator environment. Thanks to the compact design, the systems of SC Link, DFH and HTS current leads will be tested at the surface in nominal cryogenic conditions and brought down in the LHC underground areas, after full qualification, already connected.

The novel Cold Powering Systems for HL-LHC attracted the attention of the electrical power transmission community. This included the European BEST PATHS (“BEyond State-of-the-art Technologies for rePowering Ac corridors and multi-Terminal HVDC Systems”) project that studied the potential of MgB_2 SC Links for high power transmission – gigawatt range – in replacement of convention lines in a grid network [15].

References

1. L. Rossi, G Apollinari, I Béjar Alonso, O Brüning and M Lamont, High-Luminosity Large Hadron Collider (HL-LHC) Preliminary Design report CERN-2015-05, (2015).
2. A. Ballarino, Development of superconducting links for the LHC machine, *Supercond. Sci. Technol.* 27, 044024 (2014).
3. A. Ballarino, B. Bordini, S. Giannelli, MgB_2 Transmission Lines for the Large Hadron Collider, *World Scientific Series in Applications of Superconductivity and Related Phenomena*, ISSN 2424-8533, Vol. 2, pp. 581-591, (2016).
4. K. Konstantopoulou et al., Electro-mechanical characterization of MgB_2 wires for the Superconducting Link Project at CERN, *Superconductor Science and Technology* 29(8), (2016) DOI: 10.1088/0953-2048/29/8/084005.
5. M. Sugano et al., Evaluation of Young's modulus of MgB_2 filaments in composite wires for the superconducting links for the high-luminosity LHC upgrade, *Superconductor Science and Technology* 29 (2), (2016).

6. MgB₂ Superconducting Link for the HL-LHC triplets, CERN Accelerating science, (2021). <https://hilumilhc.web.cern.ch/article/mgb2-superconducting-link-hl-lhc-triplets>.
7. A. Ballarino, S. Giannelli, A. Jacquemod, Y. Leclercq, C. Ortiz Ferrer, V. Parma, Conceptual study of the cryostats for the cold powering system for the triplets of the High Luminosity LHC, IOP Conf. Series: Materials Science and Engineering 278 (2017) 012155.
8. W. Bailey, J. Pelegrin, I. Falorio, Y. Leclercq, R. Betemps, V. Parma, A. Ballarino and Y. Yang, Distribution Feedbox for the Superconducting Link (SC Link) and Magnets of HL-LHC, J. Phys.: Conf. Ser. 1559 012076, (2020).
9. A. Ballarino, HTS current leads for the LHC magnet powering system, Physica C 372–376 1413–1418, (2002).
10. World Record Current in the MgB₂ Superconductor, CERN Bulletin, (2014). <http://cds.cern.ch/journal/CERNBulletin/2014/16/News%20Articles/1693853>.
11. Successful tests of a cooler way to transport electricity, CERN Accelerating science, (2019). <https://home.cern/news/news/accelerators/successful-tests-cooler-way-transport-electricity>.
12. Electricity transmission reaches even higher intensities, CERN Accelerating science, (2020). <https://home.cern/news/news/accelerators/electricity-transmission-reaches-even-higher-intensities>.
13. N. Grada, Th. Otto, Failure Modes of the HL-LHC Cold Powering System (WP 6a) Leading to Cryogenic and Electrical hazards, CERN EDMS N. 2303664, <https://edms.cern.ch/document/2303664>.
14. Y. Leclercq, DFX-DSHX-DFHX: safety relief devices calculations, CERN EDMS <https://edms.cern.ch/document/2365987>.
15. A. Ballarino, Ch. E. Bruzek, N. Dittmar, S. Giannelli, W. Goldacker, G. Grasso, F. Grilli, Ch. Haberstroh, S. Holé, F. Lesur, A. Marian, J. M. Martínez-Val, L. Martini, C. Rubbia, D. Salmieri, F. Schmidt, M. Tropeano, The BEST PATHS Project on MgB₂ Superconducting Cables for Very High-Power Transmission, IEEE Trans. Appl. Supercon., 26, No. 3, (2016).

Chapter 11

Warm Powering

M. Martino^a, J.-P. Burnet^b and S. Yammine^c

^a*CERN, SY Department, Genève 23, CH-1211, Switzerland*

^b*CERN, ATS-DO Unit, Genève 23, CH-1211, Switzerland*

^c*CERN, TE Department, Genève 23, CH-1211, Switzerland*

New power converters are needed for the powering of the HL-LHC circuits in the insertion regions of LHC points 1 and 5. In addition to the unprecedented precision, the HL-LHC power converters are also designed to assure very high availability in order to maximize operation time. Moreover, energy storage system will be designed to not only recuperate the magnet energy but to optimize the electrical infrastructure for accelerator applications as well. Furthermore, with an even more complex inner triplet circuit than in the LHC, a new nested circuit control needs to be developed for the HL-LHC. This chapter will present the main novelties and challenges in the development of the HL-LHC power converters.

1. Introduction

The new power converters for HL-LHC are requested to deliver even superior performance with respect to the systems developed for the LHC. The main challenges of the HL-LHC warm powering systems can be summarized as follows:

- high availability to maximize operation time;
- magnet energy storage and optimization of the electrical infrastructure;
- unprecedented precision request for the powering systems;
- handling circuit complexity: new decoupling control strategy.

This is an open access article published by World Scientific Publishing Company. It is distributed under the terms of the Creative Commons Attribution 4.0 (CC BY) License.

To ensure high availability, the architecture of the power converters will be redundant, modular and radiation tolerant in radiation exposed technical galleries. Furthermore, an energy storage system will be designed for the HL-LHC inner triplets whose interest is twofold. Firstly, it will store the magnet energy for optimal energy management. Secondly, it represents a cornerstone for the optimization of the electrical infrastructure for accelerator applications. Furthermore, a new nested circuit control is developed to handle the complexity of this circuit. This chapter will present these main novelties and challenges of the HL-LHC power converters development.

2. High Availability by means of Modularity and Redundancy

Increasing the availability of the power converters is a major challenge to increase time of beam collisions. To achieve high availability, the architecture of modern power converters for particle accelerator has to be highly modular and radiation tolerant if placed in a radiation exposed area.

Two main parts constitute a power converter: the first comprises the power part that includes the power and protection modules, and the second can be categorised as the control and measurement electronics. Concerning the power system of the power converter, there are two main advantages for introducing modularity. Firstly, the power converter can be repaired faster in case of failure while spare parts quantities are minimized. Secondly, the architecture of the power converter with modular power bricks can provide redundancy for operation. In other terms, if a single power brick fails, operation can continue smoothly without triggering a beam dump and repair can be done during a technical stop if possible. This is also known as $n + 1$ redundancy. The power converter internal architecture is illustrated in Fig. 1 including the $n + 1$ parallel implementation of the power part which is common to all power converters for HL-LHC.

The high reliability control electronics based on FGC (Function Generator and Controller) is detailed in [1]. Two types of controllers are foreseen: FG3.2 whose electronics will natively support $n + 1$ redundancy and FGCLite for radiation tolerant power converters (guaranteeing full compatibility with existing LHC ones).

The powering of the corrector magnets typically requires operation in positive and negative current. Three families of 4-quadrant power converters

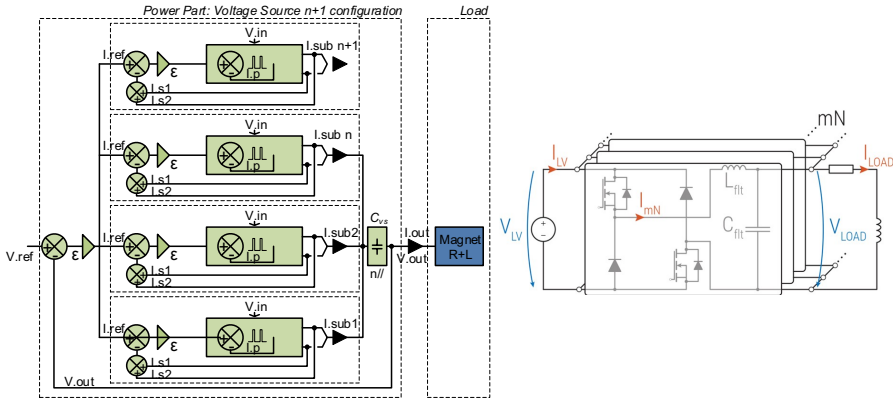


Fig. 1. Architecture of modular and redundant power converters: (left) the control scheme of the parallelization of $n + 1$ power sources to supply the final current to the load and (right) schematic illustration of the power connection of the parallel modular branches (N sub-converters composed on m branches each).

were developed for the LHC machine to cover all corrector magnet families and are rated for 60 A, 120 A and 600 A currents. With HL-LHC project, a new family of 4-quadrant power converter is required rated up to 2 kA (for some corrector magnets and trim circuits). The families developed for the LHC corrector magnets (below 600 A) are made with a unique power module rated at the maximum current, meaning with no modularity nor redundancy. In the higher currents family, the redundancy principle has demonstrated all its interest for the maintenance and for the availability of the machine. In the framework of R2E (Radiation to Electronics) Project, the 600 A converter was redesigned with introduction of redundancy. The power module is rated 400 A and two modules are placed in parallel to reach 600 A (current is limited to 600 A by the rating of the DCCT, DC Current Transformer, which is set to optimize for precision performance). In case of fault, and with an operational current set below 400 A, a power module failure will not stop the operation of the machine, as the second one will keep the magnet current constant. The redundancy is limited to 50% of the maximum current but most of the correctors operate far below their maximum current (in particular D2 correctors nominal current is 394 A so full redundancy is guaranteed up to 7 TeV).

For the new 2 kA family, the same redundancy principle will be used. The power converter will be composed of six power modules rated 400 A in

parallel. They shall be identical or based on the recently developed 400 A power modules.

3. High Current 2-Quadrant Power Converters with Energy Storage

Thyristor based power converters are widely used in particle accelerator high current applications. A main advantage of such a technology is the capability to operate in quadrant 2 where the energy is re-injected to the grid. However, these power converters are highly sensitive to grid glitches and inject harmonics to the grid where proper compensatory measures are needed.

For the HL-LHC, a new family for the 2-quadrant power converters is foreseen to be developed using switch-mode technology in order to keep the same good principles of the present LHC power converters where there is an increased immunity from grid glitches, where modularity can be easily applied, and where relatively low frequency voltage harmonics are not injected to the magnet circuit. However, the switch mode power converters developed for the high current LHC circuits are not bi-quadrant and do not provide the possibility to recuperate the energy stored in the magnet circuit during ramp-downs. The LHC solution relies on dissipating the energy stored in the magnet during ramp-downs in the resistive portion of the circuit i.e. DC cables. Therefore, as an addition to the switch-mode power converters developed for the LHC, energy management systems are studied for HL-LHC to find the best strategy to control the recovered magnet energy.

Moreover, due to several improvements of electrical storage systems like the last generation of batteries whose progress is driven by the development of electric vehicles, an Energy Storage System (ESS) that stores the magnet energy to be re-used in the following ramp-up could be envisaged [2]. The proposed scheme for energy storage is shown in Fig. 2.

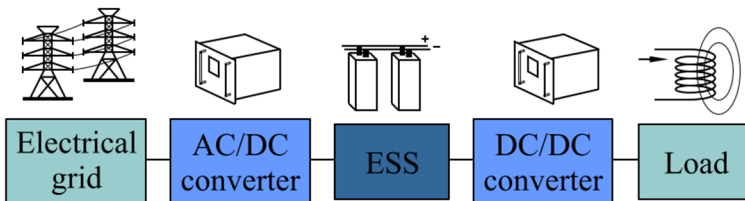


Fig. 2. Selected Energy Storage scheme.

In addition to the proper management of the energy stored in the magnet circuit, the introduction of energy storage brings another major advantage by reducing the power taken from the grid and reducing the infrastructure of the grid connection. The connection to the grid would, therefore, ensure only the losses due to the transmission chain (losses in the power converter, losses in the warm DC cables, etc.), whereas the magnet energy is provided by the electrical storage element. Moreover, the energy flow between grid, the energy storage system and the magnet would be optimized in order to maximize the lifetime of the storage element and its efficiency.

Research at CERN and within collaborations will be focused on power converter topologies, energy management and energy storage systems with a goal to keep reliability as high as possible, while reducing size and improving power quality and efficiency.

Concerning the energy storage system, many technologies were investigated, and the Lithium Titanate (LTO) batteries were chosen as baseline since they provide the best compromise between price, integration size and life cycle for the HL-LHC requirements. Fig. 3 shows an overview of the energy storage technologies (batteries and supercapacitors) and their performance.

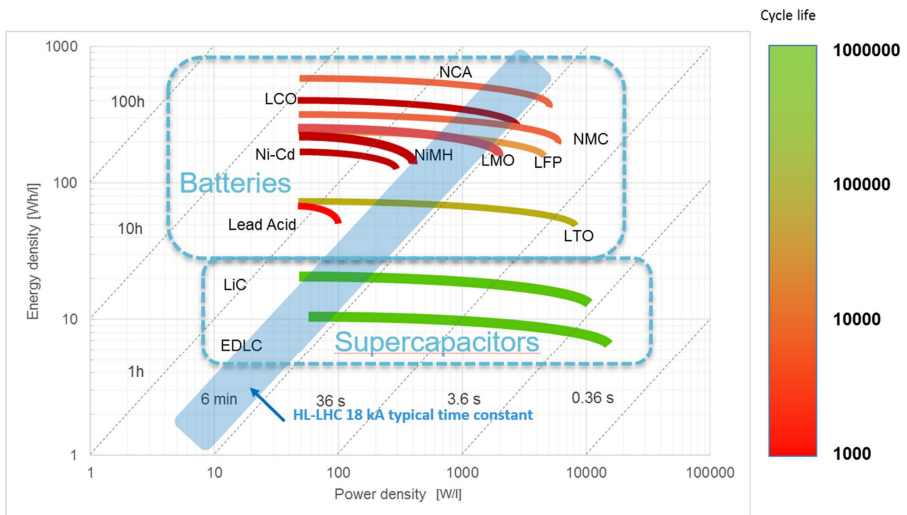


Fig. 3. Energy storage technologies and their performance in terms of energy density, power density and cycle lifetime.

4. Request for Unprecedented Precision

The new power converters for the Inner Triplets Q1-Q2a-Q2b-Q3 series and for the Separation/Recombination dipoles D1 and D2 are required to guarantee unprecedented current precision, and this represents a unique challenge in the design and more specifically in the measurement and control of the power converters' output current. The reader is referred to [3] (Chapter 6B) for proper definition of the main terms (borrowed either from metrology [4] or control theory [5]) used for the specification of power converter performance. As a reminder, throughout this chapter, relative figures are always expressed in ppm (parts-per-million) of a given reference value; for circuits currents the reference value is the rated current of the current measuring device, the DCCT (which usually coincides with the maximum value of current that can be generated by the power converter). As an example, the main power converter of the Inner Triplet Q1-Q2a-Q2b-Q3, the HCRPAFE, is rated 18 kA whereas the operating current at 7 TeV is about 16.5 kA; according to this convention one ppm amounts to 18 mA.

4.1. Accuracy classes

New accuracy classes have been defined for HL-LHC based on an update of the most useful classifications adopted for LHC. The new classification takes into account, as an example, the typical duration of a fill and is the result of a thorough estimation of the actual metrological performance of the current measurement chains of the LHC power converters [6] (the metrological performance turned out to be much better than what was specified for LHC in the design phase [7]). Its full definition is reported in [6]; only the main definitions are reported here (Fig. 4):

- **short term stability (20 min)** - variation of the delivered current (for a constant reference) during a period of 20 minutes, measured up to a frequency of 0.1 Hz
- **stability during a fill (12 h)** - variation of the delivered current (for a constant reference) during a period of 12 h, measured up to a frequency of 10 mHz
- **long term fill-to-fill stability** - variation of the delivered current for the same reference current after one year from the last calibration

- **fill-to-fill repeatability** - Fill to fill variation of the average of the delivered current (for a constant reference), measured over 10 consecutive fills.

All these parameters are defined at constant temperature; the effect of temperature change is then combined to calculate the global figures of merit summarized in Table 1. Furthermore these parameters are defined for a single converter (assuming an underlying statistical distribution), the spread among many converters is also considered in the global parameters, as an example taking the worst measured value on a set of tests or the maximum value for a uniform distribution (summarized Table 1 in column “Assumptions”). Finally, for uniformity of representation the global parameters are expressed as twice the rms, or standard deviation, value (gaussian distribution is not implied though, so twice the rms value does not translate into 95% confidence

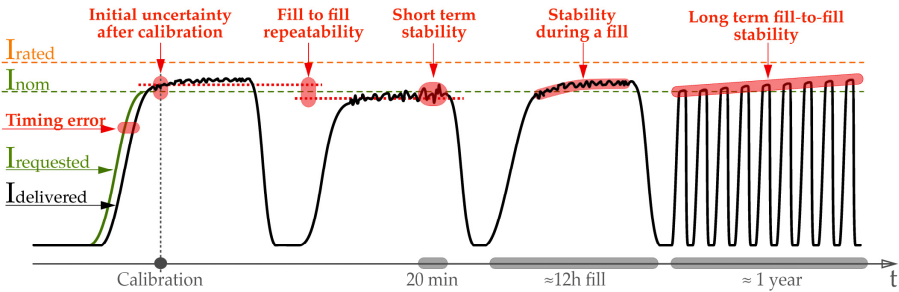


Fig. 4. Illustration of the main “precision performance” parameters together with their different time scales [8].

Table 1. Newly defined HL-LHC accuracy classes (main parameters only).

Metrological Parameter	Assumptions	Units	ACCURACY CLASSES				
			0	1	2	3	4
Short term stability (20 min)	w.c. / normal	2 x rms ppm	0.2	0.4	1.2	2.0	5.0
Stability during a fill (12 h)	max / uniform	2 x rms ppm	1.0	2.0	15.5	34	40
Long term fill to fill stability	max / uniform	2 x rms ppm	9.5	9.5	26.5	56	64
Fill to fill repeatability	w.c. / normal	2 x rms ppm	0.7	1.6	15.0	32	38
Temperature coefficient	uniform	max $ \cdot $ ppm/C	1.0	1.2	2.5	5.5	6.5
12 h Delta T for HL-LHC	constant	max C	0.5	1.0	5.0	5.0	5.0
1 y Delta T for HL-LHC	constant	max C	0.5	1.0	5.0	5.0	5.0

Table 2. Summary of precision requirements per magnet/circuit (including LHC mains for comparison). In the definition of these parameters specific frequency ranges have been considered based on the considerations presented in section 0.

Circuit Name	Equipment Code	I_{DCCT} [kA]	Accuracy Class	Stability [ppm of $I_{\text{DCCT, rated}}$ expressed as twice the rms value]		
				Short Term	During a fill (12 h)	Long Term fill-to fill
RB	HCRPTE	13	1	0.4	2	9.5
RQ(D/F)	HCRPHE	13	1	0.4	2	9.5
RQX	HCRPAFE	18	0	0.2	1	9.5
RTQX1	HCRPBAB	2	2	1.2	15.5	26.5
RTQXA1	HCRPALD	0.06	4	5	40	64
RTQX3	HCRPBAB	2	2	1.2	15.5	26.5
RCBX	HCRPBAA	2	2	1.2	15.5	26.5
RQSX	HCRPMBD	0.6	3	2	34	56
RC(S/O)X	HCRPLBC	0.12	4	5	40	64
RC(D/T)X	HCRPLBC	0.12	4	5	40	64
RD(1/2)	HCRPAFF	14	0	0.2	1	9.5
RCBRD	HCRPMBF	0.6	3	2	34	56
RQ4	HCRPHRA	4	2	1.2	15.5	26.5
RCBY	HCRPLBC	0.12	4	5	40	64
RQ(5/6)	HCRPHSB	5	2	1.2	15.5	26.5
RCBC	HCRPLBC	0.12	4	5	40	64
RTB9	HCRPMBE	0.60	3	2	34	56

interval). A summary of accuracy classes and precision parameters, per circuit, is reported in Table 2.

4.2. Impact on the beam quality – requirements from beam physics

A first thorough review of the precision and accuracy requirements for all circuit types is reported in [8].

4.2.1. DC performance

Requirements are currently based on a rather simplified model of the full transfer function from power converter output (voltage or current delivered to the load) to the magnetic field experienced by the beam. The full transfer function, for a frequency range where stray capacitances can be neglected, can

be modelled as in the following equation:

$$B_b(f) = \begin{cases} T_{B_m \text{ to } B_b}(f) \cdot T_{I \text{ to } B_m}(f) \cdot i(f) & f \leq f_0 \\ T_{B_m \text{ to } B_b}(f) \cdot T_{I \text{ to } B_m}(f) \cdot T_{v \text{ to } i}(f) \cdot v(f) & f > f_0 \end{cases} \quad (1)$$

where $i(f)$ is the (circuit) current noise, $v(f)$ is the power converter's voltage noise, $T_{v \text{ to } i}(f)$ is the overall circuit admittance, as seen at the power converter's terminals, $T_{I \text{ to } B_m}(f)$ is the transfer function from the circuit current to the magnetic field produced by the magnet, $T_{B_m \text{ to } B_b}(f)$ is the transfer function of the cold bore, beam screen etc. (which determines the magnetic field actually seen by the beam) and f_0 is a parameter set by the (digital) current regulation of the power converter. For frequencies below f_0 the current regulation is fully active, and the power converter is operating in "current control" mode, whereas for frequency above f_0 the electrical characteristics of the circuit dominate over the current regulation loop and the converter is considered to be operating in "voltage control" mode. Both $T_{B_m \text{ to } B_b}(f)$ and $T_{I \text{ to } B_m}(f)$ were assumed constant for LHC design. This approximation is rather accurate in the "current control" frequency and f_0 spans from few tenths of Hz to few Hz as for LHC and HL-LHC (performance parameters presented in 4.1 mostly cover this range of frequencies). However, such an approximation is overly pessimistic for higher frequencies where important attenuations due to different loss phenomena are indeed introduced; neglecting them would turn into an overspecification of power converters and finally extra costs. The frequency response $T_{B_m \text{ to } B_b}(f)$ for HL-LHC magnets/beam screens configurations and the LHC mains, has been thoroughly investigated in [9]: the cut-off frequency spans from about 32 Hz for HL-LHC Q1 to about 135 Hz of LHC main quadrupoles. An equivalent electrical circuit model (a generalization of the one presented in [10]) is shown in Fig. 5 (left) assuming that all the circuit current is producing magnetic field (lossless magnet) and assuming $H(s) = T_{i_{B_m} \text{ to } i_{B_b}}(s) = T_{B_m \text{ to } B_b}(s)$. With this simplified model all the effects of the power converter voltage noise $v(f)$ on the field experienced by the beam, B_b , can be translated in terms of the equivalent current i_{B_b} [11]. The overall transfer function is (for $0 \leq k \leq 1$):

$$\frac{i_{B_b}(f)}{v(f)} = \frac{H(f)}{R_c + j2\pi fL[(1-k) + kH(f)]} \quad (2)$$

It is important to highlight that the noise on the circuit current i (measured by the current measurement chain) is greater than the noise on i_{B_b} (for $f \geq f_0$):

$$\left| \frac{i_{B_b}(f)}{v(f)} \right| \cong \frac{1}{2\pi fL} \left| \frac{H(f)}{[(1-k)+kH(f)]} \right| \leq \frac{1}{2\pi fL} \cong \left| \frac{i(f)}{v(f)} \right| \quad (3)$$

In other terms the presence of a conductive beam screen, $|H(f)| \leq 1$, guarantees additional lowpass filtering of the power converter noise with respect to an ideal inductor with the same DC (differential) inductance L . The voltage noise acceptance limits currently considered, for spectral lines (and not for broadband noise) are reported in Fig. 5 (right).

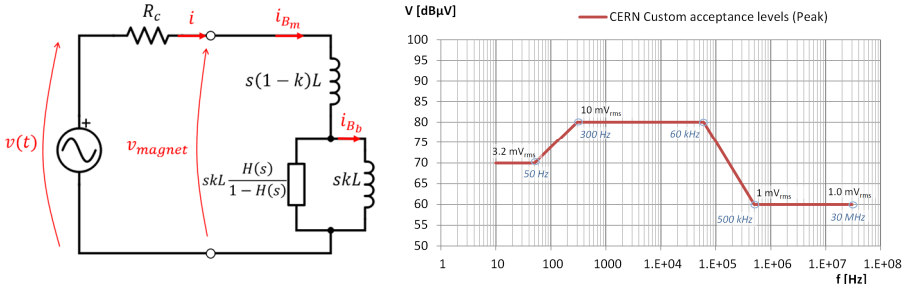


Fig. 5. (Left) Equivalent circuit of a lossless superconducting magnet with a beam screen. (Right) Output ripple limits profile (≤ 50 V DC output): maximum tolerated tone amplitude for a given f .

4.2.2. Tracking

As for LHC [12], and many other accelerators at CERN [13], the digital control algorithm is the RST, a 2-degree-of-freedom polynomial controller, implementing a dead-beat input-output relationship as in the following equation:

$$\frac{i_{ref}}{i} \cong e^{-\tau_d s} \leftrightarrow i(t) \cong i_{ref}(t - \tau_d) \quad (4)$$

In closed loop actual circuit current is approximately a delayed version of the reference current; being a design parameter, τ_d can be corrected for and the error between the two (actual versus “delayed reference”), during ramp-up and ramp-down phases, would be constrained only by the accuracy class of the power converter [6,8,14].

4.3. High precision measurement R&D for Class 0 Accuracy

The principles and main components of the high precision measurement chain of the power converters current are discussed in [1,3] and in more details in [15]. It is assumed here that the uncertainty of the power converter is equal to the uncertainty of the measurement chain in the low frequency range which can be translated into the combined uncertainty of DCCTs and ADCs (Analog-to-Digital Converter). Here, only their R&D aspects will be highlighted.

4.3.1. DCCT

The DCCT is a mature and highly reliable technology based on the concept of “zero flux” where the DCCT current can be assumed to be an extremely accurate fraction of the measurand current that nullifies the flux produced by the latter. Some improvement is however still needed to comply with Class 0 requirements: R&D activities are focusing on improvements on the summing node of the feedback loop of the “zero flux” circuit and, more importantly, in the “current to voltage” conversion stage, as voltage is always used for digitization [15]. In particular the focus is on the high-precision current sensing resistors (a.k.a. the burden resistors) or alternative “current to voltage” conversion technologies as they represent a strategic know-how for CERN [16].

4.3.2. ADC

At the end of the 90’s no ADC on the market was deemed to be able to comply with LHC Class 1 requirements, so a CERN internal development was launched which led to the DS22 (22-bit resolution Delta-Sigma ADC). Given its obsolescence and the new challenge of Class 0 [17] an R&D project was launched for its upgrade. Another direction of R&D is a completely new design based on commercial ADCs with improved performance; this included a thorough survey of the state-of-the-art in high resolution ADCs [18]. Preliminary test results are quite encouraging both for the DS24 (the upgraded version of the DS22 with 2 extra bits of resolution) and for the HPM7177 [19] (the new ADC based on the commercial Delta-Sigma chip AD7177-2, Fig. 6).

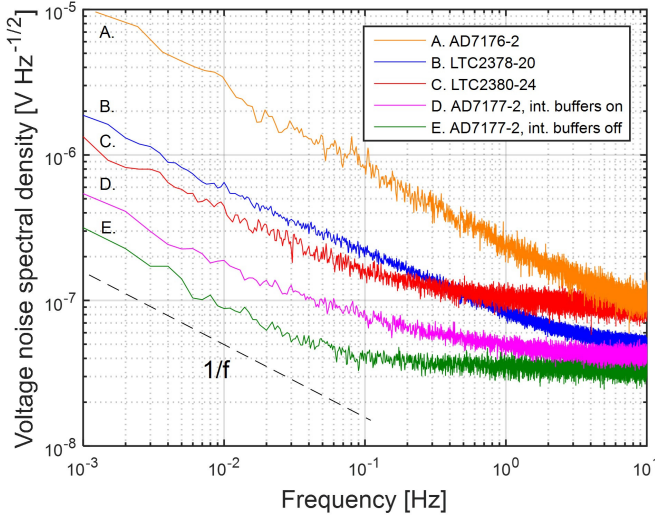


Fig. 6. Comparison of noise performance of the most promising commercial ADCs [19].

5. Handling Circuit Complexity: A New Decoupling Control

The main quadrupole circuits for the inner triplets of LHC comprise three nested circuits [12]. From the circuit control point of view, this connection represents a Multiple Input Multiple Output (MIMO) system where the action on one circuit leads to a change of state of the other connected circuits. The adopted strategy for the control of the LHC inner triplets is based on the decoupling principle and it is realized by means of dedicated hardware.

For the HL-LHC inner triplets, four nested circuits are foreseen as shown on Fig. 7. In addition to the main 18 kA circuit to feed the triplets, two 4-quadrant trim power converters are added over Q1 and Q3 (rated ± 2 kA, ± 10 V) and a 4-quadrant trim power converter over Q1a (rated ± 35 A, ± 10 V) to perform k-modulation (see Chapter 5). Therefore, even if the decoupling strategy is kept for the HL-LHC, a new solution is developed to take into account the new configuration and the new challenge of controlling a three-layer nested circuit in contrast to the two-layer nested circuit of the LHC. Given the upgraded control capabilities of the control infrastructure based on Ethernet, a full software solution is chosen. This software solution includes an inter-FGC communication where information for the different branches of the circuit is shared to perform a global control of the current circulating in each

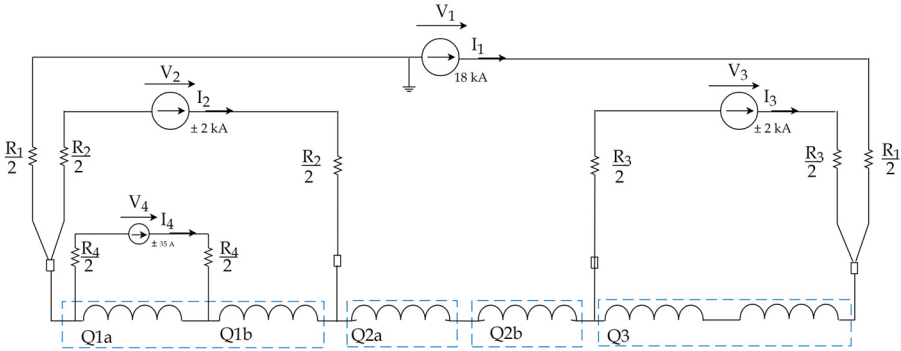


Fig. 7. Inner triplet main circuit simplified powering layout (cold diodes not shown).

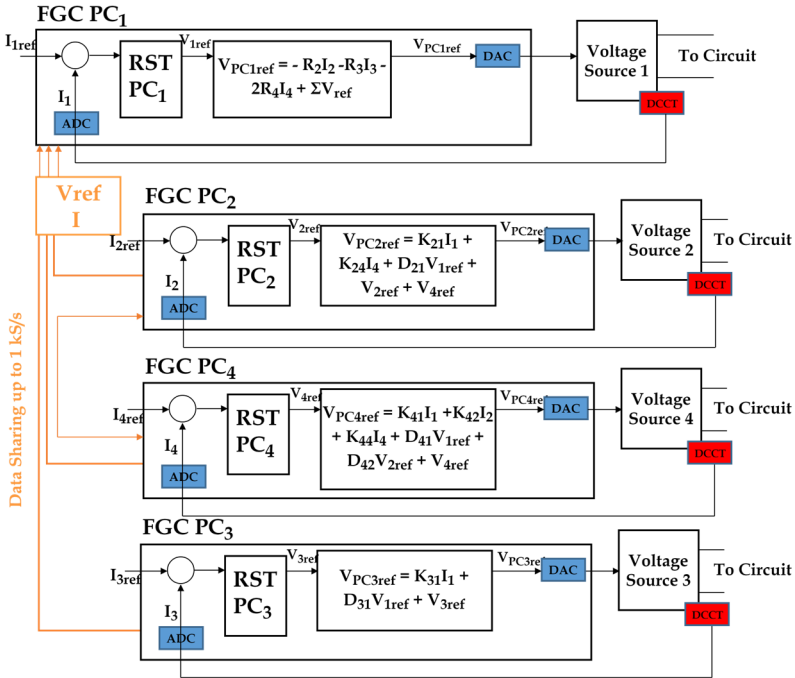


Fig. 8. Decoupling control architecture implementation.

branch. This solution will require the development of new libraries which will extend FGC control capabilities [13] beyond the current Single Input Single Output (SISO) paradigm. The state equation that describes the interaction

between the sub-circuits of the HL-LHC inner triplet is the following (with reference to Fig. 7):

$$\frac{dI}{dt} = \mathbf{A} I + \mathbf{B} V_{ref_PC} \quad (5)$$

where $I = [I_1 \ I_2 \ I_3 \ I_4]^T$ and $V_{ref_PC} = [V_{ref_PC1} \ V_{ref_PC2} \ V_{ref_PC3} \ V_{ref_PC4}]^T$.

In order to decouple the sub-systems, the reference voltages of the four converters need to be calculated as full state feedback as: $V_{ref_PC} = \mathbf{K} I + \mathbf{D} V_{ref_RST}$ by means of two decoupling matrices, \mathbf{K} and \mathbf{D} . This will transform the system from a MIMO (4x4) system into four SISO equivalent systems as follows:

$$\dot{I} = \mathbf{A} I + \mathbf{B}(\mathbf{K} I + \mathbf{D} V_{ref_RST}) = \mathbf{A}_d I + \mathbf{B}_d V_{ref_RST} \quad (6)$$

where \mathbf{A}_d and \mathbf{B}_d are diagonal matrices and the decoupling matrices are calculated as: $\mathbf{K} = \mathbf{B}^{-1} (\mathbf{A}_d - \mathbf{A})$ and $\mathbf{D} = \mathbf{B}^{-1} \mathbf{B}_d$. It can be proven that information sharing is needed between {PC1 and PC2}, {PC1 and PC3}, {PC1 and PC4} and {PC2 and PC4}; a possible implementation of the state feedback is then shown in Fig. 8. Preliminary simulations were performed and show satisfactory results [20].

References

1. I. Béjar Alonso, O. Brüning, P. Fessia, M. Lamont, L. Rossi, L. Tavian and M. Zerlauth, Editors, High-Luminosity Large Hadron Collider (HL-LHC) Technical Design Report v. 1, CERN-2020-010 (2020).
2. R. Garcia Retegui et al., Comparative analysis of interleaved methods for parallel full-bridge structures used in particle accelerator power supplies, AADECA, Argentina, (2018).
3. G. Apollinari, I. Béjar Alonso O. Brüning, P. Fessia, M. Lamont, L. Rossi and L. Tavian, Editors, High-Luminosity Large Hadron Collider (HL-LHC) Technical Design Report v. 0.1, CERN-2017-007-M (2017). DOI: <https://doi.org/10.23731/CYRM-2017-004>.
4. Working Group 1 of the Joint Committee for Guides in Metrology (JCGM/WG 1); Evaluation of measurement data — Guide to the expression of uncertainty in measurement; JCGM 100:2008.
5. W. A. Wolovich, P. Ferreira, Output Regulation and Tracking in Linear Multivariable Systems, IEEE Transactions on Automatic Control, (1979).
6. M. Cerqueira Bastos and M. Martino, HL-LHC Power Converters Requirements, EDMS: <https://edms.cern.ch/document/2048827>.

7. O. S. Brüning, P. Collier, P. Lebrun, S. Myers, R. Ostojic, J. Poole, and P. Proudlock, "LHC Design Report," editors, Tech. Rep. CERN-2004-003-V-1, CERN, Geneva, (2004).
8. D. Gamba et al., Beam dynamics requirements for HL-LHC electrical circuits, CERN-ACC-2017-0101, (2017). <https://cds.cern.ch/record/2298764>.
9. M. Morrone, M. Martino, R. De Maria, M. Fitterer and C. Garion, Magnetic Frequency Response of High-Luminosity Large Hadron Collider Beam Screens, *Physical Review Accelerators and Beams* **22**, 013501 (2019).
10. R. Shafer, Eddy currents, dispersion relations, and transient effects in superconducting magnets, Technical Report No. TM-991, (1980).
11. M. Martino, Admittance model for (superconducting) magnets for power converters control, 6th Power Converters for Particle Accelerators Workshop, Campinas, Brazil, 2018, EDMS: <https://edms.cern.ch/document/2032753>.
12. F. Bordry, D. Nisbet, H. Thiesen, J. Thomsen, Powering and Control Strategy for the Main Quadrupole Magnets of the LHC Inner Triplet System, 13th European Conference on Power Electronics and Applications, Barcelona, Spain, 8 - 10 Sep 2009, CERN/ATS 2010-022 (2009).
13. Q. King, K. Lebioda, M. Margrans de Abril, M. Martino, R. Murillo, A. Nicoletti, CCLIBS: The CERN Power converter Control Libraries, 15th International Conference on Accelerator and Large Experimental Physics Control Systems, Melbourne, Australia, 17 - 23 Oct 2015, pp.WEPGF106 (2015). DOI: 10.18429/JACoW-ICALPCS2015-WEPGF106.
14. D. Gamba et al., Update of beam dynamics requirements for HL-LHC electrical circuits, CERN-ACC-2019-0030 (2019). <https://cds.cern.ch/record/2656907>.
15. M. Cerqueira Bastos, G. Fernquist, G. Hudson, J. Pett, A. Cantone, F. Power, A. Saab, B. Halvarsson, J. Pickering, High Accuracy Current Measurement in the Main Power Converters of the Large Hadron Collider: Tutorial 53, *IEEE Instrumentation & Measurement Magazine*, (2014).
16. M. Cerqueira Bastos, M. Martino, N. Beev and C. Baccigalupi, HL-LHC Power Converters High Precision Current Measurement and Data Acquisition – a Roadmap, EDMS: <https://edms.cern.ch/document/1959515>.
17. P. Arpaia, C. Baccigalupi and M. Martino, Metrological Characterization of High-Performance Delta-Sigma ADCs: A Case Study of CERN DS-22, *IEEE International Instrumentation and Measurement Technology Conference*, Houston, Texas, USA, (2018).
18. N. Beev, Analog-to-digital conversion beyond 20 bits, *IEEE International Instrumentation and Measurement Technology Conference*, Houston, Texas, USA, (2018).
19. N. Beev, Use of a commercial integrated ADC for a metrology-grade digitizer system, *Workshop on new developments in high performance ADCs and their characterization*, National Physical Laboratory, Teddington, UK, (2019).
20. S. Yammine and H. Thiesen, Modelling and Control of the HL-LHC Nested Magnet Circuits at CERN, 20th Workshop on Control and Modeling for Power Electronics (COMPEL), Toronto, Canada, (2019).

This page intentionally left blank

Chapter 12

Machine Protection in the High Luminosity LHC

A. Apollonio^a, P. Bélanger^b, D. Carrillo^c, R. Denz^c, F. Rodriguez Mateos^c,
B. Panev^c, A. Siemko^c, J. Uythoven^c, A. Verweij^c, D. Wollmann^c and M. Zerlauth^d

^a*Former CERN member*

^b*CERN, BE Department, Genève 23, CH-1211, Switzerland*

^c*CERN, TE Department, Genève 23, CH-1211, Switzerland*

^d*CERN, ATS-DO Unit, Genève 23, CH-1211, Switzerland*

In the high luminosity era of the LHC, the energy stored in the two beams will nearly double as compared with the design value of the current LHC and the beta functions will significantly increase in critical locations. In addition, novel equipment like Nb₃Sn based superconducting magnets, crab cavities, hollow e-lenses and others will be installed. These changes require the careful review of known fast failure cases and the study of newly emerging ones. Furthermore, a new generation of magnet and circuit protection systems will be applied in the HL-LHC, which will set a new standard in this field. Finally, a high machine availability will be one of the key factors to achieve the challenging integrated luminosity goals of the HL-LHC era. Therefore, the overall availability targets in terms of the allowed number of beam dumps and fault recovery time are defined.

1. Introduction

In the high luminosity era of the LHC, the bunch intensity will nearly double as compared to the nominal LHC design and, therefore, the stored beam energy will increase to about 700 MJ in each of the two proton beams. At the same time, new accelerator equipment like Nb₃Sn based inner triplet superconducting magnets in IP1 and 5, 11 T dipole magnets for the dispersion

This is an open access article published by World Scientific Publishing Company. It is distributed under the terms of the Creative Commons Attribution 4.0 (CC BY) License.

suppressor regions of IP7, new superconducting separation and re-combination dipoles, as well as crab cavities, hollow e-lenses and other new equipment will be installed. Furthermore, the beta functions will increase at critical locations of the accelerator by up to a factor of four.¹ These changes require the careful review of already known and the study of newly emerging fast failure cases introduced by new equipment and technologies, to ensure that the existing machine protection system can safely abort the beams before damage to the experiments or accelerator equipment occurs. The results of these studies will be described in Section 2. Their impact on the required evolution and upgrades of the LHC interlock systems will be discussed in Section 3.

The protection of the new inner triplet circuits in IR1 and IR5, which are based on large aperture inner triplet Nb₃Sn quadrupole magnets depends on classical quench heaters and the novel coupling loss induced quench (CLIQ) protection system, new radiation tolerant cold power diodes and a newly developed, universal quench detection system (UQDS).¹ Furthermore, a new generation of energy extraction systems based on in-vacuum switches will be used for the protection of corrector circuits of the HL-LHC insertion magnets. The details of these next generation magnet and circuit protection systems will be discussed in Section 4. Section 5 will discuss the aspects of machine availability for the HL-LHC.

2. Fast Failures and Protection in the HL-LHC

In the following two subsections, the criticality of known fast failures resulting from the HL-LHC machine parameters and beam intensities will be summarized and new fast failures described. Finally, the expected impact of beam-dust interactions on HL-LHC performance will be described.

2.1. *Scaling of known fast failures to HL-LHC*

Injection and extraction failures are so-called ultra fast failures and the protection against them depends primarily on the use of passive protection elements. Due to the increase in bunch intensity and beam brightness some of these elements will require to be upgraded for HL-LHC.¹ The impact of particle showers from these protection elements into downstream superconducting magnets during such events has been studied, showing that the expected levels

of energy deposition of up to about 100 Jcm^{-3} in Nb-Ti based magnets are not critical. Degradation of the thermal stability of LHC type Nb-Ti superconductor strands was observed for energy depositions above 2 kJcm^{-3} , which is equivalent to hot-spot temperatures of 680 K. However, no degradation of the critical current density was observed after beam impacts with an energy deposition of about 4 kJcm^{-3} (equivalent to a hot-spot temperature of about 1200 K) in LHC type Nb-Ti strands.²

The normal conducting separation dipoles (D1) in IP1 and IP5 will be replaced by superconducting magnets. Therefore, the very fast impact on the beam due to a powering failure³ in these circuits will be mitigated due to the significantly increased circuit discharge time constants. In case of a quench or another failure in the powering of the new RD1 circuits, the beam dump will be initiated via the Powering Interlock Controller (PIC) and Beam Interlock System (BIS).

The impact of the coherent beam-beam kick on the HL-LHC has been studied and discussed in.⁴ Recently, these results have been reviewed based on simulation models bench-marked with measurement data from LHC Run 2. The results show that a significant orbit distortion of up to 1.6σ has to be expected in the second turn after a sudden loss of the coherent beam-beam kick in HL-LHC.⁵ For this reason, a hardware linking of the beam permits of the two beams at the level of the Beam Interlock System is required for high intensity operation, ensuring that the delay between the dumping of the two beams is limited to a maximum of one turn.

The LHC transverse damper (ADT) can, besides it's main functionality of damping, also be used to coherently excite the full beam or parts of it. At its maximum voltage of 7.5 kV, beam losses will reach critical levels after only 10 turns.⁵ This is sufficient for the beam loss monitors (BLMs) and the beam current change monitor (BCCM) to interlock on beam losses. However, the maximum deflecting voltage of the ADT should not be increased beyond the current value and the functionality of coherently exciting the beam should be limited to only a fraction of the full beam, e.g. 144 bunches, to gain margin between the time of interlocking and reaching critical loss levels. The effect of a partially depleted beam halo due to the use of the hollow e-lens on this time margin must be carefully studied.

A fast symmetric quench of one of the triplet magnets in IP1 has been observed in LHC Run 2. This quench caused a beam dump due to beam losses

after 242 turns. With the significantly increased beta functions in the triplets of IP1 and IP5 during the HL-LHC era, critical levels of orbit excursion due to a similar event could be reached after only about 55 turns.⁵ In such an event, the protection against excessive beam losses entirely depends on the BLMs and the BCCM, as the intrinsic delays of the quench detection system are longer. The criticality of these types of events needs to be reviewed in case of significant changes to the beam optics or the interlock thresholds in the future. Furthermore, the effect of a partial depletion of the beam halo on the protection in case of such an event has to be studied carefully.

2.2. Fast failures related to new equipment

Following a beam induced quench in one of the LHC main dipole magnets, a periodic loss pattern in the LHC collimation region was observed. These losses were traced back to an orbit excursion caused by the skew dipole kick induced on the beam by the firing of the quench heaters of the concerned main dipole.⁶ This observation triggered a detailed study of the expected effects of magnet and circuit protection elements like quench heaters and the novel CLIQ systems⁷ on the circulating beam of HL-LHC. As a result, the connection schemes for quench heater circuits in the new HL-LHC triplet, D1 and D2 magnets as well as the connection scheme of the CLIQ systems in the triplet circuits have been revised to reduce their impact on the circulating beam in a way which is coherent with protection requirements of the superconducting circuits.^{5,6} However, the effects of a spurious discharge of a quench heater in one of the triplet magnets and the D1 as well as a spurious discharge of a CLIQ unit in one of the triplet circuits, would still lead quickly to critical beam excursions. Therefore, the spurious discharges of the quench heaters of these magnets as well as of CLIQ systems have to be interlocked during HL-LHC operation and the extraction of the beams must be ensured within ten turns.⁵

During the first test of crab cavities with proton beams in CERN's Super Proton Synchrotron (SPS) in 2018⁸ dedicated machine protection tests were performed, confirming previously studied failure cases.⁹ The most critical failure case observed was due to resonant beam excitation, when the crab cavity phase crossed the betatron tune.¹⁰ This confirms the need for a fast interlock of the crab cavity voltage and phase in HL-LHC.

2.3. *Beam-dust interactions*

Micrometer-sized dust particulates, made of fine grains of solid matter, are known to have caused intensity drops in electron storage rings (TRISTAN, CESR, HERA, DORIS),^{11–13} pressure bursts in the SuperKEKB positron storage ring¹⁴ and sporadic beam losses as well as magnet quenches in the LHC.^{15–17} The presence of dust contamination in the vacuum chamber of the LHC is not fully understood and seems unavoidable, even with careful cleaning measures.¹⁸ As a result, the same phenomenon is expected to occur in the HL-LHC.

Dust sampling carried out in the vacuum system of the LHC revealed the presence of grains of different materials, with radii ranging from 1 μm to 200 μm . Experimental observations suggest that this dust was introduced during the assembly of the LHC.¹⁹ During operation, dust grains can become charged due to both electron clouds and synchrotron radiation.²⁰ Negatively charged grains are attracted by the beam of the LHC, get ionized by the passage of the high energy protons and are eventually repelled out of the beam. The inelastic interactions of the beam with dust are significant enough so that the resulting beam losses risk triggering the interlock systems and cause magnet quenches. For historical reasons, beam-dust interactions in the LHC are commonly referred to as Unidentified Falling Objects, or UFOs. Throughout LHC Run 1 and Run 2, UFOs were observed sporadically all around the LHC, with no clear source or triggering mechanism. Typical beam losses follow an asymmetric Gaussian profile lasting up to a few milliseconds, with integrated doses between 10^{-7} Gy and 10^{-3} Gy. The main mitigation strategy used to reduce the impact of UFOs was to increase the threshold of certain Beam Loss Monitors (ICBLMs) towards or above the assumed magnet quench limit¹⁶ and to profit from the conditioning effect of high intensity beam operation.²¹

The dynamics of UFOs is mainly driven by the charge-to-mass ratio of the grain, which depends on the ionization rate following the interaction with the beam. On that matter, simulations are in good agreement with measurements and indicate that UFOs must carry an initial negative charge before the interaction with the beam.²² Based on these results, UFO time profiles recorded by the LHC BLMs have been used to narrow down the size and charge distribution of the dust grains which interacted with the LHC beam during Run 2.²³ Moreover, a theoretical model for the charging mechanisms

at play in the beam pipe of the LHC was developed²⁰ and is consistent with the expected charge. However, the triggering mechanism of UFO events is still not understood and remains the main unknown related to the UFO phenomenon, in particular the sporadic release of UFOs around the LHC ring.

3. Interlocks

The machine protection of the HL-LHC will be based on the existing interlock systems already present for the LHC. The core systems related to HL-LHC are the Beam Interlock System (BIS) with the Safe Machine Parameter (SMP) system and the Power Interlock Controller (PIC) for the protection of the superconducting magnets. These three systems will have a consolidation upgrade foreseen for Long Shutdown 3, which allows for making some system changes taking into account new HL-LHC requirements.

The reaction time of the BIS is determined by the physical transmission time of the beam permit signals through optical fibres around the LHC circumference. As there is no clear requirement to have a faster beam abort, the optical infrastructure of the BIS will not be changed. The only change of the system will be the hardware linking of the beam permit signals of the two beams above a certain beam intensity. This will very likely be introduced with the implementation of an additional flag of the SMP system.

The operational limits of the passive beam absorbers (TCDQ, TCDS, TDIS) mainly depend on the intensity of a few bunches hitting these absorbers in the case of acceptable failure scenarios related to the injection or beam abort process. To obtain flexibility in interlocking and machine operation, the new SMP system will produce one or several additional flags related to the maximum bunch intensity.

Many new HL-LHC elements are important and even critical for machine protection, due to the failure modes identified in the section above. For this reason, systems like the crab cavities, will be connected to the BIS as additional interlocks. The hollow electron lens will be connected to the PIC, related to the protection of its superconducting circuits, and by this also to the BIS. A direct link between the hollow electron lens system and the BIS could be required to abort the beam, depending on the operating conditions. In this context, a link between the coronagraph and BIS can also be envisaged.

For the HL-LHC operation with increased beam intensities some areas where the BIS user connections (CIBUs) are located have been identified as requiring radiation tolerant electronics. Also the PIC equipment in the RRs will see larger radiation doses and the new electronics developed for both the CIBUs and part of the PIC electronics will be made radiation tolerant.

4. Circuit Protection

The various superconducting circuits for the HL-LHC (see also Chapter 9) will be protected against overheating due to quenches in several ways, relying on either self-protection, energy extraction, quench heaters, or a combination of quench heaters and CLIQ. Quench detection systems are implemented on all circuits except for some higher-order corrector circuits which rely on self-protection. All quench detection and protection systems are built from robust and reliable components to minimize the risk of overheating and possible degradation of the magnet performance. Realistic failure scenarios are taken into account, and sufficient redundancy in the quench detection and protection systems is implemented to cope with these failure scenarios.

The triplet circuit consists of a series of six quadrupole magnets (Q1a/b, Q2a/b, Q3a/b) powered by a main converter, two 2 kA trim converters, and one 35 A trim converter on the Q1a. Each quadrupole magnet contains eight quench heater circuits and is connected to one CLIQ unit. In case of a quench in any superconducting part of the circuit (magnet, busbar, current lead), the power converters will be switched off and all 48 quench heaters and six CLIQ units are fired, hence quickly discharging the circuit current and depositing the stored energy rather uniformly in the coils of the six quadrupole magnets.

The quench protection of the D1 and D2 magnet circuits relies on eight quench heaters connected in four electrical circuits. The D2 magnet contains as well eight spare quench heaters. In case of a quench in the superconducting magnet, busbar or current lead, the power converter will be switched off and all eight quench heaters are fired. The fast increase of the coil resistance ensures a discharge of the circuit current with a pseudo-time constant of about 0.4 s at nominal current.

The quench protection of the orbit corrector circuits in the inner triplet relies on external energy extraction. In case of a quench in the superconducting magnet, busbar or current lead, the power converter will be switched off and

the energy extraction switch will be activated, hence including an external dump resistor in the circuit. The fast discharge of the circuit current with a pseudo-time constant of about 0.4 s to 1.5 s, depending on the circuit, will ensure sufficient margin for the maximum temperature of the coil and the maximum voltage to ground.

Also the quench protection of the D2 orbit corrector circuit and the quench protection of the inner triplet skew quadrupole corrector circuit rely on external energy extraction. In case of a quench, the power converter will be switched off and the energy extraction switch will be activated, similar to the triplet orbit corrector circuits, hence dissipating most of the magnet stored energy in a dump resistor.

The higher order triplet corrector circuits covering, sextupole, octupole, decapole and dodecapole magnets are all self-protected. In case of a quench in any of the magnets of these circuits, the power converter will shut down and the quench propagation in the coils will generate sufficient resistance to discharge the current fast enough to avoid overheating of the coil. The busbars of these circuits are cryostable.

4.1. Energy extraction systems

The HL-LHC requires the introduction of 44 new energy extraction (EE) systems for protection of the new superconducting triplet and triplet orbit corrector and triplet skew quadrupole circuits. Two classes of systems, one for 600 A and another one for 2 kA have been developed to cover the HL-LHC requirements. The new EE systems introduce a novel DC switching technology, the DC in-vacuum switches, in the quench protection equipment and provide some essential features such as an ultra-fast switch opening, less maintenance and long service life operation.

The energy extraction systems use off-the-shelf in-vacuum interrupters as a switching element. To ensure high-speed reaction during opening, each interrupter is activated by an inductive-dynamic driver (IDD) mechanism based on the Thompson coil principle. The classical configuration of two redundant switches connected in series and controlled simultaneously is implemented for each system. To rupture the circuit current and extinguish the following electrical arc, the in-vacuum switches use a so-called forced commutation method. This technique is based on a strong counter-current pulse gener-

ated during the switch opening process which makes the main current in the vacuum chamber to cross zero and complete the commutation. Pre-charged capacitors controlled through thyristor switches are the sources for the IDD and counter-current auxiliary circuits. Each in-vacuum switch is a single-pole, bipolar device, built in a sliding cassette to facilitate its replacement if necessary, and connected to the power part through flexible bus bars. The power part structure is sized according to the specified current density of 1.6 A/mm^2 . A simple and reliable locking device ensures the opening status when the contact of the interrupter is opened. Optical fibers provide galvanic separation and fast links for trigger signals and digital readouts. For redundancy, two auxiliary low-voltage power supplies with status supervision are used. The switch control unit is using the IGLOO2, flash-based FPGA platform from Microsemi-Microchip to control the operation of the switch. All safety-critical signals and interlocks are redundant.

Dump resistors are custom-made, high-temperature wire wound resistors produced in industry. There are four, permanently connected in a redundant configuration, to ensure the proper resistance level and safe operation in case of a failure in one of them. The resistors are equipped with temperature sensors and thermal switches for supervision.



Fig. 1. In-vacuum switch based 2 kA energy extraction system.

The in-vacuum switch EE systems are integrated in a standard EURO rack with dimensions $600 \times 900 \times 2000$ (see Figure 1). Each 2 kA system is housed in one rack while for the 600 A version, two EE systems share one rack. The power terminals, at the top of the racks fulfil the IP20 norm.

4.2. Coupling loss induced quench systems

The coupling loss induced quench (CLIQ) system is an innovative technology for the protection of superconducting magnets in case of a quench.⁷ Its fast and effective heating mechanism, utilizing coupling losses, and its robust electrical design makes it a very attractive solution for high-field magnets. The CLIQ technology has been successfully applied to magnets of different sizes, coil geometries and types of superconductor.

The CLIQ system is composed of a capacitor bank C, a floating voltage supply S, two resistive current leads CL1 and CL2 connecting the system to the magnet, and a Bidirectional Controlled Thyristor (BCT) package, indicated as TH in Figure 2.

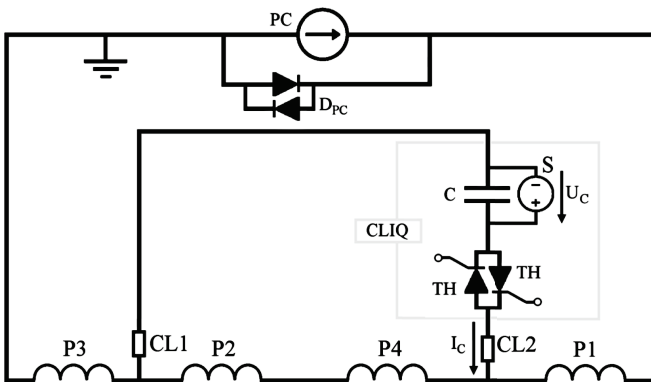


Fig. 2. Schematics of a CLIQ system connected to protect a superconducting magnet.⁷

The capacitor bank is charged by S with a voltage U_C . Upon quench detection, the thyristors are activated resulting in a current I_C discharging through CL2 causing an over-current in magnet poles P2-P4 and an under-current in magnet poles P1-P3 as compared to the nominal current in the magnet as shown in Figure 3.

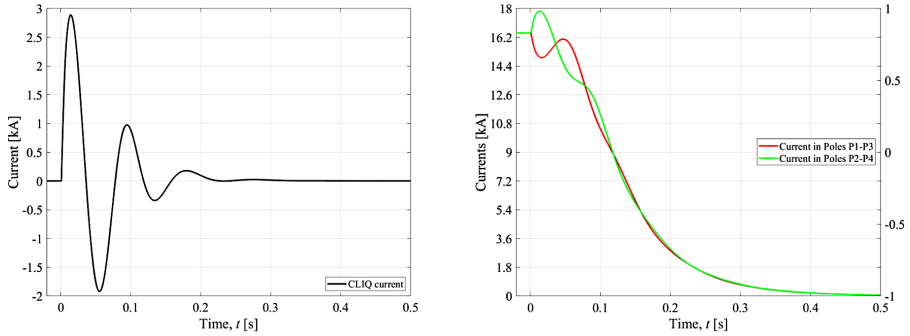


Fig. 3. Oscillation of the CLIQ current I_C (left) and current in the poles of the magnet (right) following the activation of the CLIQ thyristor as simulated with STEAM-LEDET.^{24,25}

So far eleven CLIQ units of industrial-grade have been manufactured and successfully qualified.²⁶ Compared to these, the HL-LHC version will include an improved monitoring system, enhanced electronics and a higher reliability configuration. As core component, each unit will contain a polypropylene film capacitor bank with a total capacitance of 40 mF and nominal operating voltage of 1 kV, hence discharging an energy of approximately 20 kJ into the connected magnet. Figure 4 shows units of the second generation prototypes, manufactured for the tests of prototype magnets.



Fig. 4. CLIQ prototype units of the second generation at the test lab.

4.3. Quench heater power supplies

The quench heater discharge power supplies (QHDS) are the units responsible for energizing the quench heater strips in order to dissipate the energy stored in the magnet into its full volume, hence limiting the hot-spot temperature at the location of the original quench and preventing damage to the coil. Every QHDS consists of a capacitor bank with six aluminium electrolytic capacitors arranged in two sets of three capacitors each. These are connected in series, providing a total capacitance of 7.05 mF. Figure 5 shows a simplified scheme of a QHDS.

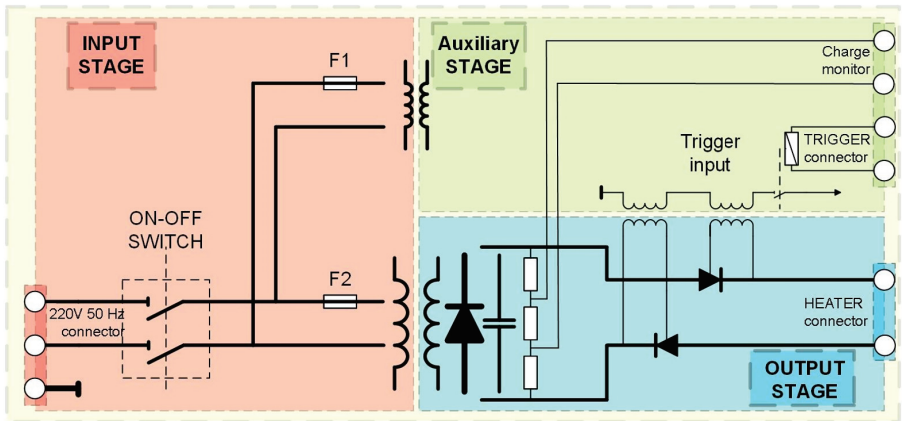


Fig. 5. Simplified electrical scheme of a QHDS unit.

The nominal operating voltage of the capacitors will be 450 V and therefore an overall voltage for the capacitor bank of 900 V is expected to deliver ~ 3 kJ to a single quench heater strip when the unit is triggered by the quench detection system.

Presently, there are over 6000 QHDS installed in the LHC and additional 256 QHDS with improved capabilities and higher reliability will be needed for HL-LHC in order to protect the 11 T dipoles (MBH), the inner triplet magnets in IP1 and IP5 as well as the new separation and re-combination dipoles D1 and D2. Figure 6 shows one QHDS for the protection of the 11 T dipole (MBH).

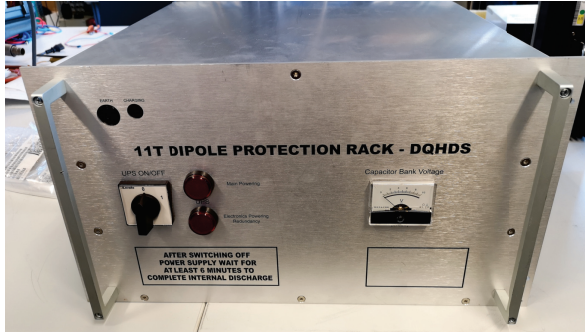


Fig. 6. QHDS for the protection of the 11 T dipole (MBH) magnets.

4.4. Cold diodes

Cold power diodes are an essential part of the protection of the new HL-LHC triplet circuits in IP1 and 5. Their role is to contain voltage and current transients within the cold part of the circuit without transmitting those effects to the superconducting link and the warm elements. Furthermore, they protect the triplet magnets from excessive quench voltages in case of a non-uniform distribution of the resistance in the magnet coils. The cold diodes will be placed in the so-called DCM, a cryostat connecting module which will be installed close to the separation dipole D1. In this position, they will be exposed to high levels of radiation from the interaction point. The expected integrated dose and fluence levels at their position by the end of life are 12 kGy and $5 \times 10^{13} \text{ cm}^{-2}$ in 1 MeV neutron equivalent (n-eq) units.²⁷

Three types of power diodes with different n-base widths were irradiated at cryogenic temperatures up to a 1 MeV n-eq fluence of $2.2 \times 10^{14} \text{ cm}^{-2}$ and 12 kGy in CERN's CHARM facility.²⁸ The forward voltage increased between approximately 43% for the diodes with very thin n-base width to about 83% for the LHC reference diode type at the end of the irradiation campaign when compared to the initial values. Partial annealing of the radiation damage has been observed after a thermal cycle to room temperature. Due to this effect, the increase of the forward voltage due to radiation damage after annealing was close to halved in all three diode types.^{2,29}

Although all three types of diodes were fulfilling the specifications for the protection of the HL-LHC triplet circuit at the end of the irradiation campaign, the most radiation tolerant (very thin n-base width) diode type was

chosen for the series production. This, together with the possibility of partial annealing through a thermal cycle, provides comfortable margin within the uncertainty of the expected integrated dose and fluence levels at the end of life of the triplet circuit.

4.5. Quench detection system

The protection and diagnostics of the new HL-LHC magnets and circuit elements require the development of a new generation of integrated quench detection and data acquisition systems (QDS). For the HL-LHC QDS a unified approach, the Universal Quench Detection System (UQDS), has been proposed³⁰ and several prototypes have been built (see Figure 7).



Fig. 7. UQDS v2.1 crate serving as the baseline prototype for the 11 T dipole (MBH) quench detection system. The crate is not equipped with top covers to illustrate its construction.

4.5.1. UQDS general architecture

As a flexible and generic system, the UQDS architecture is not connected to a specific quench detection algorithm and can be configured according to the requirements of the protected superconducting element. In case of the HL-LHC, the UQDS can be adapted to the needs of various magnet technologies and provide as well efficient protection for the novel MgB₂ high current cable links. One of the key elements of the UQDS architecture are the analogue front-end channels equipped with a high-resolution analogue-to-digital converter (ADC) of the successive approximation type. Insulated DC-DC converters and digital isolators for the serial data interfaces provide galvanic isolation of the analogue channels. In the foreseen implementation up to 16 of such channels connect to a field programmable gate array (FPGA), which processes

the acquired data and executes the quench detection algorithms. To enhance reliability UQDS units are always deployed as a set of two independent units reading signals from two redundant sets of instrumentation voltage taps. Each unit is powered by two independently monitored power supply units. The UQDS units are equipped with dedicated hardware interlocks for the activation of the protection elements of the magnet circuit such as quench heater discharge power supplies, coupling loss induced quench systems and energy extraction systems. The built-in field-bus interface provides the data link to the front-end computers of the accelerator control system.

5. Availability Aspects

Operating HL-LHC with high availability will be one of the key factors to achieve the challenging integrated luminosity goals of the HL-LHC project. The target production is set to 250 fb⁻¹ over 160 days of operation per year, which implies an average daily production of 1.56 fb⁻¹. Considering the latest reference beam parameters,¹ a HL-LHC fill colliding for 12 h (with 7.2 h levelling time) produces about 1.8 fb⁻¹. This allows setting a high-level goal for HL-LHC physics efficiency (i.e. fraction of time in collisions) of 50%, including some margin. Such a goal is in line with LHC performances during Run 2, which reported a physics efficiency of 49% in the years 2016-2017-2018. Nevertheless, a number of factors will make achieving this goal a challenge for HL-LHC. The beam energy will be 7 TeV, potentially affecting availability for what concerns the number of magnet flat-top quenches (or ‘de-training’ quenches) and beam-induced quenches (mainly induced by UFOs, see section 2.3 of this Chapter). In addition, the energy increase implies that many systems will be operated closer to their design limits. The beam dumping system in particular, whose failure rate is known to depend on the operating energy, has undergone major consolidations during LS2, which should reduce its sensitivity to higher operating voltage. Failure rates for the new system will have to be re-assessed during LHC Run 3. Thanks to available margins, it is estimated that the failure rate of power converters will not be significantly affected. In general, failures of electronics due to radiation are not expected to be a major limitation to operation, thanks to the dedicated radiation tolerant designs developed in view of the HL-LHC era, which will allow coping with increased fluences. The cryogenic system will

have to cope with increased heat loads without significantly affecting availability. The deployment of additional cryoplants in points 1 and 5 inevitably implies a higher failure rate for the system. In addition, in order to reach the set integrated luminosity goal, the performance of new HL-LHC systems (crab cavities, superconducting link, Nb₃Sn magnets) will have to be in line with the performance of present LHC systems. Back-up mitigation strategies should be defined in case of significant performance loss due to any of the new systems (e.g. use of flat optics as a back-up for the use of crab cavities). In the HL-LHC era the role of the injectors will already be of even higher importance than for today's LHC. Extended operation with levelling implies shorter optimal fill lengths than for LHC, which requires performing more machine cycles and, thus, more injections. Even with lower demand rates experienced in LHC Run 2, the injector complex has been the first contributor to LHC unavailability. Optimizing the injection process for HL-LHC beams will be a key aspect for achieving the target physics efficiency. LHC Run 3 will already offer the possibility to achieve this thanks to the production of higher brightness beams made possible by the LHC Injectors Upgrade. Figure 8 allows defining the overall availability targets for these systems in terms of number of allowed beam dumps and fault recovery time.

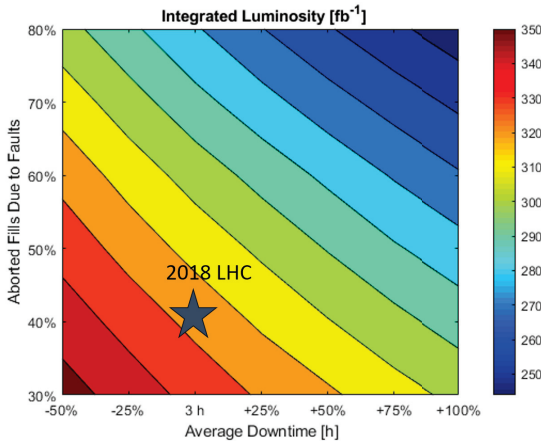


Fig. 8. HL-LHC Integrated luminosity production as a function of average downtime and number of aborted fills due to faults. The star indicates the yearly luminosity production expected in the HL-LHC era, if the HL-LHC will achieve a similar machine availability as the LHC in 2018.

References

1. I Béjar Alonso, O Brüning, P Fessia, L Rossi, L Tavian, and M Zerlauth. *High-Luminosity Large Hadron Collider (HL-LHC): Technical design report*. CERN Yellow Reports: Monographs. CERN, Geneva, 2020.
2. Andreas Will. Damage mechanisms in superconductors due to the impact of high energy proton beams and radiation tolerance of cryogenic diodes used in particle accelerator magnet systems, 2021. Presented on 23 April 2021, to be published.
3. B Goddard, V Kain, R Schmidt, and M Zerlauth. Detecting Failures in Electrical Circuits Leading to Very Fast Beams Losses in the LHC. (LHC-Project-Report-749. CERN-LHC-Project-Report-749):4 p, 2004. revised version submitted on 2004-09-23 10:55:35.
4. Tobias Baer. Very Fast Losses of the Circulating LHC Beam, their Mitigation and Machine Protection, Oct 2013. CERN-THESIS-2013-233.
5. B. Lindstrom, P. Bélanger, L. Bortot, R. Denz, M. Mentink, E. Ravaoli, F. Rodriguez Mateos, R. Schmidt, J. Uythoven, M. Valette, A. Verweij, C. Wiesner, D. Wollmann, and M. Zerlauth. Fast failures in the lhc and the future high luminosity lhc. *Phys. Rev. Accel. Beams*, 23:081001, Aug 2020.
6. Matthieu Valette, Lorenzo Bortot, Alejandro Fernandez Navarro, Bjorn Lindstrom, Matthijs Mentink, Emmanuele Ravaoli, Ruediger Schmidt, Edvard Stubberud, Arjan Verweij, and Daniel Wollmann. Impact of Superconducting Magnet Protection Equipment on the Circulating Beam in HL-LHC. *Proceedings of the 9th Int. Particle Accelerator Conf.*, IPAC2018, 2018.
7. Emmanuele Ravaoli. CLIQ. A new quench protection technology for superconducting magnets, 2015. CERN-THESIS-2015-091.
8. R. Calaga, O. Capatina, and G. Vandoni. The sps tests of the hl-lhc crab cavities. In *Proc. 9th Int. Particle Accelerator Conf. (IPAC'18)*, pages 846–849. JACoW Publishing.
9. Andrea Santamaria Garcia. Experiment and Machine Protection from Fast Losses caused by Crab Cavities in the High Luminosity LHC, 2018. CERN-THESIS-2018-142.
10. B Lindstrom, H Bartosik, T Bohl, A Butterworth, R Calaga, L R Carver, V Kain, T E Levens, G Papotti, R Secondo, J Uythoven, M Valette, G Vandoni, J Wenninger, D Wollmann, and M Zerlauth. Machine protection experience from beam tests with crab cavity prototypes in the CERN SPS. *Journal of Physics: Conference Series*, 1350:012004, nov 2019.
11. Hiroshi Saeki, Takashi Momose, and Hajime Ishimaru. Observations of dust trapping phenomena in the TRISTAN accumulation ring and a study of dust removal in a beam chamber. *Review of Scientific Instruments*, 62(4):874–885, 1991.
12. David Sagan. Mass and charge measurement of trapped dust in the CESR storage ring. *Nuclear Instruments and Methods in Physics Research*, 330:371–379, 1993.
13. F Zimmermann. Trapped Dust in HERA and DORIS, 1993.
14. S Terui, Y Suetsugu, T Ishibashi, M Shirai, K Shibata, K Kanazawa, and H Hisamatsu. Observation of Pressure Bursts in the SuperKEKB Positron Ring. *Proceedings of IPAC 2018*, 2018.

15. G. Papotti, M. Albert, B. Auchmann, E. B. Holzer, M. Kalliokoski, and A. Lechner. Macroparticle-induced losses during 6.5 TeV LHC operation. *Proceedings of IPAC 2016*, pages 1481–1484, 2016.
16. T. Baer, M. J. Barnes, F. Cerutti, A. Ferrari, N. Garrel, B. Goddard, E. B. Holzer, S. Jackson, A. Lechner, V. Mertens, M. Misiowiec, E. Nebot Del Busto, A. Nordt, J. Uythoven, V. Vlachoudis, J. Wenninger, C. Zamantzas, F. Zimmermann, and N. Fuster Martinez. UFOs in the LHC: Observations, studies and extrapolations. *Proceedings of IPAC 2012*, 2012.
17. B. Goddard, P. Adraktas, T. Baer, M. J. Barnes, F. Cerutti, A. Ferrari, N. Garrel, A. Gerardin, M. Guinchard, A. Lechner, A. Masi, V. Mertens, R. Morón Ballester, S. Redaelli, J. Uythoven, V. Vlachoudis, and F. Zimmermann. Transient beam losses in the LHC injection kickers from micron scale dust particles. *Proceedings of IPAC 2012*, 2012.
18. B. Auchmann, J. Ghini, L. Grob, G. Ladarola, A. Lechner, and G. Papotti. How to survive a UFO attack. *Proceedings of the 6th Evian Workshop*, pages 81–86, 2015.
19. P. Bélanger. Unidentified falling objects in the large hadron collider: formation, charging mechanisms and dynamics of dust particulates in a high energy proton accelerator. Master’s thesis, University of British Columbia, 2020.
20. P. Bélanger, R. Baartman, A. Lechner, B. Lindstrom, R. Schmidt, and D. Wollmann. Charging mechanisms and orbital dynamics of charged dust grains in the lhc. *Phys. Rev. Accel. Beams*, 2021. to be submitted.
21. A Lechner, M Albert, B Auchmann, C Bahamonde Castro, L Grob, E B Holzer, J Jowett, M Kalliokoski, S Le Naour, A Lunt, A Mereghetti, G Papotti, R Schmidt, R Veness, A Verweij, G Willering, D Wollmann, C Xu, and M Zerlauth. Blm thresholds and ufos. In *Proceedings of the 7th Evian Workshop on LHC Beam Operation, Evian Les Bains, France*, pages 209–214, 2016.
22. B. Lindstrom, P. Bélanger, A. Gorzawski, J. Kral, A. Lechner, B. Salvachua, and Others. Dynamics of the interaction of dust particles with the LHC beam. *Physical Review Accelerators and Beams*, 23(124501), 2020.
23. A. Lechner, P. Bélanger, B. Lindstrom, R. Schmidt, and D. Wollmann. Characteristics of dust- induced beam losses in the cryogenic arc sectors of the CERN Large Hadron Collider. *to be submitted to PRAB*.
24. Lorenzo Bortot, Bernhard Auchmann, I Cortes Garcia, AM Fernandez Navarro, Michał Maciejewski, Matthias Mentink, Marco Prioli, Emmanuele Ravaioli, S Schps, and AP Verweij. Steam: A hierarchical cosimulation framework for superconducting accelerator magnet circuits. *IEEE Transactions on applied superconductivity*, 28(3):1–6, 2017.
25. E. Ravaioli, B. Auchmann, M. Maciejewski, H. H. J. ten Kate, and A. P. Verweij. Lumped-Element Dynamic Electro-Thermal model of a superconducting magnet. *Cryogenics*, 80:346–356, 2016.
26. Felix Rodriguez-Mateos, David Carrillo, Stavroula Balampekou, Knud Dahlerup-Petersen, Mathieu Favre, Joaquim Mourao, and Bozhidar Panev. Design and Manufacturing of the First Industrial-Grade CLIQ Units for the Protection of Superconducting Magnets for the High-Luminosity LHC Project at CERN. Design and Manufacturing of the First Industrial-

- Grade CLIQ Units for the Protection of Superconducting Magnets for the High-Luminosity LHC Project at CERN. *IEEE Trans. Appl. Supercond.*, 28(3):4702504, 4 p, 2018.
27. R. García Alía, M. Brugger, F. Cerutti, S. Danzeca, A. Ferrari, S. Gilardoni, Y. Kadi, M. Kastriotou, A. Lechner, C. Martinella, O. Stein, Y. Thurel, A. Tsinganis, and S. Uz-nanski. Lhc and hl-lhc: Present and future radiation environment in the high-luminosity collision points and rha implications. *IEEE Transactions on Nuclear Science*, 65(1):448–456, 2018.
 28. Adam Thornton. CHARM Facility Test Area Radiation Field Description. Apr 2016.
 29. Andreas Will, G. D’Angelo, R. Denz, D. Hagedorn, A. Monteuuis, E. Ravaoli, F. Rodriguez Mateos, A. Siemko, K. Stachon, A. Verweij, D. Wollmann, A.-S. Mueller, and A. Bernhard. Characterization of the radiation tolerance of cryogenic diodes for the high luminosity lhc inner triplet circuit. *Phys. Rev. Accel. Beams*, 23:053502, May 2020.
 30. Reiner Denz, Ernesto de Matteis, Andrzej Siemko, and Jens Steckert. Next Generation of Quench Detection Systems for the High-Luminosity Upgrade of the LHC. *IEEE Trans. Appl. Supercond.*, 27(4):4700204, 2017.

This page intentionally left blank

Chapter 13

Interface with Experimental Detector in the High Luminosity Run

H. Burkhardt^a and F. Sánchez Galán^b

^a*CERN, EP Department, Genève 23, CH-1211, Switzerland*

^b*CERN, BE Department, Genève 23, CH-1211, Switzerland*

We describe the main general changes as relevant for the experiments, and in particular the changes in the machine-detector interface (MDI) region extending from the merging of the LHC beampipes into a single experimental chamber before the inner triplet to the start of the experimental beampipe in the experimental cavern. The geometry of this region is optimized to provide a maximum decoupling of the activities in the tunnel and inside the experimental caverns. Massive absorbers are used to strongly reduce the flux of secondary particles produced in collisions in the interaction region into the tunnel, and at the same time help to protect the experiments from beam induced losses and backgrounds. This chapter explains the main challenges within that region and how they will be solved to cope with the new requirements coming from the luminosity upgrade.

1. Introduction

The machine upgrade for high luminosity requires major changes on the machine side. Key ingredients for the luminosity increase are larger apertures in the focusing sections around the experiments and higher beam intensities.¹

The experiments are upgraded for reduced inner beam pipes with more powerful vertex detectors. This is important for physics and essential for the increased pile-up. Other key design considerations for the upgraded LHC detectors include longevity at increased radiation levels, minimisation of activation and exposure to personnel by remote handling.

This is an open access article published by World Scientific Publishing Company. It is distributed under the terms of the Creative Commons Attribution 4.0 (CC BY) License.

As is often the case in machine-detector interfacing, these are to some extent conflicting requirements, which require a coherent planning for experiments and machine together.

1.1. Overview of the main changes relevant for the experiments

In this chapter, we discuss more generally hardware changes of relevance to the experimental regions, with respect to the original design of the LHC as described in the LHC design report.² The changes required for the high-luminosity upgrade and the requests and planning of the experiments for the future running of the LHC have been discussed in several joint machine-experiments workshops.^{4,5}

Figure 1 shows the schematic layout of the LHC with its four interaction regions.

The HL-LHC design is for four experiments, the two high-luminosity experiments ATLAS and CMS at IR1 and IR5, and the ALICE and LHCb experiments installed at IR2 and IR8.

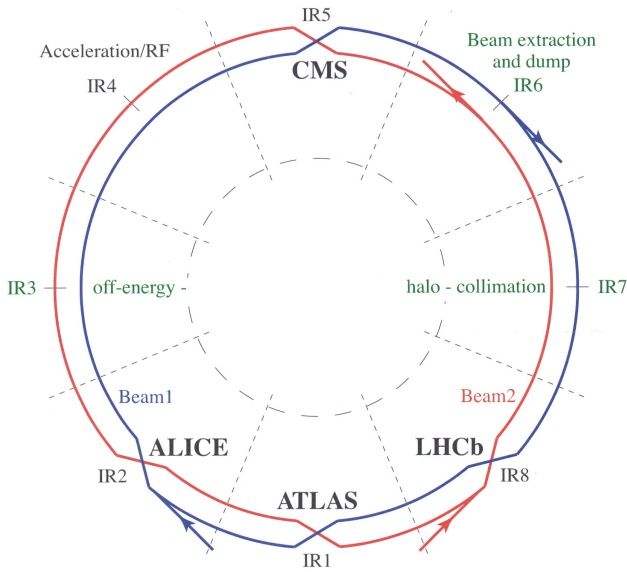


Fig. 1. Schematic layout of the LHC with its four interaction regions which provide collisions to the ALICE, ATLAS, CMS and LHCb experiments.

Table 1. Target luminosities \mathcal{L} for p-p operation for the LHC and HL-LHC. For the HL-LHC, the ATLAS and CMS target luminosities include luminosity leveling which will allow for constant luminosities for the first hours during a fill.

IR	LHC $\mathcal{L}, \text{cm}^{-2}\text{s}^{-1}$	HL-LHC $\mathcal{L}, \text{cm}^{-2}\text{s}^{-1}$	Experiment
1	1×10^{34}	5×10^{34}	ATLAS
2	1×10^{31}	1×10^{31}	ALICE
5	1×10^{34}	5×10^{34}	CMS
8	4×10^{32}	2×10^{33}	LHCb

Table 1 shows the target luminosities for the experiments in proton-proton collisions in the LHC as originally designed, and for the high-luminosity upgrade. The main luminosity upgrade is for the interaction regions IR1 and IR5 and will be implemented in the long shutdown LS3.

The ALICE and LHCb experiments installed in IR2 and IR8 already had significant detector upgrades during LS2 in 2020. LHCb has asked for a luminosity increase to $2 \times 10^{33} \text{cm}^{-2}\text{s}^{-1}$, to be implemented in RUN3. This is possible without major changes to the magnet layout in IR8 and the required detector and vacuum beam pipe upgrades can be implemented in the long shutdown LS2. It is accompanied by an improved shielding (TANb at D2), to minimize the impact of the increase in radiation and heating of cold machine elements. A second upgrade by LHCb targeting luminosities of $1\text{--}2 \times 10^{34} \text{cm}^{-2}\text{s}^{-1}$ after LS4 is currently being studied.^{6,7}

The low target luminosity for ALICE in pp operation requires collisions with large transverse offsets. The future plans for the ALICE pp programme are described in.⁸ The possibility to install an entirely new detector in IR8 in LS4 for heavy ion operation at significantly increase luminosities has been proposed⁹ and is presently under study.

In discussions with all experiments in the HL-LHC coordination working group during 2013, it was confirmed that the LHC machine upgrade design can be considered as dedicated to high-luminosity and should not be constraint by other modes of operation, which can be completed before LS3. High-beta* ($\gg 30 \text{m}$) operation is not planned after LS3. The experimental programs of the smaller dedicated forward experiments (LHCf, TOTEM) requiring special low luminosity LHC operation does not extend beyond LS3. At the same time, there is a general consensus that new ideas to fully exploit the unique physics potential of the HL-LHC without compromising its main goals should always

be welcome. Several smaller new detectors FASER, SND and MoEDAL have been proposed and will likely operate in future LHC runs, mostly in passive, parasitic mode.^{10–12}

From year 2016 in RUN2, forward detectors (Roman Pots) were successfully used in standard physics to tag forward protons at distances of 220–240 m from IP1 and IP5.¹⁴ TOTEM has now been integrated into the CMS collaboration, and expressed a strong interest for a continued operation of roman pot detectors in the space available near Q6 and possibly 420 m in standard HL-LHC runs.¹³

The magnet layout in IR1 and IR5 will change significantly. This is shown schematically in Figure 2 for the first 80 m from the interaction point and discussed in detail in the following Chapter.¹⁵ The distance of the first quadrupole magnet (Q1) from the IP will remain the same (23 m) as before the upgrade.

The most relevant machine modification for the experiments will be the installation of the new large aperture triplet magnets Q1-Q3 in IR1 and IR5. The inner coil diameter of these triplet magnets will increase by roughly a factor of two from 70 mm to 150 mm.

As presently the case, the magnet layout will be the same for IR1 and IR5, and also remain approximately left/right anti-symmetric with respect to the interaction points.

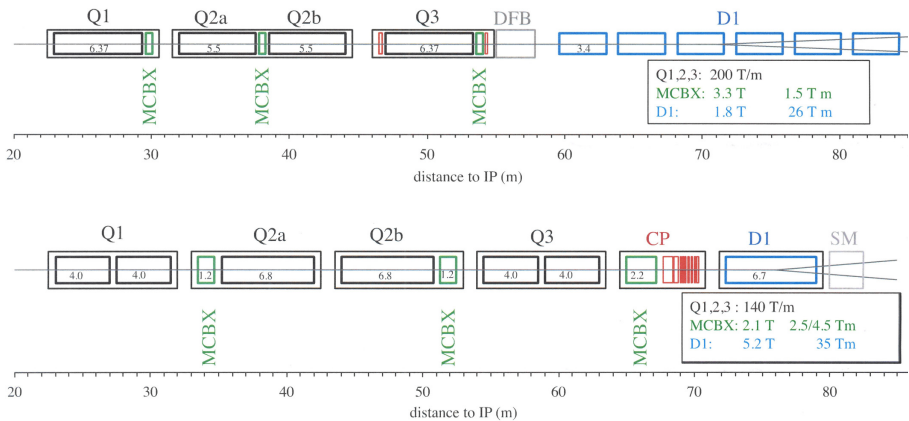


Fig. 2. Schematic magnet layout for the current LHC (top) and the HL-LHC in IR1 and IR5 (bottom) up to first separation magnet D1.

2. Experimental Beam-pipes

The four large experiments have asked for reductions of the diameter of the central beam pipes. Table 2 summarizes the original and reduced inner beam pipe radii. For ATLAS and CMS the new reduced aperture beam pipes were installed during LS1 and successfully used in LHC RUN2. The LHCb VELO¹⁶ is movable. It is only closed in stable physics to the value shown in the table, and retracted to 30 mm otherwise. Based on aperture studies, the good experience in RUN2 and detailed simulations including failure scenarios, it was agreed that the reduced central chamber sizes can be kept for HL-LHC. A further decrease from 19 mm to 16.5 mm radius for the central piece of the ALICE beam pipe over 500 mm length has been requested for LS3 and is currently under study.

Table 2. Original and reduced inner beam pipe radii at the IPs.

IP	original r_{\min} mm	reduced r_{\min} mm	Experiment	when
1	29	23.5	ATLAS	LS1
2	29	19	ALICE	LS2
5	29	21.7	CMS	LS1
8	5	3.5	LHCb, VELO	LS2

3. Failure Scenarios and Experiments Protection

Active machine protection, based on continuous beam loss monitoring (BLM) and fast beam dump (within 3 turns) has already been proven to be essential and reliable for the present LHC. It will be even more important for the HL-LHC. In addition to the protection of the machine elements described in Chapter 12,¹⁷ we will have to rely on active protection for the experiments. This implies, that we have to identify all relevant failure scenarios which may result in significant beam losses to the experiments, and to make sure that these abnormal beam losses can be detected sufficiently fast and beams be dumped before they cause any significant damage to the experiments.

Detailed studies with particle tracking have been performed for the HL-LHC. Most critical for experiments protection is the operation at top energy with squeezed beams. The potentially most relevant failures scenarios for the HL-LHC are:

- Asynchronous beam dumps¹⁸
- Crab cavity failures¹⁹
- Mechanical non-conformities, i.e. objects which accidentally reduce the aperture (example RF-fingers) or UFO's (dust particles falling through the beam) resulting in showers with local production of off-momentum and neutral particles around the experiments.²⁰

Other more or less dangerous scenarios do exist but are not expected to pose significant extra risks to the experiments, not covered by the machine protection and fast dump systems. These include:

- D1 magnet failures. The present 6 warm D1 magnets at either side of IP1 and IP5 will be replaced with single superconducting D1 magnets with longer time constants well within the capabilities of the machine protection.
- Injection (kicker) failures and grazing beam impact on injection elements (TDI).

The injection and dumping systems are described in Chapter 19.²¹

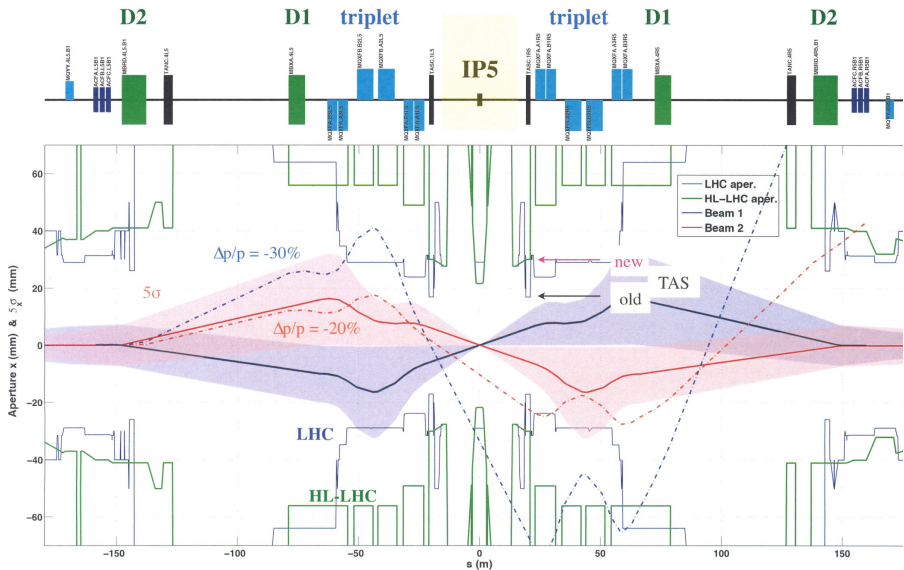


Fig. 3. Schematic view of IR5 with beam envelopes and apertures.

Figure 3 shows a schematic view of IR5 with beam envelopes and apertures. Beam-pipe apertures are shown as lines as implemented in present simulations, both for the LHC as originally build for RUN1 (dark blue lines), as well as for the HL-LHC after LS3 (green). The coloured bands show 5σ beam envelopes for $\beta^* = 15$ cm as relevant for the HL-LHC. Two off momentum tracks with $\Delta p/p = -20\%$ and -30% are also shown. A -30% track originating at 150 m from the interaction point (originating by collisions of beam particles with dust particles, for example) will pass through the enlarged HL-LHC apertures and directly hit the central experimental beam pipe.

Figure 4 illustrates the beam envelope growth induced by an immediate 90° phase jump on a single crab cavity.

High amplitude particles are removed in the LHC by the collimation system in dedicated cleaning sections far from the experiments.²² The experience in LHC RUN1 and RUN2 and detailed simulations have shown that the LHC collimation and machine protection systema are very effective to protect the machine and experiments from uncontrolled beam losses, but also require a continuous follow up of safety considerations and safe operational procedures.

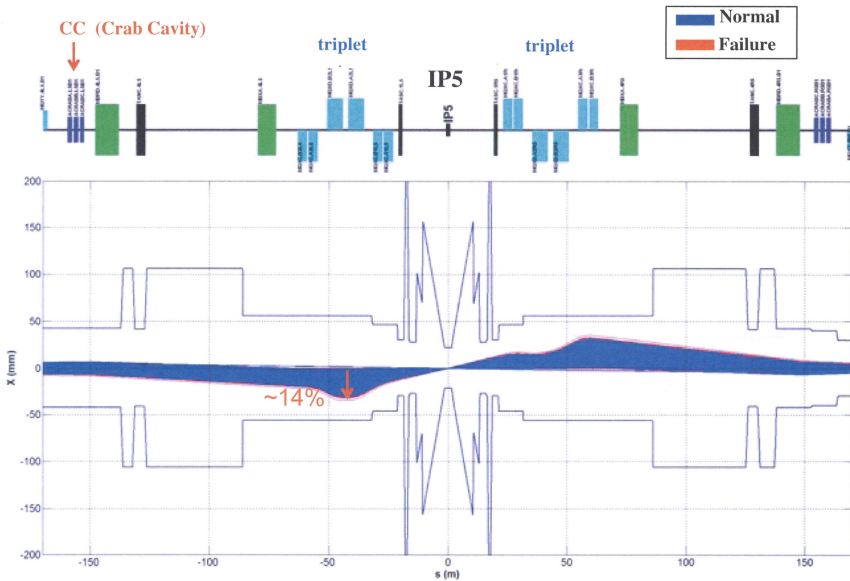


Fig. 4. Schematic view the beam envelope growth induced by a crab-cavity failure, resulting in a growth of 14% within 5 turns.

4. Machine Induced Backgrounds

Machine induced backgrounds in the LHC are generally dominated by beam gas scattering. Beam gas backgrounds scale with the beam intensity and vacuum pressure and are to a large extent generated locally in the straight section and dispersion suppressors around the experiments. Under normal conditions, they depend only weakly on optics details and collimator settings.

Background conditions have generally been very good in RUN1 and RUN2 of the LHC.²³ Signal to background ratios of the order of 10^4 were observed in good running conditions in ATLAS and CMS.

For ALICE, which operates at much lower luminosity, machine induced backgrounds are more critical. Excellent vacuum conditions (pressures below 5×10^{-9} mbar) are essential for ALICE. During part of the proton-proton operation in 2012, machine induced backgrounds in ALICE were too high to permit data taking. This was related to heating in the injection absorber (TDI) region and has already been improved for RUN2 and is not expected to cause problems for the upgraded injection and vacuum systems relevant for HL-LHC.

Continued efforts to monitor, understand and minimise backgrounds are important for all experiments. Increases in intensity and luminosity generally translate also in more heating, out-gassing and potentially increased backgrounds. There have already been major changes in running conditions in the LHC between RUN1 and RUN2. Potential reasons for an increase of backgrounds between RUN1 and RUN2 were:

- more synchrotron radiation, by the increase of beam energy from 4 to 6.5 TeV at beginning of RUN2
- electron cloud due to reduced bunch spacing, main step 50 ns \rightarrow 25 ns at beginning of RUN2
- electron cloud due to increased bunch intensities
- local heating from increased intensities.

While these effects were in fact observed, their effect was largely mitigated by many improvements on hardware and also generally improved understanding and control of the LHC, such that backgrounds in LHC2 were not an issue and in some case even better than in RUN1 (in particular for ALICE). Towards the end of RUN2, there have been first signs of a possible background

increase induced by losses on tertiary collimators for operation at low β^* . This is at present followed up by simulations comparing both LHC and HL-LHC conditions and benchmarking with the RUN2 observations of the LHC experiments, with the aim to assure that the background conditions for the experiments remain excellent also for HL-LHC.

5. Engineering Challenges

As explained in the previous sections, the luminosity reach of ATLAS and LHC at the HL-LHC era implies new constraints for the protection of the inner triplets from the machine debris. One of the most challenging comes from the fact that activation levels will increase a factor of 15–30 from the 2015 values (LS1), affecting both radiation tolerance of equipment and the ability to perform routine maintenance operations. Figure 5 shows the residual dose rates at a standard working distance in the tunnel.²⁴

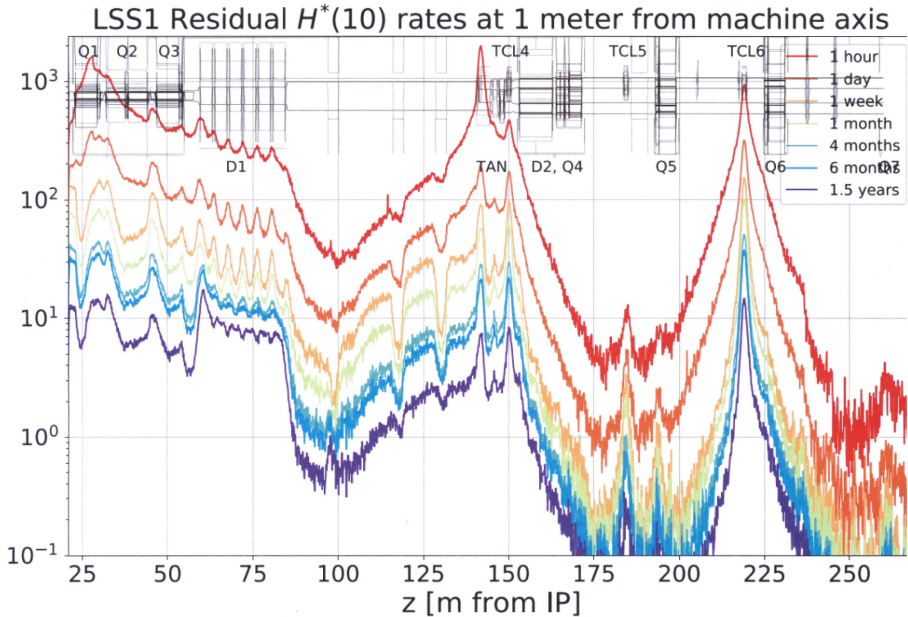


Fig. 5. Point 1 summary 1D profile of residual dose rates at 1 meter distance from beam axis, on average 40cm from outer surface of cryostats. Cooling times referenced to end of Run 3 p-p operations.

When the Proton (or ion) bunches traveling in opposite directions traverse each other at the interaction points there is a probability that two or more particles will come close enough to interact. The event generates a number of high-energy collision products, some having an electric charge (like pions+/-, protons, etc.), other being neutral (like neutrons, gammas etc.). Some of these particles leaving the IP could impinge on the front face of the inner triplet superconducting quadrupole Q1 or the superconducting dipole D2 situated in front of the vacuum recombination chamber producing a quench.

For the LHC, special purpose absorbers called TAS and TAN stop these secondary particles and concentrate the radiation, allowing a safe operation of Q1 and D2. At the same time, due to the proximity to the interaction region, ($22.1\text{m} < z$) the TAS absorbers are surrounded by a massive shielding to reduce the background radiation in the detectors generated by the interactions taking place in the TAS. In this way, TAS absorber and its surrounding are a highly radioactive environment and form an integral part of the forward shielding of both ATLAS and CMS.

The design of the upgraded TAS and TAN (namely TAXS and TAXN) and new equipment takes into account additional challenges, as the increased energy deposition, alignment capabilities and the radiation constraints and in consequence, the entire layout of tunnel equipment near the interaction regions (machine-interface region) will allow for simplified maintenance.³

The typical machine-interface region is a dead-end region extending from the end of the inner triplet Q1 to the start of the TAS ($20.8 < z < 22.1\text{m}$). Due to the shielding requirements, the access to that area is very narrow (40 cm wide passage for personnel from the tunnel wall to the elements belonging to the LHC machine and auxiliary beam line equipment's), and the space surrounding is limited in all directions. Furthermore, only 1.3 m are available longitudinally to house multiple equipment essential for operation:

- a Helium tightness dome (which secures the close region in the experimental area in case of Helium release from the triplet)
- a Beam Positioning Monitor (BPM)
- two all-metal gate vacuum valves
- a module containing a residual gas analyser + ion pump + Non-Evaporable Getter (NEG) cartridge + diverse gauges Bayard Alpert, Penning and Pirani gauges (“VAX module”)

- bellows
- services ancillaries (piping and cabling).

Routine operations of elements like the BPM's (i.e. alignment) are very difficult to perform and equipment replacement in case of failures needs to be done manually by a single person, without the possibility of lifting systems. The confined space presents also a safety risk in case of an evacuation or an intervention by the fire brigade.

6. Relocation of Vacuum Experimental Modules (VAX)

As indicated previously, multiple studies about the residual dose rates in the whole LHC machine, and in particular both in ATLAS and CMS show that the values following HL-LHC operation (3000/fb) are likely increasing by a factor which is consistently between 15 and 30 times the values measured in the First Long Shutdown (LS1).²⁴ This is of key importance for the regions close to the TAS, as there is little room to improve the current situation: No modifications of the massive steel and concrete shielding (which tightly surround the equipment) are possible, and also alignment requirements for the last BPM will now become critical for operation, thus requiring more frequent survey interventions.²⁵

The design of new equipment takes into account these constraints and the equipment in the machine-experiment cavern boundaries will be optimised for simplified maintenance. In this way, the new design focused on the use of reduced activation materials and improving (reducing time and avoiding contact during handling) or eliminating the need of interventions. Nevertheless, there is little room to improve the accessibility to the subsystems in the Q1-TAS region, as in HL-LHC will still be an extremely narrow dead-end zone where no modifications of the massive steel and concrete shielding (which tightly surround the equipment) are possible.

The situation could be substantially improved by relocating the equipment to the other side of the TAS (from the tunnel to the inside of the experimental caverns), where the massive existing forward shielding structures would have to be slightly modified, however with a negligible loss of performance for background shielding. The available "empty" space in that region is also limited during operation, but at every yearly-programmed shutdown, the massive steel shielding structures are dismantled or opened to free up space, allowing the

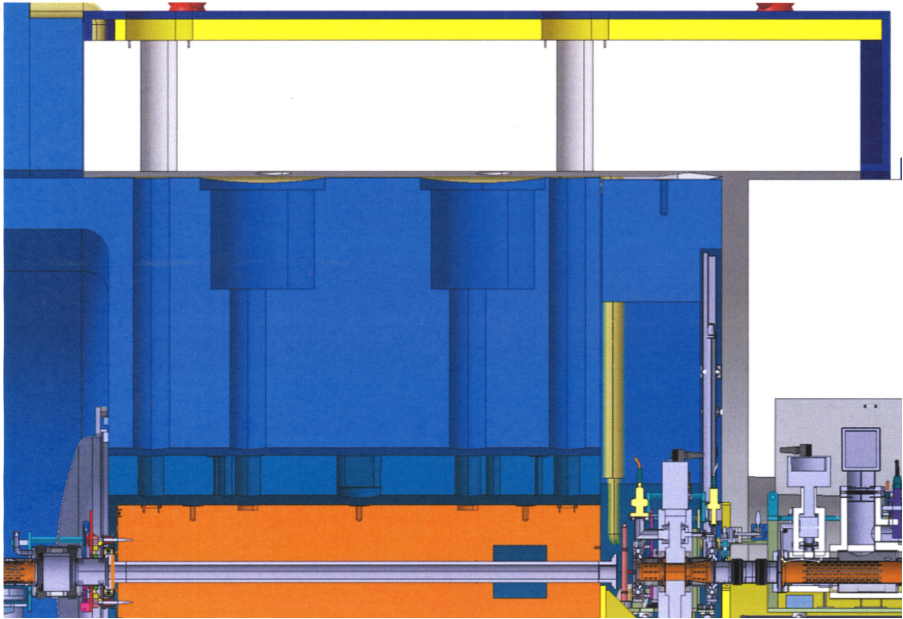


Fig. 6. 2D view of the ATLAS machine-experiment interface region, with the TAXS (orange) inside the blue, TX1S fixed steel shielding. Experimental cavern is on the right, the relocated VAX is inside the white ATLAS Forward mobile shieldings.

detectors to be opened. In this way, after the removal of the forward shielding structures, access is easier than in the tunnel and the intervention doses can be drastically reduced with the use of remote handling and keeping a much safer distance respect to the one existing at the tunnel side.

The proposed relocation requires modifications in the forward shielding regions of ATLAS and CMS to host the support and the modules while being compatible with the standard opening scenarios.

The proposal for HL-LHC started revising the need of each equipment and services. The exercise resulted first in the integration of the element requiring more interventions, the BPM within Q1 (being in secondary vacuum improves reliability, and eliminates the need of independent alignment), and second the installation of a new-cantilevered support in the experimental cavern, which includes guiding columns and self-plug-in connectors hosting both electrical and pneumatic lines. The equipment will be remotely handled and automatically plugged-onto the supports with the use of a robot attached to



Fig. 7. The CERN CRANEbot is seen here carrying a VAX module (centre of the image) inside the CMS cavern, as part of an operation test conducted in early February 2021.

the the cranes situated at the experimental caverns. An intense validation campaign followed by a successful proof of principle test in CMS cavern was performed in LS2. During the test in the CMS cavern, the robot, handled by a crane, was remotely operated to locate the VAX module on its place in the support and then uninstall it. The robot was able to grab and release the lifting rings as well as to assist in the alignment operation on the guide pins in order to correctly reach the support.

The proposed modifications in shielding structures inside the experimental caverns were advanced to LS2, where a number of subsystems were modified (in ATLAS: JTT, JFC1, JFC2, JFC3, VT chamber supports and in CMS: beampipe support and shielding inserts) and will be completed during LS3.

7. Secondaries Absorbers for HL-LHC, TAXS

The Target Absorbers for charged Secondaries and Neutral particles TAS and TAN of the present LHC will be replaced in LS3 by modified, larger aperture

absorbers referred to as TAXS and TAXN and in LS2 a new Target Absorber for Neutrals was installed at both sides of LHCb (IR8).

The high-luminosity interaction regions IR1 and IR5 of the present LHC are equipped with 1.8 m long copper absorbers called TAS at 19 m from the interaction points, located in front (IP side) of the first superconducting quadrupoles Q1, see Figure 8.

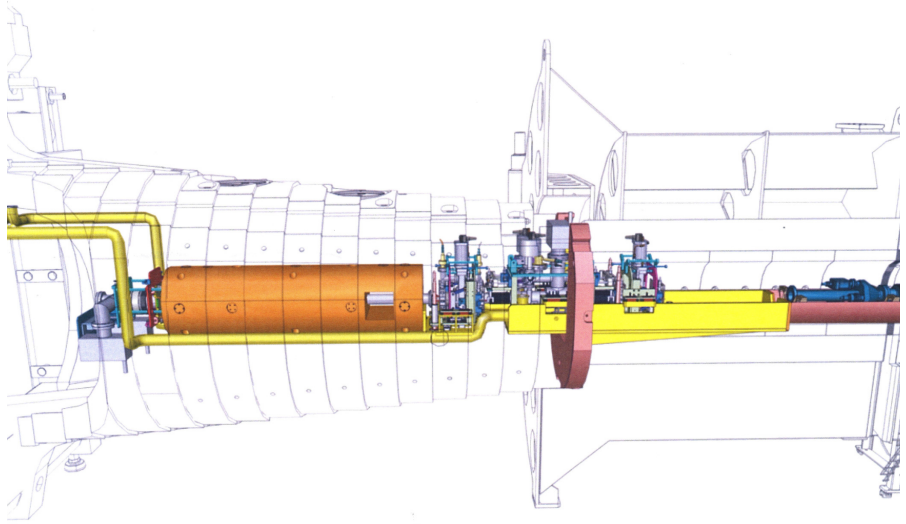


Fig. 8. 2D Layout drawing showing left side of IR5 (CMS). The TAXS (orange) is surrounded by the FIN shielding. IP is at the right, while the relocated VAX can be seen at the right of it, at the experimental side).

Their primary function is to reduce the energy flow from collision debris into the superconducting quadrupole triplet magnets. In addition, the TAS also acts as a passive protection. It reduces the flux of particles into the inner detectors of ATLAS and CMS in case of abnormal beam losses. The inner radius of the TAS as presently installed is 17 mm both in IR1 and IR5. This is significantly less than the central beam pipe radius of ATLAS and CMS. The radius of the reduced central beam pipes installed in LS1 was chosen such, that they still remain in the shadow of the TAS, including alignment tolerances and sagging. This is of direct relevance for high- β^* operation in the LHC, where the beam size is approximately constant throughout the experimental regions.

For the HL-LHC upgrade, the inner coil diameter of the triplet magnets will increase from 70 mm to 150 mm. The inner radius of the present TAS will also increase from 17 to 30 mm for the TAXS, which will be significantly larger than the radius of the central beam pipes. The material (Cu), length and outer dimensions remain as originally designed. Additional shielding will be installed around the beam screens in the triplet region. The energy deposition for the enlarged beampipe inside the TAXS to the triplet magnets has been determined by simulations and remains within specifications, see Chapter 10. The absorbed power will increase imposing an active cooling to have a TAXS compatible with beam operating temperatures.

Understanding, minimising and mitigating any un-avoidable negative impact of the machine upgrade to the experiments is a key objective of the machine detector interface for the HL-LHC.⁴ Increasing the central beam-pipes after LS3 in the same proportion as the inner TAS radius would compromise the vertex detector performance. Optimal vertex resolution for ATLAS and CMS is essential to deal with the increased pile-up after LS3. The beam pipe radii in the central detector region will remain after LS3 at the reduced values given in Table 2. Detailed tracking studies including failure scenarios further described in¹⁷ have shown that the experiments remain well protected in case of accidental beam losses in spite of increased intensities and apertures.

8. Neutral Absorbers for HL-LHC (TAXN, TANB)

There will also be major changes further outside in IR1 and IR5. The D2 magnet and neutral absorber TAN which is located in front of the D2 magnet will move by 13 m closer to the interaction points, to make space available for the installation of the crab cavities. The β -functions at the TAN will increase and require a larger aperture of the vacuum recombination chamber (Y-chamber) inside the TAN. The half-crossing angle will roughly double for the HL-LHC (from typically 142.5 to 295 μ rad) and move the neutral cone from collision debris closer to the beam aperture of the TAN. The TAN surrounds both beams and also acts as passive absorber for the incoming beam. Similar to the TAXS, energy deposited will increase in the TAXN, making an active cooling compulsory. The increase in aperture results in a reduction of passive protection compared to the present LHC, which will be minimised by closer matching of the holes through the new TAXN to the beam geometry and by addition of movable collimators.

The LHC luminosity upgrade of the LHCb detector located at the Interaction Point 8 (IP8) will also represent an increase of the inelastic collisions. Same as for IP1 and IP5, The pp collisions will produce a shower of forward particles, namely of neutrals (mostly neutrons and photons) and charged particles (mostly pions and protons), that will leave the interaction point 8 in both directions towards the machine creating a non-negligible energy deposition in the region. With these conditions and without the use of an absorber, the D2 recombination dipoles will see an energy deposition that could bring them above their safety thresholds risking quenching. For protecting these dipoles, a minimal absorber TANB (shown in Figure 15) was installed on either side of IP8 to reduce the heat load on the D2 magnets to values well below the quench level.

Four TAXN neutral particle absorbers will be installed in LS3, each unit around 125 m away on each side of IP1 and IP5. Same as for the replaced TANs, their initial goal is to protect the separation dipoles D2 and the quadrupoles of the Matching Section from the power carried off by neutrals produced at the interaction point. They will host detectors inside to study the very forward physics and to measure the relative and absolute luminosity.

The TAXNs located around IP1 and IP5 will be instrumented with the machine beam rate monitor (BRAN) and the Zero Degree Calorimeter (ZDC). Each detector is considered as a separate ‘small experiment’ to be integrated and installed inside the TAXN in the LHC tunnel.

The TAXNs, shown in Figure 9, are 30 tonne absorbers composed by 9 subassemblies. Positioned with customised pins, each subassembly is below 5 tonne in weight. The stainless steel recombination vacuum chamber is at the centre of the Absorber Box, the inner assembly of a TAXN, and it is clamped inside the two water-cooled absorber clam shells. This 4.3 m long vacuum beam chamber has a large tube facing the interaction point which transitions smoothly into two tubes going away from the IP. Both, the copper absorber and the chamber, are surrounded by heating jackets for bake-out purposes. An assembly composed of Five carbon steel (St-36) blocks surround the Absorber Box for radiation protection purposes: two Base Plates (Lower and Upper), two Lateral Shieldings and the Top Shielding. Two marble blocks are located on the IP end providing a personnel lower radiation area inside the Long Straight Section. Finally, the complete assembly is supported by three jacks which can be remote aligned to optimise the recombination chamber aperture.

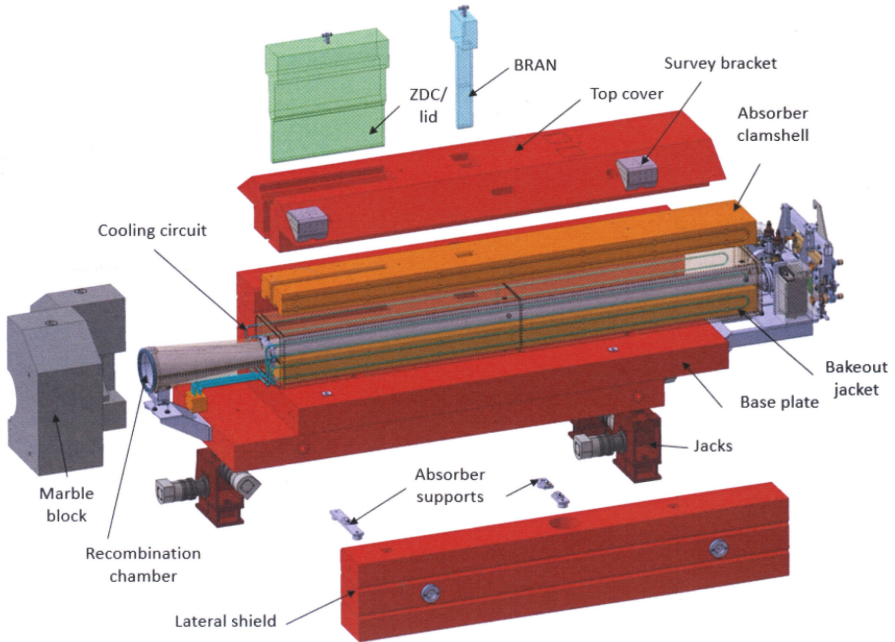


Fig. 9. TAXN developed overview. Detectors geometries represent exclusively a space reservation.

There are two open slots inside the TAXN which are accessible from the top and that will host the Luminosity and Forward Physics detectors. The BRAN is foreseen to remain installed during the complete LHC run, and the ZDC, which will be in place only during the Pb-Pb run. For this reason, a lid covers the ZDC slot during the proton-proton run providing radiation protection to personnel and equipment.

The main constraints and functionalities with which the design shall comply are:

- The heat loads from IP collision debris. The energy deposition mainly comes from neutral particles impacting the absorber block resulting in a highly peaked profile as is shown in Figure 10.
- The length of the absorber as well as the beam pipe separation of the recombination chamber allow protecting the downstream magnets from collision debris while the surrounding elements (i.e. collimators) receive a heat load that can be extracted by their cooling system.

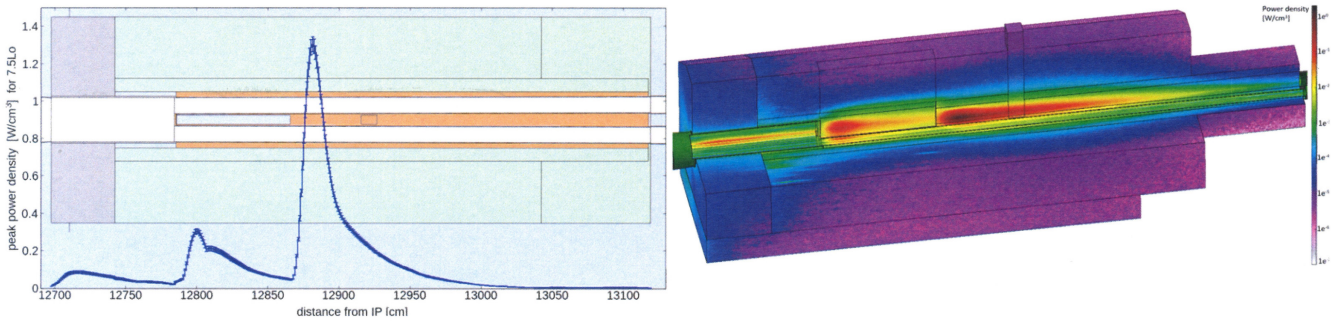


Fig. 10. Left: 2D plot of TAXN showing the heat deposition peak distribution along the beam machine axis. Right: 3D cut view showing the heat deposition distribution along the transverse plane.

- The integration of the bakeout system required to achieve the foreseen vacuum conditions for the operation of the LHC machine.
- The transverse beam aperture and impedance limits for the LHC proton and Pb-Pb beam. The beam aperture for the HL-LHC layout v1.5 flat optics at 14σ is shown in Figures 11, 12 and 13. The 12.5σ expected in the inner triplet and dipole 1 showing that there is a margin of 1.5σ in terms of aperture.
- The high expected radioactive environment.

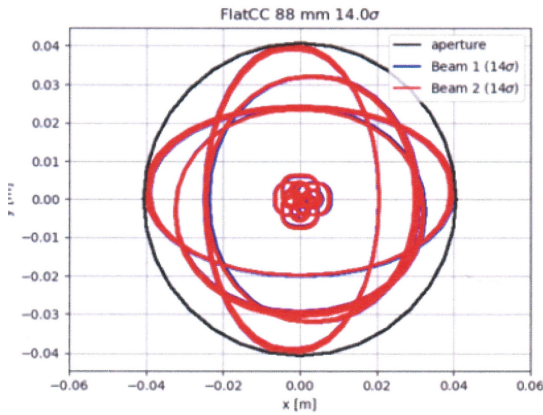


Fig. 11. Vertical transverse cross-section.

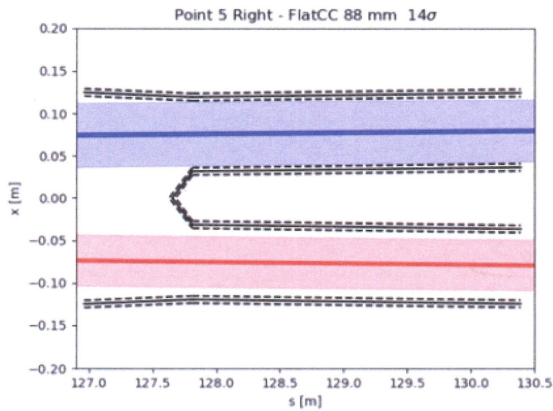


Fig. 12. Longitudinal horizontal cross section.

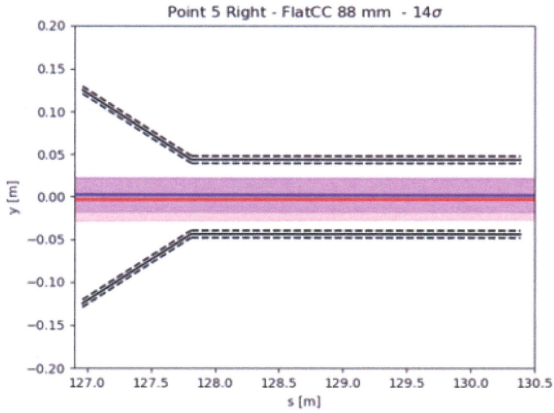


Fig. 13. Longitudinal vertical cross section.

- The alignment system of the TAXN itself and its neighbours components.
- The integration of the ZDC and BRAN detectors to provide an optimised environment for the full exploitation of their physics case and functionalities (ion or p-p runs).
- The LHC operation and tunnel integration as shown in Figure 14.

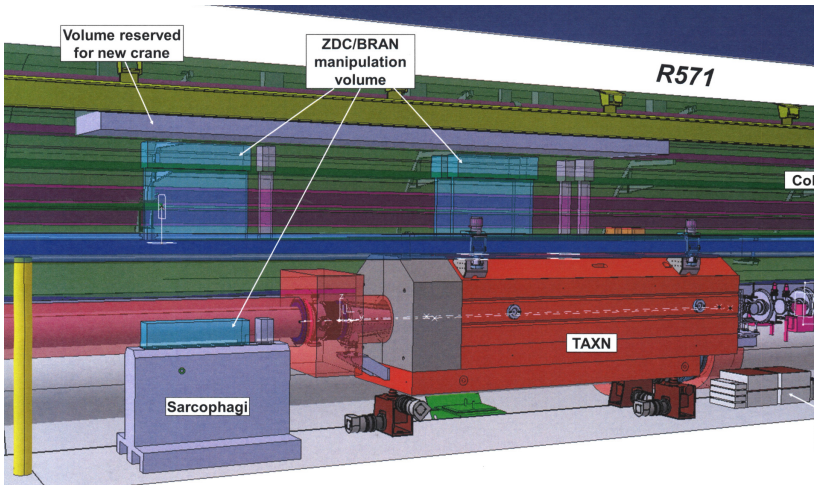


Fig. 14. TAXN integration inside the LHC tunnel.

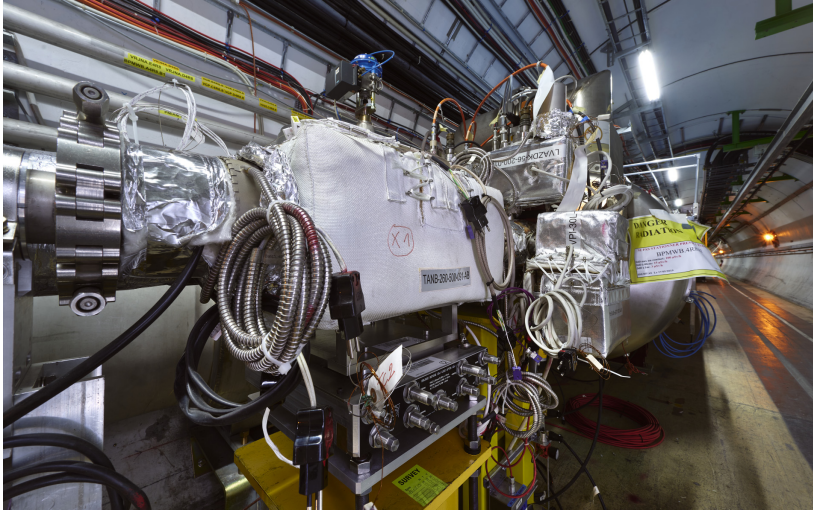


Fig. 15. The TANB absorbers were installed in the LHC tunnel to protect the accelerator components from particles produced by collisions occurring in the LHCb experiment. The alignment table can be seen below the absorber.

Similar as in IP1 and IP5, the luminosity increase require a new absorber at IR8, to protect the superconducting dipole D2, although energy deposition levels and integration constraints led to a different design without surrounding the vacuum recombination chamber. The TANB (shown after installation in Figure 15) is composed by two blocks of high density material (in this case tungsten) clamping the two beam chambers approximately 1.9m before D2 towards the IP8, on either side of IP8, creating a static mask to stop the forward neutral particles while letting the beam inside the vacuum chambers pass by undisturbed.

The continuous deposition during HL-LHC operation will activate the TANB, limiting any human activity in the region to very strict access and short time periods. Among these activities, alignment is placed as one of the most time consuming and one that obliges a closer proximity with the TANB absorber mainly due to the current design of the “standard” CERN alignment platforms. This will be much improved from LS2 as, following the ALARA (As Low As Reasonably Achievable) approach, a new alignment platform was engineered. The new alignment plate is based upon the design of the “standard” CERN alignment platforms, moving the actuators for each

degree of freedom to a single side (in this case, the transport side of the tunnel) facilitating its access, improving the ergonomics of the alignment operations and principally decreasing the time and proximity from the operator to the equipment mitigating the exposure of the professionals to the activated area.

References

1. Rossi, Lucio (ed.) (CERN); Brüning, Oliver (ed.) (CERN), “The High Luminosity Large Hadron Collider: the new machine for illuminating the mysteries of Universe”, Hackensack, NJ: World Scientific, 2015.
2. O. Brüning et al. (ed.), LHC design report. Vol. 1-3, CERN-2004-003-V-1–3.
3. Apollinari G. (ed.) (FERMILAB); Béjar Alonso I. (ed.) (CERN); Brüning O. (ed.) (CERN); Fessia P. (ed.) (CERN); Lamont M. (ed.) (CERN); Rossi L. (ed.) (CERN); Tavian L. (ed.) (CERN), “High-Luminosity Large Hadron Collider (HL-LHC): Technical Design Report V. 0.1”, CERN Yellow Reports: Monographs.
4. H. Burkhardt, D. Lacarrere, L. Rossi, Executive summary of the 1st Collider-Experiments Interface Workshop on 30 Nov. 2012.
5. ECFA High Luminosity LHC Experiments Workshop, Aix-Les-Bains, 3-6 Oct. 2016.
6. LHCb Collaboration, “Expression of Interest for a Phase-II LHCb Upgrade: Opportunities in flavour physics, and beyond, in the HL-LHC era”, CERN-LHCC-2017-003.
7. I. Efthymiopoulos et al., LHCb Upgrades and operation at $10^{34} \text{ cm}^{-2} \text{ s}^{-1}$ luminosity – first study, CERN-ACC-NOTE-2018-0038.
8. ALICE collaboration, “Future high-energy pp programme with ALICE”, ALICE-PUBLIC-2020-005.
9. D. Adamova et al., “A next-generation LHC heavy-ion experiment”, <https://arxiv.org/abs/1902.01211v2>.
10. A. Ariga et al., “Technical proposal: FASER, The forward search experiment at the LHC” CERN-LHCC-2018-036
“Detecting and Studying High-Energy Collider Neutrinos with FASER at the LHC”, CERN-LHCC-2019-012.
11. C. Ahdida et al., “SND@LHC - Scattering and Neutrino Detector at the LHC”, CERN-LHCC-2021-003.
12. B. Acharya et al., “MoEDAL Run-3 Technical Proposal”, CERN-LHCC-2021-006.
13. M. Albrow et al., “CMS-TOTEM Precision Proton Spectrometers CT-PPS”, CERN-LHCC-2014-021.
14. S. Grinstein, “The ATLAS Forward Proton Detector (AFP)”, Nucl. Part. Phys. Proc. 273-275 (2016) 1180-1184.
15. E. Todesco, “Insertion Magnets”, Chapter 6 of this book.
16. LHCb collaboration, “LHCb VELO Upgrade Technical Design Report”, CERN-LHCC-2013-021.
17. D. Wollmann, “Machine protection”, Chapter 12 of this book.

18. A. Tsinganis et al., “Impact on the HL-LHC Triplet Region and Experiments From Asynchronous Beam Dumps on Tertiary Collimators” Proc. IPAC 2017.
19. B. Lindstrom et al., “Crab Cavity Failures Combined with a Loss of the Beam-Beam Kick in the High Luminosity LHC”, Proc. IPAC 2018.
20. Tobias Baer, “Very fast Losses of the Circulating LHC Beam, their Mitigation and Machine Protection”, CERN-THESIS-2013-233.
21. C. Bracco, “Injection and Dumping Systems”, Chapter 19 of this book.
22. S. Redaelli, “Collimation System”, Chapter 8 of this book.
23. LHC Background Study group, <http://cern.ch/lbs>.
24. D. Bjorkman, A. Infantino, “Radiation Protection estimates for LS3 activities in LHC LSS1 and LSS5”, CERN-EDMS2435122.
25. F. Sanchez Galan et al., “Optimising machine-experiment interventions in HL-LHC”, IPAC 2017, Copenhagen.

This page intentionally left blank

Chapter 14

Cryogenics for the HL-LHC

S. Claudet, G. Ferlin, E. Monneret, A. Perin, M. Sisti, R. Van Weelderren,
A. Lees, V. Gahier, K. Brodzinski and L. Delprat

CERN, TE Department, Genève 23, CH-1211, Switzerland

The discovery of a Higgs boson at CERN in 2012 was the start of a major program working to measure this particle's properties with the highest possible precision for testing the validity of the Standard Model and to search for further new physics at the energy frontier. The LHC is in a unique position to pursue this program. Europe's top priority is the exploitation of the full potential of the LHC, including the high-luminosity upgrade of the machine and detectors with an objective to, by around 2030, collect ten times more data than in the initial design. To reach this objective, the LHC cryogenic system must be upgraded to withstand higher beam current and higher luminosity at top energy while keeping the same operation availability by improving the collimation system and the protection of electronics sensitive to radiation. This paper will present the conceptual design of the cryogenic system upgrade with recent updates in performance requirements, the corresponding layout and architecture of the system as well as the main technical challenges which have to be met in the coming years.

1. Overview

The upgrade of the cryogenics for the HL-LHC will consist of the following:

- design and installation of two new cryogenic plants at P1 and P5 for high luminosity insertions. This upgrade will be based on a new sectorization scheme aimed at separating the cooling of the magnets in these insertion regions from the arc magnets and considering the new feedboxes and superconducting links located in underground infrastructures.

This is an open access article published by World Scientific Publishing Company. It is distributed under the terms of the Creative Commons Attribution 4.0 (CC BY) License.

- design and installation of a new cryogenic distribution lines (QXL) at P1 and P5 in the LHC tunnel and in a new underground service galleries.
- upgrade of the existing cryogenic plant (QSRA and QURA) cooling the LHC sector 3-4 located at P4.
- cryogenic design support for superconducting devices, such as magnets, crab cavities, superconducting links, and the hollow electron lenses.

Some other options such as new cryogenic circuits at P7 for the superconducting links and displaced current feedboxes or a new cryoplant in P4 have been discarded.

2. LHC Machine Upgrades

2.1. Upgraded beam parameters and constraints

The main parameters impacting the cryogenic system are given in Table 1. With respect to the nominal beam parameters, the beam bunch population will double and the luminosity in the detectors of the high luminosity insertions at P1 and P5 will be multiplied by a factor 5 with respect to LHC nominal luminosity.

These upgraded beam parameters will introduce new constraints to the cryogenic system:

- The collimation scheme must be upgraded. As some of the new collimators will work at room temperature but be installed on the cold region, cryogenic bypasses are required to guarantee the continuity of the cryogenic and electrical distribution.
- Hollow electron lenses will be installed for halo control.

Table 1. LHC upgraded beam parameters for 25ns bunch spacing.

Parameter	Unit	Nominal LHC	Nominal HL-LHC
Beam energy, E	TeV	7	7
Bunch population, N_b	protons/bunch	1.15×10^{11}	2.2×10^{11}
Number of bunches per beam, n_b		2808	2748
Luminosity, L	$\text{cm}^{-2} \text{s}^{-1}$	1×10^{34}	5×10^{34}
Bunch length	ns	1.04	1.04

Table 2. (Continued)

Component	Q1	Q2A	Q2B	Q3	CP	D1	Intercon.	DFX	DFM	D2	CC
Beam Screen											
Temperature (K)	60-80	60-80	60-80	60-80	60-80	60-80	60-80	-	-	4.5-20	4.5-20
Total Heat Load (W)	223.1	97.3	144.8	133.0	66.9	74.0	375.8	0.0	0.0	49.8	46.0
Avg. Heat Load (W/m)	22.0	9.9	14.8	13.1	11.1	10.0	54.2 W pu	0.0	0.0	3.8	23.0 W pu
Static (W/m)	0.1	0.1	0.1	0.1	0.2	0.2	0.0 W pu	0.0	0.0	0.0	9.3 W pu
Resistive (W/m)	0.0	0.0	0.0	0.0	0.0	0.0	0.0 W pu	0.0	0.0	0.0	13.6 W pu
Beam Induced (W/m)	5.1	2.9	4.4	5.1	0.6	2.3	42.4 W pu	0.0	0.0	3.7	0.0 W pu
Collision Induced ‡ (W/m)	16.8	6.9	10.2	7.9	10.3	7.6	11.9 W pu	0.0	0.0	0.2	0.0 W pu
Thermal Shield											
Temperature (K)	60-80	60-80	60-80	60-80	60-80	60-80	60-80	60-80	60-80	60-80	60-80
Total Heat Load (W)	66.6	53.2	53.2	54.3	133.8	103.2	22.2	24.9	28.0	133.1	609.0
Avg. Heat Load (W/m)	6.3	5.4	5.4	5.4	22.2	14.0	3.2 W pu	8.2	7.0	9.5	304.5 W pu
Static (W/m)	6.3	5.4	5.4	5.4	22.2	14.0	3.2 W pu	8.2	7.0	9.5	206.9 W pu
RF Cavity (W/m)	-	-	-	-	-	-	-	-	-	-	97.6 W pu

"-" = not applicable; W pu = Watts per unit.

* Length of each interconnection unit is 1 m, except between Q3-CP which is 1.8 m and CP-D1 which is 1.13 m.

† A module unit contains 2 crab cavities.

Table 3. Total heat loads divided by group of users, LSS.R5 and IP5. Preliminary values.

Group*	IT	D2	CC	LSS_R5	IP5
Cold mass length (m)	62.7	17	-	79.7	159.4
Thermal shield length (m)	63.7	18	-	81.7	163.4
Number of units (-)	-	-	2	2(CC)	4(CC)
Cold Mass					
Temperature (K)	1.9	1.9	2	1.9-2	1.9-2
Total Design + flash (W)	1416.7	100.2	149.6	1667	3333
Total Design (W)	1173.3	83.0	127.6	1384	2768
Total Ultimate (W)	1103.4	68.7	89.9	1262	2524
Total Nominal (W)	779.4	50.7	89.9	920	1840
Dynamic - Ultimate (W)	1033.4	54.4	52.2	1140	2280
Dynamic - Nominal (W)	709.4	36.4	52.2	798	1596
Static (W)	70.0	14.3	37.7	122	244

Table 3. (Continued)

Group*	IT	D2	CC	LSS_R5	IP5
Beam Screen					
Temperature (K)	60-80	4.5-20	4.5-20	60-80	4.5-20
Total Design (W)	1685.0	74.7	97.0	1685	172
Total Ultimate (W)	1424.1	50.9	46.0	1424	97
Total Nominal (W)	1115.0	49.8	46.0	1115	96
Dynamic - Ultimate (W)	1415.8	50.9	27.3	1416	78
Dynamic - Nominal (W)	1106.7	49.8	27.3	1107	77
Static (W)	8.4	0.0	18.7	8	19
Thermal Shield					
Temperature (K)	60-80	60-80	60-80	60-80	60-80
Total Design (W)	744.9	229.6	913.5	1967	3935
Total Ultimate (W)	496.6	153.1	609.0	1312	2623
Total Nominal (W)	496.6	153.1	609.0	1312	2623
Dynamic - Ultimate (W)	0.0	0.0	195.2	195	390
Dynamic - Nominal (W)	0.0	0.0	195.2	195	390
Static (W)	496.6	153.1	413.8	1116	2233

(*) *italic* values are indicating Design Heat Load values

The design heat load values consider margins and technological requirements. They can be calculated by using the following equations:

$$\dot{Q}_{\text{installed}} = \text{MAX} [F_{\text{ov}} \cdot (F_{\text{un}} \cdot \dot{Q}_{\text{static}} + \dot{Q}_{\text{dynamic nominal}}) ; F_{\text{un}} \cdot \dot{Q}_{\text{static}} + \dot{Q}_{\text{dynamic ultimate}}] \quad (1)$$

$$\dot{Q}_{\text{installed}} = \text{MAX} [F_{\text{ov}} \cdot \dot{Q}_{\text{nominal}} ; \dot{Q}_{\text{ultimate}}] \quad (2)$$

Equation (1) is valid for the cold mass (1.9–2 K) and beam screens (4.5–20 K and 60–80 K). Equation (2) is valid for the thermal shield (60–80 K) and current leads (20–293 K). A detailed study is available on Fig. 1 which gives a global view of the heat load at 1.9 K.

4. Impact on Existing Sector Cryogenic Plants

With new cryogenic plants dedicated to the cooling of cryogenic equipment in P1 and P5, the cooling duty of the existing sector cryogenic plants will be

reduced and more equally distributed. Figures 2 and 3 show the required cooling capacities for the different temperature levels and compares them to the nominal cooling requirements and to the installed capacities (green bars).

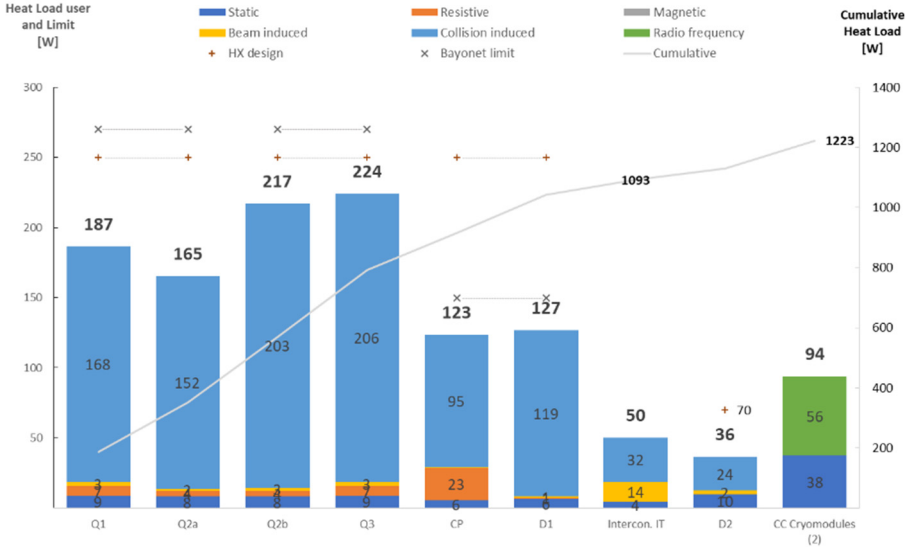


Fig. 1. Total heat load for users at 1.9 K. Preliminary values.

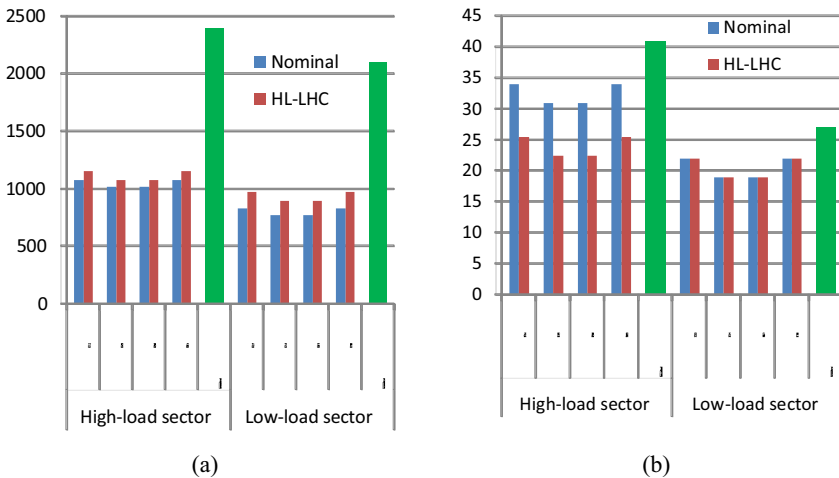


Fig. 2. Cooling capacity requirement of sector cryogenic plants: (a) cold mass; (b) current leads.

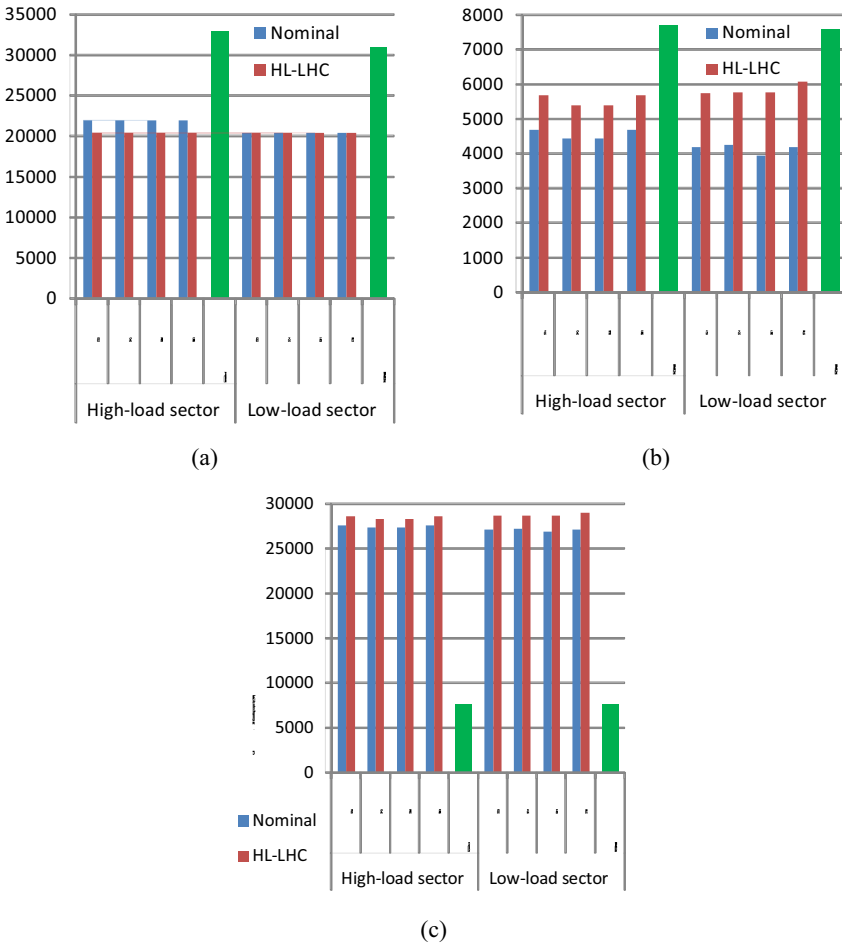


Fig. 3. Cooling capacity requirement of sector cryogenic plants: (a) thermal shields; (b) beam screen (dipole off); (c) beam screen (dipole on).

The low-load sectors equipped with upgraded ex-LEP cryogenic plants have lower installed capacity than the four cryogenic plants specially ordered for the LHC high-load sectors. For the HL-LHC, sufficient capacity margin still exists provided that the beam scrubbing of dipole beam-screens is efficient (dipole off).

5. Point 4 Cryogenics

The initial baseline considered the installation of a new cryoplant in P4. Later on, it was decided to evaluate an alternative scenario for the refrigeration part. The alternative scenario consisted of an upgrade of one of the existing refrigerators of P4 (equivalent of 2 kW@4.5 K with respect to the existing plant capacity of 16.5 kW@4.5 K) to fulfil the required cooling capacity of existing SRF modules with sufficient margin, while keeping or adapting the distribution system depending on the alternative. As a complement, a new mobile refrigerator with a cooling capacity allowing RF tests of a single cryo-module during long shut-downs was then considered, as all other cryogenic sub-systems would be stopped for maintenance and major overhauling but was finally abandoned.

The upgrade of the ex-LEP refrigerator included mainly:

- Replacement of 7 expansion turbines.
- Modification of one existing turbine.

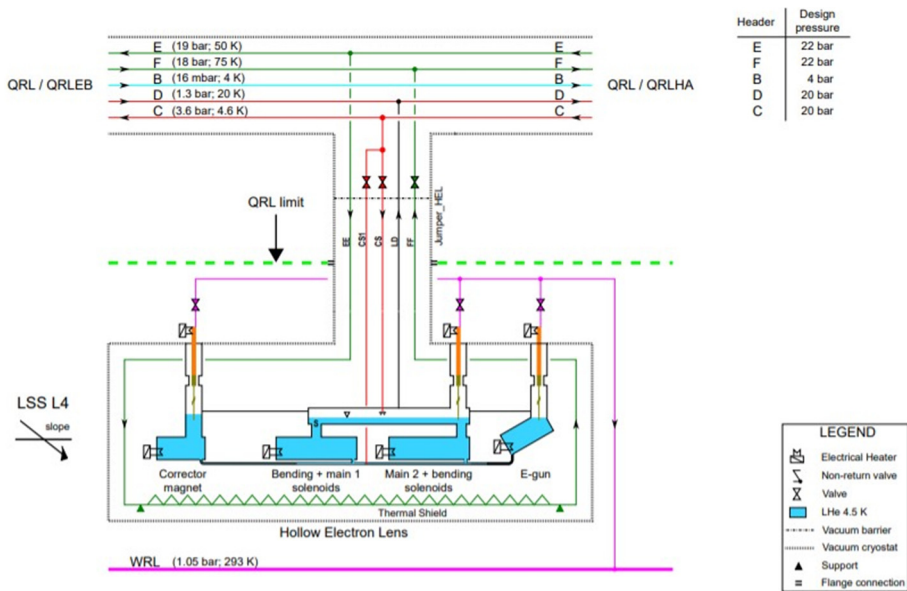


Fig. 4. Layout of the possible cryogenic layout at P4 (Hollow e-lens).

- Modification of the required piping inside the boxes or for instrumentation and service panels.

The upgrade was successfully completed during the Long Shutdown 2.

The modification of the cryogenic distribution line to allow the installation of the hollow electron lenses is under study. The schematic layout can be seen in Figure 4 [5].

6. New Cryogenics for High Luminosity Insertions at Point 1 and Point 5

The new HL-LHC cryogenic system will require new cryo-plants of about 15 kW at 4.5 K including 3 kW at 1.8 K. They will encompass new refrigeration plants and distribution lines. Figure 5 illustrates the architecture of the system. A full analysis of both systems has been done in order to optimize the cost and the sourcing strategy.

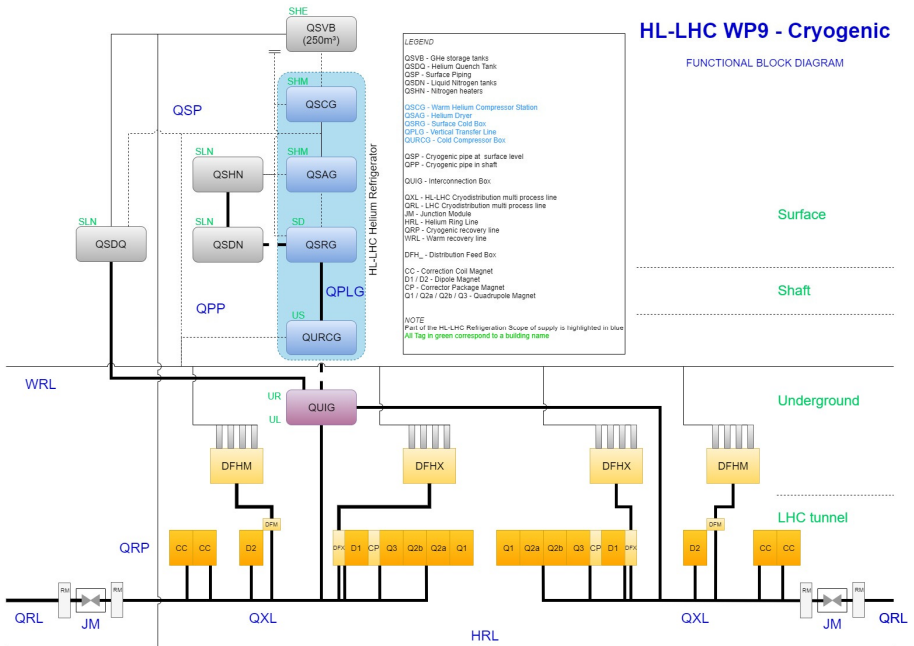


Fig. 5. HL-LHC Cryogenic architecture at P1 and P5.

The main components of the new helium refrigeration system are [7]:

- the compressor station (QSCG)
- a dryer system (QSAG)
- the 4.5 K cold box (QSRG) including 80 K and 20 K absorbers and a liquid helium phase separator
- a cryogenic vertical transfer line (QPLG) in a shaft connecting the 4.5 K surface cold box to the 1.8 K cold box located in an underground cavern
- a 1.8 K cold box (QURCG) including the cold compressors and a phase separator.

Each HL-LHC helium refrigerator shall:

- provide cooling to different magnets with an equivalent capacity of about 3 kW at 1.8 K
- supply an average helium mass flow rate of approximately 10 g/s at 4.5 K for the beam screens and recover it at around 20 K
- provide cooling to the Distribution Feed Boxes (DFH) with a liquefaction flow rate of 25 g/s
- supply an average helium mass flow rate of approximately 100 g/s at 60 K for various thermal shields and recover it at around 80 K, for a corresponding cooling capacity of 10 kW
- allow control of supply temperature between 300 K and 10 K during cool down of magnets
- accommodate heat load variation from 20 to 100% in less than one hour twice a day.

Regarding the new distribution system, it shall:

- distribute helium from the refrigerator to the different machine components in the temperature range from 4 K to 350 K with a maximum allowable pressure of 25 bar absolute
- control the helium flow to and from users as required for multiple operating modes
- have a maximum heat load for lines below 20 K ($\dot{Q}_{eq} \sim 320$ mm) lower than 0.4 W/m
- have a vacuum vessel diameter ranging from ~ 650 mm to ~ 770 mm
- house five inner headers ranging from ISO DN40 to DN300 and an actively cooled thermal shield

- integrate approximately 200 cryogenic control valves and interface to users via 32 feeding points.

Figure 6 illustrates the cryogenic distribution architecture while the following details provide details on the layout for the different components.

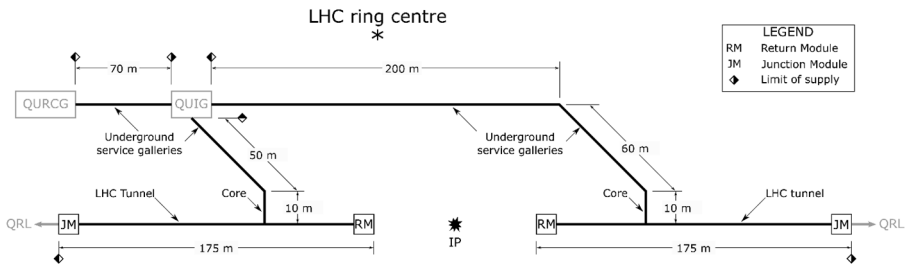


Fig. 6. Schematic of the cryogenic distribution architecture [8].

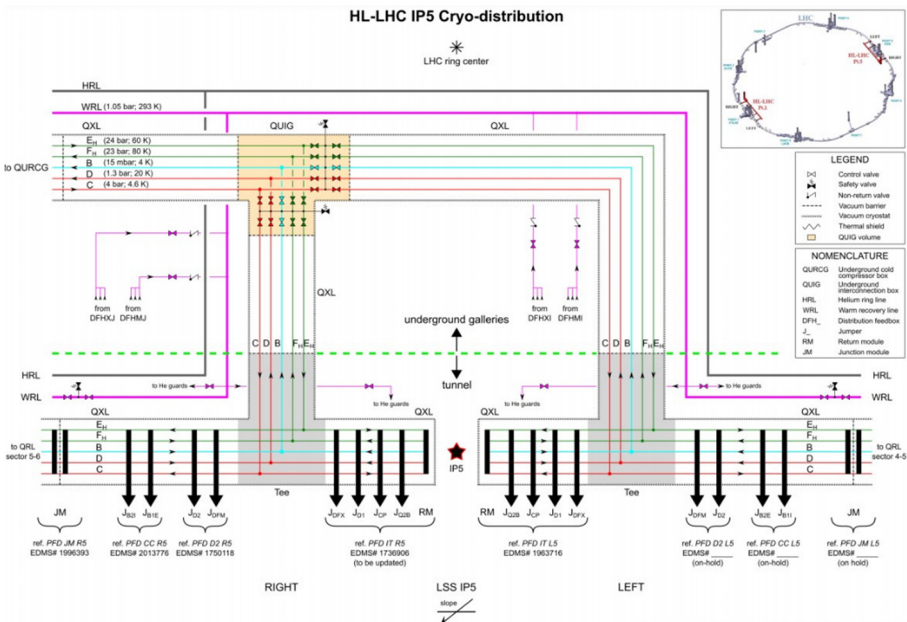


Fig. 7. Layout of the IP5 Cryodistribution [9].

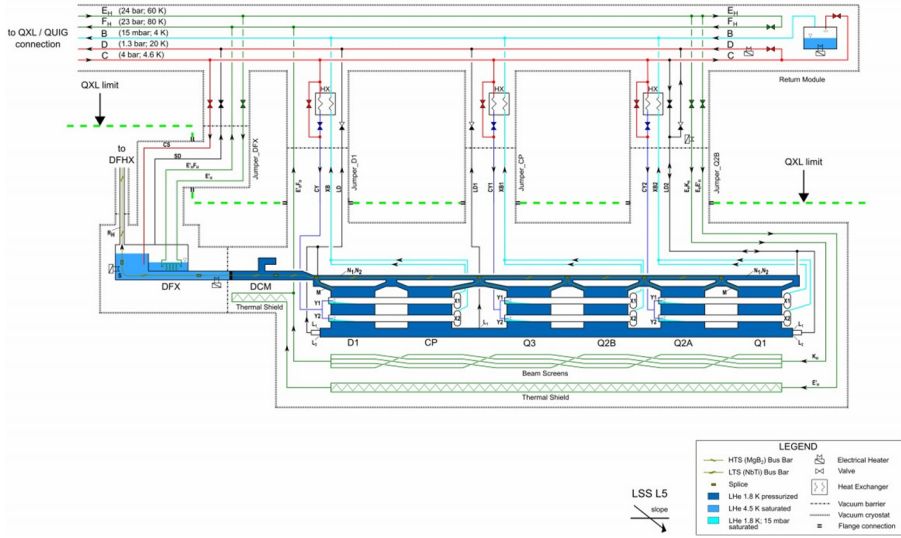


Fig. 8. Detail of the distribution for the IT magnets, CP and D1 [10].

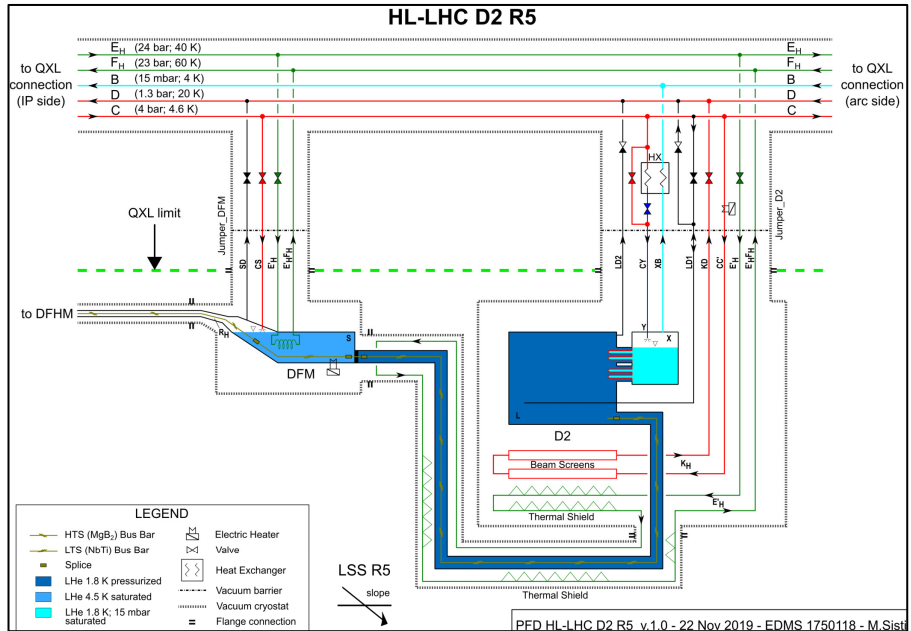


Fig. 9. Detail of the distribution for the D2 magnet [11].

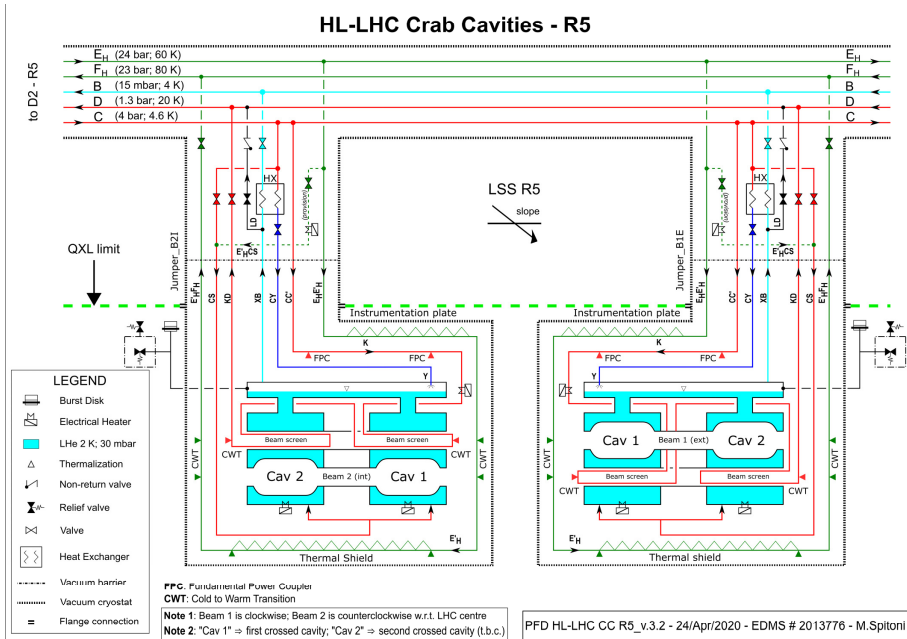


Fig. 10. Detail of the distribution for the Crab Cavities [12].

References

1. J. Poole, LHC Design Report Volume I, The LHC Main Ring, Chapter 11, CERN, (2004). EDMS: <https://edms.cern.ch/document/445856>.
2. V. Gahier, U. Wagner and P. Zijm, Heat load definition for the HL-LHC project, Updated heat load tables for the LSS.R5 for the HL-LHC. EDMS: <https://edms.cern.ch/document/1610730>.
3. M. Sisti, Process flow diagram of the HL-LHC IT L5. EDMS: <https://edms.cern.ch/document/1963716>.
4. M. Sisti, Cryo distribution IP5. EDMS: <https://edms.cern.ch/document/2025508>.
5. M. Spitoni, Process Flow Diagram of HL-LHC Hollow e-Lens in L4. EDMS: <https://edms.cern.ch/document/2314734>.
6. E. Monneret, IT-4472 Upgrade of the ex-LEP Refrigerator for HL-LHC - Point 4. EDMS: <https://edms.cern.ch/document/2001440>.
7. E. Monneret, MS-4631 - Supply of Two New Helium Refrigerators for HL-LHC at Point 1 (P1) and Point 5 (P5). EDMS: <https://edms.cern.ch/document/2382454>.
8. M. Sisti, MS-4630 - Supply of the Cryogenic Distribution Lines for the HL-LHC at Point 1 (P1) and Point 5 (P5). EDMS: <https://edms.cern.ch/document/2381328>.

9. M. Sisti, Process flow diagram of HL-LHC IP5. EDMS: <https://edms.cern.ch/document/2025508>.
10. M. Sisti, Process flow diagram of HL-LHC IT L5. EDMS: <https://edms.cern.ch/document/1963716>.
11. M. Sisti, Process flow diagram of HL-LHC D2 R5. EDMS: <https://edms.cern.ch/document/1750118>.
12. M. Spitoni, Process flow diagram of HL-LHC Crab Cavities R5. EDMS: <https://edms.cern.ch/document/2013776>.
13. V. Gahier, Process flow diagram of HL-LHC DFX/DSHX/DFHX L5. EDMS: <https://edms.cern.ch/document/2322140>.

Chapter 15

Energy Deposition and Radiation to Electronics

F. Cerutti^a, R. Garcia Alia^a and A. Tsinganis^b

^a*CERN, SY Department, Genève 23, CH-1211, Switzerland*

^b*CERN, EP Department, Genève 23, CH-1211, Switzerland*

The radiation impact on the machine elements and the electronics equipment in the high luminosity insertions is discussed, distinguishing the different loss regions, and respective mitigation measures are highlighted.

1. Collision Debris

Proton–proton inelastic collisions* taking place in the LHC inside its four big detectors generate a large number of secondary particles, mostly pions. The average multiplicity for one collision at 7 TeV beam energy is about 120 [1-4], but there are very substantial fluctuations over different events. Moving from the interaction point (IP), this multiform population evolves, even before touching the surrounding material, because of the decay of unstable particles, in particular neutral pions decaying into photon pairs. Most of these particles are intercepted by the detector and release their energy within the experimental cavern. However, the most energetic ones, emitted at small angles with respect to the beam direction, travel farther in the vacuum tube and reach the accelerator elements beyond the TAS (Target Absorber Secondaries) absorber, a protection element consisting of a 1.8 m long copper core located

* From the perspective of the radiation impact in the experimental insertions, ion–ion collisions remain in the shadow of the proton operation, because of their much lower luminosity, except for some remarkable processes, such as the Bound Free Pair Production, originating very localized losses with major implications on the LHC upgrade strategy, as discussed in Chapter 8.

at 20 m from the IP and featuring in the HL era a circular aperture of 60 mm diameter. Despite the fact that on average the number of particles per collision leaving the TAS aperture is more than one order of magnitude lower than the total number of debris particles, they carry about 80% of the total energy, 40% for each side. At the nominal HL-LHC luminosity ($5 \times 10^{34} \text{ cm}^{-2} \text{ s}^{-1}$), this represents about 3800 W per side that is impacting the LHC elements and is dissipated in the machine, in the nearby equipment and in the tunnel walls.

2. Triplet and Separation Dipole Protection

The TAS absorber is part of the interface area between the detector and the accelerator on each side of the high-luminosity IRs, namely IR1 and IR5, hosting the ATLAS and CMS detectors respectively (see Figure 1, left panel). Its protection role is not needed for luminosities up to $0.2 \times 10^{34} \text{ cm}^{-2} \text{ s}^{-1}$, as in the LHCb insertion [5], and is in fact limited to the first quadrupole, since its geometrical shadow gets quickly dashed by the effect of the magnetic field that bends a significant fraction of charged debris particles coming through the TAS aperture, in particular high energy pions, against the quite larger quadrupole aperture.

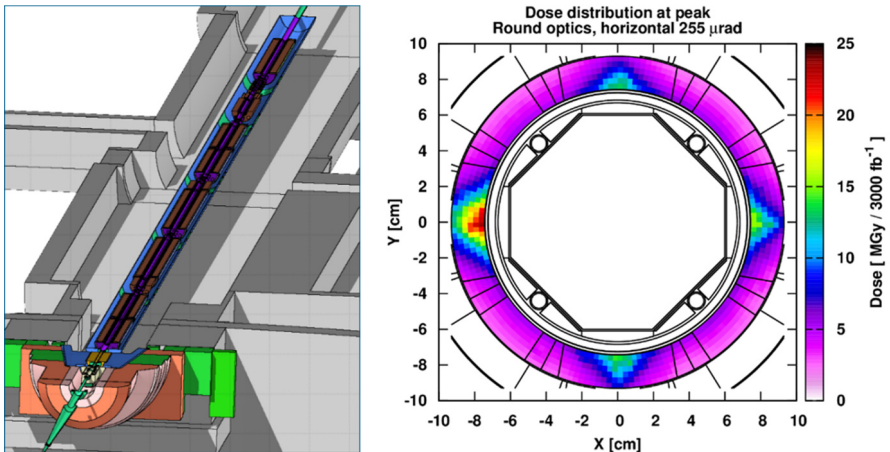


Fig. 1. Left: Geometry model [6,7] of the future machine layout outside the CMS cavern. In the forefront at the bottom, the TAS is surrounded by the visible massive shielding. Right: Dose distribution in the quadrupole coils at the most exposed location. The mid-planes hot spots are mitigated by tungsten alloy absorbers attached to the octagonal beam screen.

For this reason, the backbone element for the protection of the string of magnets up to the separation dipole (D1) will instead be the beam screen equipped with dedicated tungsten alloy absorbers all over its length, reaching their maximum thickness (of 16 mm in the first quadrupole and 6 mm elsewhere) at the magnet mid-planes, where the energy deposition is concentrated, as shown in the right panel of Figure 1.

The combination between the focusing-defocusing field configuration and the crossing plane yields a characteristic longitudinal profile for the peak dose (or power density) in the superconducting coils, as reported in Figure 2. After the HL-LHC upgrade, the weakest point becomes the IP end of the third quadrupole (Q2b) for horizontal crossing, due to the effect of the preceding interconnect, where the amount of absorbing material is limited. A careful optimization of the interconnect design, allowing for the extension of the tungsten alloy absorbers as well as their installation in the embedded Beam Position Monitor (BPM), brought the maximum dose expectation below 30 MGy for the nominal target of 3000 fb^{-1} , which is a level deemed to be still sustainable by the coil insulator. On the other hand, the maximum power density is predicted not to reach 3 mW/cm^3 at $5 \times 10^{34} \text{ cm}^{-2} \text{ s}^{-1}$, so remaining safely below the quench limit [8,9].

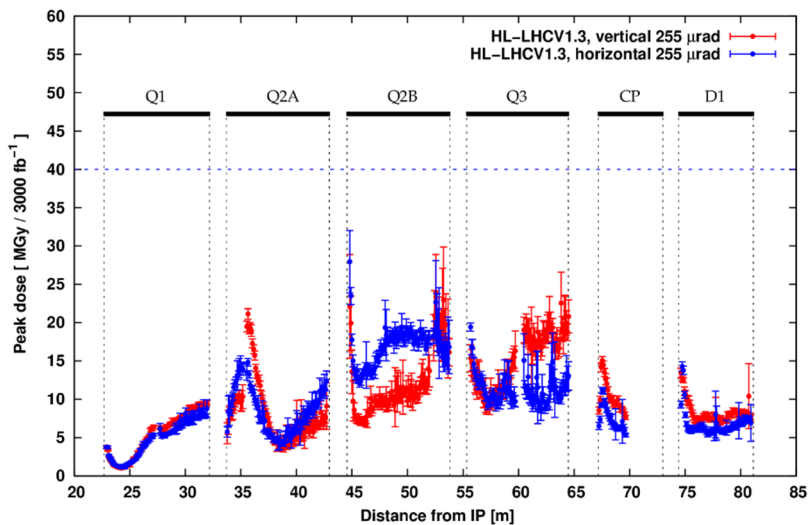


Fig. 2. Peak dose profile in the superconducting coils of the single bore magnet string after 3000 fb^{-1} , for horizontal (blue) and vertical (red) crossing.

For the same instantaneous luminosity, the total power collected by the 60 m long string of magnets amounts in the worst case (vertical crossing) to more than 1200 W, almost equally shared between the beam screen structure and the cold masses.

3. Matching Section Protection

The transition from the single bore vacuum chamber hosting the two counter-rotating beams to the two separate beam chambers is embedded in the TAN (Target Absorber Neutral), another massive absorber, with a 3.3 m long copper core, aimed at intercepting the neutral component of the collision debris, mostly photons and neutrons. The TAN absorber provides a substantial protection to the double bore recombination dipole (D2) and the four main quadrupole assemblies of the matching section (see Figure 3, left panel), including dipole correctors. However, the HL-LHC layout features the D1–D2 distance shortening, implying a lower beam separation in the TAN, coupled to a very significant enlargement of its twin pipes, due to optics requirements. These design changes, together with an almost double-crossing angle and an important increase of the mechanical aperture of the upstream elements, bring a flagrant weakening of the TAN effectiveness, further aggravated by the luminosity rise. Therefore, the cold magnet shielding has to be strengthened, by complementing the TCL (Target Collimator Long) physics debris collimators on the outgoing beam with tungsten alloy warm masks put in front of the cryostats and matching the aperture of the following beam screen, without altering the magnet design. The incoming beam bore benefits from the presence of the TCT (Target Collimator Tertiary) collimators that, while cleaning by design the incoming halo, also play a role in intercepting the debris propagating in the opposite direction. This scheme prevents the risk of debris induced quenches, keeping the power density in the coils below 1 mW/cm^3 for the reference luminosity of $5 \times 10^{34} \text{ cm}^{-2} \text{ s}^{-1}$. Respective dose values after 3000 fb^{-1} are predicted to remain below 10 MGy, except for the D2, locally exceeding by 20% that threshold. In the less favorable case of horizontal crossing, where the leakage through the TAN is maximized, the total power collected by the D2, which is the most exposed magnet, amounts to 33 W, twice as much its load for vertical crossing.

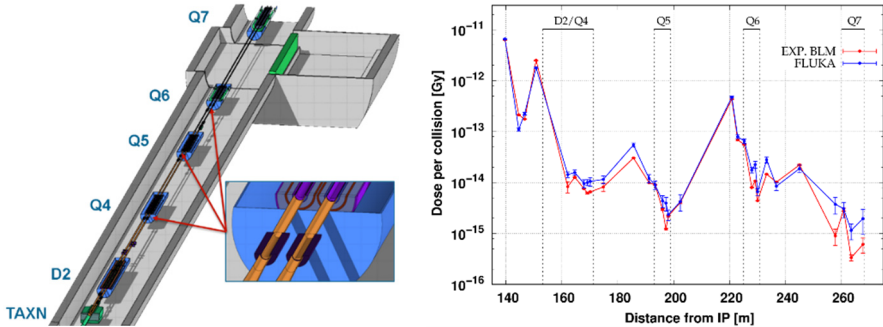


Fig. 3. Left: Geometry model of the future matching section layout. The frame zooms in on the additional TCLM masks. Right: BLM data (red) and FLUKA predictions (blue) in the present IR1 matching section for the fill #4919 of May 2016.

The matching section hot spots are displayed in the pattern of Beam Loss Monitor (BLM) data in the right panel of Figure 3, referring to the present machine layout. The first two points at about 140 m from the IP correspond to the front and rear of the TAN, while the following three peaks occur at the TCL locations, reflecting their different opening, with the TCL5 at about 185 m featuring a quite relaxed gap. The agreement quality in the absolute comparison with the simulation results gives a good confidence in the understanding of these medium distance losses, still critical even if representing only a few percent of the collision debris power.

4. Dispersion Suppressor Protection

The most forward TCL collimator, in the straight section half-cell 6, can provide a good cleaning of the initial part of the Dispersion Suppressor (DS) too, where the beam lines are bent by the LHC main dipoles, and no layout modification is planned for the HL-LHC era in IR1 and IR5. Nevertheless, beyond the TCL6 range, losses are expected in the DS odd half-cells, according to the periodicity of the single turn dispersion, and were already regularly observed, as shown by the BLM pattern in the left panel of Figure 4. In fact, they originate from protons subject to diffraction at the IP, affected by a magnetic rigidity deficit of the order of 1% and therefore destined to touch the horizontal boundary of the mechanical aperture towards the center of the ring.

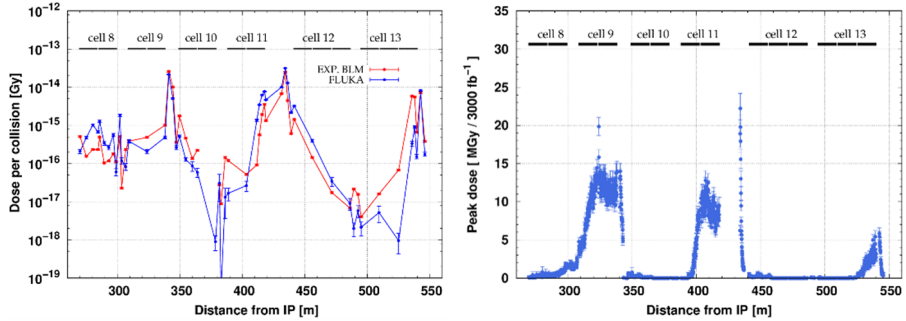


Fig. 4. Left: BLM data (red) and FLUKA predictions (blue) in the present IR5 DS for the fill #5401 of October 2016. Right: Peak dose profile in the superconducting coils of the DS magnets after 3000 fb⁻¹ for horizontal crossing.

As a consequence, the right panel of Figure 4 presents the predicted peak dose profile in the superconducting coils for the accumulation of a 3000 fb⁻¹ integrated luminosity, where the pronounced maximum at the end of the half-cell 11 is enhanced by an artificial aperture step in the simulation model at the specific interconnect between the missing dipole and the quadrupole assembly. On the other hand, actual imperfections in the machine aperture may locally worsen the picture, as well as more relaxed TCL6 gaps induce a dose increase up to the middle of the half-cell 9. In the latter, the main quadrupole cryostat hosts a dipole corrector, for which the resulting values, insensitive to the TCL6 setting, are deemed to be excessive on the left of IP1 and IP5 (taking into account the layout asymmetry), due to its lower radiation resistance, and mitigation actions, such as the introduction of an orbit bump, are being considered.

Respective peak power densities are of the order of 1 mW/cm³ for the reference instantaneous luminosity of $5 \times 10^{34} \text{ cm}^{-2} \text{ s}^{-1}$.

5. Radiation to Electronics

Radiation damage to electronics is often considered for space applications. However, it is important to note that the radiation environment encountered at the LHC, the high number of electronic systems and components partly exposed to radiation, as well as the actual impact of radiation induced failures strongly differ from the context of space applications. While for the latter application design, test and monitoring standards are already well-defined,

additional constraints, but in some cases also simplifications, have to be considered for the accelerator environment.

The mixed particle type and energy field encountered in the relevant LHC areas is composed of charged and neutral hadrons (protons, pions, kaons and neutrons), photons, electrons and muons ranging from thermal energies up to the GeV range. This complex field has been extensively simulated by the FLUKA Monte Carlo code and benchmarked in detail for radiation damage issues at the LHC. The observed radiation is due to particles generated by proton-proton (or ion-ion) collisions in the LHC experimental areas (as previously discussed in this chapter), beam losses (protons, ions) on the collimators, and distributed interactions of the beam with the residual gas inside the beam pipe. The proportion of the different particle species in the field depends on the distance and on the angle with respect to the original loss point, as well as on the amount (if any) of installed shielding material. In this environment, electronic components and systems exposed to a mixed radiation field will experience three different types of radiation damages: these are displacement damage, damage from the Total Ionising Dose (TID) and so-called Single-Event-Effects (SEEs). The latter range from single or multiple bit upsets (SEUs or MBUs), transients (SETs) up to possible destructive latch-ups (SEs), destructive gate ruptures or burn-outs (SEGRs and SEBs).

The first two groups are of cumulative nature and are measured through TID and non-ionizing energy deposition (NIEL, generally quantified through accumulated 1-MeV neutron equivalent fluence), where the steady accumulation of defects cause measurable effects which can ultimately lead to device failure. As for stochastic SEE failures, they form an entirely different group as they are due to the localized ionization by a single particle, able to deposit sufficient energy through ionization processes in order to perturb the operation of the device. They can only be characterized in terms of their probability of occurring as a function of accumulated High Energy (>20 MeV) Hadron (HEH) fluence. The probability of failure will strongly depend on the device as well as on the flux and nature of the particles. In the context of HL-LHC, several tunnel areas close to the LHC tunnel, and partly not sufficiently shielded, are or are supposed to be equipped with commercial or not specifically designed electronics, which are mostly affected by the risk of SEEs [10], whereas electronics installed in the LHC tunnel will also suffer from accumulated damage in the long-term.

The impact of radiation effects on the accelerator performance and availability can be in first term quantified by the number of beam dumps induced by SEE failures in critical equipment. In addition to the premature loss of the beam and as opposed to non-destructive SEEs, typically solved by a remote reset, destructive SEEs will also require an access to the machine for replacement, and therefore will induce machine downtime.

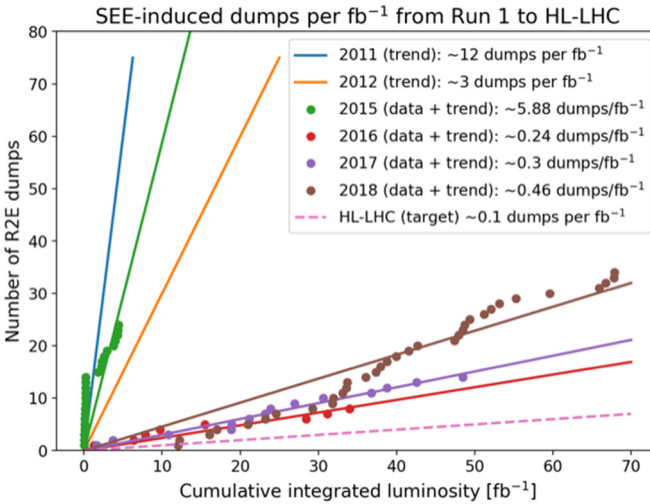


Fig. 5. Number of SEE induced dumps as a function of integrated luminosity for Run 1 and Run 2, and HL-LHC requirement.

Therefore, the number of SEE dumps per unit integrated luminosity can be used as a figure-of-merit of the R2E impact on the machine availability and is shown in Figure 5 with Run 1 and Run 2 data and HL-LHC objectives. Thanks to the LS1 mitigation measures and the Run 2 deployment of radiation tolerant systems, the <0.5 dump/ fb^{-1} requirement was fulfilled. Further development and qualification activities within the R2E project are aimed at meeting the challenging <0.1 dump/ fb^{-1} requirement for HL-LHC operation.

In addition to SEE effects, which scale linearly with integrated radiation levels and start manifesting from a very early stage in the accelerator operation, cumulative radiation damage is also a threat for the availability of critical accelerator systems, and will not manifest itself through a linear behavior with the accumulated radiation levels, but rather as a prompt failure increase, as

described in the wear-out phase of the so-called reliability bathtub curve. Therefore, the design and qualification of systems compliant with the radiation lifetime requirements is an essential ingredient to the Radiation Hardness Assurance procedure, in addition to the SEE tolerance.

Hence, defining the radiation levels to which a certain HL-LHC system will be exposed to is an essential step to be completed at a very early stage of the design specification [11]. The expected radiation levels will have an impact on the high-level system architecture as well as on the selection of electronic components and their qualification strategy.

A broad variety of radiation environments and levels are encountered in a high-energy hadron accelerator like the LHC, with gradients that can involve order of magnitude changes over just a few meters distance. As a general guideline, the radiation level intervals and respective recommendations for electronic component use are summarized in Table 1.

Table 1. Radiation level intervals and respective recommendations for electronic component use.

Lifetime Dose (Gy)	Lifetime n_{eq} fluence (cm^{-2})	Annual HEH fluence ($\text{cm}^{-2} \text{yr}^{-1}$)	R2E Category
<10	< 10^{11}	10^6 - 10^9	Only SEEs are of concern
10-200	10^{11} - 2×10^{12}	10^9 - 2×10^{10}	Standard qualification for LHC tunnel equipment; both SEEs and cumulative damage are of concern
200-3000	2×10^{12} - 3×10^{13}	2×10^{10} - 3×10^{11}	Dose interval in which most standard COTS will fail; component level SEE qualification might require Heavy Ions; system level tests in CHARM will require multiple weeks
>3000	> 3×10^{13}	> 3×10^{11}	Use of COTS typically excluded

In the rest of this chapter, we will cover several examples of radiation levels in the vicinity of IP1 and IP5 for the HL-LHC operation, where, as previously discussed, the source of the radiation environment is the collision debris.

5.1. Triplet and Matching Section

The respective dose levels as calculated with FLUKA at beam height and 1.6 m distance from the beam line towards the inside of the ring can be seen

in Figure 6. They remain above 10 kGy up to a 230 m distance from the IP. Therefore, this region is essentially excluded for commercial-off-the-shelf (COTS) components, and related accelerator equipment needs to be hosted in shielded areas, such as the UJs, ULs and RRs, which will be covered later.

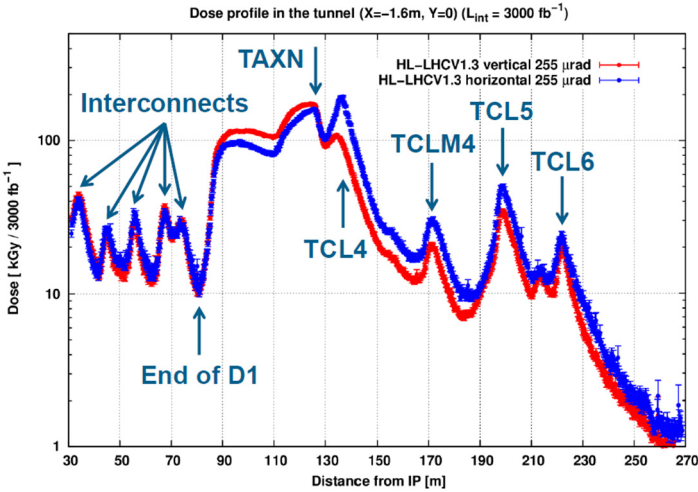


Fig. 6. Dose profile at beam height and 1.6 m from the machine axis on the internal side of the HL-LHC straight section, for vertical (red) and horizontal (blue) crossing.

Of particular interest in this interval is the area near the end of D1, which is a possible location for the cold by-pass diodes of the triplet to potentially suffer from radiation damage. The calculated radiation levels around this area can be seen in Figure 7, referring to different heights (60, 80 and 100 cm) above the vacuum chamber. Just downstream the D1, at about 83 m from the IP, where the cold-diode would be located[†], one finds at a height of 80 cm roughly 30 kGy and 1.5×10^{14} n_{eq}/cm² for the nominal HL-LHC lifetime, which can therefore be considered as specification values, excluding safety margins, for the respective diode radiation qualification.

[†] Detailed integration studies for the cold diode location are presently ongoing, in addition to further FLUKA simulations taking into consideration a more detailed description of the surroundings of the diode (e.g. diode box, DFX connection, etc.).

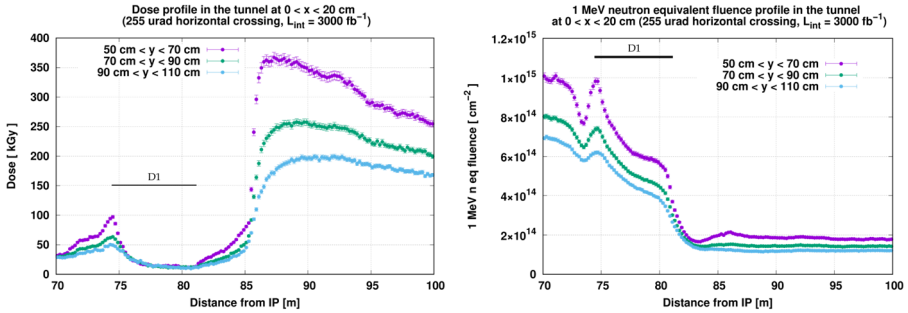


Fig. 7. Dose and 1-MeV neutron equivalent fluence in the area of the triplet-D1 string cold diode.

It is interesting to note that the D1 magnet on the one hand acts as shielding for the dose, which increases abruptly after its end, and as a neutron source on the other hand, as indicated by the following lower fluence plateau. As a consequence, finding an optimal position both in terms of ionizing dose and 1-MeV neutron equivalent becomes challenging. However, it is worth noting that in the specific case of the cold diodes, the main degradation mechanism is linked to an increase in the forward voltage related to displacement damage, therefore the neutron equivalent fluence is the main requirement from a radiation standpoint.

5.2. Dispersion Suppressor

As presented in Section 4, the Dispersion Suppressors of the high luminosity insertions feature pronounced losses in the odd half-cells. Focusing here on the equipment below the cryostats, Figure 8 shows the calculated dose profile, highlighting the regions that exceed the standard LHC tunnel qualification target of 200 Gy. As a consequence, extended intervals of the HL-LHC DS will either be excluded for equipment qualified up to 200 Gy, or host equipment (i) requiring periodic planned replacement and/or (ii) tolerant up to larger levels.

It is to be noted that, whereas relocation is a valid solution to spare the equipment from the very large radiation levels of the areas where their associated objects are operated (for instance, power converters and Quench Protection System versus their corresponding magnets), it often comes at a

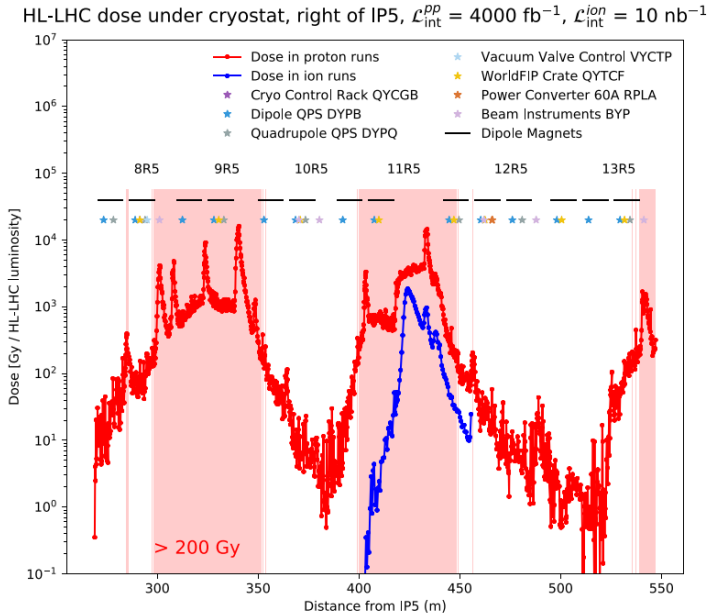


Fig. 8. HL-LHC radiation levels in the IR5 Dispersion Suppressor. A similar profile is expected for IR1.

high cabling cost, and therefore needs to be adequately balanced out with respect to the achievable radiation tolerance of the system.

Moreover, electronics in the DS will also be subject to very large particle fluence, which can have an impact in terms of possible displacement damage degradation, as well as, notably, SEEs.

5.3. Shielded Areas

In order to host electronic systems for equipment in high radiation areas, shielded alcoves were included in the LHC infrastructure. For IR1 and IR5, the most relevant alcoves, from the point of view of their still challenging radiation levels, are the UJs (Junction Chamber), ULs (Liaison Gallery between underground works) and RRs. As can be seen in Figures 9 and 10, the expected high energy hadron fluence for one HL-LHC year in these areas is as large as 10^{10} HEH/cm^2 , corresponding to roughly 10 Gy/yr and $10^{11} \text{ n}_{\text{eq}}/\text{cm}^2$.

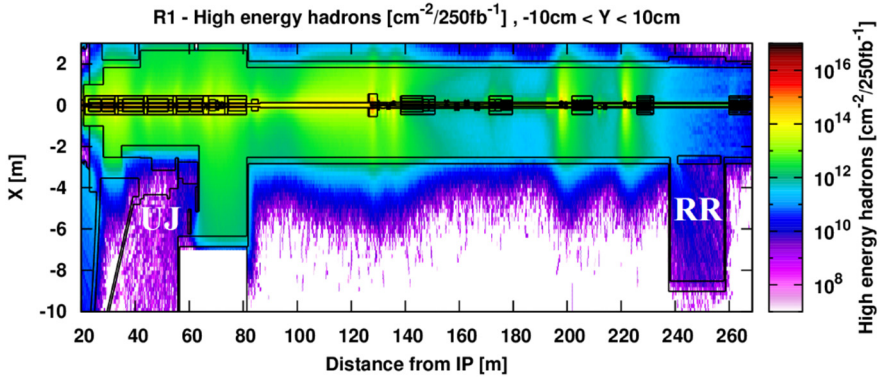


Fig. 9. HL-LHC annual high-energy hadron fluence in the IR1 straight section, including the RR and UJ shielded areas.

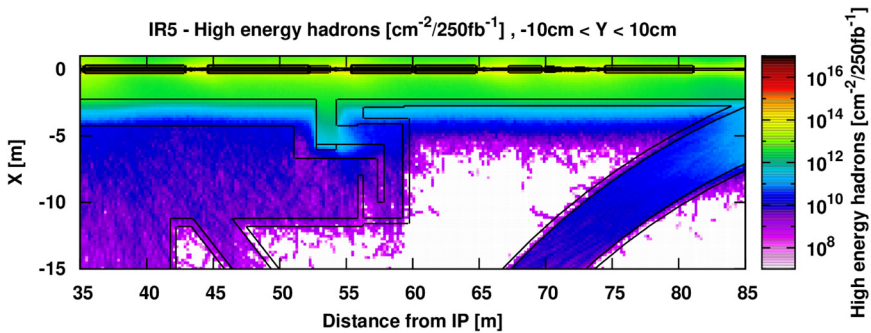


Fig. 10. HL-LHC annual high-energy hadron fluence in the IR5 triplet-D1 region, including the UJ shielded area.

In addition to Single Event Effects, which are presently the only concern for the LHC shielded areas, these levels will also potentially induce cumulative degradation of the electronics and therefore will also represent a threat to its lifetime.

5.4. Implications on Radiation Hardness Assurance

The radiation levels introduced above, along with the performance and availability requirements for the HL-LHC and its systems (for instance, many of the distributed systems exposed to radiation can only afford one

single radiation induced failure leading to a beam dump per year), imply a highly challenging Radiation Hardness Assurance approach for the HL-LHC equipment.

The associated methodology combines critical component level testing up to the typical requirement, as well as system level testing in the highly representative radiation environment of the CHARM facility [12]. In CHARM, a mixed-radiation field for the qualification of accelerator equipment is generated through the interaction of a 24 GeV/c proton beam with a 50 cm copper target.

In fact, the availability of a facility such as CHARM, unique in the world as for its capability of irradiating full large-scale systems with a radiation environment representative of the one present in the LHC accelerator, is the cornerstone of the associated qualification approach.

System level radiation tests in CHARM are typically performed on a weekly basis, corresponding to roughly 10^{16} protons on target, and during which the equipment receives a dose (depending on the actual irradiation configuration) of roughly 200 Gy, therefore compliant with the typical tunnel and shielded area radiation level requirements. As an example, the FGCLite power converter controls and the 600A and 4-6-8 kA converters have been already tested in CHARM according to the HL-LHC radiation level and availability requirements.

References

1. T. T. Bohlen, F. Cerutti, M. P. W. Chin, A. Fassò, A. Ferrari, P. G. Ortega, A. Mairani, P. R. Sala, G. Smirnov, and V. Vlachoudis, The FLUKA Code: Developments and Challenges for High Energy and Medical Applications, Nuclear Data Sheets 120, 211-214 (2014).
2. G. Battistoni et al., Overview of the FLUKA code, Annals of Nuclear Energy 82, 10-18 (2015).
3. S. Roesler, R. Engel, J. Ranft, The Monte Carlo Event Generator DPMJET-III, Proc. of the Monte Carlo 2000 Conference, Lisbon, A. Kling, F. Barao, M. Nakagawa, L. Tavora, P. Vaz eds., Springer-Verlag Berlin, 1033-1038 (2001).
4. A. Fedynitch, PhD Thesis, (2015). <https://cds.cern.ch/record/2231593/files/>, CERN-THESIS-2015-371.pdf.
5. L. S. Esposito et al., Power load from collision debris on the LHC Point 8 insertion magnets implied by the LHCb luminosity increase, IPAC2013, TUPFI022, p. 1382, (2013).

6. V. Vlachoudis, FLAIR: A Powerful But User Friendly Graphical Interface For FLUKA, Proc. Int. Conf. on Mathematics, Computational Methods & Reactor Physics, Saratoga Springs, New York, (2009).
7. A. Mereghetti et al., The FLUKA LineBuilder and Element DataBase: Tools for Building Complex Models of Accelerator Beam Lines, IPAC2012, WEPPD071, p. 2687, (2012).
8. N. V. Mokhov et al., "Protecting LHC IP1/IP5 Components Against Radiation Resulting from Colliding Beam Interactions," CERN-LHC-Project-Report-633, (2003).
9. N. V. Mokhov, I. L. Rakhno, "Mitigating radiation loads in Nb3Sn quadrupoles for the CERN Large Hadron Collider upgrades," Phys. Rev. STAB 9 (2006) 101001.
10. R. García Alía et al., "Single event effects in high-energy accelerators", Semicond. Sci. Technol., vol. 32, no. 3, p.034003 (Feb., 2017).
11. R. García Alía et al., "LHC and HL-LHC: Present and Future Radiation Environment in the High-Luminosity Collision Points and RHA Implications," in IEEE Transactions on Nuclear Science, vol. 65, no. 1, pp. 448-456 (Jan., 2018).
12. J. Mekki, M. Brugger, R. G. Alia, A. Thornton, N. C. D. S. Mota and S. Danzeca, "CHARM: A Mixed Field Facility at CERN for Radiation Tests in Ground, Atmospheric, Space and Accelerator Representative Environments," in IEEE Transactions on Nuclear Science, vol. 63, no. 4, pp. 2106-2114 (Aug., 2016).

This page intentionally left blank

Chapter 16

11T Dipole and New Connection Cryostats for Collimators

Bernardo Bordini, Luca Bottura, Arnaud Devred, Lucio Fiscarelli,
Mikko Karppinen, Gijs de Rijk, Lucio Rossi, Frédéric Savary,
Daniel Schörling and Gerard Willering

CERN, Geneva 23, CH-1211, Switzerland

This chapter describes the design of, and parameters for, the 11 T dipole [11] developed at FNAL and the European Organization for Nuclear Research (CERN) for the High Luminosity Large Hadron Collider (HL-LHC) project.

1. Introduction

The HL-LHC upgrade will yield a more intense proton beam, with a circulating current of 1.1 A per beam vs. the 0.56 A nominal current value in the LHC. The intensity of the ion beams (usually Pb ions) for ion–ion collisions will actually be increased by a factor of three: from $4 \cdot 10^{10}$ to $1.2 \cdot 10^{11}$ circulating particles per beam. This intensity increase, both for protons and ions, will increase the diffractive losses at the primary collimators, located in LHC Point 7 (P7), which may drive the energy deposition in the main dipoles located in the dispersion suppressor (DS) region above the quench limit. To avoid limiting the machine due to this effect, various countermeasures have been studied, and the solution chosen was to intercept these diffractive losses via warm absorbers (also called collimators) placed in the cold dispersion suppressor region of the LHC. The most elegant and practical way to introduce a room-temperature zone in the DS, at a location corresponding to the middle of the second dipole of the DS cell, was to substitute a regular LHC dipole (8.33 T of central field and 14.3 m of magnetic length) with a magnet of 11 T

This is an open access article published by World Scientific Publishing Company. It is distributed under the terms of the Creative Commons Attribution 4.0 (CC BY) License.

with a length of approximately 11 m, yielding the same bending strength while saving about 3.5 m of longitudinal space. The 11 T field in the magnet bore inevitably calls for Nb₃Sn technology. The space gained, thanks to the higher field and shorter length, is sufficient to insert a cold–warm–cold bypass on which to allocate all lines for cryogenic and electrical continuity of the circuits being powered in series throughout the LHC arc, as well as to install the Target Collimator Long Dispersion suppressor (TCLD). For reasons of beam dynamics and to reduce the technology risk associated with the innovative and relatively expensive Nb₃Sn superconductor, the 11 T dipole was split into two magnets of 5.5 m length, with the bypass and collimator installed in the middle. A schematic layout of the assembly with its position in the LHC is shown in Figure 1.

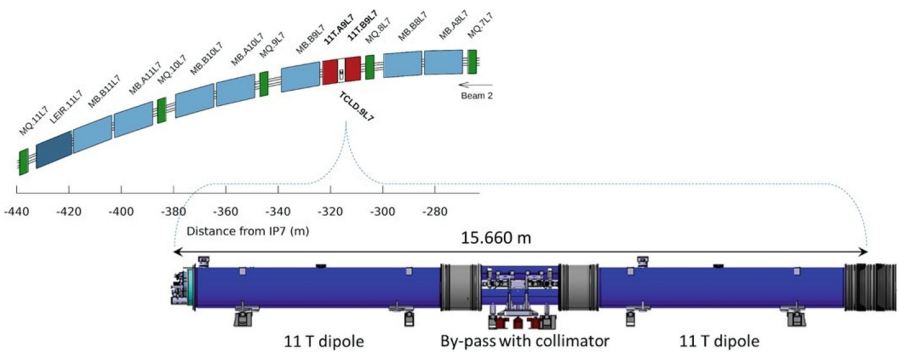


Fig. 1. Schematic of the 11 T cryo-assembly, with the bypass hosting the collimator at the center. In the dispersion suppressor (DS) cells (the array in the top where LHC dipoles are in light blue) one standard dipole is replaced by the 11 T cryo-assembly, indicated in red.

A similar DS cleaning upgrade is required for heavy ion collisions in the ALICE experiment of IP2, where secondary ion beams with different magnetic rigidity are created, which are lost in the adjacent DS. These secondary ion beams create heat deposition in the impacted magnet that could lead to a magnet quench. Bound-free pair production (BFPP) are the dominant process with the main heat deposition occurring in Cell 10 of the long arc cryostat. The same TCLD collimator assembly as foreseen for IR7 has therefore been installed as cold-warm-cold transition just without the 11 T dipole magnets on either side of IR2, replacing the previous connection cryostat in Cell 10 (see Figure 2).

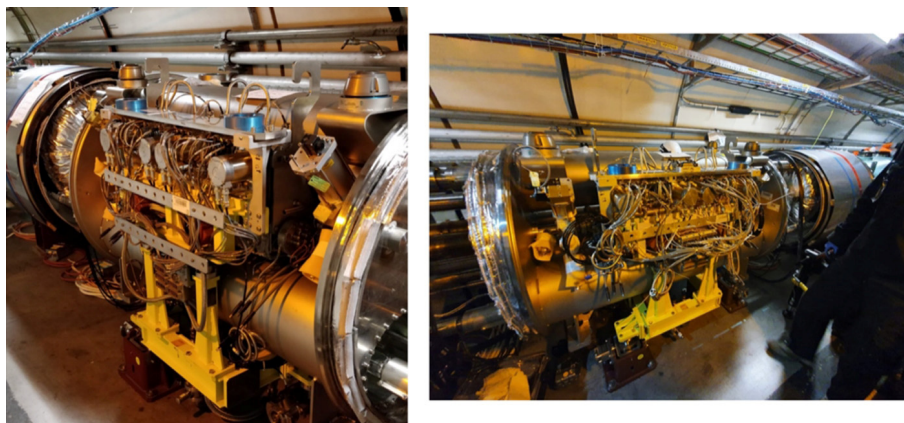


Fig. 2. TCLD assembly installed along with new connection cryostats on either side in Cell 10 of IR2, replacing the former empty connection cryostat.

2. Magnet Design

The main constraint of the 11 T magnet design stems from the fact that the 11 T dipole pair becomes a part of the LHC main circuits of the LHC sectors 67 and 78 and, as such, is powered in series with the remaining 153 LHC two-in-one-aperture dipole magnets. Each 11 T dipole magnet pair therefore must provide an integrated transfer function (ITF) as close as possible to that of the LHC main dipole magnets over the whole dynamic range, from injection energy of 0.45 TeV (7.7 T.m of bending strength) to the collision energy of 7 TeV (119.2 T.m of bending strength). These values for the bending strength must be obtained at the nominal current of the main bending (MB) circuit, *i.e.*, 760 A at the 0.45 TeV injection energy and 11.85 kA at the 7 TeV collision energy. A second condition was to respect the LHC's basic geometry: the distance between the center of the two apertures (194 mm at 1.9 K) and the position of the cryogenic and electrical lines passing through the yoke. Finally, the timescale did not allow for a long period of R&D. It was therefore decided to rely on a design concept as close as possible to that of the LHC MB dipoles, from which CERN has accumulated more than two decades of experience [1]: the two-layer cos-theta coil layout, with the force supported by a classical collar structure, a vertically split iron yoke, and an external shrinking cylinder also serving as a helium vessel. Thanks to CERN's experience and to the

FNAL program on the Nb₃Sn cos-theta layout with collars, the initial decision on the layout was taken [2,3,13].

The preliminary design study proved that all main design criteria, *i.e.*, field strength with a reasonable ITF over all of the dynamic range, critical current margin, and field quality (both at injection and at high field), could be met with the available Nb₃Sn wire properties, despite the considerable difficulties given by the various constraints. Structural and protection issues were left to a later, more detailed and realistic design.

2.1. Basic design Features

Different from the LHC main dipole magnets, the 11 T dipole magnets feature separate stainless-steel collars for each aperture, compared to common stainless-steel collars in the case of the LHC MBs. This design change was introduced to allow a better-controlled symmetric loading of the coils and make it possible to test the collared coils in a one-in-one configuration without the need for de-collaring prior to integration in the two-in-one cold mass. To maximize the use of the existing infrastructure and cold-mass assembly tooling, the outer contour of the cold mass was chosen to be identical to the LHC MBs. The location and the section of the slots' busbars was to be preserved, as well as the location of the heat exchanger in the iron yoke.

A nominal field of 11 T requires a magnet that is about 11 m long. To reduce the risks associated with the fabrication of brittle Nb₃Sn coils, the original 11 m long magnet was split into two units, each 5.5 m long and with straight coils, not being bent as the ones of the LHC MBs. The sagitta of the beam trajectory in each of the two 5.5 m long straight magnets is only around 2 mm, compared to 9 mm in a standard LHC MB. During the initial phase of the project, it was considered important to compensate for the effect of the sagitta on the free aperture by enlarging the coil aperture to 60 mm (compared to the 56 mm in the LHC MB). Later, it was however decided to use existing spare beam screens from the LHC without an increased free aperture.

The field quality targets were similar to those of the LHC MB, *i.e.*, at the 10⁻⁴ level at the reference radius of 17 mm. Special attention had however to be paid to the multipoles arising from persistent currents induced in the inherently larger filaments of the available Nb₃Sn strands and the higher

yoke saturation (with a larger magnetic flux conveyed in the same yoke as the LHC MB).

A further important advantage of this solution is the possibility of placing the collimator between the two 5.5 m long 11 T dipoles, reducing the orbit excursion.

To ensure reliable operation, the design goal was to provide an operational margin of 20% on the load line, as for other Nb₃Sn HL-LHC magnets, assuming that the only conductor performance degradation results from cabling and neglecting transverse stress effects. The initial design of the 11 T dipole is described in [2] and [3].

2.2. Conductor Choice and nominal dimensions

The parameters of the strands and the Rutherford cable were selected based on the required number of ampere-turns to generate the requested ITF under the 20% operating margin, the available coil space, and the maximum number of strands possible in the cabling machine. The finally selected strand diameter was 0.7 mm, with an expected cable thickness in the range of 1.2–1.3 mm (depending on the allowed compaction). The strand geometry and performance specification are summarized in Table 1.

The optimization of cable parameters was done jointly by FNAL and CERN [3] and included the selection of the cable cross-section geometry and compaction to achieve good mechanical stability of the cable and acceptable I_C degradation (less than 10%), incorporating a stainless-steel core (25 μm thickness), and preserving a high residual resistivity ratio (RRR) of the Cu matrix (RRR larger than 100 in extracted strands) as given in Table 2 and depicted in Figure 3.

Table 1. Nb₃Sn wire geometry and specifications

Description	Value
Strand diameter (mm)	0.70
J_c (12 T, 4.2 K) (kA/mm ²)	> 2.45
Effective filament size D_{eff} (μm)	< 41
Twist pitch (mm)	14
Cu RRR (virgin state)	> 150
Cu-to-non-Cu fraction (%)	53.5 (± 2)

Table 2. Cable geometrical parameters

Parameter	Reacted	Unreacted
Mid-thickness (mm)	1.25	1.30
Thin edge (mm)	1.15	1.19
Thick edge (mm)	1.35	1.40
Width (mm)	14.70	15.08
Keystone angle (o)	0.79	0.81

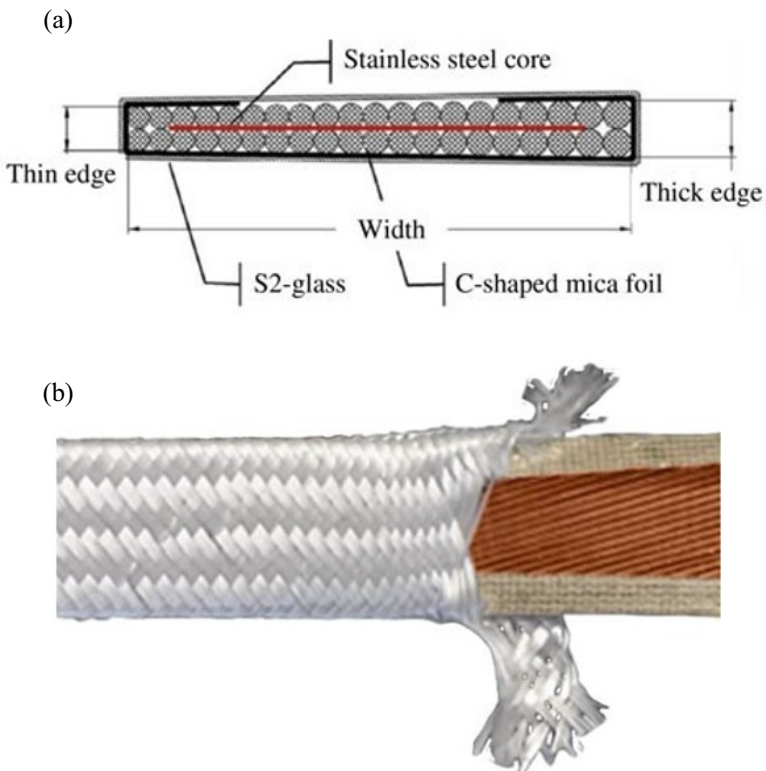


Fig. 3. Cable insulation based on S2-glass braided on mica tape (CERN insulation): (a) schematic; and (b) photograph.

The choice of filament results on the contrary in a significantly higher magnetic induction heating, being at compatible with the available cryogenic power only for a small number of magnets to be installed in the LHC [12].

2.3. Magnetic Design

The main electromagnetic design challenges of the two-in-one-aperture 11 T dipole magnet are to match the integrated transfer function of the MB, to control the magnetic crosstalk between apertures, and to minimize the magnitude and variation of non-allowed multipoles [4]. The coil cross-section was optimized using the reacted cable parameters and a 100 μm insulation layer around the cable. The early-stage preliminary design used the iron yoke shown in Figure 4(a), leaving a radial space of about 30 mm for the collars. The optimal configuration, delivering 11.21 T at 11.85 kA in a two-in-one configuration, was found with a six-block layout of 56 turns with 22 turns in the inner layer and 34 turns in the outer layer, as shown in Figure 4(b).

The coil ends were optimized first to find the optimal mechanical configuration based on easy- and hard-way strain in the cable, as well as the amount of torsion over the unit length. The lead-end optimization also included the layer jump and the transitions between the winding blocks. The relative axial positions of the end blocks were then optimized to minimize the integrated harmonics.

It was decided to use this coil design for the short models and then, before scaling up to the full length, re-optimize the coil cross-section with the experimental data from the magnetic measurements of the short model magnets along with the feed-back from coil fabrication [17,18].

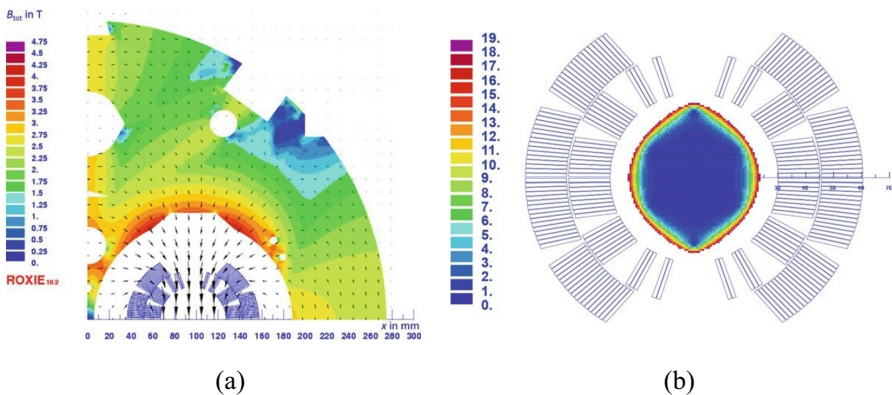


Fig. 4. (a) Two-in-one model used for coil optimization; (b) coil cross-section, with relative field errors in units.

The nature of the magnetic flux pattern in the two-in-one yoke configuration requires additional features to minimize the cross-talk between the apertures, in particular for the b_2 component. The two holes in the yoke insert reduce the b_2 variation from 16 units to 13 units. Such large cross-talk indicates that the distance between the apertures and the overall size of the yoke would ideally need to be increased for such a high field magnet.

Due to the stronger iron saturation effect, the Nb₃Sn 11 T dipole magnets will be stronger than the LHC MB at intermediate excitation levels, the peak difference being 2.4 T.m at 6.7 kA. This difference can be compensated with the foreseen 250 A bi-polar trim power converters to be installed across the 11 T dipole magnets.

Owing to the larger filament size in Nb₃Sn strands when compared to Nb–Ti strands, the scaled b_3 component due to the persistent currents in the 11 T dipole magnet is about 44 units at the LHC injection current [14]. The magnetization effects strongly depend on the current pre-cycle and the lowest current reached during the cycle, the so-called reset current, I_{res} . Using I_{res} of 100 A – being the standby current of the main dipole converters - the sextupole component can be reduced to stay within 20 units between injection (I_{inj}) and nominal current (I_{nom}), which is acceptable for the LHC [5]. In addition, as shown by the measurements, flux jumps strongly affect the filament magnetization below 1 T and reduce the projected b_3 effect, which is a beneficial effect at the expense of reproducibility.

2.4. Mechanical Design

The mechanical structure of the magnet provides optimum clamping of the superconducting coil in order to achieve minimum distortion of the conductor and avoid cable displacement, whilst maintaining at all times the stresses at an acceptable level for the strain sensitive and brittle Nb₃Sn. A detailed structural analysis was carried out to explore the optimal parameter space for the magnet assembly [15].

The design of the magnet was inspired by the 1-m-long LHC MFISC model magnet [6]. One of the main challenges of the mechanical design is to achieve a delicate balance between the risk of overloading the mid-plane turns and that of unloading the pole turns at full field. To enable a better control of coil stress, it was decided to rely on a removable pole [2]. Such a pole enables an

adjustment of the coil pre-compression by the insertion of bespoke shims of which the thickness is determined as a function of the coil size measured after vacuum pressure impregnation. An additional Cu-alloy filler wedge, which is potted together with the coil, is added to the outer layer to match the azimuthal size of the inner layer to simplify the pole wedge geometry as shown in Figure 5. In order to smoothen out the stress distribution between the inner and the outer layers and to reduce peak stresses in the coil along its interface with the pole during collaring, 2-mm-thick stainless-steel loading plates are added at the pole prior to impregnation.

The collared coils are assembled between the yoke halves and the central yoke laminations insert, and the two 15-mm-thick stainless-steel outer shells. The shells are welded together in a welding press to form the shrinking cylinder.

3. 11 T Dipole Development at CERN

The joint 11 T dipole R&D program at CERN started in 2011 with the transfer of the technology developed at FNAL, and with adjustments to the LHC MB specific design features [7]. At CERN, development was undertaken having in mind a technology suitable for scaling up to the long magnets for installation in the accelerator. In parallel to the R&D, the large tooling for the manufacturing of the long magnets was designed, procured, and installed in the CERN Large Magnet Facility.

3.1. CERN Model Design, Fabrication and Training

Twenty-three 2 m long coils were fabricated during the period of 2013–2018 and assembled in eight single-aperture and two two-in-one-aperture short models as shown in Figure 7, with several variants explored, including different strand types, assembly parameters and procedures, and the type of quench protection heaters [15].

The single-aperture magnets were trained at nominal conditions at 1.9 K with a ramp rate of 10 A/s. Some of the models included coils that were already trained in a previous assembly. The training curves are shown for the assemblies made from virgin coils (see Figure 8). In the case of magnets SP101 and SP104, the large number of training quenches and the performance limitations

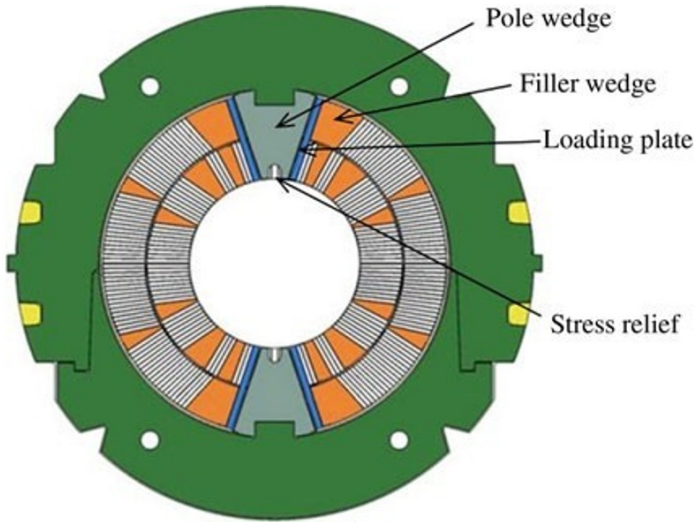


Fig. 5. Collared coil cross section.

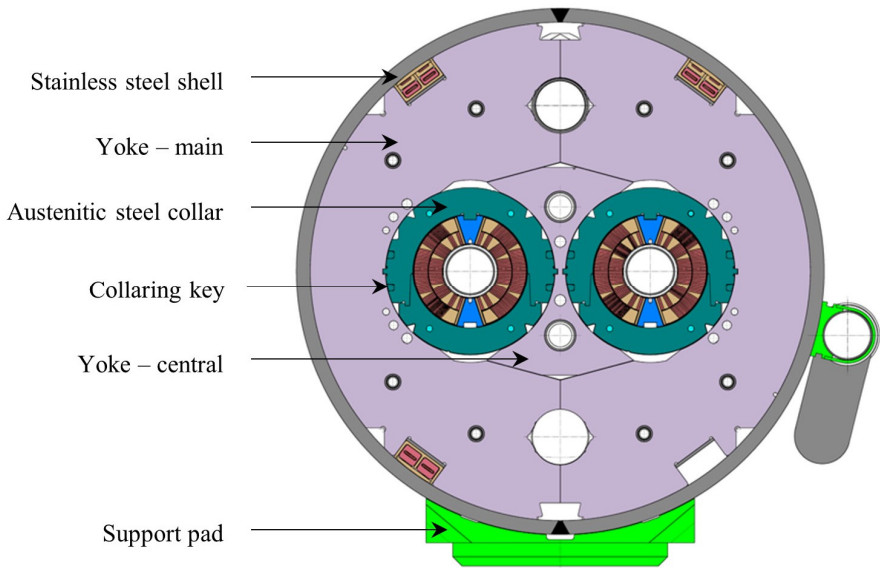


Fig. 6. Magnet cross section.

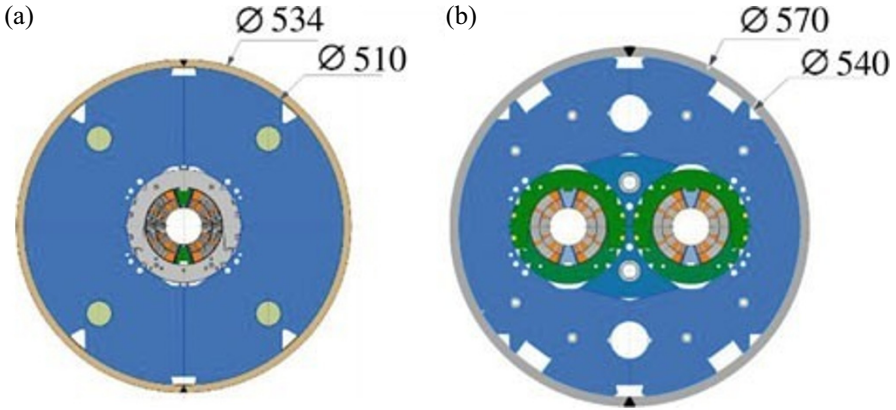


Fig. 7. CERN 11 T dipole cross-sections: (a) single-aperture; and (b) two-in-one-aperture. Dimensions are given in mm.

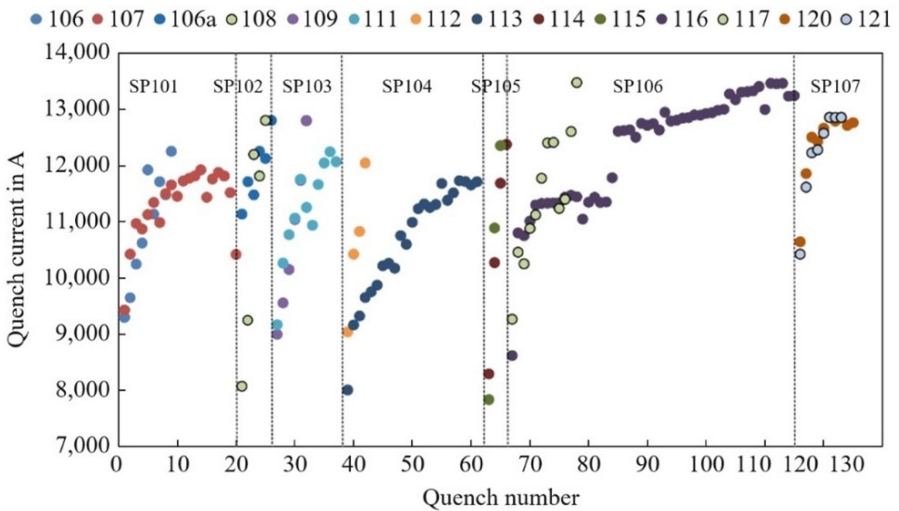


Fig. 8. Training quenches for all coils tested.

are believed to be related to issues with the layer jumps of Coils 107 (for SP101) and 112 (for SP104). There is a strong suspicion of a local non-homogeneous defect in or close to the layer jump, which may have influenced the training rate [8]. The particularly slow training of Coil 116 (SP106) may be linked with an issue in coil Block 3 of the inner layer. Following

Quench 19, as shown in Figure 8, the high MIITs ($1 \text{ MIIT} = 10^6 \text{ A}^2 \cdot \text{s}$) studies (part of the regular test program) started, and the protection was delayed, resulting in an increase of the hot-spot temperature during a quench. While additional conductor degradation driven by the hot-spot temperature was expected, the performance increased step by step, possibly due to a stress redistribution in the conductor. This magnet reached eventually 13.5 kA, with a central field of nearly 13 T.

In November 2017, a Task Force was established to review the assembly procedures of the model magnets. The Task Force focused on optimizing the collaring process parameters to cap the peak stress experienced by the coil to a value lower than 150 MPa. Model magnet SP107 was produced following the Task Force recommendations and underwent endurance testing, including 5 warm-up-cooldown (WUCD) to LHe, 10 WUCD to LN₂, and over 450 electromagnetic (EM) cycles. As shown, in Figure 9 below, the magnet repeatedly achieved nominal current, and went 3 times to ultimate current, thereby confirming design feasibility.

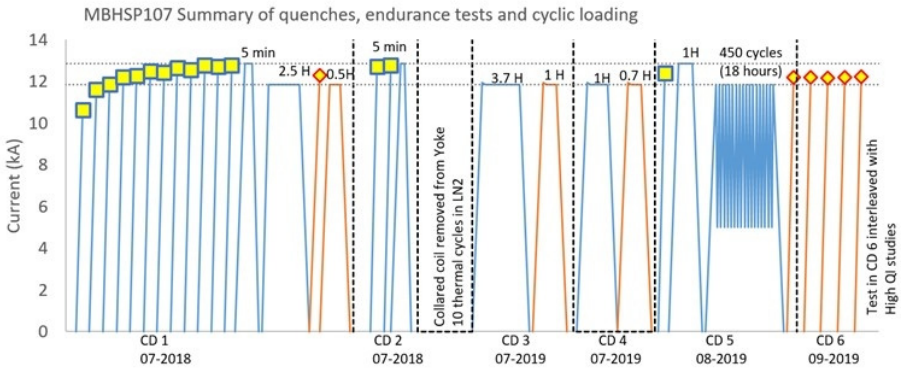


Fig. 9. Powering and quench history of model magnet SP107 issued from the 11 T Task Force (November 2017-July 2018).

3.2. Full-Scale Prototype

As a step towards scaling up the design and processes, a full-length prototype has been fabricated at CERN [10] (see Figure 10). This prototype had already the most relevant features of the final magnets (while still using a different type

of layout for the strands, the magnetic length not yet being optimized and, of course, not including the modifications subsequently introduced by the 11 T Task Force's revised design and procedures to address the limitations observed in the model coils). It has been a key learning and debugging exercise for such a complex object: indeed, this 5.5 m long dipole is the first long Nb₃Sn magnet built at CERN, aimed at providing a key demonstration of Nb₃Sn technology in an operating accelerator.



Fig. 10. The first 5.5 m long 11 T MBH dipole prototype in its cryostat at CERN ready to be transported to the test bench.

The prototype was targeting full accelerator quality in terms of quench performance, field errors, electrical robustness, protection, and geometry. Although most of the major tooling was available at CERN, recovered from the production of the Nb-Ti magnets for the LHC, significant modifications and upgrades were necessary. The largest additional tooling required to fabricate the coils were an argon oven for the reaction of the Nb₃Sn coils, and a vacuum pressure impregnation system. The design and procurement of the

contact tooling started in the middle of 2013 with the winding mandrel and curing mold, followed by the reaction fixture and impregnation mold, to finish later with the collaring tooling. Because of a tight schedule resulting from the initial project goal to install the magnets during the accelerator's Long Shut Down 2 (LS2) taking place during the years 2019–2020, an important overlap between the different phases of the project was inevitable. The assembly work profited from the large amount of experience in the assembling and collaring of long coils and the assembly of long cold masses at CERN for the LHC magnets. The magnet performance at 1.9 K appeared limited to about 8.5 kA in one of the coils which was likely due to a non-conformity (misplacement of coil end spacers) observed at the end of the reaction heat treatment and resulting in a relative movement between a coil block and an end spacer). Also, the prototype was assembled prior to the Task Force's assessment.

3.3. *Series production*

The series production of the 11 T magnets comprises four 2-in-1 magnets for installation in the LHC machine and two spare magnets. For this, 12 collared coils were to be produced and the initial plan foresaw the production of 30 single coils, of which six coils could be used to cover for possible incidents during production.

In order to cope with the tight schedule requirements, following competitive tendering, a service contract was placed with Alstom Power Services, Belfort, France, now part of General Electric. The work has been carried out at CERN in the Large Magnet Facility, where all of the necessary machines and tooling were available from the prototyping phase. All of the components and consumables have been provided by CERN. The other construction activities, like the cold mass assembly, the cryostating, the cold tests, and the final preparation prior to installation in the accelerator, were carried out by a mixed team of CERN personnel and contract labor under direct CERN technical responsibility.

The manufacture of the series collared-coil assemblies integrated all the lessons learned from the 11 T Task Force, in particular, the use of graded shims with 25 μm steps (see Section 2.4) to compensate the longitudinal variations of the azimuthal coil sizes measured after vacuum pressure impregnation, and a revised cable insulation scheme. The fiberglass braiding

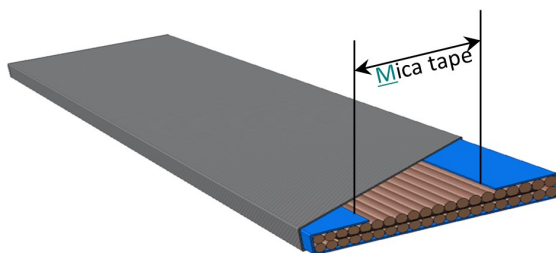


Fig. 11. Schematic view of the cable insulation. In blue, the mica tape with a gap to allow resin penetration, and in grey, the braided fiberglass.

parameters were revised in order to achieve the target thickness of $100\ \mu\text{m}$ under a compression of $5\ \text{MPa}$ (see Section 2.3). The cable insulation was actually too thick with the original braiding parameters, in the range of $135\ \mu\text{m}$ at $5\ \text{MPa}$. Furthermore, the relatively large gap of the C-shaped mica tape, initially of $7\ \text{mm}$ in order to facilitate resin penetration, was implying stress concentration along the edges of the cable. This gap was reduced to $1\ \text{mm}$ with visible smoothing of peak stress (see Figure 11). It was also verified that such a reduced gap was still allowing satisfactory impregnation conditions.

Also, it should be noted that the prototype, hybrid, S1 and S2 magnets rely on quench heaters which are impregnated with the coils, while all the subsequent magnets rely on external quench heaters like in LHC dipole magnets. The decision of taking the quench heaters out of the coils was taken in early 2019 to improve quench-heater -to-coil insulation and robustness.

In addition to a hybrid assembly, which reused the structure of the prototype, but where the collared-coil assembly with the limiting coil was replaced by the first collared-coil assembly produced by Alstom Power Services/GE, a total of five series magnet assemblies have been completed (S1 through S5). The hybrid assembly and the first four cryomagnets (S1 through S4) have been tested at nominal conditions at $1.9\ \text{K}$ in the SM18 magnet test facility. The cold mass of the fifth magnet (S5) is completed and ready for cryostating. Two more magnets (S6 and S7) are in different stages of production (from coils to collared coil). In the case of the hybrid assembly, only the new aperture was connected electrically and powered.

The new aperture of the hybrid assembly initially achieved nominal current in 2 quenches and ultimate current in 5 quenches, but exhibited detraining after a warm-up cool down cycle, with all quenches (but one) located at the

connection side of one coil head. Analysis of the WUCD procedure showed that the magnet had been subjected to large temperature gradients (in excess of 200 K), with the thermal front first hitting the magnet end where the detrainning quenches originated. The procedure was subsequently changed and a maximum ΔT of 30 K was imposed on subsequent long magnets.

Three (S1, S2, S4) out of four cryomagnets reached stable nominal performance with the requested margin (11850+100 A) after the first cooldown. Initial training was relatively fast (requiring on average 2 to 4 quenches). As illustrated in the Figure 12 below, S1 passed all mandatory LHC magnet acceptance tests in July 2019 and underwent ~ 340 power cycles to maximum current and 1 WUCD. The performance of S3, on the contrary, appeared somewhat erratic around the nominal current, with the problematic quenches originating in the same coil (see Figure 13).

In May 2020, it was observed that S2 exhibited a limitation in quench current close to the nominal value (> 11.5 kA) following intensive reliability studies with provoked quenches and two nominal thermal cycles as part of performance validation (under nominal temperature gradient for WUCD with a $\Delta T < 30$ K). In October 2020 it was observed that S4 also exhibited a - what appears to be - permanent degradation of quench current after the first thermal cycle. These results may point to a performance degradation driven by thermo-mechanical effects triggered by the combination of powering and thermal cycles, only visible in long magnets.

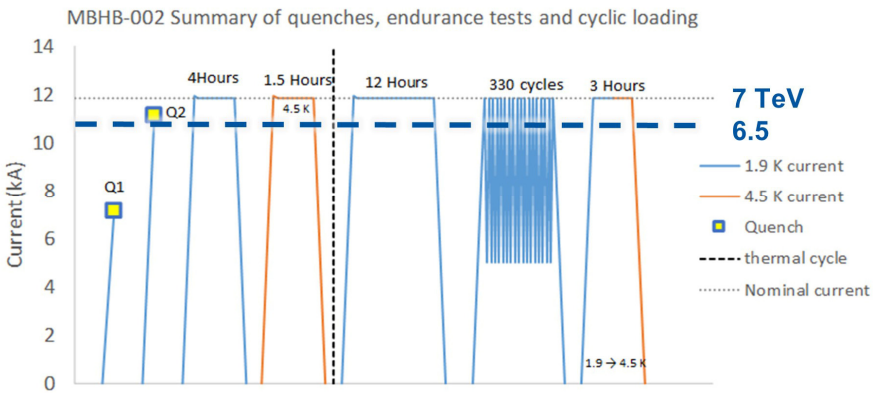


Fig. 12. Powering and quench history of first, twin-aperture, 5.5-m-long series magnet S1.

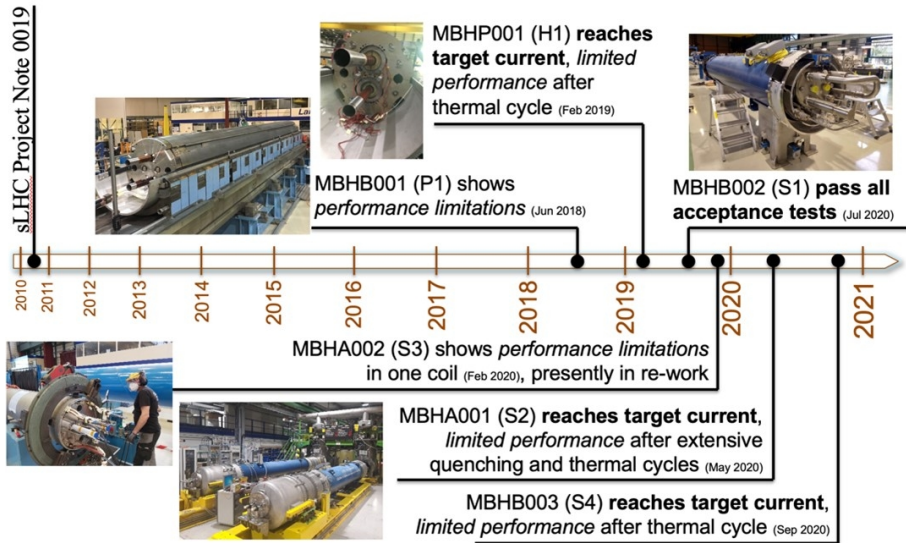


Fig. 13. Timeline of full-size 11 T dipole magnet production and cold testing.

In view of these observations, magnet testing was suspended and the installation of the 11 T dipole magnets during LS2 was given up and deferred to until after the observed degradation effect has been understood. A plan has been devised to fully understand and address the root cause of this degradation in order to assure the fully reliable operation of these magnets as well in the accelerator environment. This evaluation process has been launched at CERN at the beginning of 2021 and is still ongoing at the time of writing for this chapter.

References

1. Rossi L (2004) Experience with LHC magnets from prototyping to large scale industrial production and integration. In: Proceedings of EPAC2004. 9th European particle accelerator conference, Lucerne, July 2004, LHC Project Report 730. CERN, Geneva, p 118B. W. Bestbury, R-matrices and the magic square, *J. Phys. A.* 36(7), 1947–1959, (2003). ISSN 0305-4470.
2. Karppinen M, Andreev N, Apollinari G et al (2012) Design of 11 T twin-aperture Nb3Sn dipole demonstrator magnet for LHC upgrades. *IEEE Trans Appl Supercond* 22(3):4901504. <https://doi.org/10.1109/tasc.2011.2177625>.

3. Zlobin AV, Andreev N, Apollinari G et al (2012) Design and fabrication of a single-aperture 11 T Nb3Sn dipole model for LHC upgrades. *IEEE Trans Appl Supercond* 22(3):4001705. <https://doi.org/10.1109/tasc.2011.2177619>.
4. Auchmann B, Karppinen M, Kashikhin VV et al (2012) Magnetic analysis of a single-aperture 11 T Nb3Sn demonstrator dipole for LHC upgrades. In: *Proceedings of IPAC2012: international particle accelerator conference, New Orleans*, p 3596, (May 2012).
5. Holzer B (2014) Impact of Nb3Sn dipoles on the LHC lattice and beam optics, CERN ACC-NOTE- 2014-0063. CERN, Geneva.
6. Ahlbäck J, Ikäheimo J, Järvi J et al (1994) Electromagnetic and mechanical design of a 56 mm aperture model dipole for the LHC. *IEEE Trans Magn* 30(4):1746–1749. <https://doi.org/10.1109/20.305594>.
7. Savary F, Apollinari G, Auchmann B et al (2015) Design, assembly, and test of the CERN 2-m long 11 T dipole in single coil configuration. *IEEE Trans Appl Supercond* 25(3):1–5. <https://doi.org/10.1109/tasc.2015.2395381>.
8. Willering GP, Bajko M, Bajas H et al (2017) Cold powering performance of the first 2 m Nb3Sn DS11T twin-aperture model magnet at CERN. *IEEE Trans Appl Supercond* 27(4):1–5. <https://doi.org/10.1109/tasc.2016.2633421>.
9. Willering G, Bajko M, Bajas H et al (2018) Comparison of cold powering performance of 2-m-long Nb3Sn 11 T model magnets. *IEEE Trans Appl Supercond* 28(3):1–5. <https://doi.org/10.1109/tasc.2018.2804356>.
10. Savary F, Bordini B, Fiscarelli L et al (2018) Design and construction of the full-length prototype of the 11-T dipole magnet for the high luminosity LHC project at CERN. *IEEE Trans Appl Supercond* 28(3):1–6. <https://doi.org/10.1109/tasc.2018.2800713>.
11. D. Schoerling, A. V. Zlobin (eds.), *Nb3Sn Accelerator Magnets*, Particle Acceleration and Detection, https://doi.org/10.1007/978-3-030-16118-7_9.
12. O. Brüning et al, *LHC Full Energy Exploitation Study: Upgrade for Operation Beyond Ultimate Energy of 7.5TeV*, CERN-ACC-2020-0015.
13. G. de Rijk, A. Milanese, E. Todesco, “11 Tesla Nb3Sn dipoles for phase II collimation in the Large Hadron Collider”, sLHC Project Note 0019, 2010.
14. S. Izquierdo Bermudez, L. Bottura, and E. Todesco, “Persistent-Current Magnetization Effects in High-Field Superconducting Accelerator Magnets”, *IEEE Transactions on applied superconductivity*, Vol. 26, No. 4, (June 2016).
15. P. Ferracin, L. Bottura, A. Devred et al, “Mechanical analysis of the collaring process of the 11T dipole magnet”, *IEEE Transactions on applied superconductivity*, Vol. 29, No. 5, (August 2019).
16. S. Izquierdo Bermudez et al, “Mechanical analysis of the Nb3Sn 11 T dipole short models for the High Luminosity Large Hadron Collider”, 2019 *Supercond. Sci. Technol.* 32.
17. L. Fiscarelli, B. Auchmann, S. Izquierdo Bermudez, B. Bordini, O. Dunkel, M. Karppinen, C. Loffler, S. Russenschuck, F. Savary, D. Smekens, and G. Willering, “Magnetic Measurements and Analysis of the First 11-T Nb3Sn Dipole Models Developed

- at CERN for HL-LHC*”, IEEE Transactions on applied superconductivity, Vol. 26, No. 4, (June 2016).
18. Lucio Fiscarelli, Susana Izquierdo Bermudez, Olaf Dunkel, Stephan Russenschuck, Frederic Savary, and Gerard Willering, “*Magnetic Measurements and Analysis of the First 11-T Nb₃Sn 2-in-1 Model for HL-LHC*”, IEEE Transactions on applied superconductivity, Vol. 27, No. 4, (June 2017).

This page intentionally left blank

Chapter 17

Vacuum System

Vincent Baglin, Paolo Chiggiato and Cedric Garion

CERN, TE Department, Geneva 23, CH-1211, Switzerland

The HL-LHC project requires an important upgrade of the LHC vacuum system to ensure sufficient beam lifetime, limit the background to the high-luminosity experiments, protect the new final focusing system from ionizing radiation, increase the mechanical robustness, maximize beam aperture and mitigate electron multipacting. The technologies developed to tackle these challenges are exposed in this chapter.

1. Introduction

In the beam vacuum chambers of the Large Hadron Collider (LHC), two beams circulate in opposite direction in a 27 km circumference tunnel about 100 m underground [1, 2]. ‘Two-in-one’ superconducting magnets are cooled down with superfluid helium at 1.9 K. They provide the required magnetic field to maintain the hadron beams on a stable orbit during acceleration, from 450 GeV to collision energy, and during physics operation. In a bent trajectory, charged particles at relativistic speed emit synchrotron radiation. In the LHC at nominal energy and intensity, i.e. 7 TeV and 0.58 A, the two proton beams emit 8 kW of synchrotron radiation power, mostly in the 8.33 T superconducting bending magnets. Synchrotron radiation results in stimulated molecular desorption from the vacuum chamber walls and in the transfer of energy to the cryogenic system. To avoid an excessive cooling power, a so-called ‘beam screen’ is inserted into the magnets’ cold bore. Its main role is intercepting the heat load at a higher temperature than 1.9 K, namely in the 5-20 K range.

This is an open access article published by World Scientific Publishing Company. It is distributed under the terms of the Creative Commons Attribution 4.0 (CC BY) License.

Perforations made on the top and bottom of the beam screen provide pumping of the desorbed molecules on the cold bore. Perforations are such to produce a beam-screen transparency of 4.4% which ensures a beam vacuum lifetime longer than 100 h, well above the beam lifetime given by proton burn-off rate. These perforations limit also the heat load to the cold masses, due to proton scattering on the residual gas, at an acceptable level below 80 mW/m [3].

In the LHC experiments, $\sim 30\,000$ Higgs particles are produced per year to study in detail the Standard Model and scrutinize the appearance of new physics beyond the Standard Model. This physics goal requires a luminosity as high as $1 \times 10^{34} \text{ s}^{-1} \times \text{cm}^{-2}$ obtained by the focalization of dense proton bunches at the collision point. Despite the fact that most of the fragments produced at the collision point are intercepted by the experimental detector, there is a significant fraction of the collision debris, emitted at small angle, which escapes towards the storage ring. Indeed, from the beginning of the LHC project, it was anticipated that the large amount of debris would lead eventually to the damage of the superconducting final focusing quadrupoles located 20 to 60 m away from the collision point. Since the preliminary study for an upgrade in luminosity of the LHC, a tungsten shielded beam screen was proposed in order to mitigate the cold mass damage and heat load [4]. The insertion of tungsten in the space between the beam screen and the cold bore required a larger bore aperture provided by the new superconducting quadrupoles based on Nb_3Sn technology. Since then, the conceptual design has evolved to become a cornerstone of the upgraded vacuum system for the High Luminosity LHC (HL-LHC) [5].

The next sections will present the scientific and technological developments that build the foundation of the HL-LHC vacuum system. To this aim, we discuss in detail the performance requirements, the new HL-LHC beam screen, the new anti-multipacting surface treatment to mitigate the electron cloud build-up, a potential showstopper of the upgrade, and the modifications of the vacuum layout.

2. Performance Requirements

The HL-LHC upgrade will increase by one order of magnitude the LHC integrated luminosity with the objective to provide about 3 000 (and ulti-

mately $4\,000\text{ fb}^{-1}$ by around 2040. To do so, the instantaneous luminosity will be leveled at $5 \times 10^{34}\text{ s}^{-1} \times \text{cm}^{-2}$ to maintain the number of events per bunch crossing at an acceptable value (~ 130) for the experimental detectors. Special transversely deflecting RF cavities RF (so-called ‘crab cavities’, see Chapter 7) rotate the proton bunches to increase the virtual luminosity beyond $10^{34}\text{ s}^{-1} \times \text{cm}^{-2}$ and dynamic β^* with crossing angle adjustments are used to compensate the proton burn-off during the collisions and to keep the collision rate levelled at $5 \times 10^{34}\text{ s}^{-1} \times \text{cm}^{-2}$. The required β^* range will be attained thanks to a novel optic concept: the Achromatic Telescopic Squeeze (ATS). This concept is possible thanks to the large beam aperture available in the LHC arcs to pre-squeeze the beam and use the matching quadrupoles of the neighboring insertions to perform a final telescopic squeeze. The ATS allows to reach a much lower beam size at the collision point (β^*) for a larger proton density ($\gamma \times n_b \times N_b^2 / \varepsilon_n$) than the one of LHC, see Table 1 and Chapter 5.

The HL-LHC vacuum system shall be upgraded to cope with the increased luminosity, beam intensity and bunch population. In order to face the higher beam intensities, the vacuum beam lifetime shall be doubled with respect to LHC, thus increased to 200 h, requiring approximately half the gas density in the beam vacuum system to maintain the beam-gas losses on the cold mass below 80 mW/m. Table 2 gives for both machines the maximum number density for single gas species usually found in vacuum systems. Low mass molecules (H_2) are less critical than heavy molecules (CO_2) that have larger beam-gas cross sections.

Table 1. LHC and HL-LHC nominal beam parameters.

		LHC	HL-LHC
Energy	TeV	7	7
Luminosity (ultimate)	$\times 10^{34}\text{ s}^{-1} \times \text{cm}^{-2}$	1 (2.3)	5 (7.5)
Intensity	A	0.58	1.1
Number of bunches, n_b		2808	2760
Proton per bunches, N_b	$\times 10^{11}$	1.15	2.2
Bunch spacing	ns	25	25
β^*	cm	55	55-15
Normalized emittance, ε_n	μm	3.75	2.2
Events/crossing (ultimate)		27 (62)	131 (200)

Table 2. LHC and HL-LHC maximum acceptable number densities (m^{-3}) for single gas.

	H_2	CH_4	H_2O	CO	CO_2
LHC	1.2×10^{15}	1.8×10^{14}	1.8×10^{14}	1.2×10^{14}	7.9×10^{13}
HL-LHC	6.4×10^{14}	9.6×10^{13}	9.6×10^{13}	6.4×10^{13}	4.2×10^{13}

Table 3. Acceptable H_2 equivalent number densities (m^{-3}) in the LHC and HL-LHC experiments and IRs.

	ATLAS	CMS	IR1&5	IR2&8
LHC	1.5×10^{11}	3.1×10^{12}	5.3×10^{12}	6.5×10^{12}
HL-LHC	8.0×10^{10}	1.6×10^{12}	2.8×10^{12}	3.5×10^{12}

Similarly, the background to the LHC experiments due to beam-gas scattering in the interaction regions (IR) and inside the experimental beam pipes must be acceptable for the physics run. Table 3 gives the tolerable H_2 equivalent gas density, scaled with the beam intensity, for the LHC and HL-LHC high-luminosity experiments. As shown, the IR1 & IR5, where most of the HL-LHC upgrade is taking place, shall be designed to achieve an averaged H_2 equivalent gas density of 2.8×10^{12} H_2 equiv/ m^3 . This value corresponds to a pressure of 1×10^{-10} mbar assuming only hydrogen in the vacuum system. In the IR, the required pressure is mainly defined by the requirements of the cryo-elements and beam equipment deserving a specific attention, such as collimators, masks, etc.

3. Shielded Beam Screen

The major modification of the LHC vacuum system is taking place in the final focusing system, so-called Inner Triplet (IT), where a beam screen equipped with a tungsten alloy shielding is inserted into the cold bore to protect the cold mass from unduly deterioration due to radiation and excessive beam induced heat load (see Chapter 15) [6].

The shielded beam screen is installed along ~ 60 m. It starts at 22.5 m from the interaction point (IP) and extends inside the quadrupoles Q1, Q2, Q3, the corrector package (CP) and the dipole D1 that are all housed in a single vacuum vessel made of 6 cryostats. Two types of shielded beam screens with unit length in the range 8-11 m will be produced and inserted in a seamless 4 mm thick 316LN cold bore tube of 136.7 mm inner diameter. Most of the debris escaping the cavern through the 60 mm diameter sec-

ondary absorber (named TAXS) are intercepted by Q1. For that reason, the tungsten shielding is thicker in that position, i.e. 16 mm. The thickness is reduced to 6 mm in the other magnets located downstream of Q1. Such reduction ensures the larger aperture required in the Q2 magnet.

As shown in Figure 1, the shields are placed in the vertical and horizontal plane to intercept the charged particles debris produced at the interaction point emitted towards the cold mass in a plane depending on the crossing angle configuration. The absorbed power ranges from 15 W/m to 25 W/m at Q1. The 40 cm long absorber blocks are positioned on the beam screen tubes by pins, and they are hold in place by Ti elastic rings.

Similar to the LHC, the gas pumping towards the 1.9 K cold bore is granted by longitudinal slots punched in the beam screen shell. The transparency is set to 2% providing a total perforated area of 60 cm²/m. The perforations are located at the magnet's pole. For this reason, to protect the cold bore from direct impingement of electrons or scattered photons, electron shields are placed above the slots and clipped on the cooling tubes. The resulting pumping speed, computed by Monte-Carlo with Molflow, equals 430 ℓ/s per meter of beam screen for nitrogen at 20 °C, i.e. 15% more than in the LHC arcs.

Four 10-mm-diameter cooling tubes are laser welded on the external side of the beam screen tube. The heat load deposited on the tungsten absorbers

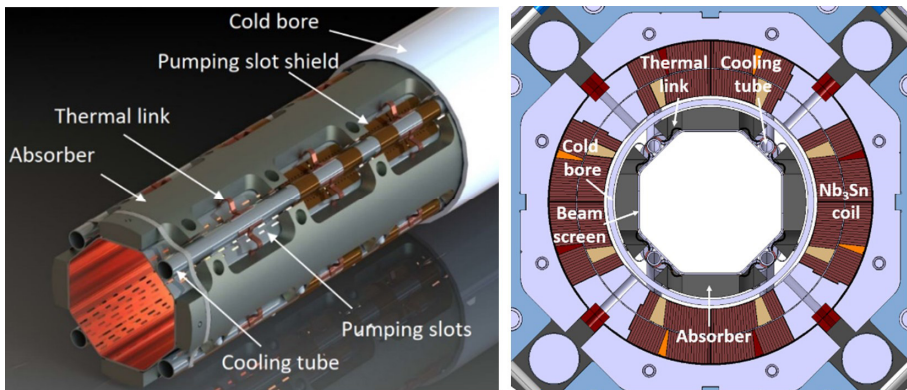


Fig. 1. Left, the Q1 shielded beam screen inserted in its cold bore tube (for illustration, one electron shield has been removed to show the slots behind); Right, cross-section of the Q1 cold mass.

is transferred to pressurized gaseous helium by Cu thermal links directly connected to the cooling tube. This thermal design has been thoroughly simulated and experimentally validated by a 1-m-long laboratory mock-up [7, 8]. The thermal links ensure a stable operating temperature of the beam screen from 60 to 80 K along the cryostat.

The beam screen aperture is maximized to provide sufficient operational margin for the beam optics. The chosen geometry of the aperture is an octagon with 99.7 mm distance between diametrically opposed faces for Q1, and 119.7 mm in horizontal/vertical plane and 110.7 mm in the 45° plane for the other magnets.

As for the LHC, the beam screen is made of Cu-colaminated high-Mn high-N austenitic stainless steel (P506). The $\sim 75 \mu\text{m}$ thick Cu layer provides an electrical resistivity of around $2.10^{-9} \Omega\cdot\text{m}$ at operating temperature, which complies with the beam impedance budget. The P506 steel provides structural robustness in the event of transitions from the superconducting to resistive state of the magnet cables (*i.e.* a ‘quench’). In such events, large forces are induced by the Foucault currents circulating in the Cu layer. These currents induce also torques and forces in the tungsten absorbers, which are designed accordingly.

An elastic supporting system using ceramic (ZrO_2) balls and Ti springs is used to support the shielded beam screen in the cold bore. Such design solution limits the heat transfer by conduction from the beam screen to the cold bore and facilitates the insertion of the ~ 500 kg shielded beam screen into the cold bore. In the occurrence of a magnet quench, the supporting system can retract and the deformed beam screen, designed to be elastic, goes in contact with the cold bore tube. In such a way, the forces due to the induced currents are homogeneously redistributed. The maximum contact force between the tungsten blocks and the cold bore is around 350 N/mm.

This mechanical design has been carefully simulated and validated in the laboratory. 2-m-long beam screen underwent a sequence of ~ 50 quenches during the prototyping phase of the HL-LHC quadrupole magnets up to 18.2 kA [9].

Between cold masses, the beam screen is interrupted, and the beam vacuum line is connected with an upgraded interconnecting system that includes tungsten shielding and a deformable RF bridge that provided continuity for the images currents (with both a DC and an RF components).

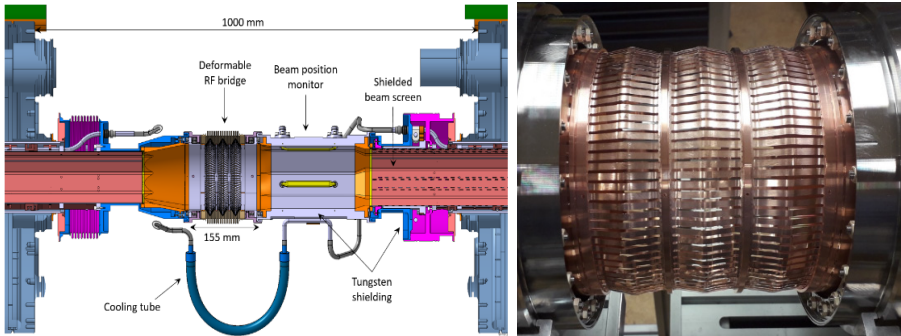


Fig. 2. Left, the HL-LHC interconnection; Right, picture of the deformable RF bridge in working position (courtesy of J. Perez Espinos, CERN).

As shown in Figure 2, the 1-m-long interconnection ensures a transition from octagonal to circular shape. It integrates a shielded beam position monitor, a cold mass shielding and a deformable RF bridge. The tungsten shielding reduces further the cold mass irradiation by the collision debris. The new RF bridge is based on a completely new design with respect to the LHC and consists of a set of V-shape convolutions manufactured from a flexible and deformable thin-walled Cu-Be element. It is produced with a single component and, consequently, it is more robust than conventional sliding RF fingers based on two independent pieces, like the LHC RF bridge. By this design feature, the risk of having an RF finger protruding into the beam aperture is eliminated [10]. In addition to the longitudinal movement, the new RF Bridge allows a transversal offset of up to 5 mm.

4. Anti-multipacting Surface Treatment

Another major upgrade of the LHC vacuum system is the introduction of an anti-multipacting surface treatment to mitigate electron cloud build-up (see Chapter 5). This phenomenon, which limits high-intensity positive-charged beam accelerators, is mainly driven by the emission of secondary electrons from the surface wall under primary electron impact.

In the LHC cryo-elements and some room temperature equipment (collimators, kickers etc.), the secondary electron yield (SEY) of the surfaces exposed to the beam is reduced by electron bombardment; this process is

called ‘beam scrubbing’. The maximum SEY, δ_{\max} , of fully scrubbed surfaces is expected to reach a value between 1.2 and 1.4, depending on the machine position and/or surface state [11, 12]. The remaining part of the LHC vacuum chambers (room temperature pipes, experimental areas) relies on a Non-Evaporable Getter (NEG) thin film that strongly mitigates the electron cloud build up (since $\delta_{\max} \sim 1.1$) while offering pumping speeds as large as $\sim 1\,000$ ℓ/s for hydrogen at 20 °C per meter of 8-cm diameter tube.

In the HL-LHC, with the advent of more intense bunch current, the electron cloud induced heat load will no longer be negligible for the IT beam screen, even with a fully scrubbed surface. Indeed, since in these magnets the beams circulate in opposite directions, the heat load may be as large as 500-1100 W (against 250-500 W at present for LHC) [13]. Moreover, the electron conditioning efficiency is strongly dependent on the electron cloud activity and surface state. To achieve a rapid commissioning of the HL-LHC vacuum system without dedicated and unpredictable “scrubbing runs”, a pre-treatment of the cryo-element’s beam screen surface is highly desirable to mitigate the electron cloud. The target of the treatment is reducing δ_{\max} down to or below one. The base line treatment is amorphous carbon (a-C) thin film coating, successfully deployed in the CERN SPS to mitigate electron cloud build-up. An alternative solution based on laser surface treatment is also under study and development [14, 15, 16].

The performance of the a-C coating was evaluated meticulously at cryogenic and room temperatures. In particular, adsorption isotherms, secondary electron and photon stimulated desorption yields were measured in the laboratory. The anti-multipacting behavior of the a-C coating was demonstrated with a mock-up installed in the SPS ring.

Adsorption isotherm measurements showed that the coating is porous (~ 300 times the Cu monolayer capacity). The high porosity is beneficial to reduce the secondary electron yield. However, at cryogenic temperatures, it amplifies the quantity of physisorbed molecules, in particular hydrogen up to ~ 60 K. For temperatures higher than 60 K, most of the physisorbed hydrogen is released. For this reason, the operating temperature of the a-C coated beam screen was set to be 60 to 80 K.

Studies with synchrotron radiation at grazing incidence with critical energy ranging from 10 to 1 000 eV were done. They revealed that the photon stimulated molecular desorption yield of a-C thin films at room

temperature is very similar to the one of oxygen-free Cu, which had allowed to define the beam screen transparency.

Finally, a demonstration of the electron multipacting suppression at cryogenic temperature was realised using the COLDEX experimental set-up in SPS that mimics a beam screen / cold bore assembly. In 2015-2016, several studies with a ~ 500 nm thick a-C coating were held during scrubbing runs and dedicated machine development periods. These studies included measurements at different temperatures 10, 20, 50, 60 K with and without pre-condensed gas (H_2 , CO, CO_2) onto the surface. The experimental results, supported by theoretical expectations derived from the PyCloud simulation code, demonstrated the absence, for LHC beams, of electron multipacting in an a-C coated beam screen with 67 mm inner diameter, located in a magnetic field free environment [17].

Figure 3 exhibits the simulated electron activity expected in the COLDEX set-up as a function of the maximum SEY. The absence of electron signal above the detection limit (10^{-10} A), together with the absence of pressure increase (larger than 10^{-10} mbar), demonstrated the anti-multipacting property of the material and showed that the maximum SEY is below 1.1 at cryogenic temperatures [18]. The measurement was performed with LHC beams in the SPS.

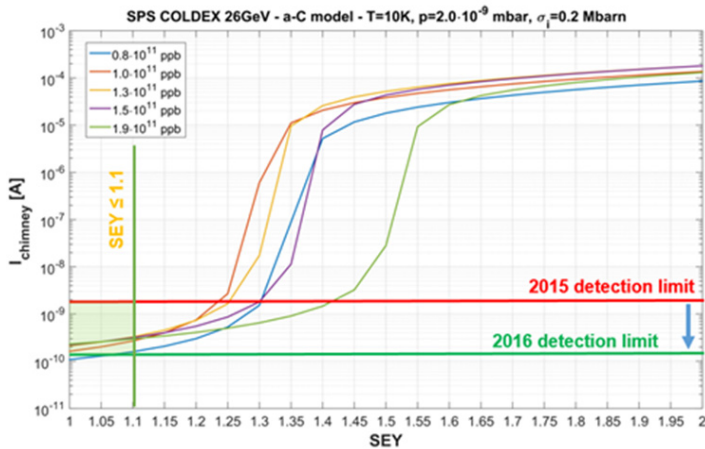


Fig. 3. Evaluation of the maximum secondary electron yield of the a-C coating from the electron activity measured with the COLDEX set-up (Courtesy R. Salemme). Figure 11-34 in [18].

The HL-LHC project foresees the modification of the IT in IR1 and IR5 that will house the a-C coated shielded beam screens. However, the triplets around IP2 and IP8 also require a specific surface treatment to reduce the beam induced heat load on the beam screen to an acceptable value. The solution chosen here was also a coating of the beam screens with a-C. Indeed, the coating technique is less expensive and less invasive than a modification of the cryogenic cooling system.

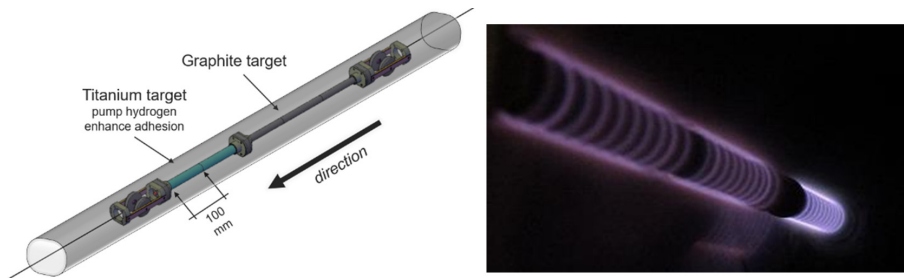


Fig. 4. Left, modular sputtering source for the in-situ coating of the LHC triplets in IR2 and 8; Right, glow discharge during the coating process (courtesy P. Costa Pinto, CERN) [14].

In order to avoid the complete dismounting of the triplets in IP2 and IP8 for the treatment, an innovative solution was worked out to perform an in-situ carbon coating by sputtering using graphite cathodes in an Ar plasma. As shown in Figure 4, a modular sputtering source, made of 100 mm long elements assembled together, was developed to allow the insertion in the tiny space left when the plug-in-modules are removed from the triplets' interconnects. The source is made of a Ti and a graphite target. The former is required to perform a pre-coating of the same material. The purpose of the Ti film is pumping H_2 during the process and enhancing the C adhesion; the removal of H_2 from the plasma is essential to achieve maximum SEY below one. Remotely controlled spools are actuated to move the targets and power the material sputtering. The whole process results in ~ 100 nm of Ti underlayer onto which is deposited a ~ 50 -100 nm C layer mixed with a ~ 150 nm Ti layer. When needed, preliminary etching of oxidized Cu surfaces may be provided by Ar inverted sputtering.

This approach will be used also for the a-C coating of a few other stand-alone magnets in the long straight sections 2 right and 8 left for the sake of

re-equilibrating the available cooling power around the LHC ring. The technique may be ultimately used also to mitigate the electron cloud build-up in the LHC arcs since, more than 15 years ago, the storage ring was not designed to operate with the HL-LHC beam.

More recently, significant collaborative efforts have been made to develop further the laser treatment of surface [16]. This technology offers the advantage to treat the material under inert atmosphere thereby simplifies the production. As shown in Figure 5, the laser ablation produces a blackened Cu surface with grooves and microstructures that results to SEY well below 1.

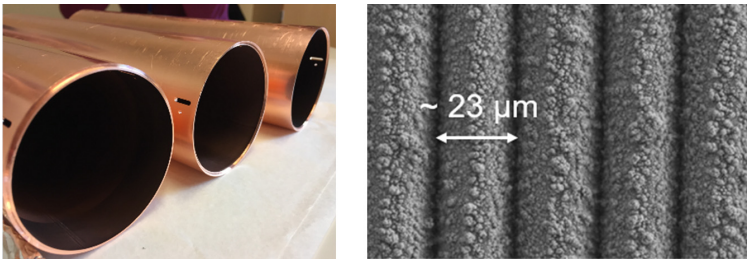


Fig. 5. Left, laser treated surface; Right, microscope view of the laser treated surface (courtesy A.T. Perez Fontenla, CERN) [17].

Beside the technical challenge to produce a mole capable of treating meters of vacuum tube, the large parameter space intrinsic to this technology, must be also studied to select the appropriate parameters compatible with the accelerator needs. As such, the behavior at cryogenic temperature during beam circulation, the surface impedance and the vacuum properties of the laser treated surface are still under intense investigation. However, the results obtained so far are very promising for a future implementation.

5. Vacuum Layout

An additional upgrade of the LHC vacuum system concerns the instrumentation of the experimental beam pipes. The experimental beam pipes are designed to be as much as possible transparent to the products of interaction and have an overall volume as small as possible to position the detectors as close as possible around the vertex. For these reasons, during the LHC design, the vacuum instrumentation was deported outside the experimental

cavern in the LHC tunnel between the secondary absorber and the first quadrupole of the IT, namely Q1.

However, during maintenance periods, this location poses important issues of safety for the personnel linked to oxygen deficiency and radiation hazards. Therefore, the HL-LHC design foresees the installation of these vacuum instruments in the experimental cavern at each extremity of the ~ 30 m long experimental beam pipe (see Chapter 13) [19]. This new layout solves not only the safety issue but, additionally, allows to install the first quadrupole, Q1, at 22.5 m from the IP, closer than in LHC (23 m), for a better beam squeeze.

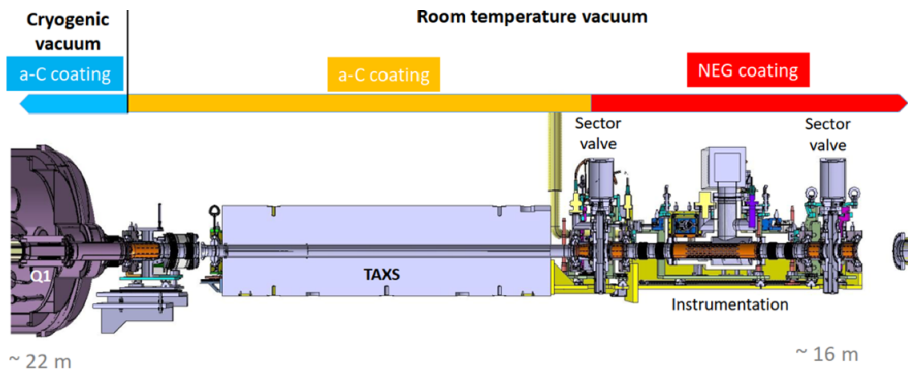


Fig. 6. The remotely connectable/disconnectable vacuum instrumentation and sector valves modules of the HL-LHC high luminosity experiments (courtesy J. Perez-Espinos).

Figure 6 shows the HL-LHC vacuum layout from Q1 to 16 m from the IP where the vacuum instrumentation for the high luminosity experiments is located. The system is made of three modules that can be independently and remotely connected/disconnected. During maintenance periods, a double valve sectorisation ensures a full decoupling between the experimental beam pipe and the triplets.

The TAXS, which separates the experimental cavern from the accelerator tunnel, is operated at room temperature with its 60-mm-diameter copper tube, which is coated with a-C. Q1 is operated at cryogenic temperature and its beam screen is carbon coated as well. Both systems are unbaked.

Similarly to the LHC, the remaining part of the long-straight-section vacuum system, including the experimental beam pipe, is coated with NEG

thin film that needs to be activated at ~ 200 °C to achieve the required pumping speed and low SEY required for the machine operation.

A last upgrade of the HL-LHC vacuum system is the implementation of a Full Remote Alignment system (FRAS), see Chapter 22, which aims to compensate the experimental cavern movements and local misalignments without intervention in the tunnel. That remote action will minimize the radiation dose to the personnel and allows more frequent alignment campaign which favors in turn to reduce the aperture margins in these locations.

The HL-LHC vacuum system layout is conceived to cope with the new remote alignment. When possible, it provides a large enough aperture to avoid component's re-alignment, deformable RF bridges to handle large transverse offset (>2.5 mm) and FRAS' supporting tables for components that require regular alignment.

The remaining part of the vacuum layout is based on the LHC design that has proven to guarantee reliable machine performance. In particular, a sector valve decouples cryogenic from room temperature vacuum sectors. The separation allows NEG activation without contamination of the cryogenic part and warming the cold part without saturating the NEG coating [2].

6. Conclusions

The HL-LHC upgrade is a major intervention on more than 1.2 km of the LHC ring. It requires an upgrade of the vacuum system and the development of new technologies to cope with the luminosity increase.

An innovative beam screen, operating at cryogenic temperature, that includes shielding and an anti-multipacting surface treatment, while maximizing the beam aperture, is one of the pillars of the upgrade. The development of an in-situ coating technology, based on a modular Ti-C sputtering target, will mitigate the electron cloud build up where required. Finally, the optimization of the vacuum system instrumentation, in particular near the high-luminosity experiments, will facilitate the maintenance of the system and limit the radiation exposure to the personnel.

The vacuum system upgrade presented here is developed and tested during 10 years to allow study, design, prototyping, construction and installation, by 2026-28, for a machine start scheduled in 2029. As for the LHC, the vacuum systems and subsystems are to be thoroughly tested in the

laboratories and accelerators. This approach ensures a proper performance of the vacuum system for the future HL-LHC. There is no doubt that most of the innovative technologies discussed above will trigger future developments for the post-LHC colliders.

Acknowledgments

The LHC vacuum system upgrade for the HL-LHC implementation is the result of team work of many colleagues, associates and collaborators of the vacuum, surfaces & coatings group. All of them deserve special recognition.

References

1. L. Evans, Ed, *The Large Hadron Collider: a Marvel of Technology*, EPFL Press.
2. O. Brüning, P. Collier, P. Lebrun, S. Myers, R. Ostojic, J. Poole, P. Proudlock Eds. *LHC Design Report, Vol 1 The LHC Main Ring*, CERN-2004-003, 2004.
3. O. Gröbner, Overview of the LHC vacuum system, *Vacuum* 60 (2001) 25-34.
4. R. Ostojic, L. Williams Eds, *Conceptual Design of the LHC Interaction Region Upgrade – Phase-I*, LHC Project Report 1163, CERN, 2008.
5. G. Apollinari, I. Béjar Alonso, O. Brüning, P. Fessia, M. Lamont, L. Rossi, L. Tavian Eds, *High-Luminosity Large Hadron Collider (HL-LHC) Technical Design Report V.0.1*, CERN-2017-007-M.
6. V. Baglin, C. Garion, R. Kersevan, Preliminary design of the High-Luminosity LHC beam screen with shielding, In *Proc. 6th International Particle Accelerator Conference, IPAC 2015*, pp 60-63, Richmond, VA, USA (May 2015).
7. C. Garion et al, Material characterisation and preliminary mechanical design for the HL-LHC shielded beam screens operating at cryogenic temperature, 2015 *IOP Conf. Ser.: Mater. Sci. Eng.* **102** 012013.
8. P. Borges de Sousa et al, Parametric study on the thermal performance of beam screen samples of the High-Luminosity LHC upgrade, 2017 *IOP Conf. Ser.: Mater. Sci. Eng.* **278** 012053.
9. M. Morrone, Thermomechanical study of complex structure in the aperture of superconducting magnets: application to the design of the High-Luminosity LHC shielded beam screen, *PhD: Imperial Coll., London: 2018-01-31*, CERN-THESIS-2018-052.
10. J. Perez-Espinos, C. Garion, Analysing and testing of a new RF bridge concept as an alternative to conventional sliding RF fingers in LHC, In *Proc. 7th International Particle Accelerator Conference, IPAC 2016*, pp 3660-3662, Busan, Korea (May 2016).
11. V. Baglin, The LHC vacuum system: Commissioning up to nominal luminosity, *Vacuum* 138 (2017) 112-119.

12. P. Dijkstal, G. Iadarola, L. Methner, G. Rumolo, Simulation studies on the electron cloud build-up in the elements of the LHC arcs at 6.5 TeV, CERN-ACC-Note-2017-0057, CERN, Geneva, Switzerland (October 2017).
13. G. Skripa and G. Iadarola, Beam-induced heat loads on the beam screens of the inner triplets for the HL-LHC, CERN-ACC-Note-2018-0009, CERN, Geneva, Switzerland, February 2018.
14. P. Costa Pinto et al, Amorphous carbon coating in SPS, In *Proc. 12th International Particle Accelerator Conference*, IPAC 2021, pp 3475-3478, Campinas, Brazil (May 2021).
15. R. Valizadeh et al, Low secondary electron yield engineered surface for electron cloud mitigation, *Appl. Phys. Lett.* 105, 231605 (2014).
16. M. Sitko et al, Towards the implementation of laser engineered surface structures for electron cloud mitigation, In *Proc. 9th International Particle Accelerator Conference*, IPAC 2018, pp 1220-1223, Vancouver, BC, Canada (May 2018).
17. V. Baglin, COLDEX: a tool to study cold surfaces in accelerators, In *Proc. 6th Electron-Cloud Workshop*, E-CLOUD'18, pp 165-178, La Biodola, Italy (June 2018).
18. R. Salemme, Space charge compensation and electron cloud effects in modern high intensity proton accelerators, *PhD: Universita di Roma Sapienza, October 2016*, CERN-THESIS-2016-337.
19. F. Sanchez Galan et al, Optimising machine-experiment interventions in HL-LHC, In *Proc. 8th International Particle Accelerator Conference*, IPAC 2017, pp 3540-3543, Copenhagen, Denmark (May 2017).

This page intentionally left blank

Chapter 18

Beam Instrumentation and Diagnostics

E. Bravin^a, R. Jones^b, T. Lefevre^a and R. Veness^a

^a*CERN, SY Department, Genève 23, CH-1211, Switzerland*

^b*CERN, BE Department, Genève 23, CH-1211, Switzerland*

1. Introduction

The extensive array of beam instrumentation with which the LHC is equipped has played a major role in its commissioning, rapid intensity ramp-up and safe and reliable operation. Much of this equipment will need consolidation by the time the LHC enters the High Luminosity (HL) era while the upgrade itself brings a number of new challenges that are currently being addressed.

Installation of a completely new final focus system in the two high-luminosity LHC insertions implies the development of new beam position monitors to equip the upgraded quadrupole magnets. In addition to replacing the current directive stripline beam position monitors, which allow independent measurement of both beams in a single aperture, eight additional beam position monitors will be added per interaction region, to further improve beam control at the collision point.

The use of crab cavities for luminosity enhancement, as part of the HL-LHC upgrade, implies new instrumentation in order to allow for the optimisation of their performance. This requires intra-bunch measurements of transverse position on a turn-by-turn basis. Several diagnostic systems are

being investigated as candidates to perform this task, including very high bandwidth pick-ups and a streak camera installation making use of synchrotron light.

The possibility prospect of using a hollow electron lens for cleaning the beam halo [see Chapter 8] has added to the beam diagnostic challenges of high luminosity LHC. Not only must the beam halo be measured, but a good concentricity and alignment between the electron and proton beam must be ensured. A coronagraph based on synchrotron light is therefore under study with the aim of being able to image a halo at a level of 10^{-5} of the core intensity, while a gas curtain monitor is under development to align the electron and proton beams within the hollow electron lens. The latter will use a high-density, supersonic, gas sheet to allow a two-dimensional image of both the hollow electron beam and the proton beam to be created via luminescence.

Upgrading the LHC also provides the opportunity of developing new instrumentation to address areas identified as currently lacking adequate diagnostics. This includes a non-invasive, beam-size measurement system, capable of delivering data throughout the LHC acceleration cycle. While wire-scanners work with low intensity beams, and the synchrotron light monitor provides the relative beam size for all beams at a fixed energy, there is currently no system that can provide accurate beam size measurements for all beams throughout the cycle. Such a measurement is essential to understand and combat emittance growth. Developments are therefore underway to provide such a monitor, with a prototype beam gas vertex detector being tested with beam in the LHC as part of the high luminosity LHC upgrade.

An upgrade or consolidation is also envisaged for several other beam diagnostic systems, including the main beam position monitoring system, the collimator beam position measurement system, the beam loss monitoring system, the luminosity measurement system and the synchrotron light monitor.

2. Beam Position Monitoring for the HL-LHC

With its 1070 monitors for orbit control, the LHC Beam Position Monitor (BPM) system is the largest BPM system in the world [1]. Based on the Wide Band Time Normalizer (WBTN) principle [2], it provides bunch-by-bunch beam position over a wide dynamic range (~ 50 dB). Despite its size and

complexity (3820 electronic cards in the accelerator tunnel and 1070 digital post-processing cards in surface buildings) the performance of the system during the first two LHC physics runs has been excellent.

2.1. *Current performance and limitations*

The position resolution of the LHC arc beam position monitors has been determined to be better than $150\mu\text{m}$ when measuring a single bunch on a single turn and better than $10\mu\text{m}$ for the average position of all bunches [3]. The main limitation on the accuracy of the BPM system is linked to temperature dependent effects in the acquisition electronics, which can generate offsets of up to a millimetre if left uncalibrated. Temperature controlled racks have been installed to limit this effect, but drifts of several tens of micrometers are still observed.

The non-linearity of the BPMs located near the interaction points has also proven to be problematic, in particular for accurate measurements during the beta-squeeze and during machine development periods. A new correction algorithm has therefore been developed, based on exhaustive electro-magnetic simulations, with the aim of bringing the residual error down to below $20\mu\text{m}$ over most of the useable BPM aperture [4]. Developed to be able to distinguish between the positions of two counter propagating beams in the same beam pipe, these BPMs also suffer from non-optimal decoupling between the beams, which is something that is being addressed for HL-LHC.

2.2. *A high-resolution orbit measurement system for HL-LHC*

At the start of the HL-LHC era the existing BPM system will have been operational for over 15 years, using components which are over 20 years old. A completely new system is therefore being developed to replace these ageing electronics. This will be a fully digital system, directly sampling opposite electrode outputs on a single channel and making use of recent advances in high resolution, fast sampling analogue to digital conversion technology and the radiation hard, high speed optical transmission systems developed for the LHC experiments. The aim will be to provide a high reliability system with improved long-term stability and reproducibility.

2.3. High directivity strip-line pick-ups for the HL-LHC Insertion Regions

In the BPMs close to the interaction regions, the two beams propagate in the same vacuum chamber. Directional strip-line pick-ups are therefore used to distinguish between the positions of both beams. The particularity of such a BPM is that signal from the beam only appears at the upstream port, with little contribution at the downstream port, which can then be used to collect the signal from the beam travelling in the opposite direction. However, when the two beams pass through the BPM at nearly the same time, there is still some interference due to imperfect directivity (some signal still appearing at the downstream port) of the strip-line. In the current design there is only a factor 10 isolation between the upstream and downstream signals, making it difficult for such a BPM to measure beams with significantly different intensities or large position offset. This effect can be minimised by installing the BPMs at a location where the two counter-propagating beams do not meet, which is a constraint included in both the current and future layout. In addition, for the HL-LHC BPMs in front of the Q2a, Q3 and triplet corrector package magnets, there is the additional constraint that tungsten shielding is required at the level of the cold bore to minimise the heat deposition due to collision debris in these magnets. A mechanical re-design (see Figure 1) coupled with extensive electro-magnetic simulations have therefore been performed to optimise the directivity under these constraints, aiming at a factor 20 or more isolation between the signals from the counter propagating beams.

2.4. Beam Position Measurement at the HL-LHC Collimators

All next generation collimators in the LHC will have button electrodes embedded in their jaws for on-line measurement of the jaw to beam position [5]. These are fitted with an orbit measurement system based on a compensated diode detector scheme [6], which has already been demonstrated to be simple and robust, and to provide a position resolution at the sub-micron level. This will provide a fast and direct way of positioning the collimator-jaws and subsequently allow constant verification of the beam position at the collimator location, improving the reliability of the collimation system as a whole.

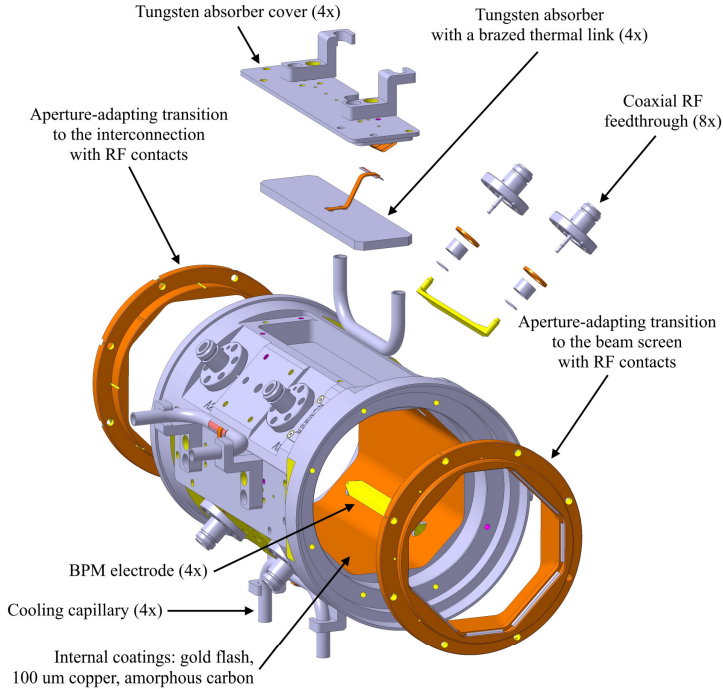


Fig. 1. Mechanical design of the Q2 directive stripline beam position monitor for HL-LHC.

3. Beam Loss Monitoring for the HL-LHC

Monitoring of beam losses is essential for the safe and reliable operation of the LHC. The beam loss monitoring (BLM) system provides knowledge of the location and intensity of such losses, allowing an estimation to be made of the energy dissipated in the equipment along the accelerator. The information is used for machine protection, to optimise beam conditions and to track the radiation dose to which equipment has been exposed. This is provided using nearly 4000 ionisation monitors distributed around the machine. These are located at all probable loss locations, with the majority mounted on the outside of the quadrupole magnets, including those in the inner triplet regions. There are also a few, fast diamond loss detectors located in the injection, dump and collimation regions to provide loss information on a bunch-by-bunch basis. While the existing system is globally believed to meet the needs of the HL-LHC, some upgrades will nevertheless be required.

The quench level signals estimated for 7 TeV running are, for some detectors, very close to the noise level of the acquisition system. This is mainly determined by the length of cable required to bring the signal from the radiation hard, ionisation chamber detector to the radiation sensitive front-end electronics. Although qualified for use in the low radiation environments of the LHC arcs the current electronics cannot be located close to the detectors in the higher radiation insertion regions. Development has therefore begun to implement these electronics in a radiation hard Application Specific Integrated Circuit (ASIC) that could sit near each detector, eliminating the need for long cables.

Two technologies are being studied for this ASIC, current to frequency conversion, as is used in the existing system, and a sigma-delta implementation. The final ASIC will need to cover a 180 dB dynamic range (corresponding to a current range from 1 pA – 1 mA) with a 10 μ s integration time, and a targeted radiation tolerance of 1MGy.

This ASIC will use standard 130 nm CMOS technology (known to be radiation tolerant to 2MGy) and be housed in a standard 64 pin Quad Flat Package (10 \times 10 mm). Each chip will have two analogue readout channels, triplicated digital circuitry with majority voting, and double communication channels for redundancy.

4. Emittance Measurement for the HL-LHC

The LHC is currently fitted with a host of beam size measurement systems used to determine the beam emittance. These different monitors are required in order to overcome the specific limitation of each individual technique.

Wirescanners are used as the absolute calibration reference but can only be operated with a low number of bunches due to intensity limitations linked to wire breakage at injection and the quenching of downstream magnets at top energy.

A synchrotron light monitor [7] provides measurements during normal operation, delivering bunch-by-bunch beam size. However, this has limitation coming from the small beam size at top energy, the multiple sources of synchrotron radiation required to produce sufficient light over the whole energy range (undulator, D3 edge radiation, central D3 radiation), and the long optical path required to extract the light. This means that the correction needed

to extract an absolute value of the transverse beam width is of the same order of magnitude as the beam width itself. An excellent knowledge of all error sources is therefore required to obtain meaningful results, something that can currently only be achieved through regular cross-calibration with wire scanners at a fixed energy.

The third system installed is an ionisation profile monitor. Originally foreseen to provide beam size information for lead ions at injection, where there is insufficient synchrotron light, this monitor has also been used for protons. However, with the intense proton beams, this monitor suffers from space charge effects at high energy, and recently had to be removed due to excessive, impedance related, radio-frequency heating.

Whilst efforts are ongoing to improve the performance of all the above systems, alternative techniques to measure the bunch-by-bunch transverse beam size and profile are under study for the HL-LHC.

4.1. A Beam Gas Vertex Emittance Monitor for the HL-LHC

The VELO detector of the LHCb experiment has shown how beam gas interactions can be used to reconstruct the transverse beam profile of the circulating beams in the LHC [8]. Currently under study is whether a simplified version of such a particle physics tracking detector can be used to monitor the beams throughout the LHC acceleration cycle. Such a concept has, up to now, never been applied to the field of beam instrumentation, mainly because of the large quantity of data treatment required. However, the advantages compared to standard beam profile measurement methods are impressive: high-resolution profile reconstruction, single-bunch measurements in three dimensions, quasi non-destructive, no detector equipment required in the beam vacuum, high radiation tolerance of the particle detectors and accompanying acquisition electronics.

This technique is based on the reconstruction of beam gas interaction vertices from the charged particles produced in inelastic beam gas interactions that are subsequently detected with high-precision tracking detectors (Figure 2). By reconstructing enough vertices, a complete two-dimensional transverse beam profile can be obtained. In order to acquire enough vertices in a reasonable time, a dedicated gas-injection system is required to provide a local pressure bump in the vicinity of the detectors. The pressure and type of gas

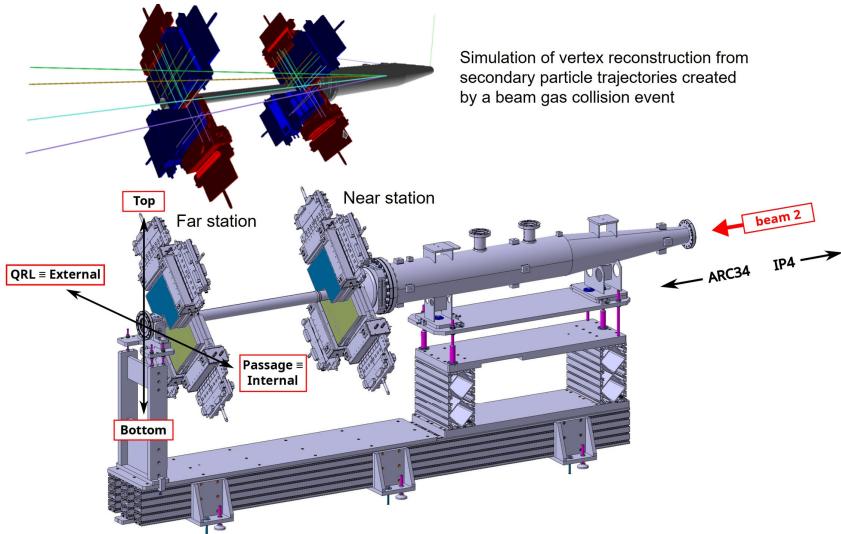


Fig. 2. The principle and design of the prototype LHC beam gas vertex detector.

used are of principal importance for the statistical and systematic uncertainties of the measured beam profiles. Prototyping of such a detector began in 2012 in collaboration with the LHCb experiment, the École Polytechnique Fédérale de Lausanne and RWTH Aachen, with the system installed in 2015 and fully operational for data taking in 2017-2018.

The installed prototype (Figure 3) has demonstrated the ability to measure both the horizontal and vertical beam size independently, with a precision better than 3% for an integration time of less than a minute [9]. This allows beam size monitoring during all operational phases, including the energy ramp for which there is currently no other instrument that can make an absolute measurement of the beam size for high intensity physics beams. These encouraging results will lead to continued R&D on such a detector, to develop a fully optimised system for installation in the HL-LHC.

4.2. Halo Diagnostics for HL-LHC

One of the major challenges for high intensity accelerators is the control of beam losses. In the case of HL-LHC the stored energy per beam is of the order of 700 MJ while the collimation system can sustain a maximum of 1 MW

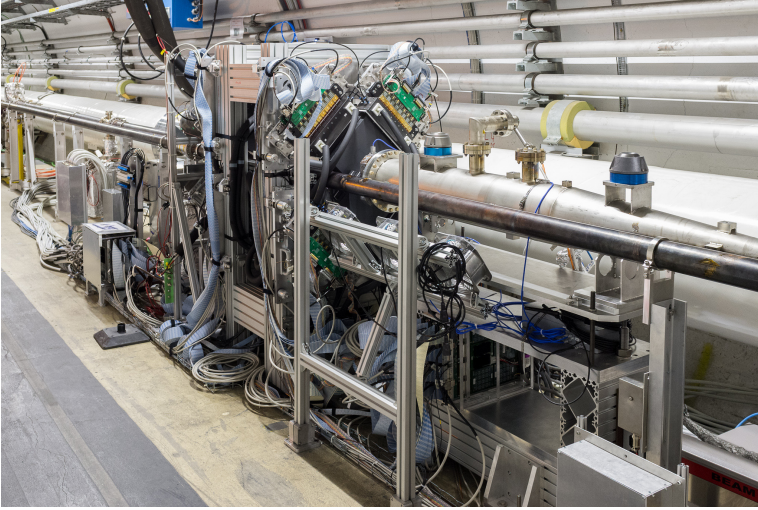


Fig. 3. The prototype LHC beam gas vertex detector

continuous power deposition. For this reason, it is very important to study and understand loss dynamics. An important mechanism for slow losses consists of populating the beam “halo”, i.e., populating the periphery of the phase-space with particles at large amplitudes (by IBS, beam-gas collisions, resonances etc.). These halo particles then gradually increase their amplitude due the non-linearity of the optics until they hit a collimator. Measurement of the beam halo distribution is important for understanding this mechanism to allow a minimisation of its effects. Moreover, in the HL-LHC crab cavities will be used to counter the geometric luminosity loss factor introduced due to the increased crossing angle. In case of failure of a crab cavity module the whole halo may be lost in a few turns. If the halo population is too high this can cause serious damage to the collimation system or to other components of the machine. The total halo population that can be absorbed by the collimation system in case of a fast loss is of the order of few 10^{-5} of the nominal beam intensity. The halo monitor for HL-LHC should thus be able to observe the halo at a level of 10^{-5} of the peak bunch intensity.

There are two main ways of measuring the beam halo: either measuring the whole transverse space with a high dynamic range monitor, or sampling only the tails using a monitor with a standard dynamic range. Both methods have already been attempted in other machines offering a good example of

what can be achieved. A third technique often used to measure the halo consists in removing it by scraping the beam and recording the loss rate during the process. This technique is, however, not suitable for the intense nominal HL-LHC beams and can only be used in dedicated low intensity experiments.

There are considerable challenges involved in adapting the standard diagnostics used for transverse beam profile measurement for halo measurements, due to the large dynamic range required and the need for continuous, non-invasive monitoring. Ionisation profile monitors and the new technique based on beam-gas vertex reconstruction provide non-invasive measurement but would require very long integration times to provide enough statistics to build-up a picture of the transverse beam tails, during which time the beam needs to remain extremely stable. Halo measurement using synchrotron radiation therefore seems the most promising technique as it can provide high dynamic range, while being non-invasive and allowing continuous monitoring of the beams at the bunch-by-bunch level.

4.2.1. *Halo measurement using Synchrotron Radiation Imaging*

Halo measurement using synchrotron radiation can be achieved by using one of the following techniques:

- high dynamic range cameras [10]
- core masking and standard cameras [11]
- performing an X-Y scan of the image plane with a photo-detector located behind a pinhole
- single photon counting with a pixelated photo-detector.

The limiting factor in all cases is likely to be the unavoidable presence of diffused synchrotron light coming from reflections in the vacuum chamber or optics, diffusion by dust particles, and diffraction. The first two can, in principle, be mitigated with an appropriate surface treatment and a clean and hermetic setup, although diffusion by scratches and defects on the optical components cannot be entirely removed. Diffraction, however, is a fundamental physics limitation.

To overcome the problem of diffraction, halo measurement using a coronagraph technique is under study, and a prototype based on a similar system installed on the Photon Factory at KEK is currently installed in the LHC [12]. Figure 4 shows the result of a test where the LHC beam was artificially blown-

up, with the halo being formed clearly visible when difference images are analysed. By combining a core image (without the coronagraph mask in place) with a halo image (with the coronagraph mask in place) a combined beam profile measurement is obtained (Figure 5). This shows that the current system is capable of detecting halo at the level of 10^{-4} . In order to push this further a new design is underway, exploiting a Cassegrain reflector telescope to allow for higher magnification, and therefore capable of achieving the specified contrast of 10^{-5} . This foresees to replace the first prototype for testing during LHC Run 3. Optimised versions will then be installed for both beams on new, specifically built synchrotron radiation lines using the light from the D4 separation dipoles in LSS4.

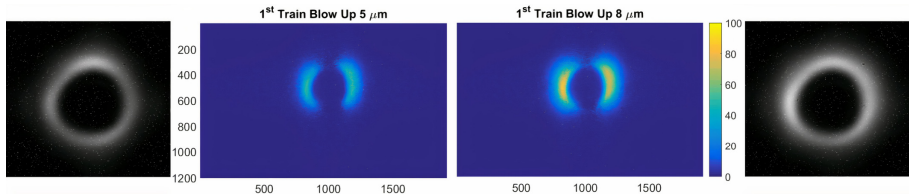


Fig. 4. Halo measurement during artificial beam blow-up. From left to right: original image, difference image after 1st blow-up, difference image after 2nd blow-up, final image.

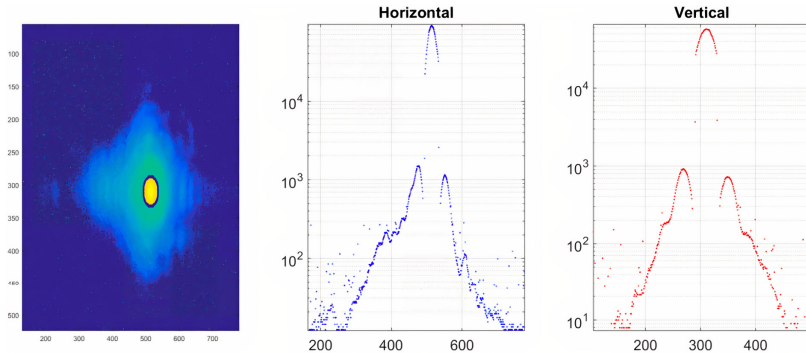


Fig. 5. Combined core and halo measurement showing a dynamic range of $\sim 10^4$.

5. Diagnostics for Crab Cavities

The crab cavities for the HL-LHC will counter the geometric reduction factor caused by a large crossing angle to enhance luminosity. These cavities will be

installed around the high luminosity interaction points (IP1 and IP5) and used to create a transverse intra-bunch deflection (head and tail of the bunch deflected in opposite directions) such that opposing bunches coming in at an angle to collide overlap fully at the interaction point. These intra-bunch deflections are compensated by crab-cavities acting in the other direction on the outgoing side of the interaction region. If the compensation is not perfect the head and tail of the bunch will travel on slightly different closed orbits around the ring and can be intercepted by the collimators or other aperture restrictions in their path. Monitors capable of measuring this orbit difference and any head-tail rotation or oscillation outside of the interaction regions are therefore required.

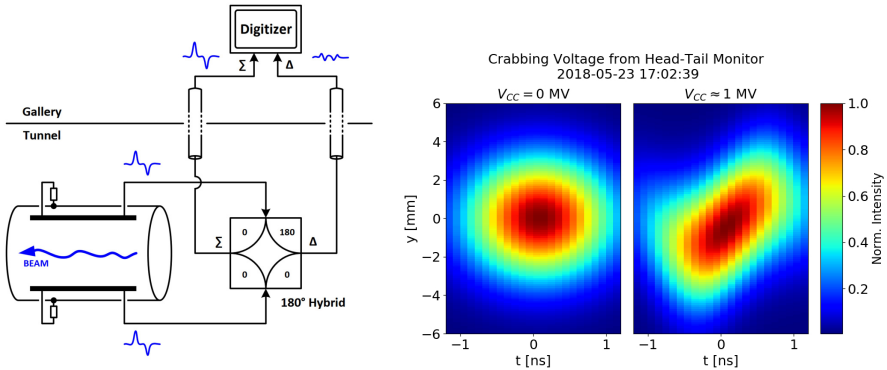


Fig. 6. Head-Tail monitor – principle of operation and reconstruction of the transverse position of the bunch with crab cavities off (left picture) and on (right picture).

5.1. Bunch shape monitoring using electro-magnetic pick-ups

Electromagnetic monitors for intra-bunch diagnostics are already installed in the LHC [13]. These so-called “Head-Tail” monitors mainly provide information on instabilities and have a bandwidth of up to several GHz. Similar monitors were essential to understand and optimise the first ever use of crab cavities in a proton synchrotron during the 2018 tests of HL-LHC prototypes in the CERN-SPS accelerator (see Figure 6).

To better understand instabilities in HL-LHC and to help with the tuning of the crab-cavities a higher granularity within the bunch (bandwidth of ~ 10 GHz) is desirable, along with an improved position resolution. Studies are

therefore ongoing to improve the existing electromagnetic pick-ups, which include optimisation of the pick-up design and the testing of faster acquisition systems.

In addition to the standard electromagnetic monitors, pick-ups based on electro-optical crystals in combination with laser pulses are also being considered [14]. Such pick-ups have already demonstrated an extremely fast time response, in the sub-picosecond range. Developed mainly for linear accelerators, this technology is now also being considered for circular machines, with a prototype recently tested on the CERN-SPS in collaboration with Royal Holloway University of London, UK [15].

5.2. *Bunch shape monitoring using streak cameras*

The use of synchrotron light combined with a streak camera is complementary to electromagnetic or electro-optical pick-ups for high-resolution temporal imaging, being able to also provide detailed longitudinal bunch profile information. Using an optical system to re-image the synchrotron light at the entrance of a streak camera allows the transverse profile of the beam to be captured in one direction (horizontal or vertical) with a very fast time resolution (below the picosecond level) [16]. Usually only one transverse axis is acquired, with the other used for the streaking (temporal profile). Using sophisticated optics, it is however possible to monitor both axes at the same time, as was demonstrated at the Large Electron Positron (LEP) collider at CERN [17].

Streak cameras can be used to observe a number of beam parameters simultaneously: bunch length, transverse profile along the bunch, longitudinal coherent motion, head-tail motion etc. The main limitations of the streak camera are the repetition rate of the acquisition, typically less than 50Hz, and the limited length of the recorded sample, which is given by the CCD size. The latter can be improved by using double scan streak cameras. Considering a CCD with 1000×1000 pixels working at 50 Hz and adjusting the optical magnification and scan speed such that the image of each bunch covers an area of about 100×100 pixels one can record a maximum of 100 bunch images per 20 ms, i.e., 5000 bunches per second. This is clearly just an optimistic upper limit with other factors likely to reduce this value.

The longitudinal resolution of around 50ps required for HL-LHC is rather easy to achieve using streak cameras, where measurements down to the sub-picosecond are now possible. In terms of transverse resolution two distinctions have to be made:

- (1) The resolution when measuring beam width. This is affected by diffraction due to the large relativistic gamma of the beam, with the diffraction disk of the same order as the beam size. Measurement of the absolute transverse beam size will therefore not be very precise.
- (2) The resolution when measuring centroid motion, i.e. the centre of gravity of the beam. This is not directly affected by the diffraction, which produces a symmetrical blur, and therefore the resolution for this type of measurement will be much better.

As head-tail motion is essentially a centroid motion, the streak camera should therefore be able to achieve the resolution of a few percent of the beam sigma necessary to quantify any residual non-closure of the crab cavity bumps.

Streak cameras are expensive and delicate devices not designed for the harsh environment inside an accelerator. Radiation dose studies are therefore required in order to verify if a streak camera can be installed directly in the tunnel or if it has to be housed in a dedicated, shielded, hutch. The latter would imply an optical line to transport the synchrotron light from the machine to the camera.

Another point to consider is the synchrotron light source. At the moment two synchrotron light telescopes are installed in the LHC, one per beam, using radiation from the D3 separation magnet in the RF insertion region of the LHC at Point 4. These telescopes already share their light amongst three different instruments, the synchrotron light monitor, the abort gap monitor and the longitudinal density monitor. It will therefore be difficult to integrate yet another optical beam line for the streak camera. The installation of additional light extraction mirrors will therefore be necessary to provide the light for the streak cameras and the halo diagnostics mentioned in the previous section. Integration studies are currently underway to incorporate a second synchrotron radiation line per beam, using the radiation produced by the D4 separation magnet near the RF insertion in Point 4. Since the crab cavities are only needed at high energy, dipole magnets can be used as the source of the visible synchrotron radiation for the streak cameras, with no need for the installation of additional undulators that are only required at injection energy, where the

dipole radiation is in the infra-red. The efficient detection of the crabbing is also dependent on the accelerator optics, requiring a favourable phase advance between the crab cavities and the synchrotron light source used.

6. Luminosity Measurement for HL-LHC

The measurement of the collision rate at the luminous interaction points is very important for the regular tuning of the machine. Accurate information about the instantaneous luminosity is provided by the LHC experiments once stable collisions are established, but this information is often not available during commissioning, machine development periods or during the beam collision process. Simple, reliable collision rate monitors are therefore needed for HL-LHC, similar to those currently available for LHC operation. This measurement is currently provided by measuring the flux of forward neutral particles generated in the collisions using fast ionisation chambers installed at the point where the two beams are separated back into individual vacuum chambers. These detectors are installed inside absorbers whose role it is to avoid that the neutral collision debris, and the secondary showers induced, reach and damage downstream machine components. As these absorbers will be re-designed for the completely different HL-LHC geometry in this region, new, adapted luminosity monitors will need to be produced.

There are several drawbacks with the current ionisation chambers, notably the need for a circulating gas circuit, and the fact that the front-end amplifiers have to be placed as close as possible to the detector in a very high radiation area, making repairs difficult. A different technology, Cherenkov radiation, is therefore being studied to provide this measurement for HL-LHC. Prototypes, with Cherenkov radiation produced in both air and in fused silica rods have been tested in the LHC during Run 2 to try to qualify the system for use in a region where the radiation dose will reach 180 MGy per year. The results indicate that the high radiation affects both systems, with a continuous degradation of the mirrors used in the Cherenkov in air monitor, and a change in transmission of the Cherenkov light produced in the fused silica rods observed. However, almost all of the transmission loss in the fused silica occurs within the first 10 fb^{-1} , with transmission remaining stable beyond this while still producing sufficient light for detection. This technology therefore looks promising as the baseline for the luminosity monitors of the HL-LHC.

7. Gas Curtain Diagnostics

With a hollow electron lens actively being studied as an addition to the HL-LHC collimation system, research and development is also underway to ensure that such an electron lens can be fitted with adequate diagnostics. One requirement is the on-line monitoring of the position of both the electron and proton beams, to ensure that the low energy, hollow electron beam is always concentric about the high-energy proton beam. This requires a non-invasive monitor capable of providing a simultaneous, two-dimensional image of both beams. In addition, this measurement must be made in close proximity to the solenoid field constraining the electron beam, preventing the collection of charged particles as an observable.

An instrument is therefore being developed, through collaboration with GSI (Darmstadt, Germany) and the Cockcroft Institute/University of Liverpool (UK), to image fluorescence generated by the interaction between these beams and a thin, supersonic, gas curtain [18]. By tilting this ‘Beam Gas Curtain’ (BGC) with respect to the beam axis, a two-dimensional image of both beams can be obtained in much the same way as for a traditional solid screen beam observation system. The instrument consists of the following main components:

- a gas generation stage consisting of a supersonic gas nozzle followed by three skimmers which select and shape the gas jet into a thin gas curtain
- an interaction chamber where the high energy proton beam and low energy hollow electron beam interact with the gas curtain
- an optical system for image generation
- an exhaust chamber which pumps the residual gas of the curtain.

There are a number of key developments required for this instrument. It is important to select a working gas that is compatible with the NEG-coated, LHC ultra-high vacuum system, whilst still producing an adequate fluorescence signal from the interaction of both keV electrons and TeV protons, preferably from the spectral line of a neutral atom or molecule to avoid image distortion from electric and magnetic fields. It is also necessary to study the production of a dense supersonic gas curtain whilst minimising the background gas load to the vacuum system, and to develop a radiation-hard imaging system that is efficient for both the electron and proton excited fluorescence signals.

Although no fluorescence cross-section data exists for protons impacting neutral gases at 7 TeV, extrapolation from lower energy experiments indicate that for the gases of choice, neon or argon, these will be between 20-30 times lower than for the low energy electrons. This, however, is compensated by the small transverse size of the proton beam, with detection of a few hundred photons considered sufficient to assess the proton beam position and shape. The electron beam is distributed over a much larger area, and it is therefore estimated that $\sim 10^4$ photons will be needed for the same purpose. Total integration times of the order of 1 s are thus expected for neon or argon as working gases.

Formation of the gas stream in the nozzle and subsequent selection and shaping in the skimmers define the gas curtain density at the interaction point with the beam. A predictive design of the gas curtain requires simulation of a continuous gas flow with a pressure range of 14 orders of magnitude, from the gas nozzle at 10 bar to the LHC machine vacuum at 10^{-10} mbar.

A hybrid simulation approach to this problem is being taken, using Computational Fluid Dynamics (CFD) from the supersonic nozzle up to the first skimmer opening and Test-Particle Monte Carlo (TPMC) assuming a quasi-molecular flow downstream of the first skimmer. This has resulted in an optimised design (Figure 7), currently undergoing laboratory testing, with promising results having already been obtained with nitrogen gas (Figure 8).

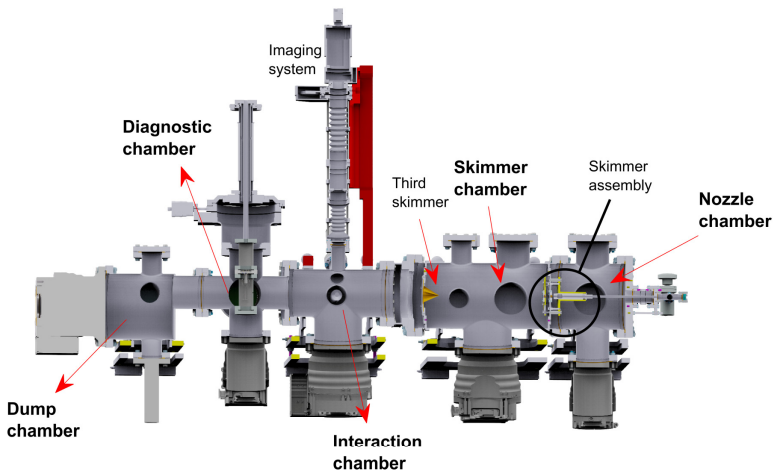


Fig. 7. Layout of the laboratory prototype gas curtain monitor.

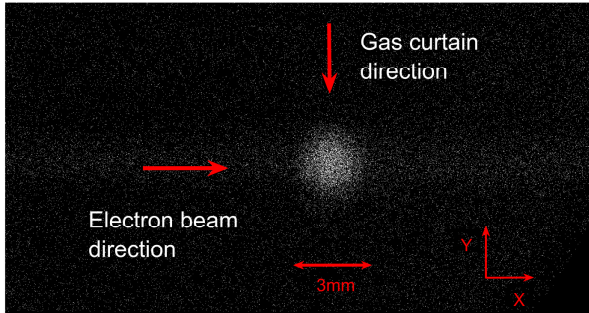


Fig. 8. Two-dimensional luminescence profile of an electron beam produced using a gas curtain.

This laboratory design must now be adapted for installation in the LHC, posing a number of additional challenges. Beam impedance concerns must be addressed by using a copper shielded sleeve with regular slots for vacuum conductance. The distance between the gas nozzle and interaction point needs to be compatible with the LHC tunnel dimensions, with the final instrument also required to fit into the 200 mm longitudinal gap between the two solenoid cryostats of the hollow electron lens. A prototype taking into account all these considerations is currently under construction with plans for installation and operation on the high energy proton beams during Run 3 of the LHC.

References

1. E. Calvo *et al.*, “The LHC Orbit and Trajectory System”, Proceeding of DIPAC, Mainz, Germany, 2003, 187.
2. D. Cocq, “The Wide Band Normaliser: a New Circuit to Measure Transverse Bunch Position in Accelerators and Colliders”, Nucl. Instrum. Methods Phys. Res. A 416, 1998, 1.
3. R.J. Steinhagen, “Real-time Beam Control at the LHC”, Proceeding of the PAC Conference, New York, USA, 2011, 1399.
4. A. Nosych *et al.*, “Overview of the Geometrical Non-Linear Effects of Button BPMs and Methodology for Their Efficient Suppression”, Proceeding of IBIC, Monterey, CA, USA, 2014, 298.
5. A. Nosych *et al.*, “Electromagnetic Simulations of an Embedded BPM in Collimator Jaws”, Proceeding of DIPAC, Hamburg, Germany, 2011, 71.

6. M. Gasiot, J. Olexa, R.J. Steinhagen, “BPM electronics based on compensated diode detectors - results from development systems”, CERN-ATS-2012-247. Proceeding of BIW, Newport News, Virginia, USA, 2012.
7. G. Trad, “Development and Optimisation of the SPS and LHC Beam Diagnostics Based on Synchrotron Radiation Monitors”, CERN-THESIS-2014-390.
8. LHCb Collaboration, “Absolute luminosity measurements with the LHCb detector at the LHC”, J. Instrum. 7 (2012) P01010, IOP and SISSA.
9. S. Vlachos *et al.*, “The LHC Beam Gas Vertex Detector – A Non-Invasive Profile Monitor for High-Energy Machines”, Proceeding of IBIC, Grand Rapids, MI, USA, 2017, 323.
10. C.P. Welsch *et al.*, “Alternative Techniques for Beam Halo Measurements”, Meas. Sci. Technol. 17 (2006) 2035c and CERN-AB-2006-23.
11. T. Mitsuhashi, “Observation of beam halo with coronagraph”, Proceedings of DIPAC’05, Lyon, France, Jun. 2005.
12. G. Trad *et al.*, “First Observation of the LHC Beam Halo using a Synchrotron Radiation Coronagraph”, Proceeding of IPAC, Copenhagen, Denmark, 2017, 1244.
13. T. Levens, K. Lasocha and T. Lefevre, “Recent Developments on Instability monitoring at the LHC”, Proceedings of IBIC, Barcelona, Spain, 2016, 852.
14. G. Berden *et al.*, “Benchmarking of Electro-Optic Monitors for Femtosecond Electron Bunches”, Phys. Rev. Letters 99, 2007, 164801.
15. S.M. Gibson *et al.*, “Enhanced Bunch Monitoring by Interferometric Electro-optic Methods”, Proceeding of IPAC, Vancouver, BC, Canada, 2018, 2353.
16. C.P. Welsch *et al.*, “Longitudinal beam profile measurements at CTF3 using a streak camera”, J. Instrum., 1 (2006) P09002.
17. E. Rossa, “Real Time Single Shot Three-dimensional Measurement of Picosecond Photon Bunches”, Proceeding of BIW, Vancouver, BC, Canada, 1994, 148.
18. V. Tzoganis *et al.*, “Design and First Operation of a Supersonic Gas Jet Based Beam Profile Monitor”, Phys. Rev. Accelerators and Beams 20, 2017, 062801.

This page intentionally left blank

Chapter 19

Injection and Beam Dump Systems

C. Bracco^a, M. J. Barnes^a, W. Bartmann^a, M. Calviani^a, D. Carbajo Perez^b, E. Carlier^a, L. Ducimetiere^a, M. I. Frankl^b, B. Goddard^a, J. Jowett^c, A. Lechner^a, N. Magnin^a, A. Perillo Marcone^a, T. Polzin^b, V. Rizzoglio^b, V. Senaj^a, L. Vega^a, V. Vlachodimitropoulos^b and C. Wiesner^d

^a*CERN, SY Department, Genève 23, CH-1211, Switzerland*

^b*Former CERN member*

^c*CERN, EP Department, Genève 23, CH-1211, Switzerland*

^d*CERN, TE Department, Genève 23, CH-1211, Switzerland*

Some of the elements of the LHC injection and extraction systems will be upgraded or replaced to adapt to the increased beam brightness and intensity of the HL-LHC beams [1; 2]. The injection main protection absorber will be replaced with new hardware which will be able to absorb and withstand **288 HL-LHC bunches** in case of an injection kicker failure. The compatibility with injection of 320 bunches (four batches of 80 HL-LHC bunches [3]) was also verified. One auxiliary injection protection collimator in Point 2 will be displaced closer to the interaction point (IP) to increase the acceptance of the ALICE Zero-Degree Calorimeter. The injection kickers, which suffered already from electron cloud, degraded vacuum and beam induced heating while operating with LHC beams, will be upgraded with several modifications to mitigate these effects. The compatibility of the LHC beam dump system with the increased beam intensities of the HL-LHC beams still needs to be fully assessed. However, the dump protection devices, as well as the dump absorber block and its entrance and exit windows needs an upgrade or replacement. The studies include the definition of the possible worst failure scenarios for the extraction and dilution kickers and the consequences on the different dump elements. Finally, the extraction and dilution system

will be upgraded to improve its reliability by reducing the risk of erratics, monitoring the status of the system and reacting faster in case of failures.

1. The LHC Injection System

The present layout of the LHC injection region, in the IR2 straight section, and the associated protection devices is shown schematically in Figure 1, an equivalent sequence of elements exists in IR8.

The beam to be injected passes through five horizontally deflecting steel septum magnets (MSI) and receives a total kick of 12 mrad. Four vertically deflecting kickers (MKI) merge the beam on to the LHC closed orbit by applying a total kick strength of 0.85 mrad. Uncontrolled beam losses resulting from MKI errors (missing pulses, erratic, partial, badly synchronized, or wrong kick strength) could result in serious damage to the downstream equipment. In particular the superconducting separation dipole D1, the triplet quadrupole magnets near the ALICE and LHCb experiments or the magnets in the arcs of the LHC machine itself could be directly hit by the beam. Also particle showers, generated by proton losses, could damage components of the detectors which are close to the beam pipe. Precautions must therefore be taken against damage and magnet quenches and collimators and beam absorber are placed at key locations in the injection regions.

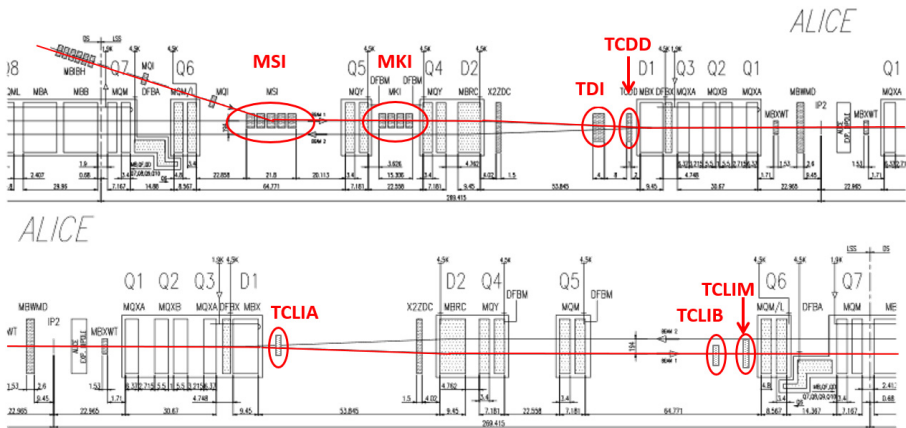


Fig. 1. Overview of the present injection system into the LHC and the associated protection devices (Beam 1, IR2). The beam is injected from the left hand side.

1.1. Upgrade of the Injection Beam Absorber TDIS

The present TDI is a movable two-sided vertical absorber which is installed at about 90° betatron phase advance from the injection kicker. Its main purpose is to protect machine elements in case of MKI malfunctions and timing errors.

The jaws of the TDIs presently installed in the LHC are 4.185 m long and accommodate blocks of graphite (6×47.1 cm), aluminium (1×60 cm) and $CuCr_1Zr$ (1×70 cm). The two latter blocks are retracted by 2 mm with respect to the graphite to avoid direct beam impact on these materials, which could lead to an excessive heating and stresses of these blocks. During the first years of the LHC operation, the TDIs in both IR2 and IR8 injection insertions were affected by several anomalies including outgassing, vacuum spikes, structural damage of the beam screens and elastic deformation of the jaws due to beam induced RF heating during the fills. Several hardware changes were already applied during the first long shutdown (LS1) and the following winter stops to mitigate the encountered problems [4]. Despite a visible reduction of the beam induced jaw deformation and of the vacuum activity, it was decided to develop a new improved design in terms of mechanics, robustness, reliability, setup accuracy, impedance and operational aspects in view of operation with higher intensity and brightness beams after LS2 [5].

Instead of having one long jaw, the new TDI (called TDIS, where the "S" stands for Segmented) will comprise three shorter absorbers (~ 1.6 m each) accommodated in separate tanks (see Figure 2 and Figure 3). The jaws of each module will all be identical except for the active absorber material. For robustness reasons, the two upstream modules will accommodate low-Z graphite absorber blocks (SIGRAFINE[®] R7550, 1.83 g/cm^3). The third module is foreseen to host higher-Z absorber materials (Ti_6Al_4V and $CuCr_1Zr$) to partially absorb and efficiently attenuate the particle showers from the low density upstream blocks.

The correct positioning of the TDIS jaws around the beam is vital for machine protection. Each module will be independently movable and redundant position measurements will be performed and checked via the Beam Interlock and the Beam Energy Tracking (BETS [6]) systems. The jaws of the third module will be slightly retracted compared to the upstream jaws to avoid direct beam impact on the higher-Z absorber blocks.

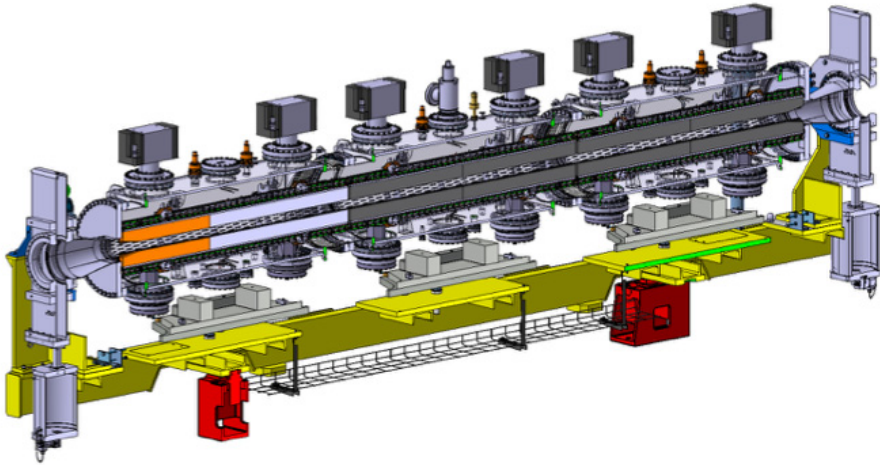


Fig. 2. The longitudinal cross section of the new TDIS showing the modules composed by different materials. The first two module jaws, starting from the right side of the figure, are made of graphite R7550 (dark grey), the last module is made of Ti_6Al_4V (light grey) and $CuCr_1Zr$ (orange).



Fig. 3. Front view of the open tank of the first TDIS module (left) and side view of the three modules installed on the common girder (right).

1.2. Supplementary Shielding of D1 Coils

The superconducting D1 separation dipole is located just downstream of the TDIS. The largest energy deposition in the D1 coils can be expected if bunches impact close to the edge of the leading TDIS absorber block since secondary particle showers can escape through the TDIS gap. During the design of the present TDI, it was found necessary to add a complementary mask (TCDD in IR2 and TCDDM in IR8) in order to prevent damage to the D1 coils for

such accident scenarios, see Figure 1. Detailed particle shower simulations [7] and damage tests at room and cryogenic temperature on NbTi cables, were carried out to determine if the efficacy of this protection system needs to be improved for HL-LHC beams. It was assessed that, in case of small beam impact parameters or grazing, the D1 magnet would certainly quench while no damage is expected. The most efficient way to further reduce the energy deposition on D1, and possibly reduce the risk of quench, consists in installing additional mask-like stainless-steel protection elements directly inside the insulation vacuum of the D1 cryostat (Figure 4). This solution offers the advantage of intercepting shower particles closer to the magnet without affecting the present machine aperture.

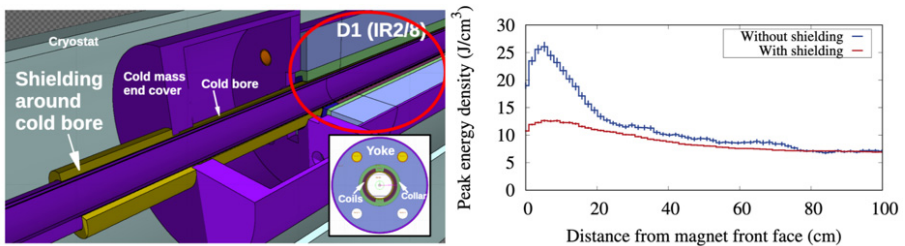


Fig. 4. 3D model of D1 cryostat where the additional shielding is installed around the cold bore to reduce the energy deposition on the magnet coils in case of injection failure (left). The expected reduction in the peak energy is also shown (right).

1.3. Displacement of Auxiliary Injection Protection Collimator TCLIA

The TCLIA is an auxiliary collimator which provides additional protection from mis-kicked beam in case of MKI failures. This device is set at an aperture of $\pm 6.8 \sigma$ (using the nominal LHC emittance of 3.5 mm mrad for the calculation of σ) during the injection process. Once the injection is completed and the MKIs are in standby, the TCLIA is opened to parking position in order not to represent anymore an aperture bottleneck. The maximum aperture at parking position for the TCLIA is ± 28 mm. This and its longitudinal position in IR2 have an impact on the acceptance of the Zero-Degree-Calorimeter (ZDC) of ALICE [8] which is a key detector used in heavy-ion operation to measure spectator neutrons and hence, the centrality of the collisions. For a given crossing angle, the ZDC is moved such that the straight-line prolongation

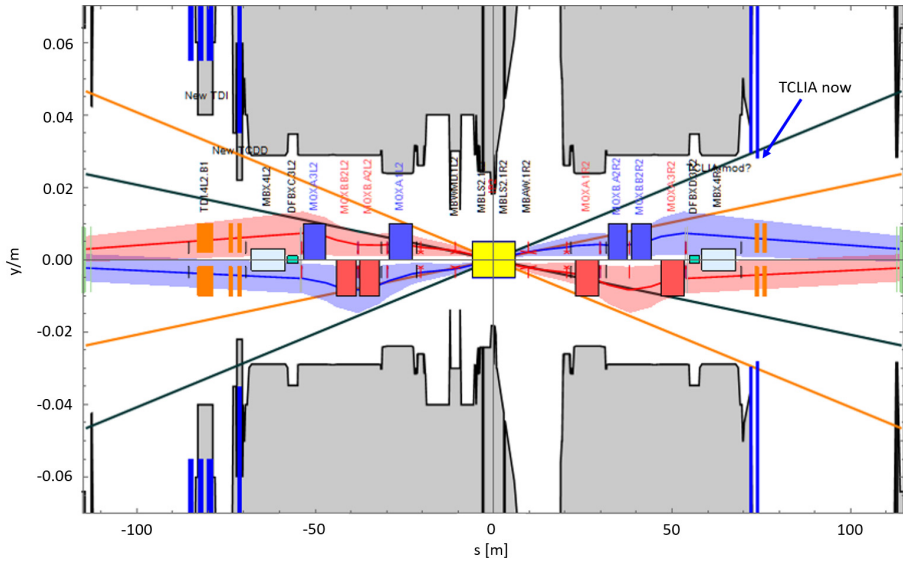


Fig. 5. IR2 aperture layout and $100\ \mu\text{rad}$ neutron cone from IP2. The present TCLIA, even when fully opened to parking, is in the line of sight of the ZDC.

from the beam at the IP passes through the centre of the ZDC. The TCLIA on the right-hand side of IP2 protrudes into this line of sight, thus shadowing the ZDC, and poses a limit on the maximum allowed crossing angle as shown in Figure 5. The present configuration limits the maximum crossing angle to $\leq 60\ \mu\text{rad}$ which is not compatible with operation with $50\ \text{ns}$ bunch spacing (i.e. the present baseline for HL-LHC Pb–Pb physics) where an angle $\geq 100\ \mu\text{rad}$ is needed. Studies were performed and it was found that the maximum TCLIA opening can be increased by $3\ \text{mm}$, without modifying the design, by pushing the setting of the mechanical end-stops and the related end-of-stroke switches to its physical limits. Moreover, the collimator will approach the IP by $2.2\ \text{m}$. These modifications will allow to achieve a crossing angle of $102.4\ \mu\text{rad}$ compatible with the $50\ \text{ns}$ Pb–Pb operation foreseen for the HL-LHC Pb–Pb exploitation.

1.4. Upgrade of the Injection Kickers MKIs

The injection kicker magnets are transmission line type magnets, each with 33 cells consisting of a U-core ferrite between two high voltage (HV) conducting

plates [9]. With high bunch intensity and short bunch lengths, integrated over many hours of a physics fill, the real part of the beam coupling impedance of the magnet's ferrite yoke can lead to significant beam induced heating. To limit the longitudinal beam coupling impedance, while allowing a fast magnetic field rise-time, an extruded ceramic tube (99.7% alumina) with up to 24 screen conductors lodged in its inner wall is placed within the aperture of each MKI magnet. A set of toroidal ferrite rings is mounted around each end of the alumina tubes, outside of the aperture of the magnet: the original purpose was to damp low-frequency resonances. To ensure reliable operation of the MKI magnets, the temperature of the ferrite yokes must not exceed their Curie point, which is $\sim 125^{\circ}\text{C}$ for the ferrite used. At this temperature the magnetic properties of the ferrite are temporarily compromised and the beam cannot be injected.

Both the MKI kickers installed in IR2 and IR8 prior to LS1 encountered a number of issues which affected operation. These include beam-induced heating, electrical flashovers, beam losses and electron cloud related vacuum pressure rise [10].

Electron cloud in the ceramic tube results in a pressure rise, which can cause an electrical breakdown and surface flash-over, hence an interlock prevents injection when the pressure is above a predefined threshold. The conditioning process of the alumina tube with beam is slow, requiring approximately 300 hours [10], and this could strongly affect beam operation in particular in case of replacement of a magnet in the middle of a run. Studies and measurements showed that a low SEY coating could mitigate multipactoring, and thus the related pressure rise, permitting more reliable operation of the injection kickers. A prototype MKI, with a 50 nm thick Cr_2O_3 coating applied by magnetron sputtering to the inner part of the alumina tube, was installed in IR8 during the winter stop between 2017 and 2018 [11]. A rapid reduction of the dynamic vacuum and faster conditioning, with respect to the original design, was observed during the scrubbing run and in operation. In addition, the Cr_2O_3 coating has not resulted in a statistically significant change in the number of UFOs (macro particles falling into the beam). The beam screen of all the MKIs was upgraded during LS1 to allow the full complement of 24 screen conductors to be installed. The modified design allowed the surface flashover rate to be further reduced [9]. The post-LS1 design also resulted in a considerable reduction of beam induced power deposition in the ferrite

yoke [12] and no limitation was encountered in operation during Run 2 [13]. A further reduction in the yoke temperature was observed in the IR8 prototype where the beam screen was modified to reduce the total power loss and move the main losses from the yoke to the ferrite rings [14]. Thermal simulations were carried out to confirm that the calculated power losses for Run 2 agreed with the temperatures measured during LHC operation. A good agreement was found and no issues were foreseen since a maximum temperature of 110°C was calculated in the first cell at the upstream end of the upgraded magnet [13]. However, for operation with HL-LHC type beams, the power deposition in the MKI is expected to be a factor of four greater than for LHC, which would be unacceptably high with the existing design [15]. Studies showed that, following the redistribution of power from the yoke to the ferrite rings, an active water cooling system just of the ferrite rings is sufficient to keep the temperature of the full magnet well below 100°C also for HL-LHC beams [16]. A complete prototype with Cr_2O_3 coated chambers, upgraded beam screen with active cooling of the ferrite rings, the so called “MKI cool” (Figure 6 [10]),

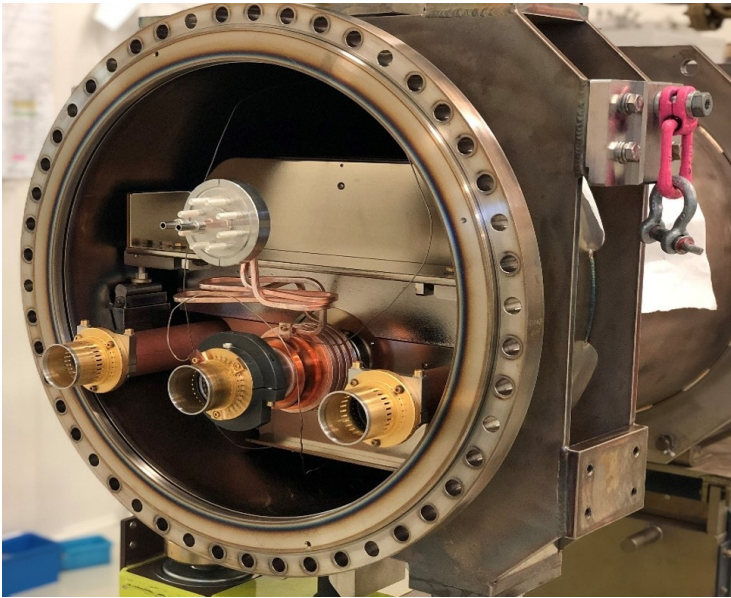


Fig. 6. Front view of the upgraded MKI-cool with the newly designed beam screen and cooling system of the ferrite cylinder.

2.1. Beam Dump System Absorbers TCDQ and TCDS

Several failure modes exist in the synchronization system and in the kicker switches that could lead to an asynchronous dump where part of the beam would be swept across the LHC aperture. Without dedicated protection devices this would lead to massive damages. The protection devices against asynchronous beam dump damages are: the TCDS, which is a fixed absorber that directly protects the downstream extraction septum MSD and the TCDQ, which is a movable absorber that protects the superconducting quadrupole Q4 and further downstream elements, including the arc and the tertiary collimators (TCTs) around the experiments. A secondary collimator with embedded beam position monitors (TCSP) is installed right after the TCDQ and allows an accurate measure of the beam center position while providing further cleaning. A fixed mask (TCDQM) is installed right upstream of Q4 to intercept secondary particle showers and thus reduce the energy deposition in the superconducting coils. The TCDQ was already upgraded in LS1. The new design, which is described in detail in [17], includes an extension of the absorber length from 6 m to 9 m, and the replacement of the higher density graphite absorber material with different grades (1.4 g/cm^3 and 1.8 g/cm^3) of carbon fibre composites (CfC). This design was supposed to be compatible with operation with HL-LHC beams. During the reliability runs performed in 2015 a new type of MKD erratic firing (Type 2), with a different rise time than the standard one (Type 1), was identified. This case is more critical since a higher number of bunches can impact the TCDQ with a large density close to the jaw surface (see Figure 8). New studies were carried out to verify the robustness of the TCDQ also for this new failure scenario [18]. Depending on the optics, the TCDQ jaw will have to be set at an aperture which could vary between 2.5 mm and 3.9 mm. No damage is expected if the TCDQ sits at ≥ 3 mm from the beam while, for smaller gaps, the peak dose could go above 2.7 kJ/g (Figure 8) corresponding to a temperature $\geq 1500 \text{ C}$. The present knowledge of the material properties at such temperature is quite poor and does not allow to exclude possible failures. Further TCDQ upgrade is not part of the HL-LHC baseline and presently, alternative mitigations (i.e. Type 2 erratic prevention, improved monitoring of the local orbit, suitable optics conditions, etc.) are being evaluated.

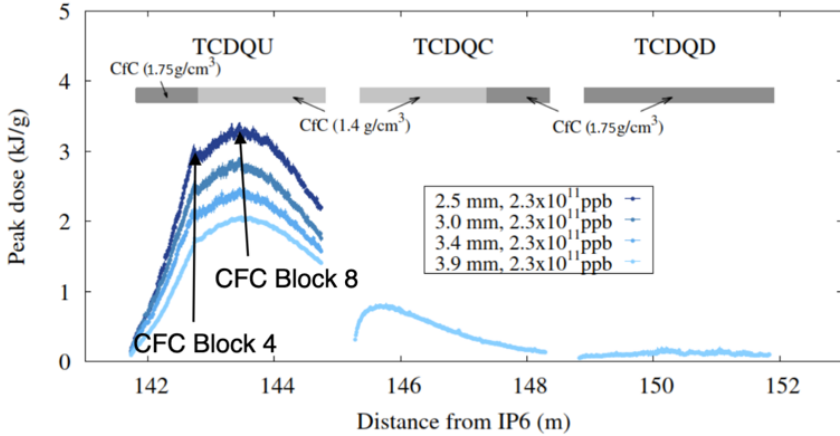


Fig. 8. Peak dose along the TCDQ modules in case of asynchronous beam dump with the TCDQ sitting at different apertures depending on the optics requirements.

The Beam Energy Tracking System (BETS [19]) monitors the position of the TCDQ as a function of the beam energy. This HW interlock was implemented in LS1 to have a redundant check of the TCDQ positioning in case of failure of the standard control system. This forbids moving the TCDQ outside pre-defined thresholds at fixed energy and might be a limitation for the ATS optics when the β -function at the TCDQ changes during the squeeze and the protection element should vary its position accordingly. In case this affects the HL-LHC β^* reach, the BETS should be upgraded to allow for TCDQ movements during the squeeze. This activity is not part of the present baseline.

The robustness of the TCDS and the protection of the MSD magnets, in case of an asynchronous beam dump with full intensity HL-LHC beams, was verified for all types of erratics [18]. A maximum energy density of 2.5 kJ/cm^3 ($\sim 1150 \text{ }^\circ\text{C}$) was calculated in the low-density blocks (graphite and CFC) and of $\geq 1 \text{ kJ/cm}^3$ in the Ti block. Thermo-mechanical studies indicate that the Ti block will experience plastic deformation and some low-Z blocks could fail due to the high stresses and elevated temperatures reached. The calculated energy deposition at the first downstream MSD septum corresponds to a temperature increase of less than 100 K ($\sim 130 \text{ }^\circ\text{C}$ absolute temperature). This temperature is not critical concerning possible changes in the magnetic properties of the steel (up to $150 \text{ }^\circ\text{C}$ is considered acceptable). Moreover the peak temperature

is reached in a peripheral part of the yoke so that no issue is expected for the insulation of the coils. Further studies are needed to evaluate if a temperature increase of up to 100 K could induce a deformation of the vacuum chamber of the circulating beam. Moreover FLUKA and ANSYS calculations have to be performed to quantify the temperature increase of the water in the MSD cooling pipes and thus evaluate the pressure rise and the consequent risk of shock-waves. The TCDS upgrade with an additional 3 m long module in front of the existing ones is included in the HL-LHC baseline.

2.2. The Beam Dump TDE

The LHC beam dump consist of an upstream window made of carbon-carbon composite on a thin stainless steel foil, a ~ 8 m long graphite dump core, a downstream Ti window and is kept under N_2 gas at higher than atmospheric pressure. The TDE and its entrance and exit windows will need to withstand the repeated dumps of high intensity HL-LHC beams. Simulation studies show that, in case of a regular dump of HL-LHC beams a peak temperature of ~ 1800 °C (a factor ~ 2 higher than for the LHC beams) will be reached in the core. In case of failure of the dilution kickers, the sweep pattern is altered (Figure 9) and significantly higher temperature and stresses can be reached.

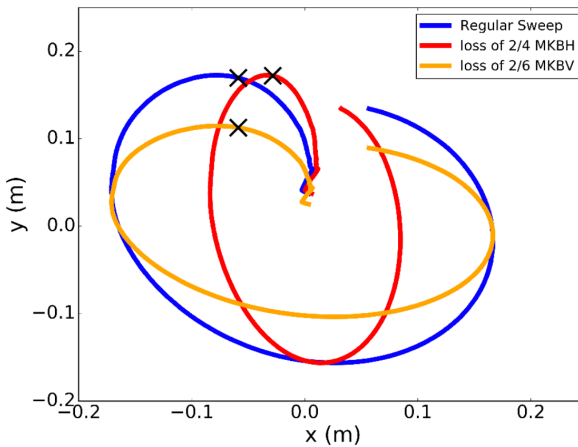


Fig. 9. Simulated beam sweep patterns at the dump for a regular sweep (blue) and the failure cases of 2 out of 4 horizontal (red) and 2 out of 6 vertical dilution kickers missing (orange). The positions of highest energy deposition are marked with a black cross.

The originally assumed worst failure scenario was the loss of two MKBs due to either the erratic firing of one kicker and perfect phase opposition with the remaining ones or a flashover simultaneously affecting two MKBs sharing the same vacuum tank. In addition, due to the smaller number of horizontal modules, their contribution in case of a failure is more critical and, for the given dilution pattern, the system is more sensitive to the loss of horizontal dilution. In case of two missing horizontal MKBs, the peak temperature can go up to 2800 °C. No information is available about the core material behavior at this temperature and mechanical characterisation studies are being performed to evaluate if any modification of the present design is needed.

The expected stress level at the present windows, also in nominal operational conditions, would be too high to insure a long term and reliable operation with HL-LHC beams [21]. For this reason they will be upgraded to ensure their survival also in case of dumps with two missing MKBs.

Moreover, during Run 2, a series of N₂ leaks appeared at the flange connections and were ascribed to large vibrations of the whole dump due to beam energy transfer during high intensity dumps. This required periodical interventions to tighten the flanges and a new nitrogen line with surface supply was built to be able to maintain the dump at the required over-pressure. Possible solutions to vibrations are being evaluated since the problem will be worsen when operating with higher intensity beams.

No dump upgrade was originally included in the HL-LHC baseline since detailed studies, identifying weaknesses and defining needed modifications, were missing. Presently, clear indications of possible limitations and required upgrades are available but key aspects, like the mechanical behavior of the core material and how to address the problem of the vibrations, are still being investigated. The goal is to having all the information to be able to define the complete upgrade strategy by 2021 in order to be ready for installation in LS3. The HL-LHC project committed to upgrade the dump with the help of the Russian in-kind contribution.

2.3. LBDS Kickers, Generators and Control System

During reliability runs, tests and operation with beam of the LBDS kickers a number of erratic triggers due to electric breakdowns and unexpected failures were encountered.

The breakdowns were located at regions with large electrical fields of around 3 MV/m at the edges of the insulators in the generators. Replacing the critical insulators and cleaning the critical areas in the generator allowed a reliable operation of the MKD system at 6.5 TeV. However, operational margins are considered too small for long-term reliable operation at 7.0 TeV for HL-LHC. For this reason a redesign of the switch stacks of the MKD generators is ongoing with the aim of keeping the electrical field below 1.5 MV/m in all areas. The replacement of the generator switch stacks is foreseen for LS2. Simultaneously, the power triggering and re-triggering system of the MKD switches will be upgraded [23]. The power triggers are presently rated at a current of 500 A and a dI/dt of 400 A/ μ s for a voltage of 3.5 kV. The upgraded system will double the current and almost double the dI/dt for a reduced voltage of 3.0 kV. The new parameters are better in line with the specifications of the manufacturer and will increase the lifetime of the GTO switches, will result in a shorter rise time and will make the power trigger less sensitive to radiation. The re-trigger system triggers all the extraction and dilution kickers as quickly as possible in case of an erratic closing of an extraction kicker switch. The present re-trigger delay is about 900 ns and the aim is to try to reduce it even further to minimise the load on the TCDQ and the ring elements, in particular the tertiary collimators, in case of an asynchronous dump. Also the diagnostic tool (IPOC) will be upgraded and a sparking activity surveillance system will be implemented to monitor the status of the generators, allow reacting in case of signs of nonconformity and provide statistics for a better understanding of the correlation between sparks and erratics. At the same time the electronics of the re-triggering system, which is becoming obsolete, will be replaced.

Beside Type 2 erratics for the MKDs, unexpected failures affected also the dilution kickers. In particular, the parasitic electromagnetic coupling, through the re-triggering line, caused the firing of neighboring MKB generators [22]. This event, combined with anti-phase could determine the loss of more than two MKBs, which was identified as the worst failure scenario in the original design of the system. Moreover, up to three MKBVs were lost, at one occasion, due to a flash-over propagation with some delay and anti-phase in two kickers sharing the same vacuum tank [24]. All these cases might have dramatic effects on the beam dump when operating with HL-LHC beams, in particular in case of MKBH failures. Different upgrade scenarios for the dilution system are being considered [25]. The MKBH generators will be upgraded to reduce

their operational voltage (presently higher than the MKBV voltage due to the lower number of MKBHs). A new re-triggering system for all the MKBs will be put in place to eliminate the risk of anti-phase in case of erratics. Different sweep patterns are then expected at the dump depending on the delay between the erratic and the execution of a synchronous dump as shown in Figure 10. The consequent energy deposition on the dump windows and the core are being evaluated for all possible relative delays. Finally, it is proposed to install two additional MKBHs per beam since this is the only fully reliable solution to reduce the risk and the sensitivity to any possible failure and open the possibility to increase the nominal sweep pattern to reduce the stresses on the dump also during nominal operation. The HL-LHC project has approved the upgrade, and implemented it in the baseline through the Russian in-kind contribution. The installation is foreseen for LS3.

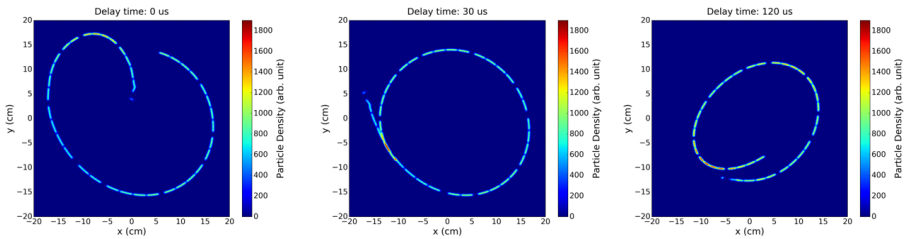


Fig. 10. Simulated sweep patterns in case of MKB re-triggering for different delays between the erratic event and the synchronous dump execution.

3. Acknowledgments

This chapter is the result of the diligent work and effort of all the WP14 members.

References

1. L. Rossi et al., *High-Luminosity Large Hadron Collider (HL-LHC): Technical Design Report V. 0.1*, CERN Yellow Reports: Monographs; 4/2017, CERN, Geneva, Switzerland, 2017.
2. E. Metral et al., *Update of the HL-LHC operational scenarios for proton operation*, CERN-ACC-NOTE-2018-0002, CERN, Geneva, Switzerland, 2018.

3. H. Bartosik et al., *Beams from the injectors*, Proceedings of 7th LHC Beam Operation Workshop, Evian, France, 2016.
4. A. Lechner et al., *TDI – Past observations and improvements for 2016*, Proceedings of 6th LHC Beam Operation Workshop, Evian, France, 2015.
5. C. Bracco et al., *Functional and operational conditions of the new TDIS beam absorber*, EDMS 1865250, CERN, Geneva, Switzerland, 2018.
6. N. Voumard et al., *Beam Energy Tracking System for MSI and TDI*, EDMS 2337989, CERN, Geneva, Switzerland, 2020.
7. A. Lechner et al., *Protection of superconducting magnets in case of accidental beam losses during HL-LHC injection*, Proceedings of IPAC, Richmond, USA, 2015.
8. J. Jowett, *ALICE ZDC aperture requirements*, EDMS 1830131, CERN, Geneva, Switzerland, 2018.
9. M.J. Barnes et al., *Reduction of surface flashover of the beam screen of the LHC injection kickers*, Proceedings of IPAC, Shanghai, China, 2013.
10. M.J. Barnes et al., *Upgrade of the LHC injection kicker magnets*, Proceedings of IPAC, Shanghai, China, 2013.
11. M.J. Barnes et al., *An upgraded LHC injection kicker magnet*, Proceedings of IPAC, Vancouver, Canada, 2018.
12. M.J. Barnes et al., *Operational experience of the upgraded LHC injection kicker magnets during Run 2 and future plans*, Proceedings of IPAC, Copenhagen, Denmark, 2017.
13. L. Vega Cid et al., *Preliminary design of a cooling system for the LHC injection kicker magnets*, Proceedings of IPAC, Vancouver, Canada, 2018.
14. M.J. Barnes et al., *Exchange of LHC kicker magnet MKI2B*, EDMS 2049157, CERN, Geneva, Switzerland, 2018.
15. V. Vlachodimitropoulos et al., *Longitudinal impedance analysis of an injection kicker magnet*, Proceedings of IPAC, Vancouver, Canada, 2018.
16. L. Vega Cid et al., *Conception and design of a cooling system for the LHC injection kicker magnets*, Nuclear Inst. and Methods in Physics Research, A 916 (2019) 296–305.
17. R. Versaci et al., *LHC asynchronous beam dump: Study of new TCDQ model and effects on downstream magnets*, CERN-ATS-Note-2012-084-MD, CERN, Geneva, Switzerland, 2012.
18. C. Bracco et al., *TCDQ AND TCDS requirements for operation with HL-LHC beams*, EDMS 2278697, CERN, Geneva, Switzerland, 2020.
19. N. Voumard et al., *The LHC Beam Energy Tracking System for the TCDQ*, EDMS 1322846, CERN, Geneva, Switzerland, 2014.
20. T. Polzin et al., *LHC main dump windows thermomechanical simulations for LHC-Run2 and HL-LHC beams*, EDMS 2029814, CERN, Geneva, Switzerland, 2018.
21. T. Polzin et al., *LHC main dump windows thermomechanical simulations for LHC-Run2 and HL-LHC beams*, EDMS 2029814, CERN, Geneva, Switzerland, 2018.
22. C. Wiesner et al., *LHC beam dump performance in view of the high luminosity upgrade*, Proceedings of IPAC, Copenhagen, Denmark, 2017.

23. N. Magnin et al., *Consolidation of retriggering system of LHC beam dumping system at CERN*, Proceedings of ICALEPCS2019, New York, NY, USA, 2019.
24. C. Wiesner et al., *Machine protection aspects of high-voltage flashovers of the LHC beam dump dilution kickers*, Proceedings of ICALEPCS2015, Melbourne, Australia, 2015.
25. C. Wiesner et al., *Upgrade of the dilution system for HL-LHC*, Proceedings of IPAC, Vancouver, Canada, 2018.

This page intentionally left blank

Chapter 20

Controls Technologies

J. Serrano, G. Daniluk, E. Gousiou and C. Roderick

CERN, BE Department, Genève 23, CH-1211, Switzerland

HL-LHC will pose new challenges on the accelerator control system. Although the overall architecture will be preserved and most of the currently deployed equipment will continue its operation, three areas have been identified for renovation in response to the new requirements: logging system, new hardware platform in the distributed I/O tier and radiation-tolerant fieldbus.

1. Overview

For the commissioning and subsequent operation of the HL-LHC, some physical elements, in particular front and back-end CPUs and storage will have been upgraded due to obsolescence. However, the overall control system strategy and architecture is sufficient for the HL-LHC needs and will not change in its conceptual structure.

Nevertheless, three areas have been identified as needing to be addressed so that the control system can respond to the new challenges: logging system, new hardware platform in the distributed I/O tier, and radiation-tolerant fieldbus.

During HL-LHC operation there will be an increase of radiation in some areas which will require re-designs and relocation of electronics. There are also new magnets which will raise the need for more diagnostics data in different subsystems. Higher data rates will also be needed during the commissioning of HL-LHC as equipment groups will need to fine-tune their systems and will

therefore require more diagnostics. In order to assure correct functionality up to the end of the HL-LHC operation period with ultimate performance, it is important to be conservative regarding the design choices and to share proven solutions as much as possible. This approach assures that proven solutions persist and that all efforts can be concentrated on making a few designs very robust instead of spreading efforts into a large number of sub-optimal designs.

2. Data Logging

The CERN Accelerator Logging Service (CALS) was designed in 2001, has been in production since 2003 and stores data from all of CERN's accelerator infrastructure and beam observation devices. Initially expecting 1TB / year, the Oracle-based system scaled to cope with 2.5TB / day coming from >2.3 million signals. It serves more than 1000 users making an average of 5 million extraction requests per day. CALS is considered as being mission-critical and the go-to service when investigating problems with equipment or unexpected beam behavior.

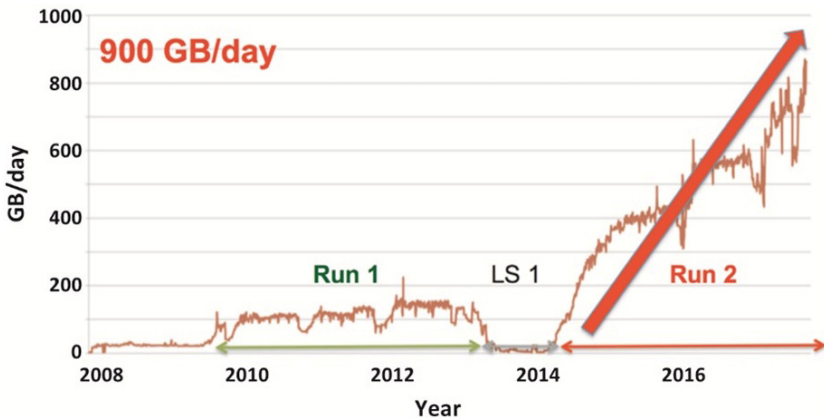


Fig. 1. Logging Service daily storage evolution in GB / day.

The CALS system has scaled well in terms of ensuring long term storage of acquired data and providing linear response times for data extractions. However, with basic accelerator operation reaching a high level of maturity, attention has turned to more complex analyses such as studying beam effects

over longer periods of time. CALS has increasingly been subjected to extraction of much larger datasets over longer periods of time to support advanced data analytics. It is in this domain, during LHC Run 2, that the CALS system quickly started to show its limits. In 2016, the NXCALS project was launched with the aim of replacing CALS from LHC Run 3 onwards. The idea is to gain operational experience with NXCALS during several years and then have time to adapt further as needed, during LS3 while still ahead of High-Luminosity LHC commissioning.

2.1. NXCALS Architecture and Technologies

In recent years, the so-called “Big Data” technology landscape has evolved significantly to support large-scale data logging and analysis, opening up new possibilities to perform efficient analysis of large data sets.

The NXCALS system is based on a microservices architecture as shown in Figure 2. The aim of this is to be able to easily upgrade or replace different aspects of the system in the future as necessary, without being forced to put in place a completely new system. From a technology perspective, NXCALS is based on in-house developments combined with open-source software such as Hadoop (HDFS and HBase) [1], Kafka [2], Spark [3], and Jupyter notebooks [4].

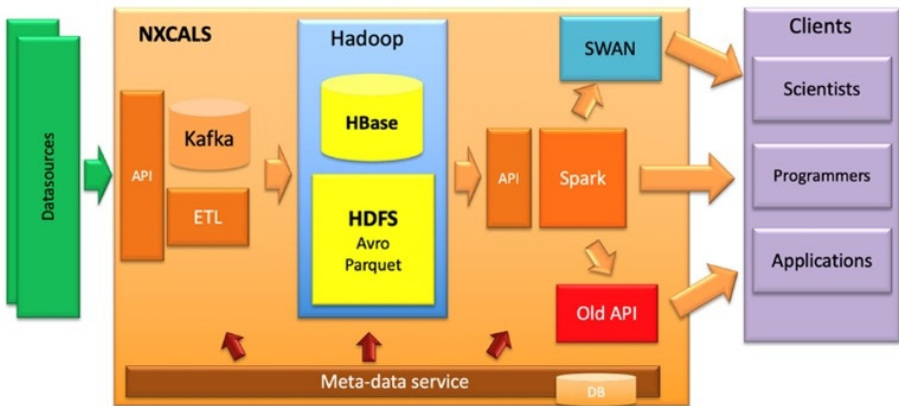


Fig. 2. NXCALS architecture.

Regarding ingestion, data is sent to the system from data acquisition processes called “Datasources”, to Apache Kafka via the NXCALS data ingestion API. Kafka is a highly reliable, high-throughput, low-latency platform for handling real-time data feeds. In NXCALS, data is stored on Kafka until it has been transferred into Hadoop by an in-house developed ETL (Extract-Transform-Load) process.

The data is stored in the Hadoop layer which is comprised of two main parts: HBase which serves as a low-latency repository from which data of the last 36 hours can be extracted by users and HDFS which serves as the long-term storage of data, in highly compressed Apache Parquet files.

A client API based on Apache Spark, with NXCALS-specific extensions, allows users of NXCALS to extract data and/or perform advanced data analysis. Spark is an analytics engine for performing large-scale distributed data processing on computing clusters. SWAN (Service for Web based ANalysis) is a CERN platform to perform interactive data analysis from the Web using Apache Jupyter notebooks.

In order to properly manage the overall coherency of the system, an in-house developed service is employed to manage the meta-data.

Finally, the core technologies used in NXCALS are based on the concept of “horizontal scalability”, which essentially means the ability to increase performance by adding more resources to the underlying infrastructure. From this perspective, the NXCALS system has the potential to adapt to the required performance needs of the future, provided sufficient resources can be financed and that sufficient physical hosting capacity is available.

3. Distributed I/O Tier Modular Kit

The HL-LHC will place challenging demands on data acquisition to/from the accelerator components which need to be controlled and diagnosed, such as the new Nb₃Sn magnets. The need for larger amounts of diagnostics information will result in a requirement for more throughput in the lower layers of the control system and will therefore affect the electronics in this tier and the communication links used to send the information up the controls stack. The current custom electronics-based controls architecture has front-end computer systems (VME or PICMG 1.3) with a large variety of reusable electronic cards to control accelerator components by sending and receiving

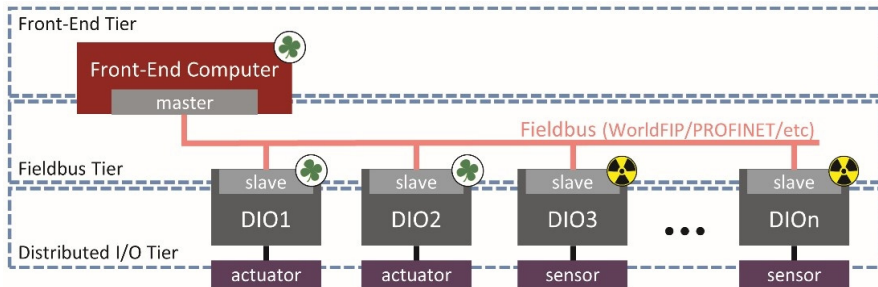


Fig. 3. Three lowest hardware layers of a typical control system.

data and carrying out calculations in real-time. In the LHC, these front-end computers typically drive a fieldbus which connects to Input/Output (I/O) modules sitting close to the accelerator, as shown in Fig. 3.

Historically, in the Front-End and Fieldbus tiers there has been a lot of sharing and reuse of design effort between equipment groups, unlike the lower Distributed I/O Tier (DI/OT) where we find many custom-made modules in different form factors.

For HL-LHC, the proposal is to extend the sharing model of the Front-End and Fieldbus to the DI/OT layer. The electronics in this layer are designed to perform early data processing and transmit to/from actuators and sensors attached to accelerator components. These I/O modules are connected to a fewer number of high-performance front-end computers which further process the data and perform the necessary calculations. By collaborating with equipment groups and providing a centralized service in the DI/OT layer, we will ensure a uniform level of quality and increase of the overall availability of electronics deployed in this tier, including those subject to radiation.

3.1. DI/OT hardware kit

In the frame of the HL-LHC project (Work Package 18) a generic and modular hardware kit (Fig. 4) is being developed in close collaboration with equipment groups, allowing different applications to benefit from a common infrastructure. The kit targets both radiation-exposed and radiation-free areas. It will consist of a 3U crate conforming to the CompactPCI Serial (CPCI-S) standard, one radiation-tolerant System Board (crate controller board for radiation-exposed systems), one non-radiation-tolerant System Board (crate controller

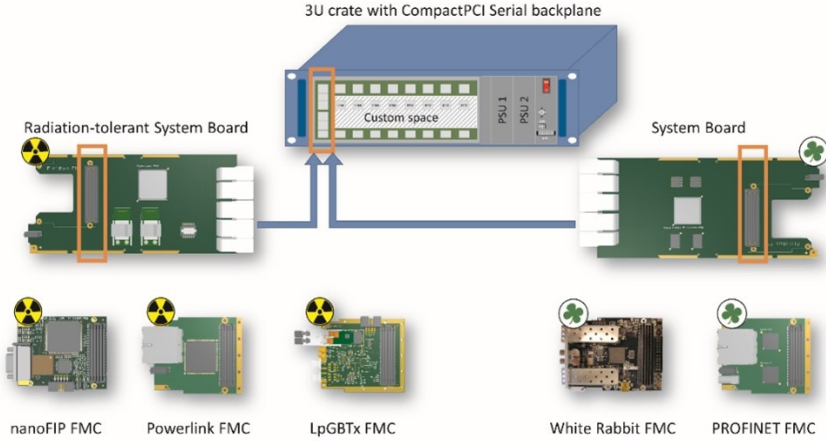




Fig. 4. Distributed I/O Tier modular and reusable hardware kit consisting of radiation-tolerant  and non-radiation-tolerant  modules.

board for radiation-free systems) and a set of interchangeable fieldbus communication mezzanines. An instance of the DI/OT crate will consist of one System Board hosting a single fieldbus mezzanine and the remaining crate slots will be filled with application-specific boards. Fieldbus mezzanines implement various communication technologies (*WorldFIP*, *Powerlink*, *LpGBTx*, *White Rabbit*, *Profinet*) and ensure control and data exchange with the Front-End tier. The System Board acts as the crate controller and interfaces with the application-specific Peripheral Boards designed by the equipment groups, plugged into the other slots of the 3U crate.

Each System Board can be programmed with desired early data processing algorithms as it features a Field Programmable Gate Array (FPGA) for the application-specific logic. A small fraction of the FPGA resources is dedicated to implement general crate monitoring services (e.g. temperatures, voltage levels, current levels, fan speeds).

Basing the kit on industrial standards (to benefit from the work already done by a large community) and designing the individual modules with experts from equipment groups and external companies (to benefit from the review of many developers) are the key principles of the project contributing to the increase in machine availability. On top of that, dedicated resources for reliability studies of all the components of the kit will provide a clear reliability assessment.

The modularity of this kit caters to different needs in equipment groups. Survey, WIC (Warm Interlocks) and PIC (Powering Interlocks) will use the full radiation-tolerant kit, including the crate, the System Board and the WorldFIP communication mezzanine. They will design their own add-in boards (Peripheral Boards) in 3U Europa card format to interface with their sensors and actuators. Other groups have their own designs for a system board and will plug one of the DI/OT communication mezzanines in it. The non-radiation-tolerant variant will be used in the Full Remote Alignment System (FRAS).

3.1.1. *DI/OT crate*

Among the various industrial standards for modular electronics, CompactPCI Serial [5] was selected as a base for the DI/OT 3U crate. The standard features a robust connector targeting transportation applications and a fully passive backplane, which makes it suitable for systems in radiation-exposed areas. Although it specifies complex protocols like PCI-Express, USB and SATA for inter-board communication, the passive backplane enables the use of the basic physical infrastructure of CompactPCI Serial without following further prescriptions on protocols. A simple communication technology (such as high-speed SPI) will be used instead, with support for automatic discovery of hardware modules. This is much more suitable for electronics in radiation-exposed areas, where the complexity of a system must be reduced as much as possible.

The fact that the DI/OT crate complies with the CPCI-S specification, enables designers to use off-the-shelf crates for lab prototyping as well as standardizes the voltages, connectors and monitoring interfaces inside the crate. However, the crates currently available on the market are not suitable “as-is” for wide deployments in HL-LHC mainly due to dimension and cost limitations. To overcome these, an open hardware crate and CPCI-S backplane are being designed in the frame of the project. The crate design will use a standard 3U sub-rack mechanical kit (available from all major crate manufacturers). It will also allow hosting boards that are longer (220mm) and wider (6 Horizontal Pitch) comparing to most common 160mm x 4 Horizontal Pitch CPCI-S boards.

To further increase the availability of DI/OT systems, the crate will be equipped with dual modular redundancy power supplies in load sharing configuration. For radiation-free areas, these will be off-the-shelf CPCI-S power supplies. However, for radiation-exposed applications, such a straightforward approach cannot be applied. Regular, switch-mode power supplies are known to fail in radiation due to both single event effects (SEE) and total ionizing dose (TID). Therefore, the vast majority of radiation-tolerant electronics currently deployed at CERN is equipped with linear power supplies. Those are less complex and thus more resilient to radiation-related effects. However, linear power supplies suffer from poor efficiency, large heat dissipation and a form factor dictated by the bulky 50Hz transformer for output powers in the order of 100W (required for DI/OT).

The first, by design radiation-tolerant, 100W switch-mode AC/DC power supply is being developed for the DI/OT hardware kit. It will be mechanically compliant with the CPCI-S standard and capable of providing 100W on +12V DC and 10W on the +5V DC power rail.

4. Radiation-tolerant Fieldbus

For the HL-LHC it has been foreseen to anticipate higher rates of data extraction from the machine by the equipment groups. Currently the only radiation-tolerant fieldbus for the accelerator is WorldFIP [6]; while operating reliably since the first LHC start-up, its bandwidth is limited to 2.5Mbps. The complexity of the Nb_3Sn magnets increases by a factor of 10 the amount of post-mortem data that needs to be transmitted for the QPS system for example, this would make the current solution based on WorldFIP sub-optimal.

An industrial solution, based on 100Mbps Ethernet, providing μs -level synchronization and supporting up to 50 slaves per segment is proposed. After a market review including leading Industrial Ethernet technologies such as Profinet, EtherNet/IP and EtherCAT, it was decided to design a radiation-tolerant implementation of Ethernet Powerlink [7]. It is the simplest of the Industrial Ethernet protocols which makes it feasible to implement a slave-node in a radiation-tolerant FPGA. Moreover, Powerlink features an open-source implementation of its stack which gives us direct access to reliable source code.

A mature option for making radiation-tolerant digital designs, is using flash-based FPGAs. Critical applications in the accelerator sector are making use of FPGA families like ProASIC3 and Smartfusion2 which have proven to be reliable for doses of a few hundred Gy. The radiation-tolerant WorldFIP slave-node for example features a ProASIC3 FPGA. The FPGA configuration is stored in flash-cells which are immune to Single Event Upsets (SEU) in the LHC environment. The pure logic is protected from SEUs by applying triple-modular-redundancy of the flip-flops, followed by voting. A more complex approach to radiation-tolerant digital designs that is being evaluated at the time of writing is instantiating a soft-core processor inside the flash-based FPGA. While replacing a complex HDL design with a real-time processor running software is a wide-spread technique outside of radiation, it has not yet been established under radiation. Fig. 5 shows the most likely scenario for the implementation of a radiation – tolerant Powerlink stack inside a flash-based FPGA. A RISC-V core is triplicated and runs software stored in ECC-protected (Error-Correction Code) memory. The data for the program resides in a separate ECC-protected memory.

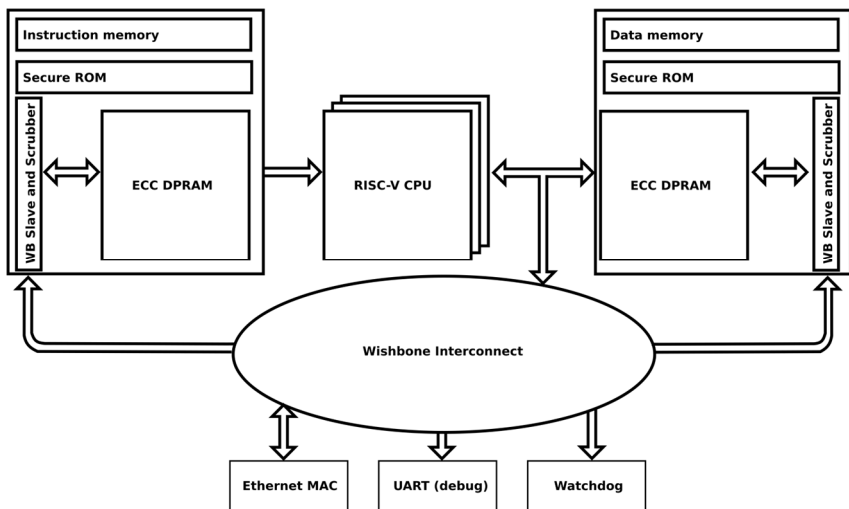


Fig. 5. Simplified block diagram of the rad-tol Ethernet Powerlink implementation.

The main challenge in our context is the validation of the RISC-V implementation in a typical flash-based FPGA and to reduce the size of the open-source Powerlink stack, originally developed for desktop systems with no memory limitations, so as to run in the amount of memory available in such FPGAs.

At the time of writing, an alternative to the flash-based FPGAs is being evaluated at CERN, the new family of low-cost and rad-hard-by-design SRAM-based FPGAs launched by the European company nanoXplore. Being rad-hard-by-design these FPGAs are tolerant to MGy doses and are immune to SEU in the configuration and the logic. They would not require triplication/voting techniques and offer memories with embedded ECC protection; this would simplify the implementation of the Powerlink stack on a RISC-V processor.

For the master side of the fieldbus, which is always outside of radiation, Powerlink being a standard, it offers commercial off-the shelf solutions, including PCIe add-in boards hosted in Linux PCs and also bus masters in Programmable Logic Controllers (PLCs). This illustrates a common theme in this work package: using industry standards as far as possible to benefit from a set of verified solutions and customizing them only as needed.

Table 1.

Aspect	LHC (2018)	HL-LHC
Logging database data rate	CALS performance limited by current architecture to 2.5 TB/day.	NXCALS horizontally scalable architecture, where performance can be increased by adding more database servers.
Resources optimization and cost reduction	Each group independently develops custom, application-specific solutions.	Common effort between groups to design a modular radiation-tolerant DI/OT ecosystem with high reliability and availability.
Efficient radiation-tolerant power supplies	Mostly linear power supplies with expensive 50Hz transformers, low efficiency (~50%) and large dimensions.	Switching mode power supply with high efficiency of at least 80%, lower cost and smaller form factor.
Radiation-tolerant fieldbus data rate	2.5 Mbps	100 Mbps

Table 2. HL-LHC systems improved by WP18.

Application	LHC (2019)	HL-LHC
Alignment and internal metrology (WP15)	Little remote diagnostics, regular personnel interventions in the tunnel.	Resources optimization and cost reduction: By-design radiation-tolerant control electronics with full diagnostics and remote alignment corrections. Efficient radiation-tolerant power supply
Warm Interlocks Controller (WP7)	Control based on commercial off-the-shelf industrial modules, not radiation-tolerant by design and not available anymore.	Resources optimization and cost reduction: By design radiation-tolerant control electronics. Efficient radiation-tolerant power supply
Powering Interlocks Controller (WP7)	Control based on legacy custom electronics and commercial off-the-shelf modules, not radiation-tolerant by design and not available anymore.	Resources optimization and cost reduction: By design radiation-tolerant control electronics. Efficient radiation-tolerant power supply
Beam Loss Monitors / Beam Position Monitors (WP13)	No link redundancy.	Resources optimization and cost reduction: Easy integration of a redundant supervision link.

5. Summary

The new Controls Technologies will provide a hardware ecosystem and improved services to the equipment groups. Table 1 highlights the main assets of the new technologies while Table 2, how the equipment groups will be benefitting from them.

References

1. <https://hadoop.apache.org/>.
2. <https://kafka.apache.org/>.
3. <https://spark.apache.org/>.
4. <https://jupyter.org/>.
5. PICMG CompactPCI Serial (CPCI-S.0) Rev 2.0.
6. <https://www.ohwr.org/projects/cern-fip/wiki/WorldFIP>.
7. <https://www.ethernet-powerlink.org>.

This page intentionally left blank

Chapter 21

Beam from Injectors: The LHC Injectors Upgrade (LIU) Project

M. Meddahi^a, G. Rumolo^b, R. Alemany^b, H. Bartosik^b, G. Bellodi^b, J. Coupard^c,
H. Damerau^d, G. P. Di Giovanni^b, A. Funken^d, R. Garoby^e, S. Gilardoni^d,
B. Goddard^d, K. Hanke^a, A. Huschauer^b, V. Kain^b, A. Lombardi^b, D. Manglunki^f,
B. Mikulec^b, F. Pedrosa^c, S. Prodon^g, R. Scrivens^b and E. Shaposhnikova^d

^a*CERN, ATS-DO Unit, Genève 23, CH-1211, Switzerland*

^b*CERN, BE Department, Genève 23, CH-1211, Switzerland*

^c*CERN, EN Department, Genève 23, CH-1211, Switzerland*

^d*CERN, SY Department, Genève 23, CH-1211, Switzerland*

^e*Former CERN member*

^f*CERN, IR Department, Genève 23, CH-1211, Switzerland*

^g*CERN, FAP Department, Genève 23, CH-1211, Switzerland*

The LHC Injectors Upgrade (LIU) project aims at increasing the intensity and brightness in the LHC injectors in order to match the challenging requirements of the High-Luminosity LHC (HL-LHC) project, while ensuring high availability and reliable operation of the injectors complex up to the end of the HL-LHC era. Fulfilling this goal requires extensive hardware modifications and new beam dynamics solutions across the entire LHC proton and ion injection chains: the new Linac4, the Proton Synchrotron Booster (PSB), the Proton Synchrotron (PS), the Super Proton Synchrotron (SPS), together with Linac3 and the Low Energy Ion Ring (LEIR) as ion PS injectors. The great majority of the LIU hardware modifications have been implemented during the 2019-2020 CERN accelerators shutdown. This chapter describes the various project phases, highlights the past and future challenges, and concludes on the expected beam parameter reach and ramp-up, together with the risks and mitigations.

1. LIU Project Goals and Phases

The LIU project aims at increasing the intensity/brightness in the injectors in order to match the HL-LHC requirements for both protons and lead (Pb) ions [1], while ensuring high availability and reliable operation of the injector complex up to the end of the HL-LHC era (ca. 2035) in synergy with the accelerator Consolidation (CONS) project [2]. This goal will be achieved through a series of major upgrades in all the accelerators of the LHC injectors chain, which are detailed in [3, 4]. The main items relevant to the desired beam performance will be addressed separately for protons and Pb ions in the next sections.

Table 1 summarises the main target parameters at the SPS exit (or equivalently, LHC injection) for both protons and Pb ions, as well as the values currently achieved. From this table, it is clear that, while for protons the main challenge lies in reaching the target single bunch parameters (double intensity and roughly double brightness), in the case of the Pb ions the single bunch parameters have been already demonstrated, but the total number of bunches in the LHC will only become accessible through a novel production scheme based on the upcoming LIU upgrades.

The LIU project was launched in 2010, with extensive beam studies taking place in Run 1 (2009 – 2013) and its first systems already installed during the injectors Long Shutdown 1 (LS1 – March 2013 to June 2014). The accelerator timeline as from 2015 up to the LIU project completion in 2021, is sketched in Figure 1 (see Ref. [5] and subsequent version updates). LIU had the peak of its execution phase during the Long Shutdown 2 (LS2: 2019 to 2020), with the installation of the largest part of its equipment.

Table 1. Beam parameters at LHC injection for protons and Pb ions, HL-LHC target and achieved in Run 2

	N (10^{11} p/b)	$\epsilon_{x,y}$ (μm)	Bunches
HL-LHC	2.3	2.1	2760
Achieved	1.15	2.5	2760
	N (10^8 ions/b)	$\epsilon_{x,y}$ (μm)	Bunches
HL-LHC	1.9	1.5	1248
Achieved	2.0	1.5	648

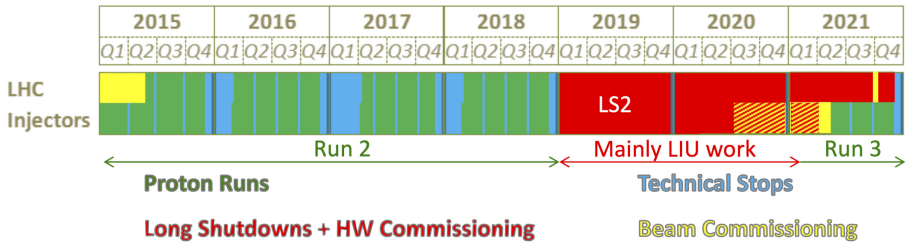


Fig. 1. LHC (upper row) and Injectors (lower row) operation schedule between 2015 and 2021. The meaning of the different colors is explained in the legend below the figure.

To define and adequately prepare the LS2 installation activities, as well as to ease the related workload, numerous project related activities had to be carried out during Run 1, LS1 and Run 2 (2010 – 2018), specifically:

- Beam simulation studies and machine measurement campaigns have been carried out to validate the assumptions made for the beam parameters as well as to explore the performance boundaries of the different machines and define strategies to cope with the various performance limitations (e.g. space charge, electron cloud, machine impedance);
- RF equipment, injection/extraction/protection devices, power supplies, beam instrumentation, etc. have been designed, built or procured and, where possible, installed during LS1 or the (Extended) Year-End-Technical-Stops – (E)YETS’s – and tested with beam;
- Cabling and decabling work was advanced compatibly with all the other maintenance activities foreseen during the yearly stops in terms of time and resources;
- All the civil engineering and infrastructures for the new buildings, as well as surface installation works, were performed in parallel with the running machines, compatibly with availability of resources;
- Linac4 was commissioned and underwent reliability and quality runs from 2016 to 2019 [6]. Tests to qualify the new PSB injection scheme were performed in 2016 — 2017 [7, 8].

The LS2 equipment installation and testing phase without beam sequentially ended for each injector synchrotron between December 2020 and March 2021, and stand-alone beam commissioning in the upgraded injectors took place. More precisely, beam commissioning first started in July 2020 for

Linac4 (which only had a relatively short technical stop after the 2019 beam quality and reliability run), and continued in December 2020 with the first beam to the PSB, March 2021 to the PS and April 2021 to the SPS. Linac3 has restarted operation in mid April 2021 after a successful test run, while the first beam to LEIR has been planned for the end of June 2021*.

Commissioning of LIU beams will have a head start in 2021 for the Pb ion beams, in preparation to the achievement of the full beam performance required for the HL-LHC Pb-Pb ion run at the end of 2022. The proton beam commissioning up to the LIU beam parameters will be gradually performed during Run 3 (2021 – 2024) to be ready after Long Shutdown 3 (LS3). This strategy will allow implementing any further hardware corrective actions during the Run 3 technical stops or LS3, if needed, as discussed more in detail further on in this chapter.

2. LIU Baseline for Protons

To fulfil the HL-LHC requirement of integrated luminosity, the proton injectors are expected to produce trains of 288 bunches (4×72) with 25 ns bunch spacing and with about double bunch intensity and 2.4 larger brightness at the SPS exit with respect to present values (Table 1, top two rows).

To reach this goal, the LIU baseline includes [3]:

- Replacement of Linac2 with Linac4. The H^- charge exchange injection into the four rings of the PSB at 160 MeV will produce beams with twice higher brightness than presently achieved out of the PSB [9];
- Increase of the kinetic energy at injection into the PS from 1.4 to 2 GeV. In combination with optimized longitudinal beam parameters at the PSB-PS transfer [10], this will allow reaching the LIU beam brightness target at unchanged space charge tune spread. The higher PSB extraction energy requires an increase of the PSB magnetic fields as well as the replacement of its main power supply and RF systems;
- Installation of longitudinal feedback against the longitudinal coupled bunch instabilities, reduction of the impedance of the 10 MHz RF system and implementation of the multi-harmonic feedback systems

* This chapter reflects the LIU progress as of May 2021

on the high frequency RF systems. These interventions are needed to increase the threshold of the longitudinal coupled bunch instabilities that presently limit LHC beams in the PS. The first and third item have been already implemented in the PS and, together with the use of the 40 MHz RF system as Landau RF system over a part of the PS cycle, have demonstrated that the PS can reliably produce the LIU target intensity. The transverse feedback system in the PS has been also made operational to gain margin in machine settings against transverse instabilities;

- Upgrade of the SPS 200 MHz RF system. The RF power will be increased by adding two new 200 MHz power plants, changing to a pulsed operation mode for increasing the peak RF power, and rearranging the 200 MHz cavities to reduce their impedance and the beam loading effect with LHC-type beams. A further reduction by a factor 3 of the High Order Modes (HOM) will be achieved through the installation of specially designed couplers. A new low-level RF for the 200 MHz RF system will be also implemented, which will allow more flexibility, beam loss reduction and new RF beam manipulations;
- Shielding of the focusing quadrupole (QF) flanges and a-C coating of the attached vacuum chambers. The goal is to increase the threshold for longitudinal beam instabilities and alleviate electron cloud transverse instabilities. Due to the limited scope of the a-C coating campaign, however, beam induced scrubbing is also expected to be required for the production of the target LIU beams;
- Upgrade of injectors protection devices and a new SPS main beam dump to cope with the increased beam intensity and brightness. The SPS extraction protection, transfer line stoppers and collimators will be either exchanged, or new interlocking systems will be added.
- Upgrade of an important fraction of the beam instrumentation, vacuum systems, and general services to comply with the performance and reliability targets.

After the implementation of the LIU upgrades, the beam parameters expected at LHC injection will match the HL-LHC target values reported in Table 1 for the LHC standard beam (trains of 72 bunches at the PS exit). This can be illustrated visually in a so-called *limitation diagram*, as shown in Figure 2: in the beam parameter space of transverse emittance versus bunch

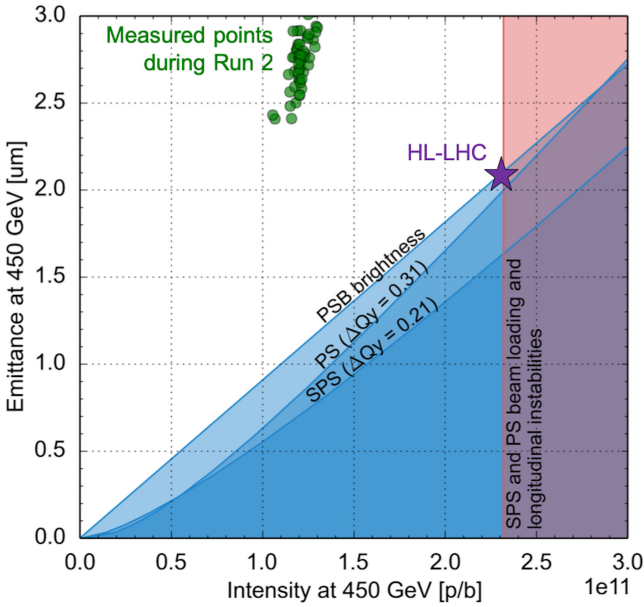


Fig. 2. Limitation diagram for LHC standard 25 ns beam. The HL-LHC target (purple star) matches the best achievable LIU parameters. Measured points from Run 2 are also displayed (green).

intensity at SPS extraction, all the boundaries for intensity and brightness limitations in the PSB, PS and SPS are plotted and the inaccessible regions are shaded. The best achievable parameter set corresponds to the point with the highest intensity and lowest emittance in the non-shaded area. As can be seen, the achievable beam parameters for the LHC standard beam match exactly the HL-LHC target values. The measured points from Run 2 are also plotted, highlighting the important challenge for the LIU project [11].

It should be mentioned that the standard beam type is considered as baseline by HL-LHC to fulfil its integrated luminosity goal over the HL-LHC run [1]. Due to the LIU improvements, also other LHC beam types will benefit and see their performance improved in post-LS2 operation. For example, both the Batch Compression Merging and Splitting scheme (BCMS) [12], which results in trains of 48 bunches out of the PS, and the 8b+4e beam, made of trains of 56 bunches from the PS arranged in alternating sequences of 8 bunches and 4 gaps [13, 14], have the potential to be produced with about

20% higher brightness with respect to the standard beam, at the expense of lower numbers of bunches in LHC. These beams are considered by HL-LHC as alternatives in case mitigation against unwanted emittance blow up and/or electron cloud effects in the LHC is needed.

On the path to define and implement the means to achieve the target beam parameters, several lessons have been learnt, which have steered and re-prioritized the activities within the LIU project and should be kept in mind for future operation. Two notable examples are described here below.

In 2018, 25 ns standard beams with the desired bunch intensity of $2.6 \cdot 10^{11}$ p/b have been successfully and reproducibly produced at the PS extraction (although the transverse emittance was still more than twice the target value). This achievement has been made possible only thanks to the installation of the broadband Finemet cavity in the PS and its deployment during Run 2. This cavity acts as the kicker for the longitudinal feedback together with other stabilising means to combat longitudinal coupled bunch instabilities on the ramp and at flat top. Figure 3 shows how the bunch intensity at the PS extraction was gradually ramped up from 2015 to 2018 as a combined result of additional RF improvements and operational optimisation [15]. As a mitigation if the target intensity could not be attained, the option of adding

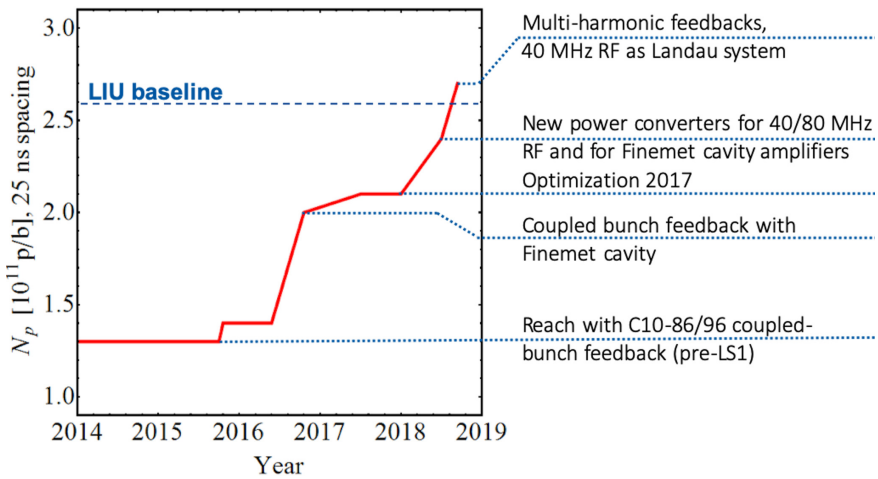


Fig. 3. Evolution of extracted bunch intensity from PS over Run 2. The LIU baseline is also represented as a horizontal dashed line.

a Landau cavity in the PS was also actively pursued in 2017 – 2018, to be ready for inclusion in the project baseline in case of confirmed need. This experience has clearly shown that 1) learning how to reach unprecedented beam parameters while operating new equipment can take a longer-than-expected commissioning time, especially if this is done in machine development mode; and 2) though eventually not needed in the baseline, having made a preliminary study for a PS Landau cavity still serves the purpose to have laid a robust ground for a possible post-LIU option, if Run 3 operation will call for lower longitudinal emittances from the PS.

The LIU project had originally amorphous carbon (a-C) coating of all the SPS dipole and quadrupole chambers in the baseline in order to suppress a large fraction of the electron cloud inside the machine. However, after the post-LS1 scrubbing experience for nominal LHC beams and the first successful scrubbing runs even with higher intensity LHC beams at 26 GeV/c already in 2015, it was decided to descope the coating to just one machine sextant and mainly rely on beam induced scrubbing also for the target beam parameters. As the scrubbing efficiency was also confirmed in the high intensity runs of 2017 - 2018, even the a-C coating of one sextant was further descoped in May 2018 during an exercise of budget reduction. Only the a-C coating of the QF chambers and some new drift chambers has been finally retained. Meanwhile, as the longitudinal coupled bunch instabilities along the cycle and at flat top had been clearly identified as responsible for limiting the bunch intensity at extraction to $2 \cdot 10^{11}$ p/b in the SPS, a campaign of impedance identification and reduction was pursued within LIU to extend the intensity reach of the project to its target value. Therefore, the shielding of the QF flanges and re-design of the HOM couplers for the 200 MHz cavities were included in the project baseline in 2016.

3. LIU Baseline for Ions

The target HL-LHC integrated luminosity with Pb-Pb in the post-LS2 era (ca. 3 nb^{-1} /year over four runs until 2029) can be met if the parameters of the Pb beam at the SPS extraction match the values in Table 1.

Thanks to an intensive campaign of machine studies and additional instrumentation installed in Linac3 and LEIR, which required an important temporary refocus of priorities and reshuffle of resources within the LIU project, the

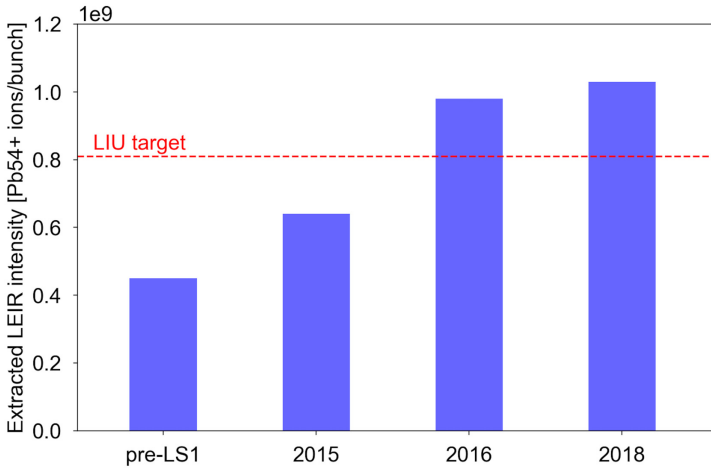


Fig. 4. Evolution of the extracted intensity from LEIR since before LS1 (2013) and over Run 2 (2015-18). The LIU target value is also displayed as a dashed line.

overall performance and reliability of the Pb ion injection chain had already a boost in 2015 [4] and has since further improved during Run 2 with respect to previous runs. As a consequence of the higher current from Linac3 after the removal of an aperture limitation at the source, optimised transfer and injections into LEIR, and mitigation of space charge at RF capture in LEIR, the intensity extracted from LEIR has more than doubled over Run 2, even exceeding the LIU target value by about 20% (see Figure 4). In the SPS the overall transmission has been also improved thanks to working point, RF and transverse feedback optimisation, and the batch spacing at injection has been successfully reduced to 150 ns by optimising the kicker switch settings and deployment of the transverse damper for ions. Globally, as reported in Table 1, the single bunch parameters achieved in 2018 at the SPS extraction already match the HL-LHC desired values, and even include a 5% margin for the additional losses expected with the future RF manipulations.

This is also displayed in Figure 5, in which both the average bunch intensity and total beam intensity per LHC fill are plotted as a function of time, when looking at the first half of the run (light blue, labeled *4 bunch scheme*). During this phase, the nominal Pb ion production scheme was used, leading to the injection into LHC of 9 trains of 4 bunches from the SPS with 100 ns between bunches and 150 ns between trains. From the plot, it is clear that the achieved

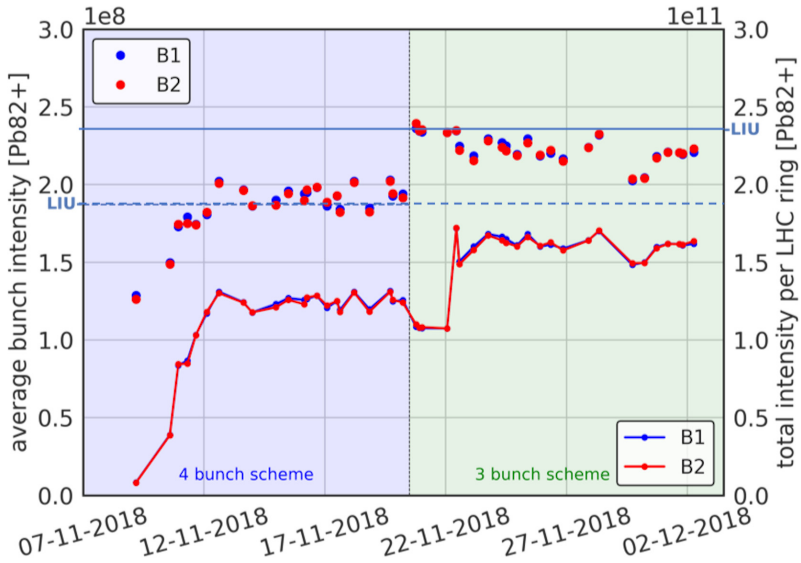


Fig. 5. Average bunch intensity (points and left vertical axis) and total beam intensity (solid lines and right vertical axis) per LHC fill as a function of time during the 2018 Pb-Pb run. The LIU goals for both are also shown as horizontal lines (dashed for bunch intensity and solid for total beam intensity).

bunch intensities at the LHC injection (red and blue dots) were always equal to or larger than the LIU target (dashed line tagged LIU) in regime operation. In addition, and later on during the run, an alternative filling scheme for LHC was set up and operationally used in the 2018 Pb-Pb run, based on the production of three bunches in LEIR and batch compression to 75 ns before the PS extraction. This scheme had the advantage of being able to pack a higher number of bunches in LHC (733 instead of 648), each with 10% higher intensity. To be noted that the potential 33% gain in bunch intensity is partly lost due to strongly nonlinear transmission through the SPS, which exhibits much higher losses for more intense bunches. Both the larger intensity per bunch and the overall larger number of bunches result in larger total numbers of ions in LHC (red and blue lines), as can be seen in Figure 5, second half of the run (light green, labeled *3 bunch scheme*). Assuming that the integrated luminosity in LHC is about proportional to the number of Pb ions that can be injected into LHC, one obtains from the 2018 run the experimental verification that the 3 bunch scheme has the potential to achieve 70% of

the HL-LHC integrated luminosity target (solid line tagged LIU), which was estimated beforehand from calculations [16, 17]. The validity of this scheme as a fallback scenario if the momentum slip stacking in the SPS is delayed or underperforms is therefore fully confirmed.

The remaining LIU item to be implemented for post-LS2 ion operation is the momentum slip stacking in the SPS to allow the transfer of 7 trains spaced by 100 ns, each train being made of 8 bunches spaced by 50 ns, to the LHC. In this configuration, 1248 bunches can be injected into the LHC. The momentum slip stacking in the SPS depends on the full deployment of new LLRF capabilities for the 200 MHz RF system, expected to be ready in the last quarter of 2021, and its feasibility has been proved in simulations [18]. In preparation for this mode of operation, dedicated machine studies were conducted in 2018 [19]. It was found that a radial displacement by 20 mm at 300 GeV (energy plateau chosen for slip stacking) does not lead to losses for the ion beam, which suggests that there would be enough momentum aperture to move only one half of the beam during the slip stacking. Unfortunately, longitudinal instabilities were observed after transition crossing and at 300 GeV, which means that stabilisation techniques (i.e. 800 MHz, longitudinal emittance blow up) will have to be studied in simulations during LS2, and then tested and commissioned in 2021 – 2022.

4. LIU Beam Commissioning in Run 3

To prepare for the restart of the injectors in 2020 – 2021, individual system tests took place during the shutdown period, followed by periods of hardware commissioning conducted by the operation teams, which in this case included also the newly installed LIU equipment. After the hardware commissioning and cold check out, blocks of variable length for stand-alone beam commissioning have been allocated for each accelerator of the injection chain. The details can be found in the general LS2 master plan [20].

The current timeline for the commissioning of the LIU beams in Run 3 is shown in Figure 6. All the pre-LS2 beams as documented through the existing beam documentation (for both protons and Pb ions) are gradually being recovered in 2021 and will serve their physics users, as they gradually come online. Conditioning of new equipment and general machine scrubbing will be needed in the SPS to recover the beam quality already for pre-LS2 beam

intensity. In order to assess the state of the machines after LS2, reference measurements are already being conducted in all machines (e.g. physical aperture, impedance) and compared with the pre-LS2 data. It should not be forgotten that the general injector operation in these two years will be challenging due to the fact that all major new LIU systems have to be commissioned with beam and operationally integrated (though not fully exploited), e.g. the new H^- charge exchange injection into the PSB, the new PSB main power supply and RF system, the PSB-PS transfer at higher energy, the upgraded 200 MHz RF system in the SPS (both for power and LLRF), the new SPS beam dump. In addition to all of this, the Pb ion beams will have to be recovered as in 2018 (both 4 and 3 bunch schemes) and commissioning of the momentum slip stacking in the SPS will have to start already in 2021 with the important challenges highlighted in the previous section and in preparation of the 2022 LHC Pb-Pb ion run. As of 2022, the intensity ramp-up of the LHC proton beams can begin. During 2022, one can expect a combined intensity and brightness ramp-up, with the bunch intensity at the SPS extraction progressively increased from the pre-LS2 $1.3 \cdot 10^{11}$ p/b to the target $1.8 \cdot 10^{11}$ p/b while the transverse emittance is tentatively decreased from the initial $2.5 \mu\text{m}$ to $1.7 \mu\text{m}$. New territory will be explored in terms of beam parameters. In fact, intensities up to $2.6 \cdot 10^{11}$ p/b were already produced up to PS extraction and even tested at SPS injection during Run 2. However, beams in the intensity range above $1.5 \cdot 10^{11}$ p/b need the upgraded SPS main RF system to be accelerated in trains longer than 12 bunches. The SPS will have to be scrubbed for this new range of intensities and the already encountered horizontal and longitudinal instabilities at 26 GeV/c will have to be overcome in order to ensure beam losses within 10% in the SPS, as required for operational deployment. Therefore, a stabilisation strategy is being developed during LS2, also relying on the search of the instability sources, and will have to be tested and demonstrated. It should be mentioned that additional beam requests from physics (e.g. light ions) may also take significant time and resources, should these requests be approved.

In 2023 – 2024 the injected intensity into the SPS will have to be further ramped up from 2 to $2.6 \cdot 10^{11}$ p/b at constant brightness, expecting an extracted intensity from 1.8 to $2.3 \cdot 10^{11}$ p/b – possibly in two steps, see Figure 6. Apart from the needed additional SPS scrubbing, new and yet unknown limitations might emerge and require additional actions to achieve the target beam param-

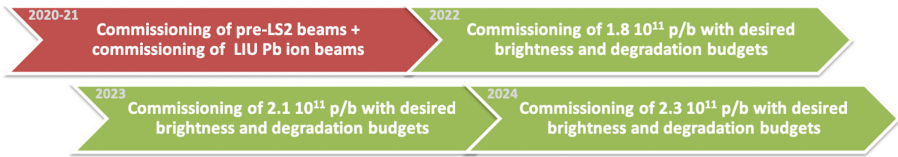


Fig. 6. Gradual intensity ramp-up to the LIU beam parameters over Run 3.

eters. Addressing these limitations and implementing measures to overcome them is part of the scope of the subject treated in the next section.

5. Beyond the LIU baseline

In the course of the LIU project, several additional items were considered at different stages for the achievement of the LIU beam parameters, but were then dropped from the baseline because of low benefit over cost ratio. A complete inventory of these options can be found in [21] with details in the references therein. However, some of them could still be revived in the post-LIU era to respond to some specific failure scenarios. In the following we will report a list of the main items, to be kept in mind during Run 3, should any of the associated failure scenarios indeed occur.

Impedance reduction of the extraction kickers in the PSB. Horizontal instabilities occurring along the PSB cycle are caused by the unmatched terminations of the extraction kickers and are cured by the transverse feedback in routine operation. Future operation might suffer due to the 160 MeV injection, which is a critical energy for the instability, and the acceleration of higher intensity beams for ISOLDE. Although this limitation is expected to be mitigated by the upgraded transverse feedback system, an impedance reduction scheme for the kicker exists and has been proved effective both in electromagnetic and beam dynamics simulations.

Landau RF system in the PS. While the LIU beam intensity has been already proved at the PS extraction, the implementation of a Landau RF system would increase the stability margin and give more potential to decrease the longitudinal emittance out of the PS, which might directly benefit the SPS losses at injection energy if they are too high. A conceptual design of this additional RF system has been performed and its efficiency has been demonstrated in simulations.

a-C coating of the dipole chambers in the SPS. Beam induced scrubbing has been shown to work for high intensity in the SPS, however large tune shifts along the batches and instabilities have been also observed, which might be due to electron cloud and limit future operation. If an active measure to suppress the electron cloud in the most critical elements of the SPS will have to be implemented, the logistics for in-situ a-C coating of selected SPS chambers will be ready and widely tested during YETS and LS2.

Further SPS impedance reduction. In addition to the shielding of the QF flanges and further suppression of the HOMs in the 200 MHz cavities, the SPS might benefit from reducing the impedance of the injection kickers (both for equipment heating and longitudinal stability) as well as from shielding the defocusing quadrupole (QD) transitions and the vacuum valves (mainly for longitudinal stability). The benefit of these measures has been shown in beam dynamics simulations. Concerning the impedance reduction of the MKP-L module of the injection kickers, a solution with longitudinal serigraphy has been found and is planned to be implemented in one of the first YETS after LS2, because it has been calculated that the heating of this element would strongly limit scrubbing and machine development for the LIU intensities during Run 3 and later routine operation in the HL-LHC era.

Wideband feedback system for the SPS. A prototype system was installed in the SPS and proved to work against vertical instabilities both in single and multi-bunch operation. An upgraded version of this system could be used against potential future vertical instabilities caused by persisting electron cloud, or a similar system could be developed ex-novo in the horizontal plane to be used against the horizontal instabilities observed in high intensity operation. In fact, the wideband feedback system in either transverse plane is a powerful means against any type of unpredicted beam instability that could rise in high intensity operation and for which the source cannot be easily suppressed.

Collimation system in the SPS. A two-stage collimation system has been designed for the SPS to intercept large momentum particle losses. Such a system could turn out to be necessary in operation with the LIU parameters and higher loss regime to reduce machine equipment irradiation and activation.

6. Conclusions

The LIU project is currently in its very final phase, with most of the new equipment installation and commissioning taking place during LS2. The project baseline in terms of design and construction of new upgraded equipment was built such that the target LIU beam parameters match the HL-LHC request for both protons and ions. This has been achieved thanks to the constantly improving machine operation and beam modelling for all injectors and to the careful steering of the project priorities towards the most critical items according to the evolving level of understanding, within the given constraints of time, resources and budget. A solid ramp-up strategy has been established for the LIU beam parameters and will be put in place during Run 3, based on a gradual exploitation of the newly installed hardware to produce baseline LIU beams in their yet unexplored parameter range by the end of 2024 for post-LS3 readiness. Although the recommissioning of the whole upgraded injectors chain will be challenging and risks still exist for the achievement of the target beam parameters, mitigation schemes and/or post-LIU options have been prepared within the project, as a pathway for successful luminosity production in the HL-LHC era.

7. Acknowledgements

We would like to thank all the current and past LIU Work Package holders as well as the numerous colleagues across all CERN departments, who have been involved in the LIU project at different levels and have contributed with their constant engagement and work to the successful execution of this project. They have made it possible to carry out all LIU activities on schedule and budget in spite of the several challenges – not only technical – encountered at the different stages of this decade long project.

References

- [1] R. Tomás *et al.*, “Beam parameter requirements from HL-LHC”, presented at the LHC Injectors Upgrade (LIU) Workshop, Montreux, Switzerland, Feb. 2019, unpublished.
- [2] M. Benedikt *et al.*, “Summary of Session 7: Accelerators and non LHC Experiment Areas Consolidation up to LS3”, in *Proc. Chamonix 2014 Workshop*, Chamonix, France, Sept. 2014, CERN-ATS-2015-002, pp. 31-32. doi:10.5170/CERN-2015-002.31.

- [3] J. Coupard *et al.*, “LIU Technical Design Report - Volume I: Protons”, CERN, Geneva, Switzerland, Rep. CERN-ACC-2014-0337, Dec. 2014.
- [4] J. Coupard *et al.*, “LIU Technical Design Report - Volume II: Ions”, CERN, Geneva, Switzerland, Rep. CERN-ACC-2016-0041, April 2016.
- [5] K. Foraz, “Long-term Schedule for the CERN Accelerator Complex”, Rep. EDMS 2311633 v1.0, Jan. 2020, <https://edms.cern.ch/document/2311633>.
- [6] A. Lombardi, “Linac4: From Initial Design to Final Commissioning”, in Proc. IPAC’17, Copenhagen, Denmark, May 2017, paper TUYA1, pp. 1217-1222.
doi : 10.18429/JACoW-IPAC2017-TUYA1.
- [7] B. Mikulec *et al.*, “Commissioning and results of the half-sector test installation with 160 MeV H⁻ beam from Linac4”, in Proc. of IPAC’17, Copenhagen, Denmark, May 2017, paper MOPIK047, pp. 619-621. doi : 10.18429/JACoW-IPAC2017-MOPIK047.
- [8] W. Weterings *et al.*, “First experience with carbon stripping foils for the 160 MeV H-injection into the CERN PSB”, AIP Conference Proceedings **1962**, 030003 (2018).
doi : 10.1063/1.5035520.
- [9] E. Benedetto *et al.*, “CERN PS Booster upgrade and LHC beams emittance”, in *Proc. of IPAC2015*, Richmond, VA, May 2015, paper THPF088, pp. 3897-3900.
doi : 10.18429/JACoW-IPAC2015-THPF088.
- [10] G. Rumolo *et al.*, “Expected performance in the injectors at 25 ns without and with Linac4”, in *Proc. Review of LHC and Injector Upgrade Plans (RLIUP) Workshop*, Archamps, France, Oct. 2013, CERN-2014-006, pp. 17-24.
doi : 10.5170/CERN-2014-006.17.
- [11] H. Bartosik *et al.*, “Injectors Beam Performance Evolution during Run 2”, presented at 9th LHC Operations Evian Workshop, Evian, France, Jan.-Feb. 2019, unpublished.
- [12] R. Garoby, *IEEE Transactions on Nuclear Science*, vol. 32, no. 5, pp. 2332-2334, Oct. 1985. doi : 10.1109/TNS.1985.4333903.
- [13] R. Garoby, “Multiple bunch splitting in the PS: Results and Plans”, Rep. CERN/PS 2001-004 (RF), Feb. 2001.
- [14] H. Damerau *et al.*, “LIU: Exploring alternative ideas”, in *Proc. Review of LHC and Injector Upgrade Plans (RLIUP) Workshop*, Archamps, France, Oct. 2013, CERN-2014-006, pp. 127-138. doi : 10.5170/CERN-2014-006.127.
- [15] A. Lasheen *et al.*, “PS intensity reach and longitudinal parameters after LIU”, presented at the LHC Injectors Upgrade (LIU) Workshop, Montreux, Switzerland, Feb. 2019, unpublished.
- [16] H. Bartosik *et al.* “LIU-SPS: Protons and Ions”, presented at LHC Performance Workshop Chamonix 2018, Chamonix, France, Jan.-Feb. 2018, unpublished.
- [17] H. Bartosik *et al.*, “Transverse beam quality and stability in the SPS (protons and ions)”, presented at the LHC Injectors Upgrade (LIU) Workshop, Montreux, Switzerland, Feb. 2019, unpublished.
- [18] D. Quartullo, “Simulations of RF beam manipulations including intensity effects for CERN PSB and SPS upgrades”, CERN, Geneva, Switzerland, Ph.D. thesis, CERN-THESIS-2019-006, Feb. 2019.

- [19] E. Shaposhnikova *et al.*, “Longitudinal beam quality and stability in the SPS (protons and ions”, presented at the LHC Injectors Upgrade (LIU) Workshop, Montreux, Switzerland, Feb. 2019, unpublished.
- [20] J. Coupard *et al.*, “Master schedule of the Long Shutdown 2 (2019-2020)”, Rep. CERN EDMS 1687788, Jan. 2019, <https://edms.cern.ch/document/1687788>.
- [21] H. Bartosik and G. Rumolo, “Beyond LS2: Possible injector upgrades to reach the LIU parameters”, Rep. CERN EDMS 2400331, Sept. 2020, <https://edms.cern.ch/document/2400331>.

This page intentionally left blank

Chapter 22

Integration, (De-) Installation and Alignment

P. Fessia^a and H. Mainaud Durand^b

^a*CERN, ATS-DO Unit, Genève 23, CH-1211, Switzerland*

^b*CERN, BE Department, Genève 23, CH-1211, Switzerland*

Optimized space allocation for each equipment is instrumental to ensure that the various systems perform according to specification and to minimize installation and maintenance time. The general optimization effort goes under the name of “integration”, and it is strictly linked to the de-installation of the previous machine, to the management of the interfaces with existing infrastructures and to the installation of the new HL-LHC equipment. One of the machine setups, which is most deeply integrated with the others, is the alignment system that plays a prominent role in allowing achieving the HL-LHC performance goals and that is conceived to minimize human presence in the machine in order to maximize operational time, to provide new operational flexibility, and – of paramount importance – to reduce the radiation dose to personnel.

1. Introduction

The HL-LHC Project requires the installation of new systems in different areas:

- (1) The beam line in the Long Straight Section around LHC Point 1 and Point 5 and, to a lesser extent, in other LHC points, is the backbone of the HL-LHC Project where the new devices will manipulate the beams in unprecedented ways, making possible to reach the Project goals. The HL-LHC alignment system extends over the whole Matching Sections [MS] of Point 1 and Point 5, intimately connecting all the elements of it

and keeping each device aligned with the beam trajectory in a new approach for proton colliders at CERN.

- (2) In each of the two mentioned LHC Points, a new complex of galleries will be excavated. It will be about 500 meters long and it will run 80 m under the surface. The new excavations will host the systems required to power and protect the superconducting magnets, the lower stages of the new cryogenic plants, the power and control systems of the new SRF crab cavities and the control racks of many other equipment currently installed along the beam line, that runs in the already existing LHC Tunnel.
- (3) On the surface, various types of infrastructures are located in an interlinked buildings complex. Such infrastructures of a total 10 new buildings cover the cooling and ventilation needs, provide the necessary connection to the electrical power lines, comprise the upper stages of the cryogenic cooling plant and host the access points to the underground galleries, two main pits of about 9 m diameter and 80 m depth.

2. HL-LHC: the Machine

The interventions necessary to upgrade the LHC will take place in all long straight sections of the LHC except for IR3 but the largest part of them will be concentrated around the high luminosity interaction points: Point 1 and Point 5.

2.1. Point 1 and Point 5

The Matching Sections around the ATLAS (at Point 1) and CMS (at Point 5) experiments will need to be extensively modified from the magnet Q5 Left of the IP (Interaction Point) to the magnet Q5 Right of the IP.

The main elements to be modified or installed are briefly listed below, starting from the LHC Arc Section and moving towards the Interaction Point (IP):

- The LHC Q5 magnet will be reinstalled in the HL configuration, but it will need to be moved to the new position required by the HL-LHC optics.
- The LHC Q4 magnet will be de-installed, modified and finally reinstalled as the HL Q4. Presently the LHC Q4 shares the cryogenic distribution with

the D2 magnet to which it is attached (semi-standalone magnet system) and the way, in which such distribution is performed, depends on the local Tunnel slope. For HL-LHC the Q4 will need to become a fully standalone unit and therefore it will be necessary to modify its cryostat and cryogenic circuitry. Both Q5 and Q4 will be electrically fed from the existing Superconducting Link that will be suitably modified. All other LHC equipment from D2 to the TAS will be de-installed and they will not be re-used in the new HL LHC configuration.

- The crab cavities cryomodules will be installed between the Q4 and the D2 magnets.
- The new HL D2 magnet will be a standalone magnet and it will be powered via a dedicated Superconducting Link. The Superconducting Link will be divided into two sections. A short one, with low temperature superconductor operated at 1.9 K, will connect the D2 to the dedicated distribution box (DFM) that will be located on the top of the D2 itself. A long section with cable in MgB_2 , operated at higher cryogenic temperature, will complete the circuit joining the DFM to the current leads that are connected to the power converters that will be installed in the new HL-LHC underground cavern, the UR. Cooled by helium gas evaporated inside the DFM, this cable will be hosted inside a semi-flexible cryostat (~130m long).
- The TAXN is the neutral absorber that will be installed around the Y chamber. This vacuum chamber element is the location where the two separate beam pipes converge into one vacuum pipe toward the IP. It is therefore also the first and more efficient location to intercept the neutral debris coming from the IP, debris that have been travelling together with the charged beam particles until this point. The large part of the mass of the TAXN, made of iron blocks with shielding function, will be recovered from the existing LHC TAN.
- The D1 is the first magnetic element belonging to the common cryostat that connects, in one unique insulation vacuum enclosure, the following elements: D1, CP, Q3, Q2B, Q2A, and Q1. The Corrector Package (CP) includes in one unit the majority of corrector magnets acting in the triplet area including also one large orbit corrector units. Two smaller ones are part of the cold mass assemblies of the Q2B and Q2A respectively. The inner triplet quadrupoles are located in the Q3, Q2B, Q2A, Q1 assemblies.

- The Q1 IP extremity is then interconnected with the TAXS, that is the first shielding element that intercepts a large fraction of the debris projected from the interaction point.
- The beam chamber belonging to the HL-LHC machine is separated from the experimental one at the level of the VAX unit. This system, composed by several modules remotely exchangeable, is sitting in the experimental cavern and connected to the TAXS. For more details, please see Chapter 13.
- Two important elements are installed out of the beam vacuum, but cryogenically linked to the D1 and electrically part of the insertion magnets chain:
 - The Cold Diode Box houses the protection diodes that are part of the magnet protection system. Such element is located on the non- IP side of the D1 and cryogenically linked to this magnet. It hosts a complex network of bus-bars allowing the connection to the
 - DFX that is the distribution feeding box where the low temperature superconductors bus-bars, running inside the magnet system in a 1.9 K He bath, are interconnected with the terminals of the MgB_2 link that is providing, similarly as for the DFM, the electrical continuity, via the current leads, between the magnet chain and the power converters installed in the new HL UR gallery.

In addition to the elements listed above, the following sets of collimators and masks protecting the active elements from the radiation showers, are part of the HL-LHC layout.

- Between Q6 and Q5 magnets:
 - mask for debris in front of the Q6
 - two tertiary collimators, one on the incoming and one on the outgoing beam.
- Between Q5 and Q4 magnets:
 - mask for debris in front of the Q5.
- Between Q4 and D2 magnets:
 - mask for debris in front of the Q4.
- Between D2 and TAXN:
 - special reinforced collimator with thicker jaws in front of the D2
 - two tertiary collimators (one for each plane) on the incoming beam.

The cryogenic fluid distribution in the LSS1 and LSS5 is guaranteed as following:

- Till Q4 (included), by a modified LHC QRL distribution line.
- From crab cavity until Q1 from the newly installed QXL distribution line. The QXL will be connected to the new cryogenic plant that will have the 1.9 K cold box installed in the US gallery.
- The QRL and QXL lines will be connected by a valve/return module installed in the area between the Q4 and the crab cavities. Its function will be to keep the two lines separated and segregated or to connect them when/if required by the cryogenic operation.

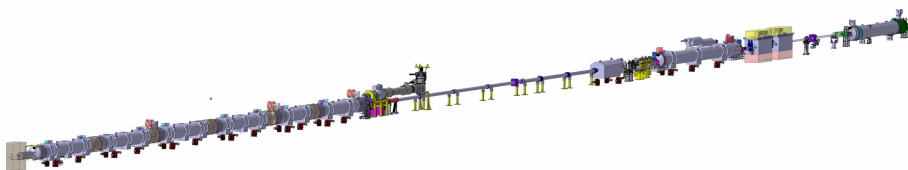


Fig. 1. Integration 3D model of the HL-LHC machine. From left to right: Q1, Q2, Q3, D1, Corrector Package, DFX, DFM, LBBR compensators, TAXN, D2, 2 Crab Cavities cryo-modules, Q4.

2.2. Point 2

Secondary ion beam, generated in the interaction point, could lead to relevant heat deposition in the Main Dipoles of the beginning of the arc. In order to limit such effect, TCLD collimators will be installed in the dispersion suppressor around IP2 (the Interaction Point hosting ALICE experiment). At those locations, the LHC lattice features two interconnection cryostats that provide continuity to the cryogenic and electrical circuits. Those units will be replaced with a modified version of the by-pass cryostat development for the collimator installation in Point 7 Dispersion Suppressor (see Chapter 8 – Collimation) in order to create a suitable installation slot for the TCLD collimators.

In Point 2 it will be also necessary to upgrade the primary injection absorbers (TDIS). The new TDIS will be at the same position as the present one as it needs to be at 90° betatron phase advance relative to the MKIs. In

reality two TDISs are required. They will be installed in the Long Straight Sections (LSS) in IP2 left side (82 m from the IP) and the other in IP8 right side (78 m from the IP). The intervention at Point 2 will be completed by the movement of 2.2 meter toward the IP of the TCLIA (auxiliary collimator). Such change is performed to increase the acceptance of the Zero-Degree Calorimeter of ALICE

2.3. Point 4

2.3.1. Cryogenic system upgrade

Interaction Point 4 will receive an upgrade of the cryogenic system to address the additional cryogenic load induced by the new accelerator operation mode. The upgrade foresees the installation of a mobile cold box and the upgrade of the existing one. The mobile cold box will be used to temporarily cope with the extra needs due to test and conditioning of the LHC main RF acceleration system while the upgrade of the existing cold box will improve the heat removal capacity in the LHC Sector 3-4 that is presently the LHC machine limitation from a cryogenic point of view.

2.3.2. New beam line elements

The Matching Sections around Point 4 will be upgraded with the installation of new beam instrumentation devices:

- **Synchrotron light diagnostic:** New synchrotron light diagnostic, looking at photon emission from the D4 bending magnet. It will be installed on the beam heading to IP4 and it will also include a new extraction mirror located ~20 meters from D4 toward D3 and an optical path to bring the synchrotron light to a detector located in a hutch in the UA gallery. The optical line will be installed through a duct to be drilled in the shielding wall. This installation is foreseen for both beams, one on each side of IP4.
- **Synchrotron light monitors:** The present synchrotron light monitors, looking at photon emission from the undulator magnet, on the beams heading away from IP4, will be upgraded.
- **High Bandwidth BPM:** To support the Crab Cavities operation, two new BPM on each beam and on each side.

- **Hollow Electron Lens:** They are not yet part of the present (approved) Project baseline, but they could efficiently complete the collimation system by providing an active control of the beam halo population and of the beam loss rate. The Hollow Electron Lenses will be equipped with BGC (Beam Gas Curtain) to visualize the position of the beams inside the equipment.

2.4. Point 6

The horizontal beam dump dilution kicker system is planned to be upgraded with the installation of two additional kicker modules. The Beam Dump block will be upgraded already in LS2 with new windows. The entire Beam Dump block is planned to be replaced during LS3 in preparation for the HL-LHC exploitation.

2.5. Point 7

In order to protect the superconducting magnets by excessive heat deposition from off-momentum proton leakage from the main collimator system itself, some special collimators (TCLD) must be installed in the Dispersion Suppression region, i.e. in the continuous cryostat. The installation of these collimators will take place during LS2 shutdown.

In order to cope with the proton losses in the dispersion suppressor area it has been decided to install two TCLD collimators one on each side of the IP. To complete such installation, it will be necessary to:

- Remove two LHC standard Main Bending magnets in the cells 9 Left and 9 Right.
- Substitute each removed dipole with a more compact magnet unit composed of two 11 T dipoles separated by a cryogenic bypass.
- Install the TCLD collimator on the top of the cryogenic bypass (see Chapter 8).

Furthermore, the collimation system will undergo major upgrade and this in order to reduce the machine impedance. As this part of the intervention is quite distributed, we refer to the relevant chapter (see Chapter 8).

2.6. *Point 8*

As mentioned in the Point 2 activity description a new primary injection absorbers (TDIS) will be installed also in Point 8 in the LSS.

In addition, as LHCb will see the delivered luminosity increased after the Long Shutdown 2, two absorbers of neutral debris are necessary to protect the D2 magnets. The two masks denominated TANB will be installed at ± 119 meters symmetrically respect to the IP8. In order to increase their efficiency, it is necessary to displace the horizontal and vertical tertiary collimator installed in the zone in order to create the space as near as possible to the magnet to be protected.

3. HL-LHC Underground Infrastructures

3.1. *The need*

During the conceptual design phase of the HL-LHC Project, the need for new underground volumes to be dedicated to the installation and operation of many equipment appeared as a necessity, but also as an opportunity. The new cryogenic cooling plant, that would have allowed cooling down separately the Matching Sections around IP1 and IP5, required installation of the 1.9 K stages in dedicated underground volumes that are not available. Similarly for the power/control electronics dedicated to: the alignment system, the magnet protection system, the machine protection system and the beam instrumentation. On the other hand, the initial concept of having the power converters installed on the surface and linked to the magnet chain via superconducting link exceeding 350 meters of length, was undoubtedly appealing, but raises several practical and technological challenges to the design of the cold powering system itself. Among others, the need to cope with a change in height of about 100 meters between the LHC Tunnel level and the surface level and a very complex vertical installation in shafts already overcrowded by the LHC services. The RF crab cavities powering and control systems were also meant to be installed on the surface and linked to the deflecting cavities via RF lines of over 100 m of length, creating issues of synchronization between the equipment installed left and right of the IP and challenges for the practical installation and operation.

For the HL-LHC Project was nevertheless mandatory to provide the maximum accessibility to the powering and controlling units of the new installed equipment and therefore it was important to install them in area free from radiation or other risks like oxygen deficiency (consequence of a possible leak/breakage in the He containment of the magnet cryostats chain).

Taking into considerations the above listed challenges a new underground cavern system was designed with the following objectives:

- (1) Provide volume for the 1.9 K cryogenic cold box installation and path to connect it to the machine, left and right of the IP.
- (2) Provide volume for the installation of the RF powering and control systems minimizing the distance between them and the deflecting cavities and the distance between the two Low Level RF setups, that control the left and right side of the IP. Provide an optimized connection path from the RF systems to the cavities.
- (3) Provide volume for the installation of all the power converters connected to the superconducting magnets and of the related magnet protection systems. Provide an optimized connection path to be used to host the superconducting links.
- (4) Ensure that all the above-mentioned systems are accessible while the machine is in operation. That means that while the new galleries shall be connected to the LHC machine Tunnel they shall guarantee, by design, that personnel operating inside them shall be preserved from radiation coming from the accelerator in standard operational and exceptional events, as well preserved from possible cryogenic leaks that could take place in the machine Tunnel itself.

3.2. *The solution*

As results of the requirements listed above, an underground gallery system at IP1 and IP5 with the following characteristics was designed and finally approved:

- (1) A 345 m long tunnel running parallel to the machine, symmetrically positioned with respect to the IP and offset by about 50 m horizontally and 10 m vertically. The main section has a diameter of 6 m while one extremity ends in a large cavern of 16 meters diameter equipped with a

vertical shaft of 9 meters diameter that connects the complex to the surface.

- (2) Four shorter tunnels, perpendicular to the tunnel described above that stick out and stop on the top of the LHC ring from which they will be separated by 7 meters of rock. In these areas, vertical cores allow the routing of the various services to the equipment installed in the LHC machine. The extremely limited openings, joining the LHC Tunnel and the new cavern, allow reducing at minimum the incoming stray radiation maximizing the area where access can be granted without supervision. Special sealing around the cores and pressurized access SAS will avoid the risk of oxygen deficiency and of importing irradiated air from the LHC Tunnel environment.

In more details the gallery complex is composed by the following units:

- UR: 345 m long, parallel to the LHC it will host the power converters system, the magnet protection equipment and the feedboxes that are the starting elements of the superconducting link systems.
- US: 50 m long large cavern placed at one extremity of the UR it will host the 1.9 K cold box, the electrical safe room, many other technical services as three main electrical transformers. US cavern will be the junction to the PM, the vertical shaft to the surface. The US extremity is segregated by a fire-resistant wall, and it is identified with the name of UW.
- UW: has the same section of the US and it is dedicated to the cooling and ventilation equipment.
- PM: the 9.2 m diameter shaft that hosts the lift, the stairs, the loading bay and the routing of the main services from the surface to the underground.
- UL (2 per IP), perpendicular to the UR, they provide the installation path from the LHC Tunnel for the cryogenic line (QXL) and the superconducting links dedicated to the final focus and D2 magnets. They end in three cores joining the LHC Tunnel vault, one dedicated to the cryogenic line, one for the superconducting links, one for power and signal cables.
- UA (2 per IP): placed at the UR extremities they host all the RF related ancillaries with the exception of the Faraday cages for the low-level RF control. They end with a small section parallel to the LHC Tunnel that runs on the top of it. Three aligned cores dive from its floor to the LHC Tunnel vault. Two will host the RF powering for the two crab cavity cryomodules, one is reserved for cables.

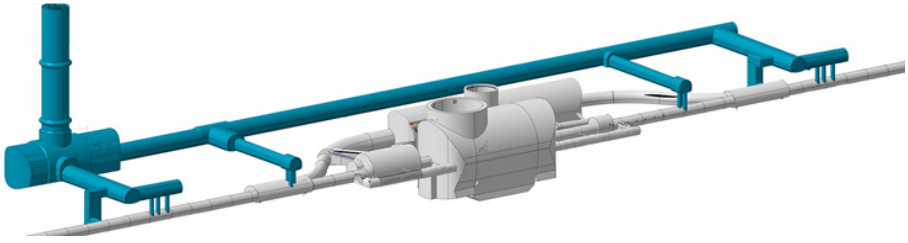


Fig. 2. Axonometric view of the HL-LHC underground Civil Engineering infrastructures as it would appear in IP5.

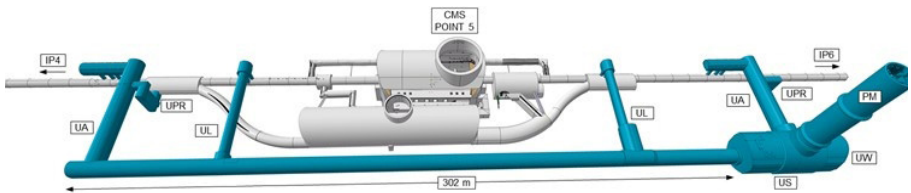


Fig. 3. View of the HL-LHC underground Civil Engineering infrastructures as it would appear in IP5.

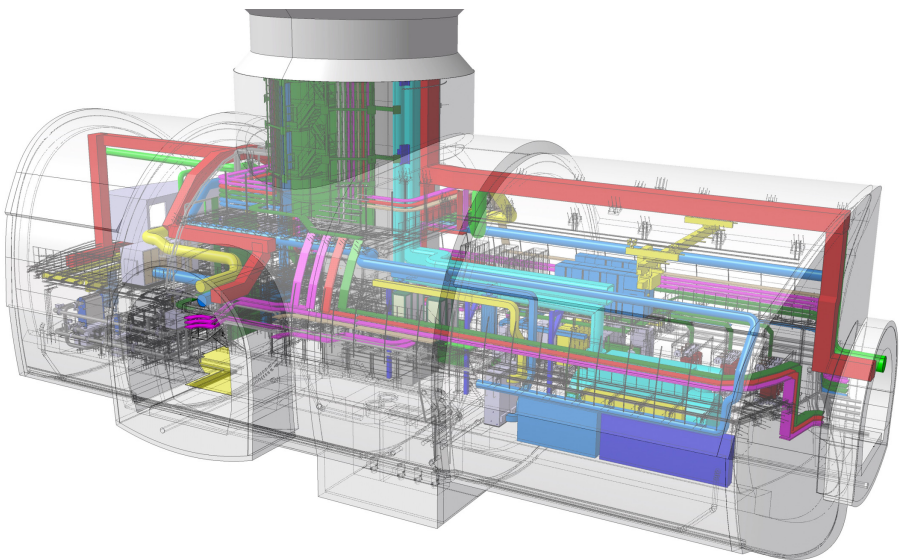


Fig. 4. The cavern (US) hosting the cold box with other technical services.

4. HL-LHC Surface Installation

4.1. *The surface building complex*

The above described underground complex will host the equipment that requires to be close to the accelerator equipment or that has an efficiency or technological or cost advantage in being near to it. There are many other equipment and systems that do not have such requirement or that need to be installed on surface. A set of buildings has therefore been designed to satisfy this demand. Point 1 and Point 5 feature the same number of new buildings, but they are distributed topologically in different ways to better suit the respective particularities of the two locations.

The buildings and their functions are listed below:

- SD: the SD building is set on the top of the big shaft, called PM, and provides, with its overhead crane and the truck unloading area, the handling capacity required for delivering equipment to the underground caverns and tunnels. In addition, the access points for the personnel area are also located here. The upper stage of the cryogenic cold box is installed inside the SD building. As the PM shaft is the only physical access to the underground for services, the design and integration of the building is quite challenging. All the cryogenic ducts, powering and signal cables, water pipes, air ducts, safety smoke extraction system, have to converge here and have to join the shaft walls in adequate positions and topological sequence in order to be adequately routed to the underground. For the same reason the interfaces of the building with the surface technical gallery system have required a detailed optimization as many cables and pipes converge here from the other infrastructures. For both Point 1 and Point 5 it was possible to identify a surface location of the SD building on the inner side of the circle drawn by the LHC Tunnel. This allowed designing the underground in exactly the same way between Point 1 and Point 5 making much easier the management of design evolution and of the integration effort. This helped also in reaching a higher standardization in the equipment to be produced and installed. Unfortunately, because of the site topology, it was necessary to have the SD buildings functionally rotated by 180° between the two sites and this will have to be taken into account in the handling of long equipment from the surface to the

underground as the direction of unloading from the loading bay will be opposite in the two cases.

- SU and SE: the SU and the SE buildings are set contiguous to the SD in order to minimize the length of the ducts and of the cables. The first SU is dedicated to the cooling and ventilation equipment while the second is dedicated to the electrical distribution and it is internally divided in high voltage and low voltage areas.
- SHM: the large SHM is a noise proof building designed to host the warm compressors of the cryogenic cooling plant. A Helium tank is connected to the building via a technical trench.
- SF: it hosts the cooling towers that are the final element of the cooling and ventilation chain
- All the above listed buildings are interconnected by a complex system of technical galleries. The network not only allows the interconnection inside the HL related domain, but it is also the link to the pre-existing infrastructure of Point 1 and Point 5.

4.2. Point 1

The topological distribution of the buildings is shown in Figure 5. The SD building with the nearby SU and SE is placed on the western edge (right side). Two technical galleries run in parallel from West to Est. The central one join the SD with the SHM and it is mainly dedicated to electrical services and cryogenic routing, the northern one, of smaller dimension join the SU building to the SF and it is mainly dedicated to the piping of the cooling circuits. The gallery moving toward northwest on the corner of the SE17 building allows the connection to the previous existing ATLAS site.

4.3. Point 5

The topological distribution of the building is in Figure 6. The SD building with the nearby SU and SE is placed as in Point 1 on the western edge (right side). One technical gallery runs southeast following the edges of the SH and SF buildings and then move straight North to connect to the main existing technical gallery of the CMS site.

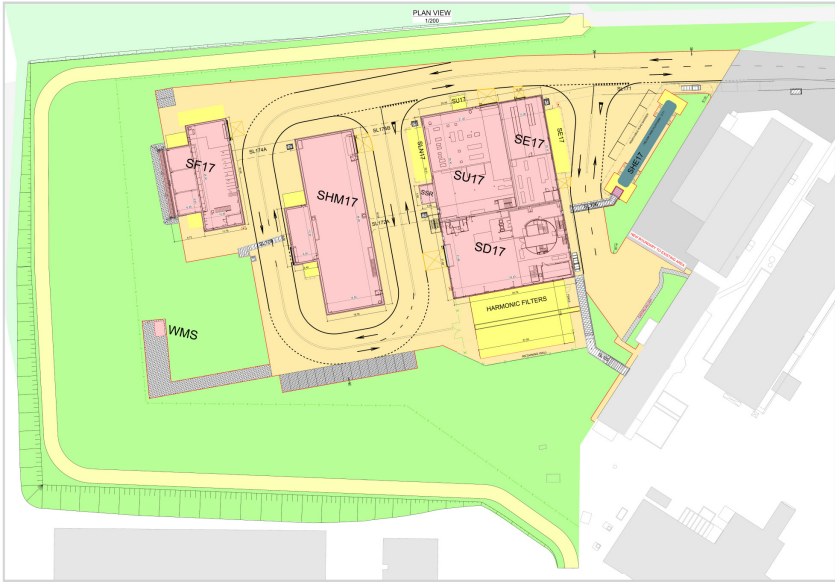


Fig. 5. The LHC Point 1 with the new HL-LHC surface building.



Fig. 6. The LHC Point 5 with the new HL-LHC surface building.

5. Survey and Alignment for HL-LHC

5.1. Geodetic aspects

One of the most urgent tasks to undertake was to provide to Civil Engineering (CE) companies reference frames and associated accurate and precise reference points from the surface geodetic network, so that they could build secondary networks to be used for all their work. From the geodetic surface reference network at CERN, 15 pillars were selected for the primary network of this project, spread over the whole surface of the LHC accelerator. These points have been determined from Global Navigation Satellite System (GNSS) observations, in order to get a precision and accuracy below 2 mm in planimetry and below 5 mm in altimetry. All points were measured simultaneously twice, stationed during 48h each time with individually calibrated geodetic antennas. The data were processed using Bernese GNSS software. The resulting coordinates were calculated in the International Terrestrial Reference System (ITRS), realization 2014 (epoch 2017.74). The coordinates

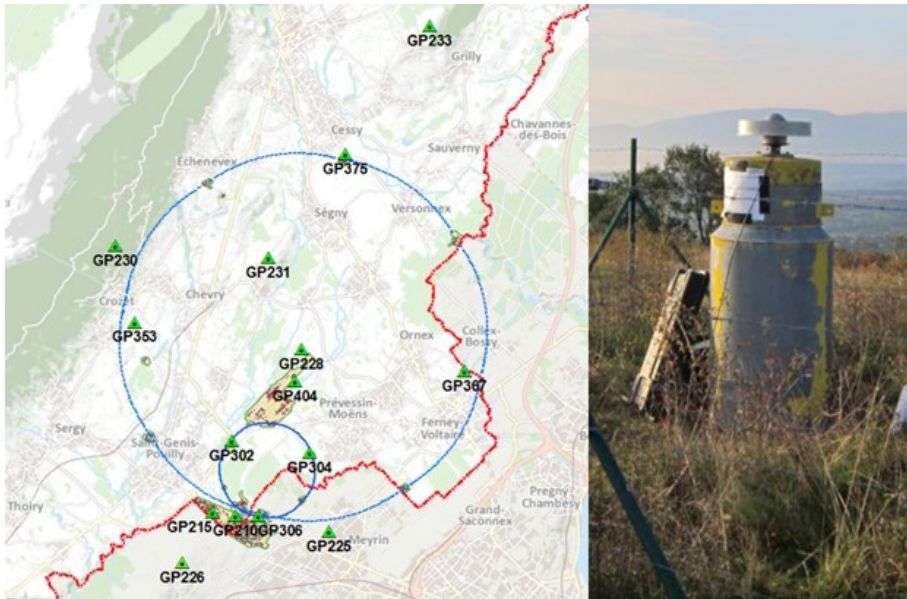


Fig. 7. Surface geodetic reference network (left) and one pillar equipped with a permanent antenna (right).

were also provided in ITRF87 (epoch98.5), the Swiss national surveying system CH1903+_LV95 and the French geodetic network RGF93_ [1].

The standard deviation of the final solution fulfils the initial requirements: the mean residuals for the Helmert transformation in a local frame using permanent stations known in ITRF2014 are 1.15 mm for the north component, 0.81 mm for the east component and 2.05 mm for the vertical component.

The post processing adapted the pillar coordinates from this measurement campaign onto the current CERN network coordinates, with a series of calculations to account for previous network measurements. Residuals of up to 15 mm were kept in final calculations. CERN provided 2D + 1 coordinates to the CE companies in the CERN mathematical orthographic projection system with orthometric heights. In this system, the (X, Y) planimetric coordinates of a point are provided together with an altitude H. The orthographic projection is a simple mathematical orthographical projection of the 3D CERN Coordinate System (CCS) coordinates of a point, onto the CCS X-Y plane, along a vector parallel to the CCS Z-axis. The altitude is the orthometric height w.r.t. a geoid model. The CERN CE team had previously provided a software package capable of transforming these coordinates into both the Cern Coordinate System, and the local reference systems at Point 1 (ATLAS_1102) and Point 5 (CMS_1503) being used for this project. Adapter plates with a standard survey instrument interface and appropriate parameters were also provided to enable the companies to station the pillars with their own geodetic/survey instruments.

The Mekometer 5000, a high precision electronic distance measurement instrument, was calibrated against a precision time source and the Survey team's calibration bench. A long-distance control baseline, consisting of 11 external pillars, over 500 m, on the Prévessin site, was then re-determined and made available for the HL-LHC CE teams to control their distance-meters.

Similarly, the Survey team's gyro-theodolite, Gyromat2000, was put back into service in order to provide the azimuths for the new underground tunnels at the bottom of the shafts. The instrument was controlled against an astronomical azimuth baseline to ensure its stability during a measurement campaign around Long Straight Sections (LSS) 1 and 5, performed during the Year End Technical Stop (YETS) 2017-2018. These measurements included a connection to the beamline elements and were processed with additional measurements from the alignment smoothing measurements. Based on these

calculations, the real beamline was calculated at the LHC Intersection Points (IP) 1 and 5. The geodetic azimuth control baseline has also been controlled with an astronomical azimuth measurement campaign. The HL-LHC CE teams were provided with reference azimuth values for the geodetic azimuth control baseline, together with the real beamline azimuth at LHC IP1 and IP5.

5.2. Requirements and context for the alignment of components

5.2.1. Requirements

The following error budget was defined in order to respect the HL-LHC beam dynamic requirements. The mechanical axes of the quadrupoles from Q1 to Q5 shall be included in a cylinder with a radius of 0.1 mm. The mechanical axes of quadrupoles from one side of the IP shall be included in the cylinder of the mechanical axes of the quadrupoles from the other side having a radius of 0.15 mm.

5.2.2. Context

The level of radiations in LSS1 and LSS5 is of primary importance. The ambient dose equivalent rate (in $\mu\text{Sv/h}$), at the Long Shutdown 4 (LS4) with ultimate luminosity, after one month of radiological cooling time, at working distance (80 cm), is shown in Table 1 below (only the maximum dose at the level of interconnections has been retained) [2] (Chapter 15).

Table 1. Maximum ambient dose equivalent rate in $\mu\text{Sv/h}$, for each component, at working distance, after one month of cooling.

	TAXS	Q1	Q2a	Q2b	Q3	CP	D1	BPM	TAXN	Colls	D2	CC	Q4	TCL	Q5
LSS1	870	1100	1100	550	700	700	550	200	800	350	350	5	50	400	100
LSS5	800	1050	1050	650	650	650	400	200	550	1300	400	5	50	600	100

Such an ambient dose equivalent rate at the level of the triplets and collimators prevent from using standard instrumentation in the area, even during a YETS.

The level of Total Ionizing Dose (TID) is also not negligible: around 1 kGy in the tunnel, except in the TAS-Q3 area with a few tens of kGy at the interconnects.

These levels mean that all interventions, designs, procedure measurements, alignment solutions will have to be designed according to the ALARA (As Low As Reasonably Achievable) principle and that all the permanent instrumentation foreseen will have to undergo irradiation tests to be qualified.

On top of this harsh environment, access will not be possible during Technical Stops (TS) in the inner triplet area.

Ground motions are also a main concern in the establishment of technical specifications dealing with alignment. Fortunately, regular measurements of ground floor points from the underground geodetic network, of machine and detectors components were performed since 2002. They can be summarized in the tables below. Table 2 shows the maximum displacements measured at the level of the beam pipe per year. Table 3 shows the maximum displacements measured at the level of the beam pipe of each component in the machine.

Table 2. Maximum displacements per year in millimeter of the beam height of ATLAS and CMS detectors.

	Radial (mm/year)	Vertical (mm/year)
IP5 (CMS)	± 0.2	Stable
IP1 (ATLAS)	+ 0.1	+ 0.3

Table 3. Maximum displacements per year in millimeter in the machine (ground floor and components beam height).

	Radial (mm/year)	Vertical (mm/year)
LSS5	+ 0.2 (4L5) ± 0.15 (any other area)	+ 0.7 (in 4L4, 4R5) + 0.2 (any other area)
LSS1	$< \pm 0.1$	+ 0.3

The vertical measurements in the cavern and in the tunnel are performed w.r.t. the same deep references: tunnel and cavern values can be added to get the maximum value.

The radial measurements in the cavern and in the machine are performed w.r.t. specific brackets in a tunnel parallel to the machine, considered as stable. Tunnel and cavern values can be added to get the maximum values.

As a summary, the maximum values concerning ground motions around IP are introduced in Table 4 below. The construction of the new galleries might have an impact on such value: we find the most important ground

Table 4. Maximum displacements year, in millimeter, between the detector and the machine (a positive vertical value means that the tunnel has a vertical displacement higher than the detector).

	Radial (mm/year)	Vertical (mm/year)
Around IP5 (CMS)	± 0.3	+ 0.7 (in 4L5, 4R5) + 0.2 (any other area)
Around IP1 (ATLAS)	± 0.2	± 0.3

motions in 4L5 and 4R5 areas, where new galleries were dug at the same time than the experimental area, beginning of 2000.

The uncertainties of measurements have to be considered as well: there is no direct link between the inner tracker and the machine from the survey and alignment point of view. An uncertainty of measurement of 0.7 mm is expected for the determination of the position of the experiment inner tracker w.r.t. the machine.

5.3. Description of the Full Remote Alignment

5.3.1. Introduction

A new strategy for alignment is proposed for HL-LHC, named Full Remote Alignment (FRA). It will allow aligning rigidly and remotely from the CERN Control room, all the components from Q1 to Q5 on both sides of the IP. The following steps will take place:

- A redetermination of the underground geodetic network, before the dismounting of the components at the beginning of LS3, to preserve the good beam geometry from Run 3.
- A fiducialisation on surface of whole components which will need later to be aligned in the tunnel, e.g. the measurement of the mechanical axis (or reference axis if possible) w.r.t. external targets.
- The initial alignment of the new components in the tunnel w.r.t. the underground geodetic network.
- Their smoothing along a straight line from Q7 Left – inner tracker detector – Q7 Right to make the first pilot beam pass through.
- After a few weeks of operation, as soon as enough luminosity will have been accumulated to check the real position of the IP, a rigid remote

re-alignment of all components from Q5 Left to Q5 Right, will be carried out according to the offsets seen in the inner tracker.

- The compensation of the ground motions all along the following years, when needed, will be performed.
- All relative misalignments between adjacent components will be recorded in order to monitor their impact on the vacuum bellows.
- The position of all other bellows, pipes, and RF waveguides will be controlled w.r.t. the tunnel main components during LSs.

Such a FRA will allow:

- An important reduction of the dose taken by surveyors, as no access will be needed for repositioning between YETS.
- A reduction in the mechanical misalignment that allows to reduce the required corrector strength and to push the accelerator performance.

A detailed study has been performed to identify the components located between Q1 and Q5 for which remote alignment using sensors and actuators is mandatory. The access conditions and radiation level have been considered and other components that are compliant with such a remote alignment, e.g. vacuum pipes with sufficient aperture not needing a repositioning along the 10 years of lifetime of HL-LHC have been identified as well.

5.3.2. *Methods and means to detect the position of the components.*

Alignment systems combining measurements of transverse offsets w.r.t. a stretched wire (Wire Positioning System), vertical measurements w.r.t. a water surface (Hydrostatic Levelling System) and inclinometer measurements are proposed. These systems, already used for the monitoring of the position of the LHC low beta inner triplets are robust, precise and accurate (sub-micrometric resolution). They will provide redundant measurements allowing a better understanding and analysis of the components position.

The Hydrostatic Levelling System is based on the principle of the communicating vessels. Vessels located on the fiducials to be determined, are connected to a half-filled hydraulic network located on the non-transport area, by a water pipe and an air pipe. A capacitive based sensor will be located on each vessel to measure with no contact the vertical distance to the water surface. The difference of height between vessels can be calculated within a sub-micrometric resolution. The sensors are only made of passive components;

irradiations tests have shown that they could withstand Total Ionizing Dose of more than 5 MGy. Their remote electronics, combined with their associated acquisition system will be located in a less radioactive area (Total Ionizing Dose below 100 Gy). Three Hydrostatic Levelling Sensors per cryostat will provide the determination of three Degrees of Freedom: vertical translation, roll and pitch rotations. If the component to be monitored has a limited available space, the Hydrostatic Levelling Sensors will be replaced by an inclinometer. In the case of the inner triplet, where the roll monitoring is of primary importance, an inclinometer will be added to the three Hydrostatic Levelling Sensors to provide redundancy in the roll determination. As the LHC tunnel is settled in an inclined plane and the water surface of the Hydrostatic Levelling System follows the equipotential of gravity, additional superposed Hydrostatic Levelling sensors will be installed to catch-up the difference of height between the components aligned w.r.t. the beam line and the equipotential of gravity. This corresponds roughly to a double Hydrostatic Levelling Sensor every 30 m along the tunnel [3].

In the case of the Wire Positioning System, the water surface is replaced by a wire stretched over 200 m, from Q1 to Q5, and protected from air current by an air-tightened protection. A capacitive-based sensor, installed on each fiducial, will perform horizontal and vertical offsets measurements w.r.t. the stretched wire within a sub-micrometric resolution. Two Wire Positioning Sensors per cryostat allow the determination of four Degrees Of Freedom: radial and vertical translations yaw and pitch rotations. The catenary shape of

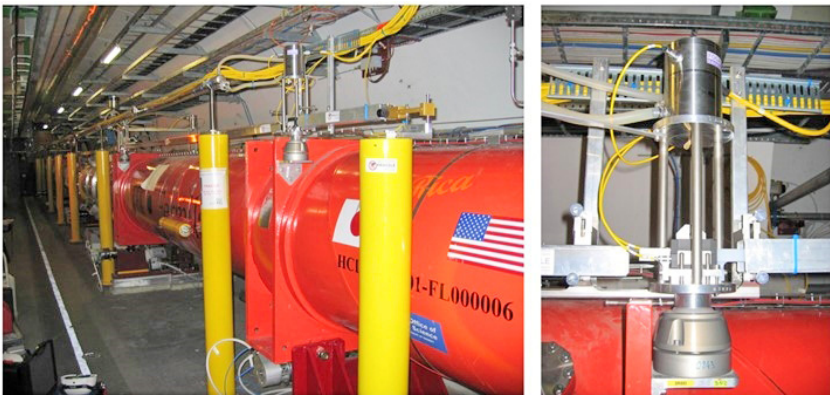


Fig. 8. Alignment systems in the LHC.

the wire in the vertical plane will be determined using a combination of Wire Positioning Sensors and Hydrostatic Levelling Sensors, in order to know at least in three locations along the wire the difference of height of the wire and to reconstruct its catenary shape within a few micrometers. Dedicated tests undertaken over 140 m long overlapping wires in a stable tunnel have shown that such a determination could be performed at an accuracy better than $10\ \mu\text{m}$ [4].

The longitudinal position of the component will be monitored by a Frequency Scanning Interferometry - based absolute distance measurement, between an optical collimator plugged on a support screwed on the ground floor, and a target (glass sphere with an external coating) located below the cryostat, providing a micrometric uncertainty of measurement.

During the initial installation of sensors, the different distances needed to compute the position of the sensor in the reference frame of the cryostat will be determined using laser tracker measurements and stored in the Equipment Management Folder database, associated with each fiducial and support. All Wire Positioning Sensors and Hydrostatic Levelling Sensors are equipped with a kinematic mount allowing their installation on a support fixed on the fiducial within a micrometric repeatability. The sensors are the object of a calibration process providing the position of the wire within the range of $\pm 5\ \text{mm}$, in the reference frame of the sensor, within an accuracy below $5\ \mu\text{m}$. The position of the ferrule of the Frequency Scanning Interferometry measuring head will be determined in the reference frame of the support materialized by 12.7 mm diameter targets, within a few micrometers [5].

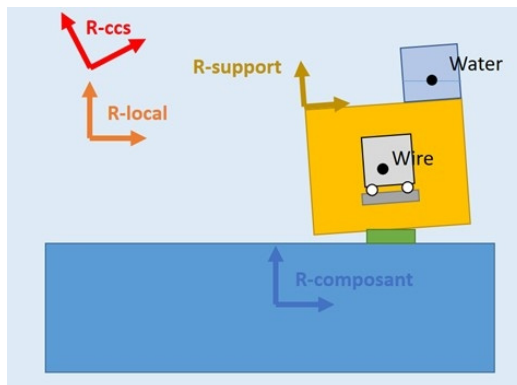


Fig. 9. Configuration of sensors and reference frames on a component.

The cold mass of the inner triplet (consisting of four quadrupoles Q1, Q2a, Q2b and Q3) will be monitored using FSI channels (see further down). During the initial installation, the reference frame of the feedthroughs, materialized by 12.7 mm diameter targets, will be determined w.r.t. the underground geodetic network and w.r.t. the reference frames of the sensors support, within a 5 μm accuracy, by laser tracker measurements (see Figure 9).

Alignment sensors will equip all the components remotely aligned. All the other components will be equipped with permanent targets allowing their automatized determination using laser tracker measurements during YETS or LS, in order to limit the dose taken by surveyors.

5.3.3. Methods and means to re-adjust the components.

The main components, e.g. cryo-assembly magnets, TAXN and crab cavities, will be supported by three motorized jacks, allowing their remote adjustment according to five Degrees Of Freedom. A longitudinal anchor will allow the initial manual adjustment of the sixth Degree Of Freedom: the longitudinal translation, using a tie-rod designed to hold vacuum and quench loads.

The smaller components, like collimators, vacuum devices and masks, needing a remote adjustment system, will be installed on universal adjustment platforms equipped with permanent radiation-hard motors [7].

The other intermediary components, which do not require remote alignment, will be supported by universal adjustment platforms on which motors can be plugged temporarily to achieve fast and efficient displacements, in combination with laser tracker measurements.

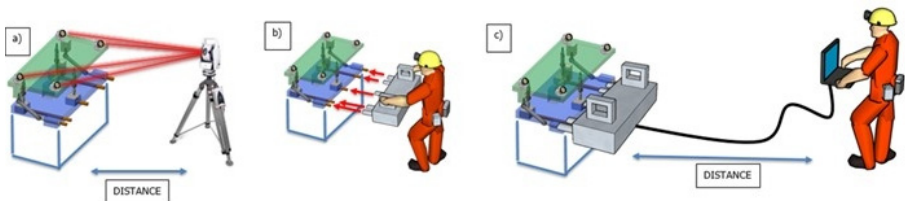


Fig. 10. Universal platform configurations: a: Platform measurement using a laser tracker; b: Installation of plug-in motors in less than one minute; c: Temporary motorized displacements.

These platforms are a simplified version of universal platforms developed for the CLIC project [6], where a solution for a fast and accurate (a few micrometers resolution) adjustment of quadrupoles was proposed and validated. These platforms have been designed in such a way that they allow an intuitive adjustment, based on simple kinematics (one adjustment knob per Degree Of Freedom), all adjustment knobs being located on the same side of the support for an easier access. The HL-LHC platform has been designed in such a way that the same type of mechanical joints providing the Degree Of Freedom can be integrated on different sizes of platforms, as each type of component has its own requirements of adjustment and associated constraints. They can be equipped with either permanent motors, either with interfaces allowing temporarily plug-in motors or with manual adjustment knobs.

5.3.4. *Crab cavities and cold mass position monitoring inside their cryostat*

Considering the tight alignment tolerances, and the fact that the cold masses of some LHC dipoles were found misaligned by up to 0.5 mm after being transported in the tunnel, it was decided that an internal permanent system will be installed to perform the position monitoring of the Inner Triplet cold masses inside their cryostat and of the two crab cavities inside their cryostat (mechanical axis inserted in a 0.5 mm diameter cylinder).

In both cases, absolute distance measurements will be performed using a CERN developed solution using Fourier analysis based Frequency Scanning Interferometry [8]. Four absolute distance measurements per sections will be carried out between an optical collimator located inside a feedthrough at the level of the cryostat (ambient temperature and atmospheric pressure) and a target (in a technical vacuum, at 4K), located either on the cold mass or on the

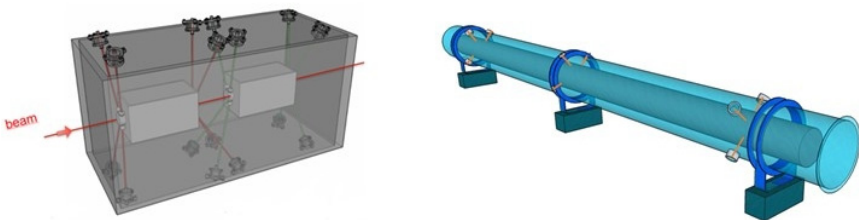


Fig. 11. Layout of FSI lines of sight for crab cavities and Inner Triplet cold masses.

Crab cavities flanges. Three sections of measurements are proposed inside each Inner Triplet quadrupole: two at the extremities and one in the middle, at the level of the cold feet. Four sections of measurements are integrated for the crab cavities: one per flange of dressed cavities [9].

The targets are 12.7 mm diameter coated glass spheres for a better reflection of the beam. For the cold masses, specific insulated supports to hold the targets have been designed, equipped with a collar, in order to place the targets at a temperature above 200 K by gathering the heat coming from the cryostat to avoid condensation on the target, and preventing this heat to be transferred to the cold mass via the support.

Irradiation tests combined with a qualification in the real environment of the SPS and cold tests achieved on a LHC spare dipole demonstrated that the Frequency Scanning Interferometry system can provide a relative monitoring of the position of the targets within a few micrometers. It can also determine the position of the components (center of the flanges for the crab cavities, center of the cold mass) within an accuracy ranging from 50 μm for the crab cavities to 120 μm for the quadrupoles.

References

1. C. Jarlskog, *CP Violation*. (World Scientific, Singapore, 1988).
2. B. W. Bestbury, *R-matrices and the magic square*, *J. Phys. A*. **36**(7), 1947–1959, (2003). ISSN 0305-4470.
3. P. X. Deligne and B. H. Gross, On the exceptional series, and its descendants, *C. R. Math. Acad. Sci. Paris*. **335**(11), 877–881, (2002).
4. D. W. Baker and N. L. Carter, *Seismic Velocity Anisotropy Calculated for Ultramafic Minerals and Aggregates*, In eds. H. C. Heard, I. V. Borg, N. L. Carter, and C. B. Raleigh, *Flow and Fracture of Rocks*, vol. 16, *Geophys. Mono.*, pp. 157–166. Am. Geophys. Union, (1972).
5. G. H. Weiss, Ed. *Contemporary Problems in Statistical Physics*, (1994). SIAM, Philadelphia.
6. R. K. Gupta and S. D. Senturia. Pull-in time dynamics as a measure of absolute pressure. In *Proc. IEEE Int. Workshop on Microelectromechanical Systems (MEMS'97)*, pp. 290–294, Nagoya, Japan (Jan., 1997).
7. L. F. Richardson, *Arms and Insecurity*. (Boxwood, Pittsburg, 1960).
8. R. V. Churchill and J. W. Brown, *Complex Variables and Applications*. (McGraw-Hill, 1990), 5th edition.
9. F. Benhamou and A. Colmerauer, Eds., *Constraint Logic Programming, Selected Research*. (MIT Press, 1993).

This page intentionally left blank

Chapter 23

The HL-LHC Technical Infrastructure

L. Tavian

CERN, ATS-DO Unit, Genève 23, CH-1211, Switzerland

The upgrade in luminosity of the LHC requires large and new technical infrastructures like civil engineering, electrical distribution, cooling, ventilation, access system, alarm system, transport, and operational safety system. This chapter describes the new technical infrastructure including layout, performance requirements and architecture as well as the main technical challenges.

1. Introduction

The HL-LHC technical infrastructure includes the civil engineering, the electrical distribution, the cooling & ventilation, the access & alarm system, the technical monitoring, the transport infrastructure, and the operational safety.

2. Civil Engineering

In terms of civil engineering, the needs of the HL-LHC consist principally of access shafts from the surface to the underground areas together with various underground caverns and galleries. Buildings are required on the surface for housing technical infrastructures such as compressors, cooling equipment, ventilation equipment, electrical equipment, helium refrigerators and helium and nitrogen storages. The HL-LHC construction work are located in the two-existing large-experimental sites, Point 1 (P1) for the ATLAS experiment, located in Switzerland, and Point 5 (P5) for the CMS experiment, located in

This is an open access article published by World Scientific Publishing Company. It is distributed under the terms of the Creative Commons Attribution 4.0 (CC BY) License.

France, and include underground and surface works at both points. At both locations, some of the new structures are located close to existing LHC infrastructure, hence, special protective measures must be taken to minimize impact on the operation of the LHC and also on the LHC infrastructure itself. For this reason, the main excavation work, which causes vibrations detrimental to the LHC luminosity, have been performed over 2 years (2019 and 2020) during the ca. 2.5-year long LS2 shutdown. The total duration of the civil engineering work extends for about 5 years starting in 2018.

2.1. *Underground civil engineering*

The underground civil-engineering at each point consists of a vertical shaft (PM, 10-m diameter, 60-m height), a service cavern (US & UW, 16-m diameter, 50-m length), a power converter gallery (UR, 6-m diameter, 300-m length), service galleries (UA & UL, 4 to 6-m diameter, 50-m length), safety galleries (UPR) and vertical linkage cores (1-m diameter, 7-m length) to the existing LHC tunnel. The civil engineering work includes the excavation, the primary concrete, the final lining and the main steel structures. Figure 1 shows a typical underground layout. Safety galleries allow the safe evacuation of personnel in case of underground fire or helium spill. These new underground structures have a useful volume of 25'000 m³ per Point.

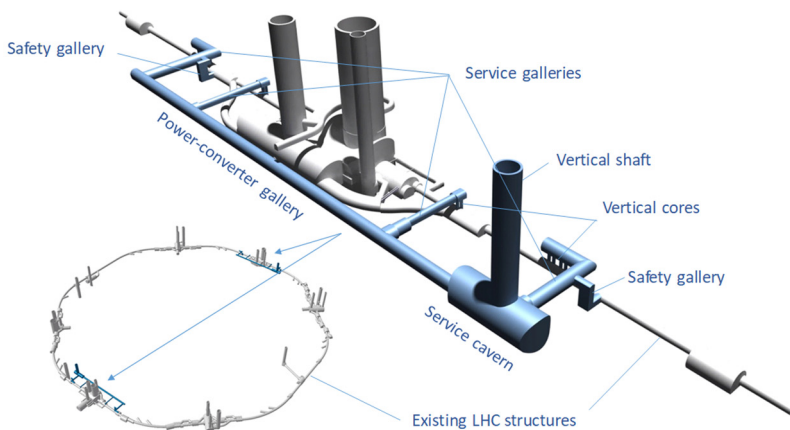


Fig. 1. Typical HL-LHC underground civil engineering structures at Point 1 and Point 5.

2.2. Surface buildings

A cluster of three buildings and two standalone buildings are required at P1 and P5. Figures 2 and 3 show the corresponding layouts. These five new buildings are a combination of steel and concrete structures, interconnected with technical galleries. The buildings represent an additional floor area of 6200 m². The head-shaft building (SD) covers the underground access shaft and integrates the main cold box of the new helium refrigerator. The ventilation building (SU) mainly contains the equipment needed for the heating, ventilation, air conditioning and smoke extraction of the underground infrastructure. This reinforced-concrete and noise-insulated building is split into two sections that house compressors and air handling units, respectively. The electrical building (SE) contains three rooms dedicated to switchgear, protection relays, switchboards, and uninterruptible power supplies (UPS). The cooling-tower building (SF) is constructed in reinforced concrete to guarantee its noise insulation. This building is split into two areas, one for the three cooling towers which extracts the heat from the primary water circuits, and one for the pump room. Finally, the cryogenic-compressor building (SHM),

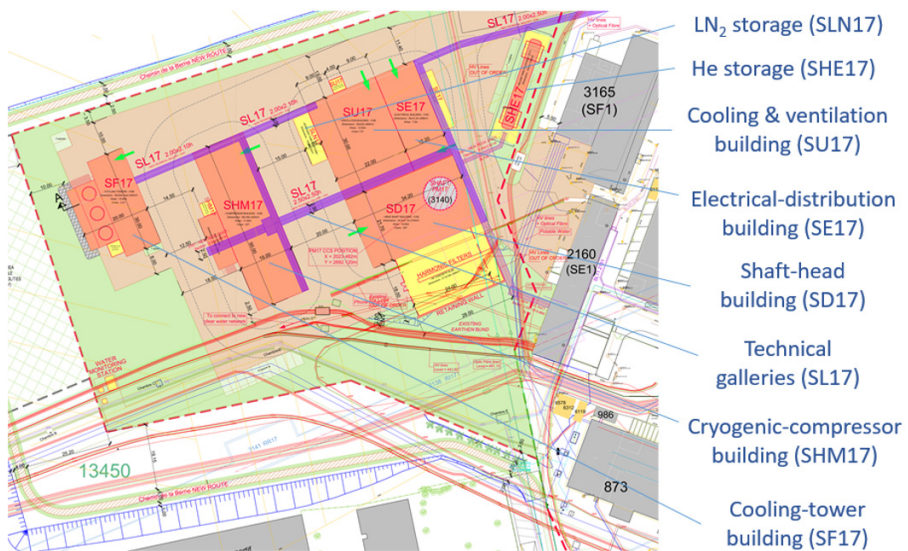


Fig. 2. HL-LHC building layout at Point 1.

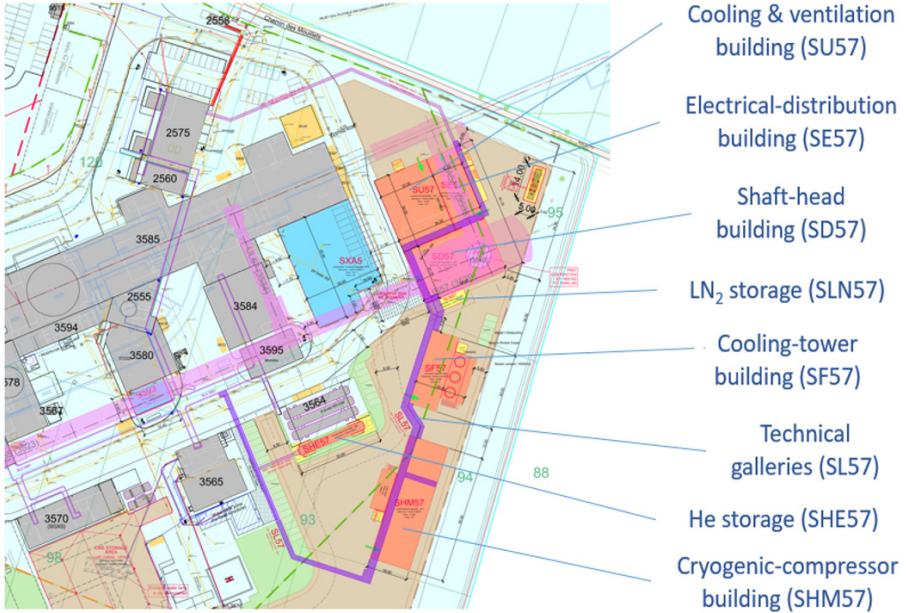


Fig. 3. HL-LHC building layout at Point 5.

also in reinforced concrete and noise-insulated, houses the cycle compressors of the new helium refrigerators.

Additional platforms for helium and nitrogen storage tanks, for harmonic filters and electrical transformers complete the layout. Environmental considerations require external drainage and oil separation systems protecting any sensitive water aquifers at the sites. The additional noise impact of the new buildings on the surrounding population is also minimized.

3. Electrical Distribution

The existing CERN electrical network is shown in Figure 4. The present strategy is to transmit electrical power to each important technical site using 66-kV independent transmission lines. The Point 5 is presently not following this strategy as this site is supplied directly from the Point 6 via an 18-kV line having a rating of 15 MVA. This rating is not adequate with respect to the new needs corresponding to 12 MVA for HL-LHC and 5 MVA for the CMS

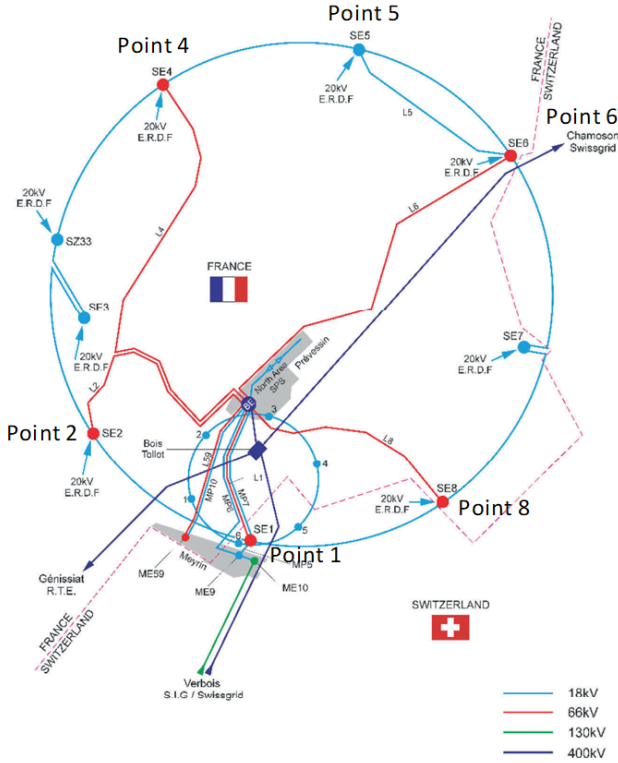


Fig. 4. Existing CERN electrical network.

experiment, which must be added to the 5 MVA presently existing. Consequently, the electrical network must be consolidated with a new 66-kV transmission line directly feeding the Point 5. On site, a new 38-MVA electrical transformer and new harmonic filters allow the distribution of 18-kV high-quality power.

At Point 1, the existing power consumption is 41 MVA. Additional loads of 11 MVA for the HL-LHC machine and 2 MVA for the ATLAS experiment bring the total electrical consumption to 54 MVA. This new power can be delivered by the existing electrical sub-station and only harmonic filters must be added for HL-LHC.

On site, electrical transformers producing 3.3-kV and 400-V networks are dry-type and therefore do not create problems in relation to oil pollution. In terms of electrical distribution, four types of electrical networks are available

for users: general services, machine network, secured network (backed-up by diesel generators) and uninterruptible power supply network (UPS). High current DC cables are available for the users as part of the distribution chain connecting the power converters and the accelerator magnets. A robust, multi-users, optical fiber infrastructure is also available.

3.1.1. High and low voltage networks

Concerning the high-voltage (18 and 3.3 kV) network distributed from the SE buildings, the main users are the cryogenic system, the radiofrequency (RF) system, the water-cooling system, the general services, the power converters and the ventilation system. Figure 5 shows the distribution of the total loads of the different systems. About 70% of the loads are distributed and consumed at the ground level.

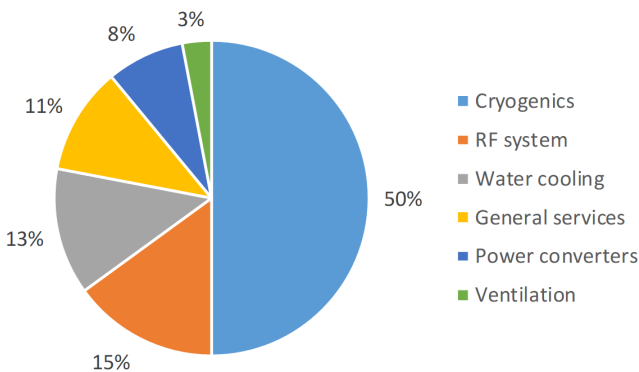


Fig. 5. Electrical load distribution.

The low-voltage (400 V) network is distributed in most of the surface and underground buildings for general services, machine network, secured network (backed-up by diesel generators) and uninterruptible power supply (UPS) network.

In the US caverns, a fireproof safe room is hosting all safety-related equipment. Secured network, supplied by diesel generators, is distributed to guarantee the supply of the critical ventilation and access system. The corresponding load is about 80 kW per point. Secured network, supplied by UPS, is constituted by several UPS units (double-conversion AC/DC)

associated with batteries and 400-V distribution switchboards. The UPS system has a 10-minute autonomy and a nominal capacity of 250 kW per point. The main UPS users are the power converters, the RF system, and the interlock & energy extraction systems. The electrical safety systems include the emergency lighting and the emergency stop system (AUG) which acts on the 18-kV distribution network.

Finally, an optical fibre infrastructure provides optical fiber links across the CERN site, including in between surface and underground buildings. This infrastructure serves a variety of systems and is designed to cover the upcoming requests and to guarantee a minimum available fiber capacity in the service areas.

The electrical distribution is controlled via industrial PLCs and SCADA supervision systems and is integrated in the existing control architecture.

3.1.2. High current DC cabling

High Direct Current (DC) cables are used between the power converters and the cold powering system. Those power cables are either conventional (air-cooled ACC) for current ratings below 600 A, or demineralized-water-cooled (WCC) for current ratings above 600 A. To limit the forces and torques on the terminal, a minimum length of straight cable (from 150 mm for 120-A cable up to 500 mm for 18-kA cable) and a minimum bending radius (from 150 mm for 120-A cable up to 800 mm for 18-kA cable) must be respected. Per Point, the resistive dissipations in the power-converter galleries of these cables are 420 kW on the water-cooling circuit and 30 kW on the air ventilation system. Figure 6 shows a water-cooled DC cable. Table 1 gives the DC cable characteristics.

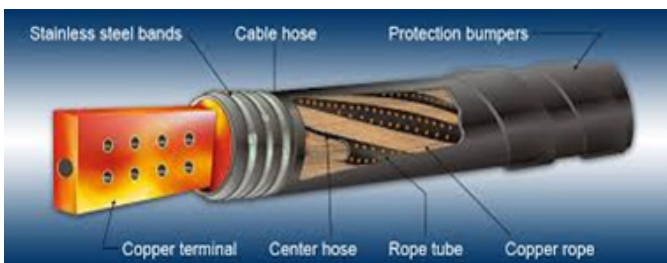


Fig. 6. Water-cooled DC cable.

Table 1. DC cable characteristics.

	Cable type	Circuit current [kA]	Section [mm ²]	From	To	# of cables [-]	Unit length [m]	Total length [m]
IT cluster	WCC	18	1300	PC	CDB	4	9	36
	WCC	14	2000	PC	CDB	2	20.5	41
	WCC	2	500	PC	CDB	16	23.3	372
	ACC	2	300	CDB	CL	56	4.4	246
	ACC	2	240	PC	EE	24	1	24
D2 cluster	WCC	14	2000	PC	CDB	2	8	16
	ACC	0.6	300	PC	CL or EE	20	3.8	76

PC: Power Converter; CDB: Circuit Disconnecter Box; EE: Energy Extraction

4. Cooling and Ventilation

The cooling and ventilation plants at P1 and P5 are mostly the same. The only difference between the two installations consists in the heating solution for the air-handling units: at P1 (in Switzerland), a dedicated extension of the super-heated water network is used; at P5 (in France), electrical heaters are deployed.

4.1. Water cooling

4.1.1. Primary water cooling

A new 3-cell cooling tower of 5 MW per cell is installed in each point. The total cooling power requirement is about 8 MW and can be supplied by 2 cells, the third cell is used as a back-up. The water supply temperature varies between 20°C and 25°C. The primary water flowrate is based on 10-K temperature difference between supply and return. Three circuits distribute the primary water in a duty and standby arrangement. Table 2 gives the circuit cooling requirements and Figure 7 shows the cooling water architecture. The pump heads are selected to provide approximately 3 bar at the connection point of each user equipment. The new plant room houses the pumps, the sand filtration, water treatment station, and frost protection systems. The pipeline is made of stainless steel and distributed in the various buildings using technical galleries.

Table 2. Primary water circuit requirements.

Circuit	From SF to	Final users	Cooling need [MW]
1	SHM and SD	cryogenics	5.4
2	UW	Power converter, RF system & cryogenics	1.6
3	SU	Water-cooled chillers	0.8

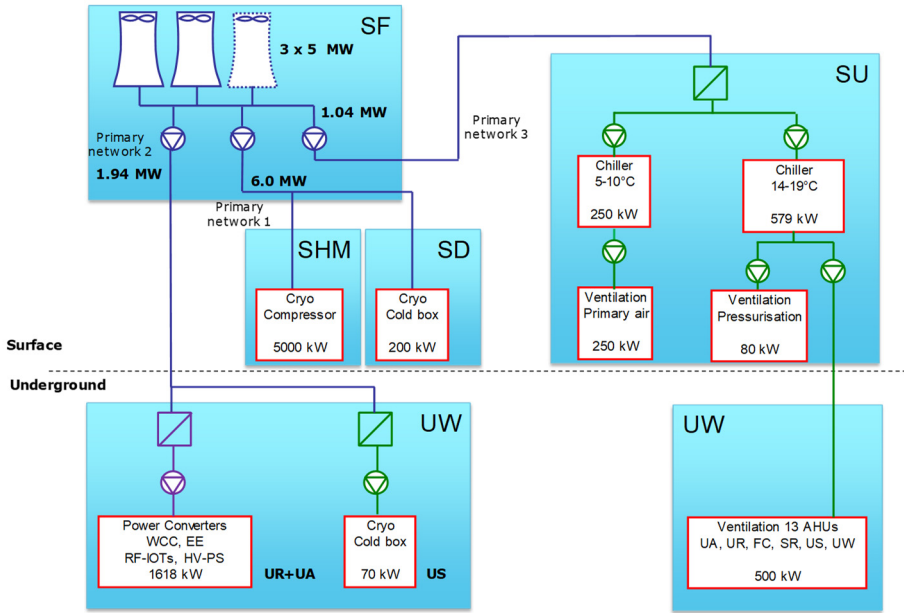


Fig. 7. Water cooling architecture.

4.1.2. Secondary water cooling

The cold compressors of the cryogenic system is cooled by a dedicated water cooling station in UW. It includes a heat exchanger of 70 kW and a duty and standby pump.

One demineralized water-cooling circuit is installed to service all the underground infrastructures. It cools the power converters, the water-cooled DC cables, and the RF system. The station includes one heat exchanger (1.6 MW), a duty and standby pump and a demineralizer, which guarantees a water conductivity below 0.5 $\mu\text{S}/\text{cm}$.

4.1.3. Chillers and cold-water cooling

Chilled water is needed for the fresh air handling unit. A duty and standby water-cooled chillers of 200 kW each are installed in the SU buildings and connected to a common 3-m³ water buffer tank. The temperature regime is 6°C at the supply and 12°C at the return. The chilled water is distributed to the fresh air-handling unit.

Cold water for air handling units is also produced in the SU buildings. Two duty and a standby water-cooled chiller of 300 kW each are installed and connected to a common 5-m³ water buffer tank. The temperature regime is 14°C at the supply and 20°C at the return. The cold water is distributed to the surface air-handling units. The water is distributed using duty and standby pumps and insulated stainless-steel pipework.

4.2. Ventilation

4.2.1. Underground ventilation

The underground temperature is maintained between 14°C and 25°C using cold water (14-20°C). The heating, ventilation, and air-conditioning (HVAC) system consists of several ventilation units located as close as possible to the equipment generating the heat load. Table 3 gives the characteristics of the underground air-handling units. When existing, the air supply and return ducts have regular spaced grids. Figure 8 shows the underground ventilation architecture.

Table 3. Underground air-handling units (per Point).

Location	Number	Capacity [m ³ /h]	Duct DN [mm]	Heat load [kW]	Comments
UR	6	8'500	n/a	90	
UA	2	15'000	900	2 x 56	
US	1	12'000	710	23	
UW	1	4'500	500	7	
Faraday cage	2	3'500	450	2 x 6	
Safe room	2	3'500	450	10	1 duty and 1 standby unit

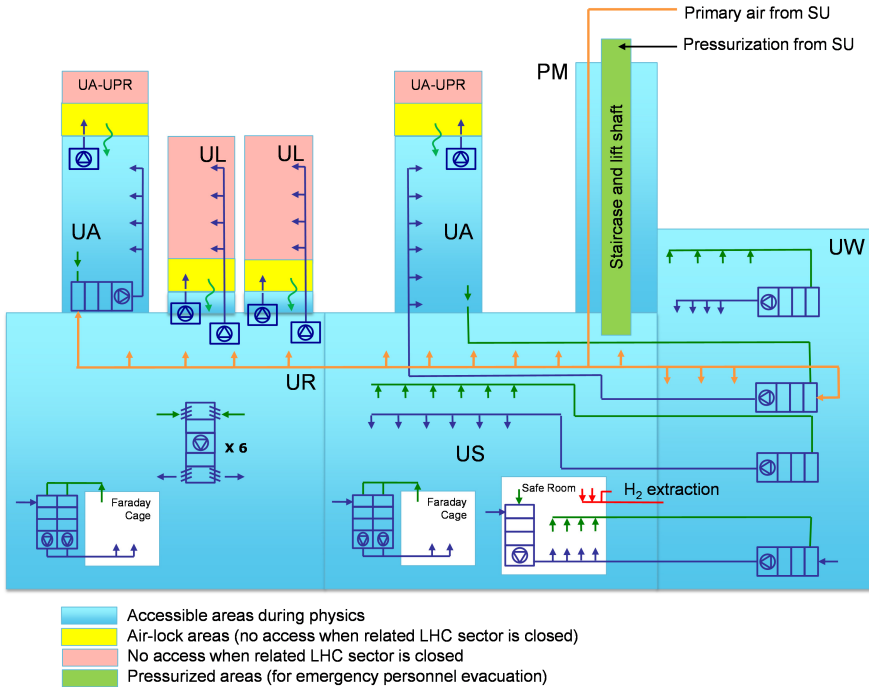


Fig. 8. Underground ventilation architecture.

The fresh air distribution in the underground structures is provided by one duty and one standby air-handling units of 15,000 m³/h each installed in SU17 and is ensuring the air renewal and the dehumidification of the tunnel. The air dew point is maintained below 12°C. Each unit uses chilled water for cooling (200 kW) and two hot water (P1) and electrical batteries (P5) (2 X 120 kW) for heating. The main supply air duct has a diameter of 800 mm thermally insulated.

A duty and standby unit of 15,000 m³/h is ensuring the pressurization of the staircase, lift shaft to the underground areas and safe area around the lift exit in the US. The supply air duct is constructed with circular ducts of 800 mm where possible. The air intake duct and supply ducts are insulated.

Two redundant ventilation systems ensure the pressurization of the airlock installed in the UA and UL service galleries. The units take fresh air from to pressurize the air-lock areas. These pressurizations prevent the migration of activated air present in the LHC tunnel.

4.2.2. Smoke extraction

Each surface building is equipped by a dedicated and independent smoke extraction system. The smoke extraction is ensured by natural ventilation using dedicated sky domes.

Two fans of 36,000 m³/h each are installed out of the SU to assure the smoke extraction form the underground buildings. A fire-resistant duct collects the smoke in the underground structures which are sectorized by doors and smoke curtains. Figure 9 shows the smoke-extraction architecture.

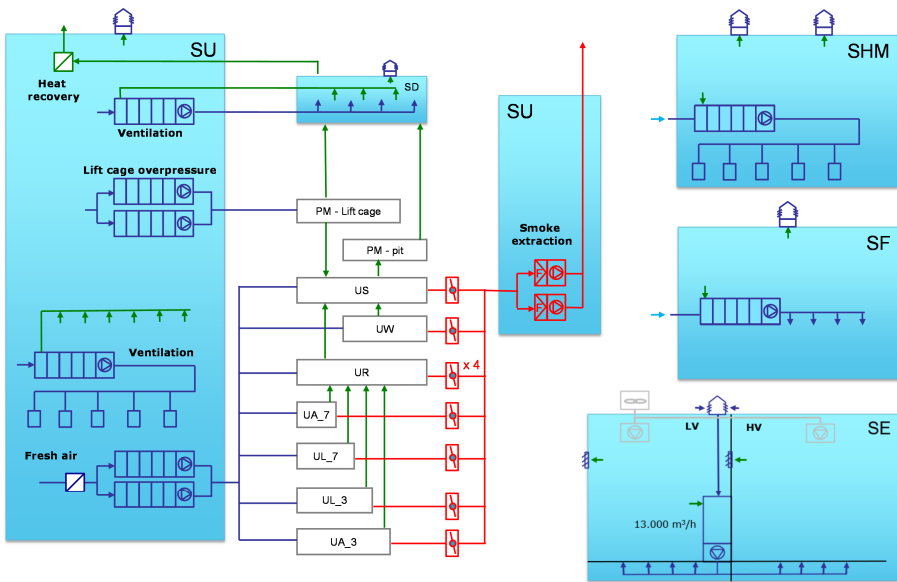


Fig. 9. Surface ventilation and smoke-extraction architecture.

4.2.3. Surface building ventilation

The required outside fresh air is provided by the ventilation systems in all the surface buildings. Depending on the building and on the required cooling capacity, the unit flowrates range from 2500 to 60'000 m³/h. The air-intake ducts are thermally insulated. The HVAC units run in free cooling mode to save energy, except the SU unit, which is designed to run both with mixed water and in free cooling. The over-pressure is released using several static

exhausts (or louvered penthouse). Figure 9 shows the surface ventilation architecture.

5. Alarm and Access System

The new underground areas must be constructed to fulfil the regulations for fire and radiation safety as well as oxygen deficiency hazards (ODH). All critical alarms are sent to the fire brigade for immediate interventions.

The LHC access safety system (LASS) ensures the personnel safety in the various operation modes of the LHC. 220 fire detectors, 74 ODH detectors, 16 radiation detectors and 50 red telephones (in direct line to the fire brigade) are equipping the new buildings and underground structures. Positions of doors allowing the access to the LHC tunnel are also monitored and interlocked with the LHC operation. An emergency evacuation system is based on audible evacuation signals triggered either automatically or manually by pushing one of the evacuation buttons. Figure 10 shows the underground access zoning and access elements.

An automatic protection safety system launches safety functions in case of fire or ODH detection. These functions are compartmentalization, evacuation, and smoke extraction. If necessary, the CERN fire brigade has the possibility

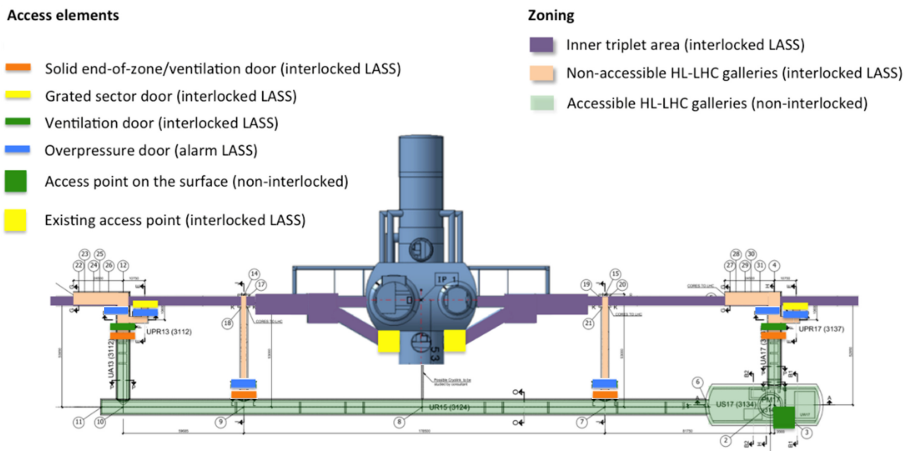


Fig. 10. Underground access zoning and access elements at Point 1 (zoning of Point 5 is similar except for existing access point and service tunnel locations).

of triggering these functions remotely and the possibility to sound safety instructions to the HL-LHC area.

For personnel access to underground structures, a control system located at the shaft lift entrance reads the personnel badges, checks the access rights, verifies the identity via biometric check, and authorizes the access if all conditions are fulfilled. Access to interlocked areas may be possible either in general mode or in restricted mode. Restricted mode is meant for accessing the machine in ready-for-beam conditions, and the user must be in possession of a safety token and the attached restricted mode key. The safety tokens ensure that the beam cannot be entered into the machine until the token is returned to its place in the token distributor. The new normally accessible underground areas of the HL-LHC are of non-interlocked type, which means that no safety tokens are necessary.

Access and safety equipment are generally powered by the CERN secure power grid. All critical functions are also secured by uninterruptible power supplies (UPS).

Concerning communication, the standard CERN GSM network (leaky feeders) is deployed in the HL-LHC structures. A TETRA secure communication system is using the same GSM network.

6. Technical Monitoring Network

All installed equipment is monitored for important operational data, events, and alarms. The low-level monitoring of each subsystem depends on the exact equipment and data collection framework used by that subsystem. Delivery of high-level surveillance and alarm information to CERN operators is realized via the CERN Technical Infrastructure Monitoring system (TIM), which acquires the required data items and alarms from the local SCADA-systems or directly from the monitored equipment.

A technical monitoring network is installed in both the surface buildings and the underground structures. This covers cabled connections to CERN General Purpose Network (GPN) and Technical Network (TN) as well as Wi-fi connections in selected areas. In underground areas, cabled connections are provided at regular distances in the galleries so that modern network-connected equipment can take advantage of it. Wi-fi coverage requires installation of a starpoint rack at approximately every 70-80 meters. All surface

buildings have cabled connections at regular distances. Wi-fi coverage is limited to the more frequented areas (control rooms, rack areas, etc.).

7. Transport and Handling

Transport and handling equipment are installed in new surface buildings and underground structures.

A lift for personnel and materiel transport is installed in the shafts. The specifications are based on LHC 3-ton lifts which cover 90% of transport requirements. The safety requirement covers LHC specific risks (over pressurized shafts in case of fire or helium leak) and the lifts are fed by UPS and have a safe communication with the fire brigade so that they are used as evacuation exits in case of incident in the underground structures.

The electric overhead cranes for surface buildings & caverns are based on requirements from users, including size and weight of biggest/heaviest object to be transported to define parameters such as clearance under hook, span, and length. These designs integrate technical and legal requirements for the crane installation, operation, and maintenance, such as the clearance above the cranes and the catwalk to provide access to the rails and to the machinery. Table 4 gives the characteristics of the main electric overhead travelling cranes.

The UA galleries are permanently equipped with manual overhead cranes travelling on rails to allow for handling and transport of the radiofrequency components. In both Points, one UL gallery is permanently equipped with

Table 4. Main electric overhead travelling crane characteristics.

Location	Capacity [t]	Height hook [m]	Lifting height [m]	Hopper		Speed	
				Length [m]	Span [m]	Max [m/min]	Min [m/min]
SHM17 / 57	20	6	6	50	15	5	0.25
SD17 / 57	25	10	100	28.4	16.1	20	0.5
SF17 / 57	3.2	9	9	23	10	5	0.25
SU17 / 57	7.5	8	8	16	14	5	0.25
US17 / 57	5	7.5	7.5	26	12	5	0.25
UW17 / 57 (top)	3.2	3.2	3.2	15	6	5	0.25
UW17 / 57 (floor)	3.2	3.2	3.2	15	6	5	0.25

manual cranes travelling on rails to allow for handling and transport during maintenance of cryogenic components. These manual overhead cranes have a capacity of 1 ton.

Hoists complete the handling equipment inventory. Water sumps are equipped with heavy lifting pumps that need to be maintained. The support for the hoist is permanently installed on site. Only one hoist unit is requested and is used on demand and moved from one point to another. The equipment, tools and materials necessary for the maintenance of the equipment located in the UW cavern upper floor are transported from the US side. A small hopper with a dedicated 500 kg hoist is permanently installed to lift the tools and consumables. In the SHM buildings, a hoist on a rail is required to transfer the load in the second bay of the building.

For installation of the large cooling & ventilation equipment and all heavy equipment's located in the UW upper floor, a 5-t drawbridge is permanently installed inside the shaft of the US caverns in Points 1 and 5.

8. Operational Safety

Doors and their corresponding frames are required to guarantee the sectorization, the safety and the evacuation of personnel in the caverns and underground galleries. The corresponding instrumentation and controls of these doors are handled by the LHC access safety system (see Section 5). Smoke curtains are also required to implement fire compartments for smoke extraction. In addition, at the surface, sectional doors are installed on the main buildings. The SHM sectional doors are equipped with an anti-noise curtain. Table 5 gives the characteristics of the doors and curtains.

For the radioprotection of personnel, all UA galleries are equipped with 12-t mobile-shielding doors with electrical motors. The dimensions are: 2 m x 0.8 m x 2.8 m. These doors are moving on dedicated ground rails. In addition, 102 t of steel and 48 t of concrete blocks are used in the construction of shielding walls in the UL galleries.

Four firefighting vehicles are located in the UA galleries. These vehicles are composed of a tractor and a trailer. In addition, CO₂ fire extinguishers are periodically distributed in underground structures and surface buildings.

Table 5. Doors and curtain characteristics.

Type	Location	Total number	Size LxH [m x m]	Resistant category		Comment
				Fire	Pressure	
Ventilation and fire-resistant door	UA airlock system	4	1.3 x 2.4	EI 120	n/a	
Ventilation and end-of-zone door	UA airlock system	4	1.3 x 2.4	n/a	n/a	
End-of-sector door	UPR LHC side	4	1 x 2.1	n/a	n/a	Grating
Fire- & pressure-resistant door	UPR LHC side	4	1 x 2.1	EI 120	60 mbar	
Fire- & pressure-resistant door	UA	4	1.5 x 2.4	EI 120	60 mbar	
Fire-resistant door	UR	2	2.8 x 2.8	EI 90	n/a	
Fire-resistant door	UW	4	3 x 3	EI 90	n/a	1/3 - 2/3
Fire-resistant door	Safe room	2	2 x 2.45	EI 120	n/a	
Ventilation and end-of-zone door	UL airlock system	4	1.1 x 2.15	n/a	n/a	
Fire- & pressure-resistant door	UL airlock system	4	1.1 x 2.15	EI 120	60 mbar	
Ventilation and fire-resistant door	US lift airlock	2	2 x 2.65	EI 120	n/a	
Sectional door	SD	2	6 x 6	n/a	n/a	wall mounted
Sectional door	SF	2	4 x 4	n/a	n/a	wall mounted
Sectional door	SHM	2	5 x 5	n/a	n/a	wall mounted
Sectional door	SHM (CV room)	2	4 x 5	n/a	n/a	wall mounted
Sectional door	SU	2	5 x 5	n/a	n/a	wall mounted
Smoke curtain	UR	6	n/a	EI 90	n/a	
Smoke curtain	UA entrance	4	n/a	EI 90	n/a	
Smoke curtain	UL entrance	4	n/a	EI 90	n/a	
Noise curtain	SHM	2	5 x 5	n/a	n/a	

This page intentionally left blank

Chapter 24

HL-LHC IT String and Hardware Commissioning

M. Bajko and M. Pojer

CERN, TE Department, Genève 23, CH-1211, Switzerland

The HL-LHC IT String is the test stand to validate the collective behavior of the Inner Triplet (IT) magnets and circuits in conditions as near as possible to the operational ones.

1. Introduction

The HL-LHC project's goal is to upgrade the present LHC machine through modification and replacement of parts of the existing accelerator by new technologies that enable HL-LHC to reach its goals [1]. To reduce the risks associated to such upgrade and to these innovative technologies, all major components are tested individually at CERN or at collaborators' premises. The individual component tests are, however, not totally representative of their behavior in the machine, as the magnets and other major components connect in the HL-LHC in a common electrical and cooling circuit through which they may interact with each other. Therefore, the HL-LHC IT String installation, in an existing surface building, allows the validation and testing of a complete Inner Triplet (IT) region of the HL-LHC under nominal working conditions, checking the collective behavior of its components [2]. The HL-LHC IT String is a major intermediate milestone for the HiLumi project that will also allow the verification of a system integration and a smoother hardware commissioning of the final machine, installed in the underground areas.

2. Description of the HL-LHC IT String

The HL-LHC IT String, located in the SM18 (the CERN Magnet Test Facility building), will represent the IT zone of the left side of HL-LHC Point 5 with the exception of the inclination of the tunnel that will be not represented in the IT STRING bringing the difference between the Point 5 and Point 1 to be negligible. The IT STRING will not include the matching section region modified for HL-LHC.

2.1. *The magnets of the HL-LHC IT String*

The HL-LHC IT String will be composed by the Q1, Q2a, Q2b, Q3 (all together called the IT quadrupoles), the CP (magnet Corrector Package) and the D1 (separation dipole) cryo-magnet assemblies. These cryo-magnets contain more than one magnet each: a total of 21 superconducting magnets using NbTi- or Nb₃Sn-based technology will be required to set-up the test stand.

2.2. *Powering*

In the HL-LHC IT String, as for the HL-LHC tunnel installations, the magnets are powered via a Superconducting Link System, referred to as Sc link hereafter, composed mainly by the MgB₂ link and the current leads that use high temperature superconducting cables. On one side, the Sc link is connected to the magnets and on the other side to the room temperature DC connections. In both cases, interface devices, the so-called DFX and DFHX respectively, are setup to properly perform the connections. The leads are linked to the power converters via copper bus-bars, water-cooled cables or air-cooled cables (WCC/ACC), depending on the circuit. As in the HL-LHC, the so-called Circuit Disconnecter Boxes (CDB) will be installed between the power converters and the Sc link system allowing fast and safe disconnection of the circuits from the powering system in case of needed intervention. Although the main circuits could be powered with converters presently used for the testing of main LHC magnets and already installed in the test hall, the IT String will be powered with new higher precision 2 quadrant power converters through the Sc link, exactly as planned in the HL-LHC operation. The Sc link will be the first of the series production. The WCC or ACC linking the power

converters, the circuit disconnecter boxes and the current leads will be adapted in their length to cope with the particularity of the integration of the IT zone into the surface building.

2.3. Cryogenic cooling

The cooling of the magnets is done via a dedicated cryogenic valve box, installed for this purpose in the existing test facility. It will allow the HL-LHC IT String test stand to be connected to the global cryogenic system of the test hall and thus to cool down the magnets to superfluid helium temperature. The Sc Link will be cooled with helium gas generated in the DFX on the magnet side. The gas will flow through the High Temperature Superconducting system, including the current leads. Finally, it will be recovered at room temperature, near the DFHX, and sent back to the cryogenic system. The magnets are designed to work at 1.9 K, cooled with superfluid helium. The HL-LHC IT String cooling is independent from the cooling of the rest of the SM18 test facility, where both individual magnets and Radio Frequency (RF) cavities will be under qualification tests in parallel to the IT String operation. Although the cooling and pumping capacities were increased to cover the total need of the tests, thanks to the common efforts of the HL-LHC project and the TE department, a close coordination of the tests and the IT String operation will be necessary during the operation. In its final configuration, the test stands, and so the HL-LHC IT String will be able to profit from a 35 g/s liquid helium production and 12 g/s pumping capacity. The most demanding events in terms of cooling during the hardware commissioning of the IT String or during the study phase -quenching of the magnets- are likely to happen during extended working hours, leaving the possibility to re-cool the system to the operational temperature during the night. The total energy dumped into the He bath can be as high as 39 MJ [3] in case the circuits are powered and quenched at ultimate current. This energy is mostly coming from the circuits of the Q1-Q3 magnets.

2.4. Circuit protection

The magnet and circuit protection of the HL-LHC IT String will be the same as in the tunnel, as one of the major goals of the test stand is to verify the

protection efficiency and confirm the working principles. The protection against quenches (sudden transitions from superconducting to normal state) is assured by a detection system and a reaction one. Concerning the quench detection system, this is built on the same logic of the units installed in the LHC, but it is based on a new and more powerful generation of electronics. As for the reaction system, three types of elements are used: coil active heating, energy extraction and bypass diodes. The systems combination depends on the circuits and the characteristics of each of them. One of the most innovative protection elements is the CLIQ discharge system, which, acting directly on the magnet conductor, allows the rapid and uniform warm up of the magnets during quench events. In such cases, these units of capacitor banks are discharged directly into the magnets, using the heat generated by the coupling current in the Rutherford cables to quench and evenly distribute the warm up to the entire magnet. This method is combined with the more classical way of protection, in which heater strips integrated into the magnet coils are heated up by the discharge of capacitor banks, with the result of a more homogenous and faster distribution of the quench area. The heater strips (called quench heaters), besides providing redundancy to CLIQ at intermediate and high currents, are necessary for protection at low current.

The energy extraction system is used only for corrector magnets and consists of a switching element that allows dissipating the inductive energy stored in the magnets into an external dump resistor. The bypass diodes are integrated into the inner triplet magnets and allow to route the current in an alternative path during quenches.

2.5. *Alignment system*

In the framework of the HL-LHC project, an innovative alignment system has been developed to perform a fully remote precise positioning, monitoring and realignment of the magnets, allowing more frequent alignment campaigns while minimizing the dose exposure to personnel working in the tunnel [4]. This new system will monitor the position of the cold masses in the cryostat guiding the adjustment through motorized jacks. The distance measurements will be done by Frequency Scanning Interferometry (FSI). To determine the position of the cold mass in the cryostat the system will use 14 Wire

Positioning Sensors (WPS), 18 Hydrostatic Levelling Sensors (HLS) and 6 sensors for the longitudinal position. Despite the many similarities between the IT String test and the final configuration in the LHC, the inclination in the tunnel will not be implemented in the IT String as none of the component owners considered it necessary. The experience acquired by operating the magnets with the LHC slope is reckoned sufficient, also by the most affected system, i.e. cryogenics, to design, build and operate the new IT zone without testing it in the IT String.

2.6. *Vacuum system*

The major difference between the HL-LHC IT zone and the IT String is the vacuum system. The HL-LHC IT String, in fact, will not be equipped with beam screens. This decision was taken in order to achieve the maximum cost optimization for the test installation without sacrificing essential measurements [5]. It was judged that the learning of the LHC and some off-line test on individual magnets and validations in the laboratory can entirely address the questions related to the beam screen. These tests have been performed on model magnets, and therefore in time for fine-tuning the system if necessary. Hence, the design of the vacuum system aims to have a common beam and insulation vacuum.

3. HL-LHC IT String Validation Program

3.1. *Performance test of components before installation*

Each component will be tested individually before its installation in the IT String. In particular, the magnets are tested at the collaborators' premises and/or at CERN at nominal operational conditions. For example, the individual magnets will be powered up to nominal current, and to ultimate if required by the testing protocol. At each step of the test, their electrical integrity will be checked.

In general, acceptance and qualification test of the components are under the responsibility of each work package. The IT String test aims to complement them, as a system test.

3.2. *Electrical circuit integrity test*

The Electrical Quality Assurance (EIQA) [6] tests will be performed to assess the integrity of the dielectric insulation of the circuits and will be done at predefined and agreed levels of voltage for each circuit and during all steps of assembly and cool-down. The integrity of the instrumentation and protection systems wiring will be verified. The IT String allows to test the revised and adapted EIQA procedures for the HL-LHC.

3.3. *Cryogenic system test*

The cryogenic system test will focus on the cool down of the magnet chain and the thermal behaviour, after a quench, of the cold and warm powering systems, composed of the magnets, bus-bars, cold diodes, Sc links, cold boxes, current leads, alignment systems, warm cables and power converters. The ultimate heat load capacity for individual test of each pair of heat exchangers is evaluated to be 500 W for Q1-Q2a and Q2b-Q3 and 250 W for D1-CP. The main objective of the cryogenic tests is to get advanced information on the cryogenic characteristics of the cold mass cooling system, the quench relief system and on transient effects.

3.4. *Vacuum system test*

The IT String design does not include beam screens and therefore there is no test planned to verify heat deposition. Those verifications will be addressed with independent studies. The insulation vacuum will be qualified through a leak test with different sealing options. The other singularity of the vacuum system of the IT String, i.e. the single vacuum region for both beam screen and cryostat, may be the most important deviation from the operational configuration. The experience accumulated with LHC is applicable to the HL-LHC IT String and allowed to make this decision, and thus reducing the costs for the IT String [5].

3.5. *Powering of the IT magnets*

The HL-LHC will require the development of new high precision power converters as well as energy storage systems for the 18 kA power converters

that have never been used in the LHC. The magnets will be powered individually or in series (for the Q1 to Q3 assembly) where the fields of Q1, Q1a and Q3 will be adjusted with trim circuits. The IT String will be the first and unique occasion to test the series powering before the commissioning in the tunnel. The IT String test is the occasion to validate the crowbar circuit system and the impact of flux jumps on current regulation and precision.

The cold powering system is composed mainly of the HTS current leads and the Sc link, which relies on cooling with helium gas. The gas has a temperature range from 4.2 K up to 35 K - 50 K. The use of MgB_2 and HTS materials enables safe operation of the superconducting components, for which a temperature margin of at least 10 K is guaranteed. Although the Sc link will go through qualification tests, the IT String setup will also validate the lambda plate in its final configuration, and the connection between the warm powering, cold powering, and magnet systems through superconducting bus-bars and other equipment. The complete warm and cold powering systems will only be tested in the IT String before their installation into the LHC tunnel.

3.6. Quench detection and Magnet protection system test

A careful detection and protection system test is performed before powering the magnets at low and intermediate current. For Nb_3Sn magnets in particular, the appearance of flux jumps was found in the low and medium current range, with amplitudes ranging from 10 mV up to 2 V, and characteristic times of 10 to 20 ms. The quench detection is based on electronics called Universal Quench Detection System (uQDS), as planned for HL-LHC. This system is tested on the magnet test benches and set up to cope with the flux jumps, but the cross-talk between magnets in the Sc link hosting the various feeding cables may amplify flux jumps effect and thus trigger the protection system unnecessarily. These events, called trips, imply in most cases a non-negligible loss of machine availability, as triggering the magnet protection implies heat deposition into the cryo-magnets. Similarly, the protection of the magnets is relying on the quench heaters and the DAQ and control system that are only tested on a magnet circuit in the HL-LHC IT String before its very first installation in the tunnel.

To qualify the systems approximately 200 quenches at different energy levels are planned.

3.7. *Powering interlock test*

The interlock system validation will be one of the most critical tests. The HL-LHC interlock will integrate and handle, with a given logic, signals from all subsystems. The overall system test will only be possible in the IT String, as the interlock system used on the benches for the test of individual cryo-magnet assemblies is a dedicated one, not necessarily working in the same conditions as in the tunnel.

3.8. *Alignment system test*

The required accuracy of the relative positioning of the cryostats is in the order of magnitude of micrometers with an absolute alignment error of ± 0.1 mm with respect to the referential system of SM18. The complete system test is essential, as it is the very first time that the FSI based system is used in a chain of magnets and in real installation and working conditions. The test will confirm the alignment repeatability of cryostats with respect to an external reference, validate the full remote alignment and monitoring systems before ordering the series systems, and allow the study of the impact of vacuum or cold conditions.

3.9. *DAQ test*

In general, every system will have its associated Data Acquisition (DAQ) system and control system. The debugging of those systems is done in the IT String, aiming to improve the efficiency during hardware commissioning. The communication between systems and the data exchange for the good diagnostics of the events will be one of the major goals of the IT String. Dedicated DAQ or control software for the HL-LHC IT String are not foreseen, but rather those that are already used in the LHC or their updated version for the HL-LHC.

3.10. *Performance tests*

The aim of the performance tests will be to investigate the capability of the different subsystems to work together and within the specified conditions.

The HL-LHC IT String test plan includes the powering up to nominal current values and a complete thermal cycle of the circuits.

3.11. *Quality assurance*

The IT String will give the opportunity to validate and test all Quality Control (QC) steps, as well as installation and test procedures.

4. The HL-LHC IT String in the SM18 Test Hall

The SM18 facility (building 2173 at CERN) was the host building for the LHC String 1 [7] and String 2 [8] test installations and for the testing of the LHC magnets prior to installation in the tunnel. For the 3rd time, the facility is the place where this String experiment will be installed and operated.

The choice of the place was essentially based on the available installations and infrastructures that would allow such a test. The project included a significant contribution to the upgrade of several systems, although not dimensioned for the simultaneous HL-LHC IT String operation and full component testing at the same time. A space of 120 m length is available as of 2021 to begin the installation of the test stand. Both primary and demineralized water system, together with the electrical network, were upgraded with a joint effort of the HL-LHC project and the TE department completed in 2019. A major upgrade of the cryogenic cooling system for an additional 35 g/s liquid helium production capacity started in 2019. These modifications allow the parallel test of the individual components both for magnets, and RF systems in the same building [9]. An important coordination and scheduling work will be required during the IT String operation as the pumping capacity remains limited to 12 g/s.

Figure 1 illustrates the integration of the HL-LHC IT String test stand in the SM18 hall and Figure 2 illustrates in detail the aforementioned components of the String.

5. The HL-LHC IT String Timeline

One of the main goals of the IT String is to test and confirm the nominal operational conditions and the *collective behavior* of the entire IT setup, before

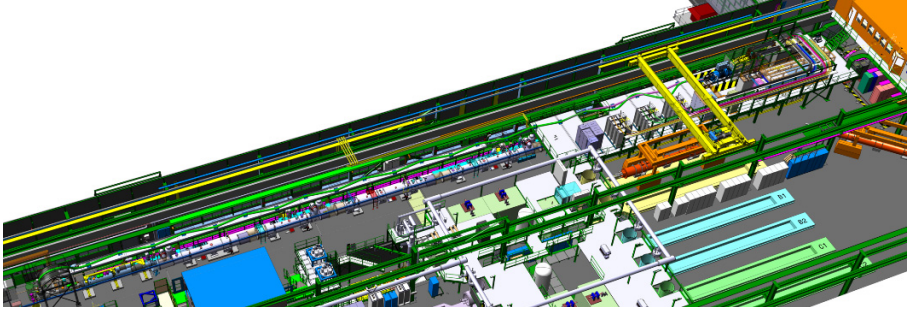


Fig. 1. The HL-LHC IT String in the SM18 hall.

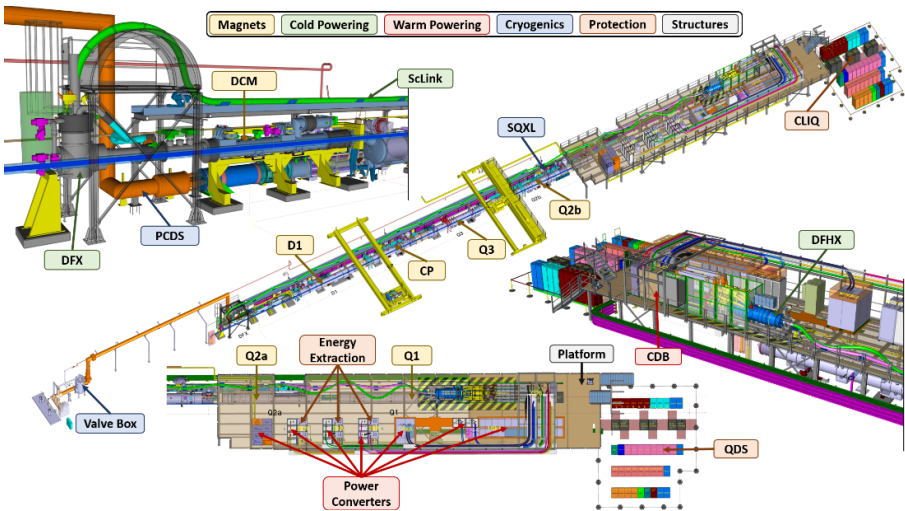


Fig. 2. Components of the HL-LHC IT String.

the installation of the magnets and main components in the LHC tunnel. The delivery schedule of the cold masses, around mid-2022, is the key element defining the critical path of the installation, which will start in 2021. The cryogenic distribution system should be ready by the end of 2021, as well as the metallic structure, allowing the placement of the powering system on top of the magnets, an interesting disposition from both safety and space allocation point of view. The IT String will be prepared for an effective operation of at least 1 year. The operation period could be extended by 4 months, dedicated to a complete thermal cycle and operation to ultimate conditions. The HL-LHC

IT String will be ready for dismantling before the end of 2024 with the option of an extension of the test plan.

6. Hardware Commissioning

6.1. Commissioning of the superconducting circuits

6.1.1. Electrical Quality Assurance tests

As stated in [10], the objective of the EIQA tests is to validate each individual superconducting circuit before powering, to gather all the necessary electrical parameters for operation, and to track all the data acquired and to manage the related non-conformities.

EIQA at warm

At the end of the installation and connection of all magnets and the superconducting link, resistance measurements and a high voltage qualification of all circuits will be performed: to check whether the circuit is closed and all instrumentation sound, determine a reference resistance value at warm, and to validate the galvanic insulation versus ground (and coil vs quench heaters, for those magnets with quench heaters). The values of voltages to be applied and the maximum acceptable leakage current values are being finalised [11-17].

EIQA at cold

Similar tests will be performed at cold, with larger test voltages applied. The circuits and the corresponding link will be cooled down to their nominal temperature. For the high voltage qualification of all lines, this will be performed to validate the galvanic insulation versus ground and the capacity of all lines to withstand the mutual high voltages developed during a fast change of current in the different circuits (typically during a fast abort or quench). The high voltage qualification also includes testing of all the elements that are electrically connected to the tested circuit. Such elements are:

- the instrumentation and feedthrough systems
- the magnet protection units
- the temperature sensors with the related tunnel cabling and electronics

- the tunnel cabling for routing the voltage taps used for the protection of the superconducting circuits.

In addition, impedance measurements will be performed, with the aim of determining the impedance of the magnet systems as a function of the frequency. The results of these measurements are used to spot possible inter-turn shorts, and for determining the settings to adjust the power converter regulation.

6.1.2. *Powering tests*

The HL-LHC magnets present several peculiarities [18] that have to be kept in mind for their commissioning. The most relevant are: the fact that all magnets will be cooled down to 1.9 K; that Nb₃Sn will be used extensively for the first time; that the current of the inner triplet will be the highest in the machine (18 kA); and, importantly, that some of the high current magnets will be protected only via energy extraction in a dump resistor without quench heaters. In addition, the powering scheme of the inner triplet will be different from the present one with implications in case of a quench of one of the magnets. The HL-LHC baseline foresees 11 T magnets in the DS, where NbTi and Nb₃Sn magnets will be powered in series, with the addition of a trim (locally connected to the 11 T magnets via resistive, 120A-like current leads) to compensate for the different transfer functions, with important implications on the powering and the protection of the circuit [19].

The powering of all circuits up to nominal current will be done in steps. At the end of each step, online and offline analyses are performed by equipment owners and protection experts to assess the performance of all hardware in the circuit. In particular, for the powering of individual circuits, several cycles at different current levels will be performed to study the performance of the magnets, the efficiency of the protection mechanisms (by provoking fast aborts and even quenches), and to check all functionalities of the powering interlocks and of the power converters (via provoked powering failures). A typical series of tests includes:

- at minimum operational current, testing of the full interlock chain, with the verification of cryogenic signals, power permit, powering failure, circuit quench transmission, and fast power abort requests;

- at low current, a check of the power converter performance and verification of all protection functionalities, by means of provoked slow and fast power aborts, with energy extraction;
- repetition of a series of power aborts and, possibly, simulation of quenches from progressively higher current levels, with increasing stored energy (e.g. 25%, 50%, and 100% of the stored energy at nominal current).

Before starting a new powering test, all previous tests must have been validated. The validation includes approval by power converter and powering interlock experts, magnet owners, and protection experts. Cryogenics experts should also confirm the correct operation of their installations and instrumentation. The criteria for approval, the parameters, and the relevant information to be stored will be discussed in due time. The first time that these procedures will be applied is during the test of a full string of magnets (reproducing from Q1 to D1), powered by a superconducting link. All valuable data extracted from the test on the IT String will help to adapt and improve the powering procedure steps and criteria to be used in the LHC tunnel.

After the individual test of all circuits up to the design current, the common powering of a set of circuits will be done for magnets that are in the same cryogenic envelope and are powered from the same link (usually referred to as the powering of a group of circuits). The objective of this powering is to validate the simultaneous operation of all magnets in nominal conditions; current cycles similar to those applied in normal operation should be used for the powering of a group of circuits. What is important at this stage is the behavior with combined powering in critical conditions, such as the fast power abort of a circuit when the others are at full current. For the inner triplets, in particular, quenching of a triplet quadrupole might induce a quench in a nearby quadrupole or corrector magnet if the current in this related circuit is not extracted fast enough. These tests should be performed on all the magnets and could even trigger the change of detection thresholds and protection configurations. Once more, all tests should be approved by a group of experts and recorded for future reference. Particular attention also has to be paid to those circuits that are not equipped with heaters and are protected by energy extraction on a dump resistor. For such circuits, a precise estimate of the energy absorbed by the cold mass during a quench has to be made, not only in the case of standalone operation on the bench tests, but also in the more severe conditions of combined powering in the tunnel. Eventually, the protection

threshold should be adapted to reduce energy deposition in the coils and improve magnet safety during powering.

6.1.3. *Magnet training*

Operations at 7 TeV should be established during Run 3. In the process, extensive experience will be gained with the dipole training required to get to the requisite current level. The effects of a full thermal cycle will also be given by the commissioning following the Long Shutdown 2 (LS2). A sound estimate of the number of quenches required after the LS3 will hence be possible and well optimized procedures will be in place to assure an effective retraining campaign. Nevertheless, few information is available for the (re-)training of the Nb₃Sn magnets; extremely useful data should come from the String in this respect. Sufficient time should be foreseen in the schedule for the training to 7 TeV.

6.2. *Hardware commissioning of the HL collimation system*

The mechanics and controls of the collimation system should be identical to that of the Run 3 configuration and required tools should be well debugged and validated by the time of the HL-LHC. The collimator settings, controls and operational sequences should be intensively re-tested during the hardware commissioning phase. A dedicated test to address the reproducibility of collimator movements during critical operational sequences (such as the ramp) will be performed. Before any beam is injected into the machine, the machine protection (MP) functionality of the collimation system must be guaranteed. Each collimator is connected to the beam interlock system (BIS) and has more than 20 interlocks that will need to be verified. The jaw positions and collimator gaps are monitored via six linear variable differential transformer (LVDT) sensors. These signals are interlocked with inner and outer limit values, making a total of 12 interlocks per collimator. In addition, there are a total of six energy-dependent and β^* -dependent limit functions and an interlock to protect from 'local' mode collimation control. The temperature of the collimators is also monitored and interlocked with minimum and maximum adjustable settings.

The main upgrade of the collimation system for HL-LHC will ensure cleaning of beam halo and will keep losses in high luminosity experimental regions at an appropriate level. For this, the project foresees the installation of local collimation in the dispersion suppressors. The installation of the new collimators (TCLDs) around Point 2 (made possible by the replacement of the connection cryostats by new ones incorporating the collimators) should be completed by the end of the LS2 and the eventual installation of TCLDs between two 11 T dipoles at point 7 (the cryo-assembly will replace one conventional LHC dipole) could be completed by the end of the LS3. These collimators feature the latest design improvements, including embedded BPMs for fast alignment. Unlike other hardware commissioning tests (such as for the magnets), most of the collimation commissioning will not impact the length of the shutdown, since the tests are individually executed in the shadow of other activities (the main exception being the testing of the interlock system where the BIS needs to be available).

6.3. Commissioning of the cryogenic systems

The HL-LHC foresees numerous modifications of the cryogenic system [20]. Among them are:

- the power upgrade for IR1 and IR5;
- the upgrade of the cooling capacity for Sector 3-4 (Sector 4-5 requires less cooling requirements as compared to Sector 3-4 thanks to the new HL infrastructure at P5) to compensate for the additional heat loads of the SRF in P4;
- the new cooling system for the superconducting links;
- the cooling loop for the crab cavities.

The operation of all systems, together with the time needed to qualify and tune the systems, will be detailed later. Provisionally, an approximate time of three weeks is considered to be mandatory to commission the scheme for the superconducting magnets.

References

1. I. Béjar Alonso, O. Brüning, P. Fessia, M. Lamont, L. Rossi, L. Tavian and M. Zerlauth, “High-Luminosity Large Hadron Collider (HL-LHC): Technical Design Report,” CERN-2020-010, ISBN 978-92-9083-587-5.
2. M. Bajko et al., “The Inner Triplet String Facility for HL-LHC: Design and Planning,” 12th International Particle Accelerator Conference (IPAC), Campinas, Brazil, 2021.
3. A. Perin, M. Sisti, S. Claudet, R. Van Weelderen, M. Bajko and F. Dhalla, “The Cryogenic System and Planned Cryogenic Tests For the Future High Luminosity LHC IT Magnet String,” IEEE Transactions on Applied Superconductivity, vol. 29, no. 5, pp. 1-4, Aug. 2019.
4. A. Herty, R. De Maria, P. Fessia, D. Gamba, M. Giovannozzi and J. Hansen, “HL-LHC Full Remote Alignment Study,” 10th Int. Particle Accelerator Conf. IPAC 2019, Melbourne, Australia, JACoW Publishing ISBN:978-3-95450-208-0 doi:10.18429/JACoW-IPAC2019-THPGW057A.
5. M. Bajko, “IT STRING Configuration and Options,” 66th HL-LHC TCC.
6. D. Bozzini et al., “Electrical Quality Assurance of the Superconducting Circuits during LHC Machine Assembly,” European Particle Accelerators Conference EPAC08, 2008, Genoa, IT.
7. P. Faugeras, “Assembly and Commissioning of the LHC Test String,” Particle Accelerators Conference PAC95, 1995, Dallas, USA.
8. R. Saban et al., “The Preparation of the Cryomagnets and the Assembly of the LHC Test String 2,” Particle Accelerator Conference PAC2001, 2001, Chicago, USA.
9. M. Bajko et al., “Upgrade of the CERN Superconducting Magnet Test Facility,” 7 p. - IEEE Trans. Appl. Supercond. 27 (2017) 9500307.
10. R. Mompou, N. Catalan Lasheras, G. D'Angelo, M. Bednarek and J. Ludwin, “ElQA Qualification of the Superconducting Circuits during Hardware Commissioning,” LHC-DE-TP-0007, EDMS 788197, <https://edms.cern.ch/document/788197>.
11. T. Da Rosa and F. Rodriguez Mateos, “Electrical Design Criteria for the HL-LHC Inner Triplet Magnets,” LHC-MQXF-ES-0001, EDMS 1963398, <https://edms.cern.ch/document/1963398>.
12. T. Da Rosa and M. Bednarek, “Electrical Design Criteria for the HL-LHC D1 Dipole,” LHC-MBXF-ES-0008, EDMS 2187266, <https://edms.cern.ch/document/2187266>.
13. T. Da Rosa and M. Bednarek, “Electrical Design Criteria for the HL-LHC D2 Dipole,” LHC-MBRD-ES-0004, EDMS 2363904, <https://edms.cern.ch/document/2363904>.
14. T. Da Rosa and M. Bednarek, “Electrical Design Criteria for the HL-LHC 11T Dipole,” LHC-LMBH-ES-0004, EDMS 1995595, <https://edms.cern.ch/document/1995595>.
15. T. Da Rosa and M. Bednarek, “Electrical Design Criteria for the HL-LHC D2 Orbit Corrector,” LHC-MCBRD-ES-0006, EDMS 2363906, <https://edms.cern.ch/document/2363906>.

16. T. Da Rosa and M. Bednarek, “Electrical Design Criteria for the HL-LHC High Order Corrector Magnets,” LHC-M-ES-0014, EDMS 2060633, <https://edms.cern.ch/document/2060633>.
17. T. Da Rosa and M. Bednarek, “Electrical Design Criteria for the HL-LHC Nested Orbit Correctors,” LHC-MCBXF-ES-0004, EDMS 2363905, <https://edms.cern.ch/document/2363905>.
18. E. Todesco, “Chapter 3: Insertion Magnets, High-Luminosity Large Hadron Collider (HL-LHC): Preliminary Design Report,” pp. 61-79 10.5170/CERN-2015-005.61.
19. A. Antoine, R. Denz, L. Grand-Clement, S. Izquierdo Bermudez, F. Menendez Camara, H. Prin, I. Romera Ramirez, J. Steckert, G. Willering, D. Wollman and S. Yammine, “11T Dipole Circuit – Powering and Protection,” LHC-MBH-ES-0001, EDMS 1764166, <https://edms.cern.ch/document/1764166>.
20. S. Claudet, “Chapter 9: Cryogenics for the HL-LHC, High-Luminosity Large Hadron Collider (HL-LHC): Preliminary Design Report,” pp. 161-169 10.5170/CERN-2015-005.161.

This page intentionally left blank

Chapter 25

SRF Cryogenic Test Facility for the HL-LHC

L. Tavian^a, G. Vandoni^a and W. Venturini Delsolaro^b

^a*CERN, ATS-DO Unit, Genève 23, CH-1211, Switzerland*

^b*CERN, SY Department, Genève 23, CH-1211, Switzerland*

Several test stands were assembled for testing integrated operation of individual components with and without beam. Amongst these, at CERN, the SPS SRF test stands allows to qualify crab cavity modules with beam, while the test facilities situated in the SM18 buildings underwent important upgrades for testing SRF single-crab-cavities, SRF modules, superconducting cryomagnets and cold powering systems. Other test stands are available off-site in the framework of collaborations. This chapter describes the test facilities at CERN and presents a summary overview of the other test facilities outside of CERN.

1. Introduction

The HL-LHC requests that superconducting devices (RF cavities, magnets and links) to be individually tested prior to their final installation. For this purpose, existing test facilities have been upgraded and a new cryogenic test stand has been created to test crab cavities (Chapter 7) in operation with proton beams. Collaborations with external institutes have also boosted cryogenic test capability for the project, off CERN site. This chapter describes these different test facilities, with emphasis on the SPS crab cavity test stand and SM18 facilities and the list of off-site facilities.

2. The SPS SRF Test Stand

With the SPS stand aims to provide a test bench to explore the operational performance of superconducting RF crab cavities – and more generally, SRF cavities – throughout a wide range of proton beam parameters, as described in Table 1, under safe conditions for the equipment and the personnel.

Table 1. SPS beam parameters as used for the 2018 tests.

Energy	26 – 450	GeV	Coast energy	55, 120, 270	GeV
Intensity	$0.05 - 1.3 \times 10^{11}$	p/bunch	Bunch length	< 2.0	ns
RF Voltage	3.0 – 7.0	MV			
Long. emittance	0.35 – 0.5	eVs	Betatron tunes	26.12, 26.18	
$\beta_{x,y}$	40, 80	m	Dispersion	-0.5	m

The choice of long straight section 6 – a region dedicated to beam extraction to the LHC and North Area – was dictated by a conveniently large tunnel section, low radiation dose and the presence of a 15 m long free drift zone, close to the access tunnel. The advantages of the presence of a substantial underground technical alcove, a 20 tons freight lift with large spans and the BA6 surface technical hall were further assets. To minimize impact of the tests on beam time, infrastructure and services were designed to allow for full remote control. The SPS main RF is synchronized to the test bench RF via a 4 km, ~1 s delay long fibre optics link. The SPS beam instrumentation is used to monitor orbit centering, RF phase scans, bunch rotation.

2.1. The test bench

To overcome critical aperture restriction by the cavities for extracted beams and mitigate the potential detrimental impact of the cavities operation on the beam during normal operation, a motorized lateral translation table was designed as integral support of the test stand. The remotely steered table movement spans 51 cm with positioning reproducibility and precision of some microns. Two overhead rails hooked at the tunnel vault hold chain hoists for handling of heavy equipment (up to 4 tons) on the table during installation work.

The beam vacuum line is split into two branches by two Y-shaped articulated vacuum chambers fitted with highly flexible bellows: one branch has SPS standard round pipe for circulating and extracted beam, while the other connects to the beam vacuum of the cryomodule under test. Thanks to the articulated continuous vacuum line, the module is parked out of the beamline during regular operation and is transferred into the beamline during cavity tests without the need to break the beam vacuum. Vacuum valves sectorize the zone, separating cold from warm areas. Neighboring vacuum chambers are carbon-coated to reduce secondary electron emission and thus mitigate electron cloud and related pressure increase. Two button beam position monitors are inserted in the cryomodule vacuum sector. The cryomodule rests on the transfer table via three jacks allowing for positioning range of ± 4.5 mm.

Space economics and equipment modularity directed the choice of cryogenics towards a displaceable helium refrigerator, with movable compressor and cold-box connected to a fixed distribution system. The cold-box, installed underground in a technical alcove, is fed by warm helium gas from the surface compressor and boosted to 7 g/s liquefaction rate by liquid nitrogen from a vertical transfer line. Liquid helium is conveyed to the proximity cryogenics equipment of the cryomodule via an 80 m transfer line flanked by 2 valve-boxes. Connection to the ancillary distribution unit on the moving table is via flexible lines. Refrigeration up to 3.5 g/s at 1.9 K is attained with two large pumping units located close to the test stand.

Two Inductive Output Tubes (IOT) of 60 kW cw, installed in the surface building, supply RF power to the two cavities via coaxial transmission lines. Flexible connection to the cavity power couplers on the cryomodule and ancillary RF charges and circulators is achieved via two V-shaped RF transmission lines with rotating joints.

Cryomodule instrumentation, in particular the frequency scanning interferometric position monitoring of the cavities, is connected with flexible yet robust cables and optical fibers, bundled and protected to follow the table movement. Few water lines for RF charge-and-circulator cooling are also conveyed from the distributed SPS water supply lines to the transfer table via flexibles.

An integrated set of interlocks protect the equipment and the SPS. It is thus impossible to set the table into movement if the vacuum valves are not closed, protecting the SPS against leaks from the dynamically stressed vacuum

bellows. Likewise, the position of the table dictates the beam permit or the beam extraction command. Protection of personnel against cryogenic hazard in an elsewhere warm machine is ensured by a distributed network of oxygen deficiency detectors. The SPS access system steers also the interlocking of RF power to the cavities, to eliminate the risk of exposure to X-rays.

In the future, the test stand could be easily upgraded to test superconducting magnets in proton beams.

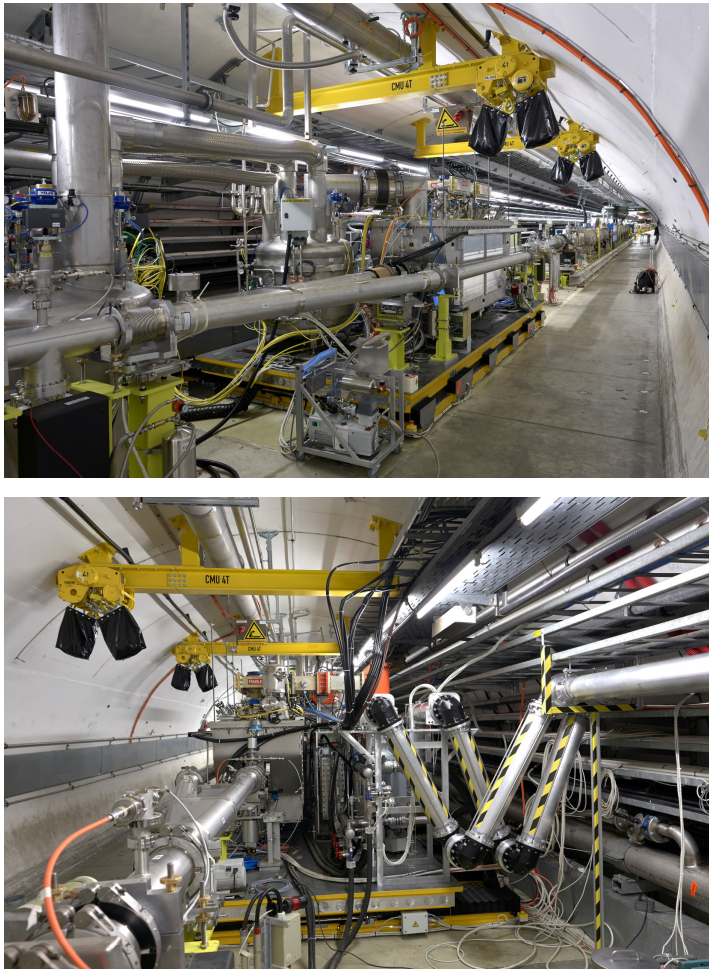


Fig. 1. The SPS SRF test stand, seen from upstream (top) and downstream (bottom).

3. The SM18 SRF Test Stand

The SM18 facility hosts also a large, fully equipped superconducting RF preparation and testing area. The SRF facilities comprise a 254 m² complex of clean rooms, staged from ISO5 to ISO4 class, partially joined in a cascade of communicating spaces and equipped with a high pressure ultra-pure water rinsing cabinet with rotating and translating nozzle, delivering up to 1 m³/hr of 18 MOhm-cm water at 100 bar. The four vertical cryostats for single cavity testing and 2 large bunkers for cryomodule testing, are entirely screened in concrete for radiation protection. An accelerator-grade access system ensures the protection of personnel. The test benches, connected to the cryogenic system of SM18 via an underground transfer line, share a large preparation area equipped with supporting structures for the cryostat inserts. The vertical cryostats can operate between 4.5 K and 1.9 K. They feature earth magnetic field compensation, presently in upgrade, pumping systems and vacuum diagnostics in dust-free, slow pumpdown mode, and Oscillating Superleak Transducers and Transition Edge Sensors for second sound detection. The two bunkers are connected to RF power systems – one klystron of 300 W and solid-state amplifiers up to 20 kW. SRF cavity locking is achieved by means of modern digital LLRF systems based on self-excited loops, as well as on traditional phase locked loops. All remote control and testing equipment for each of the 4 cryostats and the two bunkers is located in a dedicated control room.

4. The Test Facilities for Cryomagnets and Cold Powering Systems

The current CERN cryogenic test facilities located in the SM18 buildings, designed for the series test of LHC superconducting devices, have been upgraded to fulfil the new HL-LHC needs. A new test bench allows for vertical tests of magnets at nominal current (up to 20 kA) before their final integration. In addition, five existing LHC horizontal test benches will be upgraded by increasing their test current up to 20 kA and by adapting their mechanical interfaces to the new HL-LHC cryomagnets. One existing LHC horizontal test bench will be upgraded, increasing its test current to 20 kA and adapting their mechanical interfaces to the cold powering assemblies of the superconducting link, more detail in Chapter 10. The existing test bench used to qualify the

superconducting link demonstrators will be upgraded for the individual qualification tests of the series of HTS current leads. In order to fulfil the test rate of the HL-LHC series components in parallel with the test of the Inner Triplet String (see Chapter 24), the installed helium liquefaction capacity has been increased from 750 to 1800 l/h by adding a new liquefier.

In the framework of collaborations, cryogenic test stations are available in different institutes for testing superconducting magnets and RF crab cavities. Table 2 list the different test facilities available for the qualification of HL-LHC devices (see also Chapter 26).

Table 2. Available test facilities.

Test facility location	HL-LHC devices	Test conditions*
CERN SPS	RF crab-cavity cryomodules	at 7 MV and 2 K with proton beam
	Q2A & Q2B magnets	at 20 kA and 1.9 K (V)
	Q1, Q2A, Q2B & Q3 cryomagnets	at 20 kA and 1.9 K (H)
	D1 and D2 cryomagnets	at 13 kA and 1.9 K (H)
	Corrector magnet packages	at 0.2 - 2 kA and 1.9 K (H)
CERN SM18	SC links and current feed boxes	at 0.6 - 20 kA and 4.5 - 300 K
	Current leads	at 0.6 - 20 kA and 20 - 300 K
	Cold diodes	at 20 kA and 4.5 K
	RF crab-cavity cryomodules	at 7 MV and 2 K (H)
	Dressed crab cavities	at 7 MV and 2 K (V)
US FNAL	Q1 & Q3 cryomagnets	20 kA and 1.9 K (H)
US BNL	Q1 & Q3 cryomagnets	20 kA and 1.9 K (V)
US JLAB	Dressed crab cavities	at 7 MV and 2 K (V)
Canada TRIUMF	RF crab cavity cryomodules	at 7 MV and 4.5 K (H)
Japan KEK	D1 magnets	at 13 kA and 1.9 K
	Q2 & CP corrector magnets	at 2 kA and 1.9 K (V)
Sweden FREIA	Dressed crab cavities	at 7 MV and 2 K (V)
	D2 magnet models and prototypes	at 13 kA and 1.9 K (V)
Italy INFN	CP corrector magnets	at 0.2 kA and 4.5 K (V)
China IMP	D2 corrector magnets	at 0.6 kA and 4.5 K (V)
France CEA	Q4 model	at 16 kA and 1.9 K (V)

* Horizontal test (H), Vertical test (V)

Chapter 26

The International Network of Test Infrastructures for the HL-LHC Magnets and Cold Powering System

M. Bajko

CERN, TE Department, Genève 23, CH-1211, Switzerland

This chapter describes the test facilities upgraded in the framework of HL-LHC for testing magnets, cryo assemblies, SC Link systems, HTS leads and cold diodes at CERN, and at the collaborators' premises.

1. Introduction

Within the HL-LHC project, more than 100 superconducting magnets are to be tested. This includes models and prototypes, and encompasses the period of 2018-2024. They are of different types and sizes, based on either NbTi or Nb₃Sn technology, which are designed-and-fabricated at CERN, at collaborating laboratories, or in industry. The testing criteria varies at different phases of the project. For example – during the R&D phases – the main purpose of testing was to obtain design feedback. Meanwhile – during serial production – the main purpose is qualification.

The HL-LHC employs innovation not only in magnet technology, but also in cold powering, quench detection and quench protection. Test infrastructures for these various systems have been set up at CERN and collaborating sites [1,2]. For example, the cold powering system uses MgB₂ – for the superconducting link (Sc link). It transports up to 150 kA between the power converters and the magnets via current leads (CLs) using REBCO conductor (see Chapter 10). Dedicated test stands have been set up to qualify both the Sc link and the CLs before their integration into the LHC tunnel.

This is an open access article published by World Scientific Publishing Company. It is distributed under the terms of the Creative Commons Attribution 4.0 (CC BY) License.

This chapter describes the various test stands of CERN and of collaborating institutes, that have been upgraded, developed, or constructed for testing major components as described here before.

2. Cold Powering Test Facilities for Superconducting Magnets

Testing the superconducting magnets is part of the QA process. It assesses the soundness of the construction and the suitability for machine operation. In addition, during construction, the test is also an integral part of the construction chain: it must produce feedback on time to be included in eventual corrective actions in the construction process. It's also a key milestone for triggering acceptance and passage of responsibility between firms and/or institutes (in case of industrial orders), or among institutes (in case of in-kind contribution).

2.1. Test facilities at CERN

The CERN Superconducting Magnet Test Facility, placed in the building named SM18, an acronym sometimes used to refer directly to the test facility, is a unique asset for the accelerator magnet programs. Its history dates back more than thirty years. After testing the first generation LHC dipoles and quadrupoles at the beginning of the nineties a prototype test bench, construction of the twelve horizontal test benches started in the mid-1990s, reaching its final configuration in 2004. Between 2004 and 2008, SM18 hosted the series test of all LHC superconducting magnets [3]: approximately 1700 cryostated magnet assemblies, for a total of 2000 test runs. Since the end of LHC series tests, the horizontal test benches of SM18 are still regularly used to qualify spare magnets [4], to study magnet operation limits [5], or to characterize off-line the magnetic behavior of the LHC magnets by repeating selected and adjusted operation cycles [6]. The first upgrade of SM18 took place in the period of 2009 to 2013. At that time, three vertical test cryostats – originally hosted in a separate test hall (also known as the Block 4), used mainly for R&D, magnet model and component tests – were migrated to SM18. In the same time frame, a cryogenic feed-box, originally planned for the test of Nb-Ti links (with up to 600 A) in supercritical helium, was upgraded to provide up to 20 kA, and a variable temperature He flow of up to 10 g/s and at 100 K.

This test station was used to power a Fast Cycled Magnet [7] and superconducting current links [8].

In spite of its unique capacity, it was clear that SM18 would not be able to cope with the demands of new projects such as the HL-LHC. For this reason, SM18 has undergone a fundamental redesign [9–17], upgrading its test stands and service infrastructures.

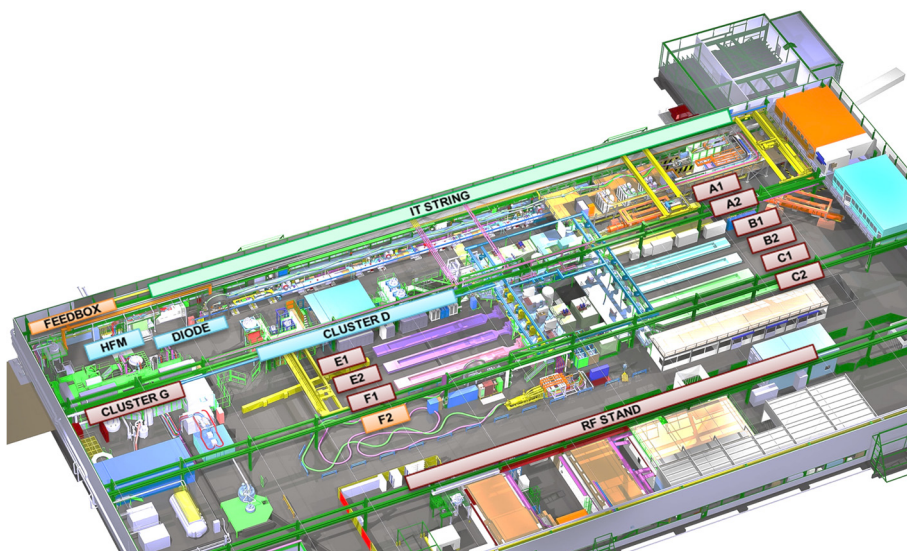


Fig. 1. Test benches at CERN for the HL-LHC

2.1.1. Service infrastructure upgrade

The increased quantity and dimensions of test installations, the greater dimensions of the magnets to be tested, and the larger currents required, led to an increased demand for general services. Following HL-LHC planning, during the serial production between 2020 and 2025, most of the testing installations will work in parallel to cope with a rate of 30-40 tests/year. This includes standard tests of LHC spare magnets as well as special tests. The impact of this program was translated into the needs of each of the service infrastructures, with particular consideration given to the simultaneous operation of horizontal benches, the vertical cryostat, the Sc Link, the RF cavities, and the IT String (as described in Chapter 24) in the SM18 test

facility. In this evaluation, contingency was taken for a hypothetical scenario where the test stands would need to re-qualify 50 spare magnets for the LHC within a shortened timeframe (max. 5 months), as was the case in 2009 [18].

The cryogenic cooling system is one of the most critical infrastructures for the test stands. SM18 is equipped with a 6 kW refrigeration system, used as a liquefier, delivering saturated, liquid He at 1.6 bar, and a 25 m³ LHe Dewar for storage. The initial liquid production capacity of 27 g/s was estimated to be insufficient when compared to the demand of up to 60 g/s. An upgrade has then been completed successfully in 2020, with the installation of an additional He liquefying system with 35 g/s capacity. Two warm pumping units are shared between the magnet test stands and the RF test stands for 1.9 K operation. These units are expected to be sufficient for long term operation. Nonetheless, to improve flexibility in 1.9 K operation, the two warm pumping units were connected to share, as required, their total pumping capacity of 12 g/s at 6 mbar between the RF cavity and magnet test benches [19].

Demineralized water is used to cool the power converters, the water-cooled cables and the switches. The LHC magnets are powered in the test stand in a range between 0.12–12 kA, while the HL-LHC needs are higher, in some cases reaching 22.5 kA. This leads to an increased consumption of demineralized water, estimated to be a total of 150 m³/h during the time the operation of the IT String or the SC link test stand. Hence an upgrade to the demineralized water station was also necessary to cope with the increased demand.

Upgrading the demineralized water station and increasing the installed cryogenic power triggered an upgrade of the primary water station, resulting in more than 5.7 MW of extra capacity.

Such modifications in and around SM18 also required an upgrade to the electrical distribution network – both for the machine, as well as the general and UPS networks to cope with the demand of different test stands. An additional 3 MVA transformer installed in 2019 ensured that the Cluster F horizontal test stand's new 20 kA power converter can be powered in parallel with all of the IT String's power converters. The UPS network's capacity typically relating to cryogenics or protection system triggers, has been upgraded to 100 kVA, ensuring approx. 10 min autonomy at 80 kW of total consumption.

A compact, 25 t capacity overhead crane equipped with a cable of sufficient length to allow installation at the -3 m level was required. It was later

completed with a 10 t crane, to ensure the handling of the SC link system and its safe installation into the IT String.

2.1.2. Vertical test stands for magnets

The HL-LHC magnets' overall dimensions and their powering characteristics justified an investment into vertical test stands comprised of a cryostat, powering circuits, and associated protection circuits. The most critical magnets of the upgrade were undoubtedly the Nb₃Sn quadrupoles of the Inner Triplet (IT) [20–22]. All quadrupoles have identical design, with a cold mass outer diameter of 630 mm (to be compared to the 550 mm of a standard LHC cold mass). The nominal current is 16.5 kA at 1.9 K, the ultimate design value is 18 kA, and the expected short sample limit is 21.5 kA. The operating current density and stored energy per unit mass of these magnets is significantly higher than in the LHC, requiring 3x faster detection and protection reaction times. This needs to be viewed in relation to the fact that Nb₃Sn is affected by an intrinsic voltage noise caused by flux jump spikes. Besides the high gradient IT quadrupoles, the cryo-assemblies of Q2a/Q2b also contains combined horizontal and vertical dipole corrector magnets, built with Nb-Ti, and operated at a nominal current of 1.4 kA.

Two new test stands were designed and installed, mainly in response to the requirements of the HL-LHC and future needs of magnet tests for the development of future generation colliders at CERN.

The first test stand is referred to as the High Field Magnet (HFM) test stand. It has a cryostat with a large inner diameter of 1500 mm, a useful length of 2.5 m, and is prepared for operation at 4.2 K and 1.9 K. The design of this cryostat and its ancillary equipment was primarily driven by the test of the FReSCa2 magnet, but considering its size, it could host any other larger magnet such as the models of the IT quadrupole for the HL-LHC, or future high field models. The insert is equipped with two pairs of current leads: one for 20 kA and one for 15 kA. They are powered independently, allowing, for example, the FReSCa2 magnet with a nested HTS insert coil to be tested [12,13]. The 20 kA power converter is shared among all the other vertical test stands of cluster G. An additional (existing) 10 kA converter, only usable for the HFM test stand, has been installed specifically for the insert circuit [23].

The second test stand is referred to as “cluster D”, as it occupies the area formerly taken by the horizontal benches with the same name (D1-D2). It has a smaller diameter of 800 mm, but a longer length of up to 5.2 m, and can similarly operate at 4.2 K or 1.9 K. The diameter was chosen to be able to host all HL-LHC magnet models (the largest cold mass is the IT quadrupole being 630 mm in diameter), with some margin for future magnets. The choice of the length was somewhat more involved. While model magnets are typically 1 m to 2 m long, the final length main magnets can be several metres long, e.g. the 7.15 m HL-LHC Q2. Between these two limits there are a number of LHC and HL-LHC magnets of different lengths. In an attempt to maintain maximum test flexibility, the depth of the 1.9 K bath was finally chosen to be 5.2 m, which is the maximum allowed in practice by the existing building and crane geometry. The present maximum height under the crane hook is 5.5 m. Additional headroom is necessary to latch the magnet under the test insert and install the insert in the cryostat. This is achieved by installing the cryostat in a pit, the working level of which is -3 m with respect to the floor (see Figure 2). The base of the cryostat is installed at a depth of -10 m.

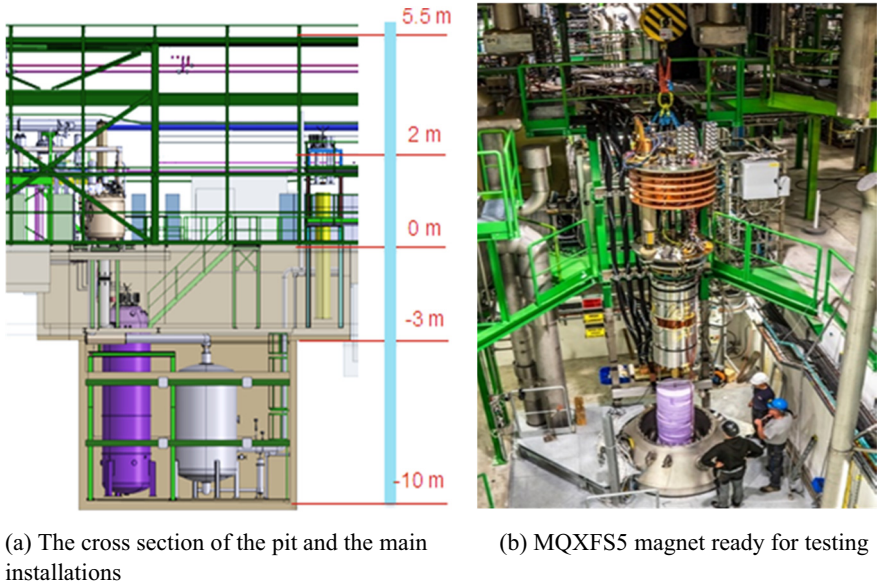


Fig. 2. Cluster D

This way, all HL-LHC magnets can be tested in such an installation, except for the IT quadrupole Q2 and the 11 T dipole. Concerning powering, the insert of cluster D is also equipped with two pairs of current leads: one for 30 kA and one for 15 kA, thus reproducing the powering topology of HFM. For now, the plan is to equip this test stand only with the main powering circuit. The main characteristics of the two new test stands are reported in Table 1.

Table 1. Main characteristics of the new vertical cryostats

NEW VERTICAL CRYOSTATS			
		CLUSTER D	CLUSTER G*
Cryostat	Diameter [mm]	800	1500
	Useful length [m]	5.2	2.5
	Lambda plate	Stainless Steel (SS)	
	Lambda plate sealing	ePTFE	ePTFE
Cooling	Operational temperature [K]	4.2/1.9	4.2/1.9
	He gas recovery buffer [m ³]	8	10
	Pre-cooling with 80 K He gas	yes	
Power	Primary circuit [kA]	30	20
	Secondary circuit [kA]	15	15
EE	Switch type	IGBT	thyristor
	Dump resistor [mOhm]	modular	

* This particular cryostat, the 4th in the cluster G, is designed for testing the FReSCa2 magnet.

Although very different in dimensions, the designs of the two new test stands have many similarities. The HFM and cluster D cryostats are pre-cooled from 300 to 80 K by high pressure He flow chilled directly using liquid N₂. This contributes to a more efficient global cooling boosted by the dimensions of the heat exchangers integrated into the cryostat.

Finally, due to the stored magnetic energy being so high, and the sheer number of expected tests and quenches, the test stands have been equipped with a cold He recovery buffer to collect the exhaust during a quench. Both the HFM and cluster D have a cold buffer with a capacity of 10 m³ and 8 m³, respectively. After a quench – the cold He gas, upon attaining a pressure of 5 bar – is recovered from the cryostat to the buffer. The cold gas remains then available for cooling the cryostat, if necessary, or can be redirected into the system for recovery in the cycle.

While HFM reuses existing infrastructure, a large part of the circuit for cluster D had to be rebuilt. With the goal of minimising the cost of the SM18 upgrade project, it was decided that the two 15 kA capacity power converters already present in the test stands will be reused. Their capacity had been boosted by an increase in water flow, and by connecting them in a parallel configuration in order to deliver up to 30 kA. It should be noted that although this current level largely exceeds present demand – 30 kA of powering capacity is an interesting option for future developments. The electrical powering circuit of HFM and cluster D is designed to withstand up to 3 kV. The consequence was that to fully benefit from such a power converter, the whole electrical circuit required dimensioning for 30 kA. Starting with the warm, water-cooled copper cables, through the energy extraction (switch and dump resistor) system, and all the way through to the current leads.

Given the challenges of increased stored energy and operating current density – and to avoid potential damage to the R&D magnets during training and provoked quenches – an energy extraction system with a reaction time below 1 ms had been specified. The energy extraction system comprises of a switch and an external dump resistor. To achieve this fast reaction time, it had been decided that a switch using IGBT technology would be built. The switch for the 30 kA circuit is composed of 4 modules, 7.5 kA each. The switch – one of the most challenging elements of the test stand – was designed and built entirely at CERN [14].

Finally, the current leads for both HFM and cluster D were also designed at CERN. Component fabrication took place partially at CERN and partially in industry. The final assembly and tests have been done at CERN. The current lead design relies on classical vapor-cooled technology – the same as all other current leads used in SM18 test stands.

2.1.3. *Horizontal test stands for cryo assemblies*

At the time of testing for the LHC, the SM18 hall was composed of 6 test clusters, each of them having two benches – called 1 and 2 – sharing a common powering and data acquisition (DAQ) system. Each cluster, named from A to E, was equipped with a dedicated electrical circuit for the main magnets and a secondary circuit(s) for the correctors. In the last 10 years, renovation works have been taking place with the goal of upgrading and optimising the SM18

test hall for HL-LHC magnets and future projects. One of the clusters had been transformed to a vertical test stand called cluster D, as described here before.

Each bench can host any of the LHC cryo-magnet assemblies, i.e. up to a maximum length of 16 m and a mass of 35 tonnes. The benches are designed to sustain vacuum forces acting on the cryostat ends up to 8 tonnes. Each cluster is equipped with a main powering circuit, i.e. power converter, warm cables and current leads, up to values of 13 kA/±16 V, and two powering circuits for correctors, up to 600 A/±12 V. There are neither switches, nor energy extraction (EE). Cluster A offers additional testing flexibility due to a different main circuit, equipped with a 17 kA/±61 V power converter. Cooling of the magnets is either at 4.2 K, or 1.9 K, whereby in the latter case the heat exchanger must be located in the magnet being tested, while the test bench only provides helium pumping and phase separation.

To respond to the requirements of HL-LHC serial production, the main part of the horizontal test facility required modifying the cryogenic interface and an upgrade of the electrical circuit: both the high current part (from 13 kA to 20 kA) and the low current for the corrector circuits (from 600 A to 2 kA). On some benches, the energy extraction system had to be integrated with the new CLIQ protection system, as well as the universal quench detection system (uQDS). This ensures that, at least on test bench, it is fully representative of all the systems in the tunnel configuration, prior to the HL-LHC IT String test. The testing strategy for the HL-LHC cold masses was defined so as to have redundancies, and therefore to minimise the risk of using ageing test benches. Therefore, for the most demanding tests – those of the 11 T dipoles and the triplet quadrupoles – two independent test benches were defined. Test benches C1 and C2 were modified and dedicated to the 11 T dipole, while benches A2 and F1 will be dedicated to the quadrupoles. Bench B1 was chosen to be the test stand for D1, and bench C2 for D2. The Corrector Package (CP) is foreseen to be tested on the A2 bench.

The major modification regarded powering circuits were to upgrade the 13 kA circuits to 20 kA and to change the 600 A corrector circuits without Energy Extraction (EE) into 2 kA circuits with EE (benches A2 and F1). Another important modification was the interface between the cold masses of type Q2 and the Cold Feed Units (CFU) of SM18. This is because the cooling channels of the LHC and HL-LHC magnets – with respect to the benches – are not aligned. The modification of the benches was done in two stages. Stage

one – ensuring a partial solution for the prototype magnets. Stage two – a full modification for the series testing [24,25].

2.1.4. *Current leads test stand*

All the superconducting current lead assemblies (DFLH), assembled in the corresponding DFH, will be entirely qualified at nominal operational conditions in SM18 test benches and in the HL-LHC IT String, as described in Chapter 24. A type test is planned to be performed of all the pre-series leads to validate their manufacturing and design, and about 10% of the total number of each current lead assembly type, as quality control and for eventual troubleshooting. Therefore, the tests should cover aspects of cooling, powering, and protection.

The leads are using copper for the heat exchanger part, and HTS for the lower part (below 50 K), that is then connected to the MgB_2 conductor of the SC Link. The joints between HTS and copper are done during the manufacturing process, while HTS to MgB_2 is done during the assembly of the DFH. In the test station, the cold connection between leads or from leads to the power converter will be done at the level of the MgB_2 -HTS joint. To avoid damage on the HTS side, the joints will be clamped [26].

2.1.5. *SC Link test stand*

SM18 also hosts a cryogenic powering test stand for the HL-LHC's SC link system, prior to the ultimate test that is in the HL-LHC IT String, as described in Chapter 24.

An early test stand had been set up during the R&D phase of the project in order to give design feedback during the development phase. This test stand consists of a cryogenic feed-box allowing one to test with supercritical He up to 100 K and with a powering capacity of up to 20 kA. The so-called DEMO program with several tests and configurations was completed on that test stand. The most complex test was one that allowed the flow of counter current with two 20 kA power converters and several lower current power converters. This was to check electromagnetic compatibility and cross talk between conductors during the powering of a 60 m SC link equipped with HTS leads and a He recovery system.

To accommodate serial production, the test stand should allow simultaneous testing of several electrical circuits ranging between 0.12-16.5 kA, to qualify the SC link through the current leads. An adequate system for He gas recovery is also necessary. It is worth noting that the cryogenic cooling capacity required for the SC link test is 7 g/s of He gas flow in steady state and up to 10 g/s for short periods of time, at a typical inlet temperature of 5 K and an outlet temperature of 30 K. In order to optimize the test infrastructure at CERN, the aim was to reuse, as much as possible, the equipment designed and used for the LHC main dipole and quadrupole cold mass qualification tests in SM18.

Cluster F of the SM18 test hall, as described earlier, and shown in Figure 1, is going to be dedicated to the HL-LHC SC link, and is therefore going through essential transformation and adaptation. The electrical circuits composed by the SC link and the interface modules, current leads, and converters will be completed with water-cooled and air-cooled cables, depending on the respective needs. Where possible, existing cables will be reused. Regarding cooldown and warmup, the liquid helium inlet will be via the existing CFB of the F2 bench. For the outlet, the upgrade of the test bench will require a warm helium gas recovery system next to the DFHx/m module. It will collect He circulating all along the link, and exiting the current leads. There are no major modifications foreseen to the CFB in order to accommodate the interconnection of the SC link to the test bench. This interconnection will be done by means of a DFX module for the first SC link assembly, and by means of a dedicated interconnection module for the rest. The reasoning is that at least one DF module should be tested in nominal operating conditions, but there is no need to cold test all of them.

A warm helium gas ($T > 280$ K expected) recovery system from the current leads of the DFH module is implemented [27]. There are four different current rating circuits: 18 kA, 7 kA, 2 kA and 0.6 kA, that will make use of four different power converters. The 2 and 18 kA power converters are needed also for the magnet testing on the F1 test bench and they are to be installed as part of the upgrade program for the magnet test bench. The 7 kA circuit is an existing one on the closest bench in what is called cluster E. From the electrical point of view, the most demanding test will be performed on the DFHx-DSHx assembly, which will need all of the above-mentioned power converters at the same time.

The quench detection system will be, as in the machine, the so called uQDS developed for the HL-LHC.

The so-called Patch Panel Interface (PPI) will provide the flexibility needed for testing operations, while having a fixed connection to the current leads. This will simplify design and manufacturing, and prevent any potential damage to the current leads during test [28]. It will be placed upstream of the DFH current leads and will perform the role of the circuit disconnecter box (CDB), albeit without circuit opening capabilities, and being driven manually.

2.1.6. *Cold diodes test stand*

Cold diodes can be tested in the vertical test cryostat developed for the testing of the LHC cold diodes at 4.2 K and 20 kA in the SM18 vertical test facility (Cluster G).

2.2. *Test facilities at collaborators' premises*

As with magnet design and fabrication, the HL-LHC collaborators play an important role – they also participate in testing activities. Several test stands have been upgraded or built with the purpose of allowing testing of one or several types of magnets or cryo magnets.

2.2.1. *Test stands in US laboratories*

Vertical test cryostat at BNL (USA)

In order to test the AUP-built MQXFA magnets, the vertical superconducting magnet test facility of the Superconducting Magnet Division (SMD) at BNL has been upgraded to perform testing in superfluid He at 1.9 K and 1 bar. This has involved extensive modifications to the 40-year old, 4.5 K cryogenics plant and vertical test facility at the SMD. The SMD has five vertical test cryostats, of which the 6.1 m deep Test Cryostat 2 was modified by inserting a new, redesigned inner He vessel, with a 4.5 K heat shield, into the existing outer Dewar. This extended the useful length by 200 mm in order to accommodate wider and longer magnets, up to 5 m long, and can therefore accept the MQXFA quadrupole magnets which approach 5 m in length. The facility is equipped with a 24 kA powering circuit associated with an IGBT based Energy

Extraction system, and the recently CERN designed CLIQ protection system is integrated to the magnet protection circuit. The variation of current thresholds is dealt within the software, and is therefore automatic during ramps. In addition, the ability to set a variable current threshold in the software is new feature of the test stand. It is necessary when working with Nb₃Sn magnets to avoid false alarms of the quench detection system. This test facility allows for testing of all US-collaboration-produced magnets in vertical position prior to their integration into a cold mass. In total, 27 MQXFA type magnets are to be tested in that test cryostat, including models and prototype magnets. At the time of writing 6 MQXFA magnets have been tested in the BNL facility, that is now in full operational mode [29,30].

The Horizontal test stand at FNAL (USA)

In order to test AUP-built LQXFA/B cryo-assemblies, the horizontal test stand also known as Stand 4, located in Industrial Building 1 (IB1) of the APS-TD in FNAL, is being upgraded. Various improvements have been made to improve overall reliability of the cryo-plant. Four extra tanks were added to the existing six buffer tanks for storage of helium gas. FNAL is in the process of procuring a new liquefier, increasing the total LHe production rate to 600 l/h and total liquid storage volume to 14,000 l. At the test stand, the feed box contains a liquid helium vessel within the vacuum vessel, and the liquid-nitrogen-cooled thermal shield. A removable insert includes the helium vessel top plate with three 15 kA vapour-cooled current leads and an instrumentation tree, displacers, a liquid-nitrogen-cooled baffle shield, a support plate (formerly the lambda plate) with instrumentation and power feedthroughs, and the power bus. The 15 kA current leads have been successfully tested up to 20 kA operation. The adapter box is an extension of the feed box and contains features required to test the HL-LHC Cryo-Assemblies. The adapter box allows for the use of the old feed box without modifications to accommodate the new design of the Cryo-Assembly. The separation between the 4.5 K and 1.9 K temperature levels is within the adapter box. In total, one prototype and ten series magnet tests are foreseen on that test stand to fulfil the primary test objectives that are the qualification and acceptance of the LQXFA/B cryo assemblies for the HL-LHC, including field and alignment measurements (apart from the quench performance) at 1.9 K [30,31].

2.2.2. *The test stand at INFN-LASA (Italy)*

In their LASA laboratory in Milan, INFN Italy is hosting a test stand able to test both superconducting radio frequency (RF) cavities, and magnets. For the HL-LHC project, the charmingly-titled DISCORAP¹ was modified to allow testing, in optimal conditions, the high-order corrector (HO) magnets designed and produced within Italian collaboration. The cryostat with an inner diameter of 697 mm and an operating pressure of 4.5 bars, shielded actively with LN₂, allowed initially to test magnets with lengths of up to 5 m and weights of 5 tonnes. In that space a second cryostat was inserted, called MAGIX, with 515 mm in diameter and 3000 mm in length for operation in 4 K and up to 500 A. The test configurations are such that regroups several magnets for the same cool down. The test stand is equipped with magnetic measurement shafts as well. Also, at LASA the experience of the HL-LHC is fundamental to making plans that are underway for a test bench – at 4.2 K – to serve the next generation dipole magnet development [32].

2.2.3. *The test stand at FREIA (Sweden)*

FREIA in Sweden has established with the HL-LHC project, in 2016 for cryogenic testing of both Sc RF cavities and magnets for HL-LHC. Within this collaboration agreement, the vertical magnet test facility has been designed to allow testing corrector magnets of type MCBXFA/B, MCBRD, etc. The test facility required the construction of a vertical test cryostat with 1.1 m in diameter and 2.65 m below the lambda plate for 1.9 K operation. The test stand is equipped also, as are the vertical test cryostats at CERN, with two independent powering circuits composed of a 2 kA power converter, and an Energy Extraction system using IGBT switches. The quench detection system is entirely compatible with the one used in SM18 at CERN, using the CERN developed POTAIM cards. The test stand is, however, not equipped with a magnetic measurement shaft [33].

2.2.4. *The test stand at CEA (France)*

CEA in Saclay, within the project STAARQ, designed a double bath vertical cryostat with a pressurized superfluid bath to test the MQYY type magnets.

For these 4 m long, double aperture, large bore (90 mm), large diameter (614 mm), heavy (8.9 t) magnet – this vertical cryostat modification is quite challenging. Taking this opportunity, the Saclay team upgraded the whole infrastructure in 4 main parts: internal and external cryogenics, the He liquefier and the powering, safety and acquisition system. This test cryostat, although not financed by HL-LHC, allows for the testing of an MQYY magnet in the vertical position [34].

2.2.5. The test stand at IMP (China)

The test stand in IMP is being developed following the collaboration agreement between HL-LHC and China for the production and testing of the MCBRD corrector magnets. The test stand consists of a vertical cryostat of 700 mm in diameter, allowing one to test the magnets at 4.2 K. Although the acceptance criteria of the HL-LHC magnets are at 1.9 K superfluid He temperature, a derogation was given to the collaboration to test the magnets at 4.5 K, but at a higher current. The tests are done with energy extraction. Magnetic measurement can be performed with a rotation probe [35].

2.2.6. The test stand at KEK (Japan)

Japan is responsible for the design and production of the D1 magnets. They are also responsible for the cold powering test in the vertical cryostat at KEK of the MBXF magnet. The magnet test cryostat allows tests at 4.2 and 1.9 K of a magnet as long as 7.5 m, with a diameter of 700 mm. The test cryostat had been equipped with a new header, allowing the test with an anti-cryostat with 141.3 mm in diameter and 15 kA current leads, for a nominal operational mode of the D1 magnet at 12 kA. The powering circuit is equipped with an Energy Extraction system with thyristor-based switches and variable dump resistors. A new DCCT has been added to the accurate and stable current measurements. Magnets, and one prototype will be tested in that cryostat for the HL-LHC [36].

Table 2. Summary table of available test facilities

Test Location	Bench Name	Device Name	Test Condition
CH CERN	A2, F1	Q2a, Q2b	Horizontal, 20 kA + 2 x 2 kA, 1.9 K
	A2, A1	Q1, Q3	Horizontal, 20 kA, 1.9 K
	B1, A1, A2	D1	Horizontal, 13 kA, 1.9 K
	C2	D2	Horizontal, 13 + 2 x 0.6 kA, 1.9 K
	A2	CP	Horizontal, 2 x 2 kA, *EE+ 8 x 0.12, 1.9 K
	C1	11T	Horizontal, 20 kA, 1.9 K
	F2	SC link	Horizontal, 0.6-20 kA, 20-300 K
	Feed Box	HTs leads	Vertical, 0.6-20 kA, 20-300 K
	Diode	Diode	Vertical, 20 kA, 4.2 K
	HFM	MQXFS, MBH	Vertical, 20 kA, *EE, 1.9 K
	Cluster D	MQXFS, MCBXFA/B, MCBRD	Vertical, 30 kA, EE, 1.9 K, 2 x 2 kA, EE
US FNAL	Stand4	Q1, Q3	Horizontal, 20 kA, 1.9 K
US BNL	SMD	LQXFA	Vertical, 24 kA, 1.9 K
Japan KEK		MBXF	Vertical, 15 kA, 1.9 K
Sweden FREIA	GERSEMI	MCBXFA/B	Vertical, 2 x 2 kA EE* + 1.9 K
Italy INFN	LASA	HO correctors	Vertical, 13 kA, 1.9 K
China IMP		MCBRD	Vertical, 0.6 kA, 4.5 K
France, CEA	SAARQ	MQYY	Vertical, 16 kA, 1.9K

References

1. M. Bajko, "Magnet Test Plan Including collaborations, String and test Stand", 7th Collaboration Meeting HL-LHC Madrid, November 2017. EDMS 1951035, <https://edms.cern.ch/document/1951035>.
2. M. Bajko, HL-LHC Interaction Region Magnets; Magnet and Cold Powering system Test Plan HL-LHC C&S Review 2019 November 2019 EDMS 2270772 CERN internal document; unpublished, <https://edms.cern.ch/document/2270772>.
3. V. Chohan, "Testing of the LHC Magnets in Cryogenic Conditions: Operational Issues & Challenges", Proc. APAC '07, January 2007, India, CERN CDS LHC-Project-Report-984.
4. G. Willering et al., "Performance of CERN LHC main dipole magnets on the test bench from 2008 to 2016", IEEE Transactions on Applied Superconductivity, 27(4) (2017), 4002705.

5. E. Todesco et al., "Training Behavior of the Main Dipoles in the Large Hadron Collider", *IEEE Transactions on Applied Superconductivity*, 27(4) (2017), 4702807.
6. E. Todesco et al., "The Magnetic Field Model of the Large Hadron Collider: Overview of Operation at 3.5 and 4 TeV", *Proceedings of International Particle Accelerator Conference (IPAC 2012)*, 20-25 May 2012, USA.
7. G. Willering et al., "Fast Cycled Magnet Demonstrator Program at CERN: Instrumentation and Measurement Campaign", *IEEE Transactions on Applied Superconductivity*, 24(3) (2014), 4004405.
8. A. Ballarino, "Development of superconducting links for the Large Hadron Collider machine, *Superconductor Science and Technology*, 27(4) (2014), 044024.
9. M. Bajko, L. Bottura, L. Rossi, "Superconducting magnet test facility SM18 upgrade for HL-LHC", November 2015, EDMS 1439872, <https://edms.cern.ch/document/1439872>.
10. L. Rossi, "LHC upgrade plans: Options and strategy", *Proceedings of International Particle Accelerator Conference (IPAC 2011)*, 4-9 September 2011, Spain.
11. H. Bajas et al., "Test set-up for the cooling of heavy magnets by controlled way down to 77 K", *Physics Procedia* 67 2015 331-337.
12. A. Van De Craen et al., "New vertical cryostat for the high field superconducting magnet test station at CERN", CEC2013, Anchorage, USA.
13. V. Benda et al., "Cryogenic design of the new high field magnet test facility at CERN", *Physics Procedia* 00 2014 000-000.
14. G.-J. Coelingh et al., "Test Results of a 7.5 kA Semi-Conductor Prototype Switch as Modular Switchgear in Energy Extraction Systems for the HL-LHC Magnet Test Facility", IPMHVC2016, San Francisco, USA.
15. M. Bajko et al., "Superconducting magnet test facility SM18 upgrade for HL-LHC: cluster A", January 2016, EDMS 1552135, <https://edms.cern.ch/document/1552135>.
16. V. Mertens, "Evolution of the Electrical Power Requirements from the Upgrade of the Sm18 Test facility and the Technical Infrastructure of the SM18 and LHC PT 1.8", August 2017, EDMS 1604702, <https://edms.cern.ch/document/1604702>.
17. L. Serio, "SM18 Cryogenic Infrastructure Upgrade Proposal", March 2016, EDMS 1571317, <https://edms.cern.ch/document/1571317>.
18. M. Bajko et al., "Superconducting magnet test facility SM18 upgrade for HL-LHC: cluster F", January 2016, EDMS 1562479, <https://edms.cern.ch/document/1562479>.
19. V. Mertens, "Upgrade of the superconducting test facilities in SM18 (B2173), Project proposal - Scope and cost estimate", August 2016, EDMS 1561688, <https://edms.cern.ch/document/1561688>.
20. E. Todesco et al., "A first baseline for the magnets in the high luminosity LHC insertion regions", *IEEE Transactions on Applied Superconductivity*, 24(3) (2014), 4003305.
21. G. Sabbi, "Nb3Sn IR Quadrupoles for the High Luminosity LHC", *IEEE Transactions on Applied Superconductivity*, 23(3) (2013), 4000707.
22. P. Ferracin et al., "Magnet design of the 150 mm aperture low-beta quadrupoles for the high luminosity LHC", *IEEE Transactions on Applied Superconductivity*, 24(3) (2014), 4002306.

23. S. Yammine, “Upgrade of the Electrical powering Circuits of the SM18 Test facilities for the HL-LHC”, November 2020, EDMS 1758151, <https://edms.cern.ch/document/1758151>.
24. M. Bajko, “Functionalities of the test bench for the HL-LHC Q2 cold masses in SM18”, September 2020, EDMS 2416565, <https://edms.cern.ch/document/2416565>.
25. M. Bajko, “The Cluster F upgrade for the testing of the HL LHC IT cold masses and the SC link System”, February 2018, EDMS 1890553, <https://edms.cern.ch/document/1890553>.
26. F. Mangiarotti, “Functionalities of the test bench for the HL-LHC Superconducting Current Leads in SM18”, October 2020, EDMS 2425482, <https://edms.cern.ch/document/2425482>.
27. G. Rolando, “Functional Specification for HL-LHC SC link test bench on CFB F2”, January 2021, EDMS 2305251, <https://edms.cern.ch/document/2305251>.
28. S. Ferradas, “Functionalities of the Test Bench for the HL-LHC SC-Link Assembly in SM18”, June 2021, EDMS 2418464, <https://edms.cern.ch/document/2418464>.
29. F. J. Muratore, (2018, May), “News from the BNL test facility”, presentation at the 2nd International Magnet Test Stand Workshop, New York, USA. Retrieved from <https://indico.cern.ch/event/704235/contributions/2931975/>.
30. S. Feher (FNAL), private communication, June 2021.
31. S. Stoynev (2019, June), “News from the FNAL test facility”, presentation at the 3rd International Magnet Test Stand Workshop, Uppsala, Sweden. Retrieved from <https://indico.uu.se/event/596/contributions/963/>.
32. M. Statera (2019, June), “News from the LASA test facility”, presentation at the 3rd International Magnet Test Stand Workshop, Uppsala, Sweden. Retrieved from <https://indico.uu.se/event/596/contributions/942/>.
33. R. Ruber (2019, June), “The FREIA laboratory”, presentation at the 3rd International Magnet Test Stand Workshop, Uppsala, Sweden. Retrieved from <https://indico.uu.se/event/596/contributions/930/>.
34. R. Vallcorba Carbonell (2016, June), “Test Stand @ CEA”, presentation at the 1st International Magnet Test Stand Workshop, Geneva, Switzerland. Retrieved from <https://indico.cern.ch/event/507584/contributions/2027922/>.
35. N. Dongsheng (2019, June), “News from the China test facility”, presentation at the 3rd International Magnet Test Stand Workshop, Uppsala, Sweden. Retrieved from <https://indico.uu.se/event/596/contributions/940/>.
36. T. Nakamoto (2016, June), “Test Stand @ KEK”, presentation at the 1st International Magnet Test Stand Workshop, Geneva, Switzerland. Retrieved from <https://indico.cern.ch/event/507584/contributions/2027926/>.

Chapter 27

Beam-beam Long Range Compensation: From Concept to Validation

Y. Papaphilippou and G. Sterbini

CERN, BE Department, Genève 23, CH-1211, Switzerland

The compensation of the long-range beam-beam interactions using DC wires is presently under study as an option for enhancing the Large Hadron Collider (LHC) performance in the framework of the High-Luminosity LHC (HL-LHC) Project. After the installation of four wire demonstrators in the LHC, a successful experimental campaign was performed, with various beam conditions and wire set-ups. In parallel, a simulation framework was established to support the experimental results in terms of the impact of the wires on dynamic aperture and thereby lifetime, for both LHC and HL-LHC.

1. Introduction

The beam-beam effect [1], related to the electromagnetic interaction between two beams, is one of the major limiting factors of collider performance. In the case of the Large Hadron Collider (LHC), the head-on effect (HO) takes place during collisions at the interaction point (IP), and the long-range effect (LR) occurs between bunches of the two beams travelling in the same beam pipe, on either side of the IPs, before they get fully separated. The detrimental impact of the beam-beam long range (BBLR) effect on the particle dynamics has been extensively studied in various colliders [2–6], including the LHC, since its design phase [7–10], operation [11, 12] and for its high luminosity upgrade HL-LHC [13, 14].

Due to the fact that BBLR kicks occur at an almost constant phase advance of $\pi/2$ and taking into account the horizontal/vertical beta functions anti-symmetry with respect to the IP, local compensation can be achieved by placing symmetrically at each side and parallel to the corresponding crossing plane, devices mimicking their field at large distance, such as electron lenses [15] or technically simpler DC current carrying wires [16]. These proposals triggered several numerical and analytical BBLR correction studies [17–25], complemented by experimental efforts in rings, such as the SPS [26], RHIC [27], DAΦNE [28] and the Tevatron [29].

In order to explore the potential of BBLR compensation for improving beam lifetime in the HL-LHC era [30, 31], four wire demonstrators were designed, embedded in the jaws of tertiary collimators (TCTs) and incrementally installed in LHC during 2017 and 2018 [32]. The hardware design choices and the experimental program goals were elaborated in two workshops [33, 34]. In the following sections, we summarise the hardware setup and the main outcomes of this experimental campaign [35], including the numerical simulations guiding the experiments [36]. Finally, we review the simulation studies exploring the wire configuration parameters in order to maximise DA for the HL-LHC nominal optics [37], thereby establishing specifications for a possible wire implementation.

2. Experimental Wire Compensation in the LHC

2.1. Experimental Setup

During 2018, all four wire demonstrators, labelled L1, R1, L5 and R5, were available for experimental studies in the LHC on Beam 2 (B2), in the left and right side of the high luminosity IPs, IP1 (ATLAS) and IP5 (CMS) (see Figure 1). For round ATS optics [38], the crossing angle between the two beams and thereby the wires lie in the vertical (horizontal) plane in IP1 (IP5). These copper wires with round cross-section diameter of 2.48 mm are embedded in both jaws of tertiary collimators [32]. Each wire can carry up to 350 A across with effective length of ≈ 1 m. The cooling of the wire (≈ 1 kW of dissipated power at 350 A) is guaranteed by the cooling circuit of the collimator jaw. The four wires can be powered with four independent power converters. Depending on the configuration of the electrical connection one

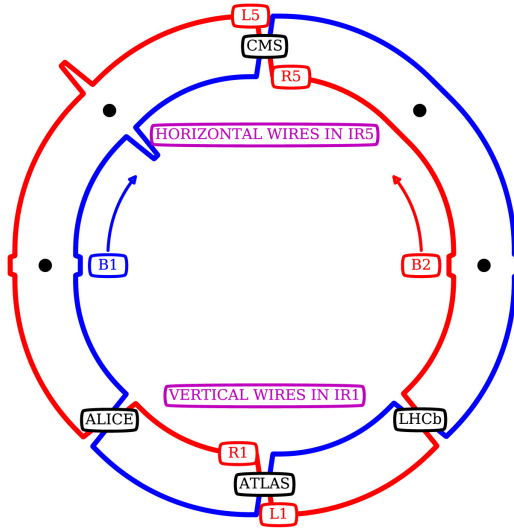


Fig. 1. A sketch representing the location of the four wire demonstrators in LHC during 2018.

or both wires at the TCT jaws can be powered by the same power converter. To compensate the dipolar and quadrupolar effect of the wire, an orbit and tune feed-forward were implemented, using the orbit corrector and the two quadrupoles closer to the wire. During the experiments, in addition to the orbit feed-forward, the LHC orbit feedback was enabled, whereas the LHC tune feedback was off. The longitudinal position of the wires, s , (see Table 1) was driven by the technical constraints of their integration in the collider, as the special wire-equipped collimators replaced existing operational ones, with the exception of L1.

The jaws of the collimator are motorized and, thanks to pick-ups placed on them [39], a precise horizontal and vertical alignment of the wire with respect to B2 can be achieved. In all the compensation experiments, the wires were powered only at top energy of 6.5 TeV and when the beams were colliding. The constraints of the demonstrators and the LHC collimation hierarchy [41] set a minimal transverse B2-wire distance, depending also on the beam intensity, as dictated by machine protection considerations. The experimental program was therefore split in two stages, the Low Intensity (LI) and the High Intensity (HI) part. During the LI experiment, the compensation principle with low intensity in B2, composed of 2 nominal bunches and 3 trains

Table 1. LHC wire parameters, including the longitudinal position, β values referring to the ATS round optics at $\beta^* = 30$ cm [40], distance and current for the Low Intensity [LI] and High Intensity [HI] experiment. Note that in the HI experiment only two out of four wires were used (corresponding values marked with dash ‘-’).

Name	s [m]	$\frac{\beta_x [\text{m}]}{\beta_y [\text{m}]}$	distance [mm], current [A] for LI/HI exp.
L1, TLCVW.A5L1	-176.17	$\frac{430}{1271} = 0.34$	-7.41/- , 350/-
R1, TCTPV.4R1	145.94	$\frac{1826}{1279} = 1.43$	7.42/9.83, 320/350
L5, TCL.4L5	-150.03	$\frac{1127}{1768} = 0.64$	-7.15/- , 190/-
R5, TCTPH.4R5	147.94	$\frac{1798}{1204} = 1.49$	8.24/11.10, 340/350

in B1, was validated by reducing the beam-wire distance settings in the four wire-collimators down to half-gaps corresponding to 5.5 collimation sigmas σ_{coll} [41]. In the HI experiment, the compensation potential was explored with high intensity in B2 with 3 nominal LHC trains in both beams but with increased beam-wire distance. The wire collimators R1 and R5 have to be set at 8.5 σ_{coll} half-gaps, whereas the operational position limits on the L1 and L5 jaw positions prevented their use, without additional setup time. In order to partially recover the LI compensation potential, the even-multipoles contributions (quadrupole, octupole, . . .) [24] of R1 and R5 were doubled by re-configuring them, as shown in Figure 2 (quadrupolar configuration). The beam-wire centre distances in the wire plane and corresponding currents for the two configurations are summarized in Table 1.

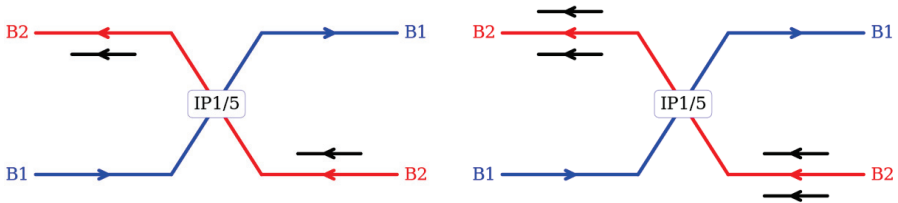


Fig. 2. A schematic representation to compare the dipolar configuration (*left*, adopted for the LI experiment) and the quadrupolar configuration (*right*, adopted for the HI experiment).

2.2. Experimental Results

Two parameters are used in order to quantify the compensation effect of the wires: (i) the beam losses and therefore the beam lifetime and (ii) the effective cross-section [42] of the bunches σ_{eff} , defined as

$$\sigma_{\text{eff}} = - \frac{1}{\sum_{IP} L_{IP}} \frac{dN}{dt}, \quad (1)$$

where L_{IP} is the instantaneous luminosity of a given IP and N is the number of protons for a given bunch. In the ideal situation, where beam lifetime is entirely dominated by particle collisions (burn-off), σ_{eff} corresponds approximately to the pp inelastic cross section (e.g., ≈ 80 mb at 6.5 TeV). The measurement procedure followed in the experiment was to setup the machine in a LR-dominated regime and, by switching regularly on and off the wire compensation, observe the behaviour of the beam losses and effective cross-section σ_{eff} .

In Figure 3 (top), the σ_{eff} evolution of the two bunches of B2 is shown during the LI experiment. The first bunch (blue curve) is colliding HO in IP1 and IP5 (PACMAN bunch) whereas the second bunch (orange curve) is experiencing, in addition to the HOs, LRs (regular bunch). The objective of the ideal compensation is to improve the lifetime of the regular bunch without degrading the one of the PACMAN. The experiments start with both bunches at the reference $\sigma_{\text{eff}} \approx 80$ mb. At 08h20, the transverse emittances of the bunches underwent a controlled blow-up for populating the bunch halo and, after that, the behaviour of the two bunches differentiates showing the clear increase of the σ_{eff} , due to LRs effect on the regular bunch. By gradually switching on the compensation, the σ_{eff} of the second bunch recovers (orange) the initial σ_{eff} almost completely, and no degradation was observed on the PACMAN bunch (blue). At 09h15, the half-crossing angle $\theta_c/2$ was reduced from 150 to 140 μrad while keeping the beam-wire separation constant. Even in this condition, the wire compensation was effective, without showing the usual losses due to the crossing angle reduction (e.g., see B1 in Figure 3 (bottom)). An additional crossing angle reduction from $\theta_c/2=140$ to 130 μrad was performed and, in this case, a moderate degradation of the σ_{eff} of the regular bunch was visible. Starting from 10h25, a partial scan confirmed that the proposed wire currents are optimal within the tested sets. In the rest of the experiment the compensation was switched on and off. The beneficial effects

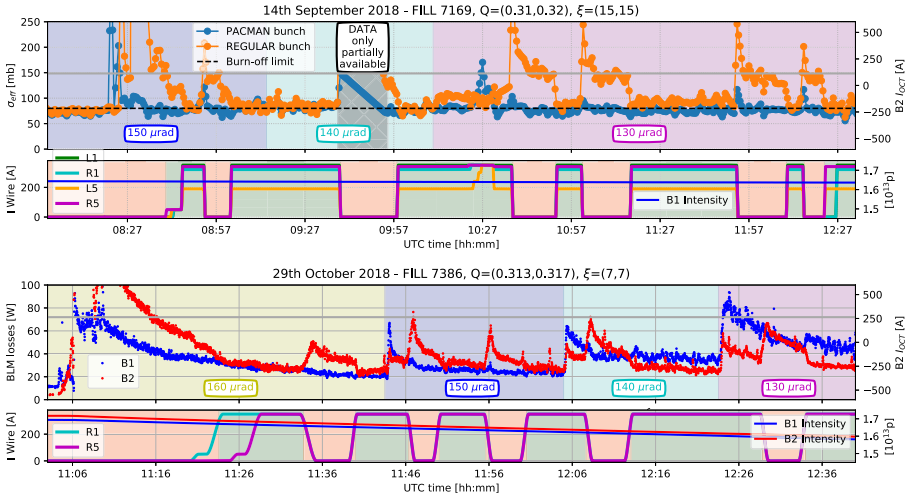


Fig. 3. Results of the Low Intensity (top) and High Intensity (bottom) experiments. Effective cross-section for PACMAN (blue) and nominal (orange) bunches and losses for B1 (blue) and B2 (red) are plotted over time. The wire currents are plotted in the bottom sub-plots.

of the wires was systematically observed. At 12h20, the compensation using only the IR5 wires was tested, confirming that, in this particular experimental setup, the IR5 wires are more effective than the IR1 ones.

In Figure 3 (bottom), the evolution of Beam Loss Monitor (BLM) losses for both beams are shown in the HI configuration, i.e. in the case where the compensation compatible with the LHC operational cycle. Tunes, chromaticity and arc Landau octupole current during the experiment were set at their operational values. After having brought the trains into collision at $\theta_c/2 = 160 \mu\text{rad}$ (11h06) and after a luminosity optimization (11h10), the B2 losses (red) were larger than the B1 ones (blue). At 11h20 the compensation was switched on and a significant reduction of the B2 losses was measured. The reproducibility of this observation was confirmed by switching off and on the wires. By reducing the $\theta_c/2$ to 150 μrad the losses increased but the ones of B2 were limited by the compensation. By switching off the compensation (11h46), the B2 losses increased significantly and they could be minimized by powering back the wires. Similar compensation scans were performed by further reducing the $\theta_c/2$ (from 150 to 140 μrad , at 12h05, and from 140 to 130 μrad , at 12h24). In all the tested configurations, the beneficial effect

of the wire compensation was systematic and reproducible, with a 20-30% reduction of the B2 losses.

3. Simulations of Wire Compensation for the HL-LHC

Tracking simulations using the HL-LHC optics version 1.3 have been undertaken in order to prove the beneficial effect of the wire [37], in the nominal and ultimate operational scenario, with round optics and crab-cavities. In order to find the best set of wire parameters for BBLR compensation, multi-parametric Dynamic Aperture (DA) scans were performed for different wire currents and distances from the beam. The four wires are located in symmetric locations at around 195 m left and right of IP1 and IP5 (next to Q4). The possible wire current and distance combinations are constrained such that two terms of the octupole-like tune-shift with amplitude are compensated [24, 37]. In the studies presented here, the optics at the end of leveling are employed with $\beta^* = 15$ cm, which is the most critical point with respect to the impact of BBLR to DA. Chromaticities are kept to 15 units in both planes and the Landau octupoles' current is either negative (-300 A) [43] or switched off. The crab-cavity effect to the beam is also taken into account.

The results of the DA scans for the nominal scenario, corresponding to 1.2×10^{11} ppb (top) and ultimate HL-LHC scenario, for 1.52×10^{11} ppb (bottom) are presented in Figure 4. These particular simulations are performed for the nominal half crossing angle of $250 \mu\text{rad}$, which corresponds to an average separation of 10.5σ for a normalised emittance of $2.5 \mu\text{m}$. For both scenarios (round optics), an optimized tune can be chosen (62.315,60.32) in order for the minimum DA for 10^6 turns, to be around the required target of 6σ for the nominal scenario, whereas, for the ultimate one, the minimum DA is slightly below 5σ [13, 14] (for zero current in the Landau Octupole). The plot axes represent the maximum wire integrated current in Am and minimum distance in beam σ of the wire R1 colorcoded with the obtained minimum DA different as compared to the uncompensated case, over 29 different initial position angles. The black curves correspond to lines with equal DA, based on a numerical interpolation. In the case of the nominal scenario, the maximum gain is around 1σ , whereas for the ultimate scenario is more than 2σ bringing the two scenarios to almost equal minimum DA of 7σ . The most striking result of these simulations is the demonstration of the existence of a large area

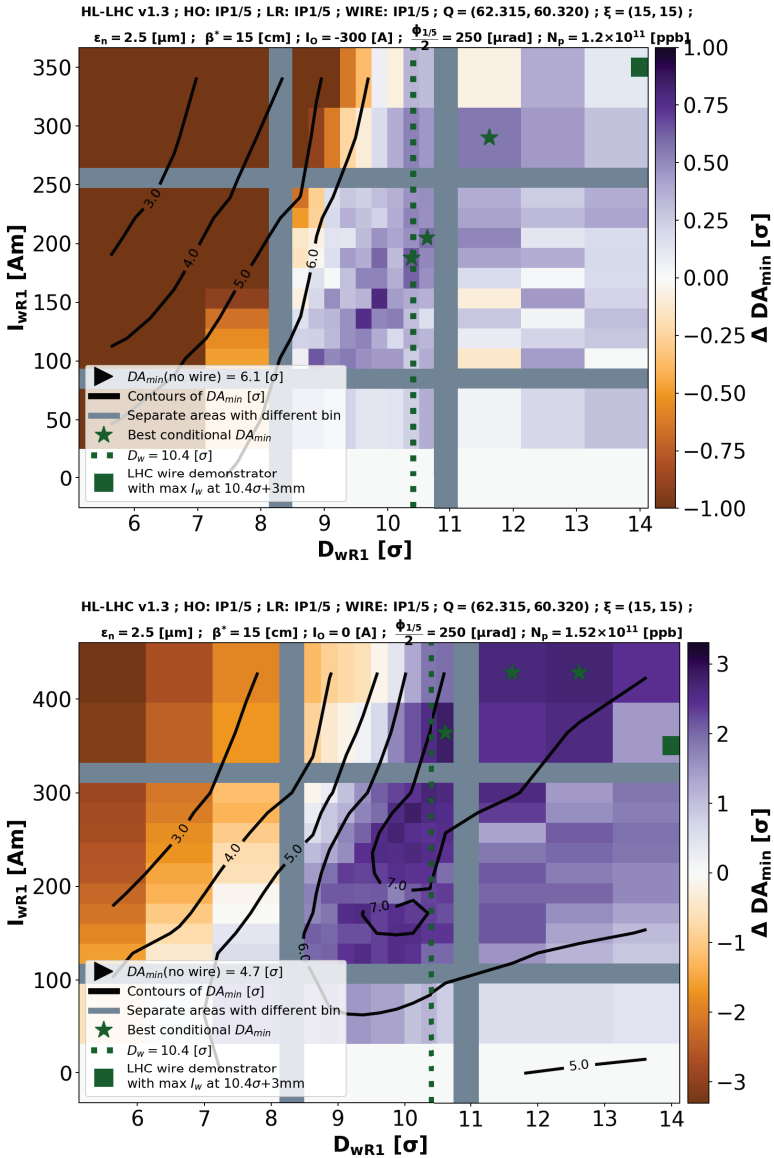


Fig. 4. Multi-parametric DA scans of wire integrated current versus distance from the beam, color-coded with the gain in minimum DA, as compared to the cases of no wires for the nominal (top) and ultimate (bottom) scenario at the end of levelling with $\beta^* = 15$ cm and nominal half crossing angle of $250 \mu\text{rad}$.

of wire and distance combinations with positive impact to the DA. In addition, the DA can be significantly improved for distances with the wire edge located above the TCT position at 10.5σ and for moderate integrated wire currents (green stars), enabling BBLR compensation without compromising machine protection considerations. Note also, that the parameters of the present LHC wire demonstrators (green square) cannot achieve the desired compensation in terms of DA, requiring a new hardware solution which is under study [45].

In Figure 5, simulation results of working point (WP) scans are presented colorcoded to the minimum DA, for the ultimate scenario. In the case without wire compensation (left), the chosen WP does not provide the target DA of 6σ . Although there are a few WPs providing, this cannot be exploited due to its proximity to the coupling resonance (marked with the dashed black line) and the implications this may have to optics distortions and collective instability issues [43]. A further drawback that was discovered through detailed DA simulations is that the optimal WP is not the same along the leveling [13, 14]. For a fixed wire current and distance beyond the TCTs obtained for the optimal WP, i.e. without further optimisation in each WP, the DA is greatly improved as shown in the right plot of Figure 5. The BBLR compensation enables a large area of WPs to guarantee a min DA above the target, thereby allowing to keep the same WP during leveling and move it even further away of the diagonal.

3.1. Improved HL-LHC scenarios

Improved nominal and ultimate scenarios can be achieved with half crossing angle at IP1 and IP5 of $\frac{\Phi_{1/5}}{2} = 190 \mu\text{rad}$ and $200 \mu\text{rad}$, respectively, as presented in Figure 6. For both cases, the DA_{\min} without wire is below 3.5σ which is catastrophic for beam lifetime and may be even difficult to handle from the collimation and machine protection point of view. With the use of wire compensators, the best configurations with wire distance above 10.4σ can provide an almost 3σ DA increase, which can guarantee good beam lifetime.

3.2. Integrated luminosity gain through wire compensators

Based on the results in Figure 6, the crossing angles during the luminosity levelling at the improved nominal and ultimate scenarios can be kept constant,

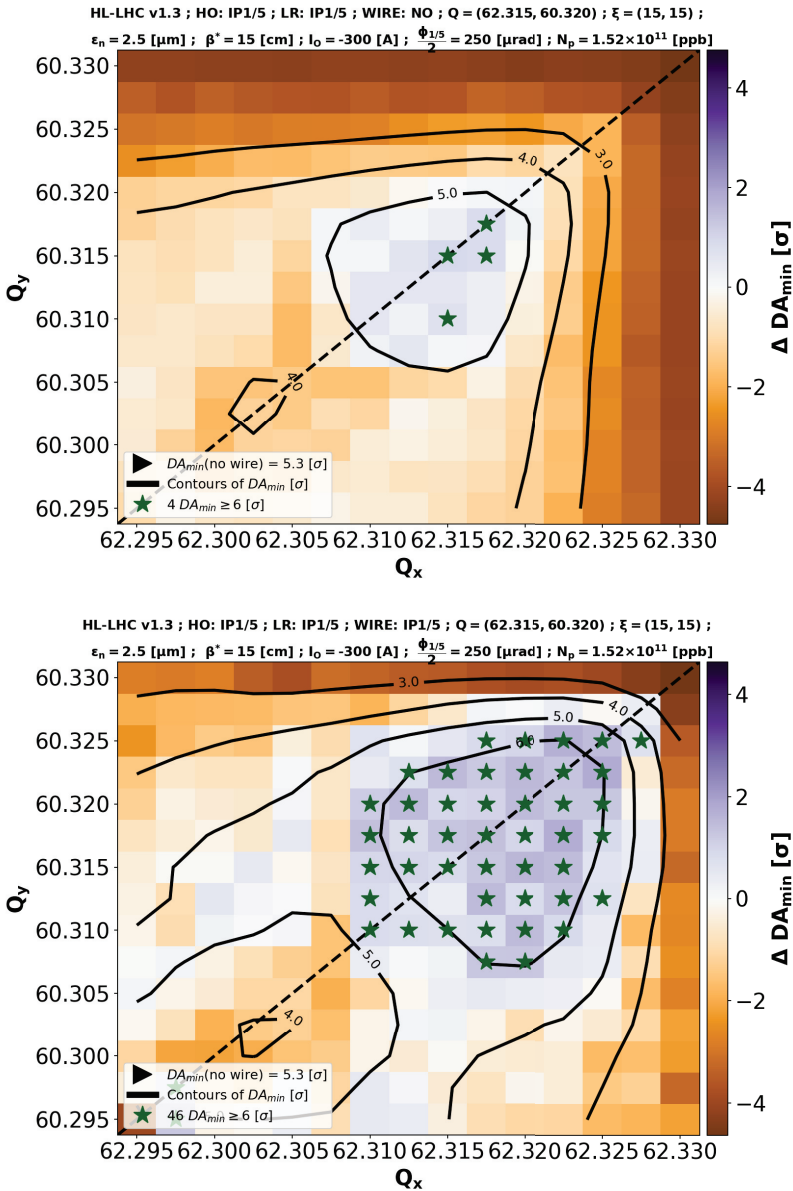


Fig. 5. Multi-parametric DA scans of horizontal and vertical tunes, color-coded with the minimum DA, for the ultimate scenario, at the end of levelling with $\beta^* = 15$ cm, without (top) and with (bottom) wire compensation.

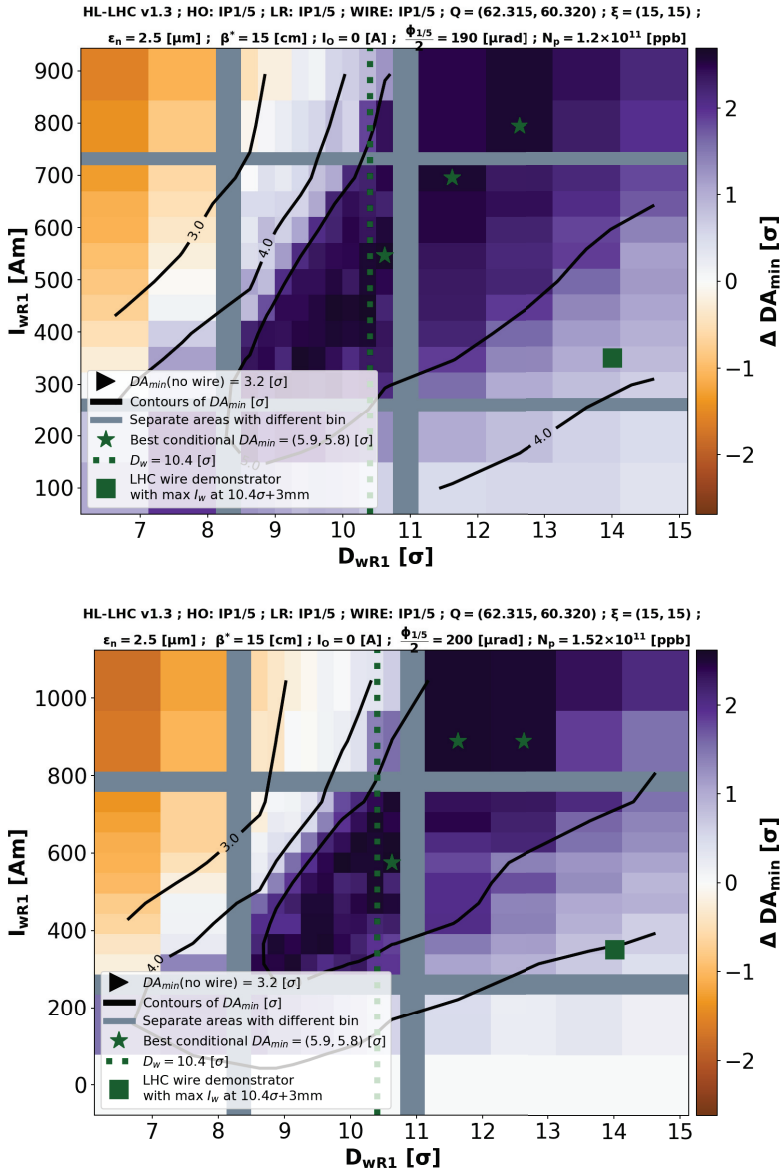


Fig. 6. Multi-parametric DA scans of wire current versus distance from the beam, color-coded with the gain in minimum DA, as compared to the cases of no wires for the nominal (top) and ultimate (bottom) scenario at the end of levelling with $\beta^* = 15$ cm and a reduced half crossing angle in IP1 and 5 of 200 μrad and 190 μrad , respectively.

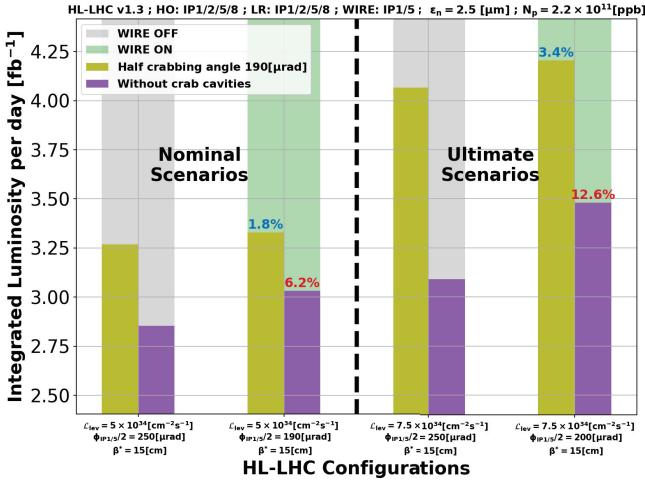


Fig. 7. The integrated luminosity per day for the current and improved nominal and ultimate scenarios of HL-LHC.

with a possibility for further reduction through levelling. Even without exploiting this margin, the luminosity levelling can be extended and the extra gain in integrated luminosity is presented in Figure 7. The scenarios that need the DC wire to be operational (improved nominal and ultimate) and with grey shade are the current nominal and ultimate scenarios (no wire compensators). With the improved nominal scenario, the gain in integrated luminosity with the crab cavities on (190 μrad crabbing) is $\sim 2\%$ over the existing nominal and $\sim 6\%$ if the crab cavities are off. The increment is more significant with the improved ultimate scenario. The gain over the current ultimate (with DA_{min} (no wire) = 4.7σ) is $\sim 3.5\%$ with crab cavities and $\sim 12.5\%$ without crab cavities.

4. Conclusions

The main results of the experimental at the LHC and simulation campaign for HL-LHC of the wire compensation are summarized. For the first time, the effectiveness of the long-range beam-beam compensation using DC wires was clearly demonstrated in an operating hadron machine. The wire demonstrators were tested in a variety of configurations showing, in all of them, their positive

impact on lifetime of regular bunches without penalising PACMAN bunches. After a convenient re-cabling of the prototypes, the compensation was also tested in the LHC operational configuration, where a reduction of 20-30% of the Beam 2 losses could be achieved. After the first clear demonstration of such a compensation during the LHC Run 2 [35], two of the four wire demonstrators have been moved from Beam 2 to Beam 1 in order to fully exploit the potential of the compensators, during operation in Run 3 [46].

The simulations have also shown that the detrimental effect from the BBLR interaction in different scenarios of the HL-LHC can be mitigated, with parameters respecting machine protection restrictions and technological feasibility. For the baseline scenario, where the minimum dynamic aperture is around 6σ , the use of wire compensators can increase the DA towards 7σ . This extra gain provides the margin for a flawless operation of the machine even in the presence of any unexpected detrimental effect (e.g. electron cloud observed during the LHC Run 2). The wire compensators can also make the ultimate scenario fully operational with DA above 7.5σ . On top of that, due to the use of wire compensators, the crossing angle of the nominal (baseline) and the ultimate scenarios can be reduced to $380\ \mu\text{rad}$ and $400\ \mu\text{rad}$ respectively, with a slight increase in integrated luminosity with crab cavities and recovering half of the lost luminosity without the crab cavities. Because of the crossing angle reduction the crab cavities voltage can be also reduced without sacrificing the machine performance. Furthermore, the strength of the correctors generating the crossing bumps, the heat load and the integrated radiation [47] that is mainly deposited in the final focus quadrupoles can be reduced, thereby increasing their lifetime. In this respect, DC wires could be considered for future upgrades of the HL-LHC baseline.

5. Acknowledgments

We would like to thank all the colleagues and collaborators contributing to the beam-beam wire compensation studies and in particular D. Amorim, G. Arduini, H. Bartosik, A. Bertarelli, R. Bruce, X. Buffat, L. Carver, C. Castro, G. Cattenoz, E. Effinger, S. Fartoukh, M. Fitterer, N. Fuster, M. Gasior, M. Gonzales, A. Gorzawski, G.-H. Hemelsoet, M. Hostettler, G. Iadarola, R. Jones, D. Kaltchev, K. Karastathis, S. Kostoglou, I. Lamas Garcia, T. Levens, A. Levichev, L. E. Medina, D. Mirarchi, J. Olexa, S. Papadopoulou,

D. Pellegrini, M. Pojer, L. Poncet, A. Poyet, S. Redaelli, A. Rossi, B. Salvachua, H. Schmickler, F. Schmidt, K. Skoufaris, M. Solfaroli, R. Tomas, G. Trad, A. Valishev, D. Valuch, J. Wenninger, C. Xu, C. Zamantzas and P. Zisopoulos.

References

- [1] E. Keil, Beam-beam interactions in p-p storage rings, in *Proc. 1st International School of Particle Accelerators "Ettore Majorana" on Theoretical aspects of the behaviour of beams in accelerators and storage rings*, Erice, Italy, 10 - 22 Nov 1976, CERN 77-13, pp. 314–340 (1977). <http://dx.doi.org/10.5170/CERN-1977-013.314>.
- [2] J. Irwin, Diffusive losses from SSC particle bunches due to long-range beam-beam interactions, Tech. Rep. SSC- 233 (SSC, Berkeley, CA, 1989). <https://cds.cern.ch/record/202623>.
- [3] *Proceeding of the Workshop on Beam-Beam Effect in Large Hadron Colliders*, Geneva, Switzerland, 1999, edited by J. Poole and F. Zimmermann. <https://cds.cern.ch/record/392054>.
- [4] T. Sen, B. Erdelyi, M. Xiao, and V. Boochoa, Beam-beam effects at the Fermilab Tevatron: Theory, *Phys. Rev. ST Accel. Beams*, **7**, 041001, (2004). <https://link.aps.org/doi/10.1103/PhysRevSTAB.7.041001>.
- [5] W. Fischer, R. Calaga, U. Dorda, A. C. Kabel, J.-P. Koutchouk, J. Qiang, V. H. Ranjibar, T. Sen, J. Shi, and F. Zimmermann, Observation of the Long-range Beam- beam Effect in RHIC and Plans for Compensation, in *Proc. 10th European Particle Accelerator Conf. (EPAC'06)*, Edinburgh, UK, paper WEPCH104, pp. 2158–2160. <https://accelconf.web.cern.ch/e06/papers/wepch104.pdf>.
- [6] V. Shiltsev and A. Valishev, Long-range beam-beam effects in the Tevatron, in *ICFA Mini-Workshop on Beam-Beam Effects in Hadron Colliders*, CERN, Geneva, Switzerland, 18-22 Mar 2013, pp. 101–107 (2014). <https://cds.cern.ch/record/1955352>.
- [7] W. Herr, Tune Shifts and Spreads due to the Long Range Beam-Beam Effects in the LHC. CERN-SL-90-06 (1990).
- [8] N. Gelfand, C. Johnstone, T. Sen, and W. Wan, Effect of the beam-beam interactions on the dynamic aperture of the LHC at collision, in *Proc. of IEEE Particle Accelerator Conference (PAC'99)*, Vol. 3 (1999) pp. 1677–1679.
- [9] Y. Papaphilippou and F. Zimmermann, Weak-strong beam-beam simulations for the Large Hadron Collider, *Phys. Rev. ST Accel. Beams*, **2**, 104001, (1999). <https://link.aps.org/doi/10.1103/PhysRevSTAB.2.104001>.
- [10] Y. Papaphilippou and F. Zimmermann, Estimates of diffusion due to long-range beam-beam collisions, *Phys. Rev. ST Accel. Beams*, **5**, 074001, (2002). <https://link.aps.org/doi/10.1103/PhysRevSTAB.5.074001>.
- [11] G. Papotti, X. Buffat, W. Herr, R. Giachino and T. Pieloni, "Observations of beam-beam effects at the LHC" doi:10.5170/CERN-2014-004.1 arXiv:1409.5208 [physics.acc-ph].

- [12] D. Pellegrini, F. Antoniou, S. D. Fartoukh, G. Iadarola, and Y. Papaphilippou, “Multi-parametric Response of the LHC Dynamic Aperture in Presence of Beam-Beam Effects”, in *Proc. 8th Int. Particle Accelerator Conf. (IPAC’17)*, Copenhagen, Denmark, May 2017, pp. 2051–2054. doi:10.18429/JACoW-IPAC2017-TUPVA009.
- [13] N. Karastathis, et al., Refining the HL-LHC Operational Settings With Inputs From Dynamic Aperture Simulations: A Progress Report, *J. Phys.: Conf. Ser.*, **1067**, 022005, (2018). <https://doi.org/10.1088/1742-6596/1067/2/022005>.
- [14] N. Karastathis and Y. Papaphilippou, Beam-beam simulations for optimizing the performance of the High-Luminosity Large Hadron Collider Proton Physics, CERN-ACC-NOTE-2020-0026, (2020). <https://cds.cern.ch/record/2715718>.
- [15] V. Shiltsev, Electron lenses for super-colliders, Particle Acceleration, Detection (Springer, New York, NY, 2015).
- [16] J. P. Koutchouk, Principle of a correction of the long-range beam-beam effect in LHC using electromagnetic lenses, CERN LHC-Project-Note 223, (2000). <http://cds.cern.ch/record/692058>.
- [17] B. Erdelyi and T. Sen, “Compensation of beam-beam effects in the Tevatron with wires,” FERMILAB-TM-2268-AD.
- [18] T. Sen and H. J. Kim, “Simulations of Beam-wire Experiments at RHIC”, in *Proc. 22nd Particle Accelerator Conf. (PAC’07)*, Albuquerque, NM, USA, Jun. 2007, paper THPAN114, pp. 3492–3494.
- [19] U. Dorda, “Compensation of long-range beam-beam interaction at the CERN LHC,” CERN-THESIS-2008-055.
- [20] H. J. Kim and T. Sen, “Simulations of Long-Range Beam-Beam Compensation in LHC”, in *Proc. 23rd Particle Accelerator Conf. (PAC’09)*, Vancouver, Canada, May 2009, paper WE6PFP031, pp. 2558–2560.
- [21] J. Qiang, “3D Strong-Strong Simulations of Wire Compensation of Long-Range Beam-Beam Effects at LHC”, in *Proc. 23rd Particle Accelerator Conf. (PAC’09)*, Vancouver, Canada, May 2009, paper WE6PFP037, pp. 2576–2578.
- [22] T. Rijoff, “Testing long range beam-beam compensation for the LHC luminosity upgrade,” CERN-THESIS-2012-377.
- [23] F. Zimmermann and H. Schmickler, Long-range beam-beam compensation using wires, *Adv. Ser. Direct. High Energy Phys.*, **24**, 243 (2015).
- [24] S. Fartoukh, A. Valishev, Y. Papaphilippou, and D. Shatilov, Compensation of the long-range beam-beam interactions as a path towards new configurations for the high luminosity LHC, *Phys. Rev. ST Accel. Beams*, **18**, 121001, (2015). <https://link.aps.org/doi/10.1103/PhysRevSTAB.18.121001>.
- [25] A. S. Patapenka, R. De Maria, Y. Papaphilippou, and A. Valishev, “Simulations in Support of Wire Beam-Beam Compensation Experiment at the LHC”, in *Proc. North American Particle Accelerator Conf. (NAPAC’16)*, Chicago, IL, USA, Oct. 2016, pp. 525–527. doi:10.18429/JACoW-NAPAC2016-TUPOB17.
- [26] F. Zimmermann, “10 Years of wire excitation experiments in the CERN SPS,” CERN Yellow Report CERN-2014-004, pp. 153–166, <http://cds.cern.ch/record/1955353>.

- [27] R. Calaga, W. Fischer, G. Robert-Demolaize and N. Milas, “Long-range beam-beam experiments in the Relativistic Heavy Ion Collider,” *Phys. Rev. ST Accel. Beams* **14** (2011) 091001. doi:10.1103/PhysRevSTAB.14.091001.
- [28] C. Milardi, D. Alesini, M. A. Preger, P. Raimondi, M. Zobov and D. Shatilov, “Dafne Lifetime Optimization with Compensating Wires and Octupoles,” arXiv:0803.1544 [physics.acc-ph].
- [29] V. D. Shiltsev, Y. Alexahin, K. Bishofberger, V. Kamerdzhev, G. F. Kuznetsov, and X. Zhang, “Experimental Demonstration of Beam-Beam Compensation by Tevatron Electron Lenses and Prospects for the LHC”, in *Proc. 22nd Particle Accelerator Conf. (PAC’07)*, Albuquerque, NM, USA, Jun. 2007, paper TUOCKI04, pp. 728–732.
- [30] Apollinari G. *et al.*, High-Luminosity Large Hadron Collider (HL-LHC): Technical Design Report V. 0.1, CERN, Geneva, Switzerland, 2017, <http://cds.cern.ch/record/2284929>.
- [31] L. Rossi and O. S. Brüning, “Progress with the High Luminosity LHC Programme at CERN”, in *Proc. 10th Int. Particle Accelerator Conf. (IPAC’19)*, Melbourne, Australia, May 2019, paper MOYPLM3.
- [32] A. Rossi *et al.*, “Progress with Long-Range Beam-Beam Compensation Studies for High Luminosity LHC”, in *Proc. 8th Int. Particle Accelerator Conf. (IPAC’17)*, Copenhagen, Denmark, May 2017, paper TUPVA115, pp. 2358–2361. doi:10.18429/JACoW-IPAC2017-TUPVA115.
- [33] “Simulations and Measurement of Long Range Beam-Beam Effect in the LHC”, 30 Nov.-1 Dec., 2015, Lyon, France, <https://indico.cern.ch/event/456856/>.
- [34] “Second workshop on Wire Experiment of Long Range Beam-Beam Effect in the LHC”, 20 March, 2017, Divonne, France, https://indico.cern.ch/event/615088.
- [35] G. Sterbini, *et al.*, “First Results of the Compensation of the Beam-Beam Effect with DC Wires in the LHC”, in *Proc. 10th International Particle Accelerator Conference (IPAC’19)*, Melbourne, Australia, 19-24 May 2019, paper WEYYPLM3, pp. 2262–2265. <http://jacow.org/ipac2019/papers/weyyplm3.pdf>.
- [36] A. Poyet, S. D. Fartoukh, N. Karastathis, Y. Papaphilippou, G. Sterbini, and K. Skoufaris, “Numerical Optimization of the DC Wires Prototypes in LHC”, in *Proc. 10th International Particle Accelerator Conference (IPAC’19)*, Melbourne, Australia, 19-24 May 2019, paper MOPMP052, pp. 566–569. <http://jacow.org/ipac2019/papers/mopmp052.pdf>.
- [37] K. Skoufaris S. Fartoukh, Y. Papaphilippou, A. Poyet, A. Rossi, G. Sterbini, and D. Kaltchev, Numerical optimization of dc wire parameters for mitigation of the long range beam-beam interactions in High Luminosity Large Hadron Collider, *Phys. Rev. ST Accel. Beams*, **24**, 121001, (2021). <https://link.aps.org/doi/10.1103/PhysRevAccelBeams.24.074001>.
- [38] S. Fartoukh, “Achromatic telescopic squeezing scheme and application to the LHC and its luminosity upgrade,” *Phys. Rev. ST Accel. Beams* **16** (2013) 111002. doi:10.1103/PhysRevSTAB.16.111002.

- [39] G. Valentino et al., “Final implementation, commissioning, and performance of embedded collimator beam position monitors in the Large Hadron Collider,” *Phys. Rev. ST Accel. Beams* **20** (2017), 081002.
- [40] The LHC optics repository, <http://cern.ch/lhcoptics>.
- [41] R. Bruce *et al.*, “Review of LHC RUN 2 machine configuration”, in *Proc. 9th Evian Workshop (EVIAN'19)*, Evian, FR, Dec. 2019.
- [42] F. Antoniou *et al.*, “Can we predict luminosity?”, in *Proc. 7th Evian Workshop (EVIAN'16)*, Evian, France, Dec. 2016, <http://cds.cern.ch/record/2289585>.
- [43] E. Metral, et al., Update of the HL-LHC operational scenarios for proton operation, CERN-ACC-NOTE-2018-0002, January 2018.
<https://cds.cern.ch/record/2301292>.
- [44] S. Fartoukh, ... The sign of the LHC octupoles, CERN-ACC-SLIDES-2014-0113, (2014)
<http://cds.cern.ch/record/1972514>.
- [45] A. Bertarelli, Wire HW design for HL-LHC and integration, Presentation in the Wire Compensation WP2/WP13 Satellite meeting, 9th HL-LHC Collaboration Meeting, 14-17 October 2019, Fermilab, Batavia, USA.
<https://indico.cern.ch/event/844153/contributions/3544326/>.
- [46] A. Poyet, S. Fartoukh, N. Karastathis, Y. Papaphilippou, A. Rossi, K. Skoufaris and G. Sterbini, “Exploiting the Beam-Beam Wire Demonstrators in the Next LHC Run 3”, in *Proc. 12th International Particle Accelerator Conference (IPAC'21)*, Online, 24 - 28 May 2021, paper MOPAB008, pp. 65–68.
<https://accelconf.web.cern.ch/ipac2021/papers/mopab008.pdf>.
- [47] F. Cerutti et al., Heat deposition and radiation dose vs operation mode and mitigation schemes, Presentation in the LHC Performance Workshop 2018, 29 January - 1 February 2018, Chamonix, France.
<https://indico.cern.ch/event/676124/contributions/2767903/>.

This page intentionally left blank

Chapter 28

Non-linear Optics Measurements and Corrections

E. H. Maclean^a, F. Carlier^a, J. W. Dilly^a, M. Giovannozzi^a, N. Karastathis^b,
T. H. B. Persson^a and R. Tomás^a

^a*CERN, BE Department, Genève 23, CH-1211, Switzerland*

^b*Former CERN member*

Nonlinear optics errors in low- β^* insertions pose a serious challenge to successful operation of the HL-LHC. LHC experience however has demonstrated that the previously assumed correction strategy, based upon ideal compensation of selected nonlinear resonances, as determined from magnetic measurements, suffers from several limitations. A beam-based correction approach yielded a positive operational impact in the LHC, and dedicated machine studies have helped establish new methods for nonlinear optics corrections in HL-LHC.

1. Motivation for Correction

Nonlinear errors in low- β^* Insertion Regions (IRs) can dramatically perturb the beam-dynamics (where β^* denotes the Courant-Snyder β function at the experimental Interaction Points, IP). At small β^* the errors in such insertions are expected to be the dominant source of nonlinear optics perturbations in both the LHC and HL-LHC. Traditionally concern in relation to nonlinear errors in the low- β IRs has focused on loss of dynamic aperture (DA, the boundary in phase space below which particle motion remains bounded for a given number of turns). DA results in beam-losses and lifetime reduction,¹ and depends on the nonlinearities present in the machine. For example, Figure 1 (left) shows simulated HL-LHC DA after 10^6 turns in the operational configuration (with beam-beam and Landau octupoles expected at end of

This is an open access article published by World Scientific Publishing Company. It is distributed under the terms of the Creative Commons Attribution 4.0 (CC BY) License.

levelling with $\beta^* = 0.15$ m), with and without normal dodecapole corrections applied in IR1 and IR5. A clear deterioration of DA is seen in the absence of nonlinear correction. Multiple studies predict that correction of nonlinear errors in experimental IRs is necessary to maintain a stable extent of phase space sufficient for productive operation in HL-LHC.

Additionally, measurement of linear optics and nonlinear observables at peak energies in HL-LHC will rely heavily on excitation of driven betatron oscillations with an AC-dipole. Machine studies in the LHC demonstrated the DA of such forced oscillations can be dramatically smaller than for free betatron oscillations.² This poses a serious challenge to HL-LHC commissioning, since a good DA will not only be required during luminosity production, sufficient forced-DA will also be necessary in order to perform optics measurements.

DA is also not the only challenge. Uncorrected IR-nonlinear errors perturb linear optics via feed-down from IR orbit-bumps. Figure 1 (right, red) shows the peak- $\frac{\Delta\beta}{\beta}$ (*peak beta-beating*, which characterises relative linear optics errors), generated in simulations of HL-LHC at end-of-squeeze due to feed-down from uncorrected nonlinear errors in the triplets and separation dipoles. Histograms over 60 instances of the errors (representative of ex-

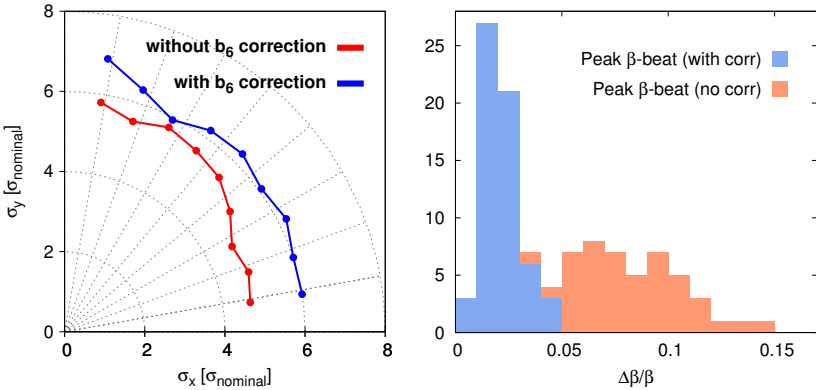


Fig. 1. Left: simulated DA after 10^6 turns during HL-LHC luminosity production, including beam-beam, with/without IR-dodecapole correction. Right: histogram over 60-seeds of simulated peak- $\Delta\beta/\beta$ in HL-LHC, without beam-beam, due to feed-down from IR orbit-bumps at 0.15 m, without (red) and with (blue) correction of all available nonlinear multipoles in the low- β^* IRs.

pected tolerances and uncertainties) are shown. In the most extreme cases, uncorrected nonlinear errors in the IRs generate a peak- $\frac{\Delta\beta}{\beta}$ which approaches machine protection limits ($\frac{\Delta\beta}{\beta} \leq 20\%$), while even more moderate cases significantly impinge on the $\frac{\Delta\beta}{\beta}$ -margin available to accommodate residuals from linear optics commissioning (typically of the order of 7% in the LHC before any orbit-bumps in the IRs, and hence any feed-down from nonlinearities, are introduced). The potential luminosity imbalance due to uncorrected feed-down can also become unacceptable, with ATLAS/CMS β^* imbalances showing comparable distributions as the peak beta-beat. The role of nonlinear errors in perturbing linear optics must therefore be considered in HL-LHC commissioning strategy.

Normal-octupole errors in the low- β^* IRs, as well as skew-octupoles and feed-down to linear coupling, can substantially distort the tune-footprint, leading to loss of Landau damping. Uncorrected normal octupole errors in the LHC have already been observed to have an impact on the instability threshold.⁴ Uncorrected normal octupole errors in the HL-LHC at end-of-squeeze could generate tune footprint distortion up to 4 times larger than those obtained in LHC.⁵ Control of collective instabilities therefore provides additional motivation for correction of nonlinear errors in the HL-LHC.

2. Motivation for Beam-based Measurement and Correction

The baseline correction strategy⁶ for nonlinear errors in HL-LHC IRs assumes the possibility of calculating ideal corrections for a wide range of nonlinear resonances based on magnetic measurements during construction, with the principle objective of optimizing dynamic aperture of free betatron oscillations. Even in this ideal case, it should be expected that beam-based measurement will still be necessary in order to validate corrections and assess residual errors: for example, quantifying residual detuning from the IRs to inform Landau damping strategy.

LHC experience however, has highlighted the limitations of the baseline approach and suggests a beam-based approach to correction may be a necessary complement to any magnetic measurements. In the LHC several discrepancies were observed between corrections based on the magnetic model and those required to minimize corresponding beam-based observables. For example,

Figure 2 shows a discrepancy between amplitude detuning expected from magnetic measurements (shown in grey, where 60 instances of the magnetic model are represented, corresponding to uncertainties in the measured errors) and that measured with beam (red). The resulting disparity in required corrections is shown in Figure 3 (center), which compares model- and beam-based settings of octupole correctors in IR1 and 5. A global discrepancy is seen at the level of 30% in amplitude detuning. Such discrepancies between the magnetic model and real accelerator could lead to sub-optimal performance.

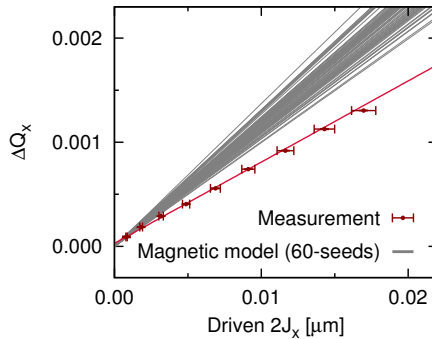


Fig. 2. Measured detuning ($\beta^* = 0.4$ m) in LHC compared to expectations from magnetic model.

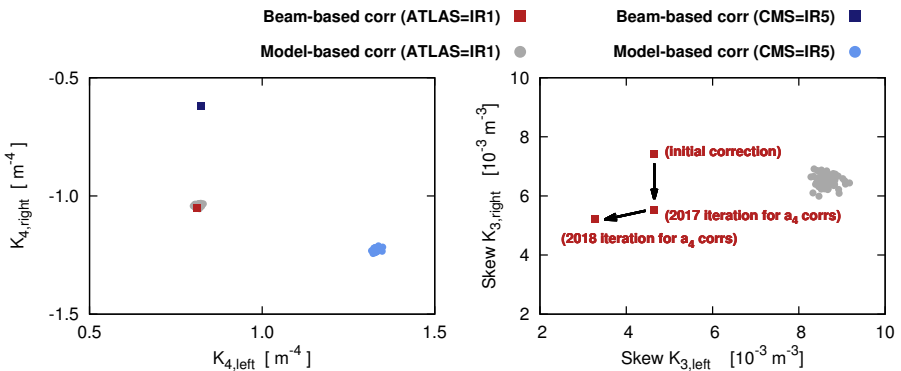


Fig. 3. Left: Beam-based normal octupole corrections in LHC IR1/5 compared to corrections from magnetic model. Right: Iterations of (beam-based) skew-sextupole corrections in LHC IR1 due to changes in skew-octupole corrector powering, compared to corrections from magnetic model.

The reason for this discrepancy is unclear. Regardless of the source however, such discrepancies motivate application of beam-based methodology to help define or improve nonlinear corrections.

Additionally, during LHC studies and commissioning it was observed that alignment errors of the high-order correctors spoiled compensation of lower-order nonlinear errors.^{8,9} For example, Figure 3 (right) shows repeated iterations of skew-sextupole corrections which had to be implemented in the LHC as a consequence of changes in skew-octupole corrector powering in 2017 and 2018. The required iterations could be identified with an anomalous 1 mm misalignment or orbit offset of the skew-octupole corrector on the right side of IR1, which introduced additional sextupole errors through feed-down once powered. Such geometric errors are not currently accounted for in the model-based correction strategy. Similarly, additional complications to a model-based correction strategy arise from the large longitudinal variation of β functions over the triplet lengths. For high-order errors (such as dodecapole sources) longitudinal variation of the error distribution within the triplet are therefore capable of causing significant changes to required corrections,¹² which are also not accounted for in the existing LHC model-based correction strategy. Such complications may be relevant to HL-LHC commissioning and motivate further development of both model- and beam-based strategies.

3. Nonlinear Optics Commissioning Experience at the LHC

A beam-based approach to nonlinear correction was adopted for LHC commissioning since 2017 (pre-2017 no IR-nonlinear corrections were performed). LHC optics commissioning strategy emphasised the interrelated nature of linear and nonlinear corrections, with several iterations of interleaved linear and nonlinear optics corrections performed. Detailed reviews of the strategy and outcome are provided.^{8–10}

Inclusion of beam-based nonlinear optics corrections into LHC commissioning strategy yielded a number of operational benefits. Of particular note, correction of nonlinear errors improved the performance of online tune measurement. This is visible in Figure 4 (left) which shows substantial reduction to noise in the tune measurement (red) as octupole correction (blue) is applied. Without this improved performance of tune instrumentation the ability to commission the linear optics in the IRs via K-modulation would be signifi-

cantly hindered, highlighting the importance of adopting an iterative approach between the linear and nonlinear optics corrections. Correction of feed-down from sextupole errors in the ATLAS and CMS insertions also significantly improved optics-related luminosity imbalance between the experiments, while better control of feed-down to linear coupling from IR-nonlinearity and better control of tune-footprint during the β^* -squeeze have been correlated with an improved performance of Landau damping since 2017.¹¹ Finally in dedicated machine studies at $\beta^* = 0.14$ m application of nonlinear corrections was observed to improve beam-lifetime during optics measurements, as seen in Figure 4 (right) which shows the change in fractional intensity for the two minutes immediately prior (red), and following (blue), application of nonlinear corrections.

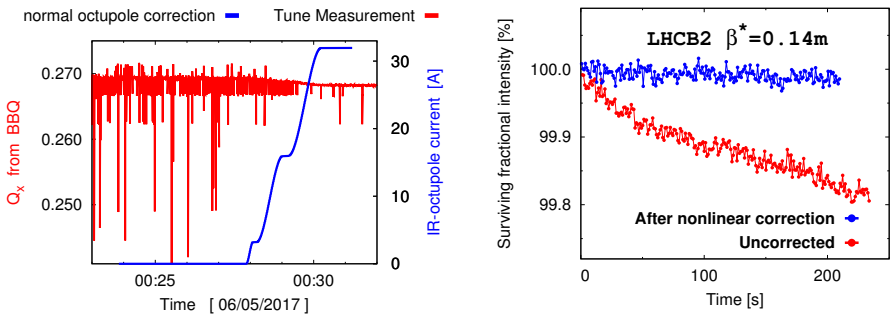


Fig. 4. Left: online measurement of LHC tune during application of octupole corrections in ATLAS and CMS insertions. Right: change in fractional intensity over 2 minutes, before and after application of nonlinear corrections in ATLAS and CMS insertions at $\beta^* = 0.14$ m during dedicated machine tests.

4. Beam-based Measurement Techniques Used at the LHC

To facilitate IR-nonlinearity correction in LHC and HL-LHC, beam-based techniques applicable to slow-cycling hadron synchrotrons were developed. Detailed reviews of the measurement techniques employed and tested at the LHC can be found in.^{8,9,12,13}

Some success had previously been obtained for IR-nonlinearity corrections at RHIC via minimization of feed-down to tune for various orbit bumps applied across an IR.¹⁴ Observation of feed-down also proved effective in the LHC.^{8,9,12} Linear and quadratic feed-down to tune was studied for various

orbit bumps in the H and V planes across each low- β IR. While the use of several custom asymmetric orbit bumps was explored in dedicated tests,²⁶ in practice studies of feed-down to tune for LHC commissioning primarily utilized the nominal crossing-angle orbit bumps, allowing correctors in IR1 and 5 to be powered in order to minimize tune shifts as a function of the operational bump.^{8,9} Figure 5 illustrates this, showing tune-shift vs IR5 crossing-angle before (red) and after (blue) sextupole correction. Where studies at RHIC focused on feed-down to tune, for LHC commissioning this was extended to also consider linear and quadratic feed-down to the f_{1001} linear coupling resonance driving term as a function of the crossing-angle orbit bumps. Optimizing tune and coupling stability vs crossing-angle was particularly relevant for crossing-angle luminosity levelling, where changes to these properties can detrimentally influence lifetime and instabilities. A primary concern during such scans is orbit leakage from the IR-bumps distorting the measurement.²⁶ Precise control of closed-orbit leakage will be a necessary prerequisite to successful nonlinear optics correction in HL-LHC.

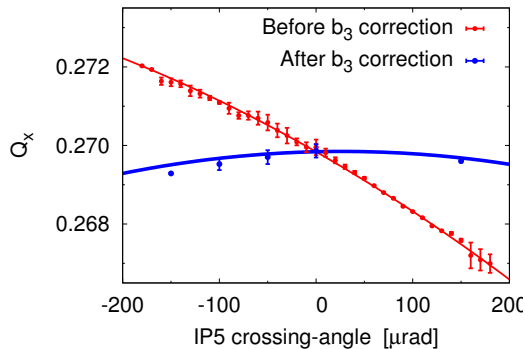


Fig. 5. Tune-shift with CMS crossing-angle, before (red) and after (blue) sextupole correction.

A further key observable developed for nonlinear optics measurements in the LHC is amplitude-detuning via AC-dipole excitation (detuning measurements via single kicks are not possible at top energy due to machine protection concerns and the beam-destructive nature of the single-kicks). Such measurements required both theoretical and experimental developments,¹⁵ but are now a routine component of LHC optics commissioning and were used in the LHC to help define normal octupole corrections in the ATLAS and CMS IRs. An

example of such a detuning measurement, used to define normal octupole corrections, is shown in Figure 2. Given the importance of high-order corrections in the HL-LHC, use of the AC-dipole was also developed for measurement of second-order detuning ($\partial^2 Q/\partial J^2$) and feed-down to first-order detuning from orbit bumps over the IRs ($\partial^2 Q/\partial J\partial\theta$) in dedicated machine tests. Both observables appear viable for study of normal/skew decapole and normal dodecapole errors at top energy in the HL-LHC.^{12,13} Examples of measurement of second-order detuning and feed-down to first-order detuning are shown in Figure 6 (left/right, respectively).

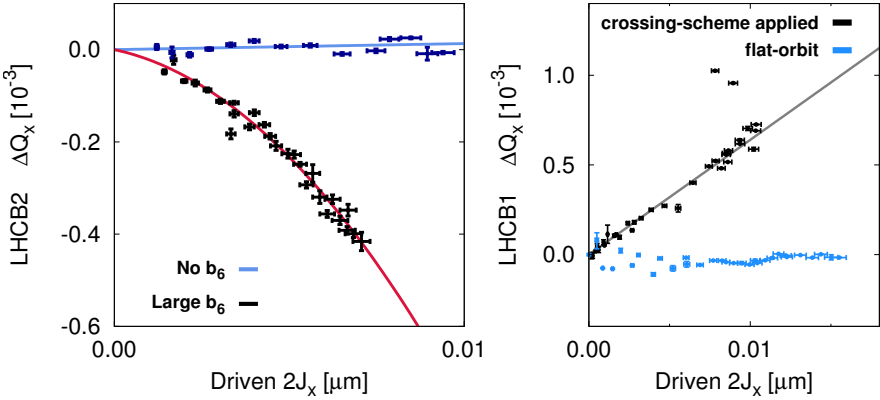


Fig. 6. Left: detuning at flat-orbit (an orbit with all IR orbit-bumps removed) with well-corrected nonlinearities (blue) and enhanced dodecapoles (red) causing a quadratic change of tune with action. Right: detuning at flat-orbit with well-corrected octupolar errors (blue), and with the IR5 crossing-angle orbit bump applied (black), causing feed-down from decapoles and dodecapoles to generate linear detuning with action.

Resonance strengths can be directly characterized by Resonance Driving Terms (RDTs). Free and forced RDTs can be measured with a single kick²¹ and AC-dipoles²² respectively. Minimization of RDTs is already used extensively in the LHC for linear coupling correction. Numerous studies of RDT measurement via AC-dipole excitation were performed during the LHC's second run. A detailed review of the methodology for AC-dipole based RDT measurement in the LHC is provided in.^{16,17} RDTs of the driven motion were successfully observed for sextupole, octupole and decapole errors.^{8,9,12,16,17} Observations of feed-down to skew-octupole RDTs were also achieved.^{12,13,16,17} Direct

beam-based correction of forced skew-octupolar RDTs was demonstrated in the LHC during 2018 commissioning,^{16,17,20} while sextupole and normal octupole RDT measurements were also used during LHC commissioning to validate corrections based on other observables.^{8,9}

Feed-down, detuning- and RDT-based measurement techniques have been developed, which proved effective in the LHC. These methods are however indirectly associated to dynamic aperture, which will be a key figure of merit to HL-LHC operation. Direct DA measurement techniques based on losses following single-kicks are impractical due to the slow machine cycle. An alternative technique, based on observing beam-loss of bunches heated to large emittance with the Transverse Damper (ADT), was demonstrated in the LHC at injection,²⁴ and later applied at 6.5 TeV.²⁵ Figure 7 (left) shows beam loss from DA observed firstly as dodecapole sources (representative of those possible at HL-LHC end-of-squeeze) are introduced (blue region), and then as corrections for sextupole/octupole errors in LHC IRs are removed (red region). DA shifts on the scale of expected errors in HL-LHC were clearly measurable, and could be associated with expected behaviours in simulation,^{12,13,25} implying direct measurement of DA is a viable observable to validate nonlinear optics corrections in HL-LHC. As described in Section 1, the DA of forced AC-dipole oscillations also represents a challenge to successful HL-LHC operation. Equally however, beam-loss via forced-DA represents a potential observable for nonlinear correction quality. During dedicated tests it was demonstrated that shifts in forced-DA could also be clearly measured for changes in nonlinear corrector powering.^{2,12,13,23}

A broad range of observables viable for study of the nonlinear optics at top energy in the LHC and HL-LHC have been developed. No individual technique was exclusively employed for study of a given multipole however, and in practice a combination of these observables were utilized for beam-based study and correction: for example normal octupole corrections were defined by a combination of detuning and feed-down studies, then validated with RDT measurements, while skew octupole corrections determined from RDT observations could be cross-checked via the quadratic feed-down to linear coupling.^{8,9} The breadth of measurement techniques now available at top energy was thus of significant benefit to the commissioning process.

5. Implications of LHC Experience to HL-LHC Commissioning

Experience from the LHC has several implications in regard to nonlinear optics correction at HL-LHC. LHC experience clearly demonstrated the importance of beam-based techniques for measurement and correction in the experimental insertions. Furthermore, while attention in regard to the nonlinear optics has traditionally (and justifiably) been focused towards preserving dynamic aperture and lifetime, LHC experience also highlighted the importance of nonlinear optics quality to the successful control of linear optics and luminosity imbalance, to the performance of beam instrumentation, and to control of Landau damping and instabilities. A particular challenge may arise if the impact from such additional effects also limit operation, since optimal corrections may differ between different figures of merit (for example between feed-down from a multipole and its directly-driven RDTs, due to different dependency on the optics functions and orbit).

The question of residual errors following correction may also be especially pertinent for some of these additional figures of merit. Figure 1 (center) showed histograms of simulated β -beating generated at HL-LHC end-of-squeeze by feed-down from nonlinear errors in IR1/5. Blue histograms demonstrate that while optics errors were reduced upon application of the ideal model-based sextupole corrections, significant optics errors could still remain ($\frac{\Delta\beta}{\beta} \leq 5\%$). While this baseline sextupole correction may be sufficient for dynamic aperture, a 5% residual beta-beat may still be unacceptable in regard to luminosity imbalance. During LHC commissioning similar residual beta-beating also remained after sextupole correction, which required additional iterations of linear optics corrections in order to achieve an acceptable luminosity imbalance. Figure 7 (right) shows histograms of simulated cross-term amplitude-detuning due to octupole errors (over 60 instances of the errors encompassing expected tolerances) at HL-LHC end-of-squeeze before (red) and after (blue) application of the ideal model-based correction. For context, the maximum detuning generated by octupole errors at $\beta^* = 0.15$ m is as large as the maximum detuning generated by the Landau octupoles. Even after corrections are applied in simulation, a large cross-term detuning remains. In some cases residual detuning after correction is still larger than any uncorrected detuning with which the LHC has been commissioned (typically $\sim 40 \times 10^3$ m⁻¹). Such residual detuning remaining after correction may still be large enough to

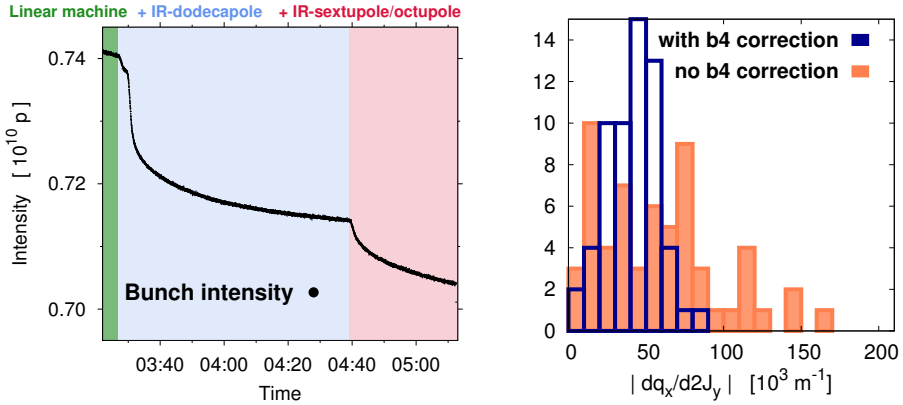


Fig. 7. Left: Beam-loss from a large emittance bunch due to reduction of DA as nonlinear errors are introduced into the LHC IRs. Right: histogram over 60-seeds of HL-LHC amplitude detuning at flat-orbit end-of-squeeze, without (orange) and with (blue) normal-octupole corrections applied in low- β^* IRs.

cause deterioration in the performance of beam-instrumentation (as discussed in Section 3) which can impede linear optics commissioning, and dependent on the β^* may also become relevant to the Landau damping of instabilities.

LHC experience has made clear that commissioning of the linear and non-linear optics are intrinsically linked. The potential for direct contributions to linear optics errors from feed-down, as well as detrimental effects on the performance of the AC-dipole and beam-instrumentation due to nonlinear errors, mean there is no guarantee linear optics commissioning will succeed at very small β^* without nonlinear corrections already in place. Equally, a reliable linear optics model is a necessary pre-requisite to the calculation of both model- and beam-based nonlinear corrections. It is anticipated that annual checks and refinement of the nonlinear optics corrections will be performed in parallel with the regular linear optics commissioning, with progressive optimization of the corrections also performed as the minimum β^* is reduced.

LHC experience also demonstrated the importance of alignment and orbit errors in the IRs to the nonlinear optics corrections. Such alignment issues meant the various orders of nonlinear multipole corrections in the LHC could not be considered independently, for example necessitating repeated recommissioning of the sextupole corrections to account for changing feed-down from the higher-orders. Optics commissioning of the HL-LHC will require an

iterative approach, both between linear and nonlinear optics corrections, and between the multipole orders. In the HL-LHC the Full Remote Alignment System (FRAS) will be used to control the alignment of IR elements with respect to the detector inner tracker and to compensate for ground motion during the year. Large changes to the alignment (of order 1 mm) are only anticipated during the commissioning phase, while during the year only small movements are expected with the aim of maintaining the magnets at their original locations. Further iterations of the nonlinear corrections may also be required during the commissioning period if any large changes to the alignment with the FRAS are performed after the initial optics commissioning.

Finally it is worth highlighting that nonlinear optics commissioning in HL-LHC assumes correction of significantly more multipole species than are currently corrected in LHC. Dedicated LHC machine studies show promise in regard to compensation of normal and skew decapoles and normal dodecapoles, however as yet no direct beam-based observable has been demonstrated for skew-dodecapole compensation.

References

1. M. Giovannozzi, *Proposed scaling law for intensity evolution in hadron storage rings based on dynamic aperture variation with time*, Phys. Rev. ST Accel. Beams 15, 024001.
2. F.S. Carlier, R. Tomas, E.H. Maclean, and T.H.B. Persson, *First experimental demonstration of forced dynamic aperture measurements with LHC AC dipoles*, (Phys. Rev. Accel. Beams, 22, 031002, 2019), <https://journals.aps.org/prab/abstract/10.1103/PhysRevAccelBeams.22.031002>.
3. R. Bruce, et al. *Updated parameters for HL-LHC aperture calculations for proton beams*, CERN-ACC-2017-0051.
4. L.R. Carver et al. *MD1831: Single Bunch Instabilities with Q" and Non-linear Errors*, (CERN-ACC-NOTE-2017-0012), <https://cds.cern.ch/record/2253143?ln>.
5. E.H. Maclean, *Non-linear IR corrections*, Presentation at the 6th HL-LHC Collaboration meeting, 14-16 November 2016, Paris, France, <https://indico.cern.ch/event/549979/contributions/2263212/>.
6. *Dynamic Aperture Studies for the LHC Separation Dipoles*, (LHC project Note 349), <https://cds.cern.ch/record/742967>.
7. E.H. Maclean et al. *First measurement and correction of nonlinear errors in the experimental insertions of the CERN Large Hadron Collider*, (Phys. Rev. Spec. Top. Accel. Beams, 18, 121002, 2015). <http://journals.aps.org/prab/abstract/10.1103/PhysRevSTAB.18.121002>.

8. E.H. Maclean *et al.* *Detailed review of the LHC optics commissioning for the nonlinear era*, CERN-ACC-2019-0029 <http://cds.cern.ch/record/2655741>.
9. E.H. Maclean *et al.* *A new approach to LHC optics commissioning for the nonlinear era*, Phys. Rev. Accel. Beams, Accepted for publication. <https://journals.aps.org/prab/accepted/7907fM9bK8d1260d11a240a5ba7078ab8655c8f08>.
10. E.H. Maclean, *New optics correction approaches in 2017*, Proceedings of the 8th Evian Workshop (Evian, 12 December 2017).
11. X. Buffat *et al.* *Transverse instabilities during run II*, Proceedings of the 9th Evian Workshop (Evian, 1 February 2019).
12. R. Tomás *et al.* Optics measurement and correction strategies for HL-LHC, CERN internal note, CERN-ACC-2022-0004.
13. E.H. Maclean, F.S. Carlier, J.W. Dilly, M. Giovannozzi, R. Tomás, Prospects for beam-based study of dodecapole nonlinearities in the CERN High-Luminosity Large Hadron Collider, in preparation.
14. F. Pilat, Y. Luo, N. Malitsky, V. Ptitsyn, BEAM-BASED NON-LINEAR OPTICS CORRECTIONS IN COLLIDERS, Proceedings of 2005 Particle Accelerator Conference, Knoxville, Tennessee.
15. S. White and E. Maclean and R. Tomás, *Direct amplitude detuning measurement with ac dipole*, (Phys. Rev. ST. Accel. Beams, 2013, 16, 071002). <http://prst-ab.aps.org/abstract/PRSTAB/v16/i7/e071002>.
16. F.S. Carlier, R. Tomás, E.H. Maclean, Measurement and Correction of Resonance Driving Terms in the Large Hadron Collider, submitted to Phys. Rev. ST. Accel. Beams.
17. F.S. Carlier, Ph.D Thesis, A Nonlinear Future - Measurements and corrections of nonlinear beam dynamics using forced transverse oscillations, Amsterdam U., 2020, CERN-THESIS-2020-025.
18. E.H. Maclean *et al.* *Report from LHC MD 2158: IR-nonlinear studies*, CERN-ACC-NOTE-2018-0021, <http://cds.cern.ch/record/2306295>.
19. J.W. Dilly *et al.* *Report from LHC MD 3311: Amplitude detuning at end-of-squeeze*, CERN note in preparation.
20. F. Carlier *et al.* *Correcting IR4 a4 using IR correctors and resonance driving terms*, Presentation to CERN LHC Machine Committee, 30 May 2018, CERN. <https://indico.cern.ch/event/733065/contributions/3023333/>.
21. R. Tomás, *Direct Measurement of Resonance Driving Terms in the Super Proton Synchrotron (SPS) of CERN using Beam Position Monitors*, CERN-THESIS-2003-010 (2003).
22. R. Tomás, M. Bai, R. Calaga, W. Fischer, A. Franchi and G. Rumolo, *Measurement of global and local resonance terms*, Phys. Rev. ST Accel. Beams 8, issue 2, 024001 (2005). <http://prst-ab.aps.org/abstract/PRSTAB/v8/i2/e024001>.
23. F. Carlier *et al.* *Probing the Forced Dynamic Aperture in the LHC at Top Energy Using AC Dipoles*, 9th International Particle Accelerator Conference, Vancouver, Canada, 29 Apr - 4 May 2018, pp. MOPMF033.

24. E.H. Maclean, M. Giovannozzi and R.B. Appleby, *Innovative method to measure the extent of the stable phase-space region of proton synchrotrons*, Phys. Rev. Accel. Beams, 22, 034002, 2019, <https://journals.aps.org/prab/abstract/10.1103/PhysRevAccelBeams.22.034002>.
25. E.H. Maclean, F.S. Carlier, M. Giovannozzi and R. Tomás, *Report from LHC MD 2171: Dynamic aperture at 6.5 TeV*, CERN-ACC-NOTE-2018-0054
26. E.H. Maclean et al. *New methods for measurement of nonlinear errors in LHC experimental IRs and their application in the HL-LHC*, Proc. IPAC 17. Copenhagen, Denmark.
27. R. Tomás et al. *CERN Large Hadron Collider optics model, measurements, and corrections* Phys. Rev. ST. Accel. Beams, 13(121004), 2010.

Chapter 29

The Role of Noise on Beam Stability and Performance in HL-LHC

X. Buffat^a, S. V. Furuseth^{a,b}, E. Métral^a, T. Pieloni^b, C. Tambasco^b and D. Valuch^c

^a*CERN, BE Department, Genève 23, CH-1211, Switzerland*

^b*EPFL, Lausanne, CH-1015, Switzerland*

^c*CERN, SY Department, Genève 23, CH-1211, Switzerland*

The beam response to an external excitation may result in a growth of the emittance, or more generally a modification of its particle distribution. The former reduces the luminosity, and the latter might lead to a loss of Landau damping of coherent instabilities. The corresponding beam dynamics model, experimental studies at the LHC as well as extrapolations to the HL-LHC are discussed in this chapter.

1. Introduction

Beam instability models at the LHC have evolved significantly over its first two runs, allowing for a significant reduction of the need for Landau octupole magnet to a level compatible with HL-LHC requirements.¹ Nevertheless, discrepancies between observations and expectations remains, especially when the beam is circulating in steady conditions for several minutes. Here we seek an understanding of this discrepancy in order to make accurate extrapolation to the HL-LHC configurations and consequently ensure that the proper mitigation measures are put in place.

Noticing that modifications of the beam distribution, beyond the reach of transverse profile measurements, could lead to drastic reduction of Landau damping, it was postulated that non-uniform diffusion mechanisms could lead eventually to instabilities.² Since the time scale of the diffusion mechanisms

This is an open access article published by World Scientific Publishing Company. It is distributed under the terms of the Creative Commons Attribution 4.0 (CC BY) License.

is usually much longer than those of coherent instabilities, a key feature of this mechanism is the existence of a latency.

We start by discussing the existing models of decoherence due to an external excitation with a broad spectrum as well as a characterisation of the present machine noise through its effect on the transverse emittance in collision in Section 2. Secondly, models of the evolution of the beam distribution in the presence of noise and electromagnetic wake fields leading to loss of Landau damping are described in Section 3. Finally, mitigation strategies are addressed in Section 4.

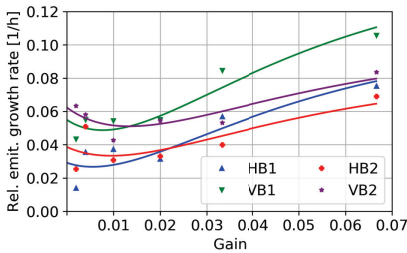
2. Decoherence

In the presence of amplitude detuning due to non-linear forces such as lattice non-linearities, octupole magnets or beam-beam interactions, a growth of the emittance is expected when the whole beam experiences a transverse kick. The decoherence is caused by the difference in oscillation frequency of the individual particles in the beam leading to desynchronization of their respective motion, often called filamentation.³ The effect of an external source of noise is usually modelled as a series of small uncorrelated kicks leading to a slow growth of the transverse emittances.

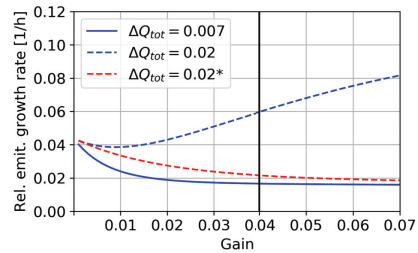
By reducing the beam oscillations faster than the decoherence mechanism, a transverse damper is capable of mitigating the resulting growth.⁴ The efficiency of such a system has limits linked to the available technology, in particular the kicker bandwidth prevents the LHC damper to act differently on the particles within a bunch. It can however act independently on each bunch.

The damper is most efficient at suppressing the effect of an external source of noise when decoherence is slow, i.e. when the amplitude detuning in the beam is small. As a result, the highest growth rate is expected when the beams are colliding due to the effect of head-on beam-beam interactions. We note that the strength of the head-on beam-beam interactions is multiplied by a factor ≈ 3 in the HL-LHC w.r.t. to the LHC due to the increase of the beam brightness and the partial compensation of the crossing angle by crab cavities (See Chapter 7). In order to probe this regime of operation, a set of experiments were conducted at the LHC by bringing in collision high brightness single bunches, which are already available from its injector chain without upgrade, their main results are reported here.

The beam dynamics models describing the emittance growth in collision could be verified experimentally at the LHC,^{4–7} the main features of the model considered as the most accurate are illustrated in Figure 1b: for a low gain, the emittance growth is dominated by the integrated machine noise floor (e.g. dipole field ripple). For a high gain, the behaviour depends on the noise introduced by the damper which is proportional to its gain, the dominant source being the measurement pickups' noise floor.⁸ This noise may overcome the beneficial effect of the damper and therefore lead to an increase of the emittance growth at high gain. This effect was observed in a dedicated experiment in the LHC, allowing for a beam-based measurement of the machine and damper pickups noise floor (Figure 1a). Whereas the causes for the machine noise floor are subject of several investigations,^{9–11} the estimated pickup noise floor is compatible with expectations with a remarkable accuracy of about 10%.⁸ A conservative extrapolation of these results, assuming an identical machine noise floor, i.e. neglecting additional source of transverse noise such as the crab cavities¹² and large β functions (See Chapter 26), shows that a reduction of the emittance growth rate below 4%/h requires an improvement of the pickups' noise floor. A new readout electronics technology was developed and tested with beam at the end of Run2 yielding promising results.¹³



(a) Measurement at LHC



(b) Extrapolation

Fig. 1. Emittance growth measured at the LHC, with high brightness single bunches featuring a beam-beam tune shift comparable to HL-LHC design, with fits of the model⁴ yielding a machine noise floor of $\approx 5 \cdot 10^{-5}$ times the r.m.s. beam size and a pickup noise floor of $0.9 \mu\text{m}$. An averaged fit is reported in dashed blue on the right, along with an extrapolation to a reduced beam-beam parameter corresponding to the present LHC configuration (solid blue) or pickup resolution improved by a factor 4 (dashed red). The black line marks the current operational damper setting corresponding to a 50-turn damping time. The value corresponding to the present LHC matches the observed growth in physics conditions.¹⁶

Through the mechanism discussed above, while the large amplitude detuning in collision seems detrimental, on the other hand it provides a strong Landau damping, much beyond the requirement.¹⁴ Decoherence is not a major concern for the preservation of the emittance in the rest of the cycle, i.e. without collision, however it remains a concern for Landau damping which is much more critical in this configuration. Indeed, since particles oscillating at different amplitudes are affected differently in the decoherence process, a modification of the beam distribution, and consequently of Landau damping, is expected. The decoherence model⁴ was extended lately to describe the corresponding time evolution of the distribution and its corresponding impact on Landau damping.¹⁵ However the noise amplitude required to lose Landau damping on a realistic time scale is not compatible with the measured noise amplitudes, suggesting that a key ingredient is missing from the model.

3. Noise and Wake Fields

In the presence of noise with a broad frequency spectrum, the beam is forced to oscillate, the amplitude of these oscillations is determined by the balance between the excitation strength and the damping strength. In particular, as for a harmonic oscillator, the beam response becomes significantly peaked at its natural frequency. In this regime, the wake fields generate an additional force with the spectrum of the beam oscillation, i.e. peaked at the natural frequency. It is important to note that; not only the wake fields shift the natural frequencies of oscillation of the beam, they can also amplify the corresponding transverse motion. We conclude that the combined effect of a source of noise with a broad frequency spectrum, a damper and wake fields results in an excitation peaked at the frequencies of the so-called coherent mode frequencies. This harmonic excitation results in diffusion of the resonant particles,¹⁷ i.e. the particles that are also responsible for Landau damping of these coherent modes, eventually leading to a loss of Landau damping.

This mechanism can be modelled with macro-particle tracking simulations (Figure 2), in particular, shows that the latency is expected to increase with the damper gain and the octupole current and decrease as the noise amplitude increases.¹⁸ An analytical model was recently developed allowing for a more detailed understanding.¹⁹

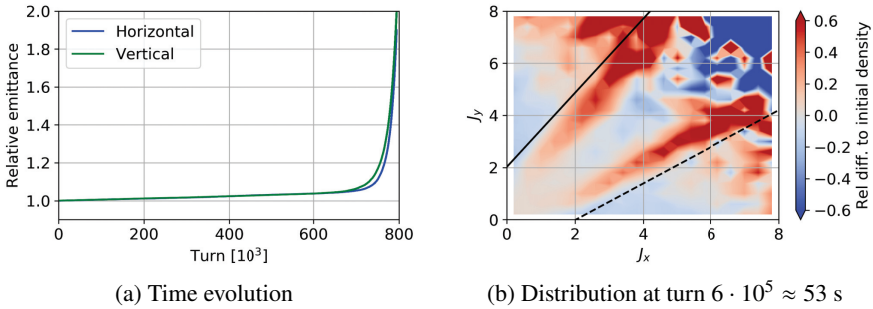


Fig. 2. Evolution of the transverse emittance from macro-particle tracking simulation with COMBI² including the effect of wake fields, transverse damper, amplitude detuning and a broad source of noise. This simulation illustrates the latency characterised by a slow growth of the emittance along with a modification of the distribution followed by an instability characterised by a fast exponential growth. The distorted distribution of transverse actions in normalised phase space at the end of the latency phase is shown. Note that the maximum normalised actions quoted on the axes correspond to an oscillation amplitude of 4 times the r.m.s. beam size. Solid and dashed lines mark the particles resonant with the most unstable modes driven by the wake fields, in the horizontal and vertical plane respectively. The simulations were performed with nominal HL-LHC settings at flat top, with an octupole current of 250 A (corresponding to approximately half of their maximum strength) and a noise amplitude of $3 \cdot 10^{-3}$, leading to a shorter time scale w.r.t. realistic configurations.

3.1. Experimental validation

While clearly visible in phase space, the expected distortion of the beam distribution is beyond the capabilities of existing transverse profile measurements. In order to measure directly the modification of the stability diagram, beam transfer function measurements were introduced in the LHC in Run2. However, a direct measurement of a distortion of the stability diagram due to noise could not be achieved so far due to various technical issues, in particular the required accuracy was not reached and the generation of instabilities by the harmonic excitation needed for the measurement itself strongly limited the investigations.^{20,21}

An indirect experimental validation of the mechanism was obtained using the damper as a controlled source of noise,¹⁹ similarly to the experiment discussed previously but without collision. The main feature of the instability, i.e. a latency that depends on the amplitude of the external excitation is shown in Figure 3.

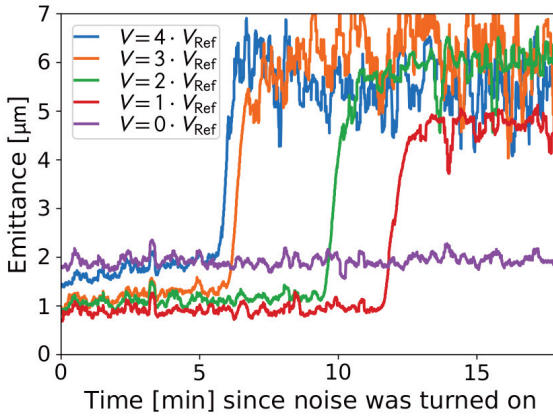


Fig. 3. Transverse emittance evolution of bunches experiencing different amplitudes of artificial noise characterised by the corresponding voltage at the electrostatic kicker, at top energy in the LHC. The latency and the instability can be clearly distinguished, with a shorter latency for bunches experiencing noise of higher amplitude. We note that the emittance growth rate is marginal during the latency phase for the low noise bunches.

4. Mitigation

The most robust mitigation addresses the root causes, i.e. the impedance (see e.g. Chapter 8) and external sources of noise. As discussed previously, the damper was identified as a source of noise and a mitigation could be put in place. Identifying the other contributors to the machine noise and minimising their impact remains the topic of experimental studies.^{9–11}

The crab cavity noise is a major concern for the preservation of the emittance in collision, however its impact on the beam stability is critical only if the cavities are enabled prior to the establishment of head-on collisions, a feature that is not required in the present baseline (see Chapter 5).

The increase of the latency with the octupole current is usually stronger than with linear,¹⁸ enhancing Landau damping is therefore a possibility. In fact, the current design accounts for an empirical factor two in the Landau damping requirements (based on experience from the LHC).

Since this instability mechanism features a latency, possibly of several minutes, its impact on the machine performance can be reduced by limiting transient times in the cycle. During Run1 and Run2, the LHC was operated

with tens of minutes spent at flat top without collision, mainly to perform the betatron squeeze. This operation is no longer required in the nominal HL-LHC thanks to the combined ramp and squeeze as well as the luminosity levelling with β^* . The establishment of collision right at the end of the ramp to improve the beam stability was already considered in Run1²² and could be implemented in the HL-LHC final operational scenario if necessary.

A detailed understanding of this mechanism is crucial to determine the optimal working point in terms of tune, chromaticity, octupole strength and damper gain, possibly allowing a reduction of the requirements for the mitigation measures mentioned above.

5. Conclusion

The impact of noise on the beam quality, and consequently on the collider performance, had been extensively studied in particular in the presence of head-on beam-beam interactions and a transverse damper.^{4,5} The models could be tested against experimental observations at the LHC, allowing for a characterisation of the integrated machine noise, under the assumption of a broad spectrum. While acceptable in the LHC, the damper pickup noise is not compatible with the required preservation of the emittance in collision in the HL-LHC, due to the larger beam-beam tune shift, thus requiring a technological improvement.

On the other hand, the noise was identified as a source of instabilities, first in simulation and later demonstrated experimentally and analytically. The main feature of this new instability mechanism is the existence of a latency, during which the beam remains stable but the combined effect of the noise and the wake fields generates non-uniform diffusion that eventually leads to a loss of Landau damping. The models are currently refined, to steer efficiently mitigation measures and determine optimal running conditions that maximise the latency to a level that does not impact the machine performance.

References

1. X. Buffat, G. Arduini, D. Amorim, S. Antipov, N. Biancacci, L. Carver, S. Furuseth, G. Iadarola, K. Li, L. Mether, E. Métral, A. Oeftiger, A. Romano, G. Rumolo, B. Salvant, M. Schenk, T. Pieloni, and C. Tambasco. Transverse instabilities during run II. In eds.

- M. Schaumann, D. Walsh, and S. Dubourg, *Proceedings of the 2019 Evian workshop on LHC beam operation*, CERN, Geneva, Switzerland (30 Jan. - 2 Feb., 2019).
2. X. Buffat. *Transverse beams stability studies at the Large Hadron Collider*. PhD thesis, EPFL (2015).
 3. D. Moehl. Sources of emittance growth. In ed. D. Brandt, *CAS - CERN Accelerator School - Intermediate Accelerator Physics*, pp. 245–270, CERN, Geneva, Switzerland (15-16 September 2003, 2006).
 4. V. A. Lebedev, Emittance growth due to noise and its suppression with the feedback system in large hadron colliders, *AIP Conference Proceedings*. **326**(1), 396–423 (1995).
 5. Y. Alexahin, A study of the coherent beam-beam effect in the framework of Vlasov perturbation theory, *Nucl. Instrum. Methods Phys. Res. A*. **480**(2), 253–288 (2002).
 6. T. Pieloni. *A Study of Beam-Beam Effects in Hadron Colliders with a Large Number of Bunches*. PhD thesis, EPFL (2008).
 7. X. Buffat, L. Barraud, E. Metral, A. Ribes Metidieri, J. Barranco Garcia, P. Goncalves Jorge, T. Pieloni, and C. Tambasco. Status of the studies on collective effects involving beam-beam interactions at the HL-LHC. Technical Report CERN-ACC-NOTE-2018-0036, CERN, Geneva, Switzerland (2018).
 8. D. Valuch, W. Hofle, J. Komppula, G. Kotzian, S. Rains, M. Soderen, and X. Buffat. ADT upgrades for HL-LHC. Presented at the 8th HL-LHC Collaboration Meeting, Geneva, Switzerland https://indico.cern.ch/event/742082/contributions/3084843/attachments/1734025/2803777/ADT_for_High_Lumi.pptx (16th Oct, 2018).
 9. X. Buffat, S. Furuseh, and D. Gamba. Emittance growth due to decoherence of external excitations in the LHC and HL-LHC. Presented at the HL-LHC WP2 Meeting, Geneva, Switzerland <https://indico.cern.ch/event/718322/contributions/2952005/attachments/1629722/2597236/2018-03-20-status-noise-expanded.pdf> (10th Apr, 2018).
 10. S. Kostoglou, H. Bartosik, Y. Papaphilippou, and G. Sterbini. Noise studies: On the 50hz harmonics perturbation. Presented at the 8th HL-LHC Collaboration Meeting, Geneva, Switzerland https://indico.cern.ch/event/742082/contributions/3084843/attachments/1734025/2803777/ADT_for_High_Lumi.pptx (16th Oct, 2018).
 11. M. Morrone, M. Martino, R. D. Maria, M. Fitterer, and C. Garion. Magnetic frequency response of high-luminosity large hadron collider beam screens. Technical Report CERN-ACC-2019-0004, CERN, Geneva, Switzerland (2019).
 12. P. Baudrenghien and T. Mastoridis, Transverse emittance growth due to RF noise in the high-luminosity LHC crab cavities, *Phys. Rev. ST Accel. Beams*. **18**, 101001 (Oct, 2015).
 13. X. Buffat, M. Albert, D. Amorim, S. Antipov, G. Crockford, S. Furuseh, J. Komppula, G. Kotzian, N. Mounet, A. Oeftiger, B. Salvant, M. Soderen, G. Trad, and D. Valuch. Noise studies with new ADT pickup electronics. Technical Report CERN-ACC-NOTE-2019-0026, CERN, Geneva, Switzerland (2019).
 14. X. Buffat, W. Herr, N. Mounet, T. Pieloni, and S. White, Stability diagrams of colliding beams in the Large Hadron Collider, *Phys. Rev. ST Accel. Beams*. **17**, 111002 (Nov, 2014).
 15. S. V. Furuseh and X. Buffat, Long-term evolution of Landau damping in the presence

- of transverse noise, feedback, and detuning, *Phys. Rev. Accel. Beams*. **23**, 034401 (Mar, 2020).
16. F. Antoniou, I. Efthymiopoulos, M. Hostettler, G. Iadarola, N. Karastathis, S. Kostoglou, S. Papadopoulou, Y. Papaphilippou, and G. Trad. What do we understand on the emittance growth? In eds. M. Schaumann, D. Walsh, and S. Dubourg, *Proceedings of the 2019 Evian workshop on LHC beam operation*, CERN, Geneva, Switzerland (30 Jan. - 2 Feb., 2019).
 17. A. Bazzani and L. Beccaceci, Diffusion in Hamiltonian systems driven by harmonic noise, *Journal of Physics A: Mathematical and General*. **31**(28), 5843 (1998).
 18. X. Buffat, D. Amorim, S. Antipov, L. Carver, N. Biancacci, S. Furuseh, T. Levens, E. Métral, N. Mounet, T. Pieloni, B. Salvant, M. Soderen, C. Tambasco, and D. Valuch. The impact of noise on beam stability. Presented at the 8th HL-LHC Collaboration Meeting, Geneva, Switzerland https://indico.cern.ch/event/742082/contributions/3084844/attachments/1733747/2804478/2018-10-16_ImpactOfNoiseOnBeamStability-expanded.pdf (16th Oct, 2018).
 19. S. V. Furuseh and X. Buffat, Loss of transverse Landau damping by noise and wakefield driven diffusion, *Phys. Rev. Accel. Beams*. **23**, 114401 (Nov, 2020).
 20. C. Tambasco. *Beam Transfer Function measurements and transverse beam stability studies for the Large Hadron Collider and its High Luminosity upgrade*. PhD thesis, EPFL (2017).
 21. C. Tambasco, T. Pieloni, X. Buffat, E. Métral, and T. Levens. MD 3292: Investigation of Landau damping by means of BTF measurements. Technical Report CERN-ACC-NOTE-2019, CERN, Geneva, Switzerland (2018).
 22. X. Buffat, W. Herr, M. Lamont, T. Pieloni, S. Redaelli, and J. Wenninger. Squeezing with colliding beams. In eds. B. Goddard and S. Dubourg, *Proceedings of the 2012 Evian workshop on LHC beam operation*, CERN, Geneva, Switzerland (17-20 December 2012, 2013).

This page intentionally left blank

Chapter 30

Crystal Collimation of Heavy-Ion Beams

S. Redaelli, R. Bruce, M. D’Andrea, D. Mirarchi and R. Rossi

CERN, BE Department, Genève 23, CH-1211, Switzerland

Crystal collimation is an advanced technique where a silicon crystal, only a few millimeters long and bent to a curvature of about $50 \mu\text{rad}$, coherently deflects the beam halo onto a collimator absorber. This technique can improve beam collimation in the HL-LHC. Since 2015, a test stand has been operational in the betatron cleaning insertion of the LHC for beam tests at the unprecedented hadron beam energy of up to $6.5 Z \text{ TeV}$, where Z is the atomic number. For the first time, channeling was observed at this energy and the crystal collimation concept was validated, demonstrating that the cleaning of lead heavy-ion beams at $6.37 Z \text{ TeV}$ can be improved by up to a factor 10. Crystal collimation has become part of the HL-LHC baseline in 2019 and will be the key upgrade for improving the cleaning efficiency for ion beam operation in Run 3.

1. The Crystal Collimation Concept and its Applications to HL-LHC

Planar channelling is a phenomenon where charged particles impinging with specific impacting conditions on a crystal are trapped by the potential produced by the parallel lattice planes. Particles follow the “channel” along the crystal. If the crystal is bent the trajectories of channelled particles [1] are deflected. For the applications discussed in this chapter, silicon (Si) crystals are used. Equivalent bending fields of up to hundreds of tesla can be achieved in a few mm long crystal, bent to produce a deflecting angle of about $50 \mu\text{rad}$. Provided that a sufficiently high efficiency is reached, channelling allows, in principle, an efficient collimation system to be built: a crystal intercepting the beam

halo, as a primary collimator, steers halo particles coherently to a well-defined point where dedicated absorbers are located. Crystals of very high purity, e.g. with atomic dislocations below 1 unit per squared cm, can nowadays be produced and bent to the required accuracy. Together with the development of goniometers for precise angular control in an accelerator environment, these advancements open the possibility to use crystals also in high-intensity, high-energy accelerators.

The crystal collimation scheme is shown illustratively in Fig. 1 (bottom plot) and compared to the LHC multi-stage collimation system based on amorphous materials (top plot), which was introduced in Chapter 8. The present collimation system, located in a dedicated insertion region (IR7), requires several secondary collimators and absorbers to catch the products developed through the interaction of the primary beam halo with collimators and to suppress the emerging secondary and tertiary halos. One single absorber per collimation plane would instead be sufficient, in theory, in a crystal-based collimation where a bent crystal replaces the primary collimator. Indeed, nuclear interactions are much reduced in this case, which translates into a reduction of dispersive losses downstream of the cleaning insertion that limit the present collimation performance (Chapter 8).

Crystal collimation might be used for betatron or off-momentum halo cleaning systems where the crystal replaces the primary collimators in the planes of interest. It cannot be used as part of the collimation systems around the experiments, e.g. to locally protect the inner triplet (a goal that is achieved by tertiary collimators) or to clean collision products (done with physics-debris absorbers). For example, the off-momentum particles emerging from the interaction points are too close to the beam core, and only separate from it where the dispersion is sufficiently large, which already occurs in the cold dispersion suppressors. The focus of crystal R&D for collimation upgrade studies has therefore been put on the betatron cleaning.

Simulations indicate a possible gain in collimation cleaning of proton beams by a factor between 5 and 10 [2], for a layout that uses the existing secondary collimators as absorbers. This is currently not possible with high stored energies: we do not have a validated solution for the design of a collimator absorber capable to dispose with sufficient efficiency of the ~ 1 MW power extracted by the crystal for the design loss scenario with 0.2 h beam lifetime in nominal HL-LHC proton operation (see Chapter 8). The

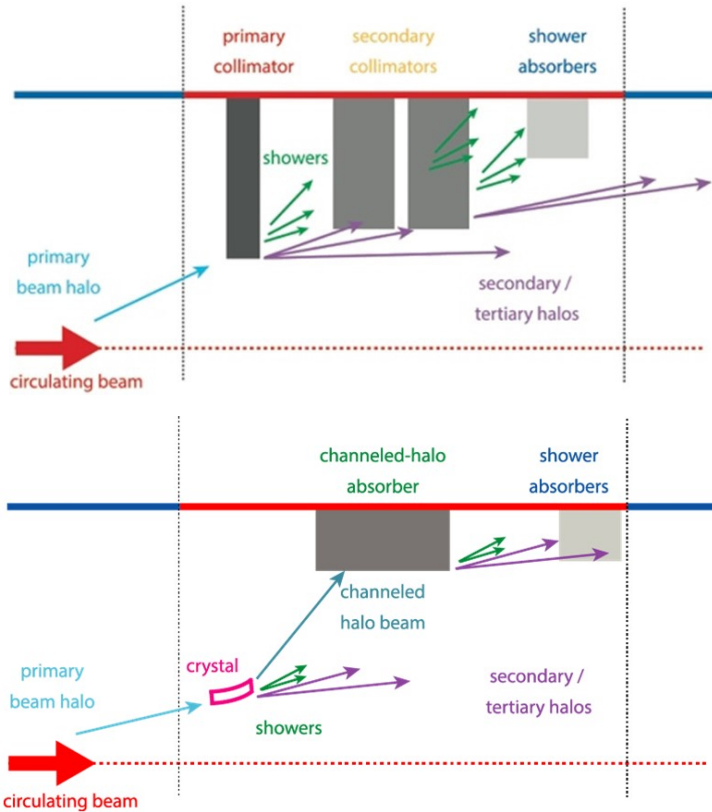


Fig. 1. Schematic illustrations of the standard multi-stage betatron cleaning system in the LHC IR7 (top) and of a conceptual implementation of a crystal-based cleaning system.

crystal collimation option is, however, directly applicable for collimating heavy-ion beams, which have a much lower intensity. Improved cleaning can be achieved thanks (see below) to the reduced probability of electromagnetic dissociation and nuclear fragmentation compared to the present primary collimators. The extracted power for design failures is more than 30 times lower and the present secondary collimators are adequate as absorbers of channelled ions. The integration of crystals into the present layout is possible for ion collimation, since crystals can be inserted into the present hierarchy without further modifications or major changes of the collimators that are used for proton operation. This approach can be seen as an “adiabatic” improvement of the collimation system, only applicable for ion beams.

The crystal collimation R&D within HL-LHC was initially motivated by the new IR7 dispersion suppressor upgrade layout, featuring only one TCLD/ 11 T dipole assembly per side of IR7 (see Chapter 8) instead of two as foreseen in the previous layout. The present baseline solution is satisfactory for the nominal ion and proton operation during HL-LHC and crystal collimation has been chosen as a mitigation measure for the delayed 11 T dipole installation and for a further improvement of the cleaning efficiency for ion operation once the 11T TCLD assemblies are installed in the LHC.

2. Experimental Validation with LHC Beams

2.1. Test stand for crystal collimation tests in the LHC

A unique crystal collimation test stand has been available in the LHC during Run 2 [2]. The initial 2015 installation with 2 crystals in Beam 1 was extended in 2017 with the addition of 2 crystals in Beam 2, enabling complete collimation tests for both beams and both horizontal and vertical planes. The layout for the horizontal plane of Beam 1 is shown in Fig. 2. The crystal primary collimator assembly is shown in Fig. 3, and the key crystal parameters

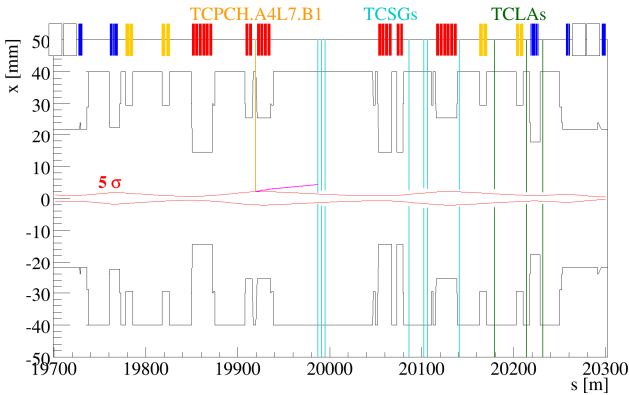


Fig. 2. Simulated horizontal trajectory of channeled halo particles for Beam 1 (magenta line) and mechanical aperture of the beam pipe (black) versus longitudinal position along the betatron cleaning insertion. The crystal (orange line) is set at 5 nominal beam sigmas (computed for a $3.5 \mu\text{m}$ emittance). Cyan and green lines indicate positions and settings of the secondary (TCSG) and shower-absorber (TCLA) collimators used to dispose of the channeled halo and of the products of its interactions with collimators.

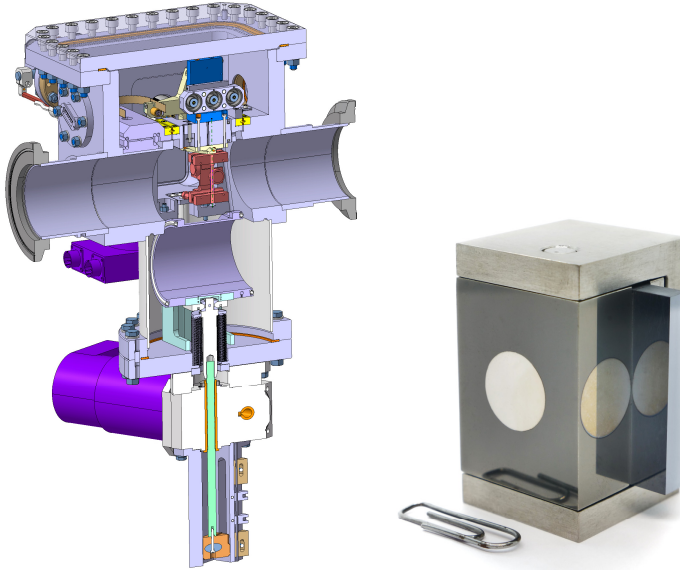


Fig. 3. Design of the prototype crystal primary collimator installed in the LHC (left) and photograph of the crystal mounted on his holder (*Courtesy of Y. Gavrikov, PNPI*). The four LHC crystal collimators use a special design of a moveable chamber that hides the crystals from the high-intensity beams when they are not used.

Table 1. Main parameters of the HL-LHC crystals

Crystal length along the beam	4 ± 0.1 mm
Total height	< 55 mm
Total weight	< 150 g
Miscut for planar channeling	< 40 μ rad
Torsion	< 1 μ rad/mm
Bending	50.0 ± 2.5 μ rad
Dislocation density	< 1 / cm^2

are listed in Table 1. The bent crystal is usually operated at 5σ and existing downstream collimators are used to intercept the channelled particles, while upstream collimators are fully open. Crystal locations and parameters have been optimized to achieve the best cleaning performance with this IR7 layout that, for protons, can only be used at low beam intensities. Silicon crystals are used in all cases, and the design specification [2] is to have 50 μ rad bending. The crystal length is 4 mm.

2.2. First demonstration of hadron channeling up to 6.5 Z TeV

The observation of planar channeling of circulating beam halos is delicate. One way to do it is by inserting the crystal in the beam as a primary collimator and by recording local losses while varying slowly the angular orientation of the crystal with respect to the circulating beam, typically with a rotational speed as low as a fraction of $\mu\text{rad/s}$ [3,4]. This so-called angular scan allows identifying the optimum crystal orientation, obtained when the impinging halo particles are nearly orthogonal to the crystal front face. The probability that they undergo channeling is, then, maximum. In this ideal condition, local beam losses directly downstream of the crystal are at a minimum because channeled particles travel within lattice planes with reduced probability to experience nuclear interactions and are instead lost at the absorber further downstream.

Beam losses at the horizontal crystal of Beam 1 as a function of the crystal orientation angle [5], re-centered to have the optimum channeling orientation at a zero angle, are shown in Fig. 4. This is a high-resolution scan performed at $0.2 \mu\text{rad/s}$ while the beam was continuously excited with the transverse

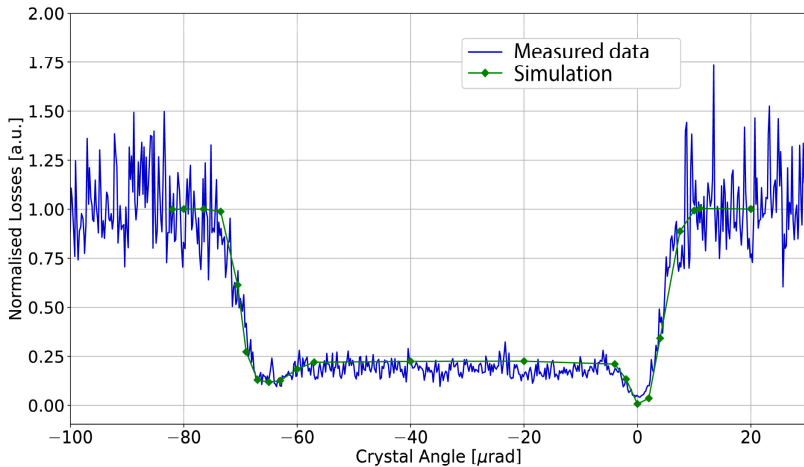


Fig. 4. Beam losses at the horizontal crystal of beam 1 as a function of the crystal orientation angle during an angular scan with proton beams at 6.5 TeV [5]. The green line shows simulations for the same conditions. The zero angle corresponds to a minimum of local losses. Losses are normalized by the values recorded in amorphous-like orientation, when channeling is prohibited, and interactions of the proton beam are like with a Si collimator of the same dimensions.

damper to obtain a desired level of primary beam losses. Data were collected with proton beams at 6.5 TeV. The green line shows simulations performed for the same conditions, proving an excellent prediction power of the tools that were developed for crystal collimation studies [6]. The flat region of losses between $-60 \mu\text{rad}$ and zero corresponds to the volume reflection [7] region.

Similar measurements, leading to the same qualitative observations, were obtained for all crystals and planes, both at injection and at top energy. Measurements are available for proton, Pb and Xe beams. A comprehensive review of available data was given at the Crystal Collimation Day event [8].

2.3. Crystal collimation cleaning and other operational aspects

The collimation cleaning inefficiency is measured by inducing beam losses in a controlled way, by injecting white noise via the transverse damper that excites the beam core until particles impinge on the IR7 collimators. The same procedure is applied with either conventional or crystal primary collimators in use, for a direct comparison of the performance of the two schemes. Figure 5 compares the standard collimation cleaning of Pb ion beams (top graph) with a crystal-based system (bottom). Losses in the most exposed cold magnets are about 8 times lower using crystals.

More systematic studies demonstrated that, with settings in IR7 similar to those used for the conventional system in 2018, the addition of one crystal at a setting 0.25σ closer to the beam than the primary collimators (i.e., 4.75σ instead of 5.0σ) could improve the cleaning for both beams and planes, by factors between 1.5 ± 0.4 and 8.0 ± 1.4 depending on the beam and plane [10]. This depends on the type of crystal used and the smallest improvement is achieved with the quasi-mosaic crystal used for the Beam 2 vertical collimation, while the strip crystals provided the best performance. Further improvements could be obtained by tightening the IR7 hierarchy in a crystal-optimized configuration that was tested in dedicated machine studies [10].

The LHC beam tests also validated critical hardware components like the high-precision goniometer that controls the crystal angle with sub- μrad resolution [9]. This is a very important result because crystal collimation should be deployed in all phases of the operational cycle, not only in static conditions. Continuous channelling was achieved during the energy ramp from 450 GeV to 6.5 TeV and in the betatron squeeze. For example, Ref. 5 shows

the crystal angle measured during the energy ramp, showing an angular RMS value below $1 \mu\text{rad}$ throughout the range. Note that the crystal moves towards the beam core by about 5 mm to keep normalized settings of 5σ , while the rotational stage moves by about $30 \mu\text{rad}$ to keep the channelling orientation. Throughout the process, and excellent angular control must be achieved to remain within the critical angle for channeling, which is reduced to about $2.2 \mu\text{rad}$ at top energy.

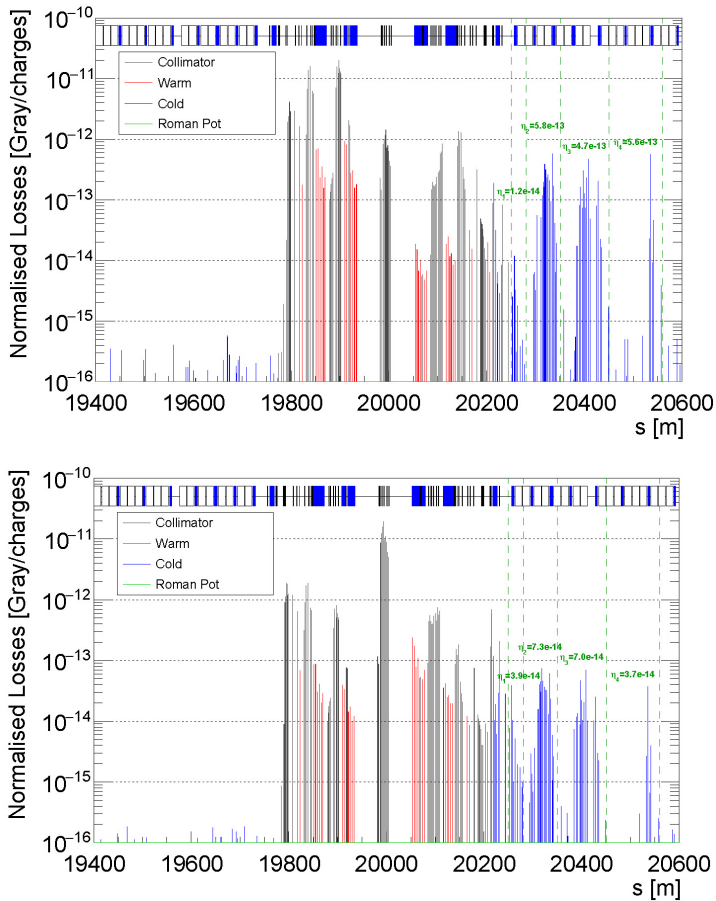


Fig. 5. Beam losses in IR7 recorded in a horizontal loss map for B1 with Pb beams at 6.37 Z TeV, for the standard (top graph) and crystal-based (bottom) system. Peak values over the selected ranges are reported in green. The crystal is installed at the coordinate 19919 m (see Fig. 2).

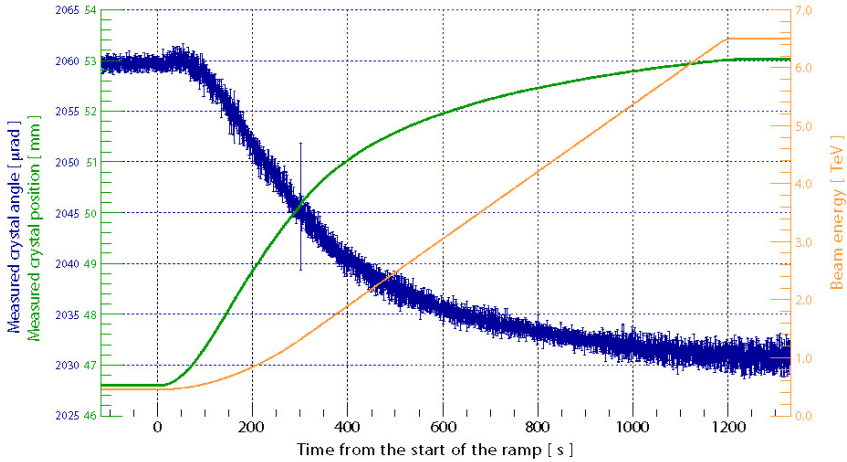


Fig. 6. Crystal position and angle as a function of time during the LHC energy ramp to 6.5 TeV (right axis), from Ref. 5.

During Pb ion operation in 2018, crystal insertions were made part of the intensity ramp up, which is the phase where the number of bunches is progressively increased, in subsequent fills, to safely approach the maximum stored energies. Crystals were successfully used in studies at the end of physics fills with up to 648 lead ion bunches, using adiabatic insertions in the standard multi-stage cleaning of IR7 as described above [10].

An important milestone was achieved at injection energy, during the high-beta run in 2018, where crystal collimation was used operationally for the first time at the LHC, to reduce beam-induced background on forward physics detectors. The crystals were orchestrated through automated sequences as the other ring collimators. Although the run was relatively short, the system showed the required stability with crystals inserted directly in channelling orientation. Significant performance improvement with respect to a standard collimation approach was observed, in good agreement with numerical simulations [11].

3. Prospect for Crystal Collimation Deployment for HL-LHC

With the promising results obtained in Run 2, crystal collimation is considered as an option to further reduce IR7 losses with lead ion beams. Crystal

collimation became part of the HL-LHC baseline after the 2019 Cost and Schedule Review and the present installation in the LHC is being upgraded during LS2 to address some non-conformities of the first prototype installations and to improve operation reliability for Run 3. Following the decision not to install 11 T dipoles during LS2, it is planned to use crystal collimation for the heavy ion beams throughout Run 3. For a complete crystal-based system, one would also add one crystal per beam and plane, for a total of 8 devices, in order to constrain the beam from both sides in each plane. The present one-side setup might indeed not be fully adequate in case of orbit drifts on the side opposite from the crystal. The specifications of four additional crystals and goniometers remain the same introduced above and available layout locations have been identified [10]. The need for such a further upgrade will be established at the beginning of Run 3 following the operational experience with the 4-crystal system.

4. Acknowledgements

The contributions by the UA9 collaboration towards the demonstration of the crystal collimation concept are strongly acknowledged. The crystals installed in the LHC and used for this publication were fabricated by PNPI and Università of, and INFN Section, Ferrara. Various groups and teams at CERN involved in the crystal installations and in the beam tests are also acknowledged: BE/ABP, BE/OP, BE/CMM and SY/STI.

References

1. A. M. Taratin, Particle channeling in bent crystals, *Phys. Part. Nucl.* **29**, pp. 437-462 (1965).
2. D. Mirarchi *et al.*, Design and implementation of a crystal collimation test stand at the Large Hadron Collider, *The European Physical Journal C* **77:424** (2017).
3. W. Scandale *et al.*, Observation of channeling for 6500 GeV/c protons in the crystal assisted collimation setup for LHC, *Phys. Lett. B* **758** (2016) 129-133.
4. S. Redaelli et al. First Observation of ion beam channeling in bent crystals at multi-TeV energies, *The European Physical Journal C* **81:142** (2021).
5. R. Rossi, PhD thesis, CERN-THESIS-2017-424 (2017).
6. D. Mirarchi *et al.*, Crystal implementation in SixTrack for proton beams, CERN-2018-011-CP.

7. Yu. M. Ivanov *et al.*, Volume reflection of a proton beam in a bent crystal, *Phys. Rev. Lett.* 97, 14 (2006), p. 144801.
8. HL-LHC Crystal Collimation Day, <https://indico.cern.ch/event/752062/overview>.
9. M. Butcher *et al.*, Controller Design for a Rotational Piezo-Based Actuator for Accurate Positioning Application in Noise Environment - in Proc. IECON'15, p. 003887.
10. M. D'Andrea, PhD thesis, CERN-THESIS-2021-022 (2021).
11. D. Mirarchi *et al.*, Reducing Beam-Related Background on Forward Physics Detectors Using Crystal Collimation at the Large Hadron Collider, *Phys. Rev. Applied* 14, 064066.

This page intentionally left blank

Chapter 31

High Field Accelerator Magnets for Next Generation Colliders – Motivation, Goals, Challenges and R&D Drivers

L. Bottura

CERN, TE Department, Genève 23, CH-1211, Switzerland

The Hadron Collider (LHC) at CERN can be regarded as the *ultimate* collider built with Nb₃Ti magnets. Its main dipoles have reached a field of approximately 8 T, which is very likely close to the highest practical field for this superconductor in accelerators. The next major step is the High Luminosity upgrade of the LHC at CERN, which among the many upgrades of the accelerator, calls for a few tens of Nb₃Sn dipole and quadrupole magnets, operated at 1.9 K and at conductor peak fields up to about 12 T. HL-LHC magnets are in the production phase, marking an historical milestone in accelerator technology and the culmination of 20 years of worldwide R&D. Here we describe the rationale for high field accelerator magnet R&D beyond HL-LHC, consisting of two complementary axes: (i) development of an ultimate Nb₃Sn technology, increasing the field reach and achieving maturity and robustness level required for deployment on a large scale and (ii) demonstrating suitability of high-temperature superconductors for accelerator magnet applications. We start with a review of the state-of-the-art, review the main goals, and identify the drivers for an R&D program responding to the declared priorities of the European Strategy Upgrade. This chapter is intended as the starting point in the formation of a structured High Field Accelerator Magnet R&D Program.

1. Introduction

High Field Magnets (HFM) are among the key technologies that will enable the search for new physics at the energy frontier. Starting from the Tevatron

This is an open access article published by World Scientific Publishing Company. It is distributed under the terms of the Creative Commons Attribution 4.0 (CC BY) License.

in 1983 [1], through HERA in 1991 [2], RHIC in 2000 [3] and finally the LHC in 2008 [4], all frontier hadron colliders were built using superconducting (SC) magnets. All colliders listed above made use of the highly optimized superconducting alloy of Nb and Ti [5], and it is a well-accepted fact that the LHC dipoles, with a nominal operating field of 8.33 T when cooled by superfluid helium at 1.9 K, represent the *end-of-the-line* in terms of performance of accelerator magnets based on this material* [6].

At the same time approved projects and studies for future circular machines call for the development of superconducting magnets that produce fields beyond those attained in the LHC [7]. This is the case of the High-Luminosity LHC upgrade (HL-LHC) [8], which is currently under construction at CERN and collaborating laboratories, and the Future Circular Collider design study (FCC) [9], structured as a worldwide collaboration coordinated by CERN. Similar studies and programs are on-going outside Europe, such as China's Super proton-proton Collider (SppC) [10]. Significant advances in SC accelerator magnets were driven by past studies such as the Very Large Hadron Collider at Fermilab [11] and the US-DOE Muon Accelerator Program [12]. Similarly, first considerations on ultra-high-field (20 T) HTS dipoles were fostered by the High-Energy Large Hadron Collider study at CERN [13]. Finally, new accelerator concepts such as muon colliders presently considered at CERN and collaborators [14] will pose significant challenges on the magnetic system. These High Energy Physics (HEP) initiatives provide a strong and sustained pull to the development of SC accelerator magnet technology beyond the LHC benchmark, towards higher fields.

Having reached the upper limit of Nb-Ti performance, all above projects and studies are turning towards other superconducting materials and novel magnet technology. On-going activities encompass both *Low-Temperature and High-Temperature Superconductors* (LTS and HTS respectively). Besides the R&D driven directly by the projects and studies listed above, it is important to recall the coordinated efforts that have led to the present state-of-the-art in

* Nb-Ti can produce field well in excess of the LHC nominal field of 8.33 T, as recently demonstrated by the spectacular achievement of ISEULT, a record full-body MRI solenoid operating at 11.7 T (see <https://www.cea.fr/english/Pages/News/Iseult-MRI-Magnet-Record.aspx>). However this is done at winding current densities that are typically one order of magnitude smaller than what is needed to build the compact windings of an accelerator magnet, and in a solenoid configuration which is magnetically twice as effective when compared to a dipole.

HFM for accelerators. The largest effort over the past 30 years was dedicated to the development of Nb₃Sn [15] conductor and magnet technology. A strong focus was given in the end of the 1990's by the US-DOE programs devoted to Nb₃Sn conductor and magnet development [16,17,18]. These programs unfolded as a collaboration among the US-DOE accelerator Laboratories and associated Institutions, and are now continuing in consolidated form under the US Magnet Development Program [19]. On the EU side the first targeted EU-wide activities were initiated under the EU-FP6 CARE (Coordinated Accelerator Research in Europe) [20] initiative, and in particular the Next European Dipole Joint Research Activity (NED-JRA) [21]. NED-JRA ran from 2004 to 2009, and was followed by the EU-FP7 EuCARD [22]. The main fruit of these collaborations is FRESCA2, the magnet that still detains with 14.6 T the highest dipole field ever produced in a clear bore of significant aperture.

As described elsewhere in detail [8], HL-LHC is presently the forefront of accelerator magnet technology and construction at the highest field ever attained. The results achieved with the nominal performance of the 11 T dipoles [23] and QXF quadrupoles [24] demonstrate that Nb₃Sn has the ability to surpass the state-of-the-art Nb-Ti mentioned earlier. At the same time, it is clear that the solutions successfully implemented for the design and manufacturing of the HL-LHC Nb₃Sn magnets will need to evolve to improve robustness, industrial yield and cost before the full potential of the material can be realised.

Finally, the interest in the exceptional high-field potential of High-Temperature Superconductors (HTS) for many domains of applied superconductivity has not spared accelerator magnets. Copper oxide compounds containing rare-earths (REBCO [25]) and bismuth (BSCCO [26]) are in a stage of early technical maturity, and their application to the generation of ultra-high magnetic fields has been proven recently. Laboratories and industry have shown that HTS are capable of producing fields in the range of 28 T in commercial NMR solenoids [27] to 45.5 T in small experimental solenoids in background field [28]. As discussed later in more detail, HTS technology for accelerator magnets is only at its promising beginning [29]. This is an area where we expect to see fast progress, along the path initiated in various laboratories, and fostered in Europe by the EuCARD [22], EuCARD2 [30], ARIES [31] and the on-going I-FAST [32] EU projects.

In this chapter we start with a review of the state-of-the-art of high-field dipole demonstrators, models and long magnets relevant to accelerator technology, derive the main goals and identify the drivers of an R&D program responding to the declared priorities of the European Strategy Upgrade. This chapter is intended as the starting point in the formation of a structured High Field Accelerator Magnet R&D Program.

2. Historical Perspective

2.1. Highest Field Attained

The result of the efforts briefly outlined above can be appreciated graphically in Figure 1, which reports the steady increase of field produced by dipole magnets built with LTS Nb_3Sn over the past forty years. The data is a loose collection of results obtained with short demonstrator magnets (simple configurations that lack an aperture for the beam and are not built with other constraints such as field quality), short model magnets (short version of magnets that are representative of the full-size accelerator magnets), and full-size accelerator magnets.

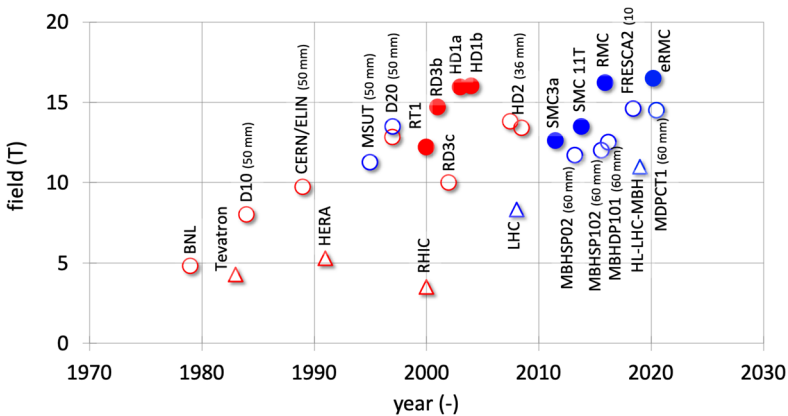


Fig. 1. Record fields attained with Nb_3Sn dipole magnets of various configurations and dimensions, and either at liquid (4.2 K, red) or superfluid (1.9 K, blue) helium temperature. Solid symbols are short demonstrator, i.e. “racetracks” with no bore, while open symbols are short models and long magnets with bore. For comparison, superconducting collider dipole magnets past and present are shown as triangles.

We can trace first significant attempts back to the 1980's, at BNL [33] and LBNL [34]. This work eventually led to the achievements of D20 [35], in the 1990's, and the 16 T field attained with the demonstrator HD1 at LBNL [36], in the 2000's. Fields in the 16 T range were obtained at CERN [37] in 2015, and surpassed in 2020 [38] as a result of the push provided by FCC-hh. It is interesting to note here how the work in the 1900's and 2000's described above [39] has laid the foundations for the construction of the HL-LHC Nb₃Sn magnets. And yet, the R&D program itself was largely funded by HEP in the US, as well as EU initiatives in Europe, i.e. essentially independent of a specific HEP project.

We also see in Figure 1 that the timeline for progress in Nb₃Sn magnet technology is relatively slow. It took about ten years for CERN and associated laboratories [20,21,22], to reproduce the results obtained in the US, from conductor R&D, i.e. highest performance of PIT conductor achieved in 2008 [40], to the field level of 16.2 T in RMC03, achieved in September 2015 [37]. This gives a good benchmark for the time scale necessary to enter into this field of technology, including the procurement of the required infrastructure (e.g. heat treatment furnaces, impregnation tanks) and the development of the necessary skills. The end result of this work is the record magnet FRESCA2, built in collaboration between CERN and CEA, and generating a field of 14.6 T in an aperture of 100 mm diameter [41]. This field level has been reproduced recently by a high-field model dipole built within the scope of the US-MDP program [42] as a step towards the highest field that can be attained with a cos-theta coil configuration (4 layers).

Finally, the plot shows the remarkable achievement in the development of Nb₃Sn accelerator magnets, and in particular the MBH 11T dipole for HL-LHC built at CERN in collaboration with industry (GE-Alstom) [23]. Initiated in 2010, and profiting from the previous developments outlined above, it took a decade to produce the first magnet unit that met all stringent requirements for accelerator operation. The first such magnet, MBHB002, was tested in July 2019 and also retains the record within its class [43]. Though successful in achieving the specified performance, the 11T program has also pointed out that there are still problems to be resolved, on the long-term reliability of the specific design as well as the robustness of the manufacturing solutions, which will need to be addressed and resolved before this class of magnets can be used in an operating accelerator.

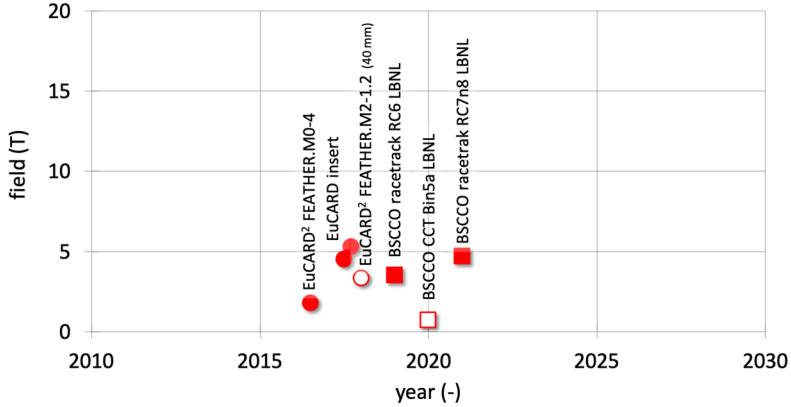


Fig. 2. Record fields attained with HTS short demonstrator magnets producing a dipole field. All tests performed in liquid helium (4.2 K). Solid symbols are magnets with no bore (e.g. racetracks), while open symbols are magnets with bore. Round symbols are magnets built with REBCO, square symbols with BSCCO-2212.

While Nb_3Sn is baseline for the high field magnets of HL-LHC, as well as the next step in SC accelerator magnet technology, great interest and significant progress was achieved recently in HTS accelerator magnet technology, reported graphically in Figure 2. The general interest in the potential of this class of material with spectacular performance coagulated at about the same time in the EU and US, i.e. in the mid of the 2000's. On the US side, efforts were coordinated by the US-DOE sponsored Very High Field Superconducting Magnet Collaboration [44], which targeted Bi-2212 as HTS high-field conductor. This activity has now flown into the scope of US-MDP [19] now addressing both BSCCO-2212 and REBCO in various cables (Rutherford and CORC) and magnet (racetracks and canted cos-theta) configurations [45-47]. As anticipated, in the EU the first seeds initiated already with the EU-FP7 EuCARD collaboration [22], and were pursued intensely with the follow-up EU-FP7 EuCARD2 [30] and EU-H2020 ARIES [31] programs. Much of the conductor effort in Europe was directed to REBCO, with a conscious choice mainly driven by the perceived potential and simpler magnet technology [29]. The result of these activities are small demonstrator magnets that have reached bore field in the range of 3 to 5 T in stand-alone mode. Figure 2 shows clearly that this is the beginning of the path that will hopefully lead to results comparable to Nb_3Sn . The next step beyond the

further development of the technology is to use these small-size demonstrators as inserts in large bore, LTS background magnets to boost the central field and quantify the ability to break the barrier of LTS magnet performance, while at the same time exploring this new range of field.

2.2. Discussion

We can draw a number of conclusions from this rather simplified but interesting review of achievements:

- Lead times for the development of high-field magnets are long, the cycle to master new technology and bring novel ideas into application has typical duration in excess of a decade. It is hence important to pursue R&D in parallel with scoping studies of new accelerators, to anticipate demands and guarantee that specific technology is available for a new HEP realization at the moment when the decision of construction is taken.
- The development of novel SC magnet technology at the high field frontier requires specific infrastructure, often of large size. The necessary investment is considerable. Continuity is hence important in a program that requires such infrastructure and the associated investment.
- The development of high field magnets naturally spans over many fields of science and requires a broad mix of competencies, implying a research team assembled as a collaboration ranging from academia to industry. As for the infrastructure, one such research team needs considerable investment for its constitution and operates most effectively with continuity.

These considerations point to the need of a sustained and inclusive R&D program for high-field superconducting accelerator magnets as a crucial element for the future of HEP, as underlined by the strong recommendation emitted by the European Strategy Group 2020 [48]. Not only should such program respond to the demands driven by specific projects and studies, it should also unfold as a continuous line of structured R&D, ready to respond to future HEP requests, and capable of feeding HEP with opportunities. The program should include both LTS and HTS materials in a synergic manner and encompass the whole spectrum from conductor to accelerator magnets, including the key technologies that are necessary for the realization of its goals. Though we have stressed how such an R&D has long lead time, with cycles of the order of ten years, the timeline should strive to match the upcoming

deadlines for critical decision, and in particular the ESPP process which has a cycle of about 7 years.

An important matter underlying the above considerations is: cost. In this respect we have to consider not only the construction cost of magnets (a very significant challenge for future accelerators, which will be explicitly covered later in this chapter), but also the cost of the R&D itself, which may limit the scope and stretch the timeline, against the wish for a fast turn-around. This is especially true for HTS materials, which explains why the scale of the demonstrators described earlier, as well as the future ones, shall be kept intentionally small (i.e. *inserts* in background field). An effective R&D program will hence include practical consideration of cost and will need to rely on a high degree of synergy.

Given the ambitious scope, the long-term engagement, and the cost, one such program will have to be of collaborative nature, with strong partnership among national laboratories, universities and industry. The R&D program should capitalize on the state-of-the-art and achievements obtained so far, remaining in a line of continuity with the work outline presented earlier, which is largely still on-going. Indeed, an R&D program with the characteristics outlined is consistent with the plans of other organizations in HEP already mentioned earlier [19,49], as well as other research fields relevant to our discussion [50-53]. Last but not least, it will be important to measure the impact of the R&D program against its relevance and impact towards other applications in science and society.

3. Goals of the High Field Magnets R&D Program

The above elements, in the context of present and future demands from HEP, were included in the process of upgrade of the European Strategy for Particle Physics (ESPP). The ESPP consultation and synthesis process started with the Open Symposium of Granada, in May 2019 [Granada], and was completed in June 2020 with the endorsement of the ESPP update by the CERN Council [48,54]. The references quoted contain strong and precise statements relevant to R&D activities on high field accelerator magnets, namely:

[...] the particle physics community should ramp up its R&D effort focused on advanced accelerator technologies, in particular that for high-field superconducting magnets, including high-temperature superconductors;” [48]

and

“The accelerator community, led in Europe by CERN with partners in the United States and Japan, is investing efforts in the design of high-field magnets based on Nb₃Sn superconductor. [...] A focused, mission-style approach should be launched for R&D on high-field magnets (16 T and beyond); this is essential for a future hadron collider, to maximise the energy and to minimise the development time and cost. Development and industrialisation of such magnets based on Nb₃Sn technology, together with the high-temperature superconductor (HTS) option to reach 20 T, are expected to take around 20 years and will require an intense global effort.” [54]

It is important to put the R&D mentioned above in the context of the request that:

“Europe, together with its international partners, should investigate the technical and financial feasibility of a future hadron collider at CERN with a centre-of-mass energy of at least 100 TeV and with an electron-positron Higgs and electroweak factory as a possible first stage.” [48]

The above statements have been translated in the following two long-term technical goals of the HFM R&D:

- (1) Demonstrate Nb₃Sn magnet technology for large scale deployment, pushing it to its practical limits, both in terms of maximum field as well as production scale. The drivers of this first objective are to exploit Nb₃Sn to its full potential, which we think is not yet unfolded, developing design, material and industrial process solutions that are required for the construction of a new accelerator. We separate the search for maximum field from the development of accelerator technology by defining the following two dependent and linked sub-goals:
 - (a) Quantify and demonstrate Nb₃Sn ultimate field. This effort consists of the development of conductor and magnet technology towards the ultimate Nb₃Sn performance. The projected upper limit is presently 16 T dipole field (the reference for FCC-hh). This field should be intended as a target, to be quantified and measured against the performance of a series of short demonstration and model magnets.
 - (b) Develop Nb₃Sn magnet technology for collider-scale production, through robust design, industrial manufacturing processes and cost reduction. The present benchmark for Nb₃Sn accelerator magnets is the HL-LHC, with an ultimate field in the range of 12 T, and a production of the order of a few tens of magnets. Nb₃Sn magnets of this class should be made more *robust*, considering the full spectrum

of electro-thermo-mechanical efforts, and the processes adapted to an industrial production on the scale of thousand magnets. The success of this development should be measured against the construction and performance of long demonstrator and prototype magnets, initially targeting the 12 T range.

- (2) Demonstrate suitability of HTS for accelerator magnet applications, providing a proof-of-principle for HTS magnet technology beyond the reach of Nb₃Sn. The *Leitmotiv* of this program is to break the evolutionary changes of LTS magnet technology, from Nb-Ti to Nb₃Sn, by initiating a revolution that will require a number of significant innovations in material science and engineering. A suitable target dipole field for this development is set for 20 T, significantly above the projected reach of Nb₃Sn (see above). Besides answering the basic question on field reach and suitability for accelerator applications, HTS should be considered for specific applications where not only high field and field gradient are sought, but also higher operating temperature, large operating margin and radiation tolerance are premium.

In addition, it is also important to underline that the HFM R&D program is intended as a focused, innovative, mission-style R&D in a collaborative and global effort, signified at multiple instances in the documents already quoted, such as:

“Innovative accelerator technology underpins the physics reach of high-energy and high-intensity colliders [...] The technologies under consideration include high-field magnets, high-temperature superconductors [...]” [48]

“The particle physics community must further strengthen the unique ecosystem of research centres in Europe. In particular, cooperative programmes between CERN and these research centres should be expanded and sustained with adequate resources in order to address the objectives set out in the Strategy update.” [48]

“Deliverables for this decade should be defined in a timely fashion and coordinated among CERN and national laboratories and institutes.” [48]

“The implementation of the Strategy should proceed in strong collaboration with global partners and neighboring fields.” [48]

It is possible to represent graphically the main objectives in the form reported in Figure 3, where we plot a length of dipole magnets produced (i.e. magnet length times the number of magnets) vs. the *bore field*. The blue line gives an idea of the state-of-the-art, bounded on one side by the nearly 20 km

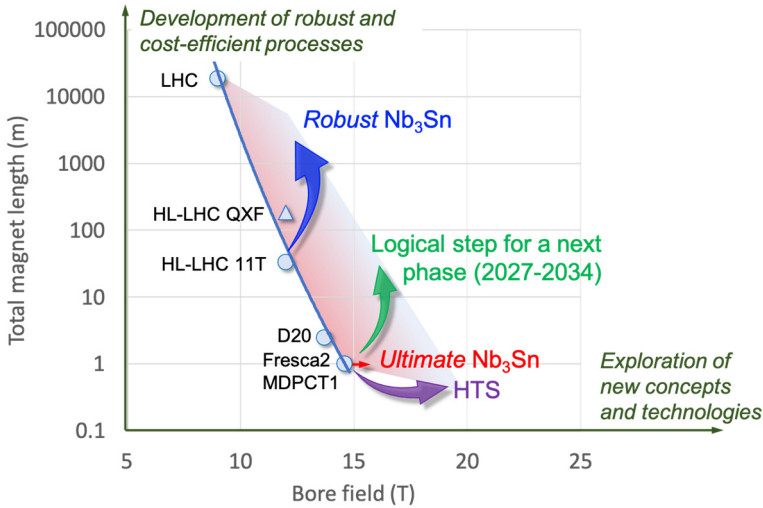


Fig. 3. Graphical representation of the objective of the HFM R&D program in this phase, 2021-2027. Both fronts of maximum field (red for Nb₃Sn, purple for HTS) and large-scale production (blue) are intended to be advanced at the same time. Also represented, in green, a possible evolution for the longer term, 2027-2034.

of Nb-Ti LHC double-aperture magnets in the range of 9 T ultimate field, and at the high-field end by single model magnets approximately 1m in length and in the range of 14.5 T maximum field. The HL-LHC point marks the production of 6 dipoles of 5.5 m length with 12 T ultimate field. The objectives listed above can be represented in this plot as an extension of the field reach by moving along the horizontal axis (magnetic field) thanks to advances in Nb₃Sn and HTS magnet technology, as well as an extension of the production capability by moving along the vertical axis (magnet length) thanks to the development of robust and efficient design and manufacturing processes. Note for clarity that the symbols at higher field (Nb₃Sn at 16 T, HTS at 20 T) and longer magnet length (5 km) represent targets, providing the desired R&D direction, and they should not be read as specified performance.

The *parallelism* in the development is an important element of the program. We believe this is necessary to provide the requested significant advances within a time frame of five to seven years, i.e. responding to the notion of a mission-style R&D that needs to feed the discussion for the next iteration of the European Strategy for Particle Physics with crucial deliverables.

The graphical representation of Figure 3 discussed above only defines the first step in the R&D, which should enfold in the 2021-2027 period. Naturally, once it is proven that the field reach can be extended, and the actual level is demonstrated, we can foresee the need of a follow-up phase. This should enfold in the period 2027-2034, being dedicated to proving the new generation of high field magnets on a scale of magnet prototype, i.e. several meters of cumulated magnet length. This is represented by the green arrow in Figure 3, whereby the choice of the field level, and the actual magnet length to be realized, are again, only indicative, and will depend on the results of the R&D in the coming few years.

A further element in support to the R&D targets formulated above, is that they respond directly to the demands coming from principal stakeholders. As evident from the quotations of the reference ESPP documents, the HFM R&D targets formulated for Nb₃Sn magnets stems directly from the demands of an FCC-hh [9]. In the staged approach described here, they are also compatible with the allotted development time of the integrated FCC program [55]. Indeed, the parallelism proposed has the advantage that it will provide options for an earlier decision on magnet technology towards the construction of the next hadron collider.

At the same time, while we recognize that the development of capture, cooling, acceleration and collider magnets for a muon collider [14] remains a formidable task, to be addressed by dedicated and targeted studies, an R&D on high-field Nb₃Sn and HTS magnets along the lines outlined above will be highly relevant to develop suitable design and technology solutions.

Examples that will become clearer in the following discussion are: (i) HTS conductor and coil winding technology towards the 20 T target, including partial- and no-insulation windings, whose results could be applied to the ultra-high field solenoids of the capture and cooling section, or to the high-field collider magnets; (ii) the study of stress management in Nb₃Sn magnets towards their ultimate performance, directly applicable to large aperture dipole and quadrupoles for the high-energy collider main ring and IR magnets; or (iii) considering HTS magnet operation at temperature above liquid helium, not mentioned explicitly above but relevant to understanding operating margin in the high heat load and radiation environment of the high-energy collider ring.

4. Challenges of High Field Magnets

A number of challenges will need to be mastered to progress towards the goals stated above [56]. Below we give a short description of the main ones, quantifying them by providing relevant orders of magnitude.

4.1. Superconductor

The prime rime challenge to achieve high magnetic fields of interest to HEP is to have a conductor that has, and retains, a high engineering current density J_E in operating conditions. A target of $J_E \approx 600$ A/mm² is appropriate to yield a compact and efficient coil design [57,58]. The J_E target should be reached with limited training, well retaining the training *memory*, and making use of the highest possible fraction of the current carrying capacity of the specific superconductor. Most importantly, all known high field superconductors (Nb₃Sn and HTS) are brittle and exhibit sensitivity to stress and strain in accordance with the specific material and conductor architecture. Though the failure mechanisms and levels can be very different among them, e.g. in the very brittle multi-filamentary Nb₃Sn and BSCCO vs. more robust REBCO tape, it is of paramount importance that the state of stress and strain state in the various constituents of a coil is mastered and controlled throughout all magnet fabrication and operation conditions. This is a major change of paradigm in the design and construction of high field magnets beyond Nb-Ti technology.

The above J_E target translates to specifications for the performance of LTS and HTS materials that have commonalities and differences. In the case of Nb₃Sn the target of J_E requires a minimum critical current density in the superconductor, J_C , of the order of 1500 A/mm² at the reference design conditions of the magnet (set to 16 T and 4.2 K) [59]. This target is at the upper end of the state-of-the-art Nb₃Sn, and still requires pursuing the on-going work on basic material and wire fabrication [60]. For HTS, the target J_E is actually already largely exceeded by the present production standards of REBCO and BSCCO materials [61,29]. The main challenge in this case is, instead, finding configurations and processes suitable to assemble single tapes and wires in high-current cables, and making sure that the extraordinary current density is retained in the magnet, avoiding the degradation induced by electro- or thermo-mechanical stress and strain.

Besides J_E , and in common to both LTS and HTS, other performance parameters need to be met. These requirements range from the high mechanical strength and good tolerance to stress and strain indicated earlier (see also next section), magnetization and the equivalent filament size (to limit flux jumps, persistent currents and AC losses), internal resistance (to promote current sharing and facilitate joints), including production quality (homogeneous long lengths are needed for magnet fabrication), and last but not least, cost [62].

The two tables below report the targets for Nb_3Sn and HTS wires and tapes performance as they were set a few years ago within the scope of the FCC conductor development program [60] and the EuCARD2 [61], followed by the ARIES [31] HTS development programs. The target values in the table include considerations of magnetization, strength, internal resistance and cost beyond engineering current density. These targets are in some instances

Table 1. Performance targets for Nb_3Sn conductor for large scale HEP applications, from [58].

Strand diameter	(mm)	0.5 ... 1
Non-Cu J_C (16 T, 4.2 K) ⁽¹⁾	(A/mm ²)	≥ 1500
$\mu_0\Delta M$ (1 T, 4.2 K) ⁽²⁾	(mT)	≤ 150
D_{eff} ⁽³⁾	(μm)	≤ 20
RRR ⁽⁴⁾	(-)	≥ 150
Allowable $\sigma_{transverse}$ ⁽⁵⁾	(MPa)	≥ 150
Allowable range of $\epsilon_{longitudinal}$ ⁽⁶⁾	(%)	$\geq \pm 0.3$
Unit Length	(km)	≥ 5
Cost (16 T, 4.2 K) ⁽⁷⁾	(EUR/kAm)	≤ 5

NOTES

- (1) Critical current density referred to the non-Copper cross section of the wire
- (2) Width of the persistent current magnetization loop
- (3) Effective filament diameter derived from magnetization target and assumed JC scaling matching the target
- (4) Residual Resistivity Ratio, customarily defined as the ratio of resistance at 293 K to resistance just above the superconductors transition but below 25 K
- (5) Intended as the average stress applied transversally that the wire can withstand with no degradation of current carrying capacity
- (6) Intended as the range of longitudinal strain that the wire can withstand with no degradation of current carrying capacity
- (7) Computed based on a Cu:non-Cu ratio of 1.

Table 2. Performance targets for HTS REBCO conductors for demonstration to HEP applications, modified from [30] and [31] and complemented with peeling strength and internal resistance targets.

J_E (20 T, 4.2 K) ⁽¹⁾	(A/mm ²)	≥ 1200
$\sigma(Ic)$ ⁽²⁾	(%)	≤ 10
$\mu_0\Delta M$ (1.5 T, 10 mT/s) ⁽³⁾	(mT)	≤ 300
Minimum σ_{peel} ⁽⁴⁾	(MPa)	≥ 25
Allowable $\sigma_{\text{transverse}}$ ⁽⁵⁾	(MPa)	≥ 200
Allowable range of $\epsilon_{\text{longitudinal}}$ ⁽⁶⁾	(%)	≥ ±0.3
Internal ρ_{specific} ⁽⁷⁾	(nΩ/cm ²)	≤ 10
Unit Length	(m)	≥ 100

NOTES

- (1) Engineering current density referred to the cross section of the whole tape
- (2) Spread (1-sigma) of the engineering current density over production batches
- (3) Width of the persistent current magnetization loop
- (4) Intended as peeling strength of the layers in the tape, derived from an estimate of the internal stress in a tape operated at 20 T
- (5) Intended as the average stress applied transversally on the broad face of the tape with no degradation of current carrying capacity
- (6) Intended as the range of longitudinal strain that the tape can withstand with no degradation of current carrying capacity
- (7) Intended as specific transverse resistivity among the layers of the tape, based on lowest range of measurements in industrial tapes.

challenging, but for most of them it has been shown that they can be achieved if taken one by one. The true challenge will be to reach them in combination and translate them into conductor engineered for production in large series.

4.2. Forces and stresses

Electromagnetic forces in dipoles scale with the square of the bore field [57,58,63], as shown schematically in Figure 4 where we have reported the horizontal and vertical electromagnetic force that are applied to a coil quadrant of dipole magnets built and designed in the past 30 years. Dipoles with bore field in the range of 16 to 20 T will therefore experience an electromagnetic force larger by a factor four to six with respect to the one experienced by the LHC dipoles, approaching the level of 10 MN/m per coil quadrant. The corresponding electromagnetic stress in the coil also increases with the field. While this value is in the range of 80 MPa for the HL-LHC 11...12 T Nb₃Sn

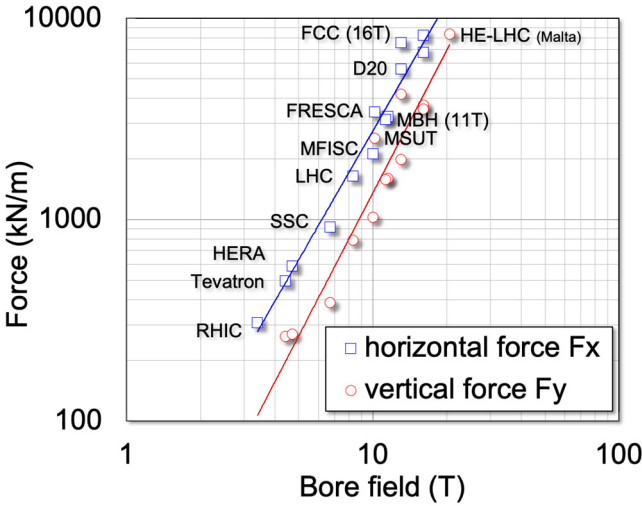


Fig. 4. Scaling of horizontal and vertical force applied on a coil quadrant of accelerator dipoles (Tevatron, HERA, RHIC, LHC, HL-LHC MBH (11T)), prototypes (SSC), models (MFISC, MFRSCa, MSUT, D20) and designs (FCC, HE-LHC). The scaling plot is an improved and augmented version of initial work reported in [57,58].

magnets, it will reach design values in the range of 150 to 200 MPa for 16 T magnet with the desired $J_E \approx 600 \text{ A/mm}^2$. This poses significant challenges in the mechanical design and the resulting stress on coil and structures, to the point that mechanics of a high-current density coil becomes the first true limiting factor to magnet performance. In fact, this is not new, being a common feature across all types of high-field magnets, solenoids [64] and fusion magnets [65].

This has driven the development of new mechanical solutions and stress management concepts for high field accelerator magnets, deviating from the cos-theta collared coils paradigm already successfully implemented in Nb-Ti accelerator magnets. Notably, recent years have witnessed a progression from collared/cos-theta coils to block- or common-coils [66,67] which mitigate the issue of azimuthal stress by moving the regions of high-stress away from the region of peak field, bladder-and-key loading [68] that avoids over-stressing the coil during assembly and pre-loading at warm, and stress-managed cos-theta [69] and canted-cos-theta [70] that provide means to avoid the accumulation of electro-magnetic stress in the coil.

The new concepts mentioned above need to integrate the demands stemming from the brittle superconducting phases discussed earlier, taking into account fracture mechanisms and material limits, the fact that the coil itself is a complex composite structure with highly non-linear properties, its interfaces, and ensuring that under no condition stress and strain exceed materials allowable limits. The difficulty is exacerbated by the fact that the coils for high field magnets, as they are presently built, are stiff and significantly less accommodating towards geometric errors, manufacturing and assembly tolerances. The new concepts will hence have to respond to the need for mechanical precision, naturally increasing as interfaces become highly stressed. Indeed, tolerances have already been reached with the HL-LHC magnets practical limits for manufacturing in large series, of the order of 20 μm .

Finally, in order to achieve the required confidence in mechanical design and construction, it is likely that new material models and corresponding constitutive equations will have to be developed. These will provide the realistic material description needed for the advanced multi-physics modeling capable to resolve the stress and strain fields with the required accuracy along the whole life span of the magnet, from manufacturing, through thermal cycles, to cyclic powering and quenches.

4.3. *Stored energy*

The energy stored in the magnetic field of a dipole also increases approximately with the square of the bore field [57,58,63], shown schematically in Figure 5. We have collected in there the values measured or computed for the same set of magnets considered for the scaling of forces. Aiming at the range of 16 to 20 T, the increase in stored energy with respect to the LHC will also be a factor of 4 to 6, ranging from 1 to 3 MJ/m per aperture. This in itself may result in severe limitations on the powering of strings, both from the point of view of their inductance (voltage required to ramp the string of dipoles), as well as magnet protection (energy density and dump time). In addition, the energy per unit volume, that drives the peak (hot-spot) temperature during a quench, also increases. The HL-LHC Nb₃Sn magnets, with a design hot-spot limited to 350 K, have values in the range of 80 to 100 MJ/m³. This value reaches 200 MJ/m³ for the most compact 16 T FCC designs. As for magnet mechanics, this is in fact the second true limitation to magnet performance.

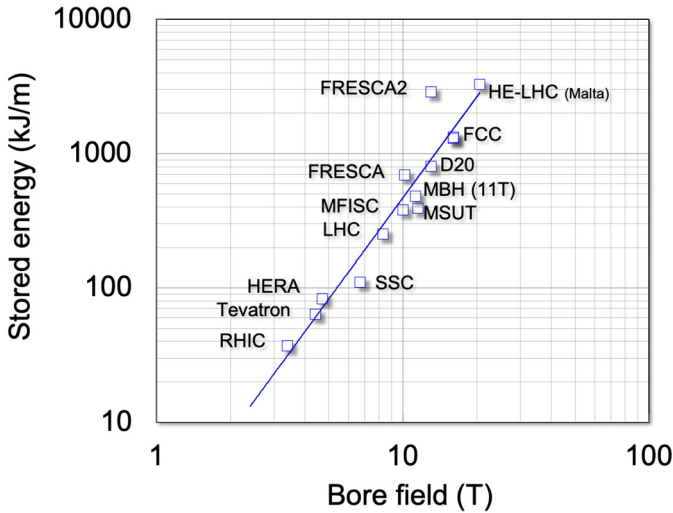


Fig. 5. Scaling of stored energy per unit length for the dipole magnets considered in Figure 4 (values refer to one aperture in case of the LHC, 11T, FCC and HE-LHC). The scaling plot is an improved and augmented version of initial work reported in [57,58].

To power magnets with larger stored energy, electrical engineering considerations would favor large voltage or current, or a combination of both. However, increasing terminal voltage significantly above the range of 1 to 2 kV or cable current significantly above the range of 10 to 20 kA is not a trivial matter, so that a future accelerator of the size of FCC may need to rely on a high level of circuit segmentation to reduce circuit inductance. This implies additional system complexity, but was successfully demonstrated and operated at the LHC. In essence, the range of magnet operating voltage and current is not expected to change significantly.

A direct consequence is that in order to keep the hot-spot temperature in the coil after a quench below reasonable values (around 300 K to 400 K, but actual damage limits are not well assessed), the quench detection and protection will need to act at least three to five times faster than in the LHC. This is already challenging for Nb_3Sn , but becomes a tantalizing task for HTS, whose quench propagation speed is one order of magnitude slower than in LTS, and quench detection based on established instrumentation would take an order of magnitude longer. Besides, quench initiation and evolution in the case of HTS is a much different process than the well characterized behavior

of LTS. In fact, though relatively unexplored, the large difference in quench initiation and propagation in HTS vs. LTS may actually be an opportunity to develop alternative schemes, e.g. profiting from early low voltage quench initiation to anticipate the evolution, or the relatively long time scales of voltage development to improve measurement sensitivity.

The challenges posed by magnet powering and protection have multiple facets, and they will need to be addressed in an integrated manner. There is a remarkable parallel between the magnet protection and magnet mechanics challenges. Firstly, detection and protection in the regime of stored energy and energy density described above will require new magnet concepts, especially for HTS (e.g. non-insulated or partially-insulated windings [71]) as well as novel detection and protection techniques (two selected examples are fiber optics for quench detection [72], and alternative active quench protection methods [73]). Secondly, measurement and characterization of the thermo-mechanical and dielectric properties and limits of coils and structures will be a mandatory step to ensure that the design are safely within allowable's. Finally, comprehensive multi-physics models with augmented accuracy will be the main tool guiding design and analysis in the extended regime of field, stored energy, temperature and voltages.

4.4. Cost

Considering the size of a new collider for the search of physics beyond the LHC, and the quantum increase in the requested magnet performance, cost is the third limit to the new technology. For this reason, it is important to include challenging and yet realistic cost targets in the study and development of new magnet concepts and materials.

An indication of a suitable cost target can be taken from the analysis of Ph. Lebrun [74] on the ratio of the cost of the technical systems to the center-of-mass beam energy, reported in Figure 6. The analysis is based on the accelerators built at CERN, excludes civil engineering, and we can roughly assume that for hadron accelerators the cost of the magnet system is half of the total accelerator cost. The result achieved with the LHC, with a specific cost of 250 kCHF/GeV, is the present benchmark, and a rather arbitrary extrapolation to the projected energy of an FCC at 100 TeV center-of-mass gives an expectation of 70...80 kCHF/GeV. At this early stage, a tentative value of

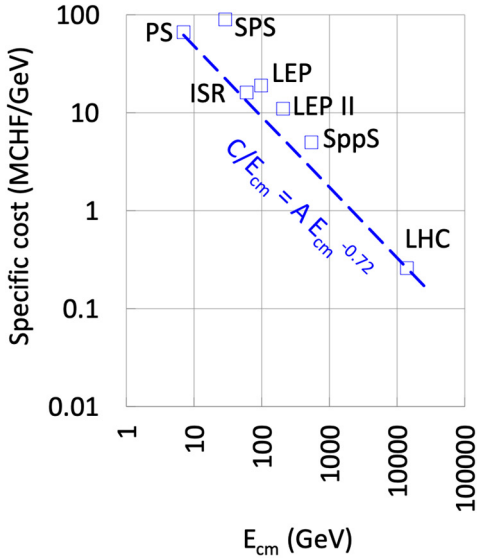


Fig. 6. Scaling of accelerator cost (excluding civil engineering) to the center-of-mass beam energy of accelerators built at CERN. Note that the data include accelerators of different magnet technology (e.g. resistive vs. superconducting) and with large disparity among the relative cost of the various accelerator systems (e.g. magnets vs. RF).

100 kCHF/GeV can be taken as a challenging but suitable benchmark. The scaling of magnet cost with beam energy may be somewhat surprising, so it is interesting to verify it by other means. The analysis in [75] provides a scaling of magnet cost purely based on the magnetic energy of the system. Projecting the cost of the LHC magnet system to an FCC, assuming a two-fold increase of the field and three-fold increase in the magnet quantity, we obtain an approximate cost of 10 BCHF, i.e. coherent with the figure of the order of 100 kCHF/GeV.

To put the cost target value in perspective, and understand the challenge, we recall that the superconductor itself is the single most expensive cost position in a high-field magnet. Normalizing to 1 AU/kg the cost of Nb-Ti, the present cost of Nb₃Sn is of about 10 AU/kg, and that of HTS is 100 AU/kg. It is clear that a substantial effort will be required to achieve feasible cost figures, starting at the level of the superconducting material.

Still, though it is clear that the construction of a large-scale machine like an FCC-hh will only be possible if targets in this range are achieved, a

successful R&D program should not be hindered by considerations of final cost. Indeed, experience has shown in many fields of science and engineering that optimal technical solutions invariably make use of the best technology available at the moment of project commitment.

5. High Field Magnets R&D Program Drivers

Driven by the challenges outlined above, we can formulate practical questions that should be addressed in priority by a High Field Magnet R&D Program. These questions are the R&D *program drivers*, and they can be broadly divided into questions of relevance for Nb₃Sn, HTS, and common to both lines of development.

For Nb₃Sn high-field accelerator magnets the following leading questions can be drawn from the earlier discussion, and will need to be addressed largely looking at the pioneering Nb₃Sn development that has led to the milestone HL-LHC magnets, the present reference technology:

- Q1: What is the practical magnetic field reach of Nb₃Sn accelerator magnets, driven by conductor performance, but bounded by mechanical and protection limits, and in particular is the target of 16 T for the ultimate performance of Nb₃Sn accelerator magnets realistic?
- Q2: Can we improve robustness of Nb₃Sn magnets, reduce training, guarantee performance retention, and prevent degradation, considering the complete life cycle of the magnet, from manufacturing to operation?
- Q3: Which mechanical design and manufacturing solutions, from basic materials, composites, structures and interfaces need to be put in place to manage forces and stresses in a high-field Nb₃Sn accelerator magnet?
- Q4: What are the design and material limits of a quenching high-field Nb₃Sn magnet, and which detection and protection methods need to be put in place to remain within these limits?
- Q5: How can we improve design and manufacturing processes of a high-field Nb₃Sn accelerator magnet to reduce risk, increase efficiency and decrease cost as required by an industrial production on large scale?

For HTS high-field accelerator magnets, the leading questions are more essential to the potential and suitability for accelerators, with the awareness that the body of work in progress is not yet at the point where a reference technology

can be defined:

- Q6: What is the potential of HTS materials to extend the magnetic field reach of high-field accelerator magnets beyond the present and projected limits of Nb₃Sn, and in particular is the target of 20 T for HTS accelerator magnets realistic?
- Q7: Besides magnetic field reach, is HTS a suitable conductor for accelerator magnets, considering all aspects from conductor to magnet and from design to operation?
- Q8: What engineering solutions, existing or to be developed and demonstrated, will be required to build and operate such magnets, also taking into account material availability and manufacturing cost?

Finally, common to Nb₃Sn and HTS:

- Q9: What is the specific diagnostics, instrumentation and infrastructure required for a successful HFM R&D, taking into account present and projected needs, and aspects ranging from applied material science to production and test of superconductors, cables, models and prototype magnets?
- Q10: What is the quantified potential of the materials and technologies that will be developed within the scope of the HFM R&D program towards other applications to science and society (medical, energy, high magnetic field science), and by which means could this potential be exploited at best?

6. Conclusions and Perspectives

The LHC is in the preparation phase before it enters another period of physics production, possibly reaching its nominal energy, and the next step magnets for accelerators, the Nb₃Sn 11T and QXF of HL-LHC, are in production and test. It is time to build on these developments to prepare for the evolution beyond these two technical milestones. The material presented and discussed in this chapter is a solid starting point and provides clear indications of the direction that a High Field Magnet R&D should take to respond to the technical challenges of the next step in accelerator magnets, along the following two principles:

- Nb₃Sn: demonstrate technology for large-scale accelerator deployment
- HTS: demonstrate suitability for accelerator magnet applications.

As discussed extensively, the goals pronounced here are also intimately bound to the demands stemming from the 2020 update of the European Strategy for Particle Physics, making direct reference to the needs deriving from the agreed accelerator strategy of the coming years.

R&D drivers have been identified, translating the general direction into practical questions that need to be explicitly addressed by *R&D Lines of Work*. As they have been formulated and discussed, it becomes natural to group the program drivers in R&D lines dedicated to: (i) conductor R&D (Nb₃Sn and HTS), (ii) magnet R&D (Nb₃Sn and HTS), and (iii) cross-cutting technology developments such as magnet protection, materials and models, instrumentation and diagnostics, and infrastructures for test and production. Finally, a dedicated line of work should be envisaged to probe and quantify the benefits of the technical development for other fields of research, industry and society.

These R&D Lines provide the framework of the upcoming HFM R&D Program which will move along the program drivers in a collaborative and global effort, strengthening the unique *ecosystem* of research centers in Europe, with strong focus on promoting the innovation required to extend the physics reach of future colliders.

References

1. R.R. Wilson, "The Tevatron", Fermilab Report TM-763, 1978.
2. R. Meinke, "Superconducting Magnet System for HERA", IEEE Trans. Mag. 27(2) (1991) p. 1728.
3. M. Anerella, et al., "The RHIC magnet system", Nucl. Inst. Meth. Phys. Res. Sect. A, 499(2-3) (2003) pp. 280-315.
4. "CERN 2004 LHC Design Report: The Main Ring Design Report", Vol 1 CERN-2004-003, L. Evans and P. Bryant Eds., 2008 LHC Machine JINST 3 S08001.
5. J.K. Hulm, R.D. Blaugher, "Superconducting Solid Solution Alloys of the Transition Elements", Phys. Rev., 123(5) (1961) 1569.
6. L. Rossi, "The Large Hadron Collider and the Role of Superconductivity in One of the Largest Scientific Enterprises," IEEE Trans. Appl. Supercond., vol. 17, no. 2, pp. 1005–1014, Jun. 2007.
7. L. Bottura, G. de Rijk, L. Rossi, E. Todesco, "Advanced Accelerator Magnets for Upgrading the LHC", IEEE Trans. Appl. Sup. 22(3), (2013) p. 4002008.

8. “The High Luminosity Large Hadron Collider”, O. Bruening and L. Rossi Eds., Advanced Series on Directions in High Energy Physics, 24, World Scientific, 2015, ISSN 1793-1339. See also: L. Rossi, C. Sutton and A. Szeberenyi, “Superconductivity leads the way to high luminosity”, CERN Courier, Jan 28, 2013; “EU supports the LHC high-luminosity study”, CERN Bulletin, Issue No. 45-46/2011; “The light at the end of the tunnel gets brighter”, CERN Bulletin, Issue No. 32-34/2014.
9. A. Abada, et al., “FCC-hh: The Hadron Collider”, *Eur. Phys. J. Spec. Top.* 228 (2019) pp. 755–1107.
10. A. Apyan, et al., “CEPC-SPPC Preliminary Conceptual Design Report”, IHEP-CEPC-DR-2015-01, IHEP-AC-2015-01, 2015.
11. P. Limon, “Design study for a staged Very Large Hadron Collider”, FERMILAB-TM-2149 (2001), <https://doi.org/10.2172/781994>.
12. Steve Geer, “Muon Colliders and Neutrino Factories”, *Annual Rev. of Nucl. Part. Sci.* 59, pp. 347–365, 2009. See also: “Muon colliders and Neutrino Factories,” W. Chou Ed., ICFA Beam Dynamics Newsletter No. 55, August 2011.
13. R. Assmann et al., “First Thoughts on a Higher-Energy LHC”, CERN-ATS-2010-177 (2010). See also: A. Abada, et al., “HE-LHC: The High-Energy Large Hadron Collider”, *Eur. Phys. J. Spec. Top.* 228, pp. 1109–1382 (2019).
14. J.P. Delahaye, et al., “Muon Colliders” (2019) arXiv:1901.06150 [physics.acc-ph].
15. B.T. Matthias, et al., Superconductivity of Nb₃Sn, *Phys. Rev.*, 95(6) (1954) p. 1435.
16. R. Scanlan, “Conductor development for high energy physics-plans and status of the US program”, *IEEE Trans. Appl. Sup.* 11(1), (2001) pp. 2150-2155.
17. R. Kephart, et al., “The U.S. LHC Accelerator Research Program: A Proposal” (2003), available at: <http://www-td.fnal.gov/LHC/USLARP.html>.
18. G. Ambrosio, et al., “Nb₃Sn High Field Magnets for the High Luminosity LHC Upgrade Project”, *IEEE Trans. Appl. Supercond.*, 25(3) (2015) p. 4002107.
19. S.A. Gourlay, S. Prestemon, A.V. Zlobin, L. Cooley, D. Larbalestier, “The U.S. Magnet Development Program Plan” (2016), available at: <https://atap.lbl.gov/wp-content/uploads/sites/22/2016/01/MagnetDevelopmentProgramPlan.pdf>.
20. R. Aleksan, “Coordinated accelerator research in Europe – Final Report” (2004), available at: <https://cordis.europa.eu/project/id/506395/reporting>.
21. A. Devred, et al., “Status of the Next European Dipole (NED) activity of the Collaborated Accelerator Research in Europe (CARE) project”, *IEEE Trans. Appl. Sup.*, 15(2), pp. 1106–1112, 2005.
22. G. de Rijk et al, “The EuCARD High Field Magnet Project”, *IEEE Trans. Appl. Sup.* 22(3), (2012) p. 4301204.
23. M. Karppinen, et al., “Design of 11 T Twin-Aperture Nb₃Sn Dipole Demonstrator Magnet for LHC Upgrades Model for LHC Upgrades”, *IEEE Trans. Appl. Sup.* 22(3), (2012) p. 4901504.
24. P. Ferracin, et al., “Magnet Design of the 150 mm Aperture Low-beta Quadrupoles for the High Luminosity LHC”, *IEEE Trans. Appl. Sup.* 24(3), (2013) 4002306.

25. M. K. Wu, et al. Superconductivity at 93-K in a new Mixed-Phase Y-Ba-Cu-O Compound System at Ambient Pressure, *Phys. Rev. Lett.*, 58(9) (1987) p. 908.
26. H. Maeda, Y. Tanaka, M. Fukutomi, and T. Asano, A New High-Tc Oxide Superconductor without a Rare Earth Element, *Jpn. J. Appl. Phys.* 27(2) (1988) L361-4.
27. “Bruker Announces World’s First 1.2 GHz High-Resolution Protein NMR Data”, Press Release available at: <https://ir.bruker.com/press-releases/press-release-details/2019/Bruker-Announces-Worlds-First-12-GHz-High-Resolution-Protein-NMR-Data/default.aspx>.
28. S. Hahn, et al., “45.5-Tesla Direct-Current Magnetic Field Generated with a High-Temperature Superconducting Magnet”, *Nature*, 570 (2019) pp. 496–499.
29. L. Rossi, C. Senatore, “HTS Accelerator Magnet and Conductor Development in Europe”, *Instruments*, 5(8) (2021), <https://doi.org/10.3390/instruments5010008>.
30. L. Rossi, et al., “The EuCARD2 Future Magnets Program for Particle Accelerator High-Field Dipoles: Review of Results and Next Steps”, *IEEE TAS*, 28(3) (2018) 4001810.
31. L. Rossi, et al., “REBCO coated conductor development in the ARIES program for HTS accelerator magnets”, Invited presentation to ASC 2018, Superconductivity News Forum, available at: https://snf.ieeeccsc.org/sites/ieeeccsc.org/files/documents/snf/abstracts/1MOr2A%E2%80%94Rossi_amended.pdf.
32. “Innovation Fostering in Accelerator Science and Technology”, H-2020 Proposal 101004730 to EU Call INFRAINNOV-04-2020. See also: “High five for CERN European Union projects”, *CERN News*, 23 November 2020, available at: <https://home.cern/news/news/cern/high-five-cern-european-union-projects>.
33. W.B. Sampson, et al., “Nb₃Sn dipole magnets”, *IEEE Trans. Magnetics* 15 (1979) pp. 117-118.
34. C. Taylor, et al., “A Nb₃Sn Dipole Magnet Reacted after Winding”, *IEEE Trans. Magnetics* 21 (1985) pp. 967-970.
35. A.D. McInturff, et al., “Test results for a high field (13 T) Nb₃Sn dipole”, PAC’97, Vancouver, May 1997, p. 3212.
36. A.F. Lietzke, et al., *IEEE Trans. Appl. Superconduct.* 14 (2004) p. 345.
37. J.C. Perez, et al., “16 T Nb₃Sn Racetrack Model Coil Test Result”, *IEEE TAS* 26(4) (2015), 4004906.
38. “A demonstrator magnet produces a record magnet field”, *CERN news release*, available at: <https://home.cern/news/news/accelerators/demonstrator-magnet-produces-record-magnet-field>.
39. D. Schoerling, A. Zlobin (eds) *Nb₃Sn Accelerator Magnets. Particle Acceleration and Detection*. Springer, Cham. https://doi.org/10.1007/978-3-030-16118-7_12.
40. T. Boutboul, L. Oberli, A. den Ouden, D. Pedrini, B. Seeber, G. Volpini, “Heat Treatment Optimization Studies on PIT Strand for the NED Project”, *IEEE Trans. Appl. Sup.* 19 (3), (2009), pp. 2564-2567.
41. E. Rochepault, P. Ferracin, CEA–CERN Block-Type Dipole Magnet for Cable Testing: FRESA2, In: Schoerling D., Zlobin A. (eds) *Nb₃Sn Accelerator Magnets. Particle*

- Acceleration and Detection. Springer, Cham. https://link.springer.com/chapter/10.1007%2F978-3-030-16118-7_12.
42. A. Zlobin, et al., “Development and First Test of the 15 T Nb₃Sn Dipole Demonstrator MDPCT1”, IEEE TAS 30(4) (2020), 4000805. See also: “Fermilab achieves 14.5-tesla field for accelerator magnet, setting new world record”, Fermilab News, available at: <https://news.fnal.gov/2020/07/fermilab-achieves-14-5-tesla-field-for-accelerator-magnet-setting-new-world-record/>.
 43. A. Devred, “Status of the 11 T dipole and CERN magnet programs beyond HiLumi”, presentation at 9th HL-LHC Collaboration Meeting, Fermilab, USA - 14-16 October 2019, available at: <https://indico.cern.ch/event/806637/contributions/3487461/>.
 44. A. Tollestrup and D. Larbalestier, Very High Field Superconducting Magnet Collaboration, Presented at Eucard2 HTS Magnet Program Meeting, CERN, 26 July 2011, available at: <https://indico.cern.ch/event/148320/contributions/1386701/>.
 45. X. Wang, et al., “Development and performance of a 2.9 Tesla dipole magnet using high-temperature superconducting CORC® wires”, Superconductor Science and Technology 34(1) (2020), 015012.
 46. T Shen, L Garcia Fajardo, “Superconducting accelerator magnets based on high-temperature superconducting Bi-2212 round wires”, Instruments 4 2) (2020), p. 17.
 47. L. Faiardo, et al., “First demonstration of high current canted-cosine-theta coils with Bi-2212 Rutherford cables”, Superconductor Science and Technology 34(2) (2021), 024001.
 48. The European Strategy Group, “Update of the European Strategy for Particle Physics”, CERN-ESU-013, June 2020.
 49. Q.J. Xu, “High Field Superconducting Magnet Program for Accelerators in China”, Proceedings of IPAC 2019, Melbourne, Australia, 4359, 2019.
 50. V. Corato, et al., “EU Progress in Superconductor Technology Development for DEMO Magnets”, Fusion Engineering and Design, 136 B, 1597-1604, 2018.
 51. Opportunities in High Magnetic Field Science, National Academies Press, 2005, ISBN: 978-0-309-09582-2.
 52. High Magnetic Field Science and Its Application in the United States, Current Status and Future Directions, National Academies Press, 2013, ISBN: 978-0-309- 38778-1.
 53. Final Report Summary - EMFL (Creation of a distributed European Magnetic Field Laboratory), EU Grant agreement ID: 262111, available at: <https://cordis.europa.eu/project/id/262111/reporting>.
 54. The European Strategy Group, “Deliberation Document on the 2020 update of the European Strategy for Particle Physics”, CERN-ESU-014, March 2020.
 55. M. Benedikt, “Future Circular Collider The Integrated Programme (FCC-int)” (2018), available at: https://fcc-cdr.web.cern.ch/reports/EPPSU18_FCCint.pdf.
 56. L. Bottura, “Taming the superconductors of tomorrow”, CERN Courier, 11 May 2020.
 57. L. Rossi and L. Bottura, “Superconducting Magnets for Particle Accelerators”, Reviews of Accelerator Science and Technology, Vol. 5 (2012) pp. 51-89.
 58. L. Bottura and L. Rossi, “Magnets for Particle Accelerators and Colliders”, in APPLIED SUPERCONDUCTIVITY – Handbook on Devices and Applications, (P. Seidel, editor)

- Wiley-VCH publisher, 2015, pp. 448-486, Print ISBN: 978-3-527-41209-9 e-pub ISBN: 978-3-527-67065-9
59. A. Ballarino, L. Bottura, "Targets for R&D on Nb₃Sn conductor for High Energy Physics", *IEEE Trans. Appl. Supercond.*, vol. 25(3) (2015), 6000906.
 60. A. Ballarino, et al., "The CERN FCC Conductor Development Program: A Worldwide Effort for the Future Generation of High-Field Magnets", *IEEE Trans. Appl. Supercond.*, vol. 25(3) (2015), 6001709.
 61. A. Badel, et al. "Advances in the Development of a 10-kA Class REBCO cable for the EuCARD2 Demonstrator Magnet", *IEEE Trans. Appl. Sup.*, 26(3), 4803908, 2016.
 62. L. Cooley, A.K. Ghosh, R.M. Scanlan, "Costs of high-field superconducting strands for particle accelerator magnets", *Sup. Sci. and Tech.*, 18(4), (2005), pp. R51- R65(15).
 63. M. Wilson, *Superconducting Magnets*, Clarendon Press, Oxford (1983).
 64. B. Montgomery, *Solenoids Magnet Design*, Interscience (Wiley) (1969).
 65. R.J. Thome and J.M. Tarrh, *MHD and Fusion Magnets, Field and Force Design Concepts*, John Wiley & Sons (1982).
 66. G. Sabbi, "The HD Block-Coil Dipole Program at LBNL", pp. 285-310, in D. Schoerling, A. Zlobin (eds) *Nb₃Sn Accelerator Magnets. Particle Acceleration and Detection*. Springer, Cham. https://doi.org/10.1007/978-3-030-16118-7_12.
 67. R. Gupta, "Common-Coil Nb₃Sn Dipole Program at BNL", pp. 371-394, in D. Schoerling, A. Zlobin (eds) *Nb₃Sn Accelerator Magnets. Particle Acceleration and Detection*. Springer, Cham. https://doi.org/10.1007/978-3-030-16118-7_12.
 68. S. Caspi, et al., "The use of pressurized bladders for stress control of superconducting magnets", *IEEE TAS* 11(1) (2001), pp. 2272–2275.
 69. I. Novitski, et al., "High-Field Nb₃Sn Cos-theta Dipole with Stress Management", *FERMILAB-CONF-17-340-TD*, 2017.
 70. D. I. Meyer and R. Flasck, "A new configuration for a dipole magnet for use in high energy physics applications", *Nucl. Instrum. Method*, 80(2) (1970), pp. 339–341. See also: S. Caspi, et al., "Design, fabrication, test of a superconducting dipole magnet based on tilted solenoids", *IEEE TAS*, 17(2) (2007), pp. 2266–2269.
 71. S. Hahn, et al., "Current Status of and Challenges for No-Insulation HTS Winding Technique", *TEION KOGAKU (J. Cryo. Super. Soc. Jpn.)*, 53(1) (2018), pp. 2-9. See also: S. Hahn, et al., "HTS Pancake Coils without Turn-to-Turn Insulation, *IEEE TAS*, 21 (2011), pp. 1592-1595.
 72. Joel H. Schultz, "Protection of superconducting magnets", *IEEE TAS*, 12(21) (2002), pp. 1390-1395.
 73. E. Ravaioli, "CLIQ A New Quench Protection Technology for Superconducting Magnets", Ph.D. Thesis, University of Twente, 2016, ISBN 978-90-365-3908-1.
 74. Ph. Lebrun, Private Communication, 2014.
 75. M.A. Green and B. Strauss, "The Cost of Superconducting Magnets as a Function of Stored Energy and Design Magnetic Induction times the Field Volume", *IEEE TAS*, 18(2) (2008), pp. 248-251.